

Characterization and Modeling of the Thermomechanical Fatigue Behavior of Brake Disks for High Speed Trains



Peter Raninger

Montanuniversität Leoben

A thesis submitted for the degree of
Doctor rerum montanarum (Dr. mont.)

Reviewer A: Univ.-Prof. Dr. Thomas Antretter,
Institute of Mechanics, Montanuniversität Leoben, Austria

Reviewer B: Univ.-Prof. Dr. Philippe Dufrénoy,
Laboratoire de Mécanique de Lille, Polytech Lille,
Université des Sciences et Technologies de Lille, France

I dedicate this thesis to my parents who gave me all the means to come so far.

Affidavit

I declare in lieu of oath, that I wrote this thesis and performed the associated research myself, using only literature cited in this volume.

Leoben, November 2014

Acknowledgements

I need to express my deepest gratitude and appreciation for my supervisors Dr. Ecker and Prof. Antretter for the multitude of technical and scientific discussions and the limitless support of my work. In phases of PhD and project related issues they have always been available with advice and guidance. Often I wonder how they make 25 days of vacation fit into 365 days of work per year — actually I'm sure they do not.

I want to thank Prof. Dufrénoy for the warm welcome at LML where I was able to spend half a year with a very likeable research group full of ideas and spirit. I am very glad for all the scientific discussions and the support of Prof Dufrénoy for my thesis.

I was lucky to have a very motivated and capable student in the project who contributed largely with his software on thermal image processing. Thank you Thomas!

The contribution of TMF data and scientific discussions with Dr. Winter and DI Strohhäussl were essential for this thesis and I send many thanks to AMB. I hope that the collaboration will continue.

I want to thank the MCL and its staff for the support and the available infrastructure, which made this thesis possible from a multitude of relevant perspectives. Special thanks to Mag. Egger for the kind discussions on the project budget, to Prof. Ebener and Dr. Marsoner for their support with the experimental program and Dr. Gänser for his help on the fracture mechanical evaluations.

I want to thank my mother for her patience every time when she asked me on the phone when I would visit her the next time and I answered: "Very soon". Monika, now you see the reason why in the end it took me a while and I hope you will forgive me.

A special person must be mentioned at this point whose patience with me was infinite over the last months, my girlfriend Petronela. She supported me on all the way even during the stage where my thoughts drifted away uncontrolled in the middle of a conversation because I was thinking of "that one special paragraph" in my thesis. Without you I would not have made it to the end.

I am very glad to share my office with Manuel and Martin and I hope the good atmosphere created by technical and private discussions will stay as it is.

Financial support by the Austrian Federal Government (in particular from Bundesministerium für Verkehr, Innovation und Technologie and Bundesministerium für Wissenschaft, Forschung und Wirtschaft) represented by Österreichische Forschungsförderungsgesellschaft mbH and the Styrian and the Tyrolean Provincial Government, represented by Steirische Wirtschaftsförderungsgesellschaft mbH and Standortagentur Tirol, within the framework of the COMET Funding Programme is gratefully acknowledged.

Abstract

The friction brake system in trains is essential in view of safety considerations. Despite the fact that in modern trains regenerative systems dissipate most parts of the kinetic energy in routine brake applications there are good reasons why a robust friction brake system is mandatory. It must be able to stop the train without further assistance in every possible in-service situation, since other systems are prone to failure. This is not only relevant for emergency braking but also for more frequent service brakings with comparable levels of dissipated energy.

The brake blending between different brake systems, such as the friction brake, the regenerative system and track brake/eddy current brake provides a wide range of design options for the brake system and the brake management. For railway applications a great number of disk geometries and materials is available, and multiple types can be used simultaneously on the same train type. Optimized brake blending between different disk sets of the friction brake system is thus required as well.

The main objective of this work is the development of a simulation tool for the design of brake disks and the brake management on high speed trains that ensures safe in-service operation and at the same time prevents oversizing. For this reason, both the characterization and the modeling of the thermomechanical fatigue behavior of railway brake disks is carried out in the scope of this work. The reference disk, that is used for component testing is a wheel mounted brake disk. This type is used for multiple unit trains, where the engines are spread over the axles of the whole train and little space is available for the usually applied axle mounted brake disks. Wheel mounted brake disks consist of two friction rings, which are mounted to the opposing sides of the wheel. The mechanical system is thus different from axle mounted brake disks, where both friction surfaces are part of one component. A major factor for the fatigue life of brake disks is the characteristics of the thermal distribution on the friction surface which is highly non-uniform. Only scarce information is available on these characteristics for wheel mounted brake disks as well as the corresponding damage mechanisms.

The investigations in this work follow a threefold strategy consisting of 1) the systematic investigation of thermal images obtained from a test rig program, 2) a profound damage analysis and 3) the thermomechanical modeling of the braking process. The thermal images provide the necessary information on the thermal evolution on the friction surface. The damage analysis reveals the governing mechanisms for crack initiation and growth. Based on the obtained information a strategy for finite element modeling is developed, which includes the braking process, the non-uniform thermal loading, the viscoplastic behavior of the disk material and the damage behavior. In a final step the simulation results are compared to the results from component testing for verification purposes.

Kurzfassung

Die Reibungsbremse ist aus Sicherheitsgründen ein wesentlicher Bestandteil jedes Zuges. Obwohl regenerative Bremssysteme in modernen Zügen den Großteil der kinetischen Energie dissipieren, ist eine robust ausgelegte Reibungsbremse verpflichtend. Sie muss den Zug in jeder möglichen Situation im Betrieb problemlos ohne das Mitwirken weiterer Bremssysteme abbremsen können, denn die anderen Systeme könnten ausfallen. Dies betrifft nicht nur Notbremsungen, sondern auch andere, häufigere Bremsungen im Betrieb mit ähnlicher Energiedissipation.

Innerhalb des Bremsmanagements (Blending) zwischen den einzelnen Systemen wie der regenerativen Bremse, der Magnetschienenbremse/ Wirbelstrombremse und der Reibungsbremse sind viele Kombinationen der einzelnen Systeme möglich. Im Eisenbahnbereich steht eine Vielzahl von Scheibengeometrien und Materialien zur Verfügung und mehrere Varianten können in ein und demselben Zug verwendet werden. Ein optimiertes Bremsmanagement zwischen den einzelnen Scheibensätzen der Reibungsbremse ist daher ebenfalls notwendig. Das Hauptziel dieser Arbeit ist die Erarbeitung einer Simulationsmethodik, die sowohl die Entwicklung neuer Bremsscheiben-Designs, als auch die Planung des Bremsmanagements effizienter macht. Die entwickelten Bremssysteme müssen sicher sein, aber eine Überdimensionierung soll vermieden werden. Aus diesem Grund werden sowohl eine umfassende Charakterisierung, als auch die Modellierung des thermomechanischen Ermüdungsverhaltens im Rahmen dieser Arbeit behandelt. Der Bremsscheibentyp, der als Referenz für Komponententests verwendet wird, ist eine Radbremsscheibe. Dieser ist typisch für Triebzüge, bei denen der Antrieb auf die Achsen des Zuges verteilt ist und nicht ausreichend Platz für die normalerweise eingesetzten Wellenbremsscheiben bleibt. Radbremsscheiben bestehen jeweils aus zwei Reibringen, die an den gegenüberliegenden Seiten des Rades befestigt werden. Das mechanische System unterscheidet sich daher von demjenigen der Wellenbremsscheiben, bei denen beide Reibflächen Teil einer Komponente sind. Die Lebensdauer von Bremsscheiben wird wesentlich durch die Charakteristik der Temperaturverteilung auf der Reibfläche beeinflusst. Diese ist für Radbremsscheiben aktuell nicht genau bekannt, Ähnliches gilt für die zugehörigen Schädigungsmechanismen.

Diese Arbeit verfolgt drei Zugänge zu diesem Problem: 1) Die systematische Untersuchung der Thermokameradaten von Komponententests, 2) eine umfassende Charakterisierung der auftretenden Schädigung und 3) das thermomechanische Modellieren des Bremsprozesses. Die Thermokameradaten liefern die notwendigen Informationen über die Temperaturentwicklung auf der Reibfläche. Die Schadensanalyse identifiziert die relevanten Mechanismen für das Initiieren und Wachstum von Rissen. Diese Informationen bilden die Basis für die Modellierung mit der Finite-Elemente-Methode, die den Bremsprozess, das viskoplastische Materialverhalten des Bremsscheibenmaterials und das Schädigungsverhalten umfasst. Am Ende der Arbeit werden die Simulationsergebnisse mit den Komponententests verglichen und verifiziert.

Contents

| | |
|--|--------------|
| Contents | xi |
| List of Figures | xv |
| List of Tables | xxvii |
| 1 Introduction | 1 |
| 1.1 Brake systems used in trains | 1 |
| 1.2 Typical problems with brake disks | 5 |
| 1.3 Some general remarks on thermal and thermomechanical fatigue | 6 |
| 1.3.1 TMF testing | 8 |
| 1.3.2 Typical TF/TMF damage | 9 |
| 1.4 Motivation and summary of the present work: TMF life assessment | 13 |
| 1.5 The tribological systems in focus | 15 |
| 1.5.1 Disks | 15 |
| 1.5.2 Pads | 16 |
| 1.6 Test rig program | 18 |
| 2 Theoretical background | 23 |
| 2.1 Material physical processes in fatigue | 23 |
| 2.1.1 Dislocation movement and plasticity | 23 |
| 2.1.2 Crack initiation | 26 |
| 2.1.3 Small crack growth | 28 |
| 2.1.4 Long crack growth | 30 |
| 2.1.5 Final fracture | 35 |
| 2.2 Material physical processes in creep | 36 |
| 2.2.1 The stages of creep — Overview | 36 |
| 2.2.2 Creep mechanisms | 37 |
| 2.3 Material physical processes in viscoplasticity and creep fatigue interaction | 44 |
| 2.4 Tensor basics | 48 |
| 2.5 Overview of material models | 51 |
| 2.5.1 Plasticity models | 53 |
| 2.5.1.1 Yield criterion | 57 |

CONTENTS

| | | |
|----------|--|------------|
| 2.5.1.2 | Hardening rule | 60 |
| 2.5.1.3 | Flow rule | 65 |
| 2.5.1.4 | Consistency condition | 67 |
| 2.5.2 | Creep models | 70 |
| 2.5.2.1 | Constant amplitude creep | 71 |
| 2.5.2.2 | Variable amplitude creep | 73 |
| 2.5.2.3 | Continuum mechanical framework | 78 |
| 2.5.2.4 | Integration of creep laws in the continuum mechanical framework | 81 |
| 2.5.3 | Viscoplastic models | 84 |
| 2.6 | General service life assessment concepts | 87 |
| 2.6.1 | Empirical life prediction models | 89 |
| 2.6.2 | Isothermal application of damage parameters | 91 |
| 2.6.3 | Cycle counting | 96 |
| 2.6.4 | Concepts for service life assessment at high and varying temperatures | 97 |
| 2.6.4.1 | Miner rule and Robinson rule | 98 |
| 2.6.4.2 | Strain Range Partitioning method | 101 |
| 2.6.4.3 | Method of Neu-Sehitoglu | 102 |
| 2.6.4.4 | Non-isothermal application of damage parameters | 103 |
| 2.7 | Infrared thermography | 105 |
| 3 | Characterization of loading conditions | 111 |
| 3.1 | Introduction | 111 |
| 3.2 | Camera system | 113 |
| 3.3 | Data processing | 113 |
| 3.4 | Results | 125 |
| 3.4.1 | Development of the thermal distribution during individual brake cycles | 126 |
| 3.4.2 | Development of the thermal distribution over several brake cycles | 130 |
| 3.4.3 | Reproducibility of thermal patterns | 134 |
| 3.4.4 | Impact of pad replacement | 138 |
| 3.4.5 | Thermal distribution in tests carried out on scaled test rig | 142 |
| 3.4.6 | Discussion of the thermal gradients in view of TMF | 148 |
| 4 | Characterization of damage | 153 |
| 4.1 | Introduction | 153 |
| 4.2 | Investigations and methods | 153 |
| 4.2.1 | Global disk deformation | 154 |
| 4.2.1.1 | Coordinate measurement machine | 155 |
| 4.2.1.2 | Harmonic analysis | 155 |
| 4.2.2 | Residual stresses | 156 |
| 4.2.2.1 | Measurement technique | 157 |
| 4.2.2.2 | Investigation methodology | 158 |
| 4.2.3 | Microstructure | 159 |

| | | |
|----------|---|------------|
| 4.2.3.1 | Background information on the characterization of metallurgical transformations | 160 |
| 4.2.3.2 | Investigation methodology | 162 |
| 4.3 | Results | 162 |
| 4.3.1 | Preliminary studies | 163 |
| 4.3.2 | Evolution of the global disk deformation | 165 |
| 4.3.3 | Distribution and evolution of the residual stresses on and under the friction surface | 170 |
| 4.3.4 | Distribution and evolution of the microstructure on and under the friction surface | 177 |
| 4.3.5 | Damage in brake disks tested on the scaled test rig | 187 |
| 4.3.6 | Discussion of residual stress formation in view of TMF | 189 |
| 5 | Modeling of the TMF behavior of brake disks | 191 |
| 5.1 | General considerations and motivation | 191 |
| 5.2 | Modeling strategies | 193 |
| 5.2.1 | Geometry | 194 |
| 5.2.1.1 | Selection of a representative geometrical model | 194 |
| 5.2.1.2 | Choice of element type | 195 |
| 5.2.2 | Thermophysical properties | 197 |
| 5.2.3 | Thermal boundary conditions | 199 |
| 5.2.4 | Thermal loading | 200 |
| 5.2.4.1 | Uniform loading | 200 |
| 5.2.4.2 | Non-uniform loading | 202 |
| 5.2.5 | Material law | 203 |
| 5.2.5.1 | Modeling of cyclic plasticity | 203 |
| 5.2.5.2 | Experiments for the characterization of the mechanical material behavior | 207 |
| 5.2.5.3 | Sampling and sample manufacturing | 209 |
| 5.2.5.4 | Parameter identification | 210 |
| 5.2.6 | Mechanical boundary conditions | 210 |
| 5.2.7 | Life time estimation models | 212 |
| 5.2.7.1 | Modeling of service life until crack initiation | 213 |
| 5.2.7.2 | Modeling of the fracture mechanical service life | 226 |
| 6 | Simulation results | 233 |
| 6.1 | Results for material A — Uniform loading | 233 |
| 6.1.1 | Temperature evolution | 233 |
| 6.1.2 | Disk coning and waviness | 235 |
| 6.1.3 | Damage mechanical evaluation of service life | 237 |
| 6.1.4 | Influence of disk wear | 242 |
| 6.1.5 | Fracture mechanical evaluation of service life | 244 |
| 6.2 | Results for material A — Non-uniform thermal loading | 250 |
| 6.2.1 | Temperature evolution | 251 |
| 6.2.2 | Disk coning and waviness | 254 |

CONTENTS

| | | |
|----------|---|------------|
| 6.2.3 | Damage mechanical evaluation of service life | 255 |
| 6.2.4 | Fracture mechanical evaluation of service life | 258 |
| 6.3 | Comparison of the simulations to the results from the test rig program. | 261 |
| 6.4 | Material comparison | 264 |
| 6.4.1 | Impact of thermophysical properties | 264 |
| 6.4.2 | Application maps for material selection | 266 |
| 6.4.3 | Alternative assessment for online health monitoring | 268 |
| 7 | Conclusion | 273 |
| A | Supplementary background information | 277 |
| A.1 | Dislocation structures | 277 |
| A.2 | Determination of fracture mechanical quantities | 278 |
| A.3 | Tensor notation | 289 |
| A.4 | Thermodynamic potential | 290 |
| A.5 | Dissipation potential | 290 |
| A.6 | Tertiary creep | 292 |
| B | Source codes | 295 |
| C | Sample geometries and sampling positions | 301 |
| C.1 | LCF | 302 |
| C.2 | TMF | 303 |
| C.3 | Fracture toughness | 304 |
| C.4 | Crack propagation | 305 |
| C.5 | Thermal diffusivity | 306 |
| C.6 | Heat capacity | 307 |
| C.7 | Thermal expansion | 308 |
| C.8 | Positions for residual stress measurements and metallographic specimens | 309 |
| D | General data and standards | 313 |
| D.1 | Extract from DIN 27205-5:2005-10: Zustand der Eisenbahnfahrzeuge - Bremsen - Teil 5: Radbremsscheiben | 313 |
| D.2 | Analytical solution for semi-elliptical cracks under tensile and bend loading according to FKM guideline | 314 |
| D.3 | Data sheet for thermal imaging system | 315 |
| | References | 317 |

List of Figures

| | | |
|------|---|----|
| 1.1 | Brake systems used in trains based on [1]. | 2 |
| 1.2 | Wheel mounted brake disk [2]. | 5 |
| 1.3 | Thermal surface gradients according to [3]: 1) local contact asperities, 2) gradients on hot bands, 3) hot bands (fire rings), 4) macroscopic hot spots, 5) ideal case: almost uniform contact pressure. | 6 |
| 1.4 | Stresses caused by a thermal gradient: a) thermal fatigue (TF), b) TF with additional mechanical loading (TMF), e.g. due to external constraint. | 7 |
| 1.5 | a) In phase (IP) TMF and out of phase (OP) TMF b) Clockwise and counterclockwise diamond TMF. | 9 |
| 1.6 | a) Cracks at the friction surface: A) network of small cracks, B) radial crack, C) tangential crack and b) Hot spot pattern after braking [4]. | 10 |
| 1.7 | Schematic deformation-mechanism diagram based on [5]. | 11 |
| 1.8 | Approach to service life prediction of a brake disk exposed to TF/TMF. | 16 |
| 1.9 | Wheel disk assembly without caliper and pads. | 17 |
| 1.10 | Mounting of the disk to the wheel. | 17 |
| 1.11 | Pad types used in the test rig program. | 18 |
| 1.12 | Flexible pad type in assembled condition. | 18 |
| 1.13 | Overview of the test rig program. | 20 |
| 1.14 | a) Schematic of the evolution of energy input over time b) Test bench used for component tests. | 21 |
| 2.1 | Overview of fatigue mechanisms (based on [6; 7]). | 24 |
| 2.2 | Dislocation structures in fcc single crystals. | 25 |
| 2.3 | Kitagawa-Takahashi diagram and evolution of crack propagation threshold, both based on [8; 9; 10]. | 28 |
| 2.4 | Regimes of fracture mechanics [11; 12]. | 30 |
| 2.5 | a) Meaning of the stress intensity factor K for the case of an ideal brittle material, b) idealized stress field due to ideal-plastic deformation in monotonic plastic zone , c) idealized stress field solely due to load after load reversal illustrating the formation of a cyclic plastic zone, d) approximation of the real stress field after load reversal as superposition of stress fields b) and c) [13]. | 32 |
| 2.6 | Characterisation of long crack propagation behavior. | 33 |

LIST OF FIGURES

2.7 Comparison of testing procedures applied in the project. 34

2.8 Correlation between S-N curve, crack propagation curve and Kitagawa-Takahashi plot. 35

2.9 Overview of creep mechanisms (based on [14]). 36

2.10 Deformation maps for a material a) without b) with phase transformation [15]. 39

2.11 Deformation map for pure iron [15] with a schematic $\sigma - T$ path for TF loading. 45

2.12 Illustration of an isothermal mechanical hysteresis loop and the corresponding mechanical quantities (based on [8; 16]). 53

2.13 Rheological models for plasticity: a) elastic-ideal plastic (Saint-Venant model), b) linear kinematic hardening (Prager model), c) elastic-piecewise linear plastic (generalized Saint-Venant model), d) $\sigma - \epsilon$ response for a)-c) and Ramberg-Osgood. 54

2.14 a) non-linear isotropic hardening, b) linear kinematic hardening [17]. 55

2.15 Evolution of the yield stress for a) isotropic and b) kinematic hardening (both non-linear in this case) based on [18]. 56

2.16 Illustration of the von Mises yield surface with isotropic and kinematic hardening. 57

2.17 Overview of hardening behavior: a) ideal plastic, b) hardening. 60

2.18 Material exhibiting cyclic softening in a strain controlled LCF test a) with $R_\epsilon = 0$ b) with $R_\epsilon < 0$ 61

2.19 Overview of common strategies for the modeling of kinematic hardening: a) linear (bilinear) hardening, b) piecewise linear (multilinear) hardening, c) non-linear hardening. 62

2.20 Illustration of a) linear and b) non-linear kinematic hardening. 64

2.21 Illustration of important principles for the definition of the flow rule. 66

2.22 Creep simulation - Comparison between time and strain hardening: a) $m=-0.5$ b) $m=0.0 \rightarrow$ Norton's law for secondary creep. 75

2.23 a) Explanation of the difference between time and strain hardening law b) General comparison of hyperbolic sine function to power law and exponential law. 76

2.24 Stress relaxation - Comparison between time and strain hardening. 76

2.25 a) Illustration of *strain hardening double* creep law for the description of primary and secondary creep b) general comparison of hyperbolic sine function to power law and exponential law. 77

2.26 Effect of plastic pre-deformation on primary creep response [5]. 81

2.27 Explicit and implicit creep formulation with a fine incrementation. The corresponding computation times are indicated in the legend. 82

2.28 Explicit and implicit creep formulation with a coarse incrementation. The corresponding computation times are indicated in the legend. 83

2.29 Illustration of automatic incrementation. The corresponding computation times are indicated in the legend. 83

2.30 Monotonic stress strain curve: a) von Mises yield surface with isotropic hardening and viscous overstress, b) corresponding $\sigma - \epsilon$ curve (based on [19]). 84

2.31 Figurative illustration of a viscoplastic potential as a set of equipotential surfaces [20]. 86

2.32 Overview of principal methods used in fatigue design (based on [6; 21]). 88

2.33 Illustration of the procedure for the test of damage parameters. 90

| | | |
|------|---|-----|
| 2.34 | Procedure for the estimation of maximum stress and strain at a notch due to a static load according to Neuber (based on [21]). a) static σ - ϵ curve, b) nominal strain compared to two possible strain distributions around a notch, c) nominal stress compared to two possible stress distributions around a notch, d) application of Neuber's rule for the determination of σ and ϵ at a notch for the elastic and the plastic case. | 92 |
| 2.35 | a) Illustration of the cyclic σ - ϵ curve, b) illustration of the construction of a stress strain hysteresis from CSSC assuming Masing behavior. | 94 |
| 2.36 | a) Schematic CSS curves obtained from incremental step test and LCF tests b) stabilized hystereses from incremental step test (shifted to common minimum position) c) stabilized hystereses from LCF tests (shifted to common minimum position) [22]. | 95 |
| 2.37 | Illustration of the interplay of CSSC, Neuber rule, Masing behavior and memory effect for the construction of hysteresis loops (based on [16; 23]). | 96 |
| 2.38 | a) Japanese Pagoda [24] b) Load spectrum, c) Rainflow Counting (based on [25]), d) Assembled hystereses. | 97 |
| 2.39 | Illustration of general TMF life prediction based on constitutive models according to Chaboche et al. | 104 |
| 2.40 | Spectrum of IR radiation. | 105 |
| 2.41 | Distribution of the specific spectral radiance for various surfaces. | 106 |
| 2.42 | Classification of IR detectors [26]. | 107 |
| 2.43 | Specific detected power for various camera systems in comparison to the full spectrum. | 109 |
| 3.1 | Position of thermal imaging system: a) position in casing, b) position in test rig (camera position is indicated). | 113 |
| 3.2 | Illustration of strategy for data processing of thermal images. | 114 |
| 3.3 | Structure of thermal image data. | 115 |
| 3.4 | Illustration of the goal of the processing technique: a) initial state, b) processed state. | 116 |
| 3.5 | Detection of disk center: a) contours within normalized image data, b) approximation of disk center, c) data from image b) on original image. | 117 |
| 3.6 | Detection of disk contour: a) normalized gradient image, b) detection of outer and inner contour. | 118 |
| 3.7 | Angular displacement between two subsequent frames. | 118 |
| 3.8 | Detection of mounting positions: a) detection of areas with minimal temperatures, b) iterative contour definition and hole detection, c) final contours indicating the mounting positions. | 119 |
| 3.9 | Detection of characteristic thermal patterns: a) global thermal pattern, b) local pattern around a mounting point. | 120 |
| 3.10 | Alternative method for the detection of relative angular displacement: temperature moment for two subsequent frames a) and b). | 121 |
| 3.11 | a) Data from cross correlation of two subsequent frames, b) deviations from the expected angular position due to missing frames. | 121 |
| 3.12 | Rotation of data frame (a) to specific angular position (b) by multiplication with rotation matrix and (c) bilinear interpolation (based on [27]). | 122 |

LIST OF FIGURES

| | |
|---|-----|
| 3.13 Average temperature as a function of the angle for the detection of pad and sensor position, a) initial data for detection of the pad, b) updated data for detection of the sensor. | 123 |
| 3.14 a) Detected positions of pad and sensor, b) Final result for the displayed frame: rotated data frame with substituted pad and sensor areas. | 124 |
| 3.15 Correlation of digital values and temperatures. | 124 |
| 3.16 Overview of tests runs and the corresponding disk sets. The numbers in brackets refer to the bake cycles where thermal image data are available. | 125 |
| 3.17 Thermal distribution for pad type 1 during cycle 10 of test run 3. The temperature field shortly after braking has started, a) and b), is focused on two circles corresponding to the mean and the outer radius. Alternating regions with higher and lower temperature levels are visible, indicating hot spots on hot bands. A distinct circle between the mean and the outer radius stays clearly cooler than the adjacent areas. In the course of the braking the hot spots increase in size and spread over the friction surface and a link to hot bands is not visible anymore. The cool ring on the outer half disappears but a higher level of thermal loading on the inner half of the disk is obvious from d) on. | 128 |
| 3.18 Thermal distribution for pad type 2 during cycle 9 of test run 7. The thermal distribution at the beginning suggests increased contact pressure along the inner and the outer circumference. Large areas with increased temperature levels build up along the inner and the outer circumference exhibiting a systematic pattern. | 129 |
| 3.19 Cumulative patterns describing the occurring temperature levels during a) Set 3, stop 10 and b) Set 7, stop 9. | 130 |
| 3.20 Thermal distribution for pad type 1 over 10 consecutive brake cycles. Reference time: 50% of brake time. On a global scale the thermal distribution from b) to j) are similar with increased thermal loading on the inner disk half. During the first emergency stop, however, the thermal input is clearly more intense on the inside. | 132 |
| 3.21 Thermal distribution for pad type 2 over 10 consecutive brake cycles. Reference time: 50% of brake time (this value differs for braking 10 due to abortion of the test). The series of thermal images reveals significant changes in the thermal distribution, which do not stabilize within 10 brake applications. Images a) and b) form a couple of inversed thermal images. After several mixed states in c) to g) the periodic inversion reappears in modified form, h)-j). The designation in brackets refers to the type of thermal configuration. | 133 |
| 3.22 Comparison of thermal patterns of the first braking of test runs 6 and 8 (pad type 2). | 135 |
| 3.23 Comparison of thermal patterns of brakings 9 and 10 of test runs 3 and 4 (pad type 1). | 136 |
| 3.24 Comparison of thermal patterns of brakings 9 and 10 of test runs 7 and 8 (pad type 2). | 137 |
| 3.25 Evolution of total brake time for a) pad type 1 and b) pad type 2. | 138 |
| 3.26 Comparison of thermal images and sum diagrams for the brake applications before and after pad replacement. | 140 |
| 3.27 Comparison of thermal patterns of brakings 44 to 50 of test run 8. The designation in brackets refers to the type of thermal configuration. | 141 |
| 3.28 Scaled test rig. | 142 |

| | |
|--|-----|
| 3.29 Evolution of the thermal distribution on scaled test rig over 201 double stops for material A. The images of the series correspond to the thermal distribution at 20% of the total brake time for each double stop. The series shows the formation of 9 hot spots situated along the disk circumference. At the beginning of the test sequence (3.29a) the formation of an inhomogeneous thermal distribution is indicated but the hot spot formation is clearly pronounced beginning with 3.29e. The maximal thermal concentration at the hot spots is reached during the final 100 double stops 3.29i-3.29j. | 145 |
| 3.30 Evolution of thermal distribution on the scaled test rig over 201 double stops for material A. The images of the series correspond to the thermal distribution at 80% of the total brake time for each double stop. The series shows the formation of 9 hot spots situated along the disk circumference. At the beginning of the test sequence (3.30a) no severe thermal surface gradients can be seen apart from an usual elevated temperature level along the disk center. Beginning with the third double stop 3.29b the formation is clearly visible. The thermal concentration at the hot spots increases over the test sequence and reaches a clear maximum state at the end 4.38a. | 146 |
| 3.31 Evolution of thermal distribution on the scaled test rig over 200 double stops for material B. The images of the series correspond to the thermal distribution at 80% of the total brake time for each double stop. In the case of material B which was exposed to less severe loading conditions no thermal surface gradient are visible apart from the usual elevated temperature levels at the disk center. | 147 |
| 3.32 Qualitative illustration of temperature-stress paths at selected positions: a) Ashby map for pure iron (based on [15]), b) thermal image and reference position for pad type 1, c) thermal image and reference position for pad type 2. | 150 |
| 4.1 a) Overview of configuration for coordinate measurements, b) close up of sensor. | 154 |
| 4.2 Illustration of the measurement positions at the inner and the outer perimeter. | 155 |
| 4.3 a) Illustration of strain and stress measurements by X-ray diffraction [28], b) illustration of the $\sin^2\Psi$ -method. | 157 |
| 4.4 a) Example for selected positions for residual stress measurement, b) Configuration for residual stress measurement. | 159 |
| 4.5 Iron carbon phase diagram [29]. | 159 |
| 4.6 Continuous TTA diagrams for two hypoeutectoid low alloyed steels with a) a ferritic-perlitic base microstructure and b) a hardened and tempered base microstructure. | 160 |
| 4.7 Characterization of phase transformations upon cooling: CCT diagram for material A (A courtesy of Schmiedag GmbH). | 161 |
| 4.8 Characterization of phase transformations upon cooling: Individual transformation temperatures for material A (A courtesy of Schmiedag GmbH). | 162 |
| 4.9 Illustration of a sample extracted for metallographic investigations, a) sample positions on disk segment, b) embedded sample with the expected regions of interest. | 163 |
| 4.10 a) Correlation of microstructure and residual stress level, b) Partially transformed region in zone 2. | 163 |
| 4.11 Correlation of a) microstructure and b) hardness. | 164 |

LIST OF FIGURES

| | |
|---|-----|
| 4.12 Measured waviness after test run 8 (friction ring 15; 100 emergency stops), a) 3D representation of measurement results b) Waviness along the inner and the outer circumference with local and global maxima. | 165 |
| 4.13 Harmonic analysis of a) friction ring 7 (200 ES) and b) 15 (100 ES). | 166 |
| 4.14 Evolution of amplitudes with increasing number of brake applications (R=335 mm). The state after bedding-in without emergency stops is indicated by the value 0.1. | 168 |
| 4.15 Evolution of the amplitudes of the orders 2, 4 and 8 as functions of the radial position. | 169 |
| 4.16 Computed disk coning from CMM measurements. | 170 |
| 4.17 Standard positions for residual stress measurements for all friction rings. | 170 |
| 4.18 Comparison of residual stresses at the positions P1, P2 and P3 for all friction rings. | 171 |
| 4.19 Residual stress measurements situated at positions with low thermal loading and less profound phase transformations. | 172 |
| 4.20 Positions for residual stress measurements on a) friction ring 5 and b) friction ring 11. | 174 |
| 4.21 Overview of residual stress measurements carried out for pad type 1. | 175 |
| 4.22 Overview of residual stress measurements carried out for pad type 2. | 176 |
| 4.23 Positions for residual stress measurements on friction ring 13 (10 ES). Two hot patches that have occurred during the last of 10 ES are indicated. | 176 |
| 4.24 a) Positions for residual stress measurements on friction ring 13 (pad type 2, 10 ES), b) thermal pattern during brake application 89. | 177 |
| 4.25 Overview of sample positions in a brake disk tested with pad type 1 (friction ring 5, 10 ES). Additionally, the figure shows the thermal loading and the microstructure in the section A-A. | 178 |
| 4.26 Overview of sample positions in a brake disk tested with pad type 2 (friction ring 13, 10 ES). Additionally, the figure shows the thermal loading and the microstructure. The yellow lines connect corresponding positions on the disk surface, the thermal image and the micrographs. | 178 |
| 4.27 Sample positions selected for the base characterization of the microstructure. | 179 |
| 4.28 Representative metallographic samples taken from brake disks, which were tested with a) pad type 1 and b) pad type 2. The transformed regions in the upper part of each micrograph is clearly visible. | 179 |
| 4.29 CCT for material A with cooling rates occurring during manufacturing and after emergency braking. | 180 |
| 4.30 Relevant portion of continuous TTA diagram for 42CrMo4. The region of typical heating rates during emergency braking is indicated as well as the corresponding transformation temperatures. | 181 |
| 4.31 a-c) Zone 3: The base microstructure consists of bainite/tempered martensite, d-f) Zone 2: Quenched microstructure after austenitization in the two phase region, g-i) Zone 1: Quenched microstructure after full austenitization. | 182 |
| 4.32 Depth of the transformed zones at characteristic positions (see Fig. 4.28) for a) pad type 1 and b) pad type 2. The average penetration depths of zone 1 and zone 2 are indicated by horizontal lines. | 183 |
| 4.33 Comparison of thermal image, microstructure and residual stresses at position 1 after 10 ES with pad type 2 | 183 |

| | |
|--|-----|
| 4.34 Comparison of thermal image, microstructure and residual stresses at position 2 after 10 ES with pad type 2 | 184 |
| 4.35 Comparison of thermal image, microstructure and residual stresses at position 3 after 10 ES with pad type 2 | 185 |
| 4.36 Comparison of thermal image, microstructure and residual stresses after 10 ES with pad type 1 | 185 |
| 4.37 Characteristic crack arrays found in disks exposed to 200/100 ES with pad type 1 and pad type 2, respectively. | 186 |
| 4.38 a) Thermal loading during test run on scaled test rig (material A) , b) overview of sample positions in the scaled brake disk. | 187 |
| 4.39 a) Microstructure around stationary hot spot in scaled brake disk made of material A, b) residual stresses. | 187 |
| 4.40 a) Thermal loading during test run on scaled test rig, b) overview of sample positions in the scaled brake disk made of material B. | 188 |
| 4.41 a) Microstructure around stationary hot spot in scaled brake disk made of material B. The ferritic-pearlitic base microstructure of the ductile cast iron is visible but no metallurgical transformations from braking, b) residual stresses. | 188 |
| 4.42 Schematic σ - T paths during TF/TMF loading at a hot spot and between hot spots. | 189 |
| 5.1 Modeling strategy for the service life prediction of a brake disk exposed to TF/TMF | 194 |
| 5.2 a) Overview wheel-disk, b) FE-geometry top view, c) FE-geometry bottom view, d) FE-mesh top view, e) FE-mesh front view | 195 |
| 5.3 a) Evolution of disk coning and b) estimated crack initiation life. | 196 |
| 5.4 Thermophysical data for material A | 198 |
| 5.5 a)-d) Boundary conditions for convection: Film coefficient for four different zones, b) boundary condition for radiation. | 199 |
| 5.6 a) Evolution of velocity during the reference emergency braking and b) the corresponding total heat flux Q into the disk | 200 |
| 5.7 a) Derivation of the loading conditions from the evolution of the velocity in Fig. 5.6a and the total energy input. The colors refer to the four terms in Eq. (5.5). b) heat flux per unit area applied by DFLUX | 202 |
| 5.8 Illustration of thermal image mapping for one brake cycle. | 203 |
| 5.9 Material exhibiting cyclic softening in a strain controlled LCF test with $R_\epsilon = 0$ and the hysteresis loop at $N=1$ and $N=\frac{N_f}{2}$ | 205 |
| 5.10 a) Tensile tests from 20°C to 800°C, b) investigation of strain rate dependence at 600°C. | 208 |
| 5.11 a) Examples for LCF hystereses at $\frac{N_f}{2}$, b) investigation of mean stress relaxation. | 208 |
| 5.12 a) Investigation of strain rate dependence, b) investigation of stress relaxation at 700°C. | 209 |
| 5.13 Exemplary sample orientation in a brake disk | 209 |

LIST OF FIGURES

| | | |
|------|---|-----|
| 5.14 | The process of parameter identification for the unified viscoplasticity model. The procedure begins with a first approximation of the parameters for the backstresses X_{1-3} and the viscoplastic potential (1). Next, the parameters for the static recovery terms R_{1-3} are approximated in four steps (2-5). Finally, the parameters for the backstresses X_{1-3} are determined again (6). In each step the weighing of the individual experiments can be chosen accordingly. If necessary the whole optimization loop can be carried out several times. . . . | 210 |
| 5.15 | a) Exemplary illustration of experimental and simulated mechanical hysteresis for $\Delta\epsilon = 0.4\%$, b) results for block tests. See Section 5.2.5.2 for more information on the tests. . . . | 211 |
| 5.16 | a) Detailed view on the fastening, b) illustration of the antisymmetric arrangement of subsequent mounting points. | 211 |
| 5.17 | Modeling of the bolts. | 212 |
| 5.18 | Mechanical boundary conditions. | 212 |
| 5.19 | a) Comparison of isothermal testing, in-phase and out-of-phase TMF testing. Mechanical hystereses for b) in-phase and c) out-of-phase TMF testing [30]. | 214 |
| 5.20 | Exemplary illustration of TMF tests carried out in the experimental program and comparison to LCF tests at T_{min} and T_{max} | 216 |
| 5.21 | a) Determination of parameter set for Manson-Coffin and b) the corresponding scatter band. $T_{90\%}$ corresponds to the scatter band enclosing 90% of the results. D_{av} refers to the average deviation and \bar{D}_{av} to the average of the absolute deviation values. | 217 |
| 5.22 | a) Determination of parameter set for Ostergren and b) the corresponding scatter band. . . | 219 |
| 5.23 | a) Determination of the parameters for the Winter model and b) the corresponding scatter band. | 219 |
| 5.24 | a) Single element for simulations at sample level, b) evolution of the element temperature. . | 220 |
| 5.25 | illustration of the simulation of a TMF test. The bars represent the length of the specimen at different stages of the test. | 221 |
| 5.26 | Comparison of the results data from a) the unified viscoplasticity model (evp) and b) the non-unified model (epc). | 222 |
| 5.27 | Experimental and simulated scatter bands for material B a) Manson-Coffin and b) Ostergren. | 223 |
| 5.28 | Experimental and simulated scatter bands for material B a) Manson-Coffin and b) Ostergren. | 223 |
| 5.29 | Experimental and simulated scatter bands for material C a) Manson-Coffin and b) Ostergren. | 224 |
| 5.30 | Experimental and simulated scatter bands for material D a) Manson-Coffin and b) Ostergren. | 224 |
| 5.31 | a) Experimental and simulated scatter bands for material E for the damage model according to Winter, b) Experimental basis for TMF tests. The boxes indicate the tested parameters and thus the area of validity for the Winter model. | 225 |
| 5.32 | a) Range of validity for material models based on LCF tests, b) Range of validity for the Manson-Coffin model and the Ostergren model. | 226 |
| 5.33 | a) 2-D illustration of a crack tip modeled with collapsed elements, b) Semi-circular half-crack in a symmetrical 3-D FE-model. | 227 |

| | |
|--|-----|
| 5.34 Analytical solutions for 3-D cracks with a) Eq. (5.28), straight crack front (P, Q, R ...forces, b ...distance of the application point of the force P from the crack front) and b) Eq. (5.29), curved crack front [31; 32] (S ...current point of interest, b_R ...distance of the normal stress σ_n at position R from the tangent in S). | 228 |
| 5.35 Illustration of the verification procedure for the virtual crack solution. | 229 |
| 5.36 a) Example of a cube model used for verification purposes, b) Comparison between FE solution and analytical solution for K_I along the front of a semi-elliptical crack | 229 |
| 5.37 a) Comparison between FE solution, analytical solution and virtual crack solution for K_I along the front of a semi-elliptical crack, b) correction functions for K_a and K_c | 230 |
| 5.38 Overview of crack propagation data collected for material A for two temperature levels and two stress ratios. | 230 |
| | |
| 6.1 Temperature evolution at a central position on the friction surface indicated by the red dot and positions underneath down to 12.5 mm depth. The mesh is finer in the surface region than at greater depths. Hence, it should be noted that the corresponding distances between the plotted lines steadily increase. Characteristic points in time are commented. | 234 |
| 6.2 Comparison of the evolution of the temperature due to different thermal input a) at the friction surface and b) in 12.5 mm depth. | 234 |
| 6.3 Values for T_{max} at the friction surface (0 mm) and 12.5 mm depth. | 235 |
| 6.4 Illustration of dynamic and static disk coning (exaggerated). The arrows show in the direction where the inner disk radius moves. | 236 |
| 6.5 a) Stabilization of maximal dynamic coning and static coning with increasing number of simulated brake cycles, b) Stabilized waviness after 10 cycles. | 236 |
| 6.6 Simulated waviness split up into individual oscillation orders. | 237 |
| 6.7 Stress-strain response during load cycle 1 and cycle 10 at the friction surface and correlation with the temperature evolution depicted in Fig. 6.1 in the form of T - ϵ hystereses. | 238 |
| 6.8 Inelastic strain in tangential direction for various depths during a) simulated brake cycle 1 and b) 10. | 238 |
| 6.9 a) Inelastic strain in tangential direction at the friction surface after load cycle 1 and 10 in tangential direction as a function of time, b) Stress versus inelastic strain. | 239 |
| 6.10 a) Comparison of the stabilized minimal and maximal in-depth distribution of ϵ_{in} for varying energy input. The regions of validity for damage mechanical (crack initiation) and fracture mechanical (crack growth) evaluations are indicated. b) The corresponding stabilized residual stress field at the end of load cycle 10. | 240 |
| 6.11 a) Predicted crack initiation life time N_f based on the Ostergren model for different values of dissipated energy E_d and brake time t_{end} , b) Local distribution of N_f on the friction surface within the validity range. | 241 |
| 6.12 Comparison between original geometry and geometry based on a wear limit of 5 mm | 242 |
| 6.13 a) Comparison of the temperature evolution in the original and the worn geometry and b) the corresponding disk coning during load cycle 10. | 243 |
| 6.14 Comparison of the original and the worn disk geometry in view of a) the stabilized hystereses at the center of the friction surface and b) estimated crack initiation life time. | 243 |

LIST OF FIGURES

| | |
|---|-----|
| 6.15 Schematic illustration of crack growth un a brake disk. The schematic crack is oriented in radial direction which is normal the main loading direction (tangential). | 244 |
| 6.16 a) Envelopes of the stress field and the resulting stress ratio in main loading direction as a function of depth and b) the envelopes of the transient temperature field. | 245 |
| 6.17 a) Illustration of the data basis for the evaluation of crack propagation based on K_{max} , R_σ and the temperature and b) simplified approach based on K_{max} and the most conservative experiment | 246 |
| 6.18 a) Correlation of K_{max} and ΔK_{eff} at room temperature as a function of R_σ for a tool steel and small scale yielding conditions (blue line). In the case of large scale yielding the red line applies [33; 34], b) Position of the virtual cracks in the brake disk. | 246 |
| 6.19 Evaluation of the stress intensity K_I during a reference brake cycle for a) a crack with a=0.4 mm and c=1.0 mm and b) a crack with a=0.8 mm and c=2.0 mm | 247 |
| 6.20 K_a for semi-elliptical cracks with different sizes in the stabilized residual stress field of the original geometry . All results are below the threshold for crack propagation, which indicates that crack growth in thickness direction is not possible. | 248 |
| 6.21 Crack propagation rates in lateral direction computed with K_c for semi-elliptical cracks with different sizes in the stabilized residual stress field of the original geometry a) 3D view and b) 2D representation. | 248 |
| 6.22 Theoretical maximum propagation rates for the original and the worn disk geometry (5 mm) exposed to the standard braking. | 249 |
| 6.23 Crack propagation rates for semi-elliptical cracks with different sizes in the stabilized residual stress field of the worn geometry (5 mm) a) 3D view and b) 2D representation. | 249 |
| 6.24 Illustration of thermal image mapping for one brake cycle. In this study the method is applied to perform the thermal image mapping for the brake sequence of 10 consecutive high energy stops represented in Fig. 3.16. | 250 |
| 6.25 a) Selected thermal image from brake cycle 7 of the 200 stop test and the section considered in the thermal image mapping, b) Corresponding temperature field in the simulation with points of interest for further investigation. | 251 |
| 6.26 a) Transient temperature evolution at the surface along the path plotted in Fig. 6.25b. The focus is laid on the incident temperature levels in the zones 1-3 rather than the evolution itself. The three zones are important in view of phase transformations as outline in Section 4.3.4, b) The corresponding data 1 mm below the surface. | 252 |
| 6.27 a) Temperature levels 2.2 mm below the radial path plotted in Fig. 6.25b and b) the data for 12.5 mm depth. | 253 |
| 6.28 a) Radial cut through the FE-model revealing the temperature field in depth direction. The three in-depth paths for further investigations indicated in Fig. 6.25b are now clearly visible, b) Upper envelopes of the in-depth temperature distributions at the three positions P1, P2 and P3. The penetration depths of the transformation zones 1 and 2 are indicated. | 253 |
| 6.29 a) Maximal dynamic disk coning per load cycle. The first ten simulations are based on uniform loading in order to stabilize the σ - ϵ field followed by the thermal image mapping, b) simulated amplitudes of the 4th and 8th order static waves. | 254 |

| | |
|---|-----|
| 6.30 a) In depth distribution of residual stress and ϵ_{in} at position P2 in tangential and radial direction at the end of brake cycle 7. The main loading direction in the bulk is oriented in tangential direction, b) Residual stress and ϵ_{in} in tangential direction at P1, P2 and P3. | 255 |
| 6.31 Illustration of the a) tangential stresses and b) principal stresses during braking. | 256 |
| 6.32 a) Mechanical hystereses for the 20 simulated high energy brakings. The applied uniform heat source during the first 10 brakings promotes the formation of a stabilized hysteresis. During the subsequent thermal image mapping completely stabilized hystereses cannot be obtained due to the varying loading conditions, b) Evolutions of the accumulated (equivalent) inelastic strain p and the von Mises equivalent stress over the course of the ten non-uniform brake cycles. | 256 |
| 6.33 Resulting distribution of the estimated N_f on the friction surface. | 257 |
| 6.34 Residual stresses a) in radial direction and b) in tangential direction after simulated brake cycle no. 17. | 258 |
| 6.35 Virtual cracks positioned in the stress field plotted in Fig. 6.34b. The crack sizes are varied and only the largest crack dimension is shown. | 259 |
| 6.36 a) Stress ratio R_σ as a function of depth at position P2 in Fig. 6.28a, b) Overview of the stress intensity factors K_a obtained at position B. | 259 |
| 6.37 Overview of propagation rates entailed by the stress intensities a) K_{c1} and b) K_{c2} at outer bounds of cracks at position A | 260 |
| 6.38 Overview of the stress intensity factors K_{c1}, K_a and K_{c2} obtained at position B. | 260 |
| 6.39 Comparison of the temperature field simulated with non-uniform loading conditions and real temperatures in terms of phase transformation temperatures. | 261 |
| 6.40 Comparison of simulated and measured disk coning. | 262 |
| 6.41 Comparison of the amplitudes of the 4th order and 8th order waviness at a) the inner and b) the outer disk circle. The experimental data after 10 emergency stops are compared to the simulated amplitudes after 10 uniform and 10 non-uniform simulations. | 262 |
| 6.42 Comparison of measured and simulated residual stress distributions a) 1 and b) 10 emergency stops. The measurements correspond to multiple positions on the friction surface. The measured results are influenced by the viscoplastic material response and the occurrence of phase transformations. The simulations only take the viscoplastic material behavior into account an aim at the description of the highest possible stress level. | 263 |
| 6.43 Comparison of measured and simulated residual stress distributions after 200 emergency stops. The measurements correspond to multiple positions on the friction surface. The measured results are influenced by the viscoplastic material response and the occurrence of phase transformations. The simulations only take the viscoplastic material behavior into account an aim at the description of the highest possible stress level. | 264 |
| 6.44 Material comparison for a) the thermal conductivity λ and b) the engineering thermal expansion coefficient α ($T_{ref} = 20^\circ\text{C}$). | 265 |
| 6.45 a) Evolution of the surface temperature for the reference braking for representatives of five different classes of metallic brake disk materials, b) Comparison of the temperature fields of materials D and E, which exhibit the greatest difference in thermophysical properties. | 266 |

LIST OF FIGURES

6.46 a) Comparison of the stabilized inelastic response for the reference braking for material A-D from the surface down to 12.5 mm depth and b) the corresponding residual stress field. 267

6.47 Qualitative material comparison with a) tensile tests at room temperature and b) LCF tests at elevated temperature. 267

6.48 Material comparison in terms of crack initiation life time. a) Validity range for each material and b) N_f versus E_d for the reference brake scenario and variable energy input. 268

6.49 Possible definitions of K_{TM} in a component: a) Evolution of $K_{TM}(t)$ in main loading direction and the governing quantities of damage and b) comparison of the results for different definitions of a characteristic K_{TM} . The results are extracted from the simulation of a reference brake cycle and material A. 269

6.50 Comparison of the K_{TM} factor obtained from the stabilized σ - ϵ field of a viscoplastic FE-calculation and K_{TM} from an elastic calculation. The results are extracted from the simulation of a reference brake cycle and material A. 270

6.51 Material comparison in terms of crack initiation life time. a) Validity range of the Winter model for each material and b) N_f versus E_d . For material E the range of valid predictions of N_f based on the Winter model is indicated in yellow. 271

A.1 Illustrative image showing the formation of an extrusion by a persistent slip band in s copper single crystals [13]. 277

A.2 Various types of dislocation structures 278

A.3 Determination of the critical load P_Q [35; 36] 278

A.4 Illustration of relevant sample dimensions at the example of an SENB specimen 280

A.5 Procedure for the measurement of a crack resistance curve (synthesized from [22; 30; 36; 37]) 282

A.6 Stress fields ahead of the crack for various loading conditions [36] 285

A.7 Testing procedure the determination of J_{IC} . a) and b) multiple specimen technique, c) single specimen technique, d) Evaluation of results [37; 38] 286

A.8 Illustration of the possible influence of the sample thickness on J_{IC} [39] 287

C.1 Positions for residual stress measurements. The images show segments tested with pad type 1 309

C.2 Positions for residual stress measurements. The images show segments tested with pad type 2 (ES...emergency stops). 310

C.3 Positions for residual stress measurements and metallographic specimens. The images show segments tested with pad type 1 311

C.4 Positions for residual stress measurements and metallographic specimens. The images show segments tested with pad type 2 (ES...emergency stops). 312

D.1 Admissible and non-admissible crack configurations and crack lengths in wheel mounted brake disks [?]. 313

D.2 Analytical solution for stress intensity factors according to FKM guideline [40]. 314

List of Tables

| | | |
|------|--|-----|
| 2.1 | Overview of empirical plasticity and steady state creep models used for the construction of damage mechanism maps [15] | 41 |
| 2.2 | Variables and constants used in Table 2.1 [15] | 42 |
| 2.3 | Overview of deformation rates occurring in the loading path indicated in Fig. 2.11 | 47 |
| 2.4 | Overview of common yield criteria [17; 18; 41] | 59 |
| 2.5 | Overview of common hardening rules based on von Mises plasticity [17] | 63 |
| 2.6 | Approaches to creep modeling [5] | 70 |
| 2.7 | Overview of empirical creep models [5; 42; 43; 44] | 72 |
| 2.8 | Overview of some empirical creep models in FE software packages | 74 |
| 2.9 | Overview of empirical models for service life estimation | 90 |
| 2.10 | Overview of life time estimation strategies at high temperatures | 98 |
| 2.11 | Illustration of the Palmgren-Miner rule | 99 |
| 2.12 | Illustration of the Robinson rule | 100 |
| 2.13 | Illustration of the Strain Rate Partitioning (based on [17]) | 101 |
| 3.1 | Test parameters for full scale test rig and material A | 112 |
| 3.2 | Test parameters for scaled test rig and material A | 142 |
| 3.3 | Test parameters for scaled test rig and material A | 147 |
| 4.1 | Meaning of stationary oscillations along the circumference. | 166 |
| 5.1 | Computation times for 10 uniform emergency brakes with different element formulations [45]. | 196 |
| 5.2 | Element types used for FE-calculations in this work | 197 |
| 5.3 | Overview of the determination of physical properties [46; 47] | 197 |
| 5.4 | Test parameters for full scale test rig and material A | 200 |
| 5.5 | Required input for uniform heat source | 201 |
| 5.6 | Parameters for the unified viscoplasticity model for material A | 205 |
| 5.7 | Parameters for the non-unified viscoplasticity model for material A | 206 |
| 5.8 | Illustration of the importance of individual mechanical experiments (orange: suitable, green: very suitable) | 207 |
| 5.9 | Parameters for LCF and TMF testing | 213 |
| 5.10 | Parameters for TMF testing for material A | 215 |
| 5.11 | Parameters for static and cyclic fracture mechanical testing | 231 |

LIST OF TABLES

| | | |
|-----|---|-----|
| A.1 | Types of tensors [18] | 289 |
| A.2 | Some tensor operations [18] | 289 |
| A.3 | Some general tensor calculus [48] | 289 |
| A.4 | Overview of variables in the thermodynamic framework of constitutive equations [17] | 292 |

Chapter 1

Introduction

The fatigue design of brake disks involves several fields of research, such as fatigue design, finite element (FE) modeling, service life estimation, fatigue testing, component testing, and damage characterization and all of these can be split up again in several sub-domains. Some of the involved topics are closely related to each other, others are not but in the end the individual results and discussions lead to the so-called big picture that this thesis strives for. The introduction is therefore meant to explain the motivation behind his work and the objectives that should be attained. Thermal fatigue (TF) and thermo-mechanical fatigue (TMF), respectively, are the principal factors limiting the service life of brake disks in the case of high energy braking. Handling their impact in view of experimental investigations and modeling is thus the paramount aspect and determines the outline of this thesis. In this chapter a summary of the necessary background information on brake systems and TMF is provided. Chapter 2 is meant to further the understanding of the most relevant aspects for the treatment of TMF and Chapters 3 to 5 deal with the specific investigations carried out in the scope of this work.

Moreover, Chapter 2 establishes the necessary links to follow the lines of thought in this work. It gives an overview of the topics treated in the thesis but the use of results is yet largely avoided. A focus is lead on the discussion of damage mechanisms as well as their physical background and numerical description. Both the introduction and the chapter about the theoretical background give references to the literature and to the sections that will develop the presented ideas in detail.

1.1 Brake systems used in trains

Over the years, several brake systems have been developed which have found their way into modern trains. Depending on the type of train and the service conditions the train has been designed for, one or more of the systems listed in Fig. 1.1 are used. In general, safety requirements demand every train to be equipped with a continuous and self-acting brake system [49]. In this context, the term continuous means that the brakes on all cars of a train can be controlled by one mutual on-board signal system. Self-acting refers to the feature that the brakes are activated automatically when the signal is lost. Due to these safety considerations, the friction based systems, although advanced in years, are still part of almost every train. Their application as well as their importance for safety, is based on G. Westinghouse's invention of the air brake, which is a fail-safe system — to control disk or tread brakes — that fulfills the above requirements.

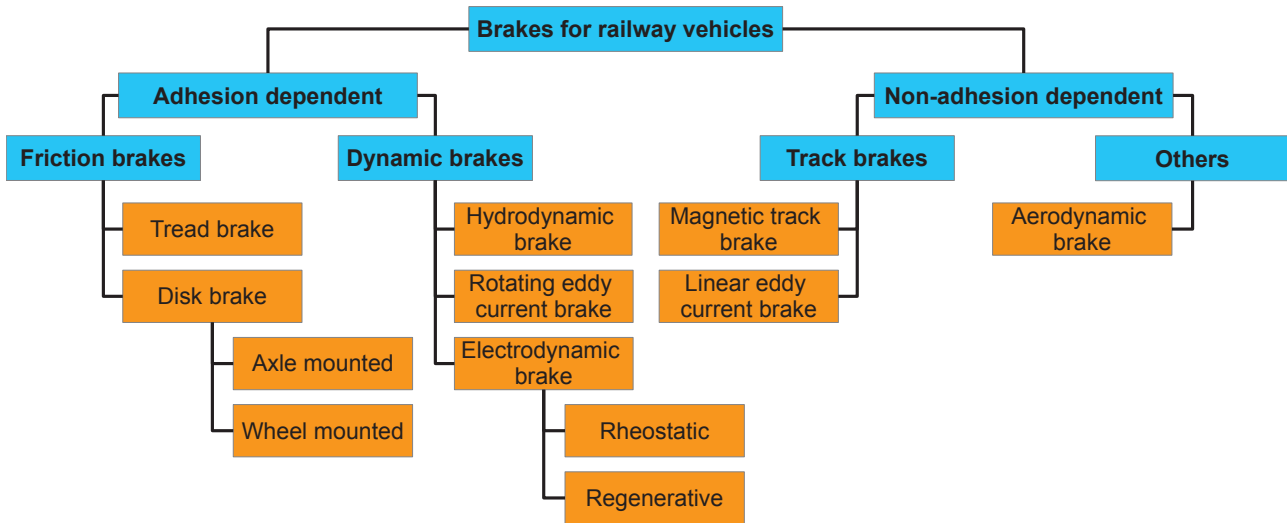


Figure 1.1: Brake systems used in trains based on [1].

The system operates with compressed air tanks mounted in each car, which are controlled by a central signal unit. This unit is a pipe system maintaining a specific air pressure. Above a certain pressure, the friction brakes are released, while they are forced closed below that pressure. In various modified forms the air brake has been used ever since in intercity trains in combination with disk and tread brakes, mostly because of its reliability. Further details on its design can be found in [2; 49].

Electrodynamic braking has been introduced into most modern motor cars. The system is wearless but dependent on the rail-wheel adhesion and braking forces are thus limited [1]. The motor is used as a generator and the resulting energy is either dissipated as heat (rheostatic braking) or fed back into the overhead line (regenerative braking). Nowadays, the latter system is frequently used to recover parts of the kinetic energy of the train. Nevertheless, there are two aspects of regenerative braking that necessitate the use of additional brake systems, like the friction brake. First, regenerative braking is efficient at high speeds but not suitable for a precise stop at a station. Second, the applicability depends on the capacity of the supply system or batteries in the current situation [50; 51].

Since multiple brake systems are normally in use, the distribution of braking force has to be managed for each relevant brake scenario, as summarized below. The necessary brake management is also called brake blending.

1. **Service brake application:** Standard brake application to reduce the speed. The electrodynamic brake is preferred unless the braking force does not suffice. In this case the friction brake is added.
 - Stopping brake application: The aim in this case is to stop the train at a given position, e.g. a train station.
 - Partial brake application: Deceleration down to a specific speed, e.g. when two trains get too close to each other the second train slows down.
 - Continuous brake application: E.g. downhill brake application where a constant speed should be maintained. Due to the high thermal loads on long downhill routes, electrodynamic braking is a crucial part in the brake blending. In the ideal case the speed is maintained by the electrodynamic brake alone.
2. **Maximum service brake application (full service brake application):** Braking with the highest

possible deceleration under service conditions. The driver uses the driver's brake valve and reduces the pipe pressure to about 3.5 bar. However, this does not correspond to maximum possible deceleration.

3. **Rapid stop:** When the driver switches to the emergency brake position of the driver's brake valve, the pressure in the pipes is reduced completely and as fast as possible. The brake application is similar to the full service brake application but faster. In modern trains a brake blending between adhesion-dependent and non-adhesion dependent brake systems is active.
4. **Emergency stop**
 - Driver's emergency brake application: This brake application is initiated by the driver operating a separate valve, namely the emergency brake valve. This valve is independent of the driver's brake valve and directly triggers the air brake.
 - Passenger's emergency brake application: The passenger operates an emergency pull-box that triggers the emergency brake valve.
5. **Automatic brake application (safety emergency brake application):** Systems monitoring the driver or the train, can cause emergency braking, e.g. in the case of damage to the pipe system or train separation.
6. **Holding brake application:** A stationary train is stopped from rolling for a limited time.
7. **Parking brake application:** A stationary train is permanently stopped from rolling.

A summary of the brake systems used for three major groups of railway transport is given in the following:

Intercity and high speed trains: The disk brake is distinctly preferred over the tread brake as obligatory friction brake system in high speed trains ($v > 200$ km/h) [52] because it has a higher limit of energy absorption. Additionally, this system does not cause any degradation of the wheel tread. It is common practice, as for the TGV, to use a certain number of brake disks on the axles, usually three or four. The limited space at the powered axles of several other train types — the space often limits the number to one axle mounted disk — made it necessary to find alternatives to the classical axle mounted brake disk. The wheel mounted brake disk (WMBD), which will be closely investigated in this work, is the predominant alternative. The disk brake is also preferred for intercity trains but recent considerations initiated the revival of the tread brake for trains operating at lower speeds. This is due to its inexpensive and space saving design. Whether these trends will be followed up or not is not clear at present.

In the case of maximum speeds exceeding 140 km/h an additional magnetic track brake has to be mounted [1]. The magnetic track brake is another friction based system commonly used for emergency braking of trains [50]. It is lowered on the rail and then magnetically attracted to it. Since it is not adhesion dependent, the braking force can exceed the adhesion limit of the wheels but it may cause damage to rails. Thus it is recommended for emergency cases only. The eddy current brake is an alternative frictionless track brake system for high speed trains based on the electro-magnetic interaction (eddy currents) between the brake and the rail. In Germany it is used instead of the track brake on ICE 3 trains [50]. Its use is complicated by the fact that the dissipated kinetic energy is induced into the rails in the form of thermal energy and proper track design is thus seminal. Additionally, acquisition and maintenance costs for this brake type are high, which is the reason why the use of the eddy current brake for service applications is limited to certain railway networks like Deutsche Bahn (DB). The use for emergency stops is unlimited.

Freight trains: Due to its cost efficiency, the tread (block) brake is state of the art in freight wagons. The

1. INTRODUCTION

wheel tread is exposed to frictional heating, however, which limits the applicability of this brake system to low energy braking, which applies for freight trains as maximum speeds are low.

Light rail transit (urban transport): The tread brake, in combination with other brake systems, is used in metro trains [53]. As noted above, besides being simpler and cheaper than other systems, the space and weight saving design of the tread brake is favorable and even necessary whenever there is no space available on the axles. This is often the case in railway vehicles for urban transport. Furthermore, the magnetic track brake is standard equipment for emergency stops in urban railway transport.

Beside the magnetic track brake two other systems are used in trams: The electrodynamic brake as previously discussed and the electrohydraulic brake. The latter refers to disk brakes operated by an electrohydraulic system instead of an air brake like in trains.

Regenerative braking (RB) is increasingly incorporated into daily service braking of railway vehicles. Although it can recover parts of the kinetic energy of the train and thus reduce the thermal load on the brake disks it cannot replace them completely. Its brake power is not sufficient for emergency stops of high speed trains [49] and for the case of a system failure the safety regulations require that the friction brake alone must be able to stop the train in every possible situation. However, the use of regenerative braking for standard service operations may permit the design of lighter disk brakes, which have to be maintained more frequently after the occurrence of an emergency stop or a system failure of the RB. This strategy is illustrated in [51] for the case of electric and hybrid cars and similar considerations could be derived for railway braking. Due to the contribution of the RB in the braking process the dissipation of kinetic energy via the friction brake is only a fraction of the total dissipated energy allowing the use of smaller system components (disks, pads, calipers, actuators). In the case of RB-failure the safety is not compromised if the friction brake is properly designed. Its service life, however, will be limited and maintenance needs to be scheduled immediately. Whether this scenario is applicable or not significantly depends on the train type and the specific track. In this context the term *high energy braking* plays a pivotal role. For most trains it refers to emergency stops only, which are rather rare events but for some train types a large number of brake events in regular service also fall in the category *high energy braking*, where the friction brake is always involved. For these train types the friction brake system is of greater importance in daily service and more conservative concepts must be applied for the design.

As mentioned above, the space available for brake disks is very limited at powered axles. A very attractive solution to this problem is the use of WMBDs (see Fig. 1.2) because they can rather easily be used where tread brakes would be mounted for applications at low speeds. Additionally, they do not cause degeneration to the wheel tread, which is usually accompanied by a significant level of noise [52]. The design of the WMBD entails a disadvantage, though. Fig. 1.2 shows that a WMBD consists of two friction rings mounted on the opposing sides on the wheel. For this reason, the loading of each ring is one-sided, which generates a significant axial distortion called coning. Furthermore, close attention needs to be paid to the thermal loading of the wheel due to the vicinity of the disk and the wheel. In order to stay within safety limits the disk design as well as the brake blending need to be chosen accordingly. These prerequisites are the reason why the maximum energy dissipation per WMBD needs to stay below 10 MJ [52].

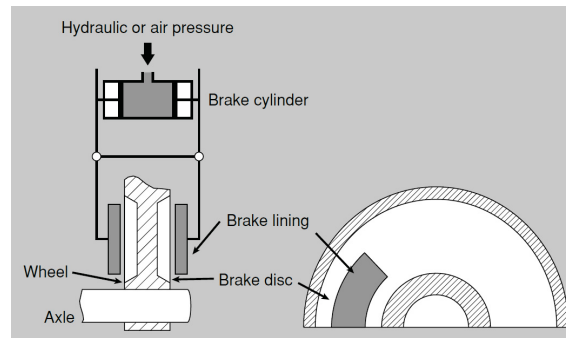


Figure 1.2: Wheel mounted brake disk [2].

In any case, the disk brake is going to remain a substantial part of each train but its role may change for certain train types. On the one hand the required service procedures may need to be adapted to new design philosophies (lighter systems with stricter maintenance regulations) in cases a light weight concept is applicable and on the other hand the disk brake may remain or become an even more substantial part in the brake blending for brake applications in service. A well grounded understanding of the in-service behavior of brake disks is thus necessary and in-depth knowledge beyond the state of the art is favorable for the development of new service concepts. For this purpose the global behavior of wheel mounted brake disks (disk coning, waviness) as well as the local behavior of the disk material are examined in this work with the goal to devise a simulation tool that can be used for the prediction of the response of brake disks to various thermo-mechanical fatigue loads. The energy levels for the WMBD investigated in this work are 5 MJ for service stops and up to 25 MJ for the case of emergency braking. This high level of thermal input must be analyzed in view of the resulting thermo-mechanical fatigue damage. This will be done by experimental means (Chapter 3, Chapter 4) and by simulation (Chapter 5).

1.2 Typical problems with brake disks

The ideal case of pad-disk contact would lead to a homogeneous distribution of contact pressure throughout the two friction surfaces. For various reasons, however, this ideal case can never be obtained and the contact areas are smaller (and are thus subjected to higher contact pressure) than commonly assumed in the design process. According to [54] the contact conditions can be considered at three levels:

1. **Global pressure variations** affecting the whole friction surface due to bulk deformation: According to [54] this large-scale effect occurs during the application of the actuation forces. It will be shown in Chapter 4 that plastic deformation on the global scale causes bulk deformation and influences the contact conditions, predominantly in the case of rigid pad types at high levels of dissipated energy.
2. **Macroscopic pressure variations** appearing as localized variations in the temperature distribution of finite size: This level involves hot spots and hot bands originating from localized deformation [54; 55] being related to the occurrence of thermo-elastic instabilities (TEI) [56; 57; 58] and plastic deformation on the local scale which may stabilize TEI patterns, as has been discussed in a more recent work [59].
3. **Frictional contact on the microscopic scale:** This last level is essential for the study of tribological

1. INTRODUCTION

processes and wear as carried out, e.g. in [60]. Processes at this level mainly influence the evolution of the friction coefficient but can also entail thermal surface gradients like hot bands as friction layers form and change due to transitions in the friction mechanism.

The inhomogeneous contact pressure attributed to effects at level 2 leads to one or more types of thermal surface gradients as discussed by Anderson [61] and Dufrénoy [3] for the case of symmetrically loaded brake disks, i.e. automotive brakes and axle mounted railway brake disks. The current work investigates the occurrence of thermal gradients on WMBD and determines if they match the literature or if there are thermal patterns unknown so far. As reported e.g. by Kasem et. al. [62], the material beneath hotspots is likely to go through metallurgical transformations, which usually entails the formation of microcracks. As will be shown in Chapter 4, high energy braking leads to plastic flow in the surface region which is accompanied by the formation of tensile residual stresses. Due to thermal gradients these stresses depend on the position on the disk. Furthermore, the local changes of the microstructure have a great impact on the in-depth stress distribution by causing a shift towards the pressure regime (It depends on the extent of metallurgical transformations and the level of plastification whether pressure stresses are obtained or not). The impact of these effects on the damage mechanisms are significant for high energy

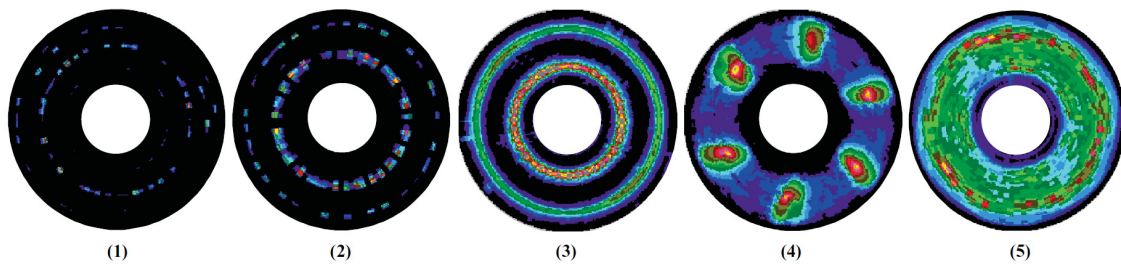


Figure 1.3: Thermal surface gradients according to [3]: 1) local contact asperities, 2) gradients on hot bands, 3) hot bands (fire rings), 4) macroscopic hot spots, 5) ideal case: almost uniform contact pressure.

braking. Yet, their consideration in fatigue design, although discussed in the literature, is not common practice in engineering. For this reason, this work will investigate approaches to tackle this problem, see Chapter 5.

1.3 Some general remarks on thermal and thermomechanical fatigue

The concept of thermal fatigue applies whenever a sample or component is exposed to thermal load cycles [63], causing inhomogeneous temperature fields. A change in temperature will result in thermal expansion or contraction and for this reason, thermal cycles causing thermal gradients will also induce stresses. This mechanism is illustrated in Fig. 1.4a) for a beam, which is thermally loaded on one side. The initial state of a component or sample before loading is that of a uniform temperature and without plastic deformation. A thermal input at the surface causes the material to expand, and as the highest temperature is at the surface ($T_1, T_2 > T_0$ and $T_1 > T_2$), the maximal thermal expansion will occur there. The regions below expand but to a lesser extent. If the component is, for the time being, imagined as a stack of individual layers — each having a uniform temperature — the variation in thermal strain (ϵ_{th}) with depth causes a mismatch of adjacent layers. If the layers expand independently of each other the mismatch does not induce stresses

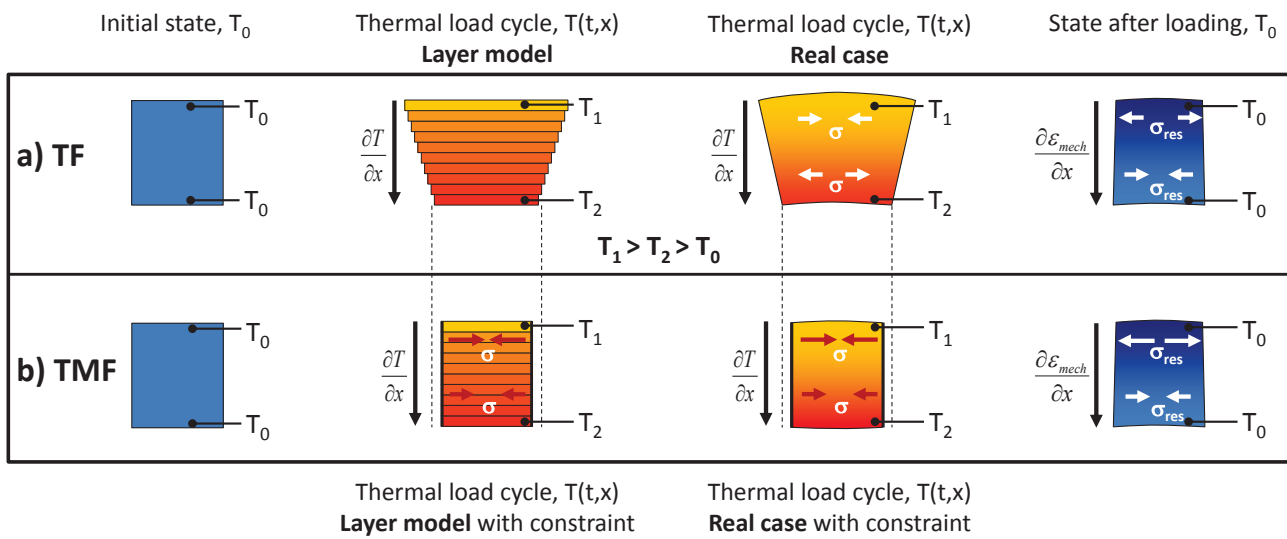


Figure 1.4: Stresses caused by a thermal gradient: a) thermal fatigue (TF), b) TF with additional mechanical loading (TMF), e.g. due to external constraint.

in the structure and a configuration like a stepped pyramid results. In the real case, the layer thickness is very small and the layers are obviously connected to each other. This gives rise to thermal stresses in the structure. These stresses are larger at the surface due to the larger mismatch. Depending on the heat input and the thermal conductivity the local stress may exceed the plastic limit (σ_y) of the material. The plastification is highest at the surface and continues in depth until the stresses are below σ_y and induce only elastic strains. This process causes plastification under pressure and thus a shortening of the material which is more pronounced close to the surface where the thermal load is applied. After the initial temperature (T_0) has been reestablished, the top layers are shorter than the layers at greater depths. This entails that the surface regions exhibit tensile residual stresses which diminish with depth and eventually change into compressive residual stresses. These mechanisms and the related formation of residual stresses are key aspects of this work. Detailed discussions follow both in the experimental and the numerical part. At elevated temperatures plasticity may not be the only deformation mechanism. At sufficiently high temperatures creep deformation at stress levels below σ_y can play a pivotal role in the formation of residual stresses, as will be discussed later on.

It should be noticed that a component exposed to a non-uniform stress field tries to reduce the stress level by bending. In the case of a simple beam, it can be shown that a linear temperature distribution can be fully compensated by bending (constant temperature gradient: $\frac{\partial T}{\partial x} = const \rightarrow \sigma_{th} = 0$). The beam is thus stress-free. In real cases, the distribution is never perfectly linear and bending can only reduce the stresses to a certain degree. Stresses are thus present. For more complex geometries, such as rings and brake disks, additional aspects add to the problem. The stresses due to a constant temperature gradient in a ring cannot simply be reduced by bending. Some symmetry planes in the cross section must remain and this limits the possible deformation. The geometry itself thus causes an internal constraint, which is not present in a the simple beam. This example is still a TF case but the transition to TMF loading is discussed in the following.

TMF occurs whenever mechanical loads accompany the mechanism described above. This process can be observed in components like turbine blades, cylinder heads, exhaust manifolds, turbo-chargers, com-

bustion engines, nuclear reactors, casting dies [34; 64] and brake disks [65]. The mechanical load can either be caused by external forces (e.g. a braking force) or in many cases from external constraints (e.g. the mounting) that oppose the thermal expansion of the component (see Sehitoglu's article in [30]). Fig. 1.4b) illustrates the impact of a constraint on the loading conditions. The initial state is free of any loading. Again its surface is subjected to an input of thermal energy but this time the sides are fixed completely. A similar thermal gradient as in case *a*) develops but now the imagined individual layers are not only constrained by their neighbors but also by the boundaries of the component. This process causes a larger loading inside the component since no expansion is possible, whereas some expansion occurs in the layers of case *a*). The corresponding stress levels are higher and plastic strains are more significant leading to a smaller fatigue life till crack initiation. In the case of TMF the fatigue life is — in the ideal case — a function of the constraint which can be described by the ratio of mechanical strain (ϵ_{mech}) to thermal strain (ϵ_{th}) [66]:

$$K_{TM} = \frac{\epsilon_{mech}}{\epsilon_{th}} \quad \text{constraint factor} \quad (1.1)$$

A constraint factor close to 0 at all positions within a component would imply that the material could freely expand everywhere. This may be the case for components with homogeneous temperature fields or theoretically for simple geometries exposed to a linear thermal gradient. For one-sided thermal input in real situations (nonlinear gradient), as in the two previous examples, which are characteristic for brake disks, this is unrealistic. Even TF, without external constraints will always cause K_{TM} to be less than 0. Nevertheless, the magnitude of the constraint factor depends on material properties and component design. Hence, the effect of the mechanical loading in TMF situations, which increases and decreases with the magnitude of K_{TM} , can also be minimized or avoided by proper design. It should be noted that in certain applications TMF can also cause positive values for K_{TM} . However, for braking only negative values are relevant.

1.3.1 TMF testing

The situation described in Fig. 1.4b) corresponds to $K_{TM} = -1$, which corresponds to a full constraint ($\epsilon_{mech} = -\epsilon_{th}$) of a sample in a TMF testing machine. This is also called *ideal out-of-phase TMF* (OP-TMF) [67] since the maximum temperature coincides with the minimum strain (Fig. 1.5a). The opposite case is called *ideal in-phase TMF* (IP-TMF). Beside the extreme cases of ideal IP-TMF with a phase angle $\phi = 0^\circ$ between temperature and mechanical strain and ideal OP-TMF with $\phi = -180^\circ$ two other rather unique TMF loading conditions exist, which are called clockwise and counterclockwise diamond loading. In both cases, the minimum and maximum strains occur at the average cycle temperature. Clockwise ($\phi = 90^\circ$) means rising strain values at the beginning of the cycle while counterclockwise ($\phi = -90^\circ$) means dropping strains (Fig. 1.5b). In between these four conditions a variety of TMF loadings can be defined by the phase angle ϕ together with the information whether the phase angle is clockwise or counterclockwise [68]. Negative values for K_{TM} correspond to out-of-phase TMF and positive values to in-phase TMF — in general not *ideal* unless $\phi = 0^\circ$ or $\phi = -180^\circ$. For example, $K_{TM} = 0.75$ means that the mechanical strain equals 75% of the thermal strain in an in-phase test configuration. General OP-TMF loading is typical for cylinder heads, casting dies and also the component treated in this work — brake disks. The

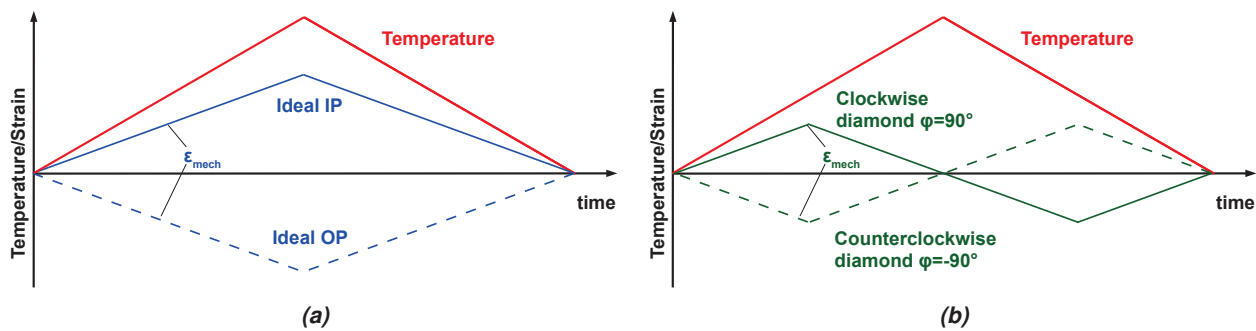


Figure 1.5: a) In phase (IP) TMF and out of phase (OP) TMF b) Clockwise and counterclockwise diamond TMF.

real loading conditions may be more complex than the presented cases but they are commonly broken down to loading conditions which can be tested in the lab. The testing under real loading conditions is restricted to component testing, but TMF testing already provides a powerful means for lab experiments very close to real conditions. In any case, TMF tests capture the real loads much more precisely than a test program based isothermal (LCF) testing. For information on the experimental setup the reader is referred to the literature, e.g. [30; 69; 70].

1.3.2 Typical TF/TMF damage

TMF damage is generally a combination of fatigue, creep and oxidative damage that finally leads to crack initiation and growth [71; 72] where the impact of the individual contributions depends on the specific TMF characteristics. As reported by Sehitoglu [30], iron-base alloys form oxide layers at temperatures above 500°C . These layers are brittle and crack easily due to a difference in volume between the oxide and the substrate, different thermal expansion and the mechanical loading. During OP-TMF the oxide forms under pressure and is exposed to tensile stresses during cooling, thus easily causing local fracture. The cracks in the oxide layer may induce crack initiation in the substrate, which is the reason for a difference in fatigue life of a factor of 2-20 between oxidizing and non-oxidizing environments. There are also metallurgical changes at elevated temperatures such as the coarsening or spheroidization of perlite lamellae above 400°C and phase transformations if temperatures above the A_1 temperature in the iron-carbon phase diagram are reached during the cycle. During the hot phase of the cycle, when austenite is present, the plastic deformation behavior is different and creep strain rates are lower (see Fig. 2.10b). This increases the complexity of the thermomechanical problem. Furthermore, a successive occurrence of austenitization and cooling results in the formation of surface cracks (see Fig. 1.6a). For brake disks this was observed in [73]. Temperature levels exceeding A_1 usually occur in the area of hot spots (see Fig. 1.6b) and hot bands. The TMF loading is largely influenced by the shape and the transient history of the thermal surface gradients. For this reason, a proper characterization and understanding of these effects is also a very important aspect in this work. On the one hand, the thermal gradients can be studied within certain limits from thermal images. On the other hand, phase transformations and initiated cracks can be made visible in metallographic samples taken after testing. Due to the significance of these two studies, they are treated in two individual chapters (Chapters 3 and 4).

Whether brake disks are subjected to TF or TMF depends on the geometry and the way they are



Figure 1.6: a) Cracks at the friction surface: A) network of small cracks, B) radial crack, C) tangential crack and b) Hot spot pattern after braking [4].

mounted. The disk type addressed in this work is based on a very flexible mounting that allows the disk to expand radially and thus also in tangential direction during heating. Additionally, each mounting point can individually move in tangential direction if hot spots are spread unevenly along the circumference. This design shifts the loading type from TMF more towards TF, which entails lower mechanical loads, as discussed above. The definition of the constraint factor (Eq. (1.1)) is still valid because in the TF case there are still internal constraints causing a mechanical load. The more general term TMF is thus preferred throughout this work. K_{TM} is the basis for TMF-testing as will be further discussed in Section 5.2.7.1.

At this point it should be mentioned that some preliminary considerations regarding material properties and their effects on TMF life expectancy — as described in [14; 74]—may help in material selection and in general discussions of TMF damage:

Young’s modulus/yield stress: In the presence of external constraints (e.g. from the mounting), the total strains occurring in the component are largely determined by the thermal expansion (α) of the material and the temperature evolution in the component. Since the plastic strains are one pivotal limiting factor of TMF-life, the material properties determining the transition from elastic to plastic deformation are crucial. Therefore, a higher yield stress (σ_y) is an advantage in terms of life expectancy but it is not the only material property to keep in mind. The key question is if and how fast σ_y is reached during a load cycle. In the presence of external constraints a low Young’s modulus (E) is thus as decisive as a high σ_y . Due to the physical relation between melting point, thermal expansion and Young’s modulus [75], a lower Young’s modulus is linked to a higher thermal expansion coefficient, which is not favorable. Evidently, the comparison between materials must involve several parameters and is thus not straightforward.

Temperature gradient: As illustrated in Fig. 1.4 the temperature gradient $\partial T/\partial x$ may cause plastic yielding and consequently limit the fatigue life. $\partial T/\partial x$ can be reduced by using optimized geometries that facilitate temperature equalization and materials with high thermal conductivity (λ). In the case of brake disks this may be achieved by increased conductivity of the material and a thinner disk design. The latter facilitates the formation of homogeneous temperature fields. It must be kept in mind though that bulk temperatures will increase that way. The models discussed in this work are capable of showing changes in the plastic disk deformation due to changes in the design, which makes design changes quantifiable in terms

of low cycle fatigue life.

Grain size: At low temperatures LCF and HCF fatigue life generally increases with decreasing grain sizes. At high temperatures the grain size has additional consequences if cycle times are long enough for diffusional creep to take effect. This is the case for gas and steam turbines, which continuously operate for weeks or months at constant temperatures in the diffusion creep region. In this regime the creep rates increase with decreasing grain sizes. For TF/TMF of brake disk comparatively short cycle times and high stress levels prevail. For this reason, dislocation creep is more relevant in the high temperature region, which is independent of the grain size.

Further influences are discussed in [14].

In TMF load cycles with high values for T_{max} plastic deformation is accompanied by creep/relaxation effects which are decisive in view of fatigue life, as has already been implied in Section 1.3. Beside plasticity, deformation mechanism diagrams (Ashby maps, Fig. 1.7) show different mechanisms for creep deformation in dependence of temperature, stress and grain size. The general section on metal physical mechanism of creep deformation, Section 2.2, will discuss Ashby maps in more detail. Plasticity is covered but from Ashby maps only limited information can be drawn on cyclic plasticity and viscoplasticity. These core subjects will be discussed in the general sections on plasticity, Section 2.1, and viscoplasticity, Section 2.3.

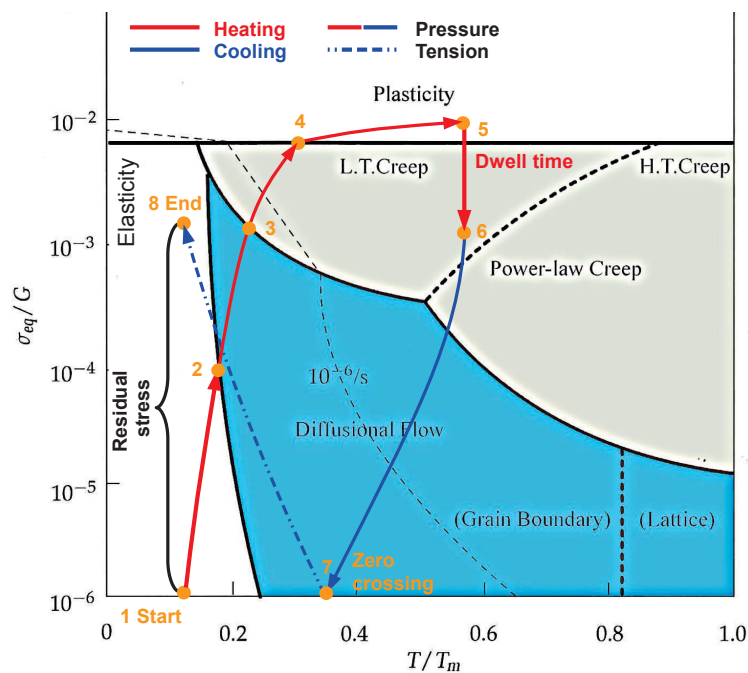


Figure 1.7: Schematic deformation-mechanism diagram based on [5].

At this point a short overview will be given in order to establish the link between the TF/TMF loading described in Fig. 1.4 at the beginning of Section 1.3 and the physical mechanisms of deformation: Beside plastic deformation above σ_y several creep deformation mechanisms prevail for certain combinations of stress and temperature. At temperatures above 0.5 times the melting point (T_m) in Kelvin and stresses close to σ_y the main deformation mechanism is dislocation creep (indicated in grey). At moderate loading, too small to cause dislocation movement, purely diffusional deformation prevails above 0.5 T_m (indicated

1. INTRODUCTION

in blue). The consideration of cycle times is important in terms of the estimated creep strain per cycle. Ashby maps contain isolines for strain rates in the various regions of the diagram and this may yield useful information on how significant creep strains are for the estimated service life. As noted above, the importance of rather slow diffusional creep mechanisms can be quickly assessed, for the two previous examples, gas turbines and brake disks. The information in Ashby maps is also useful for the definition of laboratory test parameters which in many cases do not conform to the real application ranges of the component. The simplified Ashby map in Fig. 1.7 enables us to continue the previous discussion of TF loading in more depth. We can link this general TF case to a loading path in $\sigma - T$ space. This way we can observe which mechanical effects and physical mechanisms of deformation occur. The discussion goes into some depth but many details are omitted at this point.

As noted in [5; 15; 76] plastic flow is caused by the shearing/deviatoric part of the stress state, which can be represented by the von Mises equivalent stress. For Ashby maps it is common practice to plot the normalized shear stress according to Eq. (1.2) on the vertical axis, where G refers to the shear modulus. Section 2.4 expands on tensor notation and continuum mechanical concepts used throughout this work¹.

$$\frac{\sigma_{eq}}{G} = \left(\frac{1}{2G} \mathbf{s} : \mathbf{s} \right)^{\frac{1}{2}} \quad \text{normalized shear stress} \quad (1.2)$$

$$\dot{\gamma} = (2\dot{\epsilon} : \dot{\epsilon})^{\frac{1}{2}} \quad \text{shear strain rate} \quad (1.3)$$

Or in the case of simple tension, where σ_1 and $\dot{\epsilon}_1$ refer to the uniaxial values in loading direction:

$$\frac{\sigma_{eq}}{G} = \frac{\sigma_1}{\sqrt{3}G} \quad (1.4)$$

$$\dot{\gamma} = \sqrt{3}\dot{\epsilon}_1 \quad (1.5)$$

The homologous temperature T/T_m is plotted on the horizontal axis, where T_m refers to the melting point of the material in Kelvin. As noted above, the inelastic deformation rates $\dot{\gamma}$ are usually plotted as isolines. They are computed according to Eq. (1.3), which will be explained in the Chapter 2. A schematic loading path for a component subjected to TF is indicated in the Ashby map in Fig. 1.7. This loading situation is loosely related to a material point at the surface in the graph plotted in Fig. 1.4a):

The path starts at position **1** at room temperature and at zero stress. The starting point is clearly in the elastic domain but during heating, the temperature rises and compressive stresses develop. The path passes both through the region of diffusional creep (**2-3**) and dislocation creep (**3-4**) and finally it hits the yield limit σ_y at position **4** where plastic deformation begins to occur. At this point hardening mechanisms apply, which increase σ_y . Dislocation creep is still active and the consequences of this combination of mechanisms for fatigue life form the background for areas of research such as *viscoplasticity* and *creep-fatigue-interaction*, detailed in Chapter 2. The maximum temperature in the loading path corresponds to the maximum shear stress at position 5. The temperature is maintained (dwell time, **5-6**) and recovery processes cause the stress level to decrease until the loading path is completed by the unloading branch

¹The general expression for the equivalent stress according to von Mises involves an additional factor $\sqrt{3}$ as will be explained in and Section 2.5.1.1

(6-8). During unloading, which corresponds to the reduction of the temperature to the initial value due to the removal of the external heat source, an important point occurs. At position 7 the stress changes from the compressive to the tensile regime. This corresponds to the mechanism discussed in Section 1.3. During cooling the plastification of the surface region under pressure causes the a volume element of the material to be shorter than at the beginning. When the temperature at the surface begins to cool down and the core is still hot, this shortening has an important effect. A volume element of the material further below the surface is longer and tries to stretch the surface region. This induces tensile stress at the surface and compressive stress further below. When the temperature field begins to become homogeneous and the initial temperature is approached the thermal stresses are reduced until only the residual stress remains at the end of the cycle. The residual stress built up in this example equals the vertical distance between the start and the end point.

Ashby maps are very useful for fast estimations of deformation rates and the physical mechanisms involved in the individual regions. Section 2.2 will further expand on deformation mechanism maps and the fields in Fig. 1.7, which have not yet been explained in detail. However, they do not consider other influences on the fatigue behavior, such as cyclic hardening, oxidation and cyclic metallurgical transformations. Nevertheless, the considerations from the example concerning the loading path in Fig. 1.7 largely determine the structure of the theoretical part of this thesis and the reasoning behind the experimental/simulation activities. A similar loading path as in the previous example will be elaborated in detail for a real Ashby map in Section 2.3.

1.4 Motivation and summary of the present work: TMF life assessment

As previously mentioned, this thesis is concerned with the investigation and the modeling of the mechanical response of brake disks to railway braking. To date a significant amount of literature exists on pad-disk interaction, tribology/wear and infrared thermography, e.g. [59; 62; 77; 78; 79; 80; 81]. A smaller range of articles deals with damage and failure mechanisms, e.g. [73; 82; 83; 84], and only few works have been published on the plastic deformation in brake disks, their numerical modeling and the link between plasticity and TMF fatigue life based on TMF testing. Important contributions to this field of study are [3; 83; 85] and some additional literature can be found in the automotive domain, e.g. [86]. Since these topics are key issues in improving safety as well as lowering the maintenance costs, they are addressed in this thesis. Additionally this work aims at bridging the gap between some fields of research that have never been put together in the context of service life prediction of brake disks.

On the experimental side, an analysis of the thermal loading conditions is carried out and the results are discussed in Chapter 3. The impact of these particular loading conditions on the functioning of the disks is laid out in Chapter 4, where the results of a systematic analysis of damage and processes leading to damage is shown. Chapter 5 deals with the consistent modeling of the braking process taking cyclic plasticity and thermal gradients into account. Simulation results are presented and discussed in Chapter 6. The final goal of this work is a TMF modeling strategy, so all of these points are seminal in the sense that they lead to the complete picture necessary to achieve this goal.

The flow chart in Fig. 1.8 provides an illustration of the cornerstones in the modeling strategy of

1. INTRODUCTION

TF/TMF of railway brake disks used in this work. The disk geometry is introduced at the beginning of the chart (level 1) as it is the initial point for any simulation. There is more significance to the geometry because it determines the mechanical response to the temperature field in its bulk. Automotive brake disks and axle mounted railway brake disks are loaded symmetrically, as opposed to wheel mounted brake disks, which are loaded non-symmetrically. This is why WMBDs show a different mechanical behavior that has to be considered throughout the FE modeling. Level 2 deals with the thermal loading of the disk during relevant service applications. In this work high energy emergency braking has been chosen as reference loading that determines the service life. Further details on the topic can be found in Section 1.6. In Section 1.2 an overview of the thermal loading conditions at the friction surface of brake disks has been given. Due to their complexity an individual chapter is dedicated to the investigation of thermal surface gradients in the pad-disk systems in focus (Chapter 3). Moreover attention is given to this issue in the modeling scheme as indicated in Fig. 1.8. The third level of the modeling consists of the mechanical part that eventually yields stresses and strains as well as data on the deformation of the disk. As previously mentioned, TMF shares some common ground with LCF, as it is dominated by plastic strains. The use of proper constitutive equations is therefore decisive and both Section 2.5 — in the theory part — and Section 5.2.5 — in the modeling part — attend to this subject. Additionally to the pivotal points thermal loading and cyclic viscoplasticity, a firm link to component tests is required for the three following purposes:

- Estimation of real temperature distributions in thickness direction (from metallographic investigations)
- Determination of residual stresses which are characteristic for the real TMF loading
- Determination of axial deformation (disk coning) and waviness due to real TMF loading

The results of all three investigations are meant to be used for the verification of the modeling approach. In this context, verification means to pinpoint the area of validity and the application range where the simulation scheme can be used. Both in the scientific and the industrial context, the purpose of the FE model is to provide a tool that can be used in the design process of brake disks and friction brake systems under various considerations such as the following:

1. General safety considerations: Crack initiation life, crack propagation life, damage accumulation, proof of safety standards
2. Brake disk design: Thickness, mass, shape, mounting
3. Design of friction brake systems: Selection of proper number of disks per axle, geometry types, disk materials, brake blending
4. Maintenance considerations: Is it sensible to change the disks when the wheel treads are maintained, or could the disks be safely used for more than one maintenance cycle for the wheel.

Point three may not be as self explanatory as the other three. The variety of brake disk types, materials and possibilities for the mounting is much larger for trains than for cars. When a new train type is planned the engineers have to define the brake blending, i.e. the use of the different brake systems in combination with each other for the various possible braking situations on the route. As much energy as possible is dissipated by regenerative systems and the loads on the friction brake are rather low. Still, in the event of

extreme conditions where other brake systems may fail, the friction brake alone must stop the train safely. Since more than one friction brake system is commonly used on a train (axle and wheel mounted disks, different disk sizes on motor and trailer bogies) the brake blending also affects the distribution of the braking forces on the disks during braking. In the design process it is not always evident which combinations of brake disks have to be used to meet safety standards and are not oversized at the same time. Furthermore, the brake blending should guarantee that the contribution of the individual brake applications to the overall damage is evenly distributed on all disks. Damage, in this context, is a natural process, which must not be confused with failure. The disks are designed to withstand up to a certain amount of damage accumulation which can be predicted by suitable methods. These methods prevent failure because they indicate when the disks need to be replaced. The damage evolution should be as homogeneous as possible in all disks. This way, the danger of failure of individual disks is minimized and service intervals are more predictable because all the disks are due for replacement at the same time. At least, this is the case as long as fatigue and not wear determines the lifetime.

As indicated at the bottom of Fig. 1.8, the simulation tool has to deal with three important issues, all of which are more or less related to fatigue design:

- Service life prediction, which is the main focus in the design process, as previously stated. Having a complete approach to TMF modeling at hand enables the user to obtain essential information in terms of the four points mentioned above. All of these aim at maximum safety without carrying around unnecessary weight or performing unnecessary disk replacements.
- Verification of the functioning of the design. The intense disk coning has to be compensated by the caliper construction but this is only possible within certain limits. The determination of the transient and static coning is therefore essential in order to guarantee the functioning of the disk brake.
- Investigation of possible interactions between plastic disk deformation and localizations of thermal loading. These in turn may influence the fatigue life of the disk and are thus sub-points of service life prediction. Nevertheless, it is mentioned as a separate point because pad-disk interaction is a field of study on its own and usually not included in life prediction models. For this reason, only limited studies are carried out on this topic in the scope of this work, dealing with effects due to global disk deformation.

1.5 The tribological systems in focus

1.5.1 Disks

Fig. 1.9 illustrates the assembly for the disk type in focus, which is made of a forged low-alloyed steel, subsequently designated *material A*. It is the main material in this work but its mechanical behavior will be compared to other materials at a later point in Chapter 5. As noted above, the disk type is mounted to the wheels and must consequently consist of two individual friction rings. Fig. 1.10 shows more clearly the patented system for the fastening of the rings to the wheel, which allows radial expansion, inhomogeneous tangential expansion and coning. Thermally induced stresses as well as external constraints are thus kept to a minimum.

The mounting of the disks is established with screws that pass through the wheel thus reaching the oppo-

1. INTRODUCTION

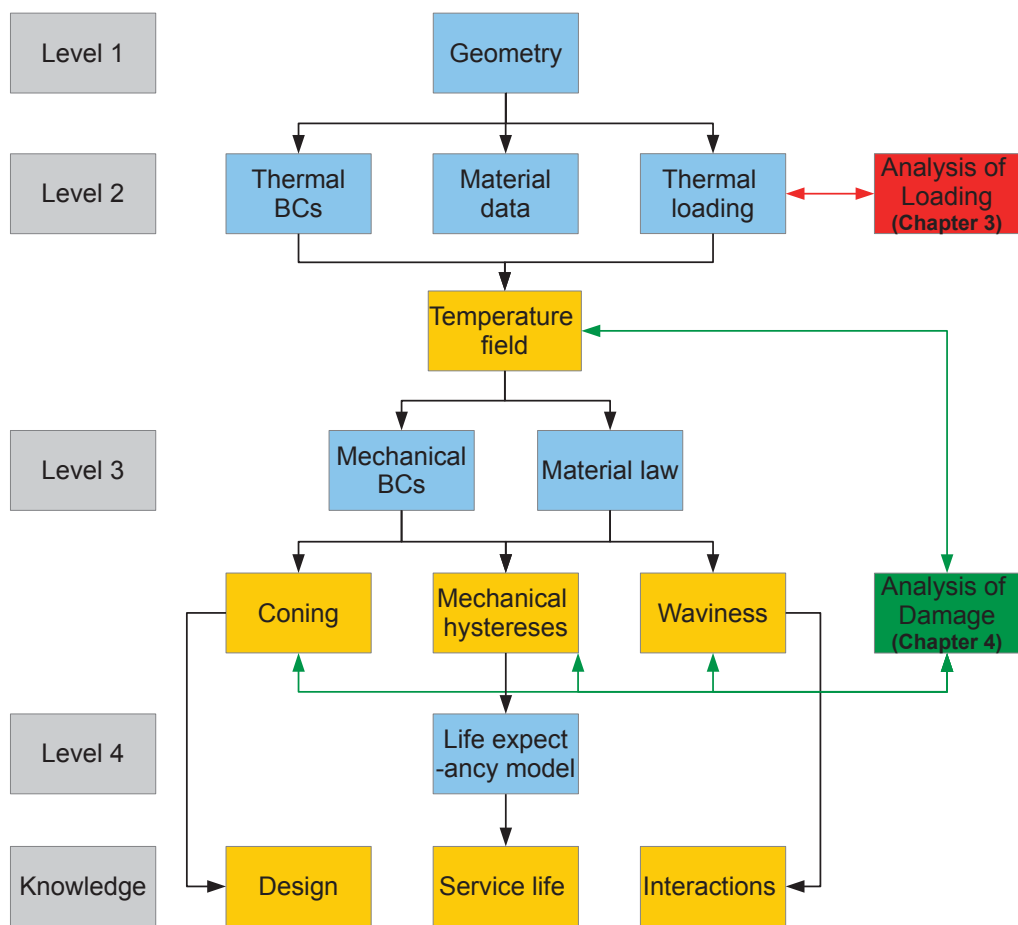


Figure 1.8: Approach to service life prediction of a brake disk exposed to TF/TMF.

site disk. This keeps the disks attached to the wheel but the torque is transmitted by sliding stones that are positioned in recesses on the reverse side of the disks. At each fastening an adapter passes through the wheel ending in a sliding block which completes the power path from the disk to the wheel in the case of braking. WMBD for high speed applications come along with the disadvantage that no split disk design exists up to now. In order to exchange the inner brake disks it is necessary to unmount the wheel, which is cumbersome and costly. This is one of the principal reasons why WMBD are exchanged when the wheels have to be removed anyway for maintenance of the wheel treads. Whether the disks have to be exchanged or not may be evident from the point of view of wear because the amount of material loss is visible due to an indicator on the disk. With regard to fatigue, the situation is not so clear and it is likely that disks are exchanged unnecessarily frequently. This problem again calls for the use of simulation tools for fatigue prediction.

1.5.2 Pads

Although the response of WMBDs to TMF loading is the core issue in this work, the role of the pads in this context must be considered to a sufficient extent. For this reason, two different pad types are included in

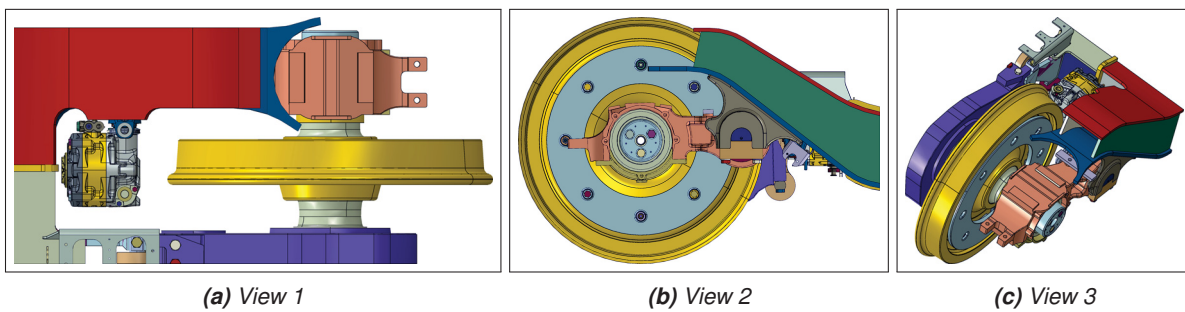


Figure 1.9: Wheel disk assembly without caliper and pads.

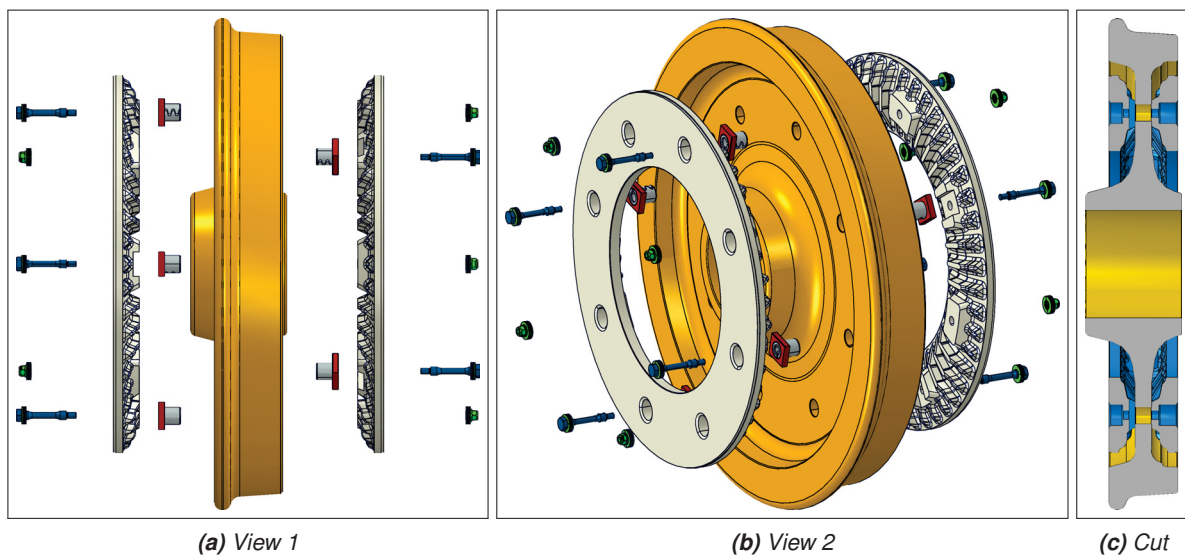


Figure 1.10: Mounting of the disk to the wheel.

component testing as will be discussed in more detail further below.

Fig. 1.11 provides an illustration of the two pad types: Fig. 1.11a shows a conventional rigid pad type that is used at lower speeds; Fig. 1.11b a flexible pad type, typically used in high speed applications. The reason why a rigid type for lower speeds is included in a study on TMF loading during high energy braking is the large difference in the expected thermal gradients and thus also in the thermal loading conditions. The loading due to the rigid pad is supposed to be different and at the same time higher than that for the flexible pad type, which is able to compensate disk deformations during intense loading. It is thus expected to get a clear picture of the possible loading conditions and damage mechanisms by testing two extreme conditions. Moreover, it might be possible to get some deeper insights in the applicability of the rigid pad type and possible criteria for pad selection.

In the case of significant disk coning the axial displacement along the radius of the disk is important but it is not the only aspect. Attention must be paid to the shape of the friction surface, which changes from a flat surface to a curved one. In other words, the axial position at mid-radius is closer to the pad than at the the inner and outer radii. For high speed braking this curvature is essential in view of homogeneous contact conditions. Flexible pad types that can adapt to the curved surface have thus been developed. As illustrated in Fig. 1.11b, the flexible pad considered in this work consists of two pad halves, which for

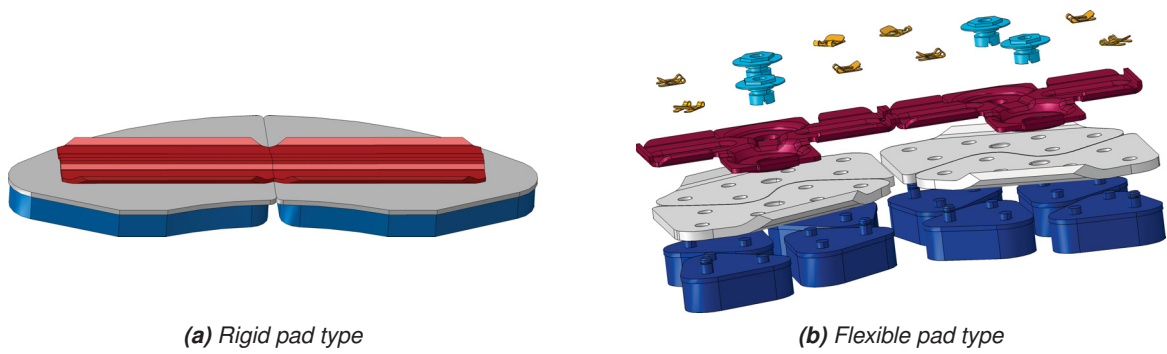


Figure 1.11: Pad types used in the test rig program.

their part, consist of 4 pins made of friction material. Two pins at a time are mounted on a back plate and each back plate is in turn attached to a support plate. The latter connection allows a rotational degree of freedom which enables the pad to adapt to the friction surface in the case of intense coning. The rigid type consists of two halves as well but each of them solely consists of a block of friction material, the back plate and a support plate for the mounting. The corresponding temperature distributions for each disk-pad combination is discussed in Chapter 3. In any case, the flexible pad is the reference case throughout this work as it is a suitable pad for the tested loading conditions, while the rigid pad is used for comparative purposes in order to have a more complete picture of possible mechanisms affecting fatigue life. Fig. 1.12 provides an additional top and bottom view of an unused flexible pad.



Figure 1.12: Flexible pad type in assembled condition.

1.6 Test rig program

Component testing is usually not practicable for design purposes because it is too expensive and time consuming. This leads to the need for material characterization in the lab and simulation tools that can be used for most parts of the design process. Nevertheless, component tests cannot always be replaced completely because experimental verification is required for critical components like brake disks. Considering the number of possible settings on a test rig with respect to loading conditions and test sequences it is imperative to identify the key mechanisms that need to be investigated and to chose the load scenario

that is best suited for that purpose. In the current work a test rig program was thus devised based on the following considerations:

- Cyclic plasticity leads to the formation of tensile residual stresses in brake disks. They build up very fast during the first cycle(s) and approach a saturation value with increasing number of load cycles.
- The plastic deformation in the disk entails global deformation that manifests itself as coning and waviness. In line with the residual stresses, changes in the global deformation are highest during the first load cycles and tend to a saturation state.
- The formation of residual stresses and global deformation as described above is true if the loading conditions are constant from one braking to the next. Spectrum loading is closer to real service conditions but they complicate the investigation of processes occurring during heavy duty braking, e.g. approaching a saturation value for the tensile residual stresses is not evident any more.
- Thermal surface gradients that are characteristic for the pad material and the pad type will appear. These gradients may or may not change with increasing number of brake applications depending on changes in the friction mechanism and changes in the disk geometry.
- The identification and characterization of the formation and evolution of thermal surface gradients is necessary for the design of the simulation method. This may be carried out in a more realistic way using spectrum loading but it is easier if the loading conditions stay constant.
- Especially in the presence of thermal surface gradients, local temperature levels may exceed the A_1 temperature, where austenite starts to precipitate from the base microstructure. The subsequent cooling period will entail metallurgical transformations leading to microstructures in those regions that are different compared to the microstructure after manufacturing.
- Phase transformations are very likely to interact with the formation of residual stresses.
 1. The plastic history before the phase transformation is deleted
 2. Compressive stresses may be induced at the disk surface if cooling rates are high enough to cause metallurgical transformation involving an increase in volume (martensite, bainite)
 3. Cyclic plasticity, the build-up of residual stresses and crack initiation are different after a phase transformation since the transformed material behaves differently.
- The investigation of the loading conditions (hot spots, hot bands, etc.) has to be carried out with the aid of a thermal imaging system. Due to changing emissivity during testing, this method has to be combined with the results of a damage analysis of the tested disks. The test rig program must thus ensure the comparability and the combination of the results of thermography and the damage analysis.
- The test rig program has to cover the loading conditions that are most decisive for the fatigue life of the brake system under investigation and the assumptions concerning the in-service conditions the project team has agreed on at the outset of this research project. It has been shown by Dufrénoy et al. that service brakings on crowded railway networks can be more demanding for the brake disks than the rare events of emergency stops. In the case of the relevant train type(s) and tracks for the current study, it was decided that emergency stops will be chosen as a reference. These emergency stops are also representative for high energy service stops relevant for the reference train type.
- In order to establish proper contact conditions that are in agreement with railway standards a bedding-

1. INTRODUCTION

in process has to be carried out for each new pad disk combination before the actual test program can be started. The braking energy is much lower than for emergency or other critical brakings, but it still cannot be excluded that plastification and thermal surface gradients take place anyway. If this is the case, those phenomena will probably have an impact on the contact conditions during the high energy stops.

Given the scope and budget of the project as well as the available time on a full scale test rig, the following conclusions have been drawn for the planning of the test rig program:

- The characterization of the formation and evolution of residual stresses during the component test is imperative because this information can be used to verify the simulation results. Constant amplitude loading (in view of the dissipated energy) is thus reasonable. The danger, however, is that the loading conditions are harsh enough to cause phase transformations down to depths exceeding the measurement range of the X-ray device used for stress measurements. This risk is accepted.
- The investigation of thermal gradients during high energy braking is sufficient for the scope of this work. Interactions with load spectra, can be modeled later on — at least at a global scale although not at the level of hot spots. Constant amplitude loading is thus sufficient.
- The comparability between thermal images and the results of damage analyses can be guaranteed by having multiple disks at hand that were exposed to a various number of load cycles. Moreover, the formation of residual stresses and phase transformations can be studied in a systematic way.
- In a test sequence consisting of identical brake events and an increasing number of brake applications, the reproducibility of thermal gradients can be investigated because corresponding braking events will appear in the test rig program.

Based on these considerations, we have agreed on a program illustrated in Fig. 1.13. Its key figures are summarized below:

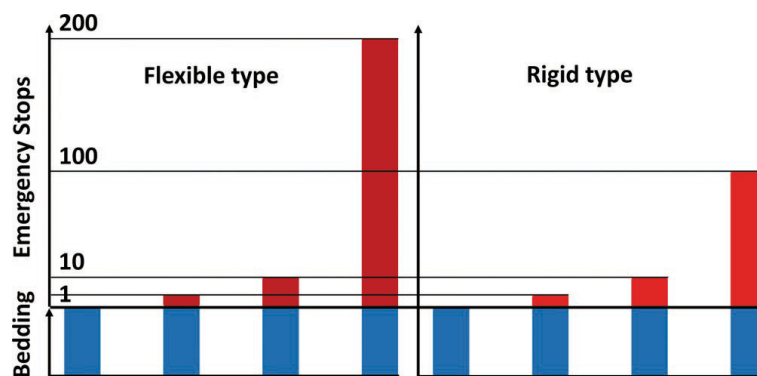


Figure 1.13: Overview of the test rig program.

- 2 test series with different pad types
- A series consists of 4 individual tests:
 1. Bedding-in process consisting of ~ 100 brakings with 5 MJ thermal input
 2. Bedding-in + 1 emergency stop with 25 MJ thermal input

3. Bedding-in + 10 emergency stops
 4. Bedding-in + 100 emergency stops (deviations from that value have occurred as illustrated in Fig. 1.13 and will be discussed in Chapter 3)
- Thermal images are taken systematically throughout the test program
 - Static and dynamic disk coning is measured systematically

The loading scenario that is carried out throughout component testing, apart from the bedding-in process, corresponds to a high energy emergency stop, as illustrated in Fig. 1.14a. The scenario is based on the assumption that all brake systems fail except the friction brake system. This means that a kinetic energy corresponding to 25 MJ must be dissipated by each brake disk corresponding to the disk type in focus. It should be noted that each brake disk consists of two friction rings and the energy values mentioned in this work always refer to the brake disks and not to individual rings. P_{max} refers to the maximum heat flux

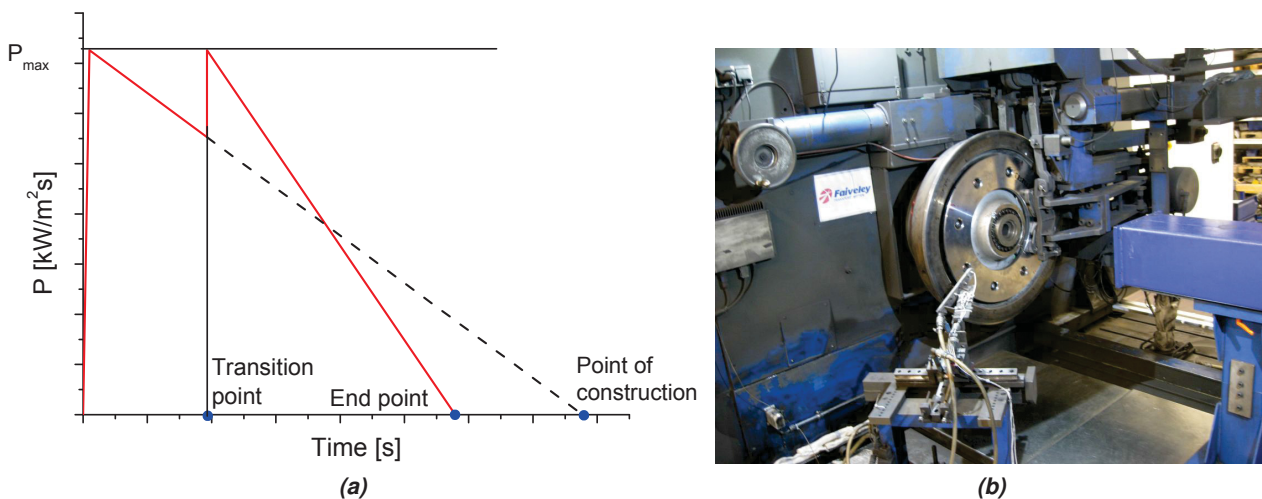


Figure 1.14: a) Schematic of the evolution of energy input over time b) Test bench used for component tests.

density specified by the disk manufacturer. For the chosen loading scenario, this corresponds to a clamping (brake) force of 45.1 kN being reached after the fill time of the brake cylinder (actuator) corresponding to t_{max1} which is reached after about 3s. According to [49], the fill time ranges from 3-5s for passenger trains and 18-30s for freight trains. In this context, 3s is a good value although it might seem slow in comparison to reaction times in passenger cars. One should keep in mind, however, that trains use air brake systems — at least for emergency braking — as explained above. The heat flux density decreases with the speed of the train which offers the possibility to increase the brake force in order to dissipate the thermal energy more quickly (t_{max2}). The initial speed is 250 km/h and the speed corresponding to t_{max2} is 190km/h. The brake application is continued to a full stop.

Fig. 1.14b shows the interior of the dynamometer test bench utilized for component testing, as previously mentioned. The test bench was manufactured by ZF and is equipped with an integrated caliper and actuator [87]. Original vehicle calipers are usually not used. Dry and wet test conditions are possible with a braked mass in the range of 315 kg up to 18315 kg. The thermal imaging system is positioned in the cuboid object on the right of Fig. 1.14b. The measurement system for static and dynamic disk coning is placed on the lower-left side of the wheel disk assembly.

Chapter 2

Theoretical background

2.1 Material physical processes in fatigue

Fig. 2.1 plots the individual stages of fatigue both in the physical and the technical context. These stages will be discussed in order to help the reader to understand the individual mechanisms, especially in the transition areas between the physical stages. The Kitagawa-Takahashi plot, a diagram with a very large and condensed amount of information, will be covered later in this subsection. It constitutes the link between the different stages shown in Fig. 2.1 and the reader should be able to see these links clearly. Section 2.2 elaborates on the effects occurring at increased temperature levels. These effects make fatigue predictions at high and varying temperatures a rather complex issue, as they start to interact with the mechanisms of pure fatigue and thus necessitate the use of proper test and simulation procedures. Fig. 2.1 illustrates the basic stages of fatigue crack formation and propagation. The whole process of fatigue is divided into five stages where distinct physical mechanisms can be detected and characterized. The end of a stage is reached when a new process starts to have an impact on the evolution of damage, where the term “damage” has not a consistent meaning throughout the five stages.

2.1.1 Dislocation movement and plasticity

The importance of dislocation structures can be discussed from the viewpoint of a macroscopic effect occurring during cyclic testing. The cyclic stress-strain response during the crack initiation stage, which is a noticeable portion of an LCF test, commonly involves increasing or decreasing hysteresis sizes on the σ -axis, for strain controlled, and on the ϵ -axis, for stress controlled, fatigue tests. This so-called cyclic hardening respectively softening depends on the dislocation substructure of the material and its changes during loading. As described by Hertzberg [37], the dislocation density of initially soft materials increases during cyclic loading, finally reaching a stable configuration characteristic for the material and the imposed strain. The material hardens until a saturation stress is reached. The dislocation structure of initially hard materials rearranges in new structures less resistant to cyclic deformation, which correspond to cyclic softening. The stabilized state for materials with high stacking fault energies (SFE) tends to be independent of the prior strain history. In pure copper, for instance, cyclic hardening and softening lead to the same stabilized condition. This phenomenon is mainly due to the increased dislocation mobility resulting from enhanced cross-slip enabled by the high stacking fault energy. The stabilized state of materials with a

2. THEORETICAL BACKGROUND

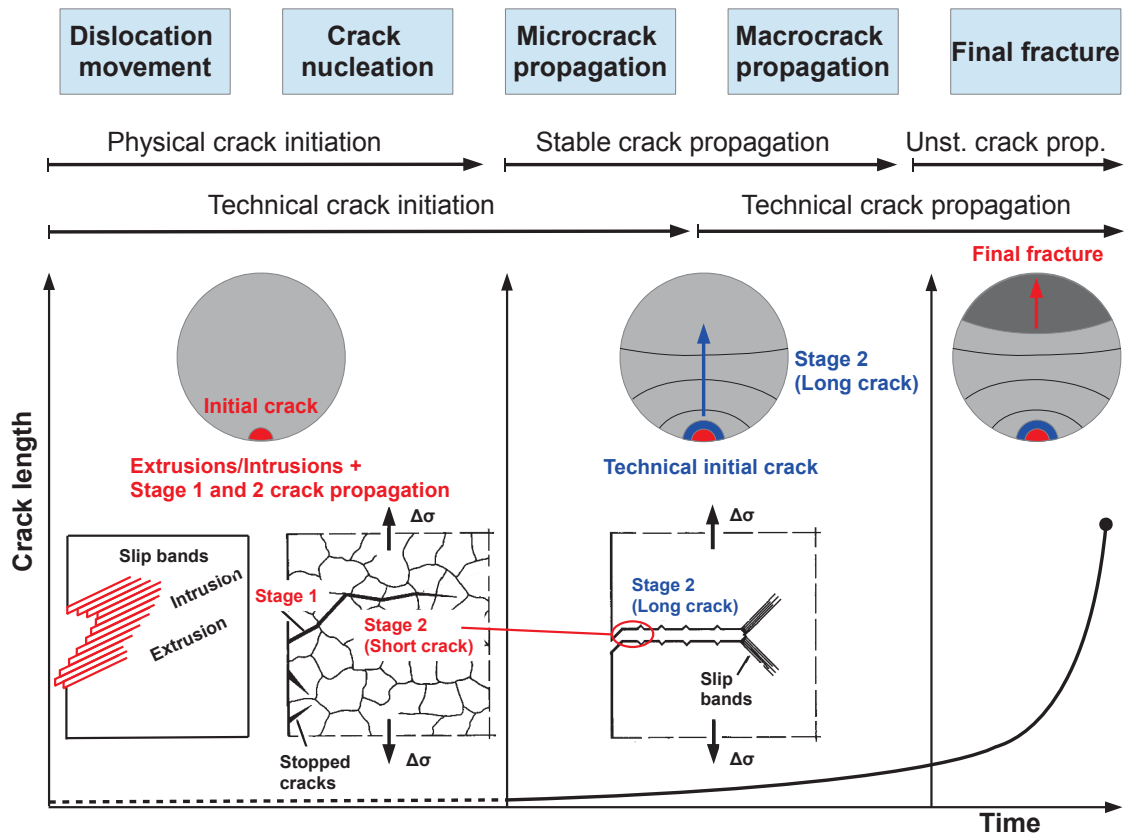
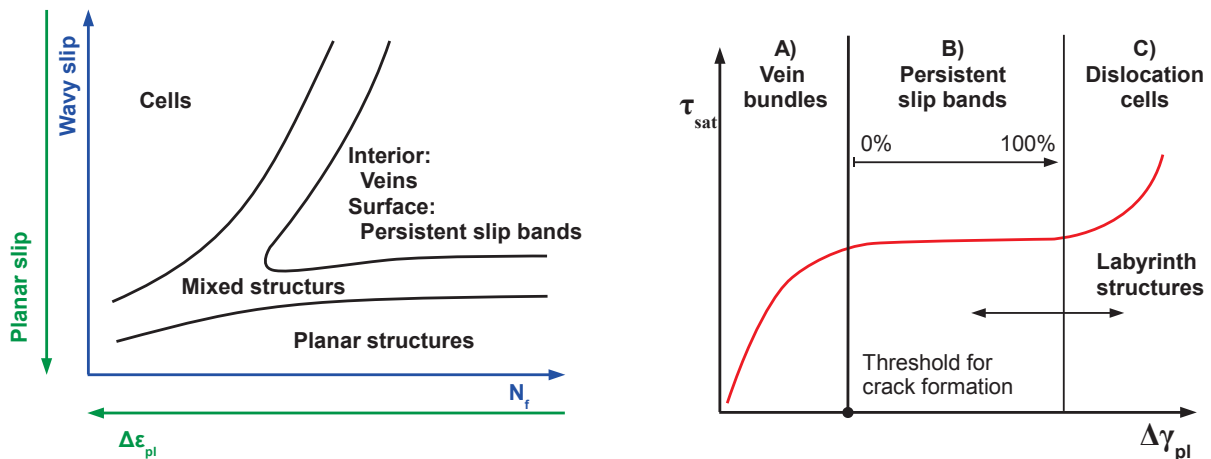


Figure 2.1: Overview of fatigue mechanisms (based on [6; 7]).

low SFE is commonly dependent on the previous strain history because the dislocation structures are not flexible enough to obtain a comparable configuration when they are cycled from a hard and soft material condition. The dislocation substructures mentioned earlier are manifold and difficult to characterize. The stabilized dislocation structures after constant amplitude loading are summarized in Fig. 2.2a and representative images from a transition electron microscope (TEM) are given in Appendix A.1. Planar slip refers to pure metals whose dislocations cannot leave their slip planes. This is caused by low SFE which prevents cross slip (unless thermally activated), leading in turn to two dimensional, planar dislocation structures. Wavy slip prevails in the case where dislocations are able to leave their planes (high SFE, cross slip is possible) causing three dimensional wavy structures, which can be very versatile, as will be illustrated further below. It should be noticed that the planar and wavy dislocation structure of alloys is mostly related to the SFE but sometimes it can be attributed to the presence of a short-range order rather than to the SFE alone [30]. This mechanism will not be further elaborated, however. The formation and evolution of dislocation structures manifests in the hardening behavior during cyclic testing but this is not their only impact on the fatigue behavior of a material. They determine how plastic strain is accumulated and concentrated in certain regions of the microstructure. The accumulated plastic strain and the related dislocation density is a measure for the fatigue damage at this stage. Dislocation structures are a complex issue taking place at microscopic level, they are thus seminal for the understanding of fatigue crack initiation, which is part of the main focus of this work. Despite the macroscopic approaches laid out in later sections it is important to be aware of the microscopic processes that are taking place. Suresh [9], Christ [22; 30], Basinski and Basinski [88] and Klesnil and Lukas [13] give very thorough insights into the



(a) Dislocation structures after cyclic stabilized cyclic loading (based on [22])

(b) Cyclic stress-strain curve for fcc single crystal oriented for single-slip (based on [9; 22])

Figure 2.2: Dislocation structures in fcc single crystals.

formation of dislocation structures and the following paragraphs shall draw on their works.

For **face centered cubic** (fcc) crystals that exhibit a wavy slip characteristic (often linked to a high stacking fault energy) the occurrence of dislocation veins, persistent slip bands (PSB) and dislocation cells can be observed in that order with increasing plastic strain amplitudes. At rather low levels of cyclic plastic strain dislocations accumulate on slip planes building veins. Edge dislocations with opposite orientations attract each other, resulting in the formation of dislocation dipoles. While screw dislocations have the possibility to annihilate each other, the number of dipoles consisting of edge dislocations evolves until they constitute the entire vein structure. In the end, the structure in the grain consists of elongated dislocation rich veins (up to 50% of the volume) separated by channels whose dislocation density is three orders of magnitude smaller. This state represents the transition state from region A to region B in the cyclic σ - ϵ curve for a fcc single crystal, shown in Fig. 2.2b (further information about cyclic σ - ϵ curves will be given in section 2.6). Since the veins can only accommodate a limited amount of plastic deformation, new structures start to appear when the imposed cyclic strain is increased. The structure of these persistent slip bands building up in the matrix of veins resembles ladders. Similarly to the veins in the matrix the rungs of the ladder structures consist of edge dislocation dipoles. Equivalently to the structure of the channels in the matrix, the channels between the rungs of the PSB contain screw dislocations but their density is three orders of magnitudes less compared to the veins and rungs, respectively. Plastic deformation concentrates in the PSBs and causes intrusions and extrusions at the surface. This is one mechanism for fatigue crack initiation since the intrusions/extrusions form sites of stress concentration. Additionally, the free surfaces on the slip planes oxidize and prevent reverse slip, at least in corrosive media. This leads to increased surface roughening and the transport of brittle material into the grain. The transition from A to B indicates the point from whereon classic fatigue crack initiation can take place. Region A is characterized by almost infinite fatigue life. A fcc single crystal oriented for single-slip (Fig. 2.2b) exhibits a cyclic stress-strain curve with a constant saturation stress in the region of mechanical loading where PSB occur (region B). This can be explained by the fact that the increasing plasticity is accommodated by an increasing volume of PSB until the PSBs fill the whole volume. Is the applied cyclic strain further increased secondary slip

2. THEORETICAL BACKGROUND

systems are activated, which appear as a new labyrinth or later on in new cell shaped structures (region C). In polycrystals the situation is similar with the exception that the density of PSBs is much higher in surface grains than in the bulk of the material. The plateau area depicted in Fig. 2.2b is thus specific for single crystals but not for polycrystals, with the exception of some coarse grained materials. In Fig. 2.2a a differentiation is thus made between the interior and the surface region.

The formation of dislocation structures in **body centered cubic** (bcc) single crystals is reported to be very different from the mechanisms previously discussed for fcc crystals. This is due to the different characteristics of screw dislocations [9]. Generally, there is a distinction between mechanisms at low and that at high strain fatigue for pure bcc metals. At low cyclic plastic strains, only edge dislocations move and hardly any hardening is observed. At higher strains, deformation involves both edge and screw dislocation, leading to the formation of a cell structure as well as to increased hardening. On the other hand, Christ concludes in [30] — after giving a review of primary sources — that the formation of dislocation structures in bcc alloys is very similar to fcc materials as long as the mobility of screw dislocations is sufficient. This is the case when testing is carried out either at very low strain rates or at high temperatures. The behavior of alloyed bcc metals is generally closer to fcc metals.

The previous discussion mostly refers to deformation in single crystals. Next, **polycrystals** will be discussed following [22]:

- In polycrystals single slip is limited to small plastic strain amplitudes.
- Multislip configurations (labyrinth and cell structures) occur thus at lower strain amplitudes as compared to single crystals. Region C will therefore grow at the expense of regions A and B.
- A differentiation between grains at the surface and in the interior must be made. The likelihood of the formation of PSBs in surface grains is much higher than in inner grains.
- As a result of the required compatibility between grains, different dislocation structures may be present in neighboring grains or even different regions inside individual grains.
- While in single crystals extrusions are the primary crack initiation sites, polycrystals are prone to surface grain boundary cracking which is due to the interaction of PSBs with grain boundaries.

A recent review on dislocation structures in single- and polycrystals and their significance from a crack initiation point of view is given in [89].

As indicated in Fig. 2.2a, there are no changes in the dislocation structure of metals with a planar slip characteristic. From transmission electron microscopy it can be seen that edge dislocations form bands with regions of low dislocation density between them. With increasing cyclic strains the dislocation density within the bands grows while their distance becomes smaller. Nevertheless, no PSBs or cells appear. A typical feature of these metals is a very slow hardening behavior which often has not even stabilized at failure.

2.1.2 Crack initiation

Plastic deformation involves dislocation movement, which is accomplished either by twinning or by slip. As slip is the primary mechanism in most polycrystalline alloys, strain localization along slip bands is primordial for crack initiation [89]. The sites where cyclic plasticity is the least constrained are at the surface or slightly beneath. At the same spot also concentrations of plastic strain are likely to occur further promoting

PSBs. The period involving nucleation and growth of a microcrack is thus a surface phenomenon that is strongly dependent on stress concentration factors (K_t) near the surface and the material structure of the grain that contains the eventual microcrack [7]. When the microcrack has successfully passed through a series of adjacent grains, the dependence on the surface condition decreases and crack propagation is increasingly governed by stress intensity factors (K) — which will be discussed further below — and bulk properties, like the crack growth resistance. In general, the preferred crack initiation sites according to Klesnil are [13]:

- Slip bands, which are the most frequent initiation sites.
- Grain boundaries, especially at high strains and high temperature. Usually PSBs are involved in this mechanism in the sense that they interact with grain boundaries.
- Surface inclusions if sufficiently large particles are present in the material.

According to Lukas [30], it makes sense to interpret the damage in the prenucleation phase of a microcrack as a function of the global plastic strain amplitude — which correlates with the local one — and the number of cycles. The appearance of damage is difficult to define and might be seen as the height and depth of extrusions and intrusions. When a microcrack has reached stage 2 growth (stage 1: crystallographic growth controlled by shear stress; stage 2: non-crystallographic growth controlled by normal stress) the appearance of fatigue damage is easier comprehensible, being simply proportional to the crack length. The period between nucleation and stage 2 growth is to some extent a special case. Usually a whole set of microcracks ($\sim 6\text{-}9\ \mu\text{m}$) forms simultaneously and their interaction is essential for the further propagation of individual cracks. The extent of damage at this stage depends on the spacing between the microcracks, which in turn can be assessed in two ways:

1. For materials loaded around the fatigue strength, the damage can be defined as the longest crack length.
2. At higher levels of stress and strain it is better to use the microcrack density as a measure for the damage, which is linked to the relaxation of strain. A large level of relaxation will prevent the nucleation of further cracks and promote the stage 2 propagation of the dominant cracks in the already existing network due to strain redistribution.

The points discussed in the last paragraphs are the basis for the development of physically based models for crack initiation. Sangid et al. [90] have published a crack initiation model based on the formation and evolution of PSBs in a polycrystalline Ni-based superalloy (U720) in dependence of the grain size, grain orientation and coincident site lattice value Σ , where $\Sigma = (\text{volume of unit cell of coincident lattice}) / (\text{volume of unit cell of crystal})$. The microstructural information is incorporated into an energy balance of PSBs that is used as initiation criterion. The rationale behind this procedure is based on the mechanisms discussed so far and the results of further investigations. The development of PSBs in polycrystalline nickel was investigated in detail by Weidner et al. in [91] with focus on the fraction of grains with PSBs in the microstructure and the volume fraction of the PSBs within these grains. Furthermore, it was found that the likelihood for the appearance of PSBs in a grain increases with the grain size which underlines the significance of the incorporation of the microstructure in a physically based crack initiation model.

2. THEORETICAL BACKGROUND

2.1.3 Small crack growth

Lukas further states that the transition from crack initiation to propagation is equivalent to the transition from a system of microcracks, whose behavior is strongly linked to local cyclic plastic strain, to crack propagation of individual cracks that behave in line with fracture mechanics. The end of the nucleation phase is thus strongly linked to the aforementioned definitions of damage. In both cases the end is marked by the formation of a small crack. The second definition, however, yields larger cracks at the end of nucleation which cannot propagate below the fatigue limit σ_F and are compatible to the transition from microstructurally to physically small cracks. In the overview given by Riemelmoser and Pippan in [92] microstructurally small cracks¹ are in the order of the characteristic length scale of the microstructure similar to the grain size. At 5 to 10 times this size the cracks are not strongly influenced by the local grains and propagate perpendicular to the main loading direction. Nevertheless, they do not yet behave like long cracks since they are too small to develop crack closure effects to the same extent as large cracks. These cracks are called physically small. Further information on microstructurally and physically small cracks is given in [10]. The second definition further implies that the end of the nucleation stage corresponds to a critical crack size where cracks initiated at σ_F stop, which typically happens when the microcrack approaches a grain boundary². This in turn is the link to the fatigue limit usually determined from S-N curves, as will be discussed in the following. This link can be visualized by the aid of Kitagawa-Takahashi (KT) diagrams, as plotted in Fig. 2.3.

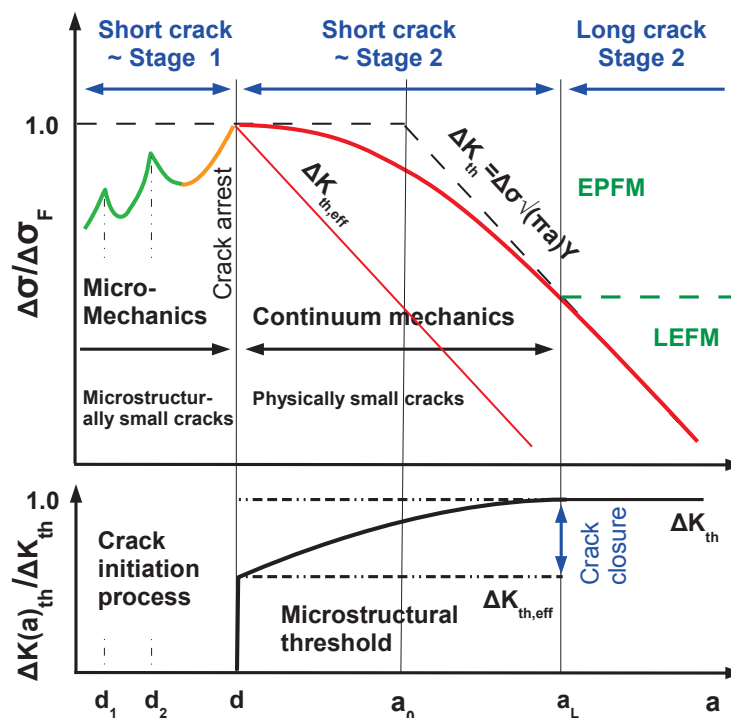


Figure 2.3: Kitagawa-Takahashi diagram and evolution of crack propagation threshold, both based on [8; 9; 10].

¹Or short cracks, the term used for the case of specimens where the crack is small in two dimensions but not the third one, corresponding to the thickness of the sample

²It should be noticed that crack arrest can also occur after the crack has grown out of the influence of microstructural barriers. In this case, the cracks are called physically small and crack arrest is linked to the formation of plastic crack closure.

The left side of the Kitagawa-Takahashi plot represents the part of fatigue where a crack nucleates and either manages to keep growing, finally becoming a physically small crack or is arrested in the microstructure of the material. Whether the former or the latter happens depends on two factors: First, the applied load and second the strongest obstacle in the microstructure through which the crack has to pass. Such an obstacle is commonly a grain boundary or a bainite/martensite lath [10] and the distance d of this obstacle from the surface equals the crack length, where a crack initiated at σ_F stops. In view of the loading there is a critical stress range $\Delta\sigma_F$ that indicates the boundary where a microscopic crack may pass or stop at d . Below d cracks are initiated but they stop at microstructural barriers at distances smaller or equal than d . This is the aforementioned physical link between the fatigue limit of an S-N curve and cyclic fracture mechanics. The propagation behavior of physically small cracks is neither governed by the local cyclic plastic strain as in the initiation phase, nor by the stress intensity factor defined for long cracks. The meaning of the stress intensity K will be discussed in detail in Section 2.1.5. At this stage it can be taken as a measure for the loading conditions at the tip of a crack. El Haddad et al. [93] investigated their propagation behavior and suggested possible means to describe the KT diagram. In line with Kitagawa and Takahashi they used a length scale according to Eq. (2.1).

$$a_0 = \frac{1}{\pi} \frac{\Delta K_{th}}{\Delta\sigma_F} \quad (2.1)$$

This signifies the transition length between the two domains in Fig. 2.3 and was not given a further physical meaning, except for being a kind of a measure for the reduced flow resistance at the surface. In [93] it was empirically shown, however, that the addition of a_0 to the actual crack length makes it possible to obtain threshold values ΔK_{th} that are independent of the crack length. Moreover, the El Haddad equation, Eq. (2.3), allows the estimation of a threshold in terms of stress for crack propagation or crack arrest, which corresponds to the thick red curve in Fig. 2.3.

$$\Delta K_{th} = \Delta\sigma_{th}\sqrt{\pi a} \rightarrow \Delta K_{th} = \Delta\sigma_{th}\sqrt{\pi a + a_0} \quad (2.2)$$

$$\Delta\sigma_{EH} = \frac{\Delta K_{th}}{\sqrt{\pi(a + a_0)}} \quad (2.3)$$

An alternative expression for the threshold is given by Chapetti [10; 94] where ΔK_{dR} signifies the microstructural threshold ($\Delta K_{th,eff}$ in Fig. 2.3) and ΔK_{thR} refers to the mechanical threshold of long cracks (ΔK_{th} in Fig. 2.3). The material parameter k (Eq. (2.5)) is a function of the microstructural and mechanical parameters used in Eq. (2.4), which are $\Delta\sigma_F$, d , and ΔK_{thR} , where d and ΔK_{thR} are computed to the microstructural threshold ΔK_{dR} (according to Eq. (2.6)).

$$\Delta\sigma_{Chapetti} = \frac{\Delta K_{dR} + (\Delta K_{thR} - \Delta K_{dR})[1 - e^{-k(a-d)}]}{Y\sqrt{\pi a}} \quad \text{for } a \geq d \quad (2.4)$$

$$k = \frac{1}{4d} \frac{\Delta K_{dR}}{\Delta K_{thR} - \Delta K_{dR}} \quad (2.5)$$

$$\Delta K_{dR} = Y\Delta\sigma_F\sqrt{\pi d} \quad (2.6)$$

2. THEORETICAL BACKGROUND

The equations above are means to estimate the critical cyclic stress range as a function of crack length where small cracks will grow. Radaj [8] gives an overview of methods to estimate the propagation rates da/dN of small cracks in the vicinity of the corresponding threshold value $\Delta\sigma_{th}$ (Fig. 2.3 top) and ΔK_{th} (Fig. 2.3 bottom), respectively.

2.1.4 Long crack growth

Fig. 2.4 provides an illustration of the various regimes of fracture mechanics, both for static as well as cyclic loading conditions. The difference between the four depicted cases a-d lies in the amount of plasticity occurring in front of the crack and in the sample in general. Fig. 2.4a) shows the case of ideal brittle behavior without any plastic deformation. Linear elastic fracture mechanics (LEFM) can be applied to characterize both fatigue crack propagation and the stability of the cracks in view of instantaneous failure in this sample. Fig. 2.4b) plots a sample with a plastic zone ahead of the crack that is smaller than 1/50 of the sample dimensions. This case is called small scale yielding (SSY) and LEFM is still applicable. Fig. 2.4c) shows the case of large scale yielding (LSY) where the plastic zone is larger than in the case of SSY and additionally plastification may occur at the back side of the specimen. In general yielding (Fig. 2.4d)) both plastic zones grow together. Materials experiencing LSY or general yielding do not follow the rules of LEFM and elastic plastic fracture mechanics (EPFM) must be applied. In the case of SSY,

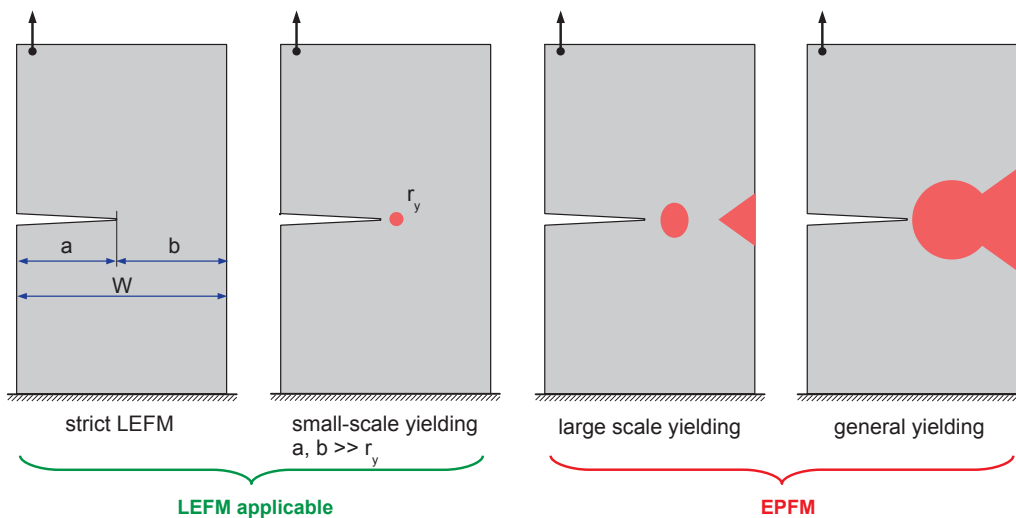


Figure 2.4: Regimes of fracture mechanics [11; 12].

the stress and strain fields ahead of the crack tip can be characterized by a single parameter, i.e. the stress intensity K , which has been already introduced in its cyclic form in Section 2.1.3, which describes the stress field in the ligament outside the plastic zone according to Eq. (2.7). Here the higher order terms take into account the evolution of σ towards the nominal stress in the cross section while the first term models a stress singularity at the crack tip as illustrated in Fig. 2.5a. Since this term fully characterizes the stresses at the tip the non-singular terms are usually neglected in LEFM [12]. However, the stresses in the elastically deformed zone cannot be described anymore when the singularity drops down to the order of the nominal stress. Plastic deformation occurs close to the crack tip, which consumes the region following

the description by K , as illustrated in Fig. 2.5b. This is one reason why the plastic zone must be small for LEFM to be valid.

$$\sigma_{ij} = \frac{K}{\sqrt{2\pi r}} f(\theta) + \text{non-singular terms } (\propto r^{\frac{m}{2}}) \quad (2.7)$$

In static fracture mechanics, K can be calculated from Eq. (2.8), where the factor Y is introduced into the equation to take the crack shape into account (e.g. Y equals 1.12 for a surface edge crack). The corresponding quantity for the case of fatigue loading is the stress intensity range according to Eq. (2.9). For complicated geometries the stress intensity can be determined on the basis of FE calculations. The procedure for determining K in this case is given in chapter “2.16.2 Stress intensity factor extraction” of the Abaqus theory manual [45], for instance. Apart from its meaning as scaling factor of the stress and strain fields it is also useful as a stability criterion because it is possible to determine a technological property K_C , called the fracture toughness, by proper experiments. Section 2.1.5 will further expand on this primordial fracture mechanical quantity.

$$K_I = Y\sigma\sqrt{\pi a} \quad (2.8)$$

$$\Delta K_I = Y\Delta\sigma\sqrt{\pi a} \quad (2.9)$$

In fatigue the status depicted in Fig. 2.5b is only a snapshot of the end of the first half cycle and a load reversal occurs subsequently. Fig. 2.5c shows the specific stress field due to the second half cycle which introduces again a plastic zone. The real situation is obtained by the superposition of the two individual stress fields as plotted in Fig. 2.5d [13]. After the superposition it becomes clear why the yield limit in the second half cycle of this simplified model is chosen as $-2\sigma_y$, since the final yield point after both half cycles ends up at $-\sigma_y$. Furthermore, the meaning of the two plastic zones with the corresponding sizes r_m and r_c becomes clearer. The quantity r_c refers to the size of the cyclic or reversed plastic zone where the cyclic change of the stress distribution yields zero mean stress, i.e. the stress distribution is completely reversed in each half cycle. The stress field in the monotonic zone on the other hand is not completely reversed, yielding non-zero mean stress over one cycle. The cyclic plastic deformation at the crack tip gives rise to fatigue crack propagation above a certain threshold for the stress intensity range ΔK_{th} , which will be further elaborated in the subsequent paragraph.

The evolution of the threshold for fatigue crack propagation in terms of stress intensity range, as shown at the bottom of Fig. 2.3, can be interpreted as R-curve (resistance curve) in analogy to static fracture mechanics [95]. From the point on where the threshold does not change with crack length any further, the build-up of crack closure effects is completed and the crack is in the long crack regime, where classical cyclic LEFM can be applied. The curves in Fig. 2.6a are each valid for a specific load ratio defined by Eq. (2.10). Due to the fact that crack closure effects vary with the tensile portion of the external load, the curve corresponding to the higher load ratio R_2 is shifted to the left, which indicates a lower threshold ($\Delta K_{th,R2} < \Delta K_{th,R1}$) for the onset of crack growth and higher propagation rates for comparable values of the stress intensity range ΔK . Nevertheless, both curves show a linear and parallel propagation characteristic in regime B as indicated in Fig. 2.6a, which is also called the Paris region. The scale on the right hand side of Fig. 2.6a illustrates that most of the service life of a component after the initiation of a

2. THEORETICAL BACKGROUND

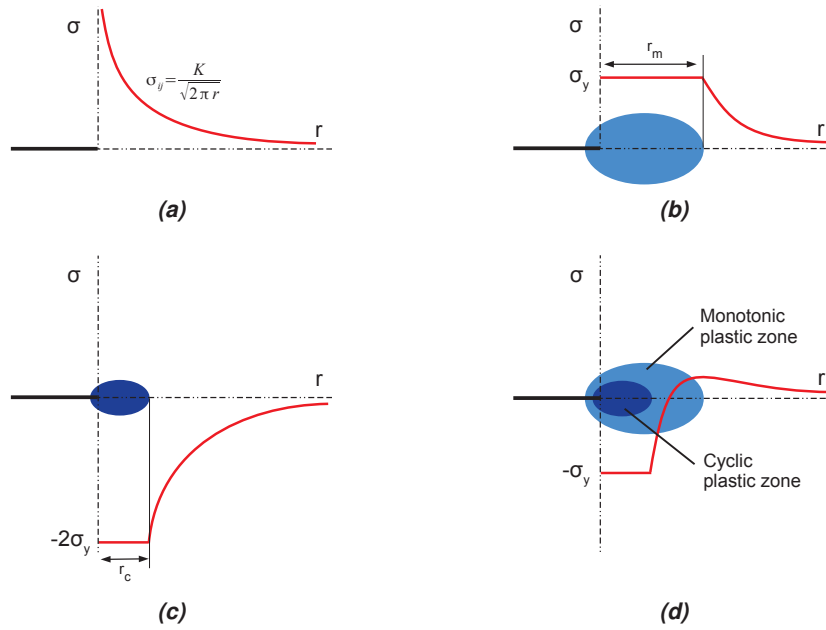


Figure 2.5: a) Meaning of the stress intensity factor K for the case of an ideal brittle material, b) idealized stress field due to ideal-plastic deformation in monotonic plastic zone, c) idealized stress field solely due to load after load reversal illustrating the formation of a cyclic plastic zone, d) approximation of the real stress field after load reversal as superposition of stress fields b) and c) [13].

technical crack, namely a crack that can be detected by non-destructive testing, is situated in the lower part of the crack propagation curve. Regime B is thus meaningful because, on the one hand, it comprises a large portion of the fatigue life and, on the other hand, crack propagation that is detectable during service checks takes place. The Paris equation, Eq. (2.11), describes crack propagation in regime B and its integrated form allows the estimation of crack elongation in the course of a specific number of load cycles (see [33]). This information can be used either for the definition of service intervals or analyses whether the component will last until the end of its service life or not. Complex loading conditions require individual tests for a set of load ratios and temperatures within the relevant range of values. It should be noted that the methods of cyclic LFM are based on the concept of similitude. This concept suggests that the propagation rate is purely a function of ΔK and R ($\frac{da}{dN} = f(\Delta K, R)$), i.e. independent of the previous loading history. In the case of overloads and variable amplitude loadings the concept of similitude does not apply and this fact must be considered for the interpretation of the results (as will be done in Chapter 6). An example for a special technique to evaluate variable amplitude loading is given in [96] but methods of this kind are not within the scope of this work.

$$\Delta R = \frac{\sigma_{min}}{\sigma_{max}} = \frac{K_{min}}{K_{max}} \quad (2.10)$$

$$\frac{da}{dN} = C \Delta K^m \quad (2.11)$$

Fig. 2.6b gives an overview of a test procedure proposed by Tabernig and Pippan [95]. They suggest precracking under pressure loading (see Fig. 2.6b, 1) upper left). During the first compressive load the

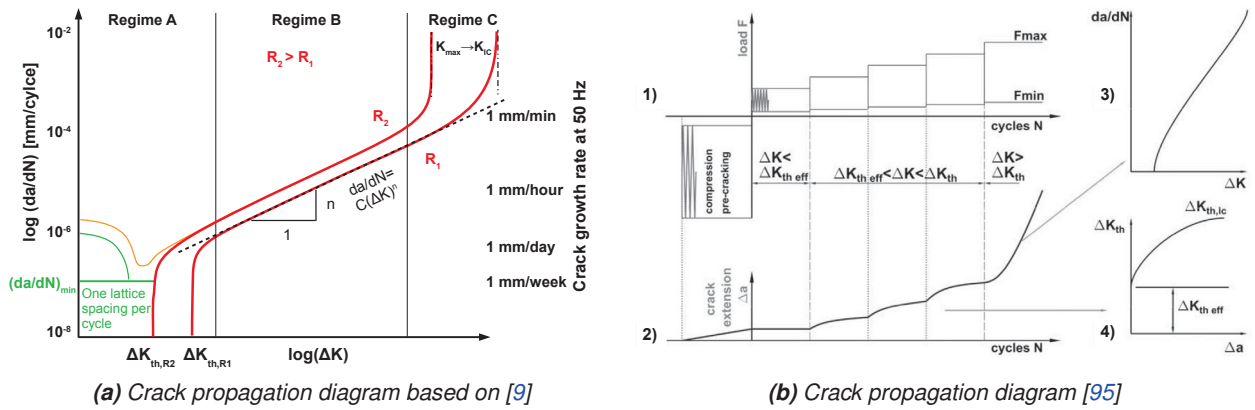


Figure 2.6: Characterisation of long crack propagation behavior.

monotonic plastic zone is formed, which induces tensile residual stress after unloading, except in the cyclic plastic zone, which is rather small in comparison. This cyclic plastic zone will move along with the propagating crack under continued loading simultaneously decreasing in size as the necessary load to close the crack continuously increases. During this process the propagation rate decreases until the crack finally reaches the end of the monotonic plastic zone formed during initial loading, where the precrack will stop. This entails a certain distribution of residual stress around the crack tip, which is favorable for the subsequent characterisation of the crack propagation behavior. The crack tip is engulfed by a small region with tensile residual stress that causes a negative closure intensity factor. This means that the crack will be open at the beginning of the fatigue growth test. As can be seen in Fig. 2.6b 1) and 2) the cyclic testing force can now be increased stepwise until the precrack begins to grow, in turn yielding the intrinsic propagation threshold $\Delta K_{eff,th}$. This value theoretically corresponds to the microstructural threshold indicated in Fig. 2.3, but the precrack might be longer than d (the distance of the largest microstructural obstacle from the surface). Due to the build-up of crack closure the crack stops and several load increments are necessary to finally produce a constantly propagating crack. The two increments, a) where crack arrest occurs for last time and b) the crack grows continually beyond that point, determine the lower and upper bound for the long crack threshold ΔK_{th} very accurately. As plotted in Fig. 2.6b, the standard crack propagation curve can be measured from that point on (3); the R-curve may be deduced from the propagation behavior prior to continuous growth (4).

This procedure allows a very thorough characterization of both the short and the long crack growth behavior. It comes with a major drawback however, since it may lead to very long testing times. The load increase must not be too coarse otherwise the R-curve would not be resolved sufficiently well. On the other hand, the load increments must not be too small either as oxide induced closure from the previous step may prevent crack propagation. According to [95] the increase of the load amplitude should be 10% or more. If little knowledge exists on the tested material, or its behavior under specific loading conditions, the determination of the threshold behavior is tedious and time consuming, since many increments may be required until the intrinsic threshold and finally the long crack threshold are found. Whenever the R-curve is not required a different procedure may be opted for. In contrast to the previous method — which will be designated *bottom-up* method — an alternative *top-down* method exists, which is in accordance with ASTM E647. The starting point of crack propagation in this context is set close to the fracture toughness

2. THEORETICAL BACKGROUND

K_{IC} and precracking is thus established at greater loads causing a longer initial crack of about 1 mm. From then on, the external load is constantly reduced until the crack stops. This way the crack propagation curve and ΔK_{th} can be found in a faster but less accurate manner. Due to the formation of crack closure at the initial stage of the experiment, the short crack regime is not accessible. Both procedures are applied in the scope of the present work and Fig. 2.7 provides a direct comparison.

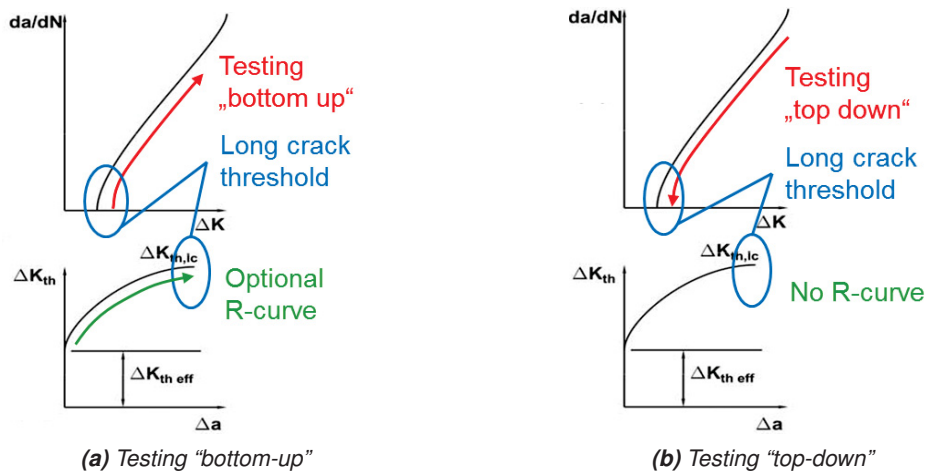


Figure 2.7: Comparison of testing procedures applied in the project.

To sum up, Fig. 2.8 illustrates the areas where the two representations, the S-N curve and the crack propagation curve, meet. The areas marked green refer to loading situations where cracks initiate but then stop due to some microstructural barriers within the first couple of grains they encounter¹. The Kitagawa-Takahashi plot contains the necessary data to understand the link between the global view of the related fatigue strength σ_F in the S-N diagram and its physical meaning illustrated by crack propagation experiments. Some further information is given by Schijve in [97]. Whether a crack shaped defect is viable under certain loading conditions or not can be determined by the aid of cyclic fracture mechanics. Moreover the propagation rate and thus the number of load cycles until a specified crack length can be computed. Examples for procedures describing the propagation of single cracks and crack arrays are described in detail in [33; 98]. Besides the information on how long it takes for a crack to reach a certain length, cyclic fracture mechanics also yields information on the maximum length a crack can obtain, because in strain controlled problems the crack driving force diminishes with increasing crack length after an initial peak, which is close to the surface region [33]. When ΔK drops below the threshold value ΔK_{th} cyclic crack propagation stops, at least if there are no loads in the load spectrum that entail ΔK values lying above the threshold. In the case the dominant cracks in the component have stopped, the only threat in terms of fatigue design is a single overload that may induce fast fracture. In the case of railway braking, for instance, the load spectra on the relevant tracks need to be analyzed. The procedures for the evaluation of possible fast fracture events are discussed in the subsequent paragraph.

¹When microstructurally small cracks continue to grow and become physically small cracks, there is still the possibility that they stop. This is due to the formation of crack closure effects, which increase ΔK_{th}

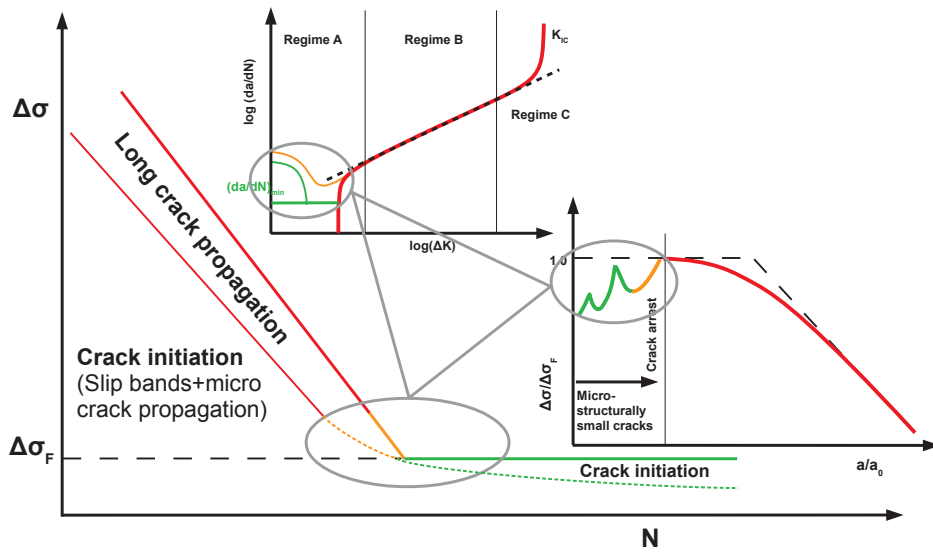


Figure 2.8: Correlation between S-N curve, crack propagation curve and Kitagawa-Takahashi plot.

2.1.5 Final fracture

Under stress controlled loading conditions the maximum stress intensity during the load cycle may increase with increasing crack length. In this case the fatigue crack propagation might not continue until the load bearing cross section has decreased to zero. Unstable crack growth will occur instead, which is equivalent to instant failure. The applicable criterion for the occurrence of unstable crack growth, at least as long as LEFM is valid, is stated in form of Eq. (2.12). The quantity on the left of Eq. (2.12) has already been introduced leaving only the quantity to the right open for discussion. Since its significance for fracture mechanics is essential in view of stability analyses of cracks, the subsequent paragraphs will expand on its physical meaning and proper testing procedures. As has already been noted, its validity is only given in the scope of LEFM and thus some methods of EPFM will also be treated towards the end of this section. The fracture toughness K_C is a quantity characterizing the tested material in view of its fracture mechanical behavior, but it also depends on the specimen type and its dimensions. For this reason it is called a technological quantity that characterizes the resistance of the material against crack propagation under similar loading conditions. Hence, K_C describes the resistance against crack growth of the material and K represents the crack driving force generated by the loading conditions. A criterion for unstable crack growth and thus failure can be defined by comparing the two quantities as shown by Eq. (2.12).

$$K_I \geq K_{IC} \tag{2.12}$$

At this point it is important to notice that it is possible to get a value for K_C which is, for the most part, dependent on metallurgical features in the material and not on the geometry. This is the classic approach described in ASTM E 399 [35], which is based on using sample geometries promoting plane strain conditions in the sample as shall be further discussed below. This quantity is commonly referred to as *plane strain fracture toughness* or K_{IC} .

Additional information on the determination of K_{IC} and alternative quantities from elastic-plastic fracture mechanics is given in Appendix A.2.

2.2 Material physical processes in creep

2.2.1 The stages of creep — Overview

At temperatures where thermally activated processes are beginning to take effect — typically at temperatures above 0.3-0.5 times the homologous temperature (T/T_S) — the previously discussed processes are becoming more complicated as further mechanisms add to fatigue damage, namely creep and oxidation. For the case of a cylindrical sample that is exposed to a fixed force in axial direction at high temperature — meaning that there is static loading without fatigue loading — the basic mechanisms of pure creep damage can be investigated, as shown in graph 2.9. Fig. 2.9a) illustrates a creep curve in terms of ϵ over time.

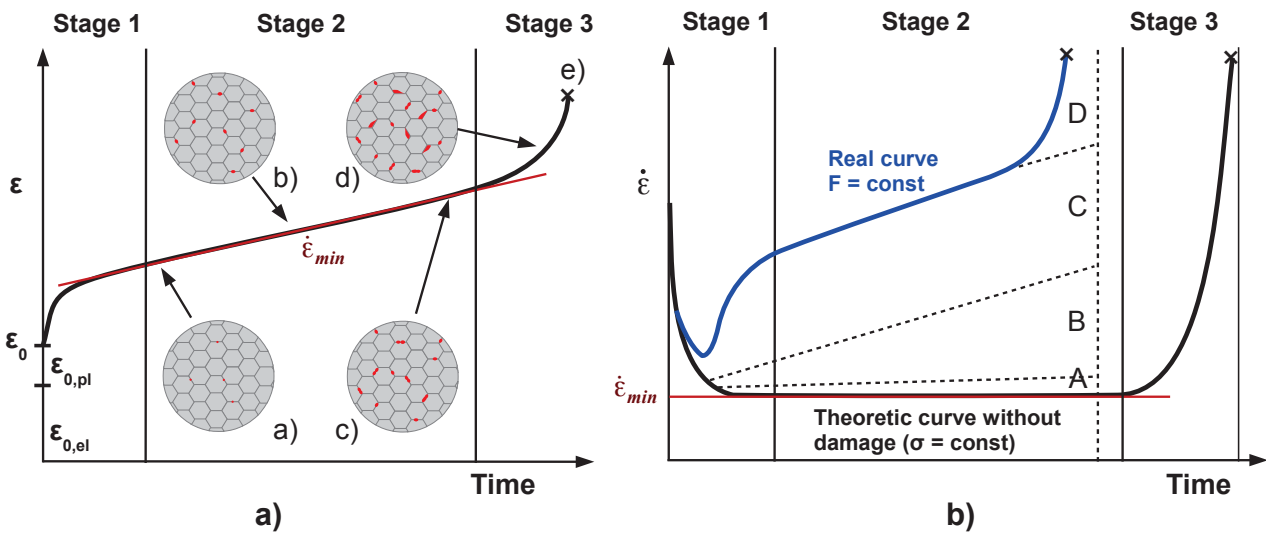


Figure 2.9: Overview of creep mechanisms (based on [14]).

When σ_0 is applied an initial strain $\neq 0$ is established immediately, consisting of an elastic and a plastic part (if $\sigma_0 > \sigma_y$). From then on a stabilization process occurs between hardening and softening (recovery) in stage 1 [14]. This process is linked to a change in the dislocation substructures that increases the resistance to dislocation motion. The equilibrium is attributed to a stable substructure and a dynamic balance between hardening and softening. This results in a constant strain rate $\dot{\epsilon}$, which is typical for stage 2 of the creep curve. A constant value for $\dot{\epsilon}$ can only be achieved, however, if the true strain ϵ_{true} is used. This part of the curve commonly constitutes the largest part of the creep life and is seminal for modeling techniques. Stage 3 is characterized by an increase of the strain rate which is due to the development of damage in the material, like pores and cracks. It should be noticed that significant deviations occur in the stages 1 and 2 between stress and force controlled experiments, since the cross section varies with increasing strain [37]. While force control is often used for engineering purposes, stress control is the first choice for scientific research on creep mechanisms and the formulation of mathematical creep laws. According to Buerger [14] the evolution of creep damage follows as indicated in Fig. 2.9a) the order:

a) Crack nuclei \rightarrow b) growth to micro-pores (cavities) \rightarrow c) chains of pores \rightarrow d) microcracks \rightarrow e) macroscopic cracks \rightarrow failure

Fig. 2.9b) shows the representation based on the strain rate $\dot{\epsilon}$ more frequently used in scientific contexts. The minimum strain rate in stage 2 is indicated, as well as possible effects that may cause a deviation from

this often simplistic behavior:

A Oxidation

A Increase of the stress level with regard to σ_0 due to a reduction of the cross section with increasing strain

A Changes of the hardening state of the material

- Changes in the dislocation structure, especially in predeformed or hardened materials
- Changes in the particle structure of dispersion hardened materials

A Formation and growth of pores and cracks

At this point it is important to notice the different often ambiguous usage of the term creep. On the one hand this term is often used in the sense of **creep deformation**, which is important from the point of view of modeling strategies in this work. As noted in Section 2.1 the crack initiation life is governed by plastic deformation. At high temperatures it is more appropriate to speak of inelastic deformation since plastic deformation is accompanied by creep deformation. These two contributions may be modeled separately by the combined use of a plasticity and a creep law. Nevertheless, other models exist that take into account the fact that a distinction between plastic and creep deformation is not necessary or even impossible. This is due to their physical link — the dislocation motion — over wide ranges of temperature and strain rates. This second type of material models are called viscoplastic models and describe all inelastic strains with one variable, the viscoplastic strain ϵ_{vp} . These models will be further elaborated in Sections 2.5.1 to 2.5.3. Apart from the meaning referring to a deformation behavior the term creep often relates to the damage behavior, i.e. **creep damage**, which is illustrated in Fig. 2.9a). Evidently this meaning is important from the point of view of models describing crack initiation life. In the present application, fatigue damage and damage due to creep/relaxation occur at the same time. The fatigue part, both governed by plastic deformation and creep deformation, prevails in the case of emergency stops since the braking process is rather short as compared to classic creep problems like steam and gas turbines. For this reason, the mechanisms leading to initiation of cracks in brake disks follow the scheme presented in rather Fig. 2.1 than in Fig. 2.9a), with the difference that also rate dependent inelastic deformation takes place. In the case of hold braking, which occurs on downhill passages on railway tracks, creep damage has a higher impact on the overall crack initiation but this is not the focus in this work. Various methods for the modeling of damage are compared in Section 2.6.

2.2.2 Creep mechanisms

Primary creep at low temperatures is commonly described by a logarithmic dependency between true strain (ϵ_t) and time, as indicated by Eq. (2.13) [37]. This behavior is called logarithmic creep and holds for $0.05 < T_h < 0.3$. For higher temperature ranges a parabolic dependency was found (Eq. (2.14))

$$\epsilon_t \propto \ln(t) \quad 0.05 < T_h < 0.3 \quad T_h = \frac{T}{T_m} \quad (2.13)$$

$$\epsilon_t = \epsilon_{t,0} + \beta t^m \quad 0.2 < T_h < 0.7 \quad (2.14)$$

2. THEORETICAL BACKGROUND

Both equations yield a decreasing strain rate with time of the form of Eq. (2.15), where n equals 1 at low temperatures (logarithmic creep) and decreases with temperature and stress. In the higher, parabolic regime, $m = 1 - n$

$$\dot{\epsilon} \propto t^{-n} \quad (2.15)$$

Eq. (2.14) can be expanded by an additional term to extend the validity of the equation to secondary creep. If m is defined as 1/3, Eq. (2.16) corresponds to the well known equation proposed by Andrade (see Table 2.7).

$$\epsilon_t = \epsilon_{t,0} + \beta t^m + \dot{\epsilon}_{t,ss} t \quad \text{ss...steady state} \quad (2.16)$$

As previously noted, the decreasing creep rate during primary creep is linked to changes in the dislocation structures. As for the case of plastic deformation and fatigue discussed in Section 2.1 the formation of dislocation structures is one pivotal physical mechanism for creep deformation and creep damage. At this point a brief summary is given for the specific condition under creep based on [14; 99]. The external, applied stress can be divided into two parts as indicated in Eq. (2.17). σ_i compensates the impact of the dislocations and other features in the region surrounding the current subdomain on the local stress field and σ_{eff} remains to act on the local dislocations causing dislocation glide and thus inelastic deformation. The decrease of $\dot{\epsilon}$ in the primary creep region is due to a decrease of the effective stress σ_{eff} . The reason for this decrease is the increase of long range internal stress linked to an increase of the dislocation density and the formation of subgrains, i.e. domains within individual grains formed by aligned edge dislocations. The stabilization of this structure is accompanied by an equilibrium between the creation and annihilation of dislocations. This state involves the stabilization of σ_{eff} and thus marks the end of primary creep.

$$\sigma = \sigma_i + \sigma_{eff} \quad (2.17)$$

Secondary creep is commonly represented by a power law of the form:

$$\dot{\epsilon} \propto \sigma^n \quad (2.18)$$

In the following the indices t for true strain and ss for steady state strain will be dropped. Eq. (2.18) is a good approximation as long as dislocation creep is the predominant deformation mechanism. This is the case for wide ranges of temperatures and stress levels. Nevertheless, at very high stress levels this relationship does not hold any more because higher strain rates are observed. After this so-called power law breakdown the steady state creep rate is better approximated by an exponential relationship. A general empirical expression defined by Garofalo is valid for both regimes:

$$\dot{\epsilon} \propto \sinh(\alpha\sigma)^n, \alpha\sigma < 0.8 \rightarrow \text{power law creep}, \alpha\sigma > 1.2 \rightarrow \text{exponential creep} \quad (2.19)$$

Both Eq. (2.18) and Eq. (2.19) are commonly available in finite element software for simulation purposes as discussed in Section 2.5.2. Apart from the creep mechanisms discussed so far a set of additional mechanisms exists as outlined in the following paragraphs. Fig. 2.10 illustrates the mechanism contribut-

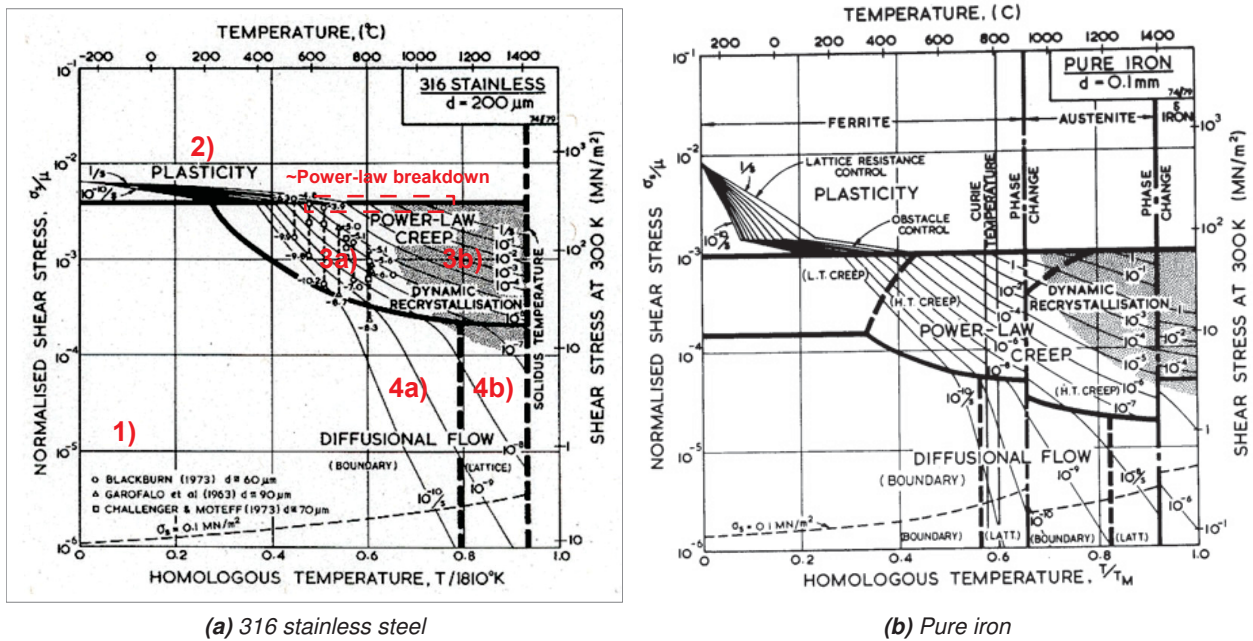


Figure 2.10: Deformation maps for a material a) without b) with phase transformation [15].

ing to creep deformation for a stainless steel and pure iron for various combinations of temperature and stress under steady state conditions. A whole set of those deformation-mechanism maps (Ashby maps) with the corresponding discussions can be found online on a web-site established by Frost and Ashby [15] or in their book [100]. Deformation-mechanism maps can be roughly divided into four regions, as indicated in Fig. 2.10a. Sometimes the elastic region is included, sometimes not and the region corresponding to boundary diffusion is plotted down to low temperatures and low stress levels:

1. **Elastic deformation:** In some representations the field for Coble creep is extended to low temperatures thus consuming the elastic region. Both possibilities are correct and make sense in view of the relevant time scale. Coble creep is active above 0K but in engineering contexts the elastic deformation will always be dominant up to $0.4 T_m$. However, in geological time frames diffusional deformation below $0.4 T_m$ is still relevant.
2. **Plastic deformation:**
 - Plastic collapse when the ideal shear strength is reached. This value is calculated from the crystal structure at 0 K, i.e. without the kinetics of dislocation formation and gliding.
 - Plasticity at low temperatures by dislocation glide, which is mainly limited by the Peierl's stress (lattice resistance) and by obstacles (grain boundaries, precipitates, particles). Although this might not be apparent due to the low rate-dependence, low temperature dislocation glide is a kinetic process which manifests itself in the mobility and the velocity of the dislocations. Besides the lattice resistance, the thermal activation of dislocation segments at obstacles is a key factor in this context and this determines the exponent in the exponential relationship between the velocity and the stress (Table 2.1). The exponent is dependent on the type of obstacle, which can be classified in two major groups: obstacles that are bypassed (dispersoids) and obstacles

2. THEORETICAL BACKGROUND

that are cut (precipitates, forest dislocations). At high deformation rates ($>10^2/s$), the limiting factor can be the interaction with lattice oscillations (phonons).

- Plasticity at low temperatures by twinning. A minimum five independent slip systems is necessary to maintain the continuity at the grain boundaries during deformation [37]. If this number is not available either premature failure may occur or, in the case of some materials, twinning may appear as an additional deformation mechanism. Deformation twinning is most frequently observed in hcp metals, while in bcc and fcc metals it only occurs at low temperatures and high strain rates. It is the least frequent mechanism in fcc apart from specific alloys.

3. **Power law creep** by dislocation glide and glide+climb. The involved mechanisms and limitations are: a) glide process, b) core diffusion controlled climb (low temperature creep), c) lattice diffusion controlled climb (high temperature creep), d) power law breakdown, f) the occurrence of dynamic recrystallization, g) Harper-Dorn creep.

Thermal activation above $0.4 T_m$ promotes dislocation glide (glide-controlled creep) which leads to creep like behavior according to a power law of the form $\dot{\gamma} \propto \left(\frac{\sigma}{G}\right)^{n1}$. This mechanism is important in ice, certain ceramics and possibly in metals below $0.4 T_m$. At higher temperatures another degree of freedom adds to the gliding, i.e. dislocation climb. This diffusional mechanism allows dislocations to bypass obstacles and to continue gliding. While the gliding determines the accumulated strain the climbing determines the speed, as the process of releasing the dislocation is the critical step (climb controlled creep). This regime can be subdivided into two areas:

- (a) Low temperature creep: Dislocation core diffusion contributes significantly to the diffusive transport (diffusion is fastest along the dislocation lines)
- (b) High temperature creep: Dislocation climb is controlled by the lattice diffusion

The creep law in both cases of climb controlled creep follows a power law. The strain rates at high stress levels often exceed the predictions of the commonly used power laws for dislocation creep, which is called the *power law breakdown*, as noted above. This change from power law creep to exponential creep delimits the power-law region for dislocation creep at high stresses and relatively low temperatures as reported in [101]. To date it was not possible to pinpoint the exact reason for this change of stress dependence. In [15] it is attributed to the transition from climb controlled to glide controlled flow, as glide contributes increasingly to the overall strain rate. Buerger [14] states that the power law breakdown is due to the change from dislocation creep to thermally activated plasticity. According to Nabarro [102], it is not clear whether the physical processes in the power law region and after power law breakdown are similar or not. There is evidence, however, that suggests that the former entails homogeneous deformation within the grains, while the latter can be attributed to grain boundary sliding.

Another interference with power law behavior occurs in the range of dynamic recrystallization. Observed strain rates exceed the power law predictions for steady state (stage 2) creep, but the deviation in this case is due to the repetitive occurrence of primary creep after regions have recrystallized. The contribution of primary creep would thus need to be considered, which is a complex issue.

A further mechanism of dislocation creep appearing in some coarse grained materials (coarse grains

¹Ashby and Frost use the shear strain rate $\dot{\gamma} = (2\dot{\epsilon} : \dot{\epsilon})^{\frac{1}{2}}$ rather than the strain rate.

suppress diffusional creep) at low levels of stress is called Harper-Dorn creep. In this case, the creep rate is lower than for the other dislocation creep mechanisms, but higher than for diffusional creep — by a factor of 1400 according to [101]. It is characterized by a linear dependency between the stress and the strain rate. The occurrence of a primary creep stage finally excluded diffusional mechanisms and indicated an independent mechanism. It is explained by climb controlled creep under conditions of a constant dislocation density. As opposed to the power law breakdown, this mechanism — if it is active in the material — bounds the power law region for dislocation climb at lower stress levels. The Harper-Dorn region is only included in the Ashby maps for aluminum and lead, but not for other materials due to lack of data [15].

4. **Creep controlled by diffusional processes:** Stress changes the chemical potential of the surface atoms in grains of polycrystals. A deviatoric part in the stress tensor causes an inhomogeneous change in this potential giving raise to a gradient in the potential. If the temperature is sufficiently high, the gradient causes a transport of material along the surface of grains and through their volume. Thus, there are two main mechanisms that are related with purely diffusional deformation (no involvement of dislocations):

- (a) Low temperature diffusion, which proceeds at grain boundaries and scales $\propto \frac{D_b}{d^3}$. Another term for this deformation type is Coble creep.
- (b) High temperature diffusion, which is lattice controlled and scales $\propto \frac{D_v}{d^2}$. This type of diffusional creep is also called Nabarro-Herring creep.

D_b refers to the coefficient of grain boundary diffusion, D_v to lattice diffusion and d to the grain size.

Usually more than one mechanism is active but one of them yields the largest contribution thus being dominant. In some cases the interaction mechanisms leads to special effects, e.g. grain boundary gliding, which occurs in the context of superplasticity [103]. The construction procedure of deformation mechanism maps begins with the collection of material data for the creep laws (Table 2.1).

Table 2.1: Overview of empirical plasticity and steady state creep models used for the construction of damage mechanism maps [15]

| Mechanism | Deformation law |
|---|---|
| Plastic deformation | |
| Plastic flow by collapse of the crystal structure | $\dot{\gamma}_1 = \infty$, when $\sigma_{eq} \geq \alpha_1 G$ $\dot{\gamma}_1 = 0$, when $\sigma_{eq} < \alpha_1 G$ |
| Discrete-obstacle controlled plasticity | $\dot{\gamma}_2 = \dot{\gamma}^* \exp \left[-\frac{\Delta F}{kT} \left(1 - \frac{\sigma_{eq}}{\tau^*} \right) \right]$, with $\dot{\gamma}^* = \frac{\alpha_2}{b} \left(\frac{\sigma_{eq}}{G} \right)^2 \beta b \nu$ and $\tau^* \propto \frac{Gb}{L}$ |
| Lattice resistance controlled plasticity | $\dot{\gamma}_3 = \dot{\gamma}_p \left(\frac{\sigma_{eq}}{G} \right)^2 \exp \left[-\frac{\Delta F_p}{kT} \left(1 - \left(\frac{\sigma_{eq}}{\tau_p^*} \right)^{\frac{3}{4}} \right)^{\frac{4}{3}} \right]$ |

2. THEORETICAL BACKGROUND

| Dislocation creep | |
|--|--|
| Power law creep (LT+HT creep) | $\dot{\gamma}_4 = \frac{A_2 D_{eff} G b}{kT} \left(\frac{\sigma_{eq}}{G} \right)^n$ $D_{eff} = D_v \left[1 + \frac{10a_c}{b^2} \left(\frac{\sigma_{eq}}{G} \right)^2 \frac{D_c}{D_v} \right]$ |
| Harper-Dorn | $\dot{\gamma}_5 = A_{HD} \frac{D_v G b \sigma_{eq}}{kT G}$ |
| Power law creep + power law breakdown | $\dot{\gamma}_6 = A_2' \frac{D_{eff} G b}{kT} \left[\sinh \left(\frac{\alpha' \sigma_{eq}}{G} \right) \right]^n$ |
| Diffusional creep | |
| Nabarro-Herring creep (lattice diffusion) + Coble creep (grain boundary diffusion) | $\dot{\gamma}_7 = \frac{42\sigma_{eq}\Omega}{kTd^2} D_{eff}, \text{ with}$ $D_{eff} = D_v \left[1 + \frac{\pi\delta}{d} \frac{D_b}{D_v} \right]$ |

Table 2.2: Variables and constants used in Table 2.1 [15]

| Var | Meaning | Var | Meaning |
|------------------|---|--------------|---|
| $\dot{\gamma}$ | Shear strain rate | α_1 | Dimensionless constant for ideal shear strength |
| α_2 | Dimensionless constant for low temperature plasticity | β | Dimensionless constant for low temperature plasticity |
| b | Magnitude of Burger's vector | ΔF | Activation energy to overcome obstacles without external stress |
| ν | A frequency | k | Boltzmann's constant |
| τ^* | Shear strength without thermal energy | L | Average obstacle spacing |
| τ_p^* | \approx Flow stress at 0K | ΔF_p | Helmholtz free energy of isolated pair of dislocation kinks |
| $\dot{\gamma}_p$ | Pre-exponential constant | A_2 | Dimensionless constant |
| a_c | cross sectional areas of dislocation core | n | Exponent of power-law creep |
| D_c | Core diffusion coefficient | D_v | Lattice diffusion coefficient |
| D_b | Boundary diffusion coefficient | δ | Effective thickness of the boundary |
| α' | Constant for power-law breakdown | D_{eff} | Effective diffusion coefficient for Power-law creep/diffusional creep |
| A_{HD} | Dimensionless constant for Haper-Dorn creep | d | Grain size |
| A_2' | $A_2 = \frac{A_2}{\alpha'^n}$ | Ω | Volume of a vacancy |

The detailed procedure for the construction can be found in the original the work [15; 100]. At this point it is sufficient to understand that critical step in the construction is the superposition of the deformation

mechanisms according to Eq. (2.20)

$$\dot{\gamma}_{net} = \dot{\gamma}_1 + \text{greatest of}(\dot{\gamma}_{plast}, \dot{\gamma}_4, \dot{\gamma}_6) + \text{greatest of}(\dot{\gamma}_5, \dot{\gamma}_7), \quad \dot{\gamma}_{plast} = \text{least of}(\dot{\gamma}_2, \dot{\gamma}_3) \quad (2.20)$$

In the case of plastic deformation, the two possible mechanisms are treated as alternatives and the strongest obstacles decide which one is active. Dislocation based and diffusion based mechanisms may add up since they involve different processes of deformation. Competing mechanisms within dislocation and diffusional creep, respectively, are treated as alternatives and the fastest one is selected. The dominant contribution to $\dot{\gamma}_{net}$ for each position in the Ashby map defines the five zones and at the boundaries two mechanisms are equally dominating. Moreover, the superposition method yields isolines for deformation rates.

The austenitic steel in Fig. 2.10a is an example for a material without phase transformations in the temperature region of interest. The flow stress is weakly dependent on the temperature since an activation energy is required for dislocations cutting each other (forest cutting). An area at high temperature is marked with dynamic recrystallization which interferes with power law creep. The regions where Nabarro-Herring and Coble creep are predominant are indicated respectively. Fig. 2.10b shows pure iron, which states an example for a material undergoing phase changes ($\alpha \rightarrow \gamma$ and $\gamma \rightarrow \delta$). As a consequence several fields occur more than once or the shape of certain fields changes abruptly at the transformation temperatures. Hence, some differences compared to Fig. 2.10a are obvious:

- Due to the high lattice resistance of bcc metals, like α -iron, the thermal activation has a greater impact on the flow stress at low temperatures (see top left of Fig. 2.10b) than the obstacles density, e.g. the dislocation density. For this reason the impact of precedent work hardening would be more apparent for the stainless steel than for pure iron if Ashby maps were determined for different hardening states.
- The power law region changes its shape at both transformation temperatures. In fact, the lower boundary could be extended from the α to the δ region since both the α and the δ phase have a bcc structure. Nevertheless, the lower boundary of austenite is different because fcc structures are more dense and diffusional creep rates are thus lower. This limits the upper stress threshold where diffusional creep prevails over dislocation creep, whose boundary is in turn lowered.
- The power law region is split in low and high temperature dislocation creep due to the different diffusion mechanisms for vacancies enabling dislocations to undergo non-conservative motions (climbing), as noted above.
- The reduction in the coefficient of lattice diffusion in the fcc region of Fig. 2.10b is more significant as compared to the drop in the boundary diffusion coefficient. For this reason the region for diffusional creep in the fcc field starts again with dominant boundary diffusion (Coble creep).
- In Ashby maps the y-axis is normalized with respect to the shear modulus G . Moving from left to right at a constant y-value does not correspond to a constant shear stress but to a decreasing one. This fact is illustrated by the dashed lines in Fig. 2.10a and Fig. 2.10b connecting points corresponding to a shear stress of $0.1 \text{ MN}/\text{m}^2$. When phase transformations occur this line comprises an important information: The other lines corresponding to certain creep rates show discontinuities at the transformation temperatures. The discontinuities appear smaller than they really are, since dif-

2. THEORETICAL BACKGROUND

ferent shear moduli are used directly before and after the transformation. The jump in the dashed line reflects the difference in the normalizations and indicates that the strain rate curves should be moved accordingly, in order to see the real discontinuity at constant shear strains.

- The loss of ferromagnetic behavior above the Curie temperature of α -iron has an impact on the rate equations used for the definition of the fields in the diagram as explained in [15]. Due to the magnetic phase change, the shear modulus does not evolve linearly with temperature any more and this must be considered in the construction of the map, although it is not directly visible.

For the case of a thermal or thermomechanical fatigue problem, the stress-temperature path for characteristic loading conditions during a cycle could be plotted on top of a deformation mechanism map, in order to identify the relevant mechanisms. This information can be used as a basis for the definition of a suitable modeling technique and the choice of constitutive equations describing the identified mechanisms.

The impact of creep damage on the overall damage behavior is becoming more pronounced the lower the strain rate is. Since industrial components are exposed to strain ranges covering several orders of magnitudes, there is no unique way how to deal with a combination of fatigue and creep mechanisms in view of a life prediction method. Either one of the damage mechanisms is predominant, which makes the second damage contribution negligible, or some sort of damage accumulation rule must be applied taking into account both mechanisms. Oxidative damage is a further contribution that is especially important if the temperature varies during the loading cycle.

2.3 Material physical processes in viscoplasticity and creep fatigue interaction

Fig. 2.11 shows again the Ashby map for pure iron but this time with a schematic loading path for a component subjected to TF. Pure iron is a first approximation for a brake disk material and the loading situation loosely relates with a material point at the surface of a brake disk in service (also compare to Fig. 1.4):

The path starts at position **1** at room temperature at a negligible stress level corresponding to zero (some stresses may be present due to manufacture). The starting point is clearly in the elastic domain. During heating, the temperature rises and compressive stresses develop. The path passes through the low temperature (LT) dislocation creep area (**2-3**) and hits the yield limit σ_y at position **3**, where the plastic deformation begins. At this point hardening mechanisms apply, which increase σ_y , but hardening is not considered in Ashby maps and assumed arbitrarily in the indicated loading path. Dislocation creep is still active and the consequences of this combination of mechanisms for fatigue life is behind the prominent topic of *viscoplasticity* and *creep-fatigue-interaction*. Both the amplitude and the duration of a load cycle can cause damage. Which one prevails depends on the exact loading path and time frame. For the assumed loading case the maximum temperature in the loading path coincides with the maximum shear stress at position **4**. The temperature is maintained (dwell time, **4-5**) and recovery processes cause the stress level to decrease until the loading path is completed by the unloading branch (**5-7**). During unloading, which corresponds to the reduction of the temperature to the initial value due to the removal of the external heat source, an important point occurs. At position **6** the stress changes from the compressive

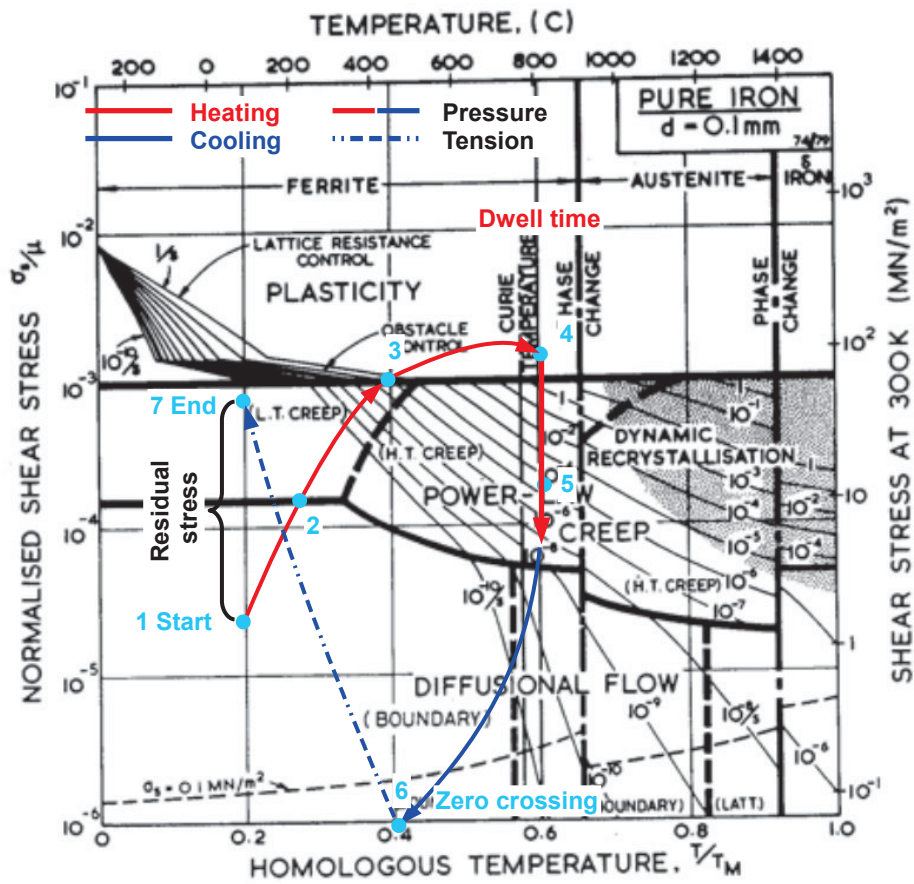


Figure 2.11: Deformation map for pure iron [15] with a schematic $\sigma - T$ path for TF loading.

to the tensile regime. This corresponds to the mechanism discussed in Section 1.3. During cooling the plastification of the surface region under pressure causes the material to be shorter than at the beginning. When the temperature at the surface begins to cool down and the core is still hot, this shortening has an important effect. The material further below the surface is of a greater length and tries to stretch the surface region. This induces tensile stress at the surface and compressive residual stress further below. At the end of the $\sigma - T$ path the temperature field becomes homogeneous and thermal stresses are reduced until only the residual stress remains. If the same load cycle is repeated several times, the residual stresses will increase, since plastic deformation occurs again. As the number of load cycles raises the magnitudes of the plastic deformation under compression and tension approach each other. If the end point meets the start point, the corresponding mechanical hysteresis is said to be stabilized. If not, as in the presented example corresponding to the initial cycle, residual stress is built up and the contribution from the current cycle to the total residual stress formation equals the vertical distance between the start and the end point. The exact value is not relevant at this point.

One aspect concerning the relation between strain and stress has not been treated so far: The **slopes** occurring in $\sigma - T$ path. The load scenario in the example corresponds to a one sided thermal heat input, as outlined in Section 1.3. The loading is thus temperature controlled and, due to the link between temperature and thermal expansion, the problem is in fact strain controlled. Between 1-2, the deformation is elastic and the slope is nearly linear according to Hooke's law. A slight curvature can be observed, due to

2. THEORETICAL BACKGROUND

the temperature dependence of the Young's modulus. When inelastic deformation occurs, the linearity in the relation between temperature and stress is gradually lost. Coble creep has no big impact on the slope, since inelastic deformation rates are insignificant between positions **1** and **2**. Actually, the boundary between the elastic region and Coble creep is rather arbitrary and often omitted. Coble creep is active at low temperatures as well, but only significant in geological time frames. At **2** the loading path enters smoothly the dislocation creep region. With increasing temperature and thermal strain the slope continuously decreases and a curvature becomes obvious. At **3** the yield limit is met and a discontinuous transition into the plastic domain occurs. Due to the contribution of time-dependent deformation mechanisms, the global deformation during the load cycle is characterized as viscoplastic rather than plastic. Due to this fact, the discontinuity at **3** is less pronounced as for the case of isothermal loading at room temperature. When **3** moves to higher temperature levels the discontinuity decreases and the same is true for slower loading conditions. In both cases the creep effects contribute more to the total inelastic deformation. The evolution of the loading path between **4** and **5** is a pivotal topic in this work, in view of its experimental characterization as well as its modeling. The necessity of proper modeling techniques leads to a thorough discussion of constitutive equations for plasticity, creep and viscoplasticity in Section 2.5. Because of the temperature controlled loading, the slope is infinity during the relaxation period between **4** and **5**. During unloading, after **5**, the same reasoning regarding the slope applies as for the loading branch between **1** and **4**.

Next, a few clarification of some terms used above will be given. The term "plasticity" implies that inelastic deformation is attributed to dislocation glide. The role of dislocations in the context of plasticity is thus essential. With increasing temperatures, however, the influence of diffusion processes becomes more and more obvious. In the dislocation creep region in Fig. 2.11 the mobility of dislocations is enhanced, since diffusion of vacancies enables dislocation climb. Due to this mechanism dislocations can bypass obstacles in the crystal structure and the meaning of a yield limit as in classical plasticity, gets lost. At the same time a rate-dependence occurs, which is due to the time dependent diffusion processes enabling dislocation climb. In the dislocation creep region the mechanisms known from classical plasticity and from creep share some common ground and interact. The corresponding inelastic deformations are rate dependent and not linked to a distinct yield limit. This phenomenon is commonly called viscoplasticity. At high temperatures and intermediate stress levels diffusion processes become dominant in the context of inelastic deformation and dislocation glide is not the main mechanism any more. This inelastic deformation is explicitly designated creep deformation and is significant for long term loading.

Additionally to the previous discussion, another point is illustrated with the following example: The **time frame**, which is set for the loading, and the individual sections in the loading path determine the contribution of the creep mechanisms to the overall creep-fatigue response of the material. The region between **1-2** is mostly elastic but Coble creep also occurs. The fastest deformation rates, however, are too low to be relevant in engineering time frames. The same reasoning applies at the beginning of the dislocation creep region after **2**. With increasing temperature and compressive stress significant deformation rates begin to occur and due to this fact, an opposing effect takes effect. The loading is strain controlled, but inelastic strains decrease the stress level. This is the reason why the stress starts to decrease before the maximum temperature is reached. Furthermore, at the beginning of the dwell time the stress along with the strain rate drop immediately by several orders of magnitude. The unloading path goes back to a residual stress state at room temperature.

Table 2.3 illustrates the meaning of deformation rates in the context of different time frames. The first data row contains some characteristic values for isolines in Fig. 2.11 and the first column contains some characteristic time periods. The main part of the table in between contains the values for the accumulated inelastic deformation for the isolines and the respective period. The time periods can be interpreted, e.g. as one load cycle and the deformation values as inelastic strain per cycle $\Delta\epsilon_{in}/\text{cycle}$. For steels under pure static tensile loading the creep rupture strain is in the order of 10% to 20% (the real value depends on a whole set of parameters, such as temperature, stress and sample geometry). The cells in Table 2.3 corresponding to the same order of magnitude are indicated in orange. They illustrate the time frames required to obtain similar states of deformation for various creep strain rates. For the case of stress controlled loading and a creep rate of $10^{-5}/s$, the rupture strain mentioned above would be obtained after ≈ 200 load cycles. For the case of strain controlled fatigue — as for brake disks — large creep deformation rates mean fast stress relaxation, which lowers the deformation rate instantaneously. Due to this fact, the stress level decreases rapidly in the indicated dwell time in Fig. 2.11 between positions 4 and 5. Creep rates much higher than $10^{-5}/s$ occur at the beginning but deformation rates significantly below $10^{-5}/s$ prevail shortly after. Hence, high creep rates at some point during a load cycle do not necessarily entail early crack initiation or even failure. The maximal possible deformation is limited by the externally applied total strain, which would only be approached by the creep strain at very high temperatures and the very beginning of the dwell time. The orange cells indicate the impact of the creep rates possibly occurring in the course of a hold time on the accumulated deformation. At a creep rate of 10^{-6} the creep rupture strain would be obtained after ≈ 2000 load cycles of 60s, for 10^{-8} after ≈ 200000 .

Table 2.3: Overview of deformation rates occurring in the loading path indicated in Fig. 2.11

| | Deformation rate of isolines [1/s] in Ashby map | | | | | | |
|-----------|---|----------|----------|----------|----------|----------|----------|
| | 1.00E-14 | 1.00E-12 | 1.00E-10 | 1.00E-08 | 1.00E-06 | 1.00E-04 | 1.00E-02 |
| | Accumulated deformation per time period [-] | | | | | | |
| 1 min | 6.00E-13 | 6.00E-11 | 6.00E-09 | 6.00E-07 | 6.00E-05 | 6.00E-03 | 6.00E-01 |
| 1 h | 3.60E-11 | 3.60E-09 | 3.60E-07 | 3.60E-05 | 3.60E-03 | 3.60E-01 | 3.60E+01 |
| 1 day | 8.64E-10 | 8.64E-08 | 8.64E-06 | 8.64E-04 | 8.64E-02 | 8.64E+00 | 8.64E+02 |
| 1 year | 3.15E-07 | 3.15E-05 | 3.15E-03 | 3.15E-01 | 3.15E+01 | 3.15E+03 | 3.15E+05 |
| 100 years | 3.15E-05 | 3.15E-03 | 3.15E-01 | 3.15E+01 | 3.15E+03 | 3.15E+05 | 3.15E+07 |

The discussion so far just aimed at a coarse description of the mechanisms involved in TF loading and their relation to deformation and damage. The real situation in brake disk involves particular $\sigma - T$ paths. Furthermore, the stresses developing during the high temperature phase are consistently in compression, while tensile stresses appear in the form of residual stresses at low temperatures, where creep is not an issue in relevant time frames of engineering components. The corresponding damage behavior under cyclic loading must thus be characterized with special TMF tests, which yield much more precise information than a creep rupture strain or a tensile strength for static loading. In summary, at this point the governing mechanism for TF/TMF loading can be identified and qualitatively discussed based on Ashby maps. The real viscoplastic deformation and its impact on crack initiation life, however, only becomes obvious from specific simulations using models describing:

- The loading conditions with the real strain rates.
- The viscoplastic material behavior.
- The damage behavior under the given loading conditions.

2. THEORETICAL BACKGROUND

Each model must be chosen properly and calibrated with proper test programs. These issues will be discussed in Sections 2.5 and 2.6 and in detail for the case of TMF loading of brake disks in Chapter 5.

2.4 Tensor basics

The subsequent sections draw on the formalism used in continuum mechanics and tensor calculus to a limited but necessary extent. This section will thus summarize the basic notations and rules from standard works, such as [5; 17; 18; 104; 105; 106; 107].

Two fundamental quantities in continuum mechanics are stress and strain. For three-dimensional stress/deformation states these can be represented by tensors, consisting of a set of values and base vectors. The values are represented in the form of a matrix X_{ij} , while the basis \mathbf{g}_i consists of the unit vectors of the coordinate system. By this representation, the values in the matrix are linked to the coordinate system and during coordinate transformations (changes of the basis) the values are changed accordingly to have the same meaning both in the new and the old coordinate system. There is a variety of ways in how to represent tensors and tensor operations, as indicated below:

$$\text{Tensor notation} \qquad \qquad \qquad \text{Index notation} \qquad \qquad \qquad \text{Symbolic notation} \qquad (2.21)$$

$$\epsilon_{ij} \mathbf{e}_i \otimes \mathbf{e}_j \qquad \qquad \qquad \epsilon_{ij} \qquad \qquad \qquad \underline{\epsilon} \qquad (2.22)$$

The tensor notation is especially useful for the derivations in a general coordinate system. In cartesian coordinates tensor calculus is simplified significantly. This is why the index notation, where the basis is not explicitly stated, is usually sufficient. Especially in continuum mechanics the symbolic notation is widely used, due to its advantage of compact representation of tensorial equations. The notation style used throughout this work is the symbolic notation proposed in [18], with deviations wherever deemed necessary. An overview is given in Appendix A.3.

Based on the principle of virtual power, the continuum mechanical derivation of the strain tensor begins with the relation between the rate of displacement vector $\underline{\mathbf{v}}$ and both the rate of deformation tensor $\underline{\mathbf{D}}$ and the rate of rotation tensor $\underline{\mathbf{\Omega}}$.

$$\underline{\mathbf{D}} = \frac{1}{2} \left[\underline{\mathbf{grad}} \underline{\mathbf{v}} + (\underline{\mathbf{grad}} \underline{\mathbf{v}})^T \right] \qquad \qquad \underline{\mathbf{\Omega}} = \frac{1}{2} \left[\underline{\mathbf{grad}} \underline{\mathbf{v}} - (\underline{\mathbf{grad}} \underline{\mathbf{v}})^T \right] \qquad (2.23)$$

According to Eq. (2.23) the decomposition of the gradient of $\underline{\mathbf{v}}$ in a symmetric and antisymmetric part yields $\underline{\mathbf{D}}$ and $\underline{\mathbf{\Omega}}$. On the condition that small deformations prevail, the strain tensor can be derived as follows:

$$\underline{\epsilon} = \int_0^t \frac{1}{2} \left[\underline{\mathbf{grad}} \underline{\mathbf{v}} + (\underline{\mathbf{grad}} \underline{\mathbf{v}})^T \right] dt = \frac{1}{2} \left[\underline{\mathbf{grad}} \underline{\mathbf{u}} + (\underline{\mathbf{grad}} \underline{\mathbf{u}})^T \right] \qquad (2.24)$$

$$\text{where } \int_0^t \underline{\mathbf{grad}} \underline{\mathbf{v}} dt = \underline{\mathbf{grad}} \left(\int_0^t \underline{\mathbf{v}} dt \right) = \underline{\mathbf{grad}} \underline{\mathbf{u}} \quad \text{for small deformations} \qquad (2.25)$$

The quantity $\underline{\mathbf{u}}$ refers to the displacement vector. For small deformations the total strain tensor is the symmetric part of the displacement gradient. The relation between the strain and the stress tensor is

defined by the material law (constitutive law), which will be subject of the subsequent sections for various types of material behavior. The simplest constitutive law is Hooke's law for linear elastic material behavior.

$$\underline{\underline{\sigma}} = \underline{\underline{\mathbf{E}}} : \underline{\underline{\epsilon}} \quad \text{general} \quad \sigma = E \epsilon \quad \text{uniaxial loading} \quad (2.26)$$

$\underline{\underline{\mathbf{E}}}$ refers to the elasticity tensor. In the case of isotropic materials the entries of the coefficient matrix contain two independent material constants, called Lamé's constants λ and G ¹. Other material properties describing the elastic material behavior are more frequently used though, since they can be directly determined from experiments. These are the Young's modulus E and Poisson's ratio ν . These are related to Lamé's constants as shown below:

$$E = G \frac{3\lambda + 2G}{\lambda + G} \quad \nu = \frac{\lambda}{2(\lambda + G)} \quad (2.27)$$

For anisotropic materials the situation is more complicated and more constants occur in $\underline{\underline{\mathbf{E}}}$ but this will not be further elaborated, since this work focuses on isotropic materials. In the case of uniaxial loading Hooke's law reduces to scalar values as indicated in Eq. (2.26). Constitutive equations describing material behavior widely assume isochoric and isotropic behavior for plastic deformation. Isochoric means that the hydrostatic stress causes elastic deformation only and does not contribute to yielding. This suggests the incorporation of deviatoric quantities ($\underline{\underline{\mathbf{s}}}$, $\underline{\underline{\mathbf{e}}}$), as well as invariants of stress and strain in material laws.

$$\underline{\underline{\mathbf{s}}} = \underline{\underline{\sigma}} - \frac{1}{3} Tr(\underline{\underline{\sigma}}) \underline{\underline{\mathbf{1}}} = \underline{\underline{\sigma}} - \sigma_m \underline{\underline{\mathbf{1}}} \quad \sigma_m = \frac{1}{3} Tr(\underline{\underline{\sigma}}) \quad (2.28)$$

$$\underline{\underline{\mathbf{e}}} = \underline{\underline{\epsilon}} - \frac{1}{3} Tr(\underline{\underline{\epsilon}}) \underline{\underline{\mathbf{1}}} = \underline{\underline{\epsilon}} - \epsilon_m \underline{\underline{\mathbf{1}}} \quad \epsilon_m = \frac{1}{3} Tr(\underline{\underline{\epsilon}}) \quad (2.29)$$

The invariants are determined from an eigenvalue problem stated in the form of Eq. (2.30), where T is a square matrix, $\underline{\underline{\mathbf{a}}}$ is an eigenvector and λ an eigenvalue:

$$\underline{\underline{\mathbf{T}}}\underline{\underline{\mathbf{a}}} = \lambda \underline{\underline{\mathbf{a}}}, \quad \underline{\underline{\mathbf{a}}} \neq 0 \quad (2.30)$$

Under consideration of the associative law Eq. (2.30) can be changed into Eq. (2.31), which indicates that eigenvectors do not possess defined lengths. For the sake of simplicity, the unit vector $\underline{\underline{\mathbf{n}}}$ can be thus applied for the solution of the eigenvalue problem of the form Eq. (2.32).

$$\underline{\underline{\mathbf{T}}}(\alpha \underline{\underline{\mathbf{a}}}) = \lambda(\alpha \underline{\underline{\mathbf{a}}}) \quad (2.31)$$

$$(\underline{\underline{\mathbf{T}}} - \lambda \underline{\underline{\mathbf{1}}})\underline{\underline{\mathbf{n}}} = 0 \quad (2.32)$$

Eq. (2.32) is a homogeneous system of equations yielding non-trivial solutions ($\underline{\underline{\mathbf{a}}} \neq 0$) if the determinant of the matrix containing the coefficients of the system of equations is non-zero:

$$det(\underline{\underline{\mathbf{T}}} - \lambda \underline{\underline{\mathbf{1}}}) = 0 \quad (2.33)$$

¹ G is also known as the shear modulus and either denoted G or μ

2. THEORETICAL BACKGROUND

Forming the determinant of Eq. (2.33) leads to the so-called characteristic polynomial, which illustrates the origin of the invariants.

$$\lambda^3 - J_1(\mathbf{T})\lambda^2 + J_2(\mathbf{T})\lambda - J_3(\mathbf{T}) = 0 \quad (2.34)$$

In the case \mathbf{T} corresponds to the stress tensor $\underline{\sigma}$, the three invariants can be stated in the following form:

$$J_1(\underline{\sigma}) = J_1^\sigma = \underline{\sigma} : \mathbf{1} = Tr(\underline{\sigma}) \quad (2.35)$$

$$J_2(\underline{\sigma}) = J_2^\sigma = \frac{1}{2} \left[(Tr(\underline{\sigma}))^2 - Tr(\underline{\sigma}^2) \right] = \frac{1}{2} [J_1^2(\underline{\sigma}) - J_1(\underline{\sigma}^2)] \quad (2.36)$$

$$\begin{aligned} J_3(\underline{\sigma}) &= J_3^\sigma = det(\underline{\sigma}) = \frac{1}{6} (Tr(\underline{\sigma}))^3 - \frac{1}{2} Tr(\underline{\sigma})Tr(\underline{\sigma}^2) + \frac{1}{3} Tr(\underline{\sigma}^3) \\ &= \frac{1}{3} [J_1(\underline{\sigma}^3) + 3J_1(\underline{\sigma})J_2(\underline{\sigma}) - J_1^3(\underline{\sigma})] \end{aligned} \quad (2.37)$$

For deviatoric quantities the second and third invariant are often defined in a simplified manner as follows:

$$J_1(\underline{\mathbf{s}}) = J_1^{\mathbf{s}} = Tr(\underline{\mathbf{s}}) = 0 \quad (2.38)$$

$$J_2(\underline{\mathbf{s}}) = J_2^{\mathbf{s}} = \frac{1}{2} Tr(\underline{\mathbf{s}}^2) \quad (2.39)$$

$$J_3(\underline{\mathbf{s}}) = J_3^{\mathbf{s}} = \frac{1}{3} Tr(\underline{\mathbf{s}}^3) \quad (2.40)$$

Experimental observations suggest that plastic flow is independent of the hydrostatic pressure, which explains the use of deviatoric quantities in constitutive equations. The definition of $J_1^{\mathbf{s}}$ is meaningless, however, since in contrast to $\underline{\sigma}$ the trace of $\underline{\mathbf{s}}$ is evidently equal to zero, as the hydrostatic part has been removed. The same procedures are applicable for other tensorial quantities, like the strain tensor, plastic strain tensor and their deviatoric formulations. Many quantities are based on the invariants, such as the equivalent stress and equivalent plastic strain according to von Mises:

$$\sigma_{eq} = (3J_2^{\mathbf{s}})^{\frac{1}{2}} = \left(\frac{3}{2} \underline{\mathbf{s}} : \underline{\mathbf{s}} \right)^{\frac{1}{2}} \quad (2.41)$$

$$\epsilon_{pl,eq} = \left(\frac{4}{3} J_2^{\epsilon_{pl}} \right)^{\frac{1}{2}} = \left(\frac{2}{3} \underline{\epsilon}_{pl} : \underline{\epsilon}_{pl} \right)^{\frac{1}{2}} \quad (2.42)$$

$$\dot{\epsilon}_{pl,eq} = \left(\frac{4}{3} J_2^{\dot{\epsilon}_{pl}} \right)^{\frac{1}{2}} = \left(\frac{2}{3} \underline{\dot{\epsilon}}_{pl} : \underline{\dot{\epsilon}}_{pl} \right)^{\frac{1}{2}} \quad (2.43)$$

The factor 3/2 in Eq. (2.41) is introduced for convenience. This way the equivalent stress in a uni-axial tension test matches the applied stress σ_1 and not $2/3 \sigma_1$ which would be confusing. The von Mises stress will be further discussed in Section 2.5.1.1. Plastic deformation in metals is isochoric, i.e. deformation does not cause changes in the volume. Based on this condition, the plastic strain tensor and plastic strain

rate tensor are by definition deviatoric. The additional coefficient used in the computation of the equivalent quantities is thus different. As noted above, in the case of the stress tensor the coefficient ensures equality of the equivalent quantity and the 11-tensor component in the event of uniaxial loading [19]. Equivalent quantities according to von Mises will be assumed in the following and no further indication will be used. An important relation for the definition of thermodynamically based constitutive equations is the Clausius-Duhem inequality (see Appendix A.4 for more details):

$$\underline{\sigma} : \underline{\mathbf{D}} - \rho \left(\dot{\Psi} + s\dot{T} \right) - \frac{1}{T} \underline{\mathbf{q}} \cdot \underline{\mathbf{grad}}(T) \geq 0 \quad \text{for small strains: } \underline{\mathbf{D}} \approx \underline{\dot{\epsilon}} \quad (2.44)$$

$\underline{\mathbf{D}}$ refers to the deformation tensor, $\dot{\Psi}$ is the specific free energy (or thermodynamic potential), $\underline{\mathbf{q}}$ the heat flux vector, s the specific entropy per unit mass and ρ refers to the mass density. According to [108], a constitutive assumption is said to be compatible with thermodynamics if Eq. (2.44) is satisfied by all processes contributing to the equation. The derivation of Eq. (2.44) from the second principle of thermodynamics is shown in [17].

2.5 Overview of material models

In [109], White and Goodman provide an introduction to the meaning of constitutive equations (CEs) for creep and plasticity modeling. CEs deliver quantitative descriptions of the relation between stress, strain and temperature for each position of a material that is considered as a continuum. The history of inelastic strains, stress and temperature generally takes part in CEs thus influencing the mechanical response in the current phase of loading. Since CEs for a general description of material behavior in arbitrary loading conditions are not available or it would not be feasible to implement them, it is common practice to select proper CEs for the application in question. The interaction between plasticity and creep mechanisms may be taken into account by internal state variables that are affected by either of the two inelastic contributions. However, superposition models are commonly used, treating creep and plasticity separately with global interactions only. These interactions may lead to unpredictable results in new loading conditions that have not been specifically tested. This point of criticism combined with the argument that all inelastic strains are fundamentally time-dependent — although this impact may not always be visible at low temperatures — gave rise to the development of unified constitutive equations. In these models only a single measure for all inelastic strains ϵ_{in} exists. The most wide-spread type of unified models is designated as viscoplastic models and a detailed discussion of these can be found e.g. in [110]. One basic characteristic of viscoplastic models is that the temperature and rate dependence of the yield stress σ_y become rather insignificant. These influences are taken into account by the yield criterion which differs from the formulation used in classical plasticity. Viscoplastic models are widely recommended and used but like other models they have some disadvantages that should be mentioned:

- Focus is laid on plastic behavior while long-term creep behavior is not covered
- Many parameters are introduced which makes the identification of these quantities difficult, especially if individual parameters affect material behavior at different time scales
- Viscoplastic models (as well as some pure creep models) tend to be numerically more expensive than classical models

2. THEORETICAL BACKGROUND

Viscoplastic models are fundamentally correct, but due to the points noted above it is also reasonable to use classical models especially for engineering purposes. Both ways will be illustrated and discussed in the modeling section (Chapter 5). Section 2.5.1 and Section 2.5.2, respectively, aim at the discussion of modeling plasticity and creep independently. Section 2.5.3 will introduce unified, i.e. viscoplastic models for cyclic inelasticity.

According to [104] the derivation of constitutive equations can be done in three different ways:

- Deductive: The derivation is carried out in a theoretic manner based on balance equations, which provide the framework for the constitutive equations. Postulates concerning material behavior are used to define the equations within the framework, staying mathematically and physically consistent. This methodology is demanding and the physical consistency must be verified by checking Eq. (2.44).
- Inductive: Experimental data are the basis for the definition of uniaxial empirical laws. In the next step these laws are extended to more general formulations, like multiaxial loading. Physical consistency is not necessarily given but this approach is well suited for the use in engineering contexts.
- Rheological: An alternative way that uses aspects of the two previous approaches is based on the definition of simple, uniaxial and physically consistent models. These are combined in various ways to model various material behavior in an illustrative way.

After the previous discussion the three main building blocks of constitutive equations can be identified in a simplified manner from a rheological point of view:

- Linear elasticity, which describes a reversible stress strain response. The spring is the corresponding representation in a rheological model.
- Plasticity, which describes irreversible deformation above the yield limit σ_y . Its rheological representation is the frictional device (skidding block).
- Viscosity, which describes time-dependent deformation after the application of the load. It can be represented by the linear and non-linear dash-pot element.

The rheological elements can be combined in multiple ways. The resulting rheological models are not related to the physical deformation mechanisms that have been discussed so far. They can be used to illustrate in the one-dimensional case the possibilities for modeling the $\sigma - \epsilon$ response for various materials and loading situations. The rheological models are thus used to establish the necessary understanding for the individual classes of material models. Subsequently, the constitutive laws are discussed from an inductive point of view. The basic deductive framework, however, is not treated in the main part of this work and is illustrated in Appendix A. All of these concepts share the convention that the total strain can be separated in a reversible ϵ_{el} and inelastic strain ϵ_{in} . Since the first one corresponds to a reversible variation of the atomic distance and the latter one to irreversible changes in the atomic structure, this separation is physically sound.

$$\epsilon_{tot} = \epsilon_{el} + \epsilon_{in} = \epsilon_{el} + \epsilon_{pl} + \epsilon_{vis} \quad (2.45)$$

At the outset of this section the focus is set on plasticity followed by a subsection dedicated to creep. The information is put together to shed light on the modeling of viscoplasticity and finally, the concepts will be applied for the case of TMF loading of brake disks in Chapter 5 and Chapter 6.

2.5.1 Plasticity models

Fig. 2.12 is a representative example of a mechanical hysteresis loop and its characteristic quantities. The exact shape of the hysteresis depends on the material and the loading conditions. For this reason, it is a crucial link between the loading and the expected life time, at least when the loading causes inelastic deformation. This is both true for testing of samples as well as the simulation of components. The hysteresis yields a set of characteristic quantities, as indicated in Fig. 2.12. In a strain controlled LCF test the total strain range $\Delta\epsilon$ is the governing test parameter, while the plastic strain range $\Delta\epsilon_{pl}$, the stress range $\Delta\sigma$, etc. are the resulting quantities. Additionally the experiment yields the information as to how many cycles the loading conditions could be tolerated. On the one hand, the hysteresis loops from lab experiments can be used to calibrate empirical life estimation models, which are able to predict the number of load cycles until crack initiation within certain limits of error. On the other hand, plasticity models – also calibrated with the lab experiments – can be used in simulations of components to obtain the quantities indicated in Fig. 2.12, which are the input parameters for the life time prediction. The life estimation models are thus the link between experiment and simulation. The combination of an experimental and a numerical procedure allows the investigation of the service life of a component (see Section 2.6). A principal requirement is a proper numerical description of the plastic response of the material to the relevant loading conditions. This issue will be addressed in this section for the case of isothermal loading.

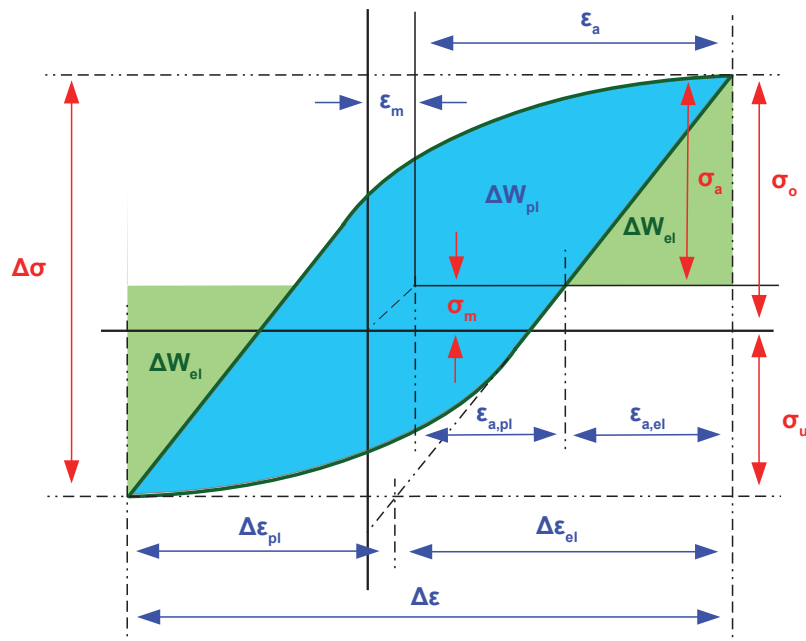


Figure 2.12: Illustration of an isothermal mechanical hysteresis loop and the corresponding mechanical quantities (based on [8; 16]).

Before the discussion of the implementation of plasticity models in the three-dimensional continuum mechanical framework, a simplified one-dimensional view on some elastic-plastic material responses to external loading will be presented in line with [17; 18; 111]. The simplest model considering plastic deformation is of the type *elastic-perfectly plastic* and can be represented by a rheological model called the Saint-Venant model illustrated in Fig. 2.13a. This model does not consider hardening and the magnitude of ϵ_{pl} is thus undefined when σ_y is reached. Two models which consider hardening are the Prager model and the

2. THEORETICAL BACKGROUND

generalized Saint-Venant model. The former one provides a linear description of the plastic region. The elastic region could be considered by an additional spring, which is connected in series. The generalized Saint-Venant model provides a multi-linear description of the $\sigma - \epsilon$ evolution above σ_y . The behavior of

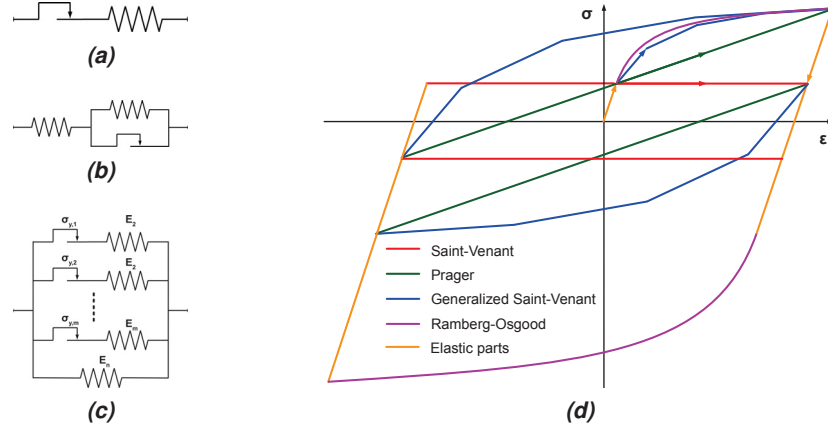


Figure 2.13: Rheological models for plasticity: a) elastic-ideal plastic (Saint-Venant model), b) linear kinematic hardening (Prager model), c) elastic-piecewise linear plastic (generalized Saint-Venant model), d) $\sigma - \epsilon$ response for a)-c) and Ramberg-Osgood.

these models can be summarized by simplified constitutive equations:

$$\text{Elastic-ideal plastic} \begin{cases} \epsilon = \epsilon_{el} = \frac{\sigma}{E} & \text{if } |\sigma| < \sigma_y \\ \epsilon = \epsilon_{pl} & \text{undefined if } \sigma = \sigma_y \text{ Sgn}(\dot{\epsilon}_{pl}) \end{cases}$$

$$\text{Elastic-plastic} \begin{cases} \epsilon = \epsilon_{el} = \frac{\sigma}{E} & \text{if } |\sigma| < \sigma_y \\ \epsilon = \epsilon_{el} + \epsilon_{pl} = \frac{\sigma}{E} + f(\sigma) & \text{if } |\sigma| \geq \sigma_y \end{cases}$$

$f(\sigma)$ refers to the function describing the evolution of the plastic strain with respect to the stress state. Fig. 2.13d presents the schematic stress strain response to external loading for each rheological model. In the case of ideal plasticity, the curve continues horizontally after σ_y is reached (approximation e.g. for mild steel after the initiation of plastic flow). The green line illustrates the behavior of the Prager model, which continues with a slope H . The stress increases with increasing strain, which is called hardening a phenomenon that is commonly observed in metals, as outlined in Section 2.1.1. According to the generalized Saint-Venant model, the hardening region is described in a multi-linear fashion. The slope of the curve changes every time when the yield limit $\sigma_{y,i}$ of an individual friction element is reached. In addition to these models, Fig. 2.13d also shows a non-linear description of hardening according to Ramberg-Osgood. However, there are more differences than the non-linearity. Attention must be paid to the mechanical behavior after load reversal. Before discussing this feature the significance of hardening needs to be further clarified: After unloading and reloading (not plotted in Fig. 2.13d), σ_y , would not correspond to $\sigma_{y,0}$ anymore, but the highest stress level before unloading. Up to this point, the deformation in the reloading path would be solely elastic. Hence, the hardening refers to an increase of the yield limit. For all the models previously mentioned, except for ideal plasticity where hardening is not considered, this behavior is clear if only monotonic loading is regarded. Nevertheless, for the behavior after load reversal,

a distinction must be made between:

- isotropic hardening
- kinematic hardening

The two cases are illustrated for the Ramberg-Osgood equation in Fig. 2.14a and the Prager model in Fig. 2.14b. In the first case, the yield limit increases steadily with increasing plastic strain and this state is maintained after load reversal. The elastic region upon reversal extends into the compressive regime until $|\sigma_y(\epsilon_{pl}^{acc})|$ is reached. From then on, the curve continues in the same manner it would have done under tension, as indicated by $A - A'$. The situation is different for the Prager model, where the yield limit under compression is not symmetric about the x-axis. At this point it makes sense to introduce the other

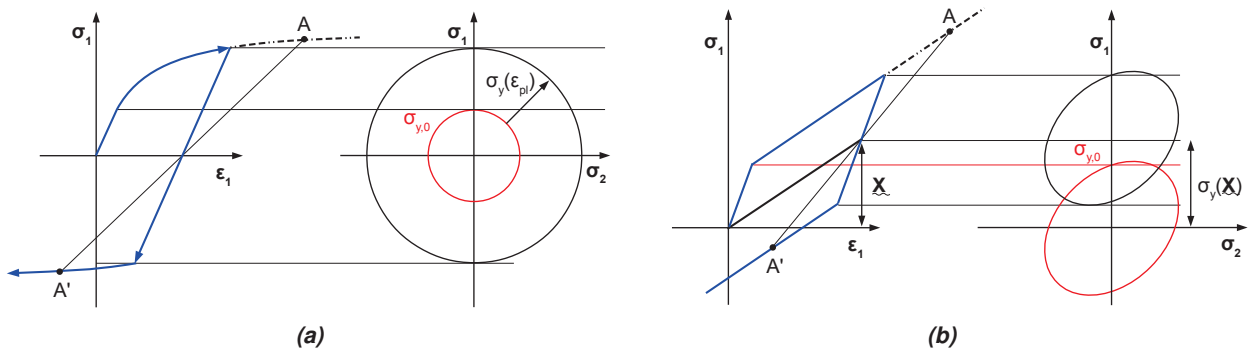


Figure 2.14: a) non-linear isotropic hardening, b) linear kinematic hardening [17].

fundamental components of every plasticity model besides the **hardening rule**. One other is the **yield surface**. In the case of uniaxial loadings, the elastic domain is limited by two scalar values $\sigma_y^{tension}$ and $\sigma_y^{compression}$. The yield surface and the corresponding yield criterion are the generalization for the multi-axial case, which can be expressed in 6-dimensional space (three normal and three shear stresses) and 3-dimensional space (principal stress space). This surface represents all stress states where the material response to the current stress state changes from elastic to plastic. In rate-independent plasticity, which is dealt with in this section, the current stress state must be within the yield surface (elastic deformation) or on it (plastic deformation). In a numerical implementation stress states outside occur but these are not permitted. Overstresses must be removed by proper algorithms that reduce the stress level to σ_y (radial return algorithm). This is linked to the computation of the corresponding plastic strains and the procedure is established by the **consistency condition**. The last component manages the direction of the plastic strain and is called **flow rule**. More light will be shed on these four components in the subsequent sections, while the first basic concepts of the yield surface fits perfectly in at this point. For isotropic hardening rules, the center of the yield surface is fixed in space and the only change in the case of plastic flow is its size. For kinematic hardening, σ_y increases as well after initiation of plastic flow but the situation after load reversal is fundamentally different. As indicated in Fig. 2.14b, the only thing that changes in view of the yield surface is its position but not its size. The yield limit after load reversal is thus not symmetric about the horizontal axis but about another position indicated by the tensorial quantity $\underline{\mathbf{X}}$, called backstress tensor or simply the **backstress**. Usually its deviatoric part $\underline{\chi}$ is used in constitutive equations. In general, an isotropic hardening is easier to numerically implement but kinematic hardening is closer to reality. In fact, the non-symmetrical behavior σ_y is called the **Bauschinger effect**. For monotonic loading, isotropic

2. THEORETICAL BACKGROUND

hardening is often the better choice, as its implementation is simpler and no difference to kinematic hardening occurs. For cyclic loading, however, the Bauschinger effect is evident for metals and thus kinematic hardening is the better choice.

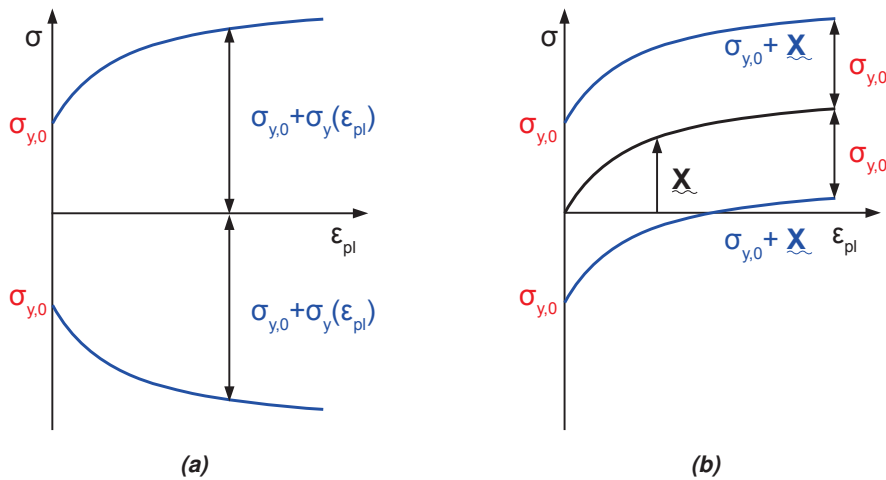


Figure 2.15: Evolution of the yield stress for a) isotropic and b) kinematic hardening (both non-linear in this case) based on [18].

Fig. 2.15 further illustrates the fundamental difference between isotropic and kinematic hardening rules by the variables governing the hardening behavior. For isotropic hardening this is a scalar quantity, the accumulated plastic strain ϵ_{pl}^{ac} . Since this internal variable can only increase, $|\sigma_y|$ can only increase but not decrease after unloading. For kinematic hardening, σ_y is a function of another internal variable, the backstress, which is not visible to an observer of the deformation process, but internally determines the effective stress state. $\underline{\chi}$ determines how the yield surface moves in space and is responsible for the fact that σ_y is not symmetric about the x-axis.

To sum up, the substantial units of models describing plasticity are:

- Yield criterion
- Hardening rule
- Flow rule
- Consistency condition

Up to this point, the difference between isotropic and kinematic hardening has been discussed, based on to exemplary hardening rules: Ramberg-Osgood and Prager. Besides their description of isotropic and kinematic hardening, respectively, there are other significant differences. Ramberg-Osgood is by definition an **empirical** and thus strictly one-dimensional law. However, it can be integrated in the three-dimensional continuum mechanical framework of a finite element software. This is also the case for empirical creep laws and proper procedures will be illustrated in Section 2.5.2. The Prager model on the contrary has been defined in a multi-axial manner right from the beginning and is thus a **continuum mechanical model**. A further difference between the two models is the non-linear nature of Ramberg-Osgood and the linear formulation of the Prager model. At least in view of modeling a tensile test Ramberg-Osgood would be preferred. In view of cyclic loading the Prager model is already very useful but it has been further improved and formulated in a non-linear manner by Armstrong-Frederick.

2.5.1.1 Yield criterion

As noted above, the yield surface represents the outer limit of the elastic domain. The yield criterion thus depends on the definition of the yield surface and on the type of hardening. It may be expressed in the three general forms each depending on the current stress state and specific hardening variables:

$$f(\underline{\sigma}, \sigma_y(\epsilon_{pl}^{ac})) = 0 \quad \text{isotropic hardening} \quad (2.46)$$

$$f(\underline{\sigma}, \underline{\chi}(\underline{\epsilon}_{pl})) = 0 \quad \text{kinematic hardening} \quad (2.47)$$

$$f(\underline{\sigma}, \sigma_y(\epsilon_{pl}^{ac}), \underline{\chi}(\underline{\epsilon}_{pl})) = 0 \quad \text{combined isotropic and kinematic hardening} \quad (2.48)$$

Fig. 2.16 plots von Mises yield surface, which is most commonly used for sufficiently ductile metals. In this case, plastic flow is governed by tangential stresses causing intercrystalline shear [17]. The von Mises criterion is an isotropic yield criterion (not to be confused with the isotropic hardening rule) and by the use of symmetry transformations of $\underline{\sigma}$ it can be shown that $f(\underline{\sigma}, \sigma_y(\epsilon_{pl}^{ac}))$ only depends on the invariants of $\underline{\sigma}$, at this point exemplary for isotropic hardening: $f(J_1^\sigma, J_2^\sigma, J_3^\sigma, \sigma_y(\epsilon_{pl}^{ac}))$ [5]. Due to the incompressibility of metals and the independence of plastic flow on the hydrostatic flow, the stress deviator \underline{s} can be applied, which further reduces the variables in f: $f(J_2^s, J_3^s, \sigma_y(\epsilon_{pl}^{ac}))$. Since the von Mises criterion draws on the shear energy the third invariant is neglected. On these grounds the plasticity theory based on the von Mises criterion is often called J_2 -plasticity [19]. Even very large but equal principal stresses will not cause yielding. The full derivation of the von Mises yield criterion starting from the elastic strain energy is carried

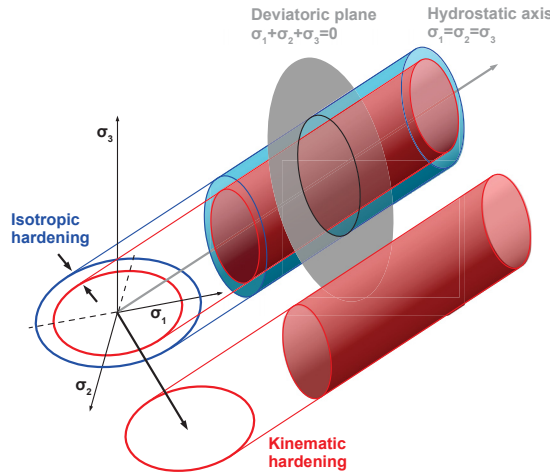


Figure 2.16: Illustration of the von Mises yield surface with isotropic and kinematic hardening.

out as follows [17]:

$$\begin{aligned} E_{el} &= \int_0^{\underline{\epsilon}_{el}} \underline{\sigma} : d\underline{\epsilon}_{el} = \int_0^{\underline{\epsilon}_{el}} \left[\underline{s} + \frac{1}{3} Tr(\underline{\sigma}) \underline{\mathbf{1}} \right] : \left[d\underline{\epsilon}_{el} + \frac{1}{3} Tr(d\underline{\epsilon}_{el}) \underline{\mathbf{1}} \right] = \\ &= \underbrace{\int_0^{\underline{\epsilon}_{el}} \underline{s} : d\underline{\epsilon}_{el}}_{\text{deviatoric} \rightarrow \text{shear energy}} + \underbrace{\int_0^{Tr(\underline{\epsilon}_{el})} \frac{1}{3} Tr(\underline{\sigma}) Tr(d\underline{\epsilon}_{el})}_{\text{hydrostatic} \rightarrow \text{volumetric deformation energy}} \end{aligned} \quad (2.49)$$

2. THEORETICAL BACKGROUND

The elastic strain energy can thus be expressed as the sum of the deviatoric and the volumetric deformation energy. For the von Mises criterion the former expression is of interested, which can be further expanded with Hooke's law $d\mathbf{e}_{el} = \frac{1}{2G}d\mathbf{s}$ (see [112] for the application of Hook's law for deviatoric quantities):

$$E_{dev} = \int_0^{\mathbf{s}} \frac{1}{2G} \mathbf{s} : d\mathbf{s} = \frac{1}{2G} \frac{s_{ij}^2}{2} = \frac{1}{4G} \mathbf{s} : \mathbf{s} \quad (2.50)$$

The equivalent stress is derived in such a way that σ_{eq} corresponds to the stress in a uniaxial tension test. Plastic flow occurs when σ_{eq} reaches the yield limit σ_y in this tension test.

$$[\boldsymbol{\sigma}] = \begin{Bmatrix} \sigma_y & 0 & 0 \\ 0 & 0 & 0 \\ 0 & 0 & 0 \end{Bmatrix} \rightarrow \mathbf{s} = \begin{Bmatrix} \frac{2}{3}\sigma_y & 0 & 0 \\ 0 & -\frac{1}{3}\sigma_y & 0 \\ 0 & 0 & -\frac{1}{3}\sigma_y \end{Bmatrix} \quad (2.51)$$

$$\frac{1}{4G} \mathbf{s} : \mathbf{s} = \frac{1}{6G} \sigma_y^2 \rightarrow \frac{1}{2} \mathbf{s} : \mathbf{s} - \frac{1}{3} \sigma_y^2 = J_2^{\mathbf{s}} - \frac{1}{3} \sigma_y^2 = 0 \quad (2.52)$$

The yield criterion, for the case of an isotropic hardening rule, can thus be written as:

$$f(J_2^{\mathbf{s}}, \sigma_y(\epsilon_{pl}^{ac})) = \left(\frac{3}{2} \mathbf{s} : \mathbf{s} \right)^{\frac{1}{2}} - \sigma_y(\epsilon_{pl}^{ac}) = \sigma_{eq}(\boldsymbol{\sigma}) - \sigma_y(\epsilon_{pl}^{ac}) = 0 \quad (2.53)$$

With the equivalent von Mises stress:

$$\sigma_{eq} = (3J_2^{\mathbf{s}})^{\frac{1}{2}} = \left(\frac{3}{2} \mathbf{s} : \mathbf{s} \right)^{\frac{1}{2}} \quad (2.54)$$

In the case of kinematic hardening, the equivalent stress is not calculated from $\boldsymbol{\sigma}$ but from an effective stress state defined by the backstress. The corresponding von Mises yield criterion reads:

$$f(J_2^{\mathbf{s}}, \boldsymbol{\chi}) = J_2^{\boldsymbol{\sigma}}(\boldsymbol{\sigma} - \boldsymbol{\chi}) - \sigma_{y,0} = \left(\frac{3}{2} (\mathbf{s} - \boldsymbol{\chi}) : (\mathbf{s} - \boldsymbol{\chi}) \right)^{\frac{1}{2}} - \sigma_{y,0} = 0 \quad (2.55)$$

It is also possible to incorporate both hardening rules which yields the subsequent yield function:

$$f(J_2^{\mathbf{s}}, \sigma_y(\epsilon_{pl}^{ac}), \boldsymbol{\chi}) = \left(\frac{3}{2} (\mathbf{s} - \boldsymbol{\chi}) : (\mathbf{s} - \boldsymbol{\chi}) \right)^{\frac{1}{2}} - \sigma_y(\epsilon_{pl}^{ac}) = 0 \quad (2.56)$$

The expression $\sigma_y(\epsilon_{pl}^{ac})$ is often written in the form $k + R$, where k is the initial size of the yield surface and R its positive or negative evolution. This notation is used e.g. by Chaboche [110; 113; 114]. From the above expressions it is clear that evolution laws for the hardening variables are pivotal elements, which will be discussed in Section 2.5.1.2.

The von Mises equivalent stress has already been anticipated in Section 2.4 but now its meaning has been clarified. The yield criterion describes a circular cylinder with $r = \sqrt{\frac{2}{3}}\sigma_y$ whose axis is coincident

¹Intermediate step with index notation.

with the space diagonal. Due to this procedure a correlation between a three dimensional stress state in the continuum mechanical framework with a scalar experimental value is later on possible. A first step from the simplified one-dimensional models, which have been discussed at the beginning of the section, towards multi-axial, numerical implementations of plasticity models has thus been established. The von Mises yield criterion is only one of many and Table 2.4 gives an overview of some common yield criteria.

Table 2.4: Overview of common yield criteria [17; 18; 41]

| Yield criterion | Formulation | Comment |
|--|--|--|
| isotropic and deviatoric | | |
| Mises | $\sigma_{eq} = (3J_2^s)^{\frac{1}{2}},$ $f = \sigma_{eq} - \sigma_y$ | Based on the total shear energy and thus the maximum shear in each principal plane |
| Tresca | $\sigma_{eq} = \text{Sup}_{i \neq j}(\sigma_i - \sigma_j),$ $f = \sigma_{eq} - \sigma_y$ | Based on the maximum shear stress occurring in one of the principal planes |
| Rankine | $\sigma_{eq} = \max(\sigma_1, \sigma_2, \sigma_3),$ $f = \sigma_{eq} - \sigma_{TS} = 0 \text{ or}$ $f = \sigma_{eq} + \sigma_{CS} = 0$ | Brittle failure criterion based on the largest principal stress. The criterion predicts failure and not yield. σ_{TS} and σ_{CS} refer to the tensile and compressive strength. |
| isotropic including effect of hydrostatic pressure (e.g. for rock mechanics) | | |
| Drucker-Prager | $f = (3J_2^s)^{\frac{1}{2}} - \frac{\sigma_y - \alpha J_1^s}{1 - \alpha}$ | Generalization of the von Mises criterion that takes the hydrostatic stress into account. A non-symmetry between tension and compression can thus be considered. α is a material parameter and for $\alpha = 0$ the criterion corresponds to von Mises. |
| Mohr-Coulomb | $f = \sigma_1 - \sigma_3$ $+ (\sigma_1 + \sigma_3) \sin \phi$ $- 2C \cos \phi$ | Extension of the Tresca yield criterion. C is the cohesion and ϕ the angle of internal friction. Due to an assumed internal friction in the material the admissible shear increases with the normal compression stress |
| Selection of non-isotropic criteria | | |
| Hill (Generalized Mises), Generalized Tresca, Generalized Burzynski, Generalized Hershey Power Yield Condition, Tsai Condition | | |

2. THEORETICAL BACKGROUND

2.5.1.2 Hardening rule

Monotonic loading: Fig. 2.17 compares ideal plastic behavior to hardening. It should be noticed that *hardening* refers to an increase of the yield stress but it is also used as a general term describing the change of σ_y with increasing loads. To distinguish the different usages, the term *hardening behavior* is commonly used for the latter one, which may refer to hardening, softening or ideal plasticity. Low carbon steels may exhibit a plateau that can be interpreted as ideal plastic behavior at the onset of plastic deformation (Lueders strain). Shortly after hardening begins and thus ideal plasticity is mostly a theoretical phenomenon. In monotonic tests usually hardening is observed. In the case of cyclic plasticity, i.e. when fatigue causes alternating loads, cyclic softening and cyclic hardening are equally important. The physical

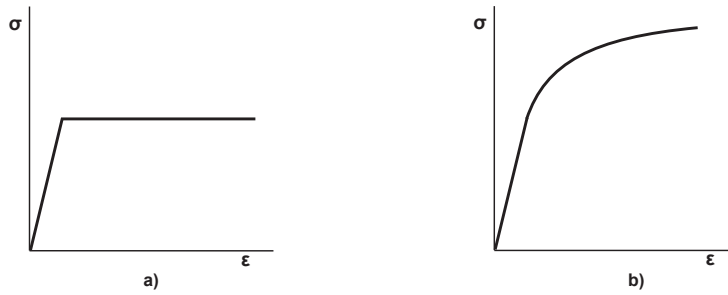


Figure 2.17: Overview of hardening behavior: a) ideal plastic, b) hardening.

explanation of hardening is the generation and interaction of dislocations, as described in Section 2.1.1. In a monotonic tension test, the yield stress usually increases with increasing stress level. This can be checked by repeated loading and unloading — back-plastification must be avoided at this point because additional effects happen that will be discussed later. The current yield stress is thus a function of the previous plastic history and in the specific case of monotonic loading it corresponds to the highest previously obtained stress. Thus, the whole hardening curve consists of representative points for the yield stress and it can be described by a hardening function [17]:

$$\sigma_y = f(\epsilon_{pl}) \quad \text{e.g. } f(\epsilon_{pl}) = kb\rho_{Def}^{\frac{1}{2}} = \sigma_{y0} + kb(\rho_{Dcur} - \rho_{Dini})^{\frac{1}{2}} \quad (2.57)$$

In this case the hardening function is based on the dislocation density ρ_D and analogous expression may be defined based on the macroscopic strains:

$$\sigma_y = f(\epsilon_{pl}) = \sigma_{y0} + K' \epsilon_{pl}^{\frac{1}{n'}} \quad (2.58)$$

$$\epsilon_{pl} = f^{-1}(\sigma_y) = \left\langle \frac{\sigma_y - \sigma_{y0}}{K'} \right\rangle^{n'} \quad (2.59)$$

Eq. (2.58) is called Ramberg-Osgood equation. K' refers to the coefficient of plastic resistance and n' is the hardening exponent. The Macaulay brackets $\langle \rangle$ indicate that ϵ_{pl} can only take positive values. For monotonic loading isotropic hardening can be modeled with Eq. (2.58). It is a purely empirical description for uniaxial loading conditions.

Fig. 2.13 plots the Ramberg-Osgood law for a hysteresis loop characteristic for cyclic loading, which implies that it can be also used for other purposes. However, the hysteresis is solely based on graphical

construction using Eq. (2.58), which is fundamentally monotonic. Graphically based constructions of hysteresis loops are used in engineering contexts in order to obtain characteristic points of the hysteresis for life time predictions. These methods draw on simple FE simulations and in the case of Masing behavior the Ramberg-Osgood equations can be used to extend the results in a simple manner to cyclic loads. This methodology will be explained in detail in Section 2.6. The subsequent paragraph will focus on more complex continuum mechanical models for cyclic loading.

Cyclic loading: Fig. 2.18a provides an illustration of a strain-controlled simulation of a cyclic tension-compression test using combined hardening. The blue hysteresis loop is the first σ - ϵ cycle in the test, starting in the compressive region. The extreme values σ_{min} and σ_{max} indicate the starting point of the cyclic softening/hardening curve plotted on the right part of Fig. 2.18a. Up to this point, the σ - ϵ response is solely due to non-linear hardening, as previously discussed. In the following cycles the extreme values become gradually lower due to cyclic softening. The two stress evolutions representing the cyclic softening can be modeled with **isotropic hardening**. The red hysteresis loop is an example for the hysteresis shape corresponding to $N_f/2$, the number of load cycles at half life of the sample. The hysteresis shape can be modeled **kinematic hardening**. In the context of LCF testing the sample's life time N_f is commonly defined as a 10% drop of the linear fit to the linear region of the hardening/softening curve. This region corresponds to the part where stable dislocation structures have formed up (see Section 2.1.1) and damage in the form of crack growth in the sample is not yet evident (the drop in stress at the end of the test indicates crack growth). The hysteresis loop at half life is characteristic for the tested loading conditions and can be used for the definition of damage parameters drawing on characteristic values of the experimental hysteresis.

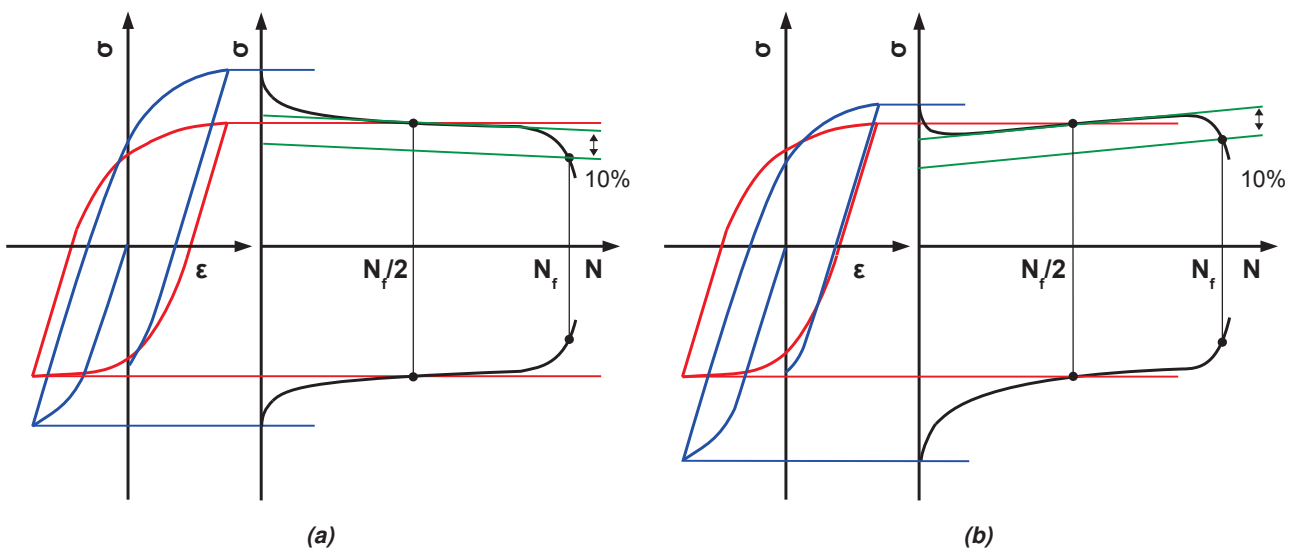


Figure 2.18: Material exhibiting cyclic softening in a strain controlled LCF test a) with $R_\epsilon = 0$ b) with $R_\epsilon < 0$.

Fig. 2.18b shows an additional effect not mentioned so far. The simulation/experiment is carried out under non-symmetric loading conditions, i.e. ϵ_{min} is larger than ϵ_{max} . At the beginning of the test the stress level is shifted into the compressive regime, i.e. the mean stress σ_m is compressive. In the course of the exper-

2. THEORETICAL BACKGROUND

iment, however, σ_m relaxes and reaches zero. This effect is called mean stress relaxation and is taken into account both by linear and non-linear kinematic hardening. Linear kinematic hardening underestimates this effect, while non-linear kinematic hardening does the opposite. Fig. 2.18b shows a slow mean stress relaxation lasting until the end of the test. In reality σ_m relaxes rapidly within the first couple of cycles. Most of the relaxation actually happens during the first cycle. The non-linear kinematic hardening rule offers an appropriate description of this phenomenon, which is relevant for the modeling of brake disks, since strain controlled loading conditions mostly prevail. The corresponding phenomenon for the case of stress controlled loading is called ratcheting, which causes a drift of the hysteresis loop along the strain axis. Both mean stress relaxation and ratcheting entail hysteresis loops that are not completely closed but for mean stress relaxation this situation stabilizes. Ratcheting does not stabilize and causes the accumulation of a significant amount of plastic strain, which is not favorable in view of the service life.

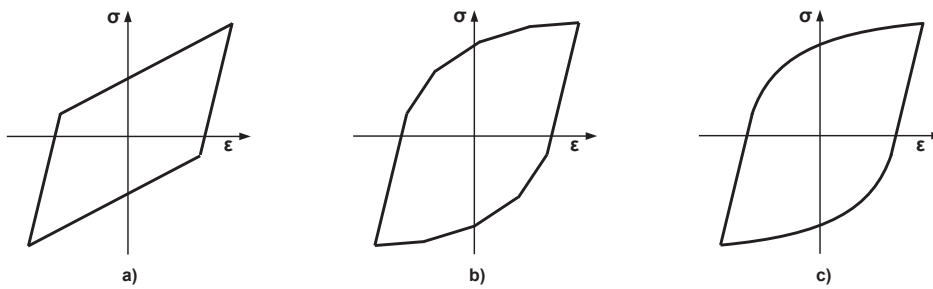


Figure 2.19: Overview of common strategies for the modeling of kinematic hardening: a) linear (bilinear) hardening, b) piecewise linear (multilinear) hardening, c) non-linear hardening.

Furthermore, the expressions *elastic shakedown* and *plastic shakedown* are important in plasticity. The later one applies if the shape of the hysteresis loop stabilizes and does not change any more, until failure. Elastic shakedown applies if the hysteresis loops decrease in size due to hardening and finally the loading is below the yield stress. The σ - ϵ response in the subsequent cycles is thus purely elastic.

Constitutive equations for cyclic plasticity aim at the direct computation of the elastic plastic response under multiaxial loading. This methodology has already been outlined in the previous section. Table 2.5 plots the three basic approaches for kinematic hardening¹: bilinear, multilinear and non-linear hardening. The former two methods are often preferred due to their simple implementation compared to the non-linear approach. A bilinear modeling, however, only considers a linear elastic region and a linear plastic region — thus bilinear — and offers a coarse approximation of the hardening behavior. The relation between σ and ϵ_{tot} is described by the tangent modulus E_T and the relation between σ and ϵ_{pl} by the hardening modulus H .

$$H = \frac{EE_T}{E - E_T} \quad (2.60)$$

The multilinear approach relativizes this drawback by combining several linear terms in one model. The non-linear approach offers the best approximation, especially if multiple terms are combined as will be discussed below. Table 2.5 summarizes the corresponding constitutive laws, which are valid for all three approaches.

¹Analogous considerations apply for isotropic hardening.

Table 2.5: Overview of common hardening rules based on von Mises plasticity [17]

| Hardening | Hardening variables | Underlying yield criterion | Yield criterion |
|-----------|-----------------------------|----------------------------|--|
| Isotropic | p | $f(J_2^\sigma)$ | $f(J_2^\sigma) - R(p)$ |
| Kinematic | $\underline{\mathbf{X}}$ | $f(J_2^\sigma)$ | $f(J_2^\sigma(\underline{\boldsymbol{\sigma}} - \underline{\mathbf{X}}))$ |
| Combined | $p, \underline{\mathbf{X}}$ | $f(J_2^\sigma)$ | $f(J_2^\sigma(\underline{\boldsymbol{\sigma}} - \underline{\mathbf{X}})) - R(p)$ |

Both isotropic and kinematic hardening rules are built upon specific internal variables V_k , which describe the current hardening state. Their definition and evolution are essential for the definition of constitutive equations. For **kinematic hardening** mostly a single tensorial quantity $\underline{\boldsymbol{\alpha}}$ is used, which often corresponds to the current plastic strain $\underline{\boldsymbol{\epsilon}}_{pl}$. While the isotropic variables can be loosely associated with the dislocation density in the current state, the kinematic quantity relates with mismatches of plastic deformation in the crystal structure [17]. The mismatch causes asymmetric yielding after load reversal, which is called Bauschinger effect and the kinematic variable is capable of describing this behavior. Since the Bauschinger effect is a primordial characteristic in cyclic loading, kinematic hardening must always be modeled for fatigue loads involving plastic strains. The most commonly used forms of kinematic hardening within the continuum mechanical framework are linear kinematic hardening law according to Prager and its extended non-linear form according to Armstrong-Frederick [110; 113]. The two formulations are depicted in Fig. 2.20. The additional term in the non-linear form is called *dynamic recovery* or *recall term* and leads to a saturation of the backstress with increasing strain. The saturation stress equals c/γ .

$$\dot{\underline{\mathbf{X}}} = \frac{2}{3} c \dot{\underline{\boldsymbol{\epsilon}}}_{pl} \quad \text{Prager} \quad (2.61)$$

$$\dot{\underline{\mathbf{X}}} = \frac{2}{3} c \dot{\underline{\boldsymbol{\epsilon}}}_{pl} - \gamma \underline{\mathbf{X}} \dot{p} \quad \text{Armstrong-Frederick} \quad (2.62)$$

Improved modeling and prediction of the hysteresis shape is achieved when multiple kinematic hardening terms with different saturation values c/γ are superimposed [113]:

$$\underline{\mathbf{X}} = \sum_i^n \underline{\mathbf{X}}_i \quad (2.63)$$

This way, the σ - ϵ response can be modeled more precisely for varying amplitudes of strain ranging from small to large values. Since linear kinematic hardening does not allow ratcheting and its non-linear counterpart yields an overestimation, ratcheting can be better modeled using a combination of linear and non-linear terms. In the classical Chaboche model two non-linear and one linear backstresses are implemented.

For **isotropic hardening** either the accumulated plastic strain p or the dissipated plastic work w_p can be

2. THEORETICAL BACKGROUND

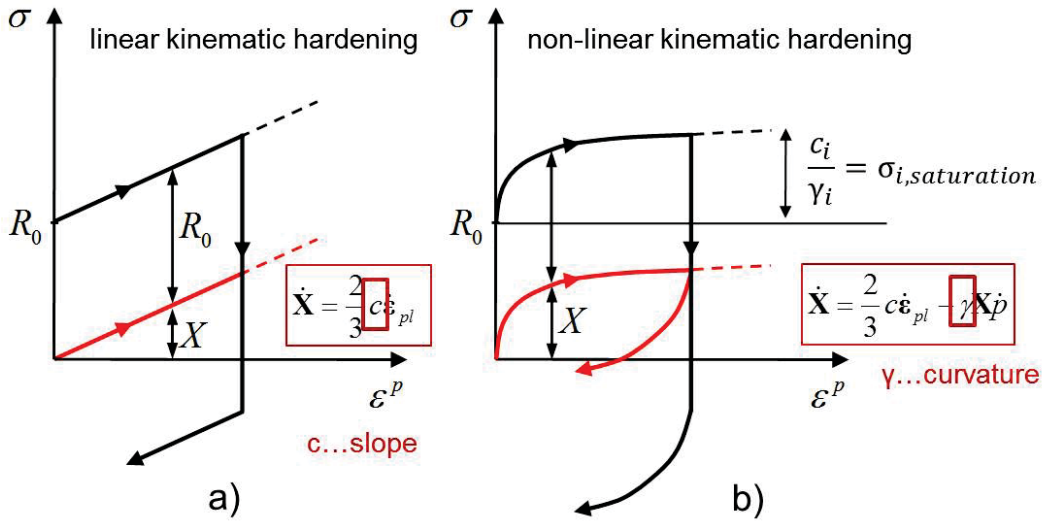


Figure 2.20: Illustration of a) linear and b) non-linear kinematic hardening.

used but p is often preferred:

$$p = \int_0^{t_{end}} \left[\frac{2}{3} \dot{\epsilon}_{pl}(t) : \dot{\epsilon}_{pl}(t) \right]^{\frac{1}{2}} dt \quad w_p = \int_0^{t_{end}} \boldsymbol{\sigma}(t) : \dot{\epsilon}_{pl}(t) dt \quad (2.64)$$

These scalar quantities are called isotropic variables or just hardening variables and R is the corresponding thermodynamic force (see Table 2.5). The isotropic hardening is based on the assumption that the work of the stress components $\boldsymbol{\sigma}$ along the plastic strain components $\dot{\epsilon}_{pl}$ equals the work of the equivalent stress σ_{eq} along the equivalent plastic strain $\epsilon_{pl,eq}$. Assuming associated flow based on the von Mises yield criterion the following expression can be derived:

$$\sigma_{eq} \dot{\epsilon}_{pl,eq} = \boldsymbol{\sigma} : \dot{\epsilon}_{pl} \quad (2.65)$$

For incremental computations as commonly applied for FE simulations, the differentials become differences. Then, p is the sum of the plastic strains of all increments: $p = \sum \Delta \epsilon_{pl,eq}$. The most common relation used for cyclic plasticity is given as follows [110; 113]:

$$\sigma_y = \sigma_{y0} + R(p) \quad (2.66)$$

$$\dot{R}(p) = b(Q - R)\dot{p} \quad (2.67)$$

$$R(p) = Q(1 - e^{-bp}) \quad \text{integrated form} \quad (2.68)$$

The material parameters b and Q define the saturation stress σ_{sat} of cyclic hardening/softening and how fast σ_{sat} is reached.

From the point of view of thermodynamics, the variables describing the thermodynamic forces can be derived from the thermodynamic potential Ψ and the internal variables. Due to the partition hypothesis,

Ψ can be split into an elastic and a plastic part (see Appendix A.4 for more information on Ψ).

$$\Psi = \Psi_{el}(\underline{\epsilon}_{el}, T) + \Psi_{pl}(p, \underline{\alpha}, T) \quad R = \rho \frac{\partial \Psi}{\partial p} \quad \underline{\mathbf{X}} = \rho \frac{\partial \Psi}{\partial \underline{\alpha}} = \frac{2}{3} c \underline{\alpha} \quad (2.69)$$

Based on this definition it can be shown that the Clausius-Duhem equation Eq. (2.44) for the intrinsic dissipation — dissipation related to plasticity — is fulfilled:

$$\underline{\sigma} : \dot{\underline{\epsilon}}_{pl} - R \dot{p} - \underline{\mathbf{X}} : \dot{\underline{\alpha}} \geq 0 \quad (2.70)$$

The corresponding constitutive equations are thus physically sound. Checking whether material models fit in the classical thermodynamic framework or not is a common procedure also for newly developed models. An example is the work of Szmytka et al. [115].

2.5.1.3 Flow rule

The yield criterion enables numerical algorithms involving plasticity models to determine from the stress state whether plastic deformation occurs or not. In the subsequent step, however, it is necessary to define what this plastic deformation looks like, if present, and this is exactly what the flow rule is meant for. The hardening laws presented in the previous section take part in this process as it will be shown. Before moving on to the continuum mechanical definition of the flow rule a distinction must be made between associated and non-associated plasticity. The latter one is a more general description of plastic behavior that requires the use of three potentials:

$$\Psi \dots \text{thermodynamic potential} \quad \Phi \dots \text{dissipation potential} \quad F \dots \text{potential surface} \quad (2.71)$$

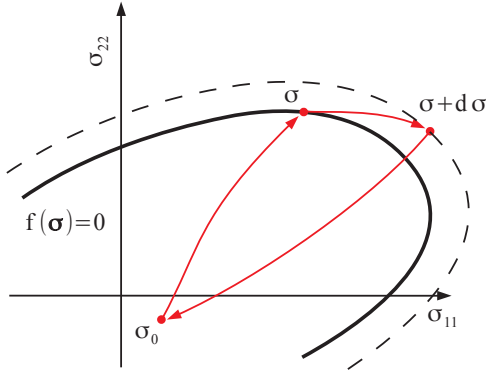
Appendix A provides additional information on the potentials. In non-associated plasticity the potential surface is used to determine the orientation of the plastic strain tensor and thus vital for the definition of the flow rule. In this work associated models are applied where the yield surface is used as potential surface: $F = f$. The subsequent derivations refer to associated plasticity, unless stated otherwise. In the French literature the framework of associated plasticity is called *formalism of generalized standard materials*.

Both for non-associated and associated plasticity, the work done in a loading-unloading cycle must be non-negative. This postulate is called Drucker's inequality, which can be stated in the form of Eq. (2.72). It should be noticed that due to Drucker's postulate the yield surface must be convex [106]. The postulate relates Eq. (2.72) to a thermodynamical background but it can also be interpreted in another manner, as stated by Lubliner [116]: The plastic strain rate cannot oppose the stress rate.

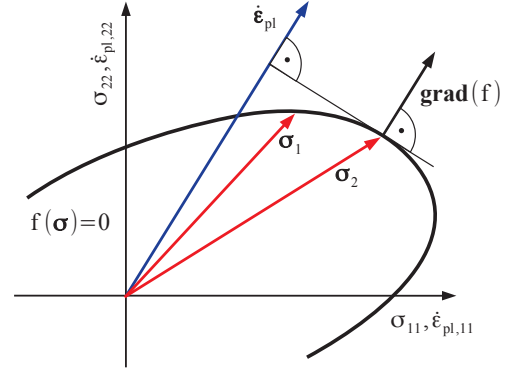
$$d\underline{\sigma} : d\underline{\epsilon} \geq 0 \quad \text{or} \quad d\underline{\sigma} : d\underline{\epsilon}_{pl} \geq 0 \quad (2.72)$$

Drucker's inequality also applies for large stress increments as is the case shown in Fig. 2.21a. σ_0 refers to the stress state at the beginning of the increment, which can be within or on the yield surface far away from the stress states during loading. An external force may cause elastic loading up to σ somewhere on the yield surface, as well as a small stress increment $d\sigma$, which causes an incremental plastic strain $d\underline{\epsilon}_{pl}$.

2. THEORETICAL BACKGROUND



(a) Illustration of Drucker's postulate [116]



(b) Illustration of the normality rule in plasticity [117]

Figure 2.21: Illustration of important principles for the definition of the flow rule.

Finally, elastic unloading back to σ_0 occurs. Ignoring the small stress increment $d\sigma$, Drucker's inequality can be stated as follows:

$$(\underline{\sigma} - \underline{\sigma}_0) : d\underline{\epsilon}_{pl} \geq 0 \quad (2.73)$$

Eq. (2.73) not only applies for work hardening materials but also work softening and perfect plastic materials. This fact gave rise to the definition of Eq. (2.73) as an individual postulate, i.e. the *postulate of maximum plastic dissipation*. The principle of maximal plastic dissipation can be further pinned down in the form of Eq. (2.74):

$$\frac{\partial}{\partial \underline{\sigma}} (\underline{\sigma} : d\underline{\epsilon}_{pl} - d\lambda f(\underline{\sigma})) = 0 \quad d\lambda \geq 0 \quad (2.74)$$

$d\lambda$ is a Lagrange multiplier that is left undetermined for now. The expression implies that from all the possible stress states fulfilling the yield criterion, the one maximizing the plastic work $\underline{\sigma} : d\underline{\epsilon}_{pl}$ is the correct one from the point of view of thermodynamics (see Appendix A for more details). Based on this knowledge, Eq. (2.74) can be transformed into the flow rule:

$$d\underline{\epsilon}_{pl} = d\lambda \frac{\partial f(\underline{\sigma})}{\partial \underline{\sigma}} \quad (2.75)$$

According to [117] the notation above is called incremental formulation. In the literature the differentials are often divided by the time increment dt . This leads to the rate formulation, which will be used in the following:

$$\dot{\underline{\epsilon}}_{pl} = \dot{\lambda} \frac{\partial f(\underline{\sigma})}{\partial \underline{\sigma}} \quad (2.76)$$

In the case of von Mises plasticity the Lagrange multiplier corresponds to the equivalent plastic strain rate \dot{p} . In line with numerical considerations, it is common practice to prescribe the plastic strain increment and to determine the stress state accordingly. In the case of plastic deformation, $\dot{\lambda}$ must thus be determined in such a way that the stress $\underline{\sigma}$ stays on the yield surface.

A further consequence from the principle of maximal plastic dissipation, besides the convexity of the yield surface, is the normality rule, which is evident from the gradient on the right side of Eq. (2.76). According to this rule, the plastic strain increment is perpendicular to the yield surface. The principle of the maximal plastic dissipation can be discussed from the point of view of the normality rule. If the plastic dissipation — the heat generated per time increment by plastic deformation — is defined by Eq. (2.77), the normality rule can be explained by a maximization problem as indicated in Fig. 2.21b.

$$W = \underline{\mathbf{s}} : \underline{\dot{\boldsymbol{\epsilon}}}_{pl} \quad (2.77)$$

Eq. (2.77) is maximized when the projection of $\underline{\mathbf{s}}$ on $\underline{\dot{\boldsymbol{\epsilon}}}$ is maximal. The position of the corresponding stress state on the yield surface is indicated by the position of $\underline{\mathbf{grad}}(f)$ that is normal to $\underline{\dot{\boldsymbol{\epsilon}}}$.

Before the next step, the computation of the plastic increment $d\underline{\boldsymbol{\epsilon}}_{pl}$, it is necessary to determine the current relation between loading conditions and yield criterion, which corresponds to one of four possible cases as illustrated in [5; 116]:

$$\left\{ \begin{array}{ll} f(\boldsymbol{\sigma}) < 0 & \text{elastic case} \\ f(\boldsymbol{\sigma}) = 0 \quad \text{and} \quad \partial f = \partial \boldsymbol{\sigma} : \frac{\partial f}{\partial \boldsymbol{\sigma}} < 0 & \text{unloading} \\ f(\boldsymbol{\sigma}) = 0 \quad \text{and} \quad \partial f = \partial \boldsymbol{\sigma} : \frac{\partial f}{\partial \boldsymbol{\sigma}} = 0 & \text{neutral loading} \\ f(\boldsymbol{\sigma}) = 0 \quad \text{and} \quad \partial f = \partial \boldsymbol{\sigma} : \frac{\partial f}{\partial \boldsymbol{\sigma}} > 0 & \text{loading} \end{array} \right. \quad (2.78)$$

In the *elastic case* and the case of *unloading* the plastic increment is zero. If one of the other cases applies, $d\underline{\boldsymbol{\epsilon}}_{pl}$ is computed with the consistency condition.

2.5.1.4 Consistency condition

Finite element simulations incorporating plasticity models are solved in an incremental way. After each increment the stress predicted at a given material point in the model is either inside, at or outside the yield surface. Which one of the cases applies has to be determined by the yield criterion. If the stress state after the so called global iteration of the FE calculation is outside the yield surface plastic deformation is indicated. The resulting plastic increment is not known at this point, but it can be determined from the condition that the stress state cannot be outside, but only on the yield surface. This condition is designated as consistency condition and can be formulated in various ways, depending on the hardening type(s) used in the simulation. The basic formulation for the case of ideal plasticity is:

$$f(\boldsymbol{\sigma} + d\boldsymbol{\sigma}) = 0 \quad (2.79)$$

Or for the cases of isotropic hardening, kinematic hardening and combined hardening:

$$f(\boldsymbol{\sigma} + d\boldsymbol{\sigma}, p + dp) = 0 \quad f(\boldsymbol{\sigma} + d\boldsymbol{\sigma}, \mathbf{X} + d\mathbf{X}) = 0 \quad f(\boldsymbol{\sigma} + d\boldsymbol{\sigma}, p + dp, \mathbf{X} + d\mathbf{X}) = 0 \quad (2.80)$$

This means that after a local iteration taking place at the current material point and involving the constitutive equations, the consistency condition must be fulfilled. At the end of the global FE iteration all stress states

2. THEORETICAL BACKGROUND

are within or on the yield surface. The corresponding procedure will be illustrated for kinematic hardening according to [19] starting with the yield criterion and the normality rule for kinematic hardening:

$$f = \left(\frac{3}{2} (\underline{\mathbf{s}} - \underline{\boldsymbol{\chi}}) : (\underline{\mathbf{s}} - \underline{\boldsymbol{\chi}}) \right)^{\frac{1}{2}} - \sigma_y \quad (2.81)$$

$$d\epsilon_{pl} = d\lambda \frac{\partial f}{\partial \underline{\boldsymbol{\sigma}}} = d\lambda \frac{3}{2} \frac{\underline{\mathbf{s}} - \underline{\boldsymbol{\chi}}}{\left(\frac{3}{2} (\underline{\mathbf{s}} - \underline{\boldsymbol{\chi}}) : (\underline{\mathbf{s}} - \underline{\boldsymbol{\chi}}) \right)^{\frac{1}{2}}} \quad (2.82)$$

In principal stress space the consistency condition in Eq. (2.80) can be stated in Voigt notation²:

$$\frac{\partial f}{\partial \underline{\boldsymbol{\sigma}}} d\underline{\boldsymbol{\sigma}} + \frac{\partial f}{\partial \underline{\boldsymbol{\chi}}} d\underline{\boldsymbol{\chi}} = 0 \quad (2.83)$$

Using Eq. (2.76), Hooke's law in incremental form, Eq. (2.82), and the evolution equation for non-linear kinematic hardening yields Eq. (2.86).

$$d\underline{\boldsymbol{\sigma}} = \underline{\underline{\mathbf{E}}} d\underline{\boldsymbol{\epsilon}}_{el} = \underline{\underline{\mathbf{E}}} (d\underline{\boldsymbol{\epsilon}} - d\epsilon_{pl}) \quad (2.84)$$

$$\frac{\partial f}{\partial \underline{\boldsymbol{\sigma}}} \underline{\underline{\mathbf{E}}} \left(d\underline{\boldsymbol{\epsilon}} - d\lambda \frac{\partial f}{\partial \underline{\boldsymbol{\sigma}}} \right) + \frac{\partial f}{\partial \underline{\boldsymbol{\chi}}} \left(\frac{2}{3} c d\epsilon_{pl} - \gamma \underline{\boldsymbol{\chi}} d\lambda \right) = \quad (2.85)$$

$$\frac{\partial f}{\partial \underline{\boldsymbol{\sigma}}} \underline{\underline{\mathbf{E}}} \left(d\underline{\boldsymbol{\epsilon}} - d\lambda \frac{\partial f}{\partial \underline{\boldsymbol{\sigma}}} \right) + \frac{\partial f}{\partial \underline{\boldsymbol{\chi}}} \left(\frac{2}{3} c d\lambda \frac{\partial f}{\partial \underline{\boldsymbol{\sigma}}} - \gamma \underline{\boldsymbol{\chi}} d\lambda \right) = 0 \quad (2.86)$$

The expression above can be solved for $d\lambda$ and Eq. (2.82) yields the plastic strain increment $d\epsilon_{pl}$.

$$d\lambda = \frac{\frac{\partial f}{\partial \underline{\boldsymbol{\sigma}}} \underline{\underline{\mathbf{E}}} d\underline{\boldsymbol{\epsilon}}}{\frac{\partial f}{\partial \underline{\boldsymbol{\sigma}}} \underline{\underline{\mathbf{E}}} \frac{\partial f}{\partial \underline{\boldsymbol{\sigma}}} + \gamma \frac{\partial f}{\partial \underline{\boldsymbol{\chi}}} \underline{\boldsymbol{\chi}} - \frac{2}{3} c \frac{\partial f}{\partial \underline{\boldsymbol{\chi}}} \frac{\partial f}{\partial \underline{\boldsymbol{\sigma}}}} \quad (2.87)$$

$$d\epsilon_{pl} = \frac{\frac{\partial f}{\partial \underline{\boldsymbol{\sigma}}} \underline{\underline{\mathbf{E}}} d\underline{\boldsymbol{\epsilon}}}{\frac{\partial f}{\partial \underline{\boldsymbol{\sigma}}} \underline{\underline{\mathbf{E}}} \frac{\partial f}{\partial \underline{\boldsymbol{\sigma}}} + \gamma \frac{\partial f}{\partial \underline{\boldsymbol{\chi}}} \underline{\boldsymbol{\chi}} - \frac{2}{3} c \frac{\partial f}{\partial \underline{\boldsymbol{\chi}}} \frac{\partial f}{\partial \underline{\boldsymbol{\sigma}}}} \frac{\partial f}{\partial \underline{\boldsymbol{\sigma}}} \quad (2.88)$$

The stress increment $d\underline{\boldsymbol{\sigma}}$ can be determined from Eq. (2.84). According procedures need to be applied for other forms of hardening.

The plastic multiplier needs to be determined numerically, since it is not known in advance, which $d\epsilon_{pl}$, will satisfy the consistency condition. This can be done either by an explicit integration scheme, as the first order forward Euler method, or an implicit integration scheme like the radial return method. Both will be briefly outlined based on [19]. In the case of the forward Euler method the total strain increment $d\underline{\boldsymbol{\epsilon}}$ and

¹A fast derivation of this expression can be illustrated for the case of uniaxial loading

²In Voigt notation tensors are represented as vectors. This way, the double contracted product becomes the scalar dot product

the estimated stress $\underline{\sigma}$ are known from the global FE iteration with the corresponding increment Δt^{global} . So far the real $\underline{\sigma}$ and $\underline{\epsilon}_{pl}$ are not known. In the local iteration concerning the plasticity model the following equations are continually updated according to:

$$\underline{\sigma}^{t+\Delta t} = \underline{\sigma}^t + d\underline{\sigma}^t \quad (2.89)$$

$$\underline{\epsilon}_{pl}^{t+\Delta t} = \underline{\epsilon}_{pl}^t + d\underline{\epsilon}_{pl}^t \quad (2.90)$$

The involved quantities, $d\underline{\sigma}^t$ and $d\underline{\epsilon}_{pl}^t$, are computed according to Eq. (2.84) and Eq. (2.88) and the iteration is continued with Δt until the global time step Δt^{global} has been reached $\sum \Delta t = \Delta t^{global}$. If hardening is considered the hardening variables must be updated as well. This integration scheme is easier to implement as an implicit scheme but there is a price to pay. Explicit schemes are only conditionally stable, i.e. the increment size Δt must be small enough or convergence might not be achieved. The choice of Δt is also relevant for the precision of the result, which will be further discussed in the scope of the integration of creep laws in Section 2.5.2.4 where the same difficulties arise. In the current context there is another issue that needs to be considered. The forward Euler scheme ensures that the yield criterion is fulfilled at the beginning of each time step in the local iteration but not at $t + \Delta t$. Due to this fact, the load point can drift away from the yield surface over several increments.

The mentioned difficulties give rise to the use of implicit methods as the radial return algorithm. This method uses a an elastic predictor function, which yields a trial stress outside the yield surface in each local increment $t + \Delta t$. Accordingly, a plastic correction is applied to bring the load point back on the yield surface, in turn rendering the plastic increment $d\underline{\epsilon}_{pl}$. This procedure may be illustrated by Eq. (2.93), where G and λ refer to Lamé's constants as previously noted:

$$\underline{\epsilon}_{el} = \underline{\epsilon}_{el}^t + \Delta \underline{\epsilon}_{el} = \underline{\epsilon}_{el}^t + \Delta \underline{\epsilon} - \Delta \underline{\epsilon}_{pl} \quad (2.91)$$

$$\underline{\sigma} = 2G (\underline{\epsilon}_{el}^t + \Delta \underline{\epsilon} - \Delta \underline{\epsilon}_{pl}) + \lambda Tr (\underline{\epsilon}_{el}^t + \Delta \underline{\epsilon} - \Delta \underline{\epsilon}_{pl}) \mathbf{I} \quad (2.92)$$

$$\underline{\sigma} = \underbrace{2G (\underline{\epsilon}_{el}^t + \Delta \underline{\epsilon}) + \lambda Tr (\underline{\epsilon}_{el}^t + \Delta \underline{\epsilon}) \mathbf{I}}_{\text{elastic predictor}} - \underbrace{2G \Delta \underline{\epsilon}_{pl}}_{\text{plastic corrector}} \quad (2.93)$$

The procedure is embedded within an implicit integration scheme where also quantities at the end of the increment are used in the computation. The resulting values correspond to the end of the increment and a drift of the load point away from the yield surface is avoided. Since implicit schemes are unconditionally stable, larger increments can be used leading to faster computation times. The result is again the plastic strain increment, the stress increment and the increments of the hardening variables if present. Stress and plastic strain at the end of the global iteration are again the summed incremental values.

For explicit FE codes the constitutive equations and their integration must be provided. Either the procedures are already implemented in scope of the standard functionality or they must be provided by user subroutines. For implicit FE codes additional information must be made available, i.e. the tangent stiffness matrix $\frac{\partial \underline{\sigma}}{\partial \underline{\epsilon}}$. The reason is that the Jacobian consisting of the load stiffness matrix and the tangent stiffness matrix is required in the integration scheme of the global FE iterations [19; 118]. Since $\frac{\partial \underline{\sigma}}{\partial \underline{\epsilon}}$ is linked to the material behavior it must be provided by the plasticity model. It should be noted, however, that FE

2. THEORETICAL BACKGROUND

software usually requires $\frac{\partial \Delta \sigma}{\partial \Delta \epsilon}$ and not $\frac{\partial \sigma}{\partial \epsilon}$. The modes of derivation of the two matrices significantly differ. The procedure for FE software and proper modifications for performance optimization are outlined in [119].

2.5.2 Creep models

The FE strategy concerning the material behavior in this work follows two corresponding ways. On the one side creep and plasticity are treated as separate phenomena and thus modeled individually. The methodology concerning the creep behavior in this case draws on empirical models which are used in continuum mechanical contexts in combination with continuum based plasticity models. On the other side a unified approach is applied which combines creep and plasticity within one model, as will be discussed in Section 2.5.3. Table 2.6 provides an overview of the four basic approaches applied for the modeling of creep and their ranges of applicability.

Table 2.6: Approaches to creep modeling [5]

| Focus and suitability | Limitations |
|--|---|
| Empirical models | |
| Study of the correlation between $\dot{\epsilon}_{cr}$ temperature and time. These models provide simple formulas for the estimation of creep conditions in structures. Methods for extrapolation of short time test data to long term behavior are available. | These models are one-dimensional and the impact of the stress state on the creep response cannot be taken into account. They operate with scalar values of stress and strain. |
| Models based on materials science | |
| Equations for the creep rate are derived from microstructural transport processes like diffusion of vacancies, climb and glide of dislocations. The main interest in this domain is the provision of correlations between microstructural characteristics like the grain size, alloying type and hardening state and the mechanical behavior as the strain rate to certain loading conditions. Kinetic equations for internal state variables, e.g. dislocation density and backstress, are thus incorporated. | These models are mostly one-dimensional and operate with scalar values of stress and strain. The form of the creep equation is very dependent on the assumed deformation and damage mechanisms at the present temperature and stress level. |
| Micromechanical models | |

Representative volume elements with an idealized microstructure and cyclic boundary conditions are used in simulations aiming for a deeper understanding of creep mechanisms in heterogeneous materials.

Since the microstructure of metals disposes of complex constituents like grain boundaries, dislocation structures, precipitates, different phases in the matrix, etc., micromechanical descriptions of creep require very complex models which limits their applicability mostly to academic research.

Continuum mechanical models

The main objective is to describe creep phenomena in idealized three-dimensional structures. Its functionality in 3D is necessary for the analysis of components. Seminal parts of these models are on the one hand balance equations and assumptions concerning the kinematics of deformation and motion and on the other hand constitutive equations describing the relation between the deformation and stress state. Microstructural features and their changes are not taken into account but their effects like hardening, recovery, aging and damage are modeled by means of internal state variables and corresponding evolution equations.

These models are phenomenological and thus describe the observed material behavior without taking the physics behind into consideration. Extensive experimental characterization of the creep behavior is necessary.

2.5.2.1 Constant amplitude creep

The creep models commonly used in simulations are empirical models that are embedded in the continuum mechanical framework. This section will focus on the empirical relations and Section 2.5.2.3 establishes the link to continuum mechanics. As outlined in [104; 120] the creep strain can be expressed as a function of σ , t and T or a product of three individual functions which depend on the physical mechanisms occurring in the range of application:

$$\epsilon_{cr} = f(\sigma, t, T) = f_1(\sigma)f_2(t)f_3(T) \tag{2.94}$$

From a physical point of view, however, it is often preferred to describe the creep behavior from the point of view of the creep rate, including the impact of the total strain (or total creep strain):

$$\dot{\epsilon}_{cr} = f_1(\sigma)f_2(t)f_3(T)f_4(\epsilon) \tag{2.95}$$

As outlined in the literature, several models for the computation of the equivalent creep rate have been proposed:

2. THEORETICAL BACKGROUND

Table 2.7: Overview of empirical creep models [5; 42; 43; 44]

| Model | Formulation |
|--|---|
| $f_1(\sigma)$, steady state | |
| Norton 1929 | $\dot{\epsilon}_{eq}^{cr} = K \sigma_{eq}^n$ (2.96) |
| Soderberg, 1936 | $\dot{\epsilon}_{eq}^{cr} = b \left[\exp\left(\frac{\sigma_{eq}}{\sigma_0}\right) - 1 \right]$ (2.97) |
| Prandtl-Nadai-McVetty, 1928/1938/1943 | $\dot{\epsilon}_{eq}^{cr} = a \sinh\left(\frac{\sigma_{eq}}{\sigma_0}\right)$ (2.98) |
| Johnson et al., 1963 | $\dot{\epsilon}_{eq}^{cr} = a_1 \sigma_{eq}^{n_1} + a_2 \sigma_{eq}^{n_2}$ (2.99) |
| Garofalo, 1965 | $\dot{\epsilon}_{eq}^{cr} = a \left[\sinh\left(\frac{\sigma_{eq}}{\sigma_0}\right) \right]^n$ (2.100) |
| Odqvist, 1966 | $\dot{\epsilon}_{eq}^{cr} = \frac{d}{dt} \left(\frac{\sigma}{\sigma_0}\right)^{n_0} + \left(\frac{\sigma}{\sigma_0}\right)^n$ (2.101) |
| $f_2(t)$, $\sigma = \text{const}$ | |
| Andrade, 1910 | $\epsilon_{eq}^{cr} = \beta t^{\frac{1}{3}} + kt$ (2.102) |
| Bailey, 1929 | $\epsilon_{eq}^{cr} = Ft^n$ (2.103) |
| McVetty, 1934 | $\epsilon_{eq}^{cr} = G [1 - \exp(-qt)] + Ht$ (2.104) |
| Leaderman, 1943 | $\epsilon_{eq}^{cr} = \epsilon_1 + A \lg(t) + Bt$ (2.105) |
| Findley, 1944 | $\epsilon_{eq}^{cr} = \epsilon_1 + \epsilon t^n \quad (n < 1)$ (2.106) |
| Philips, 1956 | $\epsilon_{eq}^{cr} = \epsilon_1 + A \lg(t)$ (2.107) |
| Graham-Walles, 1955 | $\epsilon_{eq}^{cr} = \sum a_i t^{n_i}$ (2.108) |
| $f_3(T)$ | |
| Arrhenius law | $f(T) = \exp\left(\frac{-Q}{RT}\right)$ (2.109) |
| Kauzman, 1941 | $f(T) = \exp\left(\frac{-(Q - \gamma\sigma)}{RT}\right)$ (2.110) |
| Lifshiz, 1963 | $f(T) = \frac{\sigma}{T} \exp\left(\frac{-Q}{RT}\right)$ (2.111) |
| Dorn-Tietz, 1949 | $\epsilon_{eq}^{cr} = f \left[t \exp\left(\frac{-Q}{RT} f_1(\sigma)\right) \right] f_1(\sigma)$ (2.112) |
| Penny-Marriott, 1971 | $\epsilon_{eq}^{cr} = f \left[t \exp\left(\frac{-Q}{RT}\right) \right]^n f_1(\sigma)$ (2.113) |

All variables in the expressions for $f_1(\sigma)$ are material parameters with the exception of σ_{eq} . As noted in Section 2.2 the dependency of $\dot{\epsilon}_{eq}^{cr}$ on the stress level is well covered by power-laws for the most part of the dislocation creep area in deformation mechanisms maps. At high stress levels close to the yield limit this dependency is better captured by exponential laws. The hyperbolic sine is used for the definition of creep laws covering both relationships within one model. [15] provides a discussion on a selection of hyperbolic sine laws and the meaning of the parameters used in the corresponding expressions. The temperature has two effects on the deformation behavior. First, the parameters in the creep equations have different values due to the dependence of transport mechanisms in the material on the temperature. This can be taken into account by choosing a proper function $f_3(T)$ or the temperature dependent definition of material parameters. In the later case, attention must be paid to the method used for interpolation since linear interpolation of creep data leads to unexpected results (see Chapter 5). Second, changes in the temperature affect the dominant creep mechanism and thus the governing creep equation and its temperature dependence. Due to the fact that $f_3(T)$ strongly depends on the deformation mechanism in the current temperature regime it cannot be stated in a uniform manner for all application ranges. In the Arrhenius law Q refers to the activation energy and B to Boltzmann's constant.

2.5.2.2 Variable amplitude creep

Primary creep: As stated in [43], the models treated so far can be used for constant uniaxial stress. For variable amplitude loading, as in the case of brake disks, further considerations are necessary. Altenbach [42] gives an overview of the main approaches for metals:

- Total strain theory: Assumption of a relationship between ϵ_{tot} , σ , t at constant temperature, which corresponds to a surface in $\epsilon_{tot}-\sigma-t$ space
- Time hardening theory: Assumption of a relationship between $\dot{\epsilon}_{tot}$, σ , t at constant temperature
- Strain hardening theory: Assumption of a relationship between $\dot{\epsilon}_{tot}$, σ , ϵ_{cr} at constant temperature

A combination of the functions Eq. (2.96) and Eq. (2.103) from Table 2.7 leads to an expression called the *time hardening relation* for primary creep given by Eq. (2.114) [121], which often appears in the literature.

$$\epsilon_{cr} = A\sigma^n t^m \quad (2.114)$$

If the stress is assumed constant for the subsequent derivation, the creep strain rate can be obtained in the form of Eq. (2.115):

$$\dot{\epsilon}_{cr} = A\sigma^n m t^{m-1} \quad (2.115)$$

Eq. (2.115) is called the *time hardening law* because it contains stress and time as variables. The corresponding *strain hardening law* can be obtained by solving Eq. (2.114) for t and inserting the expression into Eq. (2.115) yielding:

$$\dot{\epsilon}_{cr} = mA \frac{1}{m} \sigma \frac{n}{m} \epsilon_{cr}^{\frac{m-1}{m}} \quad (2.116)$$

2. THEORETICAL BACKGROUND

If time and strain hardening are expressed in accordance with Eq. (2.95) as in [5], the creep laws can be stated in the following form:

$$\dot{\epsilon}_{cr} = A\sigma^n t^m \quad (2.117)$$

$$\dot{\epsilon}_{cr} = B\sigma^k \epsilon_{cr}^l \quad (2.118)$$

If one creep experiment is approximated with both models, the coefficients A , n , m and B , k , l represent six individual values. However, in a similar way as before it can be shown that the two parameter sets are linked to one another:

$$b = [a(m+1)^m]^{\frac{1}{m+1}} \quad k = \frac{n}{m+1} \quad l = \frac{m}{m+1} \quad (2.119)$$

This relation of parameters is the reason for the different formulation of the strain hardening law in the commercial software packages Abaqus and Ansys as shown in Table 2.8. In Abaqus, the expressions in 2.119 are used to have the same parameters for the time and strain hardening law, while Ansys uses two independent parameter sets according to Equations (2.117) and (2.118). An additional difference is the use of an Arrhenius law for all creep equations implemented in Ansys, while this is only the case for the hyperbolic sine law in Abaqus. Temperature dependent specification of the creep parameters for time and strain hardening is thus necessary in Abaqus. In Ansys one can choose the Arrhenius law or temperature dependent parameters C1, C2 and C3 (C4=0).

Table 2.8: Overview of some empirical creep models in FE software packages

| Abaqus [45] | | |
|-------------------------|---|-------------------|
| Model | Formulation | Comments |
| Time hardening | $\dot{\epsilon}_{eq}^{cr} = A\sigma_{eq}^n t^m$ (2.120) | Primary/Secondary |
| Strain hardening | $\dot{\epsilon}_{eq}^{cr} = (A\sigma_{eq}^n [(m+1)\epsilon_{eq}^{cr}]^m)^{\frac{1}{1+m}}$ (2.121) | Primary/Secondary |
| Hyperbolic sine law | $\dot{\epsilon}_{eq}^{cr} = A(\sinh(B\sigma_{eq}))^n \exp\left(-\frac{\Delta H}{R(\theta - \theta^0)}\right)$ (2.122) | Secondary |
| User defined creep | | |
| Ansys (exemplary) [122] | | |
| Time hardening | $\dot{\epsilon}_{eq}^{cr} = C_1 \sigma_{eq}^{C_2} t^{C_3} \exp\left(-\frac{C_4}{T}\right)$ (2.123) | Primary/Secondary |
| Strain hardening | $\dot{\epsilon}_{eq}^{cr} = C_1 \sigma_{eq}^{C_2} \epsilon_{eq}^{cr C_3} \exp\left(-\frac{C_4}{T}\right)$ (2.124) | Primary/Secondary |
| Generalized Garofalo | $\dot{\epsilon}_{eq}^{cr} = C_1 (\sinh(C_2 \sigma_{eq}))^{C_3} \exp\left(-\frac{C_4}{T}\right)$ (2.125) | Secondary |
| User defined creep | | |

Secondary creep: Secondary creep in the areas denoted by dislocation creep in Fig. 2.10 can be modeled by several expressions which are often stated as power laws, as previously discussed. In this case, the functions $f_1(\sigma)$ and $f_4(T)$ are of special interest, while $f_2(\epsilon)$ and/or $f_3(t)$ only need to be considered for primary creep where the creep rate is not constant. Both Eq. (2.117) and Eq. (2.118) are often implemented in FE software packages (see Table 2.8) and for $m=0$ and $l=0$ respectively, the expressions reduce to Norton’s law for stationary creep as shown in Table 2.7.

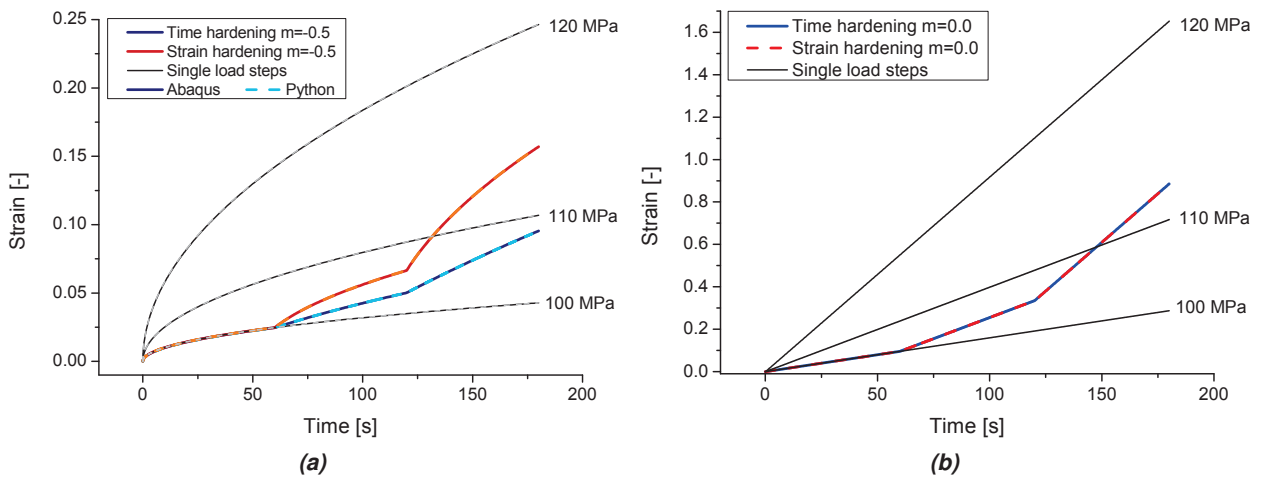


Figure 2.22: Creep simulation - Comparison between time and strain hardening: a) $m=-0.5$ b) $m=0.0$ → Norton’s law for secondary creep.

Comparison of models for primary and secondary creep: Fig. 2.22a plots the creep strain ϵ_{cr} versus time for different stress levels. The black curves correspond to constant stress conditions. In this case, both the time and strain hardening formulation yield identical results. The difference becomes apparent only for variable amplitude loading, as indicated by the colored lines. As previously discussed, both creep laws reduce to Norton’s power law for stationary dislocation creep, which is shown in Fig. 2.22b. The creep strain changes linearly with time and the slope is determined by the stress level in the form of Eq. (2.96). Hence, the creep strain rate changes with σ according to a power law, which is valid for a large portion, but not all of the dislocation creep region (see Section 2.2).

Fig. 2.25 further explains the difference between the $\epsilon - t$ paths from time and strain hardening. At first both curves follow the constant amplitude curve for 100 MPa. After 60s the stress level is increased to 110 MPa and, due to the chosen parameters for creep at high temperatures ($\sim 0.5T_m$ for steel), a significant change in the creep rate is observed (compare black lines for 100 and 110 MPa, respectively). In the case of time hardening, the variable amplitude curve continues in parallel to the 110 MPa curve — i.e. with the same curvature at the current time value. The strain hardening curve on the other hand continues with the curvature of the 110 MPa curve at the corresponding value of creep strain. This behavior explains deviation of the two curves which further increases when σ is increased to 120 MPa. It is reported in the literature that none of the creep models for variable amplitude loading is completely satisfactory [43] but the curve for strain hardening fits best.

2. THEORETICAL BACKGROUND

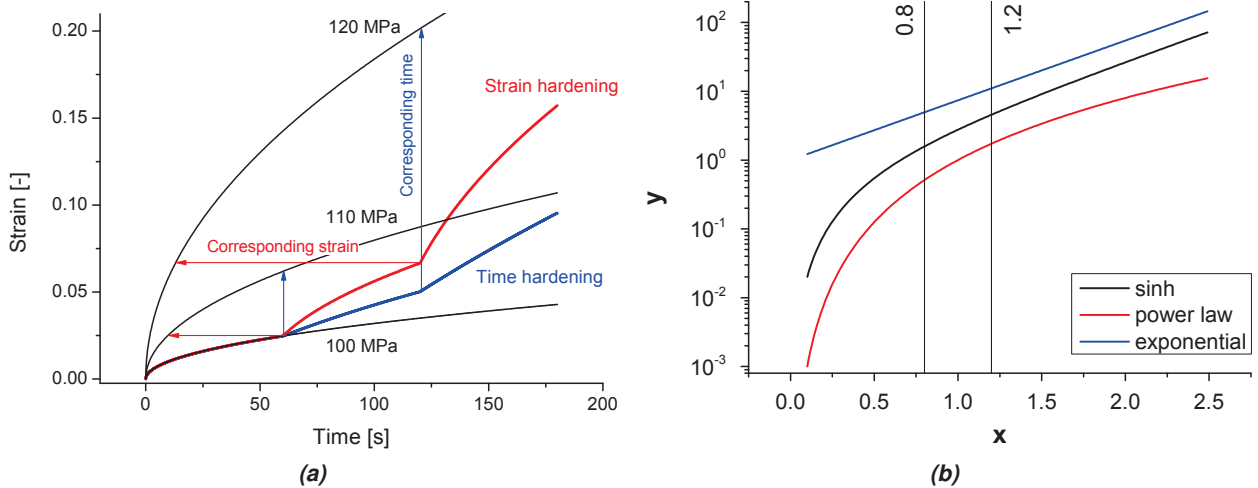


Figure 2.23: a) Explanation of the difference between time and strain hardening law b) General comparison of hyperbolic sine function to power law and exponential law.

Fig. 2.24 shows the equivalent case to Fig. 2.22 for stress relaxation. This deformation mechanism is relevant for brake disks during emergency braking. The applied displacements correspond to 0.4%, 0.6% and 0.75% total strain and each relaxation period equals 60s. The difference between time and strain hardening is less comprehensible in a relaxation experiment because the stress level, and thus the creep strain rate, continuously drop until saturation is approached. Nevertheless, a difference in the σ and $\dot{\epsilon}_{cr}$ evolution is visible. Under the assumption of stationary creep ($m=0$) both models yield the same result.

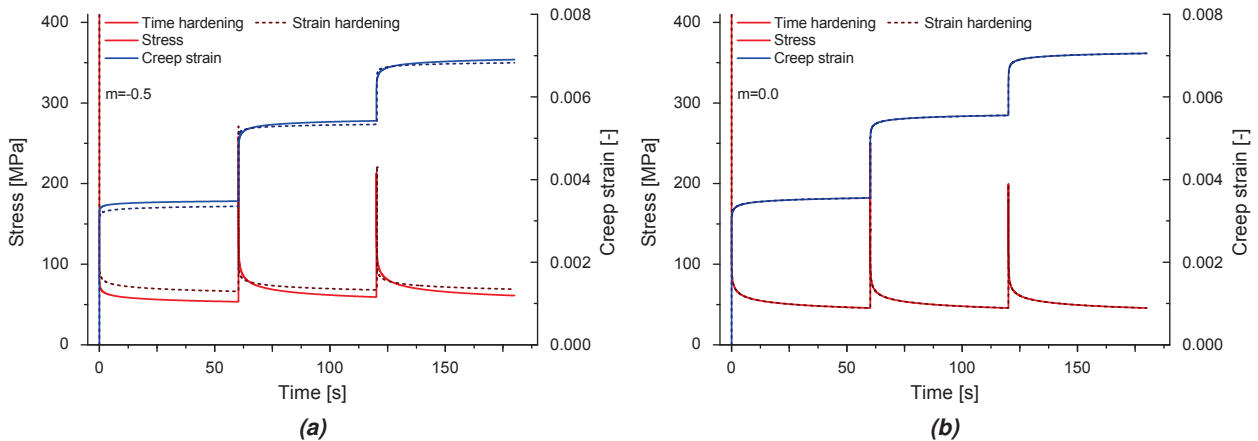


Figure 2.24: Stress relaxation - Comparison between time and strain hardening.

Combined primary and secondary creep: It is possible to choose the parameters of primary creep models accordingly to approximate the onset of secondary creep but only if the beginning of this region is of interest. Norton's power law on the other hand describes secondary creep for a large part of the dislocation creep regime. In order to cover both regimes it is possible to combine multiple time or strain hardening terms in one creep equation. Fig. 2.25a plots two strain hardening terms ($\dot{\epsilon}_{cr} = A\sigma^n \epsilon_{cr}^m$)

individually and combined. Additionally, the steady state response (i.e. $m=0$) is plotted individually for both expressions. The steady state contribution of the first term is very large compared to the second, but decreases very quickly with time if the parameter m is set to 0.5. If the second term is added — with $m=0$, of course — its steady state creep rate will dominate the creep response. This way primary and secondary creep, as well as the transition region in between can be modeled. Regarding the different number of implemented creep laws in Ansys compared to Abaqus — Table 2.8 contains all models implemented in Abaqus but only a small selection for Ansys — the difference seems to be significant and Ansys seems to offer the better support as regards the modeling of creep. It should not be disregarded, however, that the implementation of user defined creep laws is straightforward and offers the possibility to program any known empirical creep law. Code B.1 in Appendix B shows the creep subroutine that was used to simulate the *strain hardening double* creep law with a single element test (SET) in Abaqus.

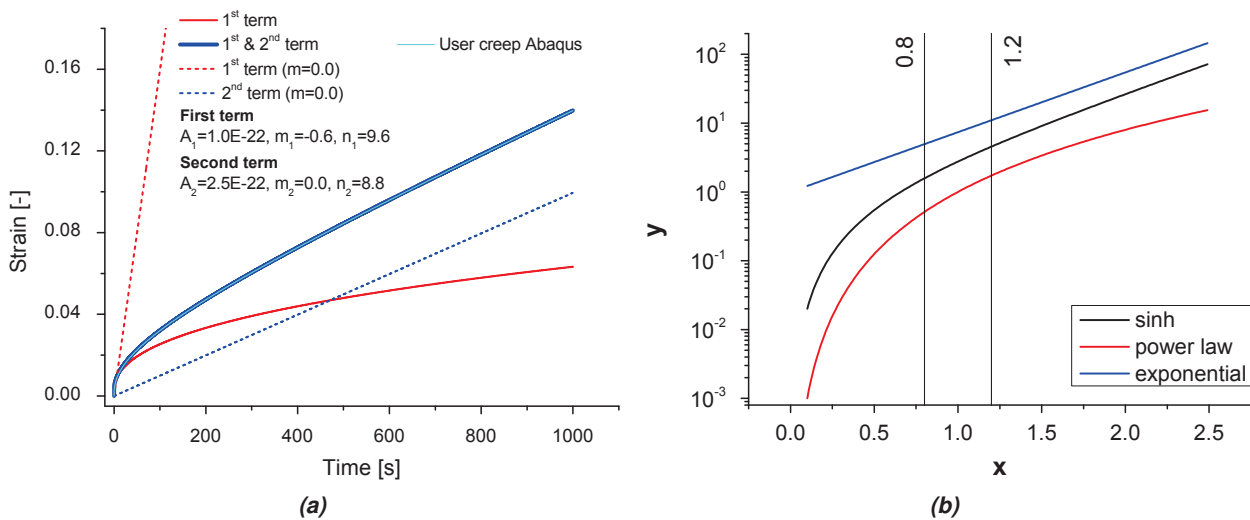


Figure 2.25: a) Illustration of strain hardening double creep law for the description of primary and secondary creep b) general comparison of hyperbolic sine function to power law and exponential law.

Combined power law creep and exponential creep: The various proportionalities between the stress level and the various creep mechanisms are discussed in Section 2.2. At intermediate temperatures and high stress levels a power law yields a proportionality that is lower than experimental observations. If this sort of behavior poses a problem for the modeling of multi-step creep experiments, the creep law according to Garofalo could be a solution. Fig. 2.25b compares a power law (red) to an exponential law in a logarithmic diagram. The hyperbolic sine function in between (black) follows the shape of the power law for values up to 0.8. After a transition the hyperbolic sine law is a straight line running parallel to the exponential function above 1.2. This behavior is also used in the Garofalo law to cover the regions of dislocation creep following a power law as well as the dislocation creep region exhibiting an exponential relationship.

Tertiary creep: Since tertiary creep is not relevant for the life estimation of brake disks the section will be closed at this point. A short discussion of the modeling of tertiary creep is given in Appendix A.6.

2. THEORETICAL BACKGROUND

2.5.2.3 Continuum mechanical framework

All creep equations have been discussed only in their empirical context so far. As previously implied, for their application in FE software, it is necessary to insert these one-dimensional equations in the three-dimensional continuum mechanical framework. Hence, most continuum mechanical creep models draw on constitutive equations based on a creep potential and a flow rule, which is equivalent to the procedures used in plasticity theory [5]. In the general context, the concept comes along with a yield criterion and a creep potential $\Phi(\boldsymbol{\sigma})$ that is used to determine the direction of deformation. Both the creep potential and the plastic potential used in plasticity theory are based on the principle of maximum dissipation rate, which allows the definition of the flow rule [121]. The inelastic strain increment $\dot{\boldsymbol{\epsilon}}_{in}$ is supposed to have the same principal directions as the deviatoric stress state $\boldsymbol{\sigma}'$, Eq. (2.28), leading to the definition of the flow rule in the form of Eq. (2.126), where $\dot{\eta}$ is a scalar factor [123]. It should be noted that in creep $\dot{\eta}$ is called proportionality factor, Lagrange multiplier or plastic multiplier as in plasticity theory [5; 19; 121].

$$\dot{\boldsymbol{\epsilon}}_{in} = \dot{\eta} \frac{\partial \Phi}{\partial \boldsymbol{\sigma}'} \quad \dot{\eta} > 0 \quad (2.126)$$

In the general formulation there is another analogy to plasticity models: In the application of the expression above it is necessary to apply the Kuhn-Tucker conditions, as noted in Section 2.5.1. However, the procedure is meaningful for plastic deformation and creep fatigue interaction. In the case of pure creep, however, the yield criterion and the Kuhn-Tucker conditions are usually dropped because the thermally activated processes leading to creep phenomena occur well below yield limits known from plasticity even at very low levels of stress. Experimental identification of yield limits is thus not possible for pure creep in contrast to plastic deformation. Eq. (2.126) still computes the direction of $\dot{\boldsymbol{\epsilon}}_{cr}$, which is oriented perpendicularly on the flow potential, while the scalar $\dot{\eta}$ indicates the magnitude of creep strain rate. The factor $\dot{\eta}$ is determined by means of the hypothesis of the equivalence of dissipation power given by Eq. (2.127). The equality between the tensorial quantities and the equivalent scalar quantities $\dot{\epsilon}_{cr,eq}$ and σ_{eq} is an assumption that facilitates the comparison between simulation and experiments.

$$P = \dot{\boldsymbol{\epsilon}}_{cr} : \boldsymbol{\sigma} = \dot{\epsilon}_{cr,eq} \sigma_{eq} \quad (2.127)$$

The plastic multiplier can thus be determined from inserting Eq. (2.127) in Eq. (2.126) and solving for $\dot{\eta}$:

$$\dot{\eta} = \frac{P}{\frac{\partial \Phi}{\partial \boldsymbol{\sigma}'} : \boldsymbol{\sigma}} = \frac{\dot{\epsilon}_{cr,eq} \sigma_{eq}}{\frac{\partial \Phi}{\partial \boldsymbol{\sigma}'}} \quad (2.128)$$

The unknown equivalent creep rate $\dot{\epsilon}_{cr,eq}$ is often defined as a function of the equivalent stress σ_{eq} according to empirical creep models that are characteristic for the relevant temperature and stress range. An example is the power law for secondary creep according to Norton and Bailey:

$$\dot{\epsilon}_{cr,eq} = K (\sigma_{eq})^n \quad (2.129)$$

Another widespread flow rule for creep modeling without yield criterion stems from Odqvist Eq. (2.130) and is based on the variational equation $\partial W = \partial \boldsymbol{\sigma} : \dot{\boldsymbol{\epsilon}}_{cr}$. $\partial W(\boldsymbol{\sigma})$ is a scalar valued function that takes the place of the creep potential.

$$\dot{\boldsymbol{\epsilon}}_{cr} = \frac{\partial W(\boldsymbol{\sigma})}{\partial \boldsymbol{\sigma}} \quad (2.130)$$

Depending on the equivalent stress both flow rules, Equations (2.126) and (2.130), may lead to the same constitutive equation, as can be seen from the definition of the dissipated energy. Keeping to Eq. (2.130) and assuming isotropic creep, the potential can be expressed in three invariants of $\underline{\sigma}$ and $\underline{\mathbf{s}}$, respectively:

$$W(\underline{\sigma}) = W(J_1^\sigma, J_2^\mathbf{s}, J_3^\mathbf{s}) \quad (2.131)$$

The appendix of [5] explains the rule for the derivative of a scalar function with respect to second rank tensor: $\Psi(J_1(\underline{\mathbf{A}}), J_2(\underline{\mathbf{A}}), J_3(\underline{\mathbf{A}}))$. The application of this rule to Eq. (2.130) yields:

$$\dot{\underline{\epsilon}}_{cr} = \frac{\partial W}{\partial J_1^\sigma} \mathbf{1} + \frac{\partial W}{\partial J_2^\mathbf{s}} \underline{\mathbf{s}} + \frac{\partial W}{\partial J_3^\mathbf{s}} \left(\underline{\mathbf{s}}^2 - \frac{1}{3} Tr(\underline{\mathbf{s}}^2) \mathbf{1} \right) \quad (2.132)$$

As noted in Section 2.4, it was found that the spherical part of the strain tensor does not contribute to plastic deformation. Equivalently, it is assumed in creep theory that the creep deformation does not entail significant volume changes (as long as tertiary creep is not involved). The spherical part of $\dot{\underline{\epsilon}}_{cr}$ is thus assumed to be zero which eliminates the first expression in Eq. (2.132) containing J_1^σ . The third term in Eq. (2.132) is non-linear in the stress deviator, which can be used to consider non-classical effects in the material behavior. These effects are commonly neglected and W reduces to a function of $J_2^\mathbf{s}$, thus forming a von Mises type potential that can be represented in terms of the equivalent stress:

$$\dot{\underline{\epsilon}}_{cr} = \frac{\partial W(\sigma_{eq})}{\partial \sigma_{eq}} \frac{\partial \sigma_{eq}}{\partial \underline{\sigma}} = \frac{\partial W(\sigma_{eq})}{\partial \sigma_{eq}} \frac{3}{2} \frac{\underline{\mathbf{s}}}{\sigma_{eq}} \quad (2.133)$$

The introduction of the equivalent strain rate yields:

$$\dot{\epsilon}_{eq} = \left(\frac{2}{3} \dot{\underline{\epsilon}}_{cr} : \dot{\underline{\epsilon}}_{cr} \right)^{\frac{1}{2}} = \frac{\partial W(\sigma_{eq})}{\partial \sigma_{eq}} \quad \dot{\underline{\epsilon}}_{cr} = \frac{3}{2} \dot{\epsilon}_{eq} \frac{\underline{\mathbf{s}}}{\sigma_{eq}} \quad (2.134)$$

Inserting Eq. (2.129) finally yields expression Eq. (2.135) which is commonly used for modeling steady state creep in structures.

$$\dot{\underline{\epsilon}}_{cr} = \frac{3}{2} K \sigma_{eq}^{n-1} \underline{\mathbf{s}} \quad \text{Odqvist law} \quad (2.135)$$

If the focus is laid on primary creep, the expressions for time or strain hardening can be inserted into Eq. (2.134) — as well as any other suitable creep law.

$$\dot{\underline{\epsilon}}_{cr} = \frac{3}{2} K \sigma_{eq}^{n-1} t^m \underline{\mathbf{s}} \quad \text{Time hardening} \quad (2.136)$$

$$\dot{\underline{\epsilon}}_{cr} = \frac{3}{2} K \sigma_{eq}^{n-1} (\epsilon_{eq}^{cr})^m \underline{\mathbf{s}} \quad \text{Strain hardening} \quad (2.137)$$

The three empirical creep laws are only approximations for the creep behavior and suffer from certain limitations, as previously discussed. Nevertheless, they can be easily implemented in the multiaxial continuum mechanical framework of a FE software.

Certain experiments revealed deviations from creep laws based on the von Mises stress, such as non-symmetric creep behavior under tension and compression. For materials showing these effects creep potentials based on all three invariants of $\underline{\sigma}$ have been defined. They are called non-classical creep equations, as noted in [5].

The continuum mechanical framework (CMF) is not only useful to incorporate empirical material laws, but also to enhance their physical meaning. Let us go back to the *strain hardening double* creep law

2. THEORETICAL BACKGROUND

for primary and secondary creep shown in Fig. 2.25a. The transition from primary to secondary creep is purely a function of the accumulated creep strain. The creep strain itself results from the current equivalent stress and time — the influence of the time diminishes when the second term becomes dominant. In the CMF it is now possible to take into account the impact of the stress state on the creep rate. As the empirical creep law enters the CMF in the form of the equivalent creep rate, the CFM can influence the creep response to the current stress state by the formulation of the equivalent stress. This procedure shall be discussed in the following in order to illustrate the possible enhancements of empirical laws within the CMF:

For transient creep effects and complex loading conditions the concepts discussed so far can be enhanced with internal state variables and evolution equations (hardening rules). One possible enhancement based on a kinematic hardening rule — kinematic hardening was already discussed for plasticity in Section 2.5.1, but the concept of an effective stress was also mentioned in the context of creep in Section 2.2. The stress tensor is split into an effective and a translation part $\underline{\mathbf{X}}$ (backstress):

$$\underline{\boldsymbol{\sigma}} = \underline{\bar{\boldsymbol{\sigma}}} + \underline{\mathbf{X}} \quad (2.138)$$

In plasticity theory the backstress is used to move the yield surface in stress space. This way mechanical hysteresis loops can be modeled. In the current context, kinematic hardening is used to consider hardening effects causing a transition from primary to secondary creep. Moreover, the impact of the stress state and the loading history on the current creep rate can be taken into account as illustrated in [5]. In analogy to plasticity theory it is assumed that only the effective part of the $\underline{\boldsymbol{\sigma}}$ is relevant for the creep strain. The creep potential is thus a function of $\underline{\bar{\boldsymbol{\sigma}}}$ and equivalently to previous discussions only the second invariant of the effective deviator $\underline{\bar{\mathbf{s}}}$ is considered in the formulation of the constitutive law:

$$W = W(\underline{\bar{\boldsymbol{\sigma}}}) = W(\underline{\boldsymbol{\sigma}} - \underline{\mathbf{X}}) \quad (2.139)$$

$$\bar{\sigma}_{eq} = (3J_2^{\underline{\bar{\mathbf{s}}}})^{\frac{1}{2}} = \left(\frac{3}{2} (\underline{\bar{\mathbf{s}}} - \underline{\mathbf{X}}) : (\underline{\bar{\mathbf{s}}} - \underline{\mathbf{X}}) \right)^{\frac{1}{2}} = \left(\frac{3}{2} (\underline{\bar{\mathbf{s}}}) : (\underline{\bar{\mathbf{s}}}) \right)^{\frac{1}{2}} \quad (2.140)$$

The above expression can be combined with the Odqvist flow rule (Eq. (2.130)) yielding:

$$\dot{\underline{\boldsymbol{\epsilon}}}_{cr} = \frac{3}{2} \frac{\dot{\epsilon}_{eq}^{cr}}{\bar{\sigma}_{eq}} \underline{\bar{\mathbf{s}}} \quad (2.141)$$

An empirical creep law $f_{1b}(\sigma)$ from Table 2.7 for steady state creep — with or without a temperature term $f(T)$ — can be inserted for $\dot{\epsilon}_{eq}^{cr}$. In contrast to previous constitutive equations, such as Eq. (2.135), there is the internal state variable $\underline{\mathbf{X}}$, the backstress, in the equation. On the one side this complicates the situation since an evolution equation has to be defined that determines how $\underline{\mathbf{X}}$ is going to change with other variables like $\dot{\underline{\boldsymbol{\epsilon}}}_{cr}$. On the other side, the model has greater capabilities. Due to the evolution of the $\underline{\mathbf{X}}$, which is influenced by the chosen evolution equation, the initial value for $\underline{\mathbf{X}}$ and the saturation value that results from the choice of parameters in the evolution equation, Eq. (2.141) can describe the transition from primary to secondary creep. Comparable results to the *strain hardening double* model (see Fig. 2.25b) can be obtained. A significant difference, however, is the treatment of the stress state. Stress states leading to the same equivalent stress could not be distinguished with Eq. (2.135), but Eq. (2.141) may yield different creep rates. An example, where this is useful, is spectrum loading with load reversals, where the creep rate before and after significantly differ.

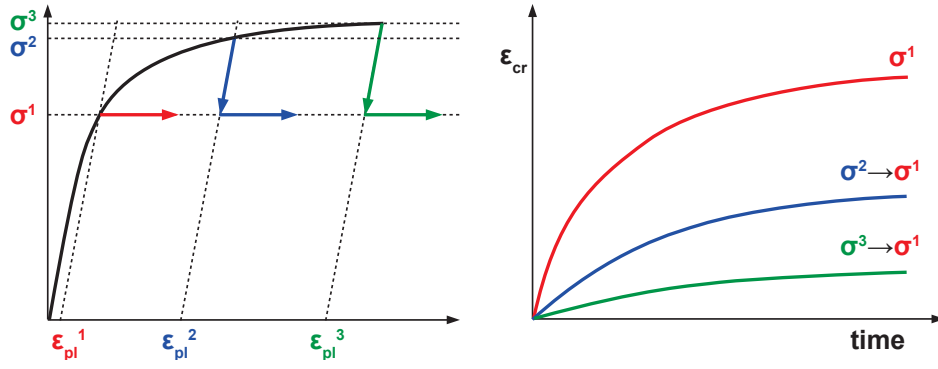


Figure 2.26: Effect of plastic pre-deformation on primary creep response [5].

Eq. (2.142) is an example for one of a whole range of possible evolution laws for the backstress. Q is the activation energy for recovery and b , c_0 are material parameters. The expression is a multiaxial application of the Bailey-Orowan recovery hypothesis, which is discussed in [99]. The procedure is thus an example how physical mechanisms may find their way in the definition of constitutive equations. Further information on Eq. (2.142) is given in [5].

$$\dot{\underline{\mathbf{X}}} = \frac{2}{3} b \dot{\underline{\epsilon}}_{cr} - c \bar{\alpha}_{eq}^{n-1} \underline{\mathbf{X}} \quad \bar{\alpha}_{eq} = \left(\frac{3}{2} \underline{\mathbf{X}} : \underline{\mathbf{X}} \right)^{\frac{1}{2}} \quad c = c_0 \exp \left(-\frac{Q}{RT} \right) \quad (2.142)$$

The creep response to the current stress state is also affected by plastic predeformation as illustrated in Fig. 2.26. This is due to the formation of dislocation structures due to plastic deformation, which shift the equilibrium state between hardening and softening mechanisms during primary creep. Furthermore, plasticity and creep can occur in the same load cycle and determine the mechanical response to external loading in a coupled manner. It is not possible to describe these effects with creep laws only. For this reason, Section 2.5.3 will focus on the modeling of viscoplasticity.

2.5.2.4 Integration of creep laws in the continuum mechanical framework

The integration of creep laws may be established by explicit or implicit methods. For explicit integration the forward Euler method is commonly applied for creep laws. As outlined in [111], the numerical statement of the problem is as follows (i refers to the current time step):

$$\Delta \underline{\epsilon}_{cr,i+1} = \dot{\underline{\epsilon}}_{cr,i+1} \Delta t_i \quad (2.143)$$

$$\underline{\epsilon}_{cr,i+1} = \underline{\epsilon}_{cr,i} + \Delta \underline{\epsilon}_{cr,i+1} \quad (2.144)$$

For the example of strain hardening, the whole algorithm can be summarized as follows:

1. $\underline{\sigma}_i$ is determined
2. $\dot{\underline{\epsilon}}_{cr,i+1} = \frac{3}{2} K \sigma_{eq,i}^{n-1} \left(\underline{\epsilon}_{eq,i}^{cr} \right)^m \underline{\mathbf{s}}_i$
3. $\Delta \underline{\epsilon}_{cr,i+1} = \dot{\underline{\epsilon}}_{cr,i+1} \Delta t_i$
4. $\underline{\epsilon}_{cr,i+1} = \underline{\epsilon}_{cr,i} + \Delta \underline{\epsilon}_{cr,i+1}$
5. $\underline{\epsilon}_{el,i+1} = \underline{\epsilon}_{tot} - \underline{\epsilon}_{cr,i+1}$

2. THEORETICAL BACKGROUND

$$6. \sigma_{i+1} = \underline{\underline{\mathbf{E}}}\epsilon_{el,i+1}$$

Steps 5 and 6 are necessary for the case of stress relaxation. For creep they are redundant since σ remains constant. Since the accumulated creep strain is part of the creep equation, it is necessary to start the algorithm with a small value for ϵ_{cr} . This can either be established by a given value or by using the time hardening law for the first increment. The laws only differ in the case of load variations which can take effect only after the first increment. For implicit integration the backwards Euler method is a common choice, which is again based on Equations (2.143) and (2.144) and can be summarized:

1. σ_i is determined
 2. $\dot{\epsilon}_{cr,i+1} = \frac{3}{2} K \sigma_{eq,i+1}^{n-1} \left(\epsilon_{eq,i+1}^{cr} \right)^m \mathbf{s}_{i+1}$
 3. $\Delta\epsilon_{cr,i+1} = \dot{\epsilon}_{cr,i+1} \Delta t_i$
 4. $\epsilon_{cr,i+1} = \epsilon_{cr,i} + \Delta\epsilon_{cr,i+1}$
 5. $\epsilon_{el,i+1} = \epsilon_{tot} - \epsilon_{cr,i+1}$
 6. $\sigma_{i+1} = \underline{\underline{\mathbf{E}}}\epsilon_{el,i+1}$
- } $\epsilon_{cr,i+1}$ and σ_{i+1} are determined iteratively

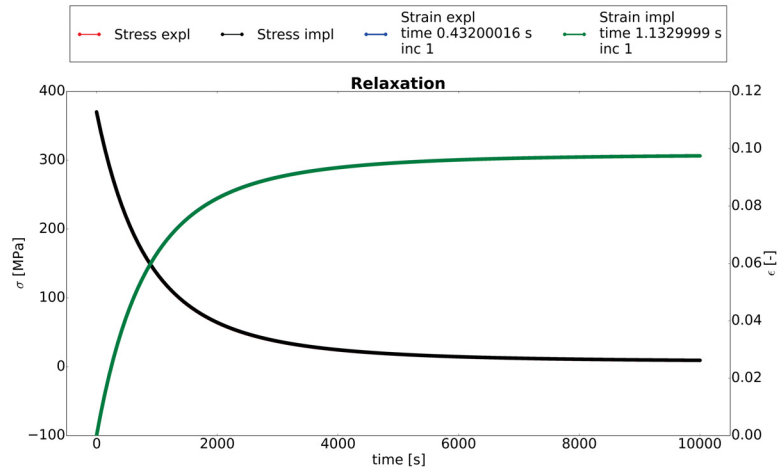


Figure 2.27: Explicit and implicit creep formulation with a fine incrementation. The corresponding computation times are indicated in the legend.

The difference between the two methods is that only quantities from the time step i are required to compute the creep strain increment $\Delta\epsilon_{cr,i+1}$ for the explicit scheme, while quantities from the subsequent time step are used in the implicit scheme. The latter one thus requires an iterative solution in each increment. In order to obtain a stable solution, the time increments must be very small in the explicit scheme compared to the implicit method. If Δt is small enough both approaches yield similar results with minimal deviations as shown for stress relaxation in Fig. 2.27. When Δt is chosen too large the numerical solution for the stress level becomes negative with the explicit method (Fig. 2.28). This non-physical solution is avoided by the implicit method, which still deviates due to the coarse incrementation, but converges in a stable manner. The stability of the implicit method is achieved at the expense of computation time. A general way to speed up a creep simulation is to use adaptive time incrementation. For the case of explicit integration, the stress level between t_i and t_{i+1} is assumed constant during the increment. Eq. (2.145) provides an objective criterion whether the time increment can be enlarged or not. A value

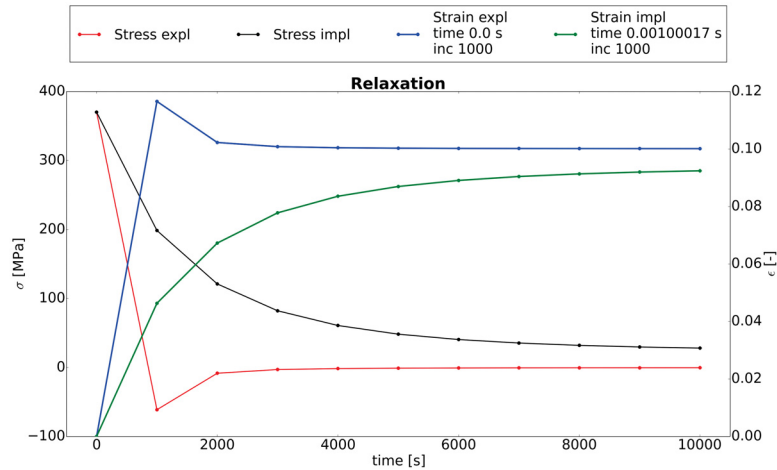


Figure 2.28: Explicit and implicit creep formulation with a coarse incrementation. The corresponding computation times are indicated in the legend.

$r_{crit} = 0.1$ means that the stress may change by maximal 10% during the increment. In the beginning of the simulation, with decreasing creep strain increments the change in the stress level falls below 10%. Eq. (2.145) illustrates the impact of this method on the computation time for the relaxation experiment mentioned previously. The step size adaptation is applied for the explicit integration method. The computation time shrinks by a factor of 100, while the computation time for the implicit scheme stays nearly constant — the latter is a requirement for the comparability of the computation times since other processes on the computer may interfere with the solution speed. Both curves are still on top of each other which stands as a verification of the procedure. This method can be used for the implicit scheme as well but other methods are available, which are controlled by the convergence of the Newton-Raphson algorithm.

$$r = \frac{\Delta\epsilon_{cr}}{\epsilon_{el}} < r_{crit} \tag{2.145}$$

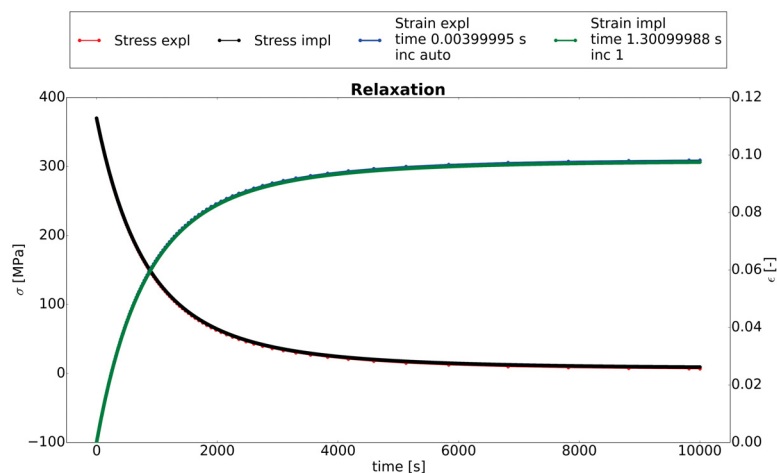


Figure 2.29: Illustration of automatic incrementation. The corresponding computation times are indicated in the legend.

2.5.3 Viscoplastic models

As noted in Section 2.3 the dislocation creep region in Ashby maps refers to a deformation mechanism that shares some common ground with both plasticity and creep. The predominant contribution to the inelastic deformation is based on dislocation glide as in rate-independent plasticity. At elevated temperatures diffusion mechanisms, namely the diffusion of vacancies in the crystal structure, start to play an important role, a role which is not obvious at room temperature because diffusion is too slow. Due to the diffusion of vacancies to the tensile/compressive field of dislocations they enable dislocation climb. Dislocations, which are stuck at obstacles as precipitates or other dislocations are thus mobilized and they can continue their gliding motion. At low temperatures these obstacles are responsible for the yield stress that has to be reached in order to enable dislocation glide. Especially at low strain rates the concept loses its meaning in the dislocation creep region, since dislocations can move at low stress levels. According to [17], viscoplastic materials share some common ground with plastic materials, as they exhibit permanent deformation after the application of a load. However, they also exhibit continuous creep flow when the load is maintained. In a similar manner to the plasticity models (Section 2.5.1) the σ - ϵ response can be illustrated for the one-dimensional case by the aid of rheological models. Here this step is omitted and the discussion starts from an empirical point of view. The elastic domain is much smaller in viscoplastic-

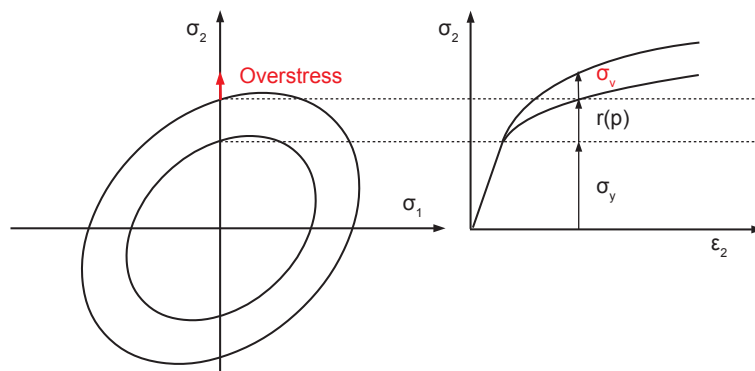


Figure 2.30: Monotonic stress strain curve: a) von Mises yield surface with isotropic hardening and viscous overstress, b) corresponding σ - ϵ curve (based on [19]).

ity compared to rate-independent plasticity to allow creep at low stresses. The current stress is free to depart from the elastic domain by the so called overstress [109]. Consequently, the consistency condition discussed in Section 2.5.1.4 in the context of rate-independent plasticity is no longer applicable. The concept of an overstress is illustrated in Fig. 2.30 plotting a tensile test at elevated temperature. For rate-dependent plasticity the achieved stress level at a certain stage during the tensile test would result from the σ_y and the contribution from isotropic hardening $R(p)$. This state is represented by the lower line in σ - ϵ diagram in Fig. 2.30. In a viscoplastic formulation the stress state may exceed the yield surface by a viscous overstress, which is a function of the strain rate. The higher the strain rate, the more the results from the viscoplastic model approach the ones from the rate-independent formulation. Rate-independent plasticity can thus be seen as a special case of viscoplasticity, when the strain rate is infinite. The situation is different for low strain rates, where higher overstresses occur.

An often used form of the viscous stress σ_v , based on the Norton equation for secondary creep (Eq. (2.96)), is given by Eq. (2.146), where K and n are material constants. This and further formulations are discussed

in [110; 113].

$$\sigma_v = K\dot{p}^{\frac{1}{n}} \quad (2.146)$$

The stress state in Fig. 2.30 can be expressed as a sum of individual contributions. In the case of uniaxial loading:

$$\sigma = X + \sigma_{y,0} + R + K\dot{p}^{\frac{1}{n}} \quad (2.147)$$

On the one hand, Eq. (2.147) shows that σ_v disappears for $n \rightarrow \infty$ or $K \rightarrow 0$. This case marks the limit where the results from the rate-dependent formulation become identical to the rate-independent formulation. On the other hand, Eq. (2.147) can be rearranged and solved for the equivalent plastic strain rate \dot{p} , as outlined in [19]:

$$\dot{p} = \left\langle \frac{\sigma - X - R - \sigma_{y,0}}{K} \right\rangle^n \quad (2.148)$$

The generalization to the multiaxial formulation yields Eq. (2.149), which is the constitutive equation of rate-dependent plasticity relating stress and plastic strain.

$$\dot{p} = \left\langle \frac{J_2(\underline{\mathbf{s}} - \underline{\boldsymbol{\chi}}) - R - \sigma_{y,0}}{K} \right\rangle^n = \left\langle \frac{\left(\frac{3}{2}(\underline{\mathbf{s}} - \underline{\boldsymbol{\chi}}) : (\underline{\mathbf{s}} - \underline{\boldsymbol{\chi}})\right)^{\frac{1}{2}} - R - \sigma_{y,0}}{K} \right\rangle^n \quad (2.149)$$

Since an overstress is admitted the consistency condition used in rate-dependent plasticity no longer applies. Moreover, it is not necessary, since \dot{p} can be directly obtained from Eq. (2.149). The normality rule still applies. Based on Eq. (2.76) and Eq. (2.82) it can be formulated for viscoplasticity and combined hardening:

$$\dot{\boldsymbol{\epsilon}}_{pl} = \dot{\lambda} \frac{\partial f}{\partial \underline{\boldsymbol{\sigma}}} = \frac{3}{2} \dot{p} \frac{\underline{\mathbf{s}} - \underline{\boldsymbol{\chi}}}{\sigma_{eq}} = \frac{3}{2} \left\langle \frac{\left(\frac{3}{2}(\underline{\mathbf{s}} - \underline{\boldsymbol{\chi}}) : (\underline{\mathbf{s}} - \underline{\boldsymbol{\chi}})\right)^{\frac{1}{2}} - R - \sigma_{y,0}}{K} \right\rangle^n \frac{\underline{\mathbf{s}} - \underline{\boldsymbol{\chi}}}{\left(\frac{3}{2}(\underline{\mathbf{s}} - \underline{\boldsymbol{\chi}}) : (\underline{\mathbf{s}} - \underline{\boldsymbol{\chi}})\right)^{\frac{1}{2}}} \quad (2.150)$$

The equation above combined with the evolution equations for $\underline{\mathbf{X}}^1$ (e.g. Eq. (2.62)) and R (e.g. Eq. (2.67)), as well as Hooke's law in rate formulation, Eq. (2.151), comprise a complete viscoplastic material model.

$$\dot{\boldsymbol{\sigma}} = 2G\dot{\boldsymbol{\epsilon}}_{el} + \lambda Tr(\dot{\boldsymbol{\epsilon}}_{el})\mathbf{1} \quad G, \lambda \dots \text{Lame's constants} \quad (2.151)$$

In analogy with the discussion from Section 2.5.1 and Appendix A, a dissipation potential can be defined $\phi^* = \Omega(\boldsymbol{\sigma}, T)$. The dissipation potential, or in this case viscoplastic potential, allows to embed the viscoplastic model in the concept of the classical thermodynamic framework [124]. In the scope of the classical Chaboche models a viscoplastic potential of Norton type is used:

$$\Omega = \frac{K}{n+1} \left\langle \frac{J_2(\underline{\mathbf{s}} - \underline{\boldsymbol{\chi}}) - R - \sigma_{y,0}}{K} \right\rangle^{n+1} \quad (2.152)$$

As illustrated by Ecker [20] the viscoplastic potential can be illustrated as a set of equipotential surfaces which connect the allowed stress states outside the elastic domain (Fig. 2.31). Each surface applies for

¹If the von Mises plasticity is used the backstress $\underline{\mathbf{X}}$ is deviatoric and thus identical to $\underline{\boldsymbol{\chi}}$. The formalism in the derivations is maintained, however.

2. THEORETICAL BACKGROUND

a specific strain rate and allows a certain overstress. The inner limit of the potential corresponds to the elastic domain, the outer limit to the case of an infinite strain rate. The maximal magnitude of the overstress is thus limited.

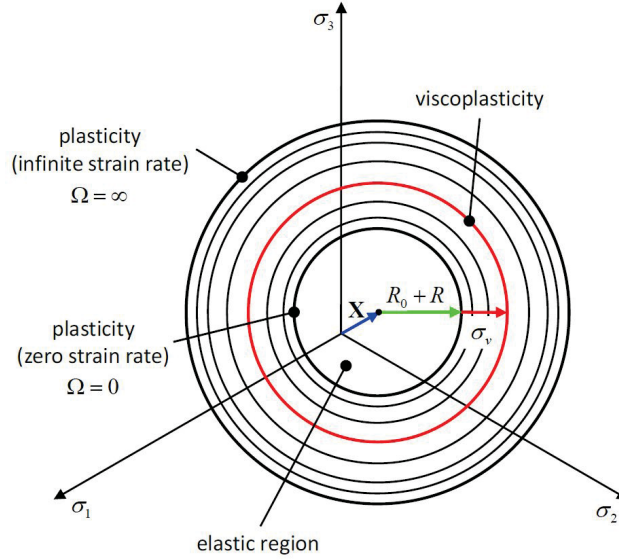


Figure 2.31: Figurative illustration of a viscoplastic potential as a set of equipotential surfaces [20].

With the aid of this potential the flow rule can be expressed in a physically sound manner:

$$\dot{\underline{\epsilon}}_{pl} = \dot{p} \frac{\partial \Omega}{\partial \underline{\sigma}} = \frac{3}{2} \dot{p} \frac{\underline{\mathbf{s}} - \underline{\chi}}{\sigma_{eq}} \quad (2.153)$$

Besides the functionality discussed so far thermal recovery can be included in the evolution laws of the hardening variables. As noted in [110] thermal recovery is attributed to two effects: 1) rearrangement of dislocations due to climb and 2) recrystallization. An example of extended evolution laws is given below, where γ^* , m , γ_r , k and Q_r are material parameters. The material parameters c , γ , b and Q are already known from Section 2.5.1:

$$\dot{\underline{\mathbf{X}}} = \frac{2}{3} c \dot{\underline{\epsilon}}_{pl} - \gamma \underline{\mathbf{X}} \dot{p} - \gamma^* [J_2(\underline{\mathbf{X}})]^{m-1} \underline{\mathbf{X}} \quad \text{kinematic hardening with recovery} \quad (2.154)$$

$$\dot{R}(p) = b(Q - R)\dot{p} - \gamma_r |R - Q_r|^{k-1} (R - Q_r) \quad \text{isotropic hardening with recovery} \quad (2.155)$$

In both equations hardening is reduced in dependence of the strain rate. In the case of dwell times complete recovery is possible in Eq. (2.154). In Eq. (2.155) recovery can be limited by the coefficient Q_r . The applicability of viscoplastic material models is thus extended and a wider range of σ - ϵ responses due to specific loading conditions can be modeled.

For distinct creep problems, as in the case of very low strain rates and long load cycles, the inelastic deformation loses its dependence on a yield limit completely. In this case the hardening terms can be omitted in Eq. (2.150), yielding Eq. (2.157). The expression can be rearranged, finally yielding Odqvist's law¹, Eq. (2.135), which has been derived in the context of pure creep models in Section 2.5.2.3. Odqvist's law is the multiaxial version of the Norton's law for the description of secondary creep as a power law. This

¹The exponent n in Eq. (2.135) and Eq. (2.157) are not identical due to the mode of derivation in the present case yielding -1 in the exponent

derivation illustrates again the dual nature of viscoplasticity taking into account both dislocation slip and creep phenomena, since it shows how plasticity and creep models are interrelated.

$$\dot{\epsilon}_{pl} = \frac{3}{2} \left\langle \frac{\sigma_{eq}}{K} \right\rangle^n \frac{\underline{\mathbf{s}}}{\sigma_{eq}} = \frac{3}{2} A \sigma_{eq}^n \frac{\underline{\mathbf{s}}}{\sigma_{eq}} = \frac{3}{2} A \sigma_{eq}^{n-1} \underline{\mathbf{s}} \quad (2.156)$$

As noted in Section 2.2.2, in most parts of the dislocation creep region in an Ashby map, the relation between stress and strain follows a power law. At the upper and lower bound of this region other relations are more appropriate. At the upper bound, which is the interesting one from the point of view of viscoplasticity, an exponential relation is sometimes observed. The transition from a potential to an exponential relation with increasing stress is called power law breakdown. Garofalo defined an empirical creep law based on a hyperbolic sine function, Eq. (2.19), which allows the modeling of both relations. Similar to Norton's law, Garofalo's law can be implemented in the viscoplastic framework, as e.g. in [125]. A discussion on alternative flow rules is given in [115] by Szmytka et al. In [115] they also present a case where even a hyperbolic sine function is not sufficient to model the relation between σ and ϵ_{cr} sufficiently well for a wide range of stress levels. Based on physical phenomena concerning dislocation glide they present an alternative flow rule, which is more physical than other models, but still applicable in the industrial context.

The material models for plasticity and viscoplasticity described in this chapter correspond to the work developed at ONERA. Further information on these models as well as alternative developments of constitutive equations is given in [110; 113]. The thermodynamic framework around the constitutive equations is laid out in [17; 114]. As noted above, there is an alternative to the unified modeling of viscoplasticity, i.e. the *plasticity-creep partition*:

$$\underline{\epsilon} = \underline{\epsilon}_{el} + \underline{\epsilon}_{pl} + \underline{\epsilon}_{cr} \quad (2.157)$$

The rate-dependent material response can thus be modeled by an appropriate combination of the plasticity models mentioned in Section 2.5.1 and the creep models in Section 2.5.2. Further insights into plasticity-creep partition modeling is given in [113].

The sections presented up to this point provide the background and the means for service life assessment concepts. An overview is given subsequently.

2.6 General service life assessment concepts

Fig. 2.32 provides an illustration of common concepts that — besides others — can be applied to the design of components against fatigue failure. Intuitively, the most straightforward approach would probably be **component** testing. The component under investigation is subjected as a whole to a series of relevant loading conditions and success or failure will reveal design issues leading to cracking or oversizing of the component. It is usually not feasible to test all possible designs in all relevant service situations as test capacities, budgets and the time available are generally by far too short. Component testing is thus limited to the final phases of component design and involves testing of specific configurations and loading conditions for verification purposes. An example is a 200-stop test on a test rig for the certification of the brake system of a new train type. For the other phases in research & development and engineering a combination of laboratory tests and numerical methods is required.

2. THEORETICAL BACKGROUND

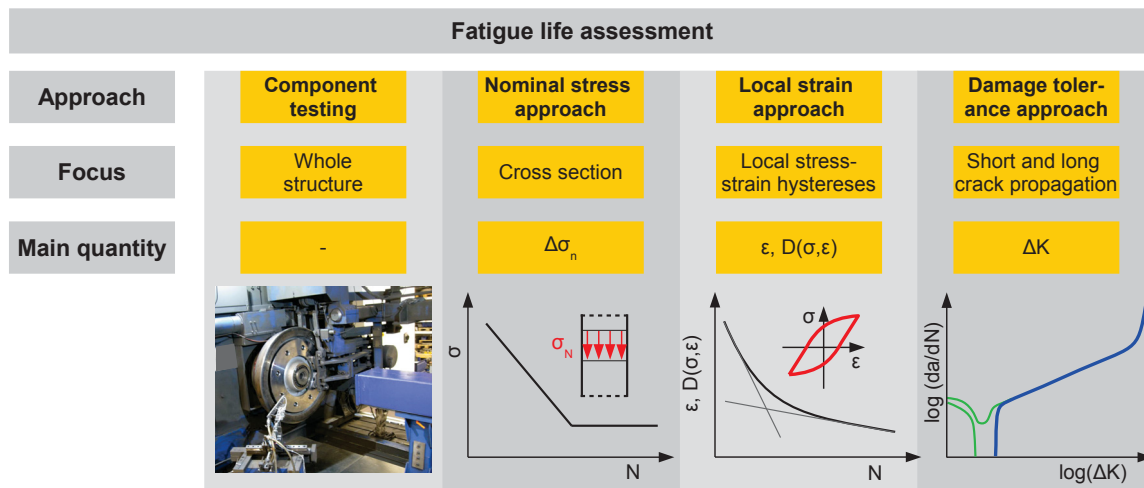


Figure 2.32: Overview of principal methods used in fatigue design (based on [6; 21]).

In the case it is possible to define a characteristic cross section with a corresponding nominal stress the engineer may opt for the **nominal stress concept**. The nominal stress concept is simple to use, which makes it widespread. It is a so-called total life approach where crack initiation and crack propagation are comprised in a Woehler curve (S-N curve). This concept fails, however, when local processes determine the failure behavior. This may be the case when cyclic plastic deformation occurs — typical for low cycle fatigue — or when load sequence effects need to be considered [16]. The position with the highest loading may thus be unknown or it may change with an increasing number of load cycles. In the case of a brake disk, damage may be a very localized problem, which is due to the formation of thermal gradients as noted in Section 1.2. This situation is further complicated by the fact that the temperature significantly varies during each brake application both on the global and the local scale. The modeling of damage is thus a complicated issue depending on a multitude of factors, which may themselves vary with the position on the disk. The **local strain concept** is based on the characterization of the local stress-strain response of the material to external loading. It only yields the service life until crack initiation based on strain-based Woehler curves (ϵ -N curves), however, and a fracture mechanical analysis may be used in conjunction with the local strain concept, as long as crack propagation is allowed in the component under investigation. Conventionally, values obtained from strain gauges attached to the component, or more frequently, results from Finite Element (FE) calculations are used in conjunction with ϵ -N curves to characterize the fatigue behavior of a component. This requires the use of appropriate constitutive equations for modeling the cyclic plastic behavior (see Section 2.5).

The **damage tolerance approach** assumes cracks to be present right from the beginning, but they are allowed as long as they remain below a critical size. The definition of a critical crack length and the characterization of crack propagation rates under the relevant loading conditions are thus paramount topics in the damage tolerance approach. Since initial flaw sizes can be detected by non-destructive testing and estimations of crack propagation rates can be carried out, it is possible to define service intervals. They are chosen in such a way that crack propagation may occur but the critical crack size will never be reached. After the period of a service interval the maximal crack sizes are determined again and the subsequent interval is chosen. Alternatively, inspection may be carried out according to a fixed schedule. The tolerable

flaw size, however, must be chosen sufficiently smaller than the critical crack length so that propagating cracks always stay below the critical length between two inspections. If the tolerable crack size is obtained the component must be repaired or replaced.

Thermomechanical fatigue (TMF) problems can be described with elaborate forms of the local strain concept, which will be discussed in depth in Section 2.6.4. The analysis can be supplemented by fracture mechanical approaches as will be shown in Chapter 5. In specific isothermal cases some simpler methods may suffice to account for cyclic plasticity, which will be discussed first before expanding on more extensive procedures.

2.6.1 Empirical life prediction models

As noted above, damage parameters are commonly used in the local strain concept in the scope of low cycle fatigue. A damage parameter is computed from one or more quantities characteristic of a stabilized load cycle. This might be the plastic strain amplitude $\epsilon_{pl,a}$ in the case of Manson-Coffin or additionally the maximum stress in the case for Smith-Watson-Topper (SWT) or even the whole hysteresis area for the plastic dissipated energy criterion. Initially they have been calibrated with isothermal experiments and also used for components exposed to isothermal loading conditions. Nevertheless they can also be applied to TMF loading provided that they are calibrated with proper TMF tests. In the case of TMF the mode of use requires more complicated simulation procedures as will be shown below. Some damage parameters are simpler than others but each of them has its own range of applicability. Manson-Coffin, which can be seen as the simplest damage parameter, just takes the stabilized plastic strain amplitude into account, which is a link to the governing mechanisms of crack initiation, as outlined in Section 2.1.2. The damage parameters of SWT and Ostergren can take into account the effect of the mean stress on crack initiation life time since they include the maximum stress of the hysteresis. This way ϵ -N curves can be transformed to more general damage parameter curves. The physical improvement is still in question since every damage parameter is merely an empirical means to link load parameters to a crack initiation life time and the most important quantity is the plastic strain. Often the damage parameter according to Smith Watson and Topper (D_{SWT}) is applied, e.g. [126], but it fails when σ_{mean} is in the pressure regime. Energy based damage parameters as the Riedler model or the dissipated plastic energy criterion are more general in the sense that they can be calibrated on the basis of an experimental program including different types of tests like low cycle fatigue (LCF) tests, thermomechanical fatigue (TMF) tests and multiaxial tests. Under specific conditions it is thus possible to obtain one parameter set that is valid for very different loading conditions, as discussed in [70; 127]. If Manson-Coffin is used for the same experimental program an individual parameter set needs to be defined for each experimental type and temperature. Table 2.9 provides an overview of a range of commonly used damage parameters with some short comments on their usage.

The calibration of a damage parameter is illustrated in Fig. 2.33. In a first step the chosen damage parameter must be computed from each data set of the experimental program that should be the basis of the final parameter set. The experimental program needs to cover all relevant loading conditions and the limits of validity must be specified accordingly for the final user. In the case of Manson-Coffin the damage parameter is $\epsilon_{pl,a}$, which must be determined from the stabilized hysteresis loops. For the other damage parameters more quantities need to be determined and computed according to Table 2.9. A possible result

2. THEORETICAL BACKGROUND

of such a procedure is depicted in Fig. 2.33b. The individual values of the selected damage parameter are plotted versus the corresponding cycles to crack initiation on logarithmic scales. The common approach

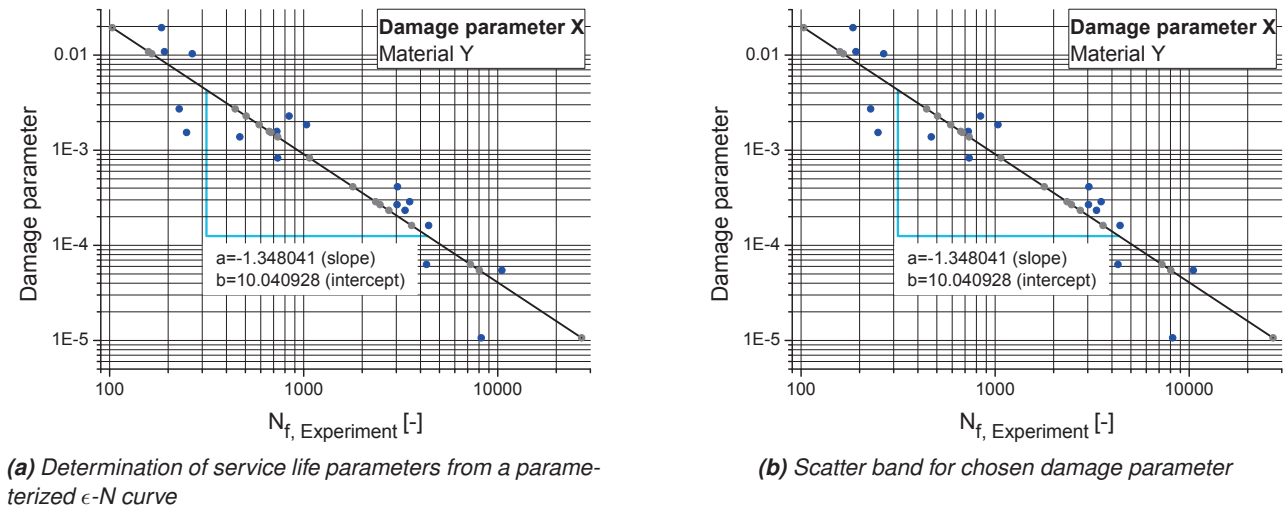


Figure 2.33: Illustration of the procedure for the test of damage parameters.

is to determine the parameters A and b of a power law, Eq. (2.158), from the logarithmic diagram. These parameters are the data set for the chosen damage parameter and experimental data set.

$$D = aN_f^b \quad (2.158)$$

Subsequently Eq. (2.158) can be solved for N_f according to Eq. (2.159) and in this form used for life time predictions. For this purpose the damage parameter D needs to be determined, usually by numerical methods, and inserted into Eq. (2.159).

$$N_f = \left(\frac{D}{a} \right)^{\frac{1}{b}} \quad (2.159)$$

A vital information for the applicability of damage parameters is the scatter, i.e. the deviation of the computed results from the experimental results. Fig. 2.33b provides an illustration of the common representation of the scatter of a specific data set. The horizontal axis shows the experimental life time, while the vertical axis refers to the results obtained from Eq. (2.159) using the previously determined coefficients a and b as well as the computed values for the damage parameter. The minimum requirement is that at least 90% of all data points must lie within a scatter band of ± 2.5 ($T_{90\%} 2.5$), indicated by the red line. The real scatter band is determined from the data set and inserted into the plot (green line in this example). Besides the scatter band some additional information is needed, as will be discussed in Chapter 5.

Table 2.9: Overview of empirical models for service life estimation

| Model | Damage parameter | Comments |
|---------------|---------------------------------------|-------------------------------------|
| Manson-Coffin | $\epsilon_{pl,a} = \epsilon_f' N_B^c$ | Most common model for LCF e.g. [25] |

| | | |
|-------------------------------------|--|--|
| Smith-Watson-Topper | $P_{SWT} = \sigma_{max} \epsilon_{a,t} = a N_B^c$ | Product of total strain amplitude and maximum stress. In contrast to Manson-Coffin the mean stress is taken into account. This is also the case for the subsequent damage parameters. [128] |
| Ostergren | $P_{Ost} = \sigma_{max} \Delta \epsilon_{pl} = a N_B^c$ | Product of plastic strain range and maximum stress, as only $\epsilon_{pl,a}$ is assumed to cause crack initiation. [129] |
| Plastic dissipated energy criterion | $P_{dpe} = \int_{cycle} \sigma : \dot{\epsilon}_{pl} dt$ | The dissipated energy yields a general link between a stabilized cycle and the corresponding N_f . The use of temperature dependent parameters is avoided. The damage parameter can be extended by expressions including the maximum stress or the maximal hydrostatic stress. [127] |
| Riedler Unified Approach | $P_R = \Delta W_u = c_u \Delta W_{u,e} + \Delta W_{u,p} = c_u (\sigma_{max} \epsilon_{a,e}) + (\sigma_a \epsilon_{a,p})$ | The damage parameter includes an approximation of the plastic dissipated energy and the elastic deformation energy. [69] |

Independently of the selected damage parameter, the required information needs to be taken from hysteresis loops that are characteristic of the loading conditions at the investigated position in the component. On the one hand, constitutive laws can be used in the simulation, which may be rather cumbersome to handle and require proper experimental programs for calibration purposes. On the other hand simpler procedures may be applied in order to estimate the stabilized σ - ϵ response of the material. The latter option is only applicable for isothermal loading and not for TMF, which is the relevant loading in the case of railway braking. Nevertheless, Neuber’s method will be discussed in the following paragraphs, being a good introduction into other strategies treated later on.

2.6.2 Isothermal application of damage parameters

Fig. 2.34 illustrates a procedure to estimate the stress and strain at a notch for loading conditions outside the elastic domain. This method was defined for static loading as described in [21] but it can be extended to cyclic loading as will be shown below. Moreover, its applicability is not restricted to notched components.

Given a notched specimen and the static σ - ϵ curve in Fig. 2.34a) the loading conditions at the notch can be approximated by the stress concentration factor K_t , Eq. (2.160), as long as the deformation is purely elastic ($\sigma_{max} \leq \sigma_y$). σ_n refers to the applied nominal stress and σ_{max} to the resulting maximum stress at the notch. The limit case is illustrated by the dashed lines in Fig. 2.34b) and c). The solid lines correspond to a higher nominal loading where plastic deformation occurs. In this case the $\sigma - \epsilon$ response is non-linear (ϵ increases over-proportionally and σ under-proportionally compared to the elastic domain) and the validity of K_t is not given anymore. Instead of K_t a stress and a strain concentration factor according to

2. THEORETICAL BACKGROUND

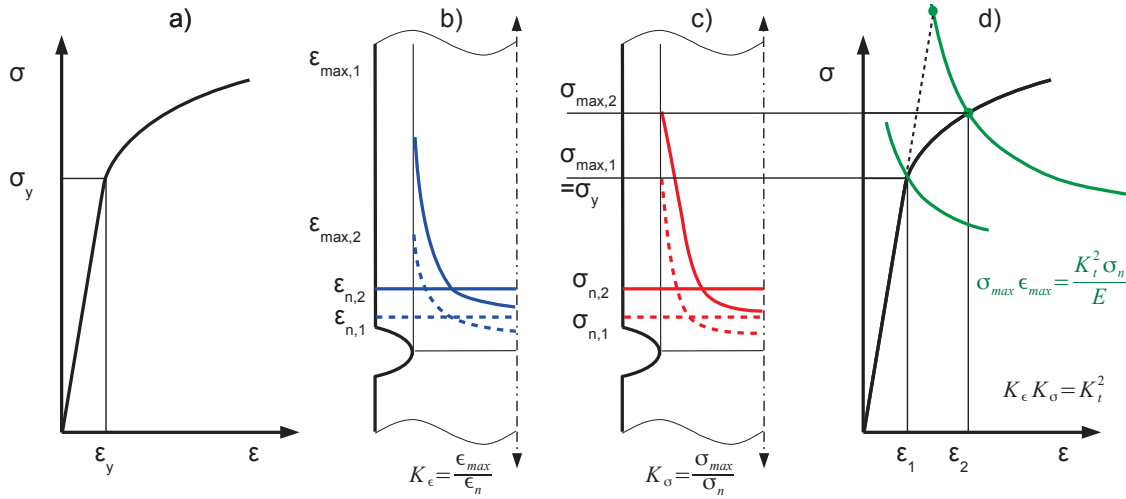


Figure 2.34: Procedure for the estimation of maximum stress and strain at a notch due to a static load according to Neuber (based on [21]). a) static σ - ϵ curve, b) nominal strain compared to two possible strain distributions around a notch, c) nominal stress compared to two possible stress distributions around a notch, d) application of Neuber's rule for the determination of σ and ϵ at a notch for the elastic and the plastic case.

Equations (2.161) and (2.162) can be defined where $K_\sigma < K_t < K_\epsilon$.

$$K_t = \frac{\sigma_{max}}{\sigma_n} \quad \sigma_{max} < \sigma_y \quad (2.160)$$

$$K_\sigma = \frac{\sigma_{max}}{\sigma_n} \quad \sigma_{max} > \sigma_y \quad (2.161)$$

$$K_\epsilon = \frac{\epsilon_{max}}{\epsilon_n} \quad \sigma_{max} > \sigma_y \quad (2.162)$$

Without plastic deformation the stress concentration factor and the strain concentration factor are equal (K_t), while two different quantities are obtained (K_σ , K_ϵ) for the case of plastic deformation at the notch. Neuber established the connection between the three stress concentration factors given by Equations (2.160) to (2.162), based on the assumption that the product of the stress concentration factors will be constant at all levels of loading (Eq. (2.163)). Inserting Eq. (2.161), Eq. (2.162) and $\epsilon_n = \sigma_n/E$ — which is valid if the nominal stress σ_n is in the elastic domain — in Eq. (2.163), yields Eq. (2.164). For a given nominal stress σ_n its right hand side is equal to a constant C and Eq. (2.164) takes the form of a hyperbola in σ - ϵ . Intersecting this hyperbola with the σ - ϵ curve as shown in Fig. 2.34d), σ_{max} and ϵ_{max} at the notch can be approximated based on the nominal stress, the stress concentration factor and the Young's modulus. As explained in [25] the Neuber approach also works if the regions remote from the notch deform non-elastically, i.e. σ_n and ϵ_n are in the plastic domain. In this case, the simplification $\epsilon_n = \sigma_n/E$ cannot be used and the nominal stress and strain have to be inserted into Eq. (2.164). This works provided that it is possible to determine these values, which is not always straightforward in the elastic-plastic case.

$$K_\sigma K_\epsilon = K_t^2 \quad (2.163)$$

$$\sigma_{max} \epsilon_{max} = \frac{K_t^2 \sigma_n^2}{E} \quad (2.164)$$

Apart from the graphical solution, the Neuber method may be carried out in a mathematical way, which can be implemented in a FE-software. In this case the σ - ϵ curve is approximated by the Ramberg-Osgood equation given by 2.165. The coefficients K' and n' are called cyclic strength coefficient and cyclic strain hardening exponent, respectively. Since the graphical solution involves the intersection of the Neuber hyperbola and the σ - ϵ curve the same can be done mathematically by equating Eq. (2.164) and Eq. (2.165) multiplied by σ_n . The corresponding expression 2.166 is solved iteratively by numerical techniques.

$$\epsilon_a = \frac{\sigma_a}{E} + \left(\frac{\sigma_a}{K'}\right)^{n'} \quad (2.165)$$

$$\sigma_{max}\epsilon_{max} = \frac{K_t^2\sigma_n^2}{E} = \frac{\sigma_n^2}{E} + \sigma_n \left(\frac{\sigma_n}{K'}\right)^{n'} \quad (2.166)$$

Eq. (2.166) may be used to determine the loading at a notch for a given nominal stress or for the transfer of the results of an elastic FE calculation for the stress and strain field at the notch to the elastic-plastic domain. The latter case is indicated in Fig. 2.34d).

The procedure noted above is also used in the scope of the local strain approach for fatigue loading. Instead of the static quantities for the loading the corresponding cyclic quantities $\Delta\sigma$ and $\Delta\epsilon$ are used. Furthermore, the stress concentration factor K_t is replaced by the fatigue notch fatigue K_f which is defined according to Eq. (2.167). In the absence of any notches, K_f equals 1.

$$K_f = \frac{\sigma_{F,unnotched}}{\sigma_{F,notched}} \quad (2.167)$$

Obviously the static σ - ϵ curve cannot be used any more and must be replaced by its cyclic equivalent, the cyclic σ - ϵ curve (CSSC), which has already been addressed in Section 2.1.1. It will be further discussed below. The Neuber method applied to fatigue problems is one of the simplified methods referred to above, since it allows to draw a conclusion about the stabilized stress-strain field based on an elastic FE computations for one or multiple fatigue cycles.

Section 2.6.2 illustrates the meaning of the cyclic σ - ϵ curve. This curve is plotted through σ_u and σ_o of stabilized hysteresis loops obtained at different levels of loading and can also be fitted with expression 2.166. In general, there are three possible ways how a cyclic σ - ϵ curve can be determined from experiments, as described in the literature (e.g. [9; 22]):

- If LCF tests are available for the construction of S-N curves, the stabilized cycles of each experiment can be used, of course separately, for each temperature
- A multiple step test (MST) can provide a similar information. One sample is tested at different levels of ϵ_a beginning with the smallest and ending with the largest. Each load level is maintained until the hysteresis has stabilized.
- Another test requiring only one sample is the incremental step test (IST). In this case the strain amplitude changes from cycle to cycle, first in an increasing manner until $\epsilon_{a,max}$ is reached and afterwards in a stepping downhill way until $-\epsilon_{a,max}$. This sequence is repeated until the hystereses do not change anymore from one block to the next. This method has the advantage that all the strain amplitudes are tested before a possible early failure occurs. Furthermore, there is no need to supervise the stabilization at each load level. The sequence can be programmed and the machine can run autonomously.

2. THEORETICAL BACKGROUND

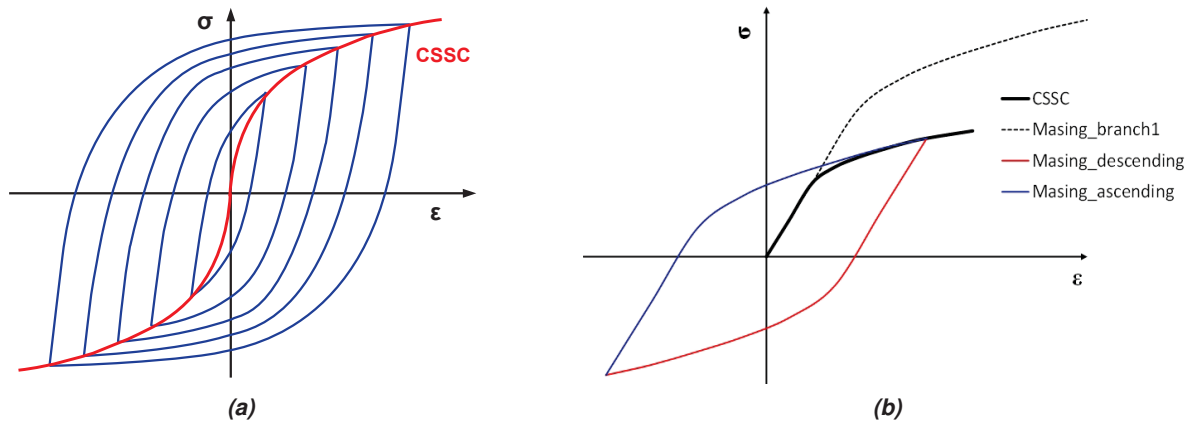


Figure 2.35: a) Illustration of the cyclic σ - ϵ curve, b) illustration of the construction of a stress strain hysteresis from CSSC assuming Masing behavior.

According to Ohrndorf in [22], the CSSC is characteristic for the dislocation structures in the material as discussed in Section 2.1.1. If these structures change with increasing load, the corresponding hystereses will not only change in size but also in shape and no unique connection between stress and strain can be found. Having established these facts, the question arises if the three methods mentioned previously will lead to the same CSSC. The answer is simply “no” because there is a major difference between the incremental step test and the other two procedures as regards the formation of dislocation structures. Section 2.1.1 discusses in detail the various structures and their evolution with increasing load. In LCF and multiple step tests a stable dislocation structure characteristic for the current load level will form. The dislocation structure in ISTs on the other hand are dependent on the largest strain amplitude in the block. Thus, the characteristic dislocation structure for $\epsilon_{a,max}$ is also present when the smaller amplitudes are tested. The difference in the result between the two methods is sketched in Fig. 2.36a where the CSSC curve obtained with an IST is compared to the curve based on LCF tests. The two CSSC intersect and the LCF based curve is higher at larger strains. This can be accounted for by the fact that the material in the incremental step test has obtained the same dislocation structure but it lags behind in terms of hardening. At lower ϵ_a , however, the dislocation structures formed at higher ϵ_a in the IST are also present at lower loads and thus cause larger stress values.

Another important difference is illustrated in Figures 2.36b and 2.36c. If the points corresponding to σ_{min} of hysteresis loops are shifted on top of each other, the upper envelope of the hystereses corresponds to the CSSC in the case of the IST but not for the LCF data. The situation in Fig. 2.36b is typical if the dislocation structure is independent of ϵ_a , which is true for special materials or most materials tested in an IST. The previously noted behavior is also called Masing behavior, which is important in view of the Neuber method for fatigue, since it yields the next point after load reversal, as will be shown later. If IST or a MST/LCF testing is more appropriate depends on the loading conditions of the component, i.e. whether the strain amplitude stays constant or varies in service. The hysteresis starting from an arbitrary point on the CSSC can be obtained rather easily if Masing behavior is assumed. In this case the shape of the descending and ascending hysteresis branch can be derived from the CSSC up to the reversal point. The stress and strain values of this part of the curve need to be multiplied by two yielding branch 1. Indicating the reversal point with σ_r, ϵ_r , the hysteresis can be plotted by two operations, as indicated in Section 2.6.2:

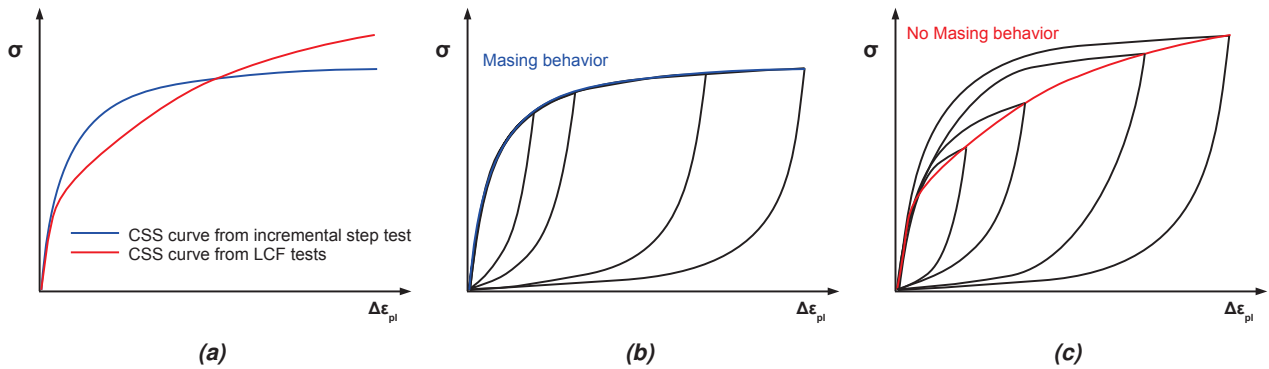


Figure 2.36: a) Schematic CSS curves obtained from incremental step test and LCF tests b) stabilized hystereses from incremental step test (shifted to common minimum position) c) stabilized hystereses from LCF tests (shifted to common minimum position) [22].

- The stress and strain values of branch1 are multiplied by -1. After that the values are shifted by σ_r and ϵ_r yielding the descending branch
- Branch1 is shifted by $-\sigma_r$ and $-\epsilon_r$ yielding the ascending branch

A detail apparently not mentioned in the literature is that the method described above also works the other way around. This means that under the assumption of Masing behavior the CSSC can be directly constructed from the hysteresis loop corresponding to the largest strain amplitude. One should be careful, however, applying this method to data from a test with constant amplitude loading because there might occur deviations as was previously noted.

The mathematical equivalent to the graphical solution is obtained by using a modified form of the Ramberg-Osgood equation given by Eq. (2.168). The descending branch of the hysteresis is obtained by applying Eq. (2.168) to a new coordinate system having its origin at the point of load reversal and inverse axes, i.e. the positive direction of both axes points in the negative direction of the original coordinate system. Eq. (2.168) can be used for each ascending or descending leg in the load spectrum but the coordinate system has to be rotated 180° and its origin has to be moved to the new point of load reversal.

$$2\epsilon_a = \frac{2\sigma_a}{E} + 2 \left(\frac{\sigma_a}{K'} \right)^{n'} \tag{2.168}$$

In case a damage Woehler line based on the damage parameter of Smith, Watson and Topper (SWT) is used for the fatigue evaluation, the required load parameters (σ_o and ϵ_a) can be determined for each hysteresis in the load spectrum. Besides the Masing behavior another criterion needs to be applied in order to construct the corresponding hysteresis loops. This criterion accounts for the so-called memory effect, which is essential in view of variable amplitude loading. If a cyclic stress strain curve is available mechanical hysteresis loops can be constructed on the basis of Neuber’s method, Masing behavior and memory effect. This approach is illustrated in Fig. 2.37, which shows a simple load spectrum on the right side and applies the following rules:

1. The initial loading branch follows the CSSC.

2. THEORETICAL BACKGROUND

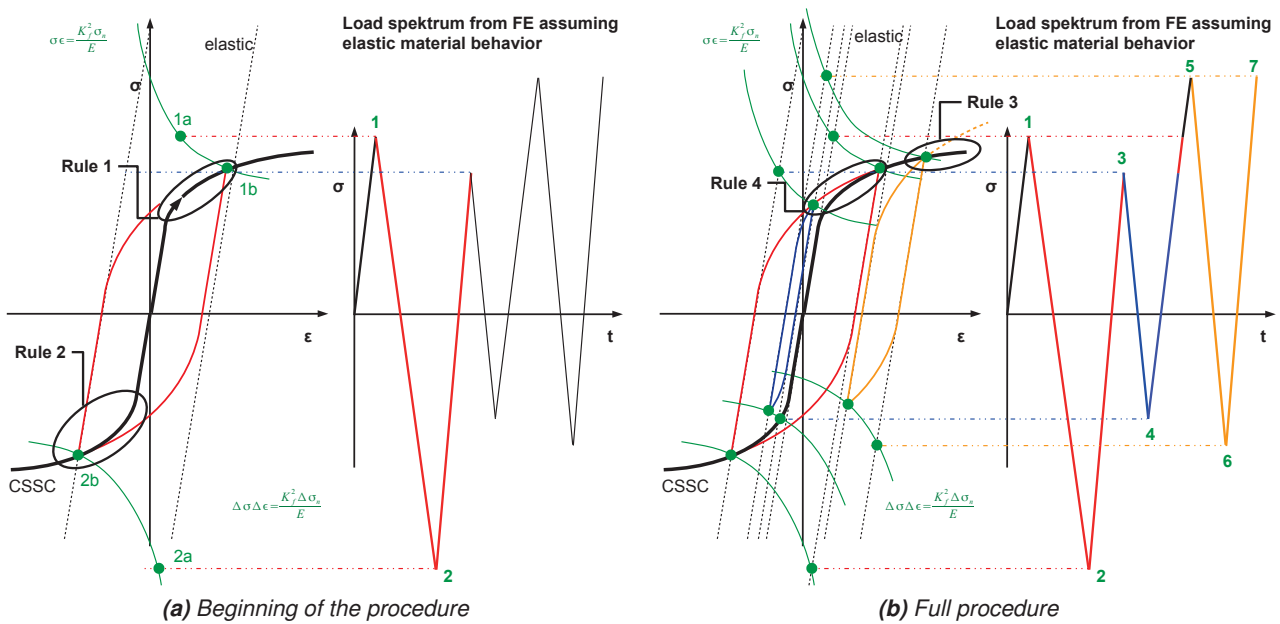


Figure 2.37: Illustration of the interplay of CSSC, Neuber rule, Masing behavior and memory effect for the construction of hysteresis loops (based on [16; 23]).

2. A hysteresis branch started on the CSSC ends if the mirrored starting point is reached on the CSSC. Afterwards the σ - ϵ path follows the CSSC if no direct load reversal occurs.
3. After closure of a hysteresis started on the CSSC, the stress-strain path continues on the CSSC.
4. The stress-strain path after closure of a hysteresis started on a hysteresis branch follows the initial branch.

2.6.3 Cycle counting

For the case of complex load spectra — isothermal or non-isothermal — it is common practice to use analysis techniques that split up the spectrum into individual hystereses. This is due to the fact that the individual closed hysteresis loops may not be evident from the measured or simulated load data alone. An overview of one and two parameter techniques is given in [22]. A very common technique is the *Rainflow Counting* well described e.g. in [9; 25]. It was inspired by the shape of the roofs of Japanese pagodas, Fig. 2.38a), and describes figuratively the flow of raindrops down the roof. In a first step the load spectrum in Fig. 2.38b) is rotated by 90° and the initial loading branch is removed. From this point on on three rules are established for the flow of the raindrops:

1. The flow stops when the drop falls of an apex which points in the direction where the drop came from and is larger or equal than the apex where the drop came from.
2. No raindrop is allowed to flow where another raindrop has already been.
3. One raindrop is started from each apex where no previous raindrop has passed by.

The graphical solution for Rainflow Counting is plotted in Fig. 2.38c). Each path of a raindrop corresponds to a positive or negative half cycle of a hysteresis. In the subsequent step after the Rainflow Counting the individual hystereses need to be assembled. In the example it is evident which half cycles match, as is shown in Fig. 2.38d), but for a complex load spectrum this is usually not the case. The classic Rainflow Counting does not take into account the mean stresses of the half cycles and thus does not require direct matching of the hysteresis branches. Even in this form, however, it facilitates the application of accumulation rules for fatigue assessment, which is necessary for variable amplitude loading.

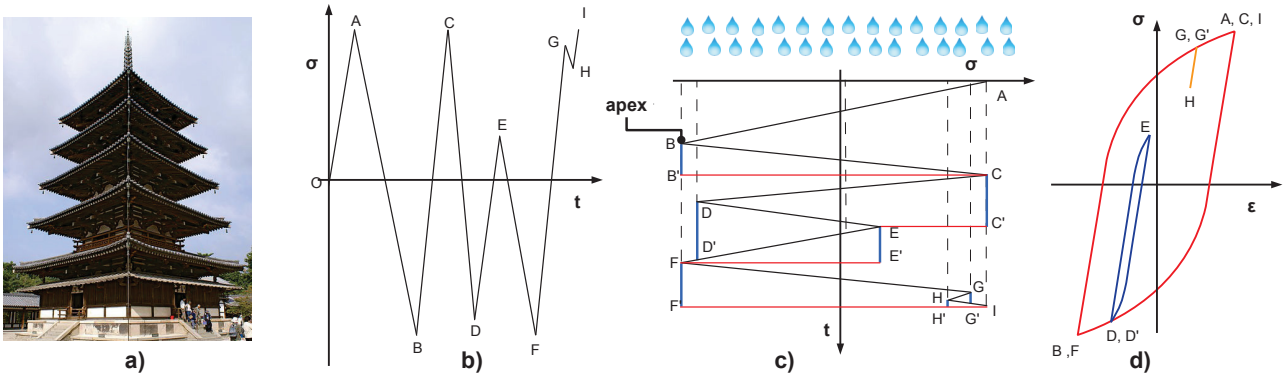


Figure 2.38: a) Japanese Pagoda [24] b) Load spectrum, c) Rainflow Counting (based on [25]), d) Assembled hystereses.

The Neuber approach combined with Masing, memory effect and cycle counting is a convenient tool for the fatigue analysis of rather simple load cycles at moderate temperatures. It might be applicable at higher temperatures (with the CSSC determined at the corresponding temperature) as long as the frequency is high enough that the pure fatigue mechanisms prevail over creep effects. In the case of thermal and thermomechanical fatigue it fails, however, since the CSSC cannot be used as an approximation of the material behavior at varying temperatures. For this case material models are required that compute the mechanical hystereses in dependence of the complex loading conditions and the previous stress strain history. This topic has already been discussed in Section 2.5.

Up to this point, the characterization of variable amplitude loading conditions has been discussed in terms of hysteresis loops. The estimation of the fatigue life, however, has been restricted to constant amplitude loading. A simple expansion of the life time prediction noted above is achieved by damage accumulation rules. These may be more complex non-linear accumulation rules, like the ones introduced by Robotnov (originally for tertiary creep, see Appendix A.6) or Lemaitre [124]. Due to its simplicity, a linear damage accumulation rule is commonly applied, i.e. the Miner rule (or Palmgren-Miner rule) [8]:

$$D_i = \frac{N_i}{N_{f,i}} \quad D = \sum_{i=1}^n \quad (2.169)$$

Additional information on the Miner rule is given in the subsequent section.

2.6.4 Concepts for service life assessment at high and varying temperatures

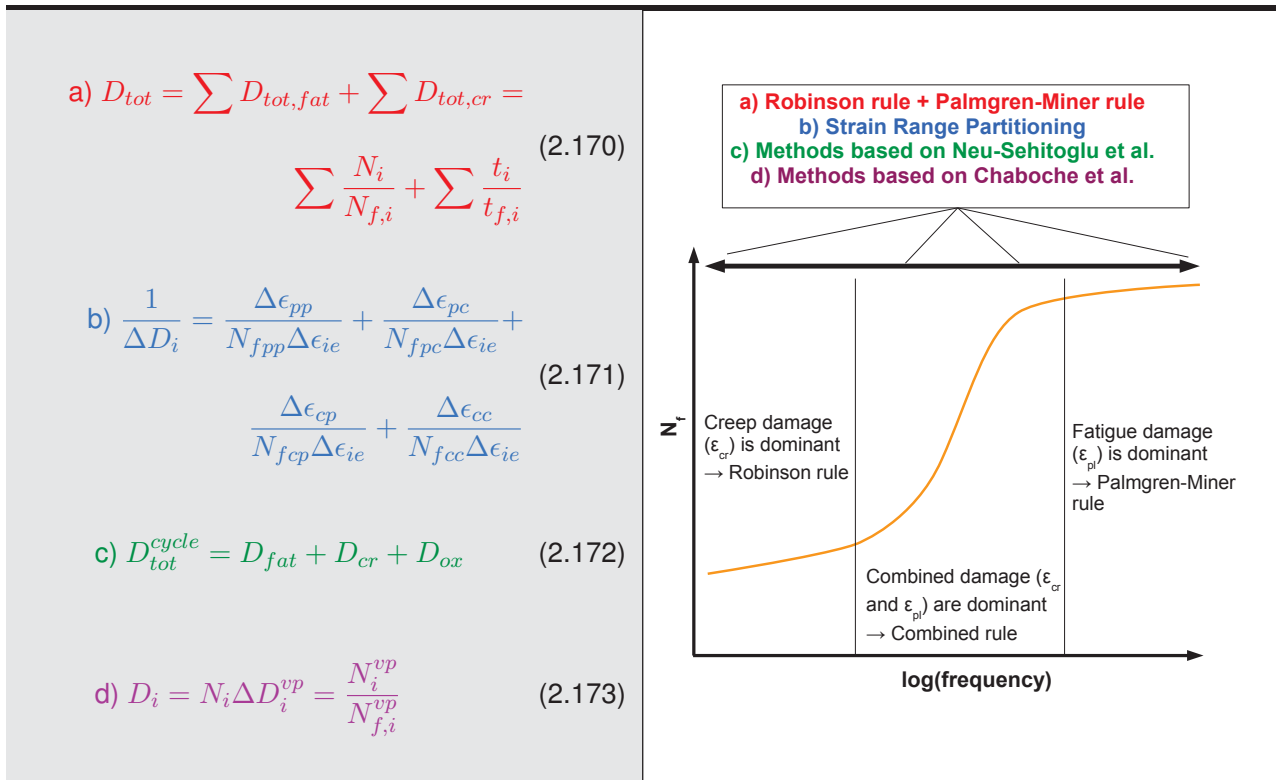
To date it has been impossible to define a standardized procedure for the determination of TMF parameters that can be used for fatigue design [70; 130]. The fact that a parameter is not sufficient to describe TMF fatigue life gives rise to a variety of more or less complicated methods outlined in the following sections.

2. THEORETICAL BACKGROUND

The models listed in Table 2.9 are suitable whenever the loading stays constant in every cycle. As mentioned in Section 1.2, however, there are changes in each cycle that are bound to happen in the thermal localizations even if the braking characteristics are identical. The question whether these phenomena are distinct enough to be taken into account or not will be dealt with in Chapter 3. Apart from variable amplitude loading on the local scale a second important point must be considered. Also the global loading of a railway brake disk varies from one braking to the next. Hence, this subsection sheds some light on the procedures that can be applied for the evaluation of damage at elevated temperatures.

Apart from the fact that the loading conditions may vary on the local scale as well as from cycle to cycle, the selected method to evaluate the damage caused by each individual cycle must take into account the two main damage mechanisms at high temperatures: fatigue and creep. Some approaches consider oxidation damage as a separate contribution to the damage evolution as will be explained later in this chapter. Table 2.10 illustrates the strategies commonly used for service life estimations (until crack initiation) at high temperatures.

Table 2.10: Overview of life time estimation strategies at high temperatures

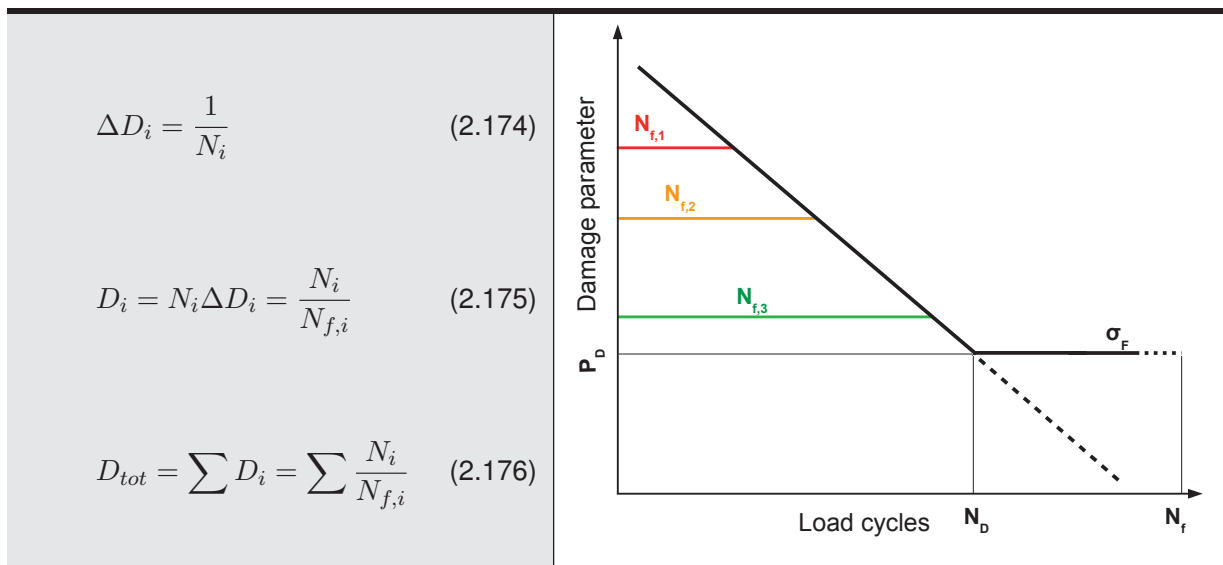


2.6.4.1 Miner rule and Robinson rule

In the case of **pure fatigue**, where no time dependent effects occur, the linear damage accumulation rule according to Palmgren and Miner, as previously mentioned, can be applied. This procedure and its modifications are well described in the literature, e.g. in [14; 131]. The method is based on an S-N-curve or an ϵ -N-curve and a processing of the load spectrum that splits up the spectrum into individual cycles

— each causing a damage according to Eq. (2.174) — that can be grouped together in load blocks. For complex loadings the rainflow-counting algorithm is often used as illustrated in Section 2.6.4.4 to identify the individual blocks. Each block leads to a partial damage ΔD_i , Eq. (2.175), and the combination of the partial damages according to Eq. (2.176) yields an estimation of the total damage. Whether failure or crack initiation is predicted depends on the methods applied for the computation of ΔD_i . HCF methods relating to S - N curves represent total life approaches, while LCF methods based on ϵ - N curves predict the number of load cycles until crack initiation. Failure/crack initiation would be expected at $D_{tot} = 1$ but since this method is on the one hand no more than an estimation and on the other hand does not take into account load series effects and changes in the material, values below 1.0 are commonly used. The load series effects refer to the occurrence of tensile or compressive overloads causing residual stresses in the opposite stress regime. The impact of load sequences on the difference between predicted and observed fatigue life are discussed in the work of Colin in [132; 133]. In any case, these effects cannot be taken into account by classical methods for damage accumulation and more complex methods need to be considered in cases they are significant. One example for HCF loading where the load sequence plays a role and a correction to some extent is possible is given for two loadings σ_{low} and σ_{high} being situated below and above the fatigue strength ($\sigma_{low} < \sigma_F < \sigma_{high}$): 1) At the beginning of the sequence, loading σ_{low} occurs followed by σ_{high} . 2) A sequence starting with σ_{high} followed by σ_{low} . In the first situation no damage is accumulated before the larger loads are applied. In the second case microcracks may be initiated during the application of σ_{high} at the beginning causing an increase of the damage during the loading with σ_{low} . The corresponding values of D indicating failure would thus be clearly different. A conservative solution can be obtained by using one of the modified forms of the Miner rule described in [8]. Another possibility is to extrapolate the S - N curve to stress ranges below $\Delta\sigma_F$, as indicated in Table 2.11. This way, also low fatigue loads contribute to the computed damage.

Table 2.11: Illustration of the Palmgren-Miner rule



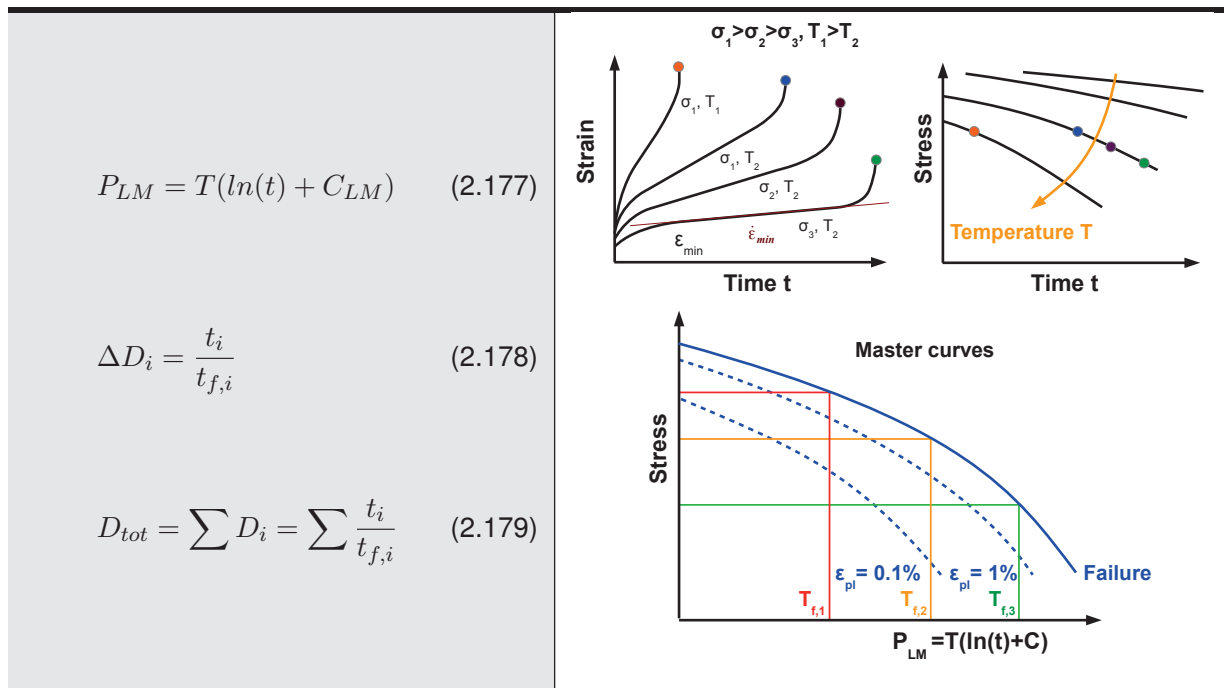
In the case of **pure creep damage** a similar methodology is applicable, which is based on the work of Robinson [14]. Since time dependent effects are clearly present, the frequency of the loading, i.e. the strain rate, has a distinct impact on the fatigue life. Thus, the use of this method requires the knowledge of

2. THEORETICAL BACKGROUND

the creep strength at the relevant temperatures and stress levels. Otherwise the procedure is equivalent to the Palmgren-Miner rule and it is prone to similar sources of error. Table 2.12 illustrates the necessary experimental basis and the application of the damage accumulation rule. Creep tests yield the evolution of strain over time for each test parameter combination of stress and temperature. The minimal strain rate $\dot{\epsilon}_{min}$ is characteristic of the equilibrium of hardening and softening mechanisms in the material, as outlined in Section 2.2. This stage is referred to as secondary creep and as its portion of the overall lifetime is much larger than those from primary creep (large hardening effects at the beginning) and tertiary creep (nucleation and growth of voids close to failure) $\dot{\epsilon}_{min}$ is an important quantity for iterative accumulation rules discussed later in this subsection. Furthermore, each creep test yields the time until fracture corresponding to each parameter pair of stress and temperature. A function $\sigma_c(t)$ can be identified for each level of temperature still leaving a great number of parameter combinations unattended to. By the aid of the Larson-Miller parameter (Eq. (2.177)) which consolidates temperature and time in one expression a single master curve can be obtained. Besides the master curve for failure additional master curves for specific values of the obtained strain are commonly used [126].

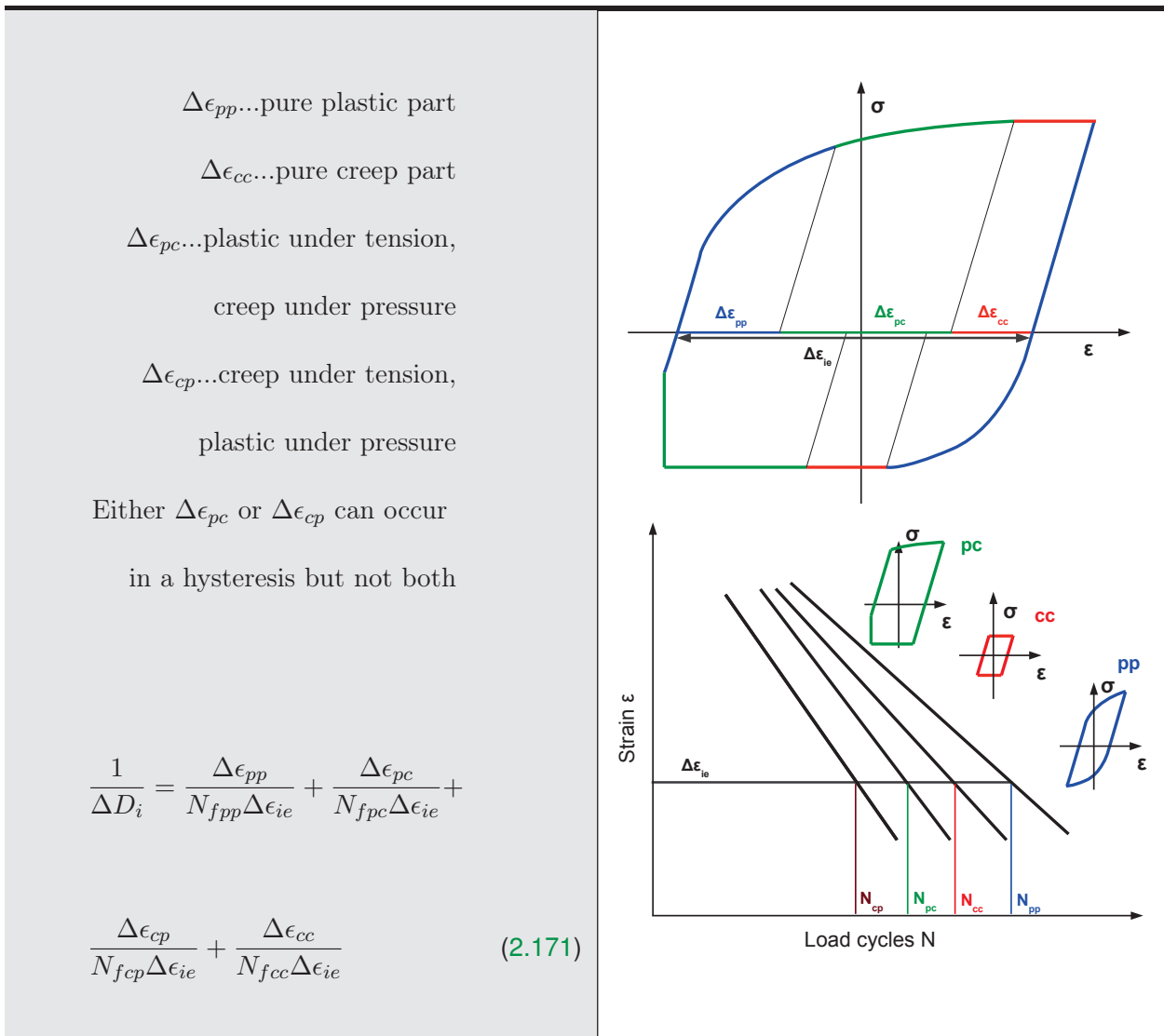
At strain rates where both damage mechanisms contribute significantly to the damage accumulation, new

Table 2.12: Illustration of the Robinson rule



strategies need to be pursued, as indicated in Table 2.10. The simplest approach is a combination of the damage accumulation according to **Palmgren-Miner and Robinson** according to Eq. (2.170). Additionally to the aforementioned errors of the two methods, another source of uncertainty appears in this formulation. Damage mechanisms behind fatigue and creep differ and thus a linear combination of both damage contributions is not admissible from the point of view of physics. This fact gave rise to more profound methods, such as the **Strain Range Partitioning**.

Table 2.13: Illustration of the Strain Rate Partitioning (based on [17])



2.6.4.2 Strain Range Partitioning method

The Strain Range Partitioning (SRP) method was first used by Manson et al. [134] and is well described in accessible literature like [14; 17]. Moreover, Manson and Halford devoted large sections of their book [135] to the SRP method. An illustration of this procedure is provided in Table 2.13:

- The relevant hysteresis for the loading in question is determined
- The inelastic strain range of the hysteresis is split into individual blocks with respect to the four base types pp, cc, pc, cp
- Cyclic testing has to be carried out for each base type yielding four data sets for Manson-Coffin.
- The estimated service life is computed according to Eq. (2.171)

According to Manson [134], this method entails one major advantage over approaches using the Robinson rule. Because the creep life is very sensitive to temperature and stress, it is necessary to characterize the

2. THEORETICAL BACKGROUND

stress-temperature interaction very precisely for the use of this time-fraction summation thus requiring a lot of creep experiments. In view of fatigue life and the corresponding scatter, however, the tension and time fracture strains and thus the Manson-Coffin parameters do not vary that severely with temperature. The four Manson-Coffin curves for 316 stainless steel discussed in [134] were determined at $\sim 590^\circ$ and could be used in a temperature range from ~ 430 to $\sim 650^\circ$. The life time prediction deviates no more than by a factor of 2 from the lifetimes determined at ~ 430 and $\sim 650^\circ$. This means that once a data set is determined for a specific temperature it can be used in a temperature range, as long as a safety factor is used.

Although this Strain Range Partitioning has some advantages over the combined Palmgren-Miner and Robinson rule, it is still not sufficient for a wide range of fatigue cases. It might not be possible to split the hysteresis into the four base types or, in the case of ratcheting, there is not even a closed hysteresis loop. Furthermore, the method is not suitable for loadings with varying temperatures, where damage mechanisms and their interactions become more difficult, as described in [71]. This gives rise to approaches going further into depth thus extending the ranges of validity of previously discussed methods.

2.6.4.3 Method of Neu-Sehitoglu

As noted in Section 1.3, TMF damage is governed by the interaction of fatigue damage, creep damage and oxidation damage. The situation is further complicated by the varying temperature during each load cycle in combination with the temperature dependence of material properties and damage mechanisms. One possible way proposed by **Neu and Sehitoglu** [72] to tackle this problem is to describe the three main mechanisms individually with physically based equations and to total the damage contributions after each cycle:

$$D_{tot}^{cycle} = D_{fat} + D_{cr} + D_{ox} \quad (2.180)$$

D_{fat} can be obtained from the Manson-Coffin relation or from its variations based on isothermal experiments at room temperature, where the impact of fatigue damage can be characterized without the influence of creep and oxidation damage. D_{fat} is thus the upper limit of the attainable fatigue life since additional damage contributions can only decrease N_f . For the description of the fatigue damage, a constitutive law has to be implemented in order to be able to consider various TMF loading conditions and to correlate strains and stresses appropriately.

D_{ox} is described by the following equation:

$$\frac{1}{N_f^{ox}} = \left[\frac{h_{cr} \delta_0}{B \Phi^{ox} K_p^{eff}} \right]^{-\frac{1}{\beta}} \frac{2(\Delta \epsilon_{mech})^{\frac{2}{\beta}+1}}{\dot{\epsilon}^{1-\frac{\alpha}{\beta}}} \quad (2.181)$$

$\alpha, \delta_0, \beta, h_{cr}, B$ are constants that need to be determined. K_p^{eff} and Φ^{ox} are both functions of the load history and include further constants that need to be identified from experiments. K_p^{eff} , the effective oxidation constant, is of the form of an Arrhenius equation and takes into account the temperature dependence of the oxidation. Φ^{ox} is the so-called phasing factor, which is a function taking into account that oxidation damage works for in-phase (IP) TMF in a different way as in out-of-phase (OP) TMF where it is more pronounced. The meaning of the variables in Eq. (2.180) and the procedure for the parameter identification from experimental data are explained in detail in [72].

D_{cr} is taken into account by the following equation:

$$\frac{1}{N_f^{cr}} = \Phi^{cr} \int_0^{t_{cycle}} A e^{\frac{-\Delta H}{RT}} \left[\frac{\alpha_1 \bar{\sigma} + \alpha_2 \sigma_H}{K} \right]^m dt \quad (2.182)$$

A and m are material constants, $\bar{\sigma}$ is the effective stress, σ_H the hydrostatic stress, K the drag stress. Φ^{cr} is again a phasing factor and α_1 and α_2 are scaling parameters that allow the consideration of different damage impact in tension and compression.

Although the approach of Neu and Sehitoglu is mostly physically founded and offers greater capabilities in terms of service life estimation, it also comes with some drawbacks:

- The computation of damage has to be carried out from cycle to cycle which can be computationally expensive
- Due to the continuous damage calculation, the equations governing the three damage contributions have to be implemented in the simulation software, which is often not a standard functionality in commercial software packages.
- The experimental program required for the parameter identification is extensive and requires complex tests in vacuum or inert gas atmosphere

2.6.4.4 Non-isothermal application of damage parameters

In Section 2.6.1 the concept of empirical damage parameters linking loading characteristics and crack initiation life times has been introduced. Subsequently, the application of damage parameters for isothermal loading was illustrated based on Neuber's method. This section illustrates that damage parameters can also be applied if the component is subjected to TMF. An approach to fatigue life evaluation at high temperatures and varying thermal loading is illustrated in Fig. 2.39. In contrast to Section 2.6.4.4 the σ - ϵ response of the material in the component must be computed with proper constitutive equations. These are elaborated in detail in Section 2.5, while their physical background is illustrated in Section 2.1 and Section 2.2. This way, the inelastic strains in the sample/component can be described, either with a single variable (ϵ_{vp}) if unified laws are used, or by separate variables (ϵ_p , ϵ_v). This is the basic requirement for the application of Manson-Coffin in the context of TMF. Test cycles carried out with different maximum temperatures and dwell times are thus described by the resulting inelastic strains. Of course, the definition of a single parameter set for Manson-Coffin is only possible if the characteristics of the TMF experiments are sufficiently close, as will be discussed in Chapter 5. Combined IP and OP testing in the experimental program, would thus require different parameter sets. Actually, the whole range of damage parameters listed in Table 2.9 may be applied provided that data from TMF tests, which are characteristic for the loading of the component are available. The more general the damage parameter is formulated, the more likely it is that differing TMF characteristics can be described with a single parameter set. Which parameter fits best thus depends on the relevant loading conditions. In the case of variable amplitude loading a linear damage accumulation rule applied in a similar fashion as noted above.

In view of the models describing the inelastic material behavior, it is common practice to use isothermal tests for identification of the parameters appearing in the material laws, although other procedures are under discussion and currently being tested [136]. The isothermal test program consists of LCF tests

2. THEORETICAL BACKGROUND

carried out in the relevant parameter range and of block tests that incorporate variable strain rates and dwell times. The calibration and the implementation of constitutive equations is laborious but provides a whole range of new possibilities, compared to the procedures illustrated in Section 2.6.4.4. The cyclic stress strain curve has been used in order to estimate the shapes of the hystereses resulting from certain loading conditions. The constitutive equations are calibrated based on the stabilized hysteresis loops of extensive experimental programs. In simulations they take complex material behavior and the load history into account and directly provide the hystereses. The results are more realistic since stress redistribution within the component is taken into account, which is not the case for elastic simulations. Instead of empirical damage parameters and linear damage accumulation rules it is possible to incorporate continuum mechanical damage models directly into the constitutive equations. Whether this improves the overall predictive quality of life prediction models or not depends on the specific application. In any case, a greater range of possibilities is at hand if suitable constitutive equations are used in the simulations.

The advantage of this procedure is thus a high level of flexibility in the modeling scheme. If the limits of validity are properly documented for the material law(s) and the chosen damage parameters, variations in the loading conditions, component design and material selection can be illustrated efficiently. This information can in turn be used for component design and process optimization. Additionally, the computation of the stress-strain response and the damage evaluation are separate. The life time evaluation can thus be carried out in the post processing of the results. Since this methodology is chosen for the numerical investigations carried out in the scope of this work, Chapter 5 expands on it in more detail.

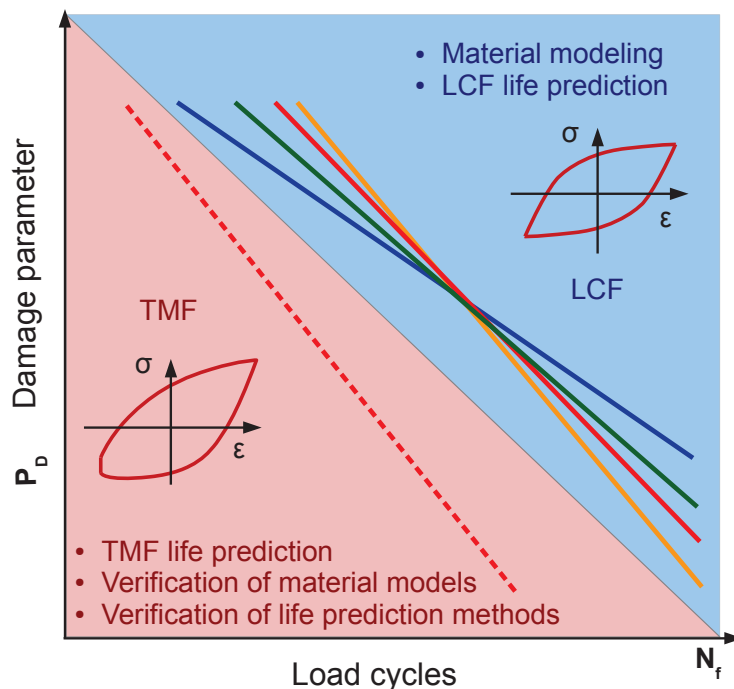


Figure 2.39: Illustration of general TMF life prediction based on constitutive models according to Chaboche et al.

2.7 Infrared thermography

Comprehensive illustrations of the general physics of radiation and infrared techniques (IRTs) can be found e.g. in [26; 137]. In addition, ample literature exists that discusses the application of IRTs for a whole range of problems, such as non-destructive inspection of spot welds [138], measurement of heat flux rates and coefficients [139] and — most relevant to this work — thermal surface gradients on brake disks [140; 141; 142; 143; 144]. In this section the basic physical laws and camera systems will be summarized.

The expression *infrared radiation* is used for the specific part of the electromagnetic wave spectrum, that spans wavelengths in the range from $\lambda=0.75$ to $\lambda=1000 \mu m$ as indicated in Fig. 2.40. All objects emit

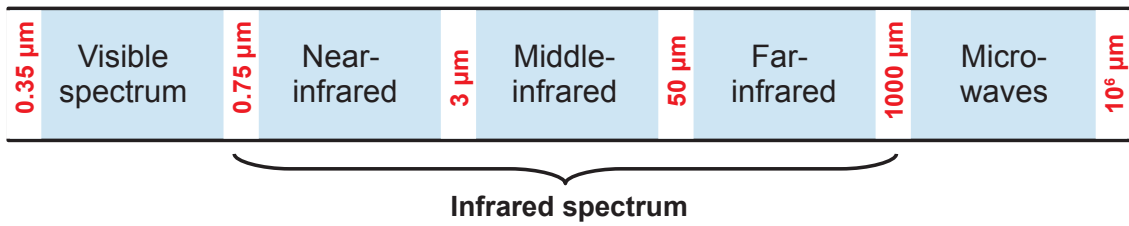


Figure 2.40: Spectrum of IR radiation.

infrared radiation and for objects having temperatures prevailing at the earth’s surface this radiation can be detected with commercial devices. The spectral distribution of the radiation emitted by a *black body* — an object that absorbs and in turn emits 100% of the incident radiation — is described by Planck’s law:

$$P_{\lambda}(\lambda, T)dAd\lambda = \frac{2\pi hc^2}{\lambda^5} \frac{1}{\exp\left(\frac{hc}{\lambda kT}\right) - 1} dAd\lambda \quad (2.183)$$

$P_{\lambda}(\lambda, T)$ refers to the power emitted by a surface dA in the spectrum $\lambda-(\lambda + d\lambda)$. The constants h and k refer to Planck’s and Boltzmann’s constant, respectively and c refers to the speed of light. The temperature must be specified in Kelvin. Fig. 2.41 plots the specific power emitted by objects of various temperatures, i.e. room temperature, 250°C, 500°C 1000°C and the temperature at the surface of the sun, $\approx 5500^{\circ}\text{C}$. The graph reveals that each body irradiates a whole spectrum and the characteristics of this radiation, λ_{min} , λ_{max} , λ_{Pmax} , $P_{\lambda, Pmax}$ for each object depend on its temperature. The derivation of each curve in Fig. 2.41 in conjunction with a minimum search yields λ_{Pmax} , the wavelength with the maximum emitted power. This way, the blue points can be determined, which correspond to λ_{Pmax} for each distribution. Additionally, red lines are plotted each representing λ_{Pmax} for a characteristic medium. Obviously λ_{Pmax} as well as the whole radiation distribution shifts to smaller wavelengths as the temperature increases. Considering the spectrum of radiation depicted in Fig. 2.40 it is thus evident that the radiation of a human body is invisible, but steel starts to glow when the temperature rises. While the intensity of the visible light increases the emitted spectrum shifts to the visible spectrum. The color changes from red to yellow and white. Red is found at the longer end of the visible spectrum ($\sim 0.75 \mu m$) giving rise to the first optical sensation when steel is heated up. The higher the temperature gets the more the optical sensation shifts to colors situated at the lower end of the spectrum, such as orange and yellow. Since the intensity increases simultaneously, all color receptors in the human eye are excited and the emitted spectrum appears to be increasingly white. The visible portion in the spectrum of heated metal is used in light bulbs with heated wires (filaments). This method is inefficient, however, since most of the emitted radiation is still in the invisible infrared spectrum (see Fig. 2.41). Both in the case of glowing/molten steel and the filament in the

2. THEORETICAL BACKGROUND

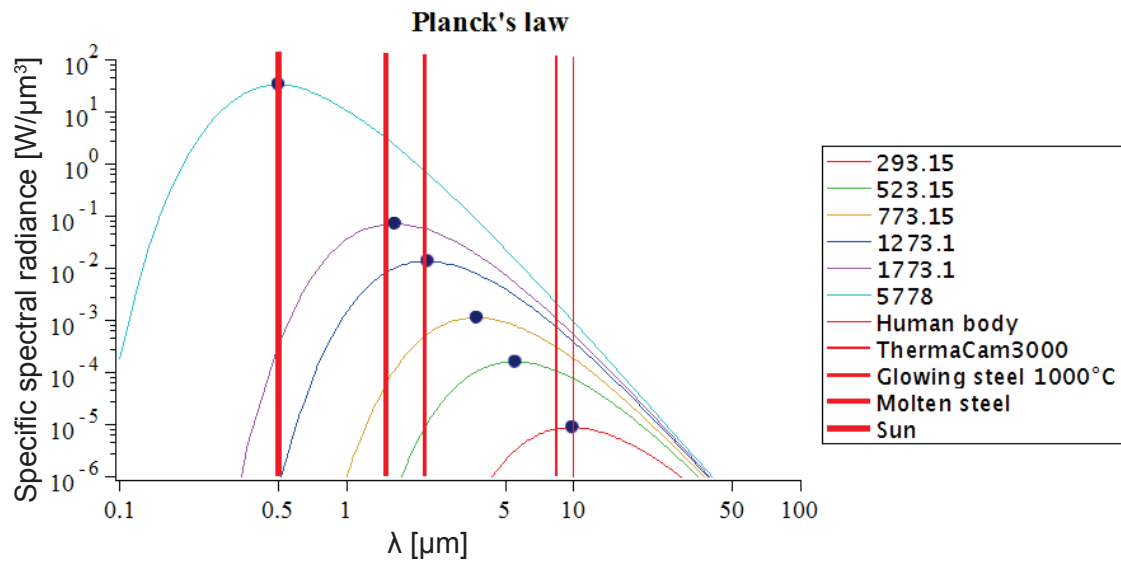


Figure 2.41: Distribution of the specific spectral radiance for various surfaces.

bulb, the infrared radiation can be felt as heat.

The German physicist Wien observed the shift of $\lambda_{P_{max}}$ to lower values and stated Wien's law which can be used to directly determine the wavelength corresponding to the maximum power:

$$\lambda_{P_{max}} = \frac{2897.8}{T} \quad \lambda_{max} \text{ in } \mu m \quad (2.184)$$

The integration of Planck's law over the entire spectrum, on the other hand, yields the total power that is emitted by an object. This corresponds to the area under the curves in Fig. 2.41. The procedure has been carried out by Stefan and Boltzmann who defined the according expression for P_{tot} :

$$P_{tot} = \epsilon \sigma A T^4 \quad (2.185)$$

The above equation only holds for black bodies, but most objects do not behave in accordance with this idealized assumption. Normally only a portion of the incident radiation is absorbed and reemitted while the other part is reflected. Kirchoff's law states this fact as:

$$\rho = 1 - \alpha = 1 - \epsilon \quad \rho \dots \text{reflectivity} \quad (2.186)$$

$\alpha \dots$ absorption

$\epsilon \dots$ emissivity

This is the reason why Eq. (2.185) is corrected by the emissivity ϵ , taking into account that a real object emits less than a black body:

$$\epsilon(\lambda, T) = \frac{P_{\lambda}(\lambda, T)}{P_{\lambda}^{BB}(\lambda, T)} \quad BB \dots \text{black body} \quad (2.187)$$

The emissivity is a function of the wavelength, the temperature and the angle between emitting and absorbing bodies, $\epsilon(\lambda, T, \theta)$. If the angular dependence is neglected, $\epsilon(\lambda, T)$ is called *hemispherical emissivity*.

The core of each IR camera is the infrared detector, which interacts in some way with the incident

radiation and converts it into a signal. In general, this signal is a voltage or a current. Fig. 2.42 provides a classification of IR-detectors which will be discussed in the following paragraphs.

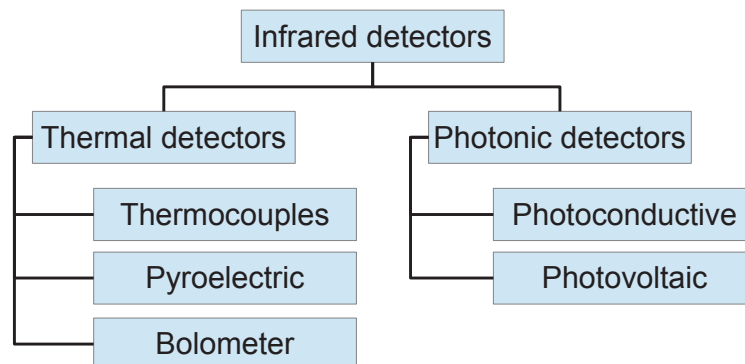


Figure 2.42: Classification of IR detectors [26].

Thermal detectors: The incident radiation changes the surface temperature of the detector and this affects physical properties of the detector material, such as electrical conductivity. The detector types of this category operate at room temperature (no cooling required) and are not subjected to any wavelength limitation. However, a sensitivity to a certain spectral band is introduced by the optics surrounding the detector. The detector is protected by a casing and a window allows radiation to pass through. There is no window material, however, that is transparent at all wavelengths. The main detector types are:

- **Thermocouples:** The Seebeck effect is utilized in junctions between two different metals. Due to this effect a difference in the potential (voltage) is introduced when the temperature between the junctions differs. In the case of IR-systems the metals are deposited as thin films on a thermally isolated substrate.
- **Pyroelectric detectors:** The pyroelectric effect in special materials is utilized to generate charges when the temperature changes.
- **Bolometer detectors:** The incident radiation heats the surface and thus the electrical conductivity changes. The core units are resistive elements with a small thermal capacity — important for detection speed — and a large temperature coefficient — absorbed radiation produces a large change in resistance.

Photonic detectors: Electrons in semiconductors are generated by excitation processes triggered by the incident photons (fundamental particles of electromagnetic radiation). Dark current, which is present in all types of photonic devices, occurs due to random generation of loaded particles. Because the dark current introduces noise into the signal, it is necessary to cool photonic detectors to operating temperatures far below room temperature (usually 200K, 90K or 77K). The advantages of such devices are a larger detectivity and faster response times, which allow the output of more frames per second (fps). The two basic types are:

- **Photoconductive detectors:** The generation of loaded particles — negatively charged electrons, positively charged holes and electron-hole pairs — increase the conductivity of the detector. For this detector type a current is applied and the potential is measured.

2. THEORETICAL BACKGROUND

- Photovoltaic detectors: Schottky barriers (semiconductor-metal combinations) or p-n junctions (combination of intrinsic and extrinsic semiconductors) are used to separate the generated electron-hole pairs by a potential barrier accompanied by an electric field. For this detector type a potential is applied and the current is measured.

In addition to the detector type there are several other important characteristics of an IR-system¹:

- Structure of the detector: Single element or array
- Size of the image: single element, line or 2D image
- For the case of a line scan or 2D image: Mechanical scanning with a single detector or use of a focal plane array (FPA)
- Frames per second and speed of storage and transmission of data
- Optic filters
- Interfaces

The simplest form of an IR-system is a pyrometer consisting of a single detector. The information obtained by a pyrometer corresponds to a single pixel of a thermal image obtained by a FPA system, where a multitude of individual detectors is arranged in an array thus delivering a whole 2D image. It is impossible, however, to manufacture all detectors perfectly identical and furthermore, the position in the array affects the amount of incident radiation. For this reason special calibration methods (NUC...non-uniformity correction) need to be applied in order to synchronize the data from each pixel. Instead of using multiple detectors in a FPA, it is also possible to have a single detector in combination with an optical system that moves the object plane systematically row by row. Some FPAs are manufactured as lines instead of matrices thus operating in line scan-mode where the information of the row is continuously evaluated and joined together. This is especially useful for high-speed applications. Some normal FPAs can optionally operate in line-scan mode.

No matter what system is used, the detection of infrared radiation is always limited to a certain spectral band. The temperature sensitivity of each system can be illustrated by integrating Planck's law (Eq. (2.183)) over the specific spectral band. Fig. 2.43 plots the obtained results for various camera systems. The red line corresponds to Stefan-Boltzmann's law, which integrates over the full spectrum $\mu = 0$ to $\mu = \infty$. Fig. 2.43 reveals that camera systems being sensitive at higher wavelengths (ThermaCam3000) receive higher specific radiation power at lower temperatures. Systems with a sensitivity to smaller wavelengths receive more radiation at higher temperatures. This is clear, since λ_{Pmax} shifts to smaller values (Wien's law) with increasing temperature. The difference between the Titanium SC7500 and the Jade camera at high temperatures is the lower limit of the detected spectral band. This value is 1.5μ for the Titanium camera, which corresponds to λ_{Pmax} of molten steel ($\sim 1650^\circ\text{C}$). The $3.0\mu\text{m}$ for the Jade camera correspond to glowing steel at 700°C . λ_{Pmax} for the ThermaCam3000 is equivalent to 90°C . The steeper the curves in Fig. 2.43 are, the higher is the contrast between neighboring points of similar — but not identical — temperature. The thermal resolution is thus higher. Since the Stefan-Boltzmann curve becomes flatter at high temperatures, a spectral sensitivity at the lower of end the IR-spectrum is important for a very precise thermal resolution. On the other hand, steep curves are problematic for objects with large temperature variations, as in the case of brake disks with hot spots. The integration time of the camera

¹IR-detector...infrared detector, IR-system...thermal imaging system consisting of the detector, the casing, interfaces, etc.

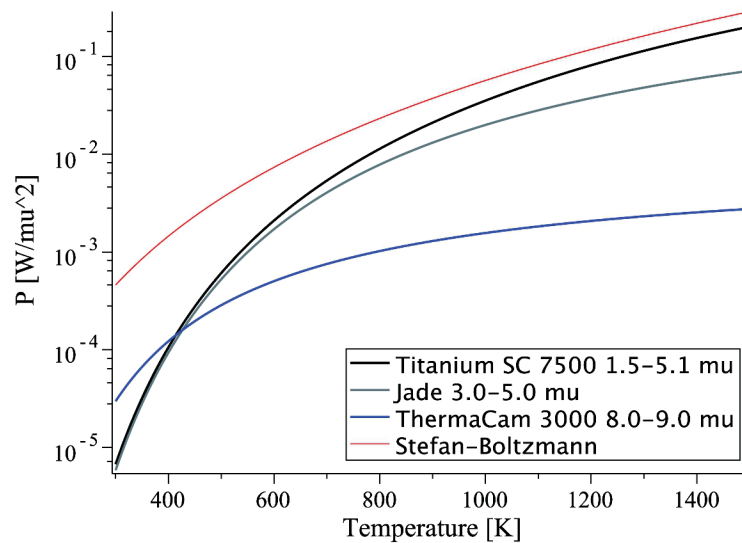


Figure 2.43: Specific detected power for various camera systems in comparison to the full spectrum.

— the time period during which the detector converts radiation to a signal — must be chosen accordingly. This means that the pixels in the section of interest on the object yield digital levels (DLs) in the range of 20% to 80% of the maximum value, which is 16384 for a 14-bit system. The first 20% of the calibration curve, correlating DLs with temperature values is very flat, which means that noise has a great influence on the result. In the last 20% of the calibration curve the sensor is close to saturation and again the results are not very precise. If the curve in Fig. 2.43 is flat, the thermal resolution is less but it is possible to fit a much greater temperature range to the desired DL range, e.g. a hot spot and the surrounding area. These considerations are important in the scope of the present study, hence the ThermaCam3000, showing a flat curve at high temperatures, is used for the infrared investigations.



Chapter 3

Characterization of loading conditions

3.1 Introduction

This chapter discusses the systematic investigation and processing of thermal image data, which is obtained from the test rig program presented in Section 1.6. Since a thorough understanding of the loading conditions is essential for the comprehension of the occurring damage mechanisms, as well as the establishment of a simulation strategy, the results presented in this chapter play a key role in this work. An overview of the goals this chapter strives for is summarized in the following list:

- Conversion of intensity data to temperature data
- Angular correlation of the individual frames of each brake test
- Analysis of the transient changes in the thermal distribution on the disk surface throughout the test rig program
- Discussion of the limits of the imaging system
- Preparation of thermal image data for simulation purposes

As noted in Section 1.6 single amplitude loading is chosen for the test rig program, i.e. only one brake characteristic is used for all individual brake applications. The test parameters for the applied stop braking scenario are summarized in Table 3.1. Each test sequence is initiated by a bedding-in-process according to UIC 541-3 consisting of about 100 brake applications until 85% of the pad are in contact with the disk. For each test run the bedding-in is followed by a sequence of two stage brake applications resembling emergency stops for the reference train type.

The subsequent paragraph will elaborate on the general configuration of test rigs making it possible to perform test runs corresponding to various brake scenarios and even changing loading conditions during two-stage braking. As stated in [79; 145] stop braking is established on a test rig by the specification of initial sliding speed, the brake force and the dissipation of a specific amount of rotational energy E_{rot} .

3. CHARACTERIZATION OF LOADING CONDITIONS

Table 3.1: Test parameters for full scale test rig and material A

| Speed range | Braking force | Braking mass | T_{ini} | Energy |
|---------------|---------------|--------------|-----------|--------|
| [km/h] | [kN] | [kg] | [°C] | [MJ] |
| Bedding (120) | 45.0 | 7900 | 80-100 | 5 |
| 250-190 | 30.1 | 9000 | 40 | 25 |
| 190-0 | 45.1 | 9500 | 40 | 25 |

The latter quantity requires some further elaborations starting with its definition. E_{rot} is computed according to Eq. (3.1), where ω_0 refers to the initial rotation speed and I_s to the simulated inertia.

$$E_{rot} = \frac{1}{2} I_s \omega_0^2 \quad (3.1)$$

The simulated inertia consists of the inertia I_r of the rotating parts (flywheel, axle, wheel, disks) and the inertia I_m generated by the electric motor, as indicated by Eq. (3.2).

$$I_s = I_r + \frac{T_m}{\dot{\omega}} \quad (3.2)$$

T_m refers to the motor torque and $\dot{\omega}$ to the deceleration of the rotating system, which results from the torque T_b generated by the brake system and I_r .

$$\dot{\omega} = \frac{T_b}{I_r} \quad (3.3)$$

Introducing the time step for motor control Δt Eq. (3.2) can be rearranged and stated in incremental form yielding:

$$I_s \Delta\omega = I_r \Delta\omega + T_m \Delta t \quad (3.4)$$

If I_s is given, the decrease of the rotation speed during a specific time increment Δt is governed by the brake torque T_b and Eq. (3.3) can be rewritten in the form of Eq. (3.5).

$$\Delta\omega = \frac{T_b}{I_s} \Delta t \quad (3.5)$$

Both the combination of Eq. (3.2) and Eq. (3.3) and the incremental forms Eq. (3.4) and Eq. (3.5) further yield:

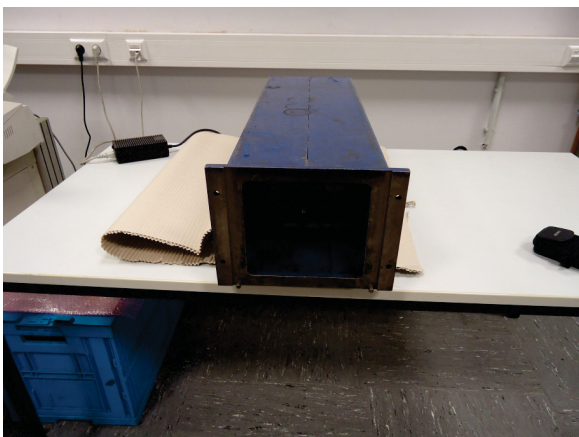
$$I_s = I_r \frac{T_b}{T_b - T_m} \quad (3.6)$$

Since the initial sliding speed (ω_0) and the dissipated energy are chosen in advance for a specific test I_s is determined according to Eq. (3.6). In Eq. (3.6) T_b results from the braking force and the mean brake radius, which are both predefined, leaving only T_m as machine parameter that has to be adjusted accordingly. Instead of ω_0 and I_s the equivalent speed v_0 and the equivalent braking mass m can be used for the characterization of the brake scenario as given in Table 3.1

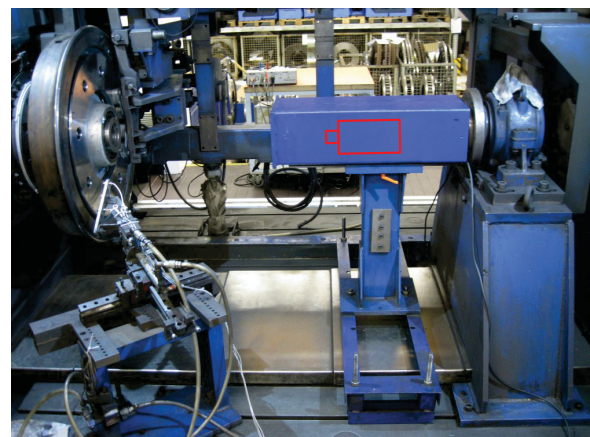
3.2 Camera system

The thermal imaging system used in the test rig is a ThermaCAM[®] SC 3000. Its maximal sensitivity is in the range of 8-9 μm , i.e. radiation within this spectral range has the greatest impact on the resulting digital level (DL), as outlined in Section 2.7. The most widespread detector material for this spectral range is GaAs. The camera thus uses a focal plane array (FPA) consisting of individual quantum well infrared photodetectors (QWIP) made of this material. In order to keep the noise level introduced by dark current as low as possible the system is cooled by a Stirling engine down to 70K. This fact introduces a lead time of about 6 min before the measurement can be started. The data acquisition rate is 50 Hz with a resolution of 320 by 240 pixels within the temperature range of -20 to 1500 °C. In this context it is crucial to notice that the real detectable temperature range is linked to the applied *integration time* (IT). This will be discussed further below. The data sheet with the complete data is given in Appendix D.

In Fig. 3.1a it can be seen that the camera is situated in a box shaped housing offering protection from airborne particles in the test rig and a barrier for incident radiation from the sides. The protective box with the imaging system can be mounted inside the test rig as shown in Fig. 3.1b. The camera was mounted throughout the test rig program for the present work and specific brake cycles were recorded. An overview of the individual sequences within the program and the monitored brakes cycles is given in Section 3.4.



(a)



(b)

Figure 3.1: Position of thermal imaging system: a) position in casing, b) position in test rig (camera position is indicated).

3.3 Data processing

The calibration of the camera system was conducted on-site assuming a constant coefficient of emissivity. After the measurements have been completed the calibration curve as well as the thermal image data were exported to Matlab[®] format. Before the data are converted to temperatures a routine for data processing is applied, as illustrated in Fig. 3.2. For the general understanding, the meaning of the calibration curve and digital levels (DLs) will be discussed right at the beginning. As previously noted, the range of detectable temperatures is rather wide for the used camera, but in each measurement only a sub-range is detectable, since one out of four settings for the integration time must be chosen in advance. The DL

3. CHARACTERIZATION OF LOADING CONDITIONS

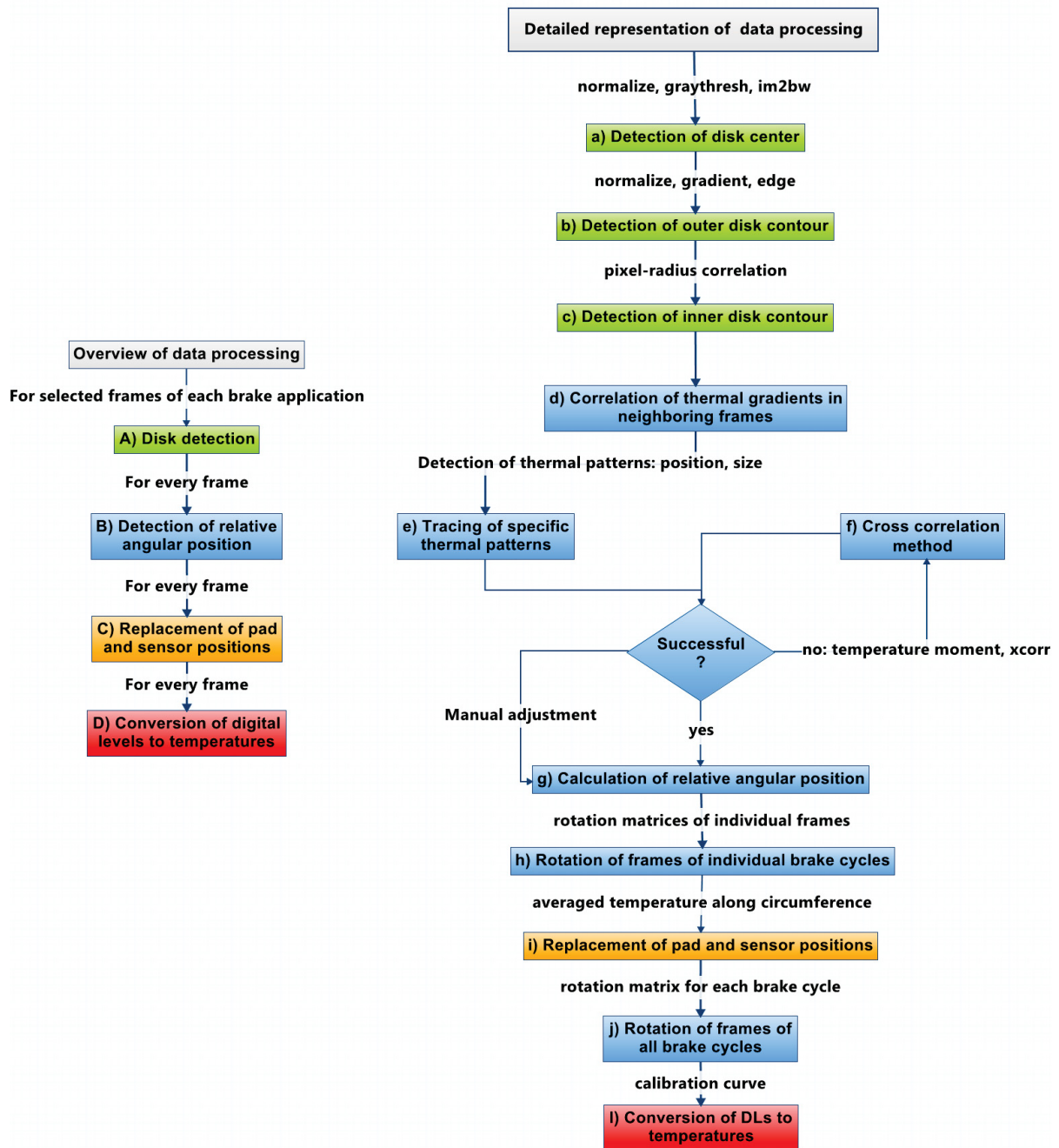


Figure 3.2: Illustration of strategy for data processing of thermal images.

represents the intensity of the incident radiation integrated over a specified time period (IT). The IT is thus the time during which the DL can increase when the detector array is exposed to radiation. When the IT is over, the DL is saved for each detector element (pixel), i.e. at this point one frame of a video has been recorded. Thereafter the DL is reset to zero. When the temperature level and thus the intensity of infrared radiation is low the IT must be set to a high value since it takes some time for the DL to reach values in the desired range between the lower and upper region of noise. For the case of high temperatures corresponding to intense radiation a low value is favorable. Otherwise the DL would saturate immediately and each pixel would yield a temperature value corresponding to a value from the uppermost region of the

calibration curve.

The ThermaCAM[®] SC 3000 uses a 14-bit system yielding a discretization of the DL in $2^{14}=16384$ steps. This means that the DL may increase during the IT from 0 to 16383, which indicates the absolute saturation value. In the range of 20% to 80% of the saturation value the correspondence between DL and temperature is linear and very precise — if it is assumed that the emissivity is homogeneous and does not change during the measurement. Increasing noise adds to the signal below and above this range since the calibration curve showing the correlation between DL and temperature flattens at the beginning and at the end.

The result of the conversion to Matlab data is a 3-dimensional data matrix for each recorded brake cycle (and a 1-dimensional list with temperature values as will be discussed later). The structure of the data array is illustrated in Fig. 3.3. The camera obtains 50 images per second regardless of the chosen integration time and each image, from now on designated as frame, comprises 320 by 240 pixels. In the present data the origin of the coordinate system is situated in the upper left corner and the individual frames are arranged along the third dimension yielding a 3-dimensional structure. Each pixel in the array corresponds to a DL. Since the thermal resolution is significantly higher in terms of DL than in terms of temperature the conversion should be carried out after the data processing. Otherwise some information is lost since a single temperature value is allocated to a whole range of DLs.

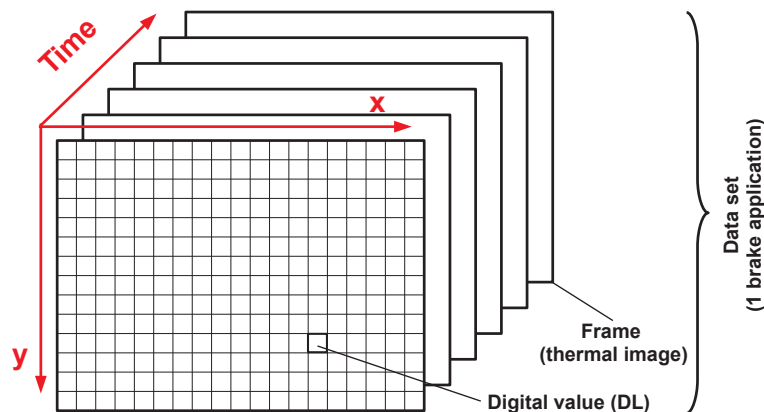


Figure 3.3: Structure of thermal image data.

The aim of the data processing is illustrated in Fig. 3.4. On the left the original data for a specific frame is shown while the image on the right represents the processed state. On the one hand the areas of the brake pad and the deformation sensor are replaced by data from adjacent frames retrieved at the corresponding positions. Since the disk rotates the areas that are covered by the pad and the sensor in one frame are visible in neighboring frames and thus a complete image can be generated. On the other hand the angular position of the disk depicted in Fig. 3.4b is rotated with respect to the original state shown in Fig. 3.4a. The application of this procedure to all the frames of a video recorded during a brake application yields a processed video showing a full view on a stationary disk with an evolving temperature field. Subsequently, the individual videos of each test run are in turn rotated to a common angular position based on a visible feature on the wheel. This way, the temperature evolution within a brake cycle as well as the thermal evolution over the test sequence is made visible and can be studied in a very comprehensive way. Furthermore, the processed temperature data are ready to be used for simulation purposes as discussed

3. CHARACTERIZATION OF LOADING CONDITIONS

in Chapter 5. The procedure developed by Kaltenbrunner et al. [146] within the scope of this work will be summarized in the following.

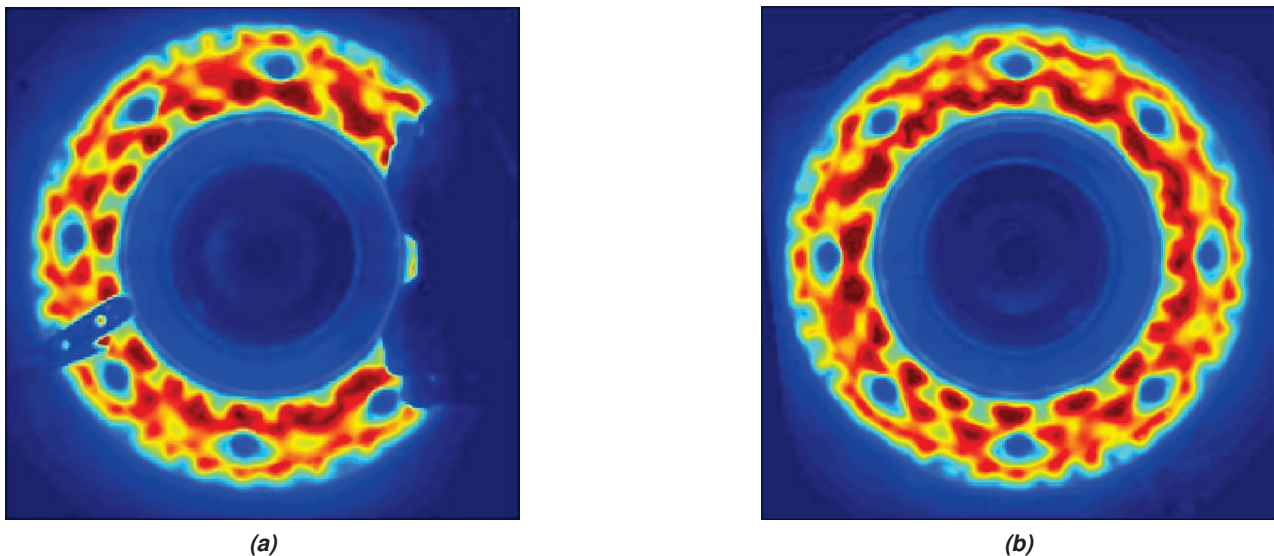


Figure 3.4: Illustration of the goal of the processing technique: a) initial state, b) processed state.

Part A) — Disk detection: Fig. 3.5 demonstrates the initial step of the Matlab procedure, which consists of the detection of the disk center, **section a)** in Fig. 3.2. For this purpose the data of a frame are converted to a binary image, i.e. a black and white image consisting of zeros and ones. This is effected by normalizing the data (the data are scaled from 0 to 1) and the subsequent use of two Matlab functions, *graythresh* and *im2bw* [147]¹. The first function determines a threshold value, and on the basis of this threshold *im2bw* converts a grey-scale image to a binary image. All the pixels below the threshold are set to zero while the ones above are set to 1. This method yields a circular distribution of data points as shown on Fig. 3.5a. The function *bwperim* makes it possible to detect the perimeter of connected objects in the binary image, i.e. the outer pixels of non-zero clusters. Subsequently, the x and y coordinates of all the perimeter pixels are accessed and stored in arrays. Afterwards the data are fitted by a circle using a least squares method. At this point a first estimate on the disk center has been obtained, but the procedure described above is carried out iteratively in order to improve the precision of the result. A variation of the method is applied in the following iterations, i.e. the range of pixels used for the fit is restricted to data within a certain distance from the disk center, which was determined in the previous iteration. The final result for one frame is depicted in Fig. 3.5b and Fig. 3.5c. The detection of the disk center is carried out for a multitude of frames, i.e. every 100th frame. The final result is the mean value of all individual results. The next steps in the data processing treat the detection of the outer, **section b)**, and inner disk contour, **section c)**. Fig. 3.5c suggests that the inner boundary of the disk has already been found in the course of the previous detection of the disk center. In general, this is not the case because the binary images often show contours situated between the disk center and the real disk contour. For this reason a different approach has to be chosen. A frame close to the end of the brake application is selected rendering the disk heated up entirely at this stage, making a proper detection more manageable. Again the data are

¹In this section Matlab functions are written in italics

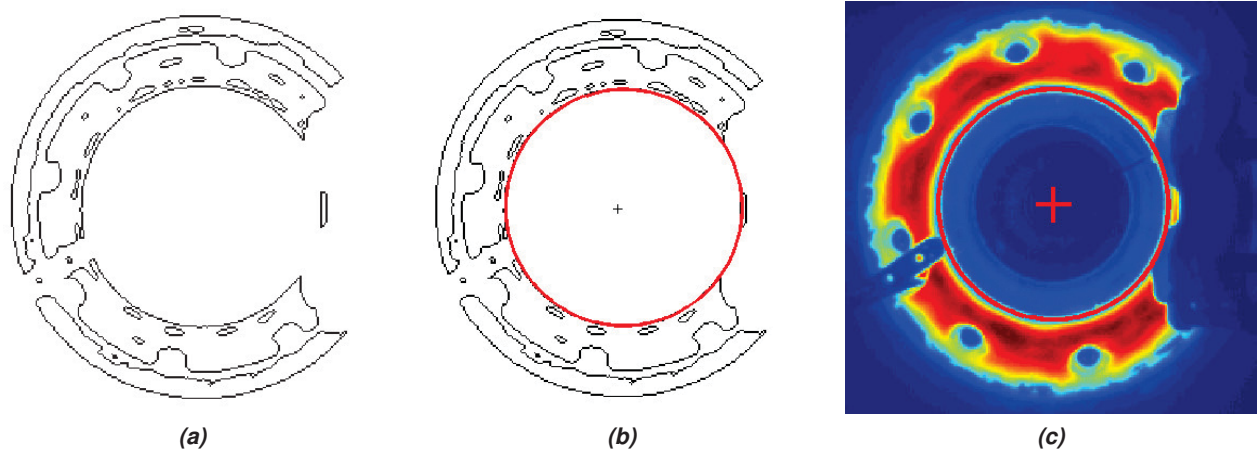


Figure 3.5: Detection of disk center: a) contours within normalized image data, b) approximation of disk center, c) data from image b) on original image.

normalized but instead of a binary image a gradient image is generated with the function *gradient*. Since 2-D data are treated the gradient function yields the gradient from pixel to pixel starting at the upper left origin both in x and in y direction. The gradient function generates two values per pixel, which can be reduced to a single value by simple averaging. The resulting values are normalized and further processed by the *edge* function. This method yields a binary image where pixels, in the present case determined by the Canny approach [147; 148], are represented by the binary digit “1”. The current state of the data processing is plotted in Fig. 3.6a. The circular structures correspond to positions with high intensity/temperature gradients. The pixels in these structures are sorted by their distance from the disk center and the estimated number of pixels corresponding to the outer circumference is used for a fit, again based on a least squares method. A similar procedure is applied for the detection of the inner contour. Since ambiguous results may occur the known ratio of outer to inner radius is used to pick the correct result. For this purpose the edge length, l_e , of a single pixel must be correlated to the corresponding length on the disk. Since the configuration of the test rig is identical for all test runs, it is sufficient to determine l_e only once. For the investigated data l_e equals 3 mm and this information combined with the outer radius and the disk center yields an estimate on the inner disk contour. As in the previous step of the data processing, several frames — in this case every 5th in the last 500 frames — are evaluated and the results are averaged. The detected inner, outer and mean radius are plotted in Fig. 3.6b. In general, the results for the disk center, section a) and the contours, sections b) and c), vary in the range of 2-3 pixels, which corresponds to deviations of 6-9 mm.

Part B) — Detection of relative angular position: The next issue that needs to be resolved is illustrated in Fig. 3.7 showing two successive frames. The red line indicates the angular position of a specific area on the disk corresponding to a hot spot. From the two images it is clear that the relative angular displacement between the individual frames of a video has to be determined. For the test sequences carried out in the scope of this study an indicator has been positioned on the wheel and should be visible in the region between the disk center and the inner disk contour. The problem in this case is that the integration time is set for a temperature range above room temperature (short integration time) and in addition to this fact the indicator is passive, i.e. it has a different emissivity than the wheel but it does not emit any radiation apart

3. CHARACTERIZATION OF LOADING CONDITIONS

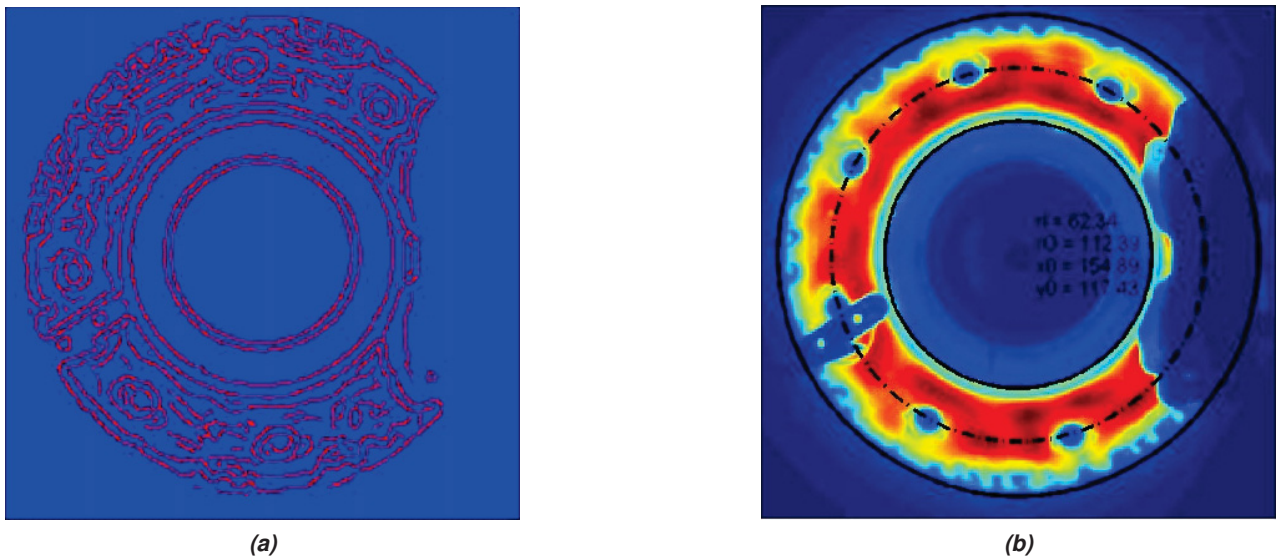


Figure 3.6: Detection of disk contour: a) normalized gradient image, b) detection of outer and inner contour.

from its natural thermal radiation. The calibration curve in Fig. 3.15, which will be discussed in more detail further below, starts with values around 60°C while the wheel and the indicator stay at room temperature throughout the test. While the pixels situated in the area corresponding to the disk obtain reasonable DL values the pixels situated on the wheel yield DL values at the lower end of the calibration curve. Despite the fact that the intensity emitted by the wheel and the indicator differ, this difference is attenuated by the noise at the lower end of the calibration curve. The lack of any visible contrast between the indicator and

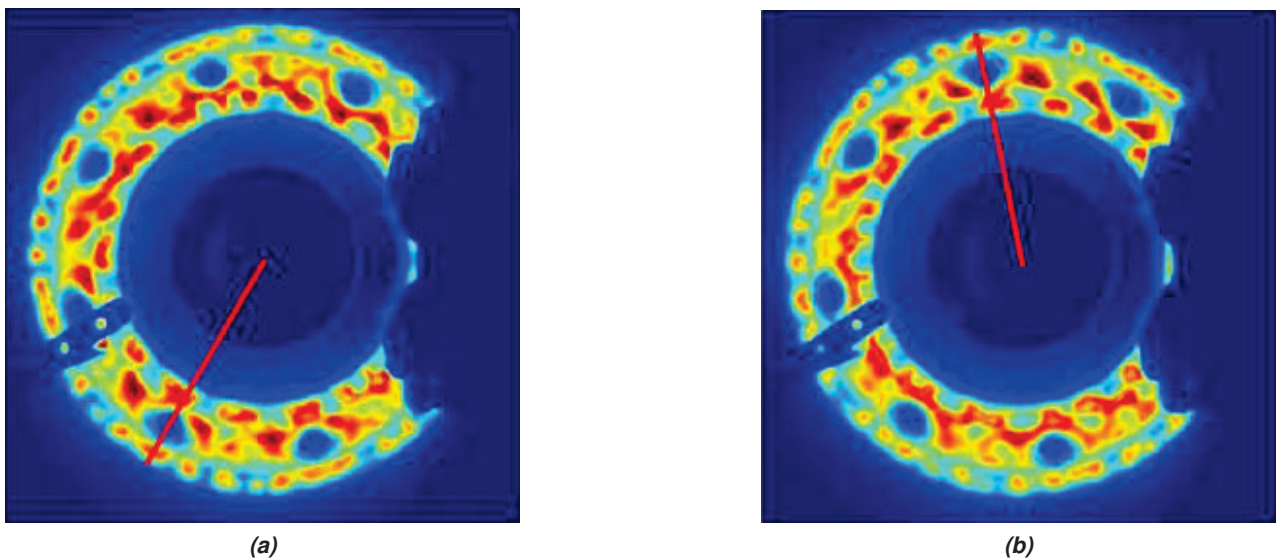


Figure 3.7: Angular displacement between two subsequent frames.

the wheel becomes evident from Stefan-Boltzmann's law. Eq. (2.185) shows that the power emitted by a radiation source correlates with the 4th power of temperature given in Kelvin. Since the camera is set for temperature levels of several hundred degrees the small differences in radiation intensity of cold parts cannot be detected. As a consequence, the relative angular displacement from one frame to the next must be

determined by tracing individual thermal patterns as already indicated in Fig. 3.7. This problem is tackled with two different strategies, indicated as **section e)** and **section f)**. The first one is to trace characteristic thermal patterns over the course of a braking. This is the standard method used in the data processing. The second method is used when thermal patterns are not sufficiently distinct and the first method fails. Then the angular displacement is determined by cross-correlation of a function defined along the angular circumference of the disk.

Section e) begins with an examination of DLs along the mean radius Fig. 3.8a. The lowest values are averaged and chosen as threshold value for the detection of the mounting points — these are always visible for the investigated disk type. The detection is carried out with the function *contour*, which encloses all values at or below the threshold. In the first attempt only a fraction of the hole areas is enclosed since temperatures increase towards the edges (Fig. 3.8b). For this reason, the threshold is iteratively increased up to a specified limit. All the contours detected in the process are analyzed based on shape, size, position and periodicity. This way all mounting points not covered by the pad or the displacement sensor are detected. Since the periodicity is known the missing holes can be added. The final state is plotted in Fig. 3.8c.

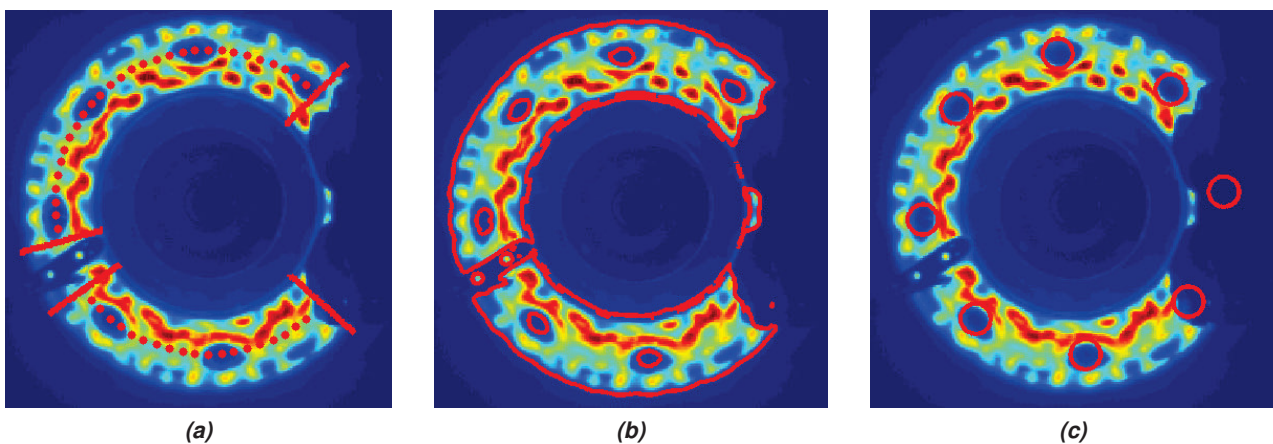


Figure 3.8: Detection of mounting positions: a) detection of areas with minimal temperatures, b) iterative contour definition and hole detection, c) final contours indicating the mounting positions.

At this stage, the relative angular displacement is limited to eight possible cases (there are eight mounting points). The subsequent procedure is cumbersome and will only be discussed briefly. One of the mounting points is selected and the thermal gradients in the adjacent area are analyzed (Fig. 3.9a). A local coordinate system is positioned at the center of the mounting point. The two largest hot spots are selected as references that should be detected in the following frame. This is effected by determining the positions of the hot spots in the local coordinate system as illustrated in Fig. 3.9b and further characterization, e.g. their size. Based on these characteristics the script tries to identify the mounting point with the two hot spots in its vicinity in the next frame. It might happen that the very position is covered by the pad and no match is obtained. In this case another mounting point is automatically chosen as new reference position. Once a match has been found the angular displacements can be determined from the position of the reference hole in the two frames.

The second method, **section f)**, for the angle detection is based on the definition of a function along the circumference of the disk that can be defined and compared in each frame. One possibility is defining a

3. CHARACTERIZATION OF LOADING CONDITIONS

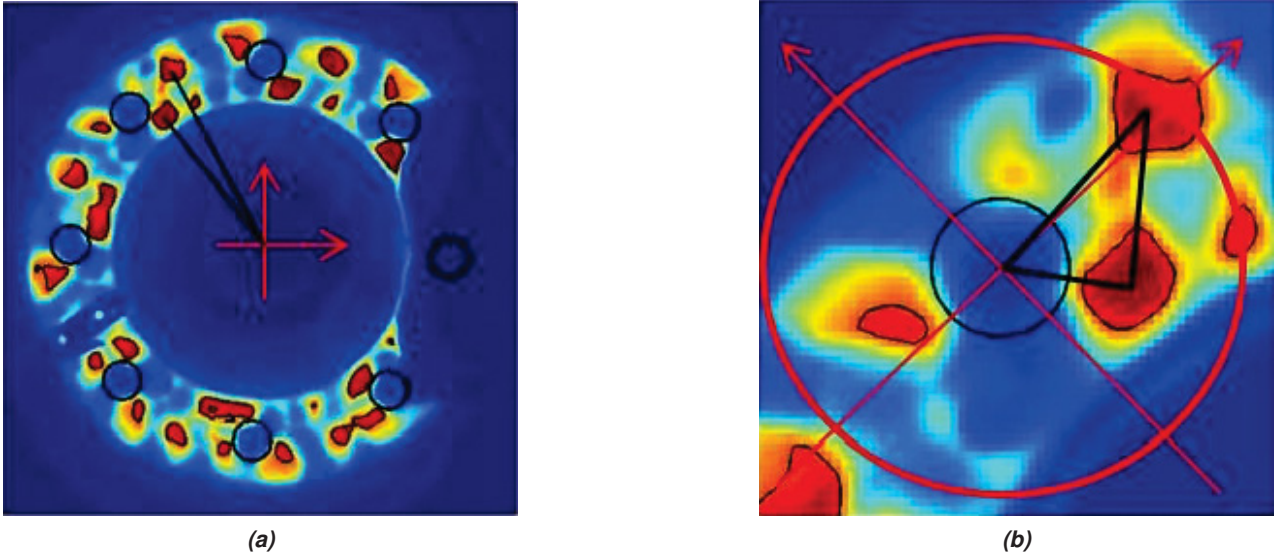


Figure 3.9: Detection of characteristic thermal patterns: a) global thermal pattern, b) local pattern around a mounting point.

temperature moment for the frame i as a function of the angular position ϕ from 0° up to 360° according to Eq. (3.7).

$$\Theta_M^i(\phi) = \frac{1}{r_a - r_i} \int_{r_i}^{r_a} T^i(r, \phi) r dr \quad r_i \dots \text{inner radius} \quad r_a \dots \text{outer radius} \quad (3.7)$$

$$\bar{\Theta}_M^i(\phi) = \Theta_M^i(\phi) - \frac{1}{2\pi} \int_0^{2\pi} \Theta_M^i(\phi) d\phi \quad (3.8)$$

For this purpose each pixel value $T^i(r, \phi)$ is multiplied by its distance r to the disk center. Thereafter, the obtained values are summed at each angular position from the inner disk radius to the outer one. Furthermore, the mean value is subtracted according to Eq. (3.8) (necessary for cross-correlation later on) and the pad and sensor areas are set to 0. The result for two subsequent frames is plotted in Fig. 3.10a and Fig. 3.10b. At this point the cross-correlation can be carried out using the Matlab function `xcorr`, which is an implementation of the following expression (for two discrete functions):

$$R_{\bar{\Theta}_M^{i+1}, \bar{\Theta}_M^i}(\psi) = \int_0^{2\pi} \bar{\Theta}_M^i(\phi) \bar{\Theta}_M^{i+1}(\phi + \psi) d\phi \quad (3.9)$$

It should be noticed that the signals must be normalized. This can be achieved by the optional argument `scaleopt` of the function `xcorr`. The angle ψ corresponds to an angular shift of $\bar{\Theta}_M^{i+1}(\phi + \psi)$ with respect to $\bar{\Theta}_M^i(\phi)$. The correlation factor R is computed as a function of ψ as depicted in Fig. 3.11a and its maximum indicates the the most probable value for the angular displacement between the data of the frames i and $i + 1$. This method is preferable when only few distinct features are discernible in the temperature field. As indicated in Fig. 3.2, section f) is only carried out if section e) fails.

A general drawback of methods relying on characteristic thermal distributions is their dependence on distinct features in the temperature field. Due to this fact the first three seconds of each braking must be omitted since temperature levels are too homogeneous. The corresponding data are included in the final results but no rotation is applied. Moreover, the method might fail for other disk-pad pairings, since thermal

patterns might be completely different. For the two pairings investigated in this study the method worked well, although for some data sets not fully automated. Manual adjustments were necessary as shown in Fig. 3.2. If the position of only one frame is misinterpreted by the procedure, all subsequent frames appear rotated. Consequently a sudden jump in the angular position occurs when the final movie is regarded. Considering that a video is made up of about 3000 frames the method must be rather fail-safe. Nevertheless, even in the case when some frames require manual adjustment, the procedure is a pivotal aid to achieve the objective of creating a stationary representation of the temperature field.

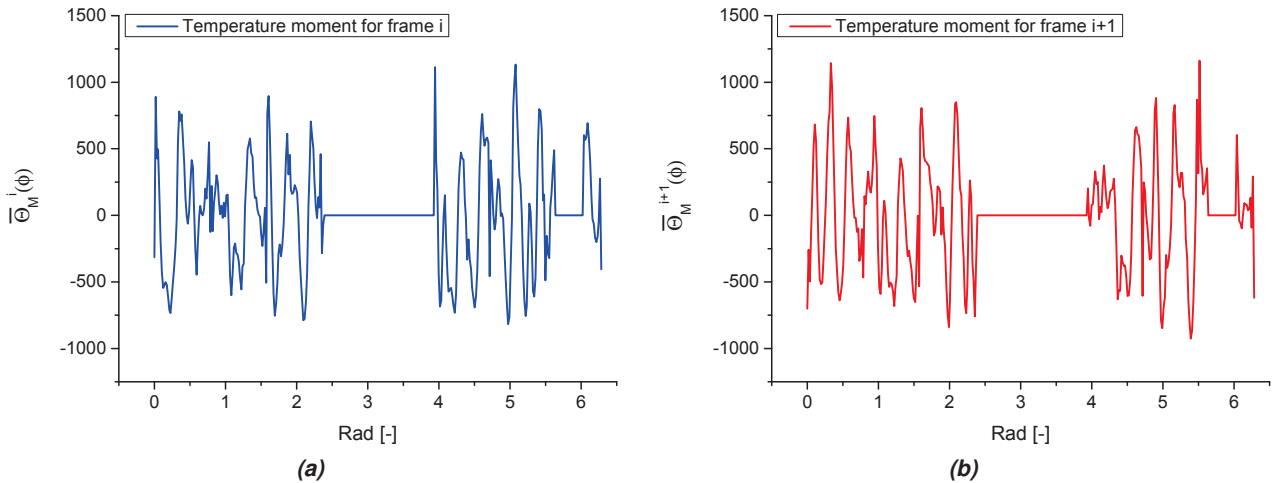


Figure 3.10: Alternative method for the detection of relative angular displacement: temperature moment for two subsequent frames a) and b).

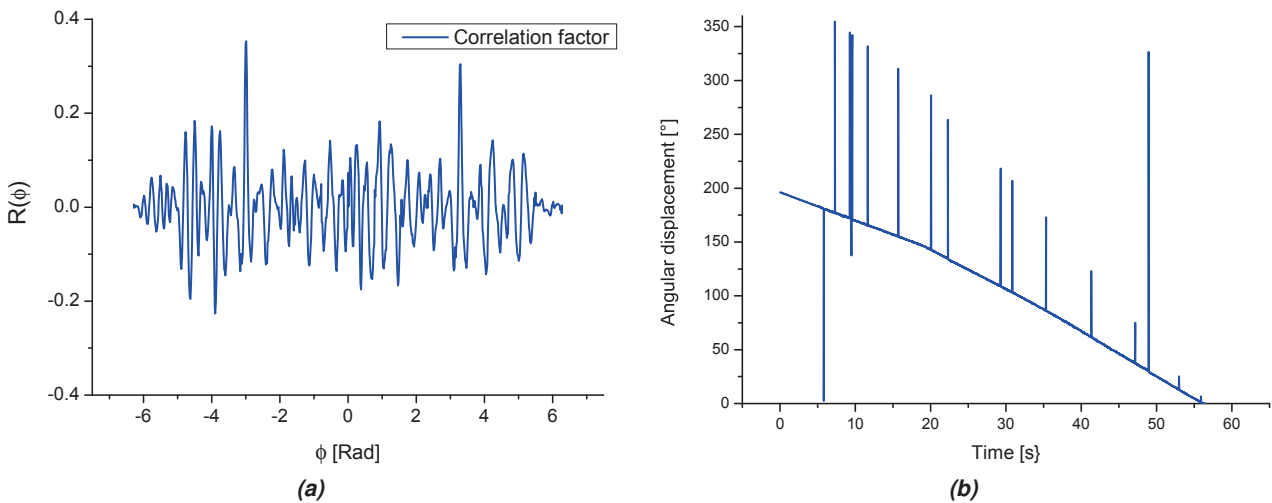


Figure 3.11: a) Data from cross correlation of two subsequent frames, b) deviations from the expected angular position due to missing frames.

The individual angles are stored to a list and can be easily plotted. Fig. 3.11b shows the result of the complete procedure described in this section for a whole brake application corresponding to roughly 3000 frames. The peaks in the evolution of the detected angles occur whenever one or more frames have not been recorded by the camera system. In each case the relative angular position deviates from the expected trend and corresponds to the sum of the angular displacements of the current frame and the

3. CHARACTERIZATION OF LOADING CONDITIONS

frames that have been left out. Each time a deviation occurs, the determined angle is verified by an additional angle detection step. In the normal procedure the angle is determined from one frame to the next, e.g. $\alpha_{100-101}$ is determined from the frames 100 and 101. If $\alpha_{100-101}$ deviates from the trend an additional evaluation step using an earlier frame, e.g. frame 99, is carried out in order to have a second result at hand. The alternative result can be obtained as follows: $\alpha_{100-101} = \alpha_{99-101} - \alpha_{99-100}$. If the results from both angle detection steps match, the deviating angular position is a correct result and the algorithm can proceed — **section e)** in the standard procedure. If the angle detection was not successful **section f)** is carried out. In cases where both methods fail, user interaction is required.

When the angles of all frames of brake cycles have been determined, the individual frames are rotated to one common angular position (**section g)**). This is done by multiplying the matrices containing the data with a rotation matrix (Fig. 3.12a and Fig. 3.12b). The rotation matrix contains the rotation angle as parameter, which is properly selected for each frame. Since the original data grid and the rotated data grid are not coincident, the rotation is accompanied by bilinear interpolation, as illustrated in Fig. 3.12c. The value of a rotated pixel (green) is computed from the four adjacent pixels in the original matrix (red).

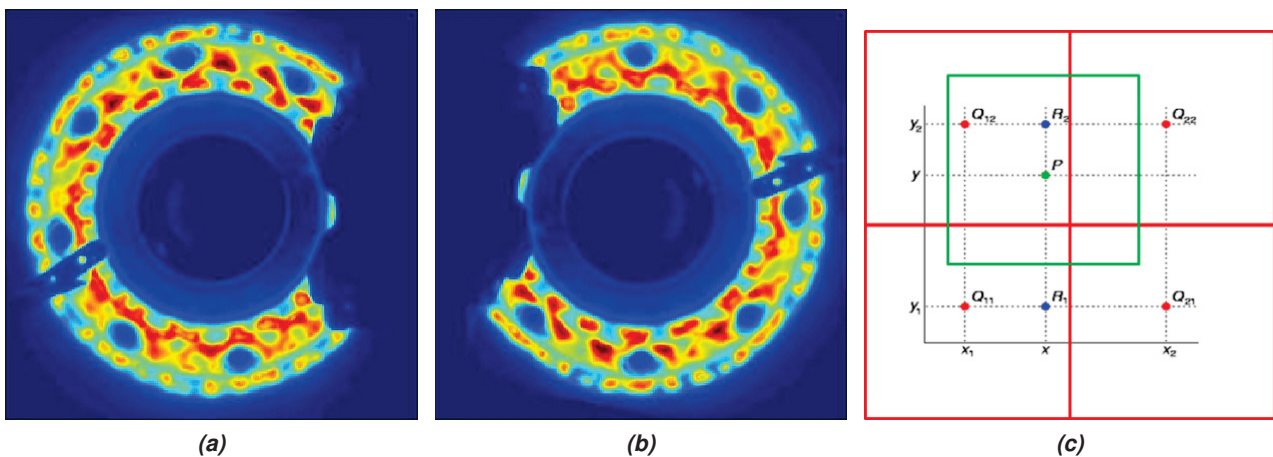


Figure 3.12: Rotation of data frame (a) to specific angular position (b) by multiplication with rotation matrix and (c) bilinear interpolation (based on [27]).

Part C) — Replacement of pad and sensor positions: In the next step of the procedure missing data underneath the pad and sensor regions are replaced¹ by data from neighboring frames. Due to the fact that there are time periods where nearly the same areas are covered in subsequent frames, these areas are replaced piecewise from multiple frames if necessary. This way, the disadvantageous situation when some areas have to be replaced by data from a point some seconds later is avoided. In each frame the temperatures are averaged along the radius between inner and outer circle for each angular position as

¹The data underneath the pad cannot be reconstructed, since the temperature values are not known. Nevertheless, in the processing the missing data are replaced with data from neighboring frames in order to obtain a complete view of the friction surface.

stated by Eq. (3.10).

$$T_m^i(\phi) = \frac{1}{r_a - r_i} \int_{r_i}^{r_a} T^i(r, \phi) dr \quad i \dots \text{frame index} \quad (3.10)$$

$$\bar{T}_m^i = \frac{1}{2\pi} \int_0^{2\pi} T_m^i(\phi) d\phi \quad (3.11)$$

A representative result is shown in Fig. 3.13a. In order to perform the following method the data are generated twice, i.e. for the angular range from 0 to 720°C. Now the global minimum is determined along with the neighboring local maxima. The maxima indicate the boundary of the pad area. This strategy works reliably if an additional criterion is satisfied. The temperature level needs to be above the average value otherwise a maximum is ignored. Now the data range in the pad region is replaced by the average temperature \bar{T}_m according to Eq. (3.11) and the procedure is repeated at the subsequent global minimum value yielding the position of the sensor (Fig. 3.13b). This method is applied to all the frames of a brake cycle and the detected angular positions are replaced as illustrated in Fig. 3.14.

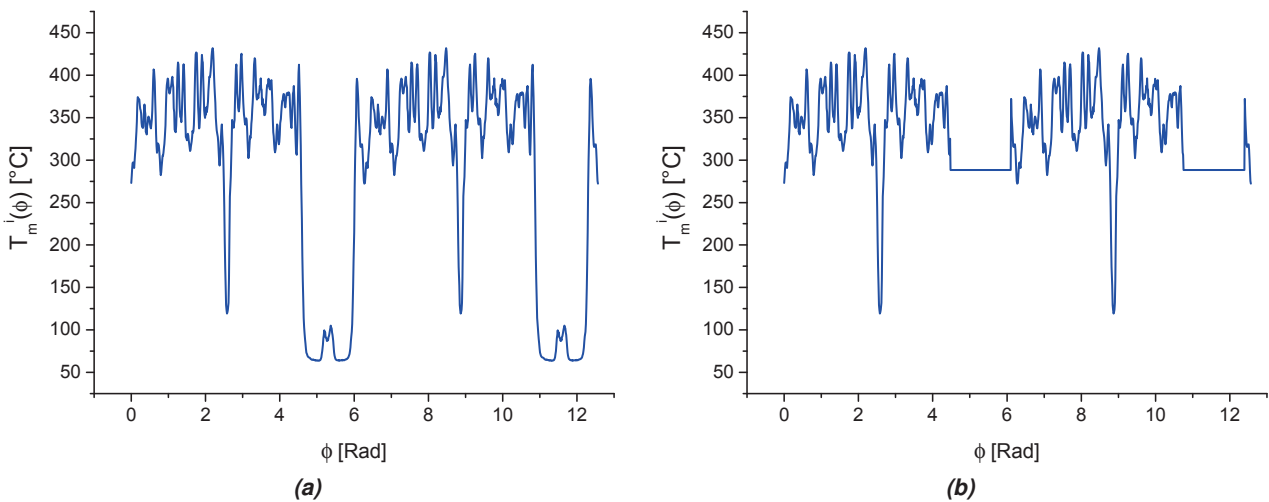


Figure 3.13: Average temperature as a function of the angle for the detection of pad and sensor position, a) initial data for detection of the pad, b) updated data for detection of the sensor.

In general, the data processing is carried out for all recorded brake applications of a test run. So far, the individual data sets have been processed but there is still an angular displacement between each data set, which must be corrected (**section j**). The displacements can be determined from certain features on the wheel, which are visible in some frames of each brake cycle. This way, a rotation matrix is defined for each data set and all frames can be rotated to a common reference position. This step is especially important for the modeling part in view of damage accumulation, where the position of each pixel must be consistent throughout the simulated sequence of brakings.

Part D) — Conversion of digital values to temperatures: Fig. 3.15 shows the calibration curve linking the digital values to temperature values. Despite the fact that a 14-bit system is used the vertical axis in Fig. 3.15 shows values from 0 to 65535. This change in the data occurs due to the data export to the Matlab format. As previously mentioned, the conversion to Matlab data yields a 3D array containing a list with temperature values for each recorded brake cycle. The list-indices correspond to DLs and the

3. CHARACTERIZATION OF LOADING CONDITIONS

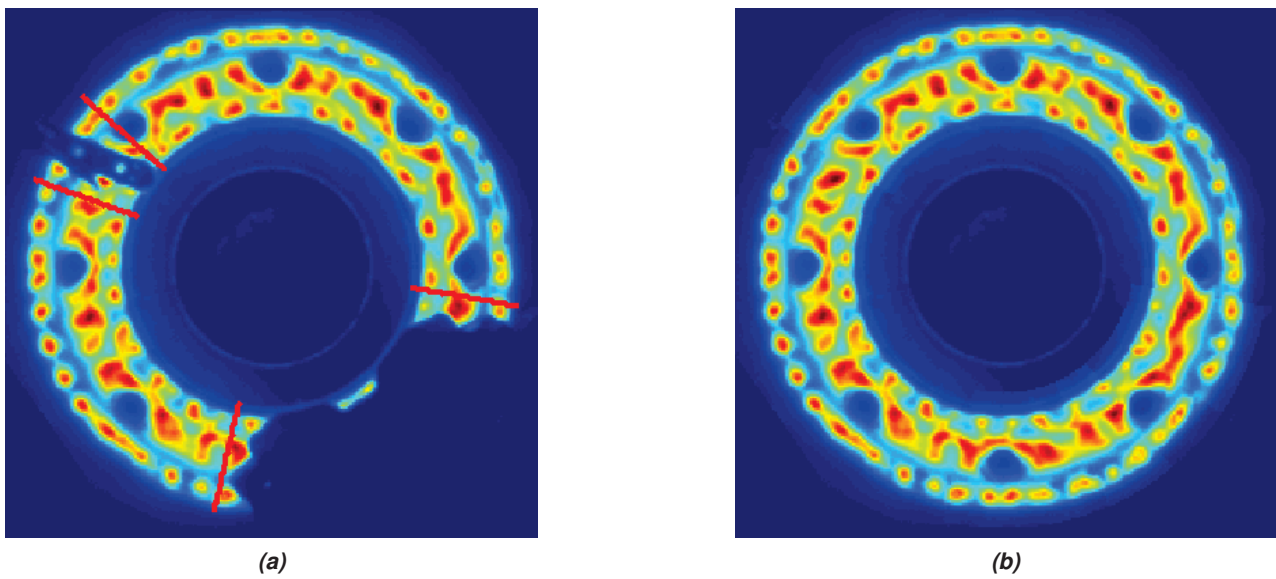


Figure 3.14: a) Detected positions of pad and sensor, b) Final result for the displayed frame: rotated data frame with substituted pad and sensor areas.

respective values to temperatures thus yielding a calibration curve. Each element in the array corresponds to a DL being in the value range of the calibration curve. The calibration curve can be applied for the conversion to temperature values by looping over all entries of the data array and matching each DL to a temperature value. Fig. 3.15 shows that the curvature at the upper and the lower end of the calibration curve is not very pronounced. This indicates that the temperature ranges below 60°C and above 870°C, have been cut-off by default since they are outside the range of validity.

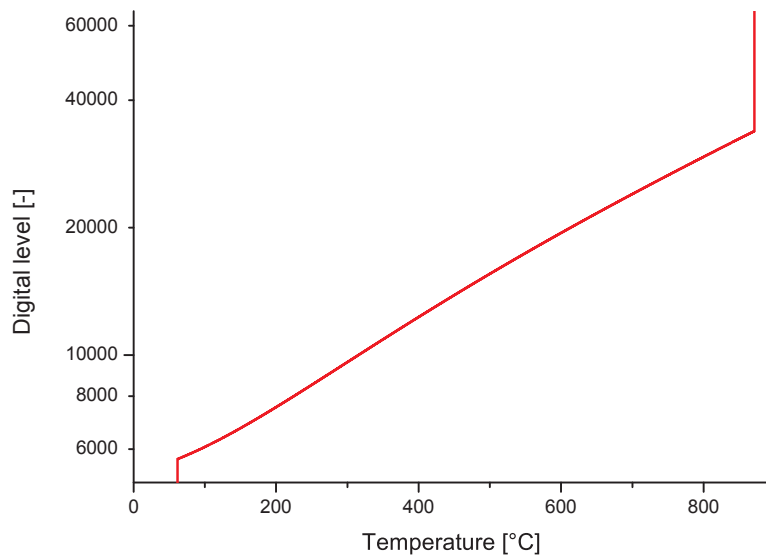


Figure 3.15: Correlation of digital values and temperatures.

The complete procedure has been applied to process the data corresponding to 40 bedding-in and 59 emergency stops. A selection of representative results will be discussed in the next section with focus on the emergency stops.

Part B of the data processing has been carried out without the aid of an indicator. The advantage of the

presented method is that it works well for the thermal image data collected in the scope of this work and it can be applied for other data, where no indicator exists. For a regular implementation of the method at a test rig further simplifications are possible: 1) a synchronization of the test bench with the thermal imaging system (the angular position of the axle can be correlated with the frames of the video), 2) the application of active indicators, i.e. infrared emitters. This way, the determination of the relative angular displacements between the frames is straightforward and the need for manual adjustments can be avoided.

3.4 Results

As noted above, the data processing is applied to the data available from the test rig program. Fig. 3.16 provides an overview of the test runs (see also Fig. 1.13) and the naming convention used for the individual disk sets. This convention will be used in the remainder of this work for the specification of the thermal image data, samples and various data obtained in scope of the damage analysis, which is treated in Chapter 4. The numbers written in brackets indicate the brake cycles in the specific test run where valid thermal image data are available for further analysis. The recorded bedding in stops are not indicated as this section will focus on emergency braking.

| Test | Test run | Side 1 (Thermocouples + thermal images): Disk name | Side 2: Disk name |
|-------------------------------|----------|---|----------------------|
| Pad type 1 (flexible) | | | |
| Bedding | 1 | 1 | 2 |
| Bedding + 1 braking | 2 | 3 | 4 |
| Bedding + 10 brakings | 3 | 5 (9 and 10) | 6 |
| Bedding + 200 Stops | 4 | 7 (1-10, 49-54, 99-103, 136,139, 148-153, 182-184, 197-199) | 8 |
| Pad type 2 (monoblock) | | | |
| Bedding | 5 | 9 | 10 |
| Bedding + 1 braking | 6 | 11 (1) | 12 |
| Bedding + 10 brakings | 7 | 13 (9 and 10) | 14 |
| Bedding + 200 Stops | 8 | 15 (1-10, 44-50, 85, 89) | 16 |

Figure 3.16: Overview of tests runs and the corresponding disk sets. The numbers in brackets refer to the brake cycles where thermal image data are available.

As outlined in Chapter 1, the test rig program is based on one reference brake cycle and in the terminology of fatigue it corresponds to single amplitude loading. This way it is possible to carry out studies on the following subjects:

- Transient changes of the temperature distribution during individual brake cycles
- Transient changes of the temperature distribution over several brake cycles
- Reproducibility of thermal distributions

3. CHARACTERIZATION OF LOADING CONDITIONS

- Impact of pad replacement within test sequences
- Thermal image data from scaled test rig

3.4.1 Development of the thermal distribution during individual brake cycles

Figures 3.17 and 3.18 show the thermal evolution at the friction surface for pad types 1 and 2, respectively in time increments corresponding to 10% of the specific total brake time. To start with representative data a more or less stabilized condition, i.e. a brake cycle at the end of the 10-stop runs, is chosen. For pad type 2 braking number 9 is selected because number 10 was aborted. Whether these brakings are really stabilized and representative will be investigated in the subsequent section. Fig. 3.17a indicates elevated though still low temperature levels compared to later stages, but the non-uniform nature of the contact conditions is already apparent. Apart from a circle on the outer disk half¹, which is still cold, elevated temperatures occur in the other disk areas. The highest temperatures appear along the mean radius and the outer radius resembling thermal gradients on hot bands reported in [3] or focal hot spots discussed in [36]. From Fig. 3.17c on, the cold ring heats up and disappears completely in Fig. 3.17e. At the same time the gradients on the inner hot band start to grow and spread over the inner half of the disk. A clear hot band pattern as in the beginning is not distinguishable anymore. The gradients on the outer hot band, on the other hand, remain until Fig. 3.17e, where the last gradients on the hot band have finally disappeared. Instead a coarser structure of hot and cold regions has formed with a higher focus on the inner disk half. The apparent coarsening of the structures is attributed to the homogenization of the temperature field, which continues until the end. The fact that the local maximal temperature levels are cut off, as indicated in Fig. 3.15, does not affect this observation. The coarsening of the thermal patterns is clearly distinguishable in the valid temperature range. The structure of hot spots on hot bands is lost during the braking and this process can also be seen on the outer disk half where the temperature levels are in general lower and can be resolved by the camera. During the second half of the braking the thermal patterns become more homogeneous until the temperature is almost the same on the greatest part of the friction surface (Fig. 3.17j).

Regarding Fig. 3.18, the situation is obviously different for pad type 2. Right at the beginning of the braking the contact pressure and thus the temperature is highest along the inner and outer perimeter preponderantly on the outer edge. Some periodic structures are visible but they are not gradients on hot bands as in the previous case discussed. The structures are distinct right from the beginning and seem to be caused by global disk deformation along the circumference. The largest size as well as a clear periodicity is obtained in Fig. 3.18d. The arrangement becomes more visible in the subsequent images: On the inner half of the disk the areas between two mounting positions are hot. The situation on the outer half is more complicated since the distribution of the hot areas is less structured. The basic arrangement is that the area directly above the holes is hot. Additionally, another hot area appears on the outer disk half situated roughly between two mounting positions. This hot area can be situated with a bias to the left or to the right, thus influencing the precise position of neighboring hot area at the hole. Based on this assumption 2 times 8 hot structures arranged along the outer circumference and 8 structures along the inner circumference are expected. Over the course of the first 70% of the braking process it can be seen that clusters of small hot

¹The terms inner and outer disk halves refers to the areas on the friction surface situated within and outside the mean radius.

structures along the inner circumference agglomerate to 8 hot structures. There is one structure that does not fit perfectly in since it is split up into three patches. In conclusion, the explanation works on the inner disk half apart from minor deviations. Counting the hot patches along the outer circumference beginning at the top in clockwise direction in Fig. 3.18e one finds alternating patterns, one patch more or less precisely above a hole and one more or less precisely between two holes. This works up to patch number 14 where one patch seems to be missing. Considering the previous image in Fig. 3.18d this patch can be interpreted as consisting of two adjacent patches. In this case the expected number of 16 is obtained. The overall distribution of the hot areas suggests the presence of a global wavy distortion of the disk being different along the inner and the outer radius. Whether the formation of this thermal distribution is an unique event or a stabilized mechanism will be discussed in Section 3.4.2.

Additionally to the two sequences the impact of the two pad types on the thermal evolution another means is available, as depicted in Fig. 3.19. The cumulative patterns illustrate the ratios between different disk areas being situated in certain temperature ranges. For instance, at the end of the braking shown in Fig. 3.19a, 5% of the friction surface are situated in the temperature range between 600 and 700°C. 40% are in the range 500 to 600°C and another 20% between 400 and 500°C. The first impression after comparing Fig. 3.19a and Fig. 3.19b might be that pad type 1 causes more severe loading conditions due to the high temperature levels. This impression is misleading, however, since the temperature level is not the only governing quantity. After a closer look at the first 20s, it can be seen that the temperature level increases much faster for pad type 2. Since the temperature in the bulk of the disk is still cold at this stage, high temperatures at the surface automatically entail high temperature gradients and thus high stress levels, which are detrimental to the component. This fact is represented by the horizontal arrow indicating a rapid change of temperature with time. Due to the fact that the temperature level increases more slowly for pad type 1 in the critical early stage of the braking, the expected stress levels are lower and loading conditions caused by pad type 1 are less damaging. The maximum temperature level that can be detected is limited by the camera settings. Thus it is not clear which pad type causes the higher temperature levels hidden in the dark red area of the cumulative patterns since the maximum temperature that is included in the calibration curve is 870°C. T_{max} , however, is a relevant quantity in view of damage, since material parameters degrade with increasing temperatures. Nevertheless, the cumulative patterns yield information in this matter. The vertical arrow in Fig. 3.19b, pad type 2, indicates large temperature gradients at the friction surface. Extended areas with low temperatures are present and smaller areas with high temperature levels. Anticipating the results from the damage analysis it can be said that the disks tested in combination with pad type 2 contain significantly more regions where phase transformations have taken place. These transformations are linked to high temperature levels and to sufficient dwell times for the formation of austenite. In the case of pad type 2 the high temperature levels are maintained for a longer time (40s) as compared to pad type 1 (25s). The thermal gradients at the friction surface are higher for pad type 2 indicating higher temperatures in certain regions of the disk surface (vertical arrow). The situation in Fig. 3.19a is distinctly more homogeneous.

As noted above, it is not clear at this point whether the thermal distributions discussed so far are characteristic for the two pad types or not. The answer to this question will be given in the next section.

3. CHARACTERIZATION OF LOADING CONDITIONS

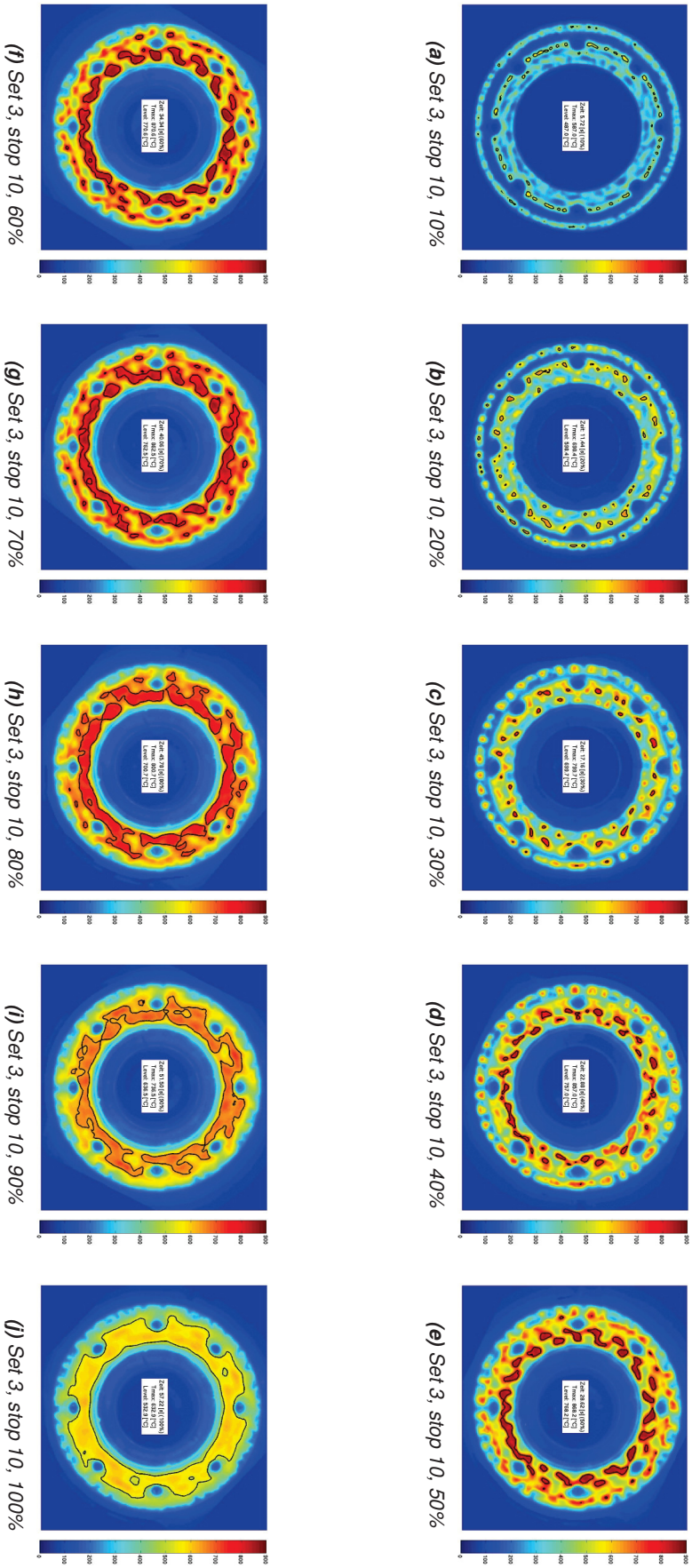


Figure 3.17: Thermal distribution for pad type 1 during cycle 10 of test run 3. The temperature field shortly after braking has started; (a) and (b), is focused on two circles corresponding to the mean and the outer radius. Alternating regions with higher and lower temperature levels are visible, indicating hot spots on hot bands. A distinct circle between the mean and the outer radius stays clearly cooler than the adjacent areas. In the course of the braking the hot spots increase in size and spread over the friction surface and a link to hot bands is not visible anymore. The cool ring on the outer half disappears but a higher level of thermal loading on the inner half of the disk is obvious from (d) on.

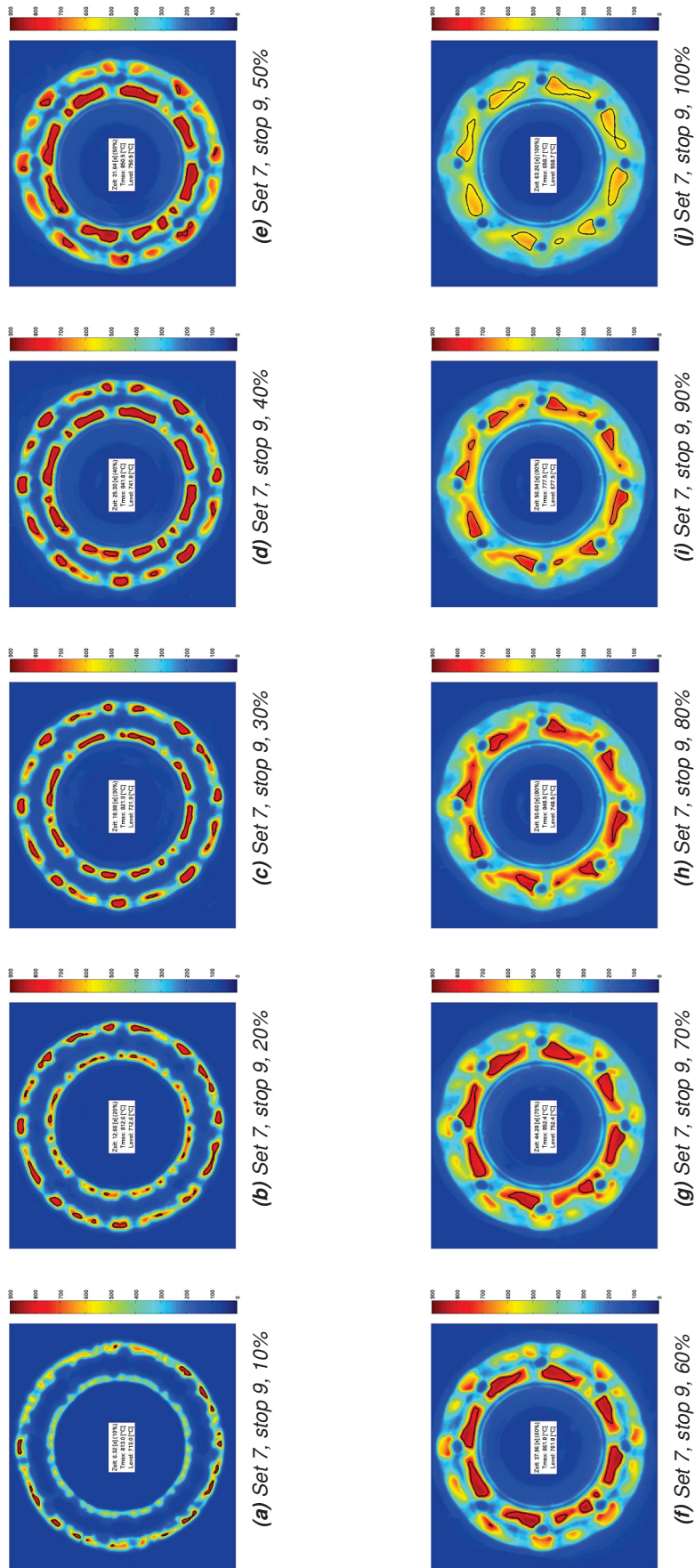


Figure 3.18: Thermal distribution for pad type 2 during cycle 9 of test run 7. The thermal distribution at the beginning suggests increased contact pressure along the inner and the outer circumference. Large areas with increased temperature levels build up along the inner and the outer circumference exhibiting a systematic pattern.

3. CHARACTERIZATION OF LOADING CONDITIONS

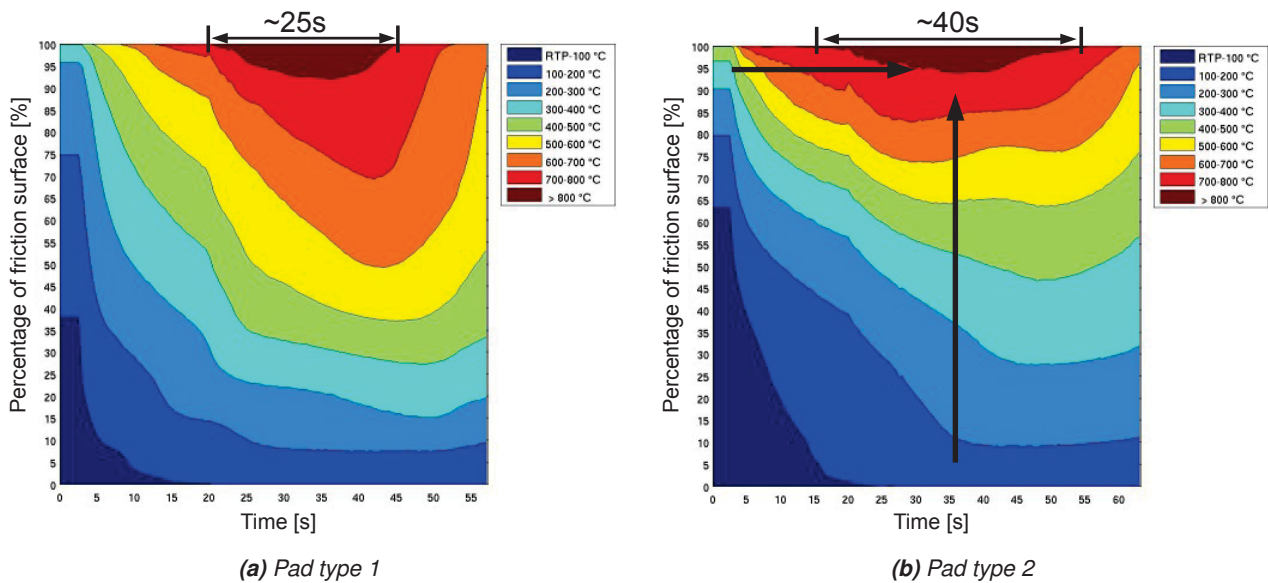


Figure 3.19: Cumulative patterns describing the occurring temperature levels during a) Set 3, stop 10 and b) Set 7, stop 9.

3.4.2 Development of the thermal distribution over several brake cycles

After one half of the total brake time, the disk temperature reaches a maximum — on average since the distribution is inhomogeneous. The highest gradients (globally) occur at an earlier stage, around 30%. Thus frames from the range of 30% to 50% of the total brake time are appropriate for further discussions. Since it was found that thermal gradients are most comprehensive at 50% this specific point in time has been chosen for the discussions in this section. Fig. 3.20 shows a sequence of processed thermal images corresponding to ten consecutive emergency stop with pad type 1 at 50% overall brake time. The corresponding image in Fig. 3.20j has already been used for the previous discussion but this time all data are taken from the beginning of test run 4, corresponding to the 200 stop test rather than the 10 stop test, where only the last two stops were recorded. Fig. 3.17e and Fig. 3.20j will be directly compared at a later point, however, with the aim to check the reproducibility of thermal patterns since they are both the tenth emergency stop in two different test runs. Right now the focus is set on the changes within a specific series. The first observation from Fig. 3.20 is the contrast between the first emergency stop (Fig. 3.20a) and the nine brake applications that follow. The increased thermal loading on the inner disk half for pad type 1 has already been noted above, but in Fig. 3.20a the situation is clearly more severe than in the case of the following brakings. The thermal patterns in Fig. 3.20b to Fig. 3.20j differ on a local scale but on a global scale the type of loading is always similar. The friction surface heats up to a base level and in more or less spot shaped areas the temperature is clearly higher. These hot regions primarily occur on the inner disk half. From this point of view the case discussed in the last section is representative for pad type 1. Still the question remains whether the situation in Fig. 3.20a might reappear, e.g. after pad replacement, or not. If this thermal pattern is a single event it might be due to the initial plastic deformation in the disk. Otherwise it is part of a bedding-process of the pad.

The series of thermal images selected for pad type 2 (Fig. 3.21) clearly suggests that the example discussed in Section 3.4.1 is not representative and is only part of a series of changing thermal patterns. The

series begins with a pattern of eight large patches corresponding to a high temperature level, designated as configuration C1. These patches cover most of the regions between the mounting points, but leave a cold gap below and above each hole. This suggests a wavy deformation of the disk with eight maxima at the center positions, between the mounting points (in the following these positions will simply be called center positions). The series continues with an almost perfect inversion of the thermal distribution depicted in Fig. 3.21b (C2). Again 8 hot patches appear, but this time they cover the areas around the holes again indicating a wavy deformation of the disk with a changed phase angle of 22.5° . This change in the thermal pattern may be explained by a high level of plastic deformation during the first brake application causing global deformation. This plastic deformation seems to change the contact conditions in the next emergency stop but the phenomenon cannot be further explained at this point. The discussion will therefore be limited to the observable changes while further explanations are left to the chapter on simulation (Chapter 5). The series continues with temperature states that cannot be clearly classified. Apparently, they constitute intermediate states between the distributions in Figures 3.21a and 3.21b. The latest point in time when the sequence of intermediate states is over is shown in Fig. 3.21h. This pattern corresponds to the initial state (Fig. 3.21a) with one difference: There is a tendency that the large patches covering the center positions are split in half, leaving a cold gap (C3). This modification occurs at some but not all center positions. The subsequent image (Fig. 3.21i) is a similar inversion as in the case of Fig. 3.21b and again the areas exhibiting the highest temperatures are arranged around the mounting points. Also in this case a modification occurs, i.e. the mean radius clearly remains at low temperature levels (C4). The cold gap in this configuration can be explained on the basis of wear of the pads. The disk deforms during heating. On the one hand this deformation appears as coning and on the other hand as a warping of the friction surface. Since the surface deforms and pad type 2 is rigid the contact pressure varies along the radius with a maximum at r_{mean} . The mean radius sticks out due to the warping and the pad wears down in this region during the first few brakings. For the largest part of the pad life, the contact pressure is higher at a greater distance from r_{mean} . This is obvious from the wear pattern on the disk after 100 emergency stops, which exhibits two valleys on both sides of r_{mean} , while the area along the mean radius is less worn. In the case of C2 and C4 the influence of wear is explicable but the situation is not clear for C1 and C3. In C4 each hot patch is split into a hot area above and a hot area below the hole due to the formation of a wear pattern on the pad (and subsequently on the disk). These areas in turn may be split into two areas positioned slightly to the left and the right of the hole, which can be related to global waviness due to the temperature field and plastic deformation. In Fig. 3.21j another clear inversion is obtained and the question arises whether this periodic inversion continues or one of the patterns stabilizes. Unfortunately, the recordings stop with braking number 10 and continue later on in the scope of pad replacement. At least in this context the continuation can be discussed in Section 3.4.4.

3. CHARACTERIZATION OF LOADING CONDITIONS

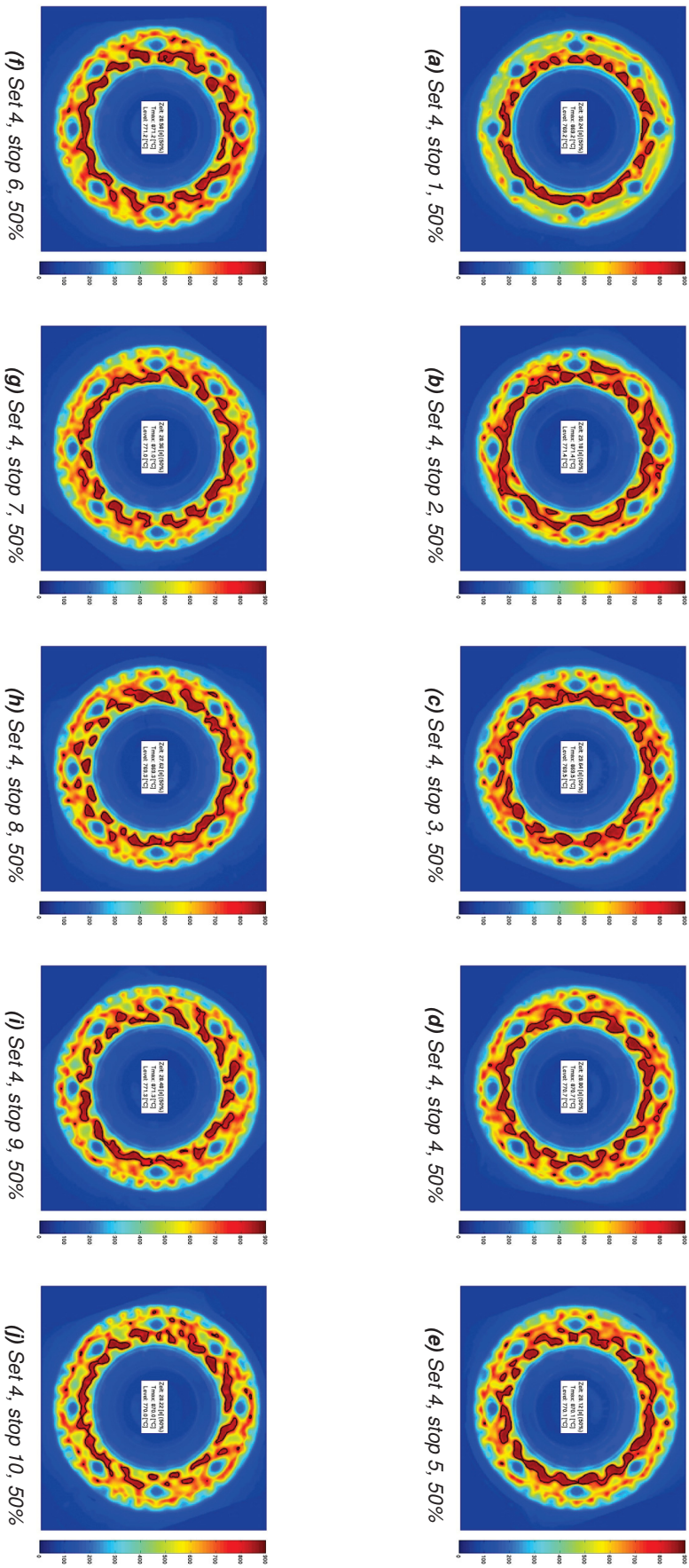


Figure 3.20: Thermal distribution for pad type 1 over 10 consecutive brake cycles. Reference time: 50% of brake time. On a global scale the thermal distribution from (b) to (j) are similar with increased thermal loading on the inner disk half. During the first emergency stop, however, the thermal input is clearly more intense on the inside.

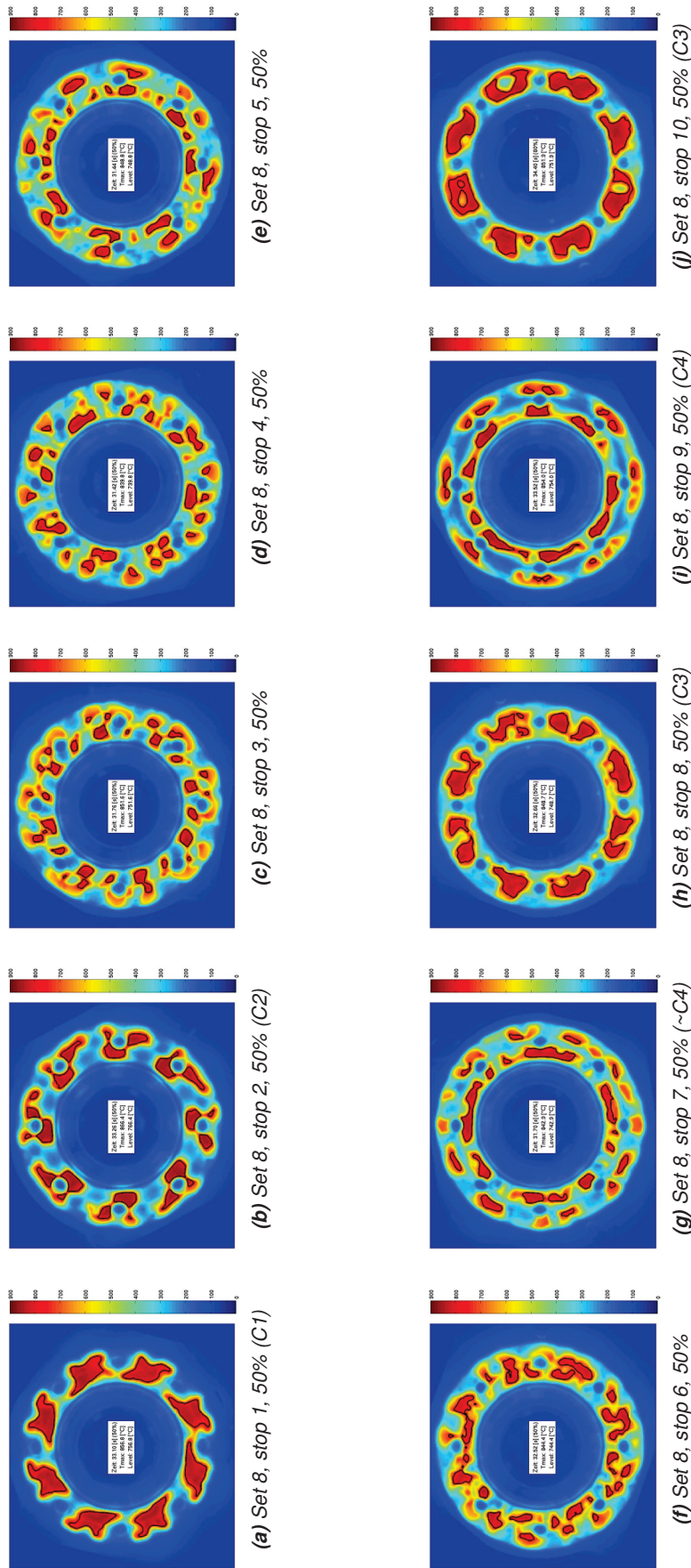


Figure 3.21: Thermal distribution for pad type 2 over 10 consecutive brake cycles. Reference time: 50% of brake time (this value differs for braking 10 due to abortion of the test). The series of thermal images reveals significant changes in the thermal distribution, which do not stabilize within 10 brake applications. Images a) and b) form a couple of inverted thermal images. After several mixed states in c) to g) the periodic inversion reappears in modified form, h)-j). The designation in brackets refers to the type of thermal configuration.

3.4.3 Reproducibility of thermal patterns

At first the reproducibility is discussed for pad type 1. Fig. 3.23 compares brakings 9 and 10, from test run 3, to the corresponding stops, from test run 4. The three images on the left show the temperature field at 10% of the total brake time (Fig. 3.23a is not available but indicated for completeness). At this stage, all three distributions are nearly identical from a global point of view, with local differences as the numbers and precise positions of the gradients on hot bands. The situation at 50% brake time is similar. In general the four thermal distributions correspond well to each other and show similar hot clusters. They are situated, for the greatest parts, on the inner disk half. On a local level the individual clusters differ in size and precise position. The thermal distribution reaches a stabilized state very fast in two independent test runs, but in view of damage accumulation it is still necessary to take multiple cycles into account, since the positions with the highest loading move on a local level with each cycle.

Fig. 3.24 depicts the corresponding data for pad type 2, viz. braking 9 and 10 from runs 7 and 8. Section 3.4.2 treated in detail the phenomenon of thermal inversion occurring in test run 8. At 10% of the brake time this inversion is not visible, but an obvious change of the contact conditions can be seen. This happens both in run 7 and 8 with a surprising accordance between the corresponding images. At this stage the reproducibility of the thermal patterns is certainly given. At the first glance this is also the case at 50% brake time, but at a second glance further discussion is required. The basic type of thermal gradients matches between run 7 and 8 and an inversion occurs in a similar manner. Nevertheless, after a closer look some differences are visible. As already mentioned in Section 3.4.1, 8 patches on the inner half are observed in braking number 10 of run 7, with one exception where the patch is split into three sub-patches. In Fig. 3.24g the situation seems to be similar but more complex. In contrast to Fig. 3.24c, three large patches are positioned directly below a hole, not in between them. Taking a look at the mounting positions it becomes evident that each patch situated below a hole has the tendency to break up into two parts, each moving further either to the left or to the right. This might lead to the situation that two patch halves from adjacent holes meet between the holes and tend to form a uniform patch, as seen in Fig. 3.24c. On the outer disk half a similar tendency is observed. The standard configuration seems to be a hot patch above each hole but each patch tends to split in two halves moving slightly to the sides. In this case 16 patches along the outer perimeter would result as was the case in Fig. 3.24c. In Fig. 3.24g, however these patches are clearly centered around the holes, while in Fig. 3.24c they appear more or less alternating at a hole and between holes. As the bottom line it can be said that differences occur between Figures 3.24c and 3.24g, but these are very systematic and conform. Looking at Fig. 3.21 and the occurring significant changes on the whole, the two patterns seem to be very close to each other. Brakings 10 in both runs correspond well to the first emergency stop shown in Fig. 3.21a, with the additional tendency that at some positions the patches are split in half by a cold stripe. This tendency is stronger in Fig. 3.24d than in Fig. 3.24h. After this discussion the reproducibility can be regarded as satisfactory.

For pad type 2 another comparison is possible, i.e. for the first emergency stop in run 6 and 8. At 10% brake time the thermal loading is concentrated at the 8 center positions for both brakings but the distribution is much more homogeneous in Fig. 3.22a. This indicates that the initial flatness of the disk and the pads as well as previous loading history consisting of the bedding-in process has some impact on the first emergency stop. At 50% brake time 8 homogeneous patches appear in both cases and the only apparent difference is the shape of these patches. In Fig. 3.22b they are more or less rectangular, while in

Fig. 3.22d the patches are more rhomboid. Nevertheless, the same type of thermal gradients is obtained in both cases and they are thus reproducible.

In conclusion, all the thermal patterns discussed in this section are reproducible with some deviations that must naturally be expected.

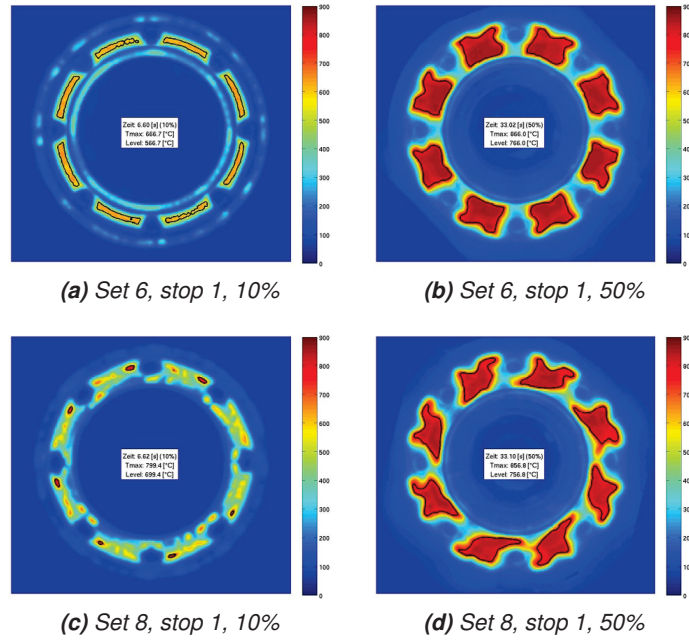


Figure 3.22: Comparison of thermal patterns of the first braking of test runs 6 and 8 (pad type 2).

3. CHARACTERIZATION OF LOADING CONDITIONS

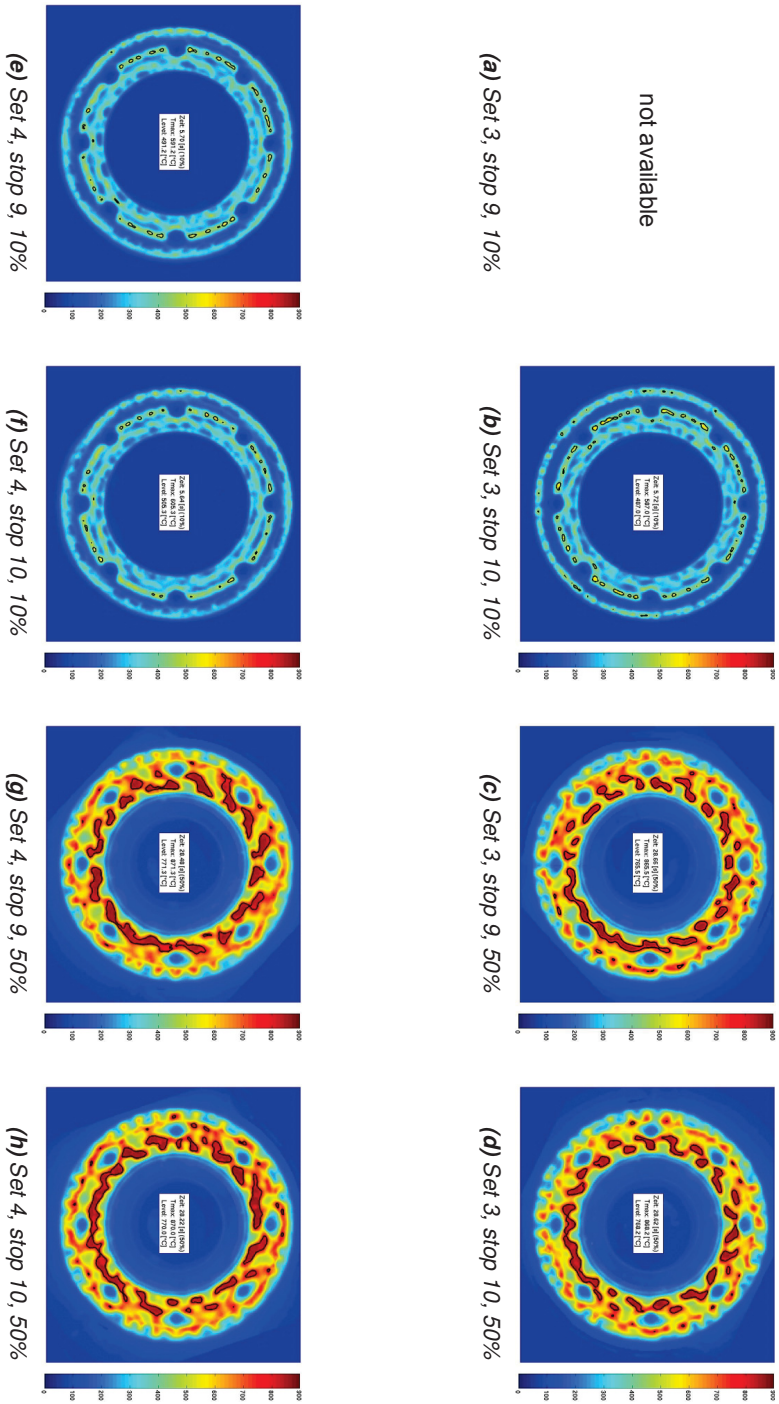


Figure 3.23: Comparison of thermal patterns of brakings 9 and 10 of test runs 3 and 4 (pad type 1).

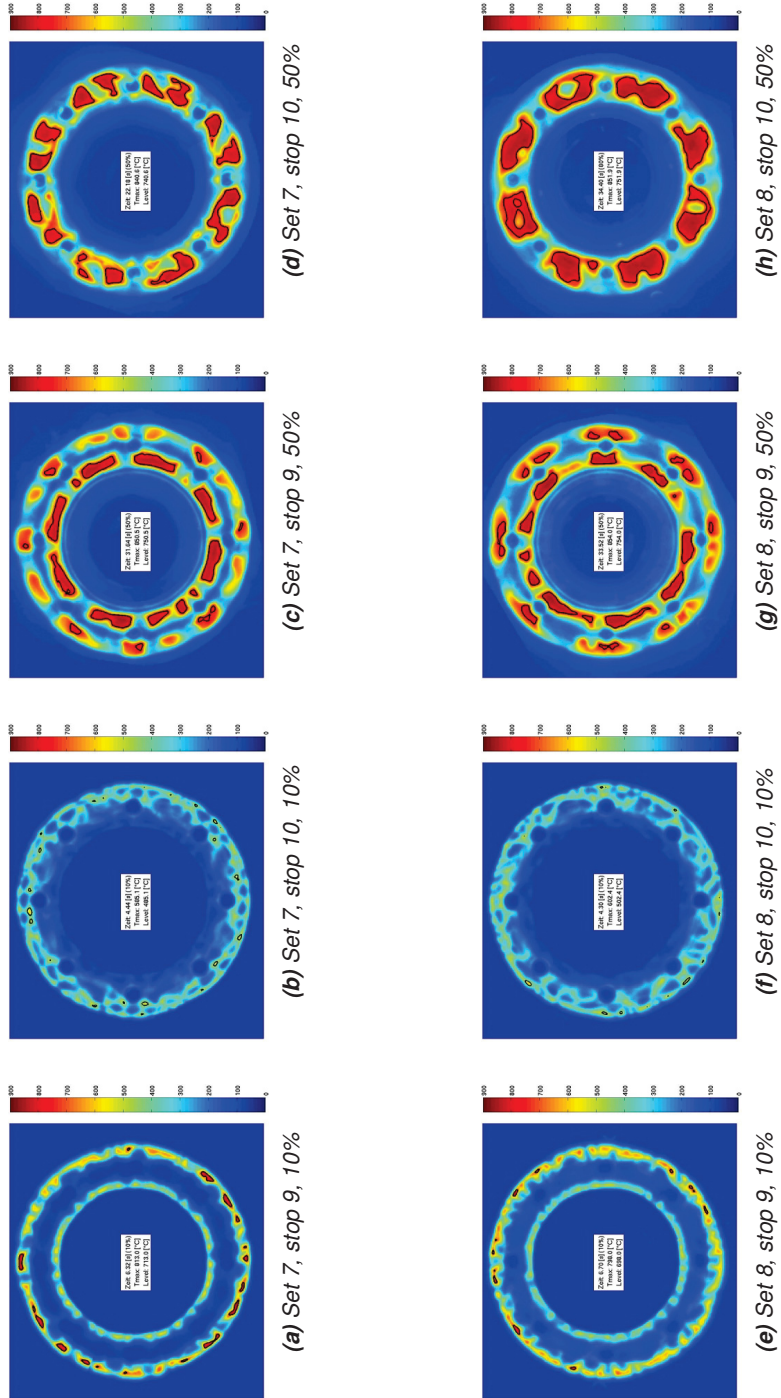


Figure 3.24: Comparison of thermal patterns of brakings 9 and 10 of test runs 7 and 8 (pad type 2).

3. CHARACTERIZATION OF LOADING CONDITIONS

3.4.4 Impact of pad replacement

Up to this point all brakings of a test run have been performed with the set of pads that was mounted at the beginning of each test run and the influence of pad replacement on resulting thermal distribution has not been considered. This topic will be investigated in the following again starting with pad type 1. In test run 4 the pads have been replaced every 50 emergency stops and the temperature evolutions in the adjacent brakings have been recorded. The two columns with thermal images on the left half of Fig. 3.26 display the temperature fields at 50% brake time before and directly after pad replacement after braking 50, 100 and 150. In all three cases the temperature level increases after pad replacement and the focus on the inner disk half seems to be amplified. The two columns to the right show the corresponding cumulative patterns, which consistently indicate a higher temperature level when new pads are applied. Not only one, but three to four brake cycles were recorded after replacement and the elevated temperature level is observable in all of them. Apparently a change in the contact conditions occurs, which is maintained for a greater number of brake cycles. At the beginning of test run 4 only the first braking yields a temperature distribution differing from the next ones. It should be noted, however, that a bedding-in procedure was applied before the test run was started. This was not the case when new pads were applied during the test run. The increased temperature level may thus be related to a bedding-in process that would be finished much faster in the case of high energy stops (25 MJ) compared to the normal low energy brakings (100 stops with 5 MJ). Nevertheless, more than 3 to 4 brakings seem to be required. The discussion can be continued from the point of view of brake time, as indicated in Fig. 3.25a, which clearly shows that the brake time decreases quickly during the brake cycles at the beginning of the test run, and it takes about 10 brakings until the minimal brake time is reached. Afterwards the brake time slowly approaches the initial value. A similar process occurs after each pad replacement, but shorter brake times are reached than during the initial 50 brakings. This accounts for the fact that the thermal level increases, since the same amount of kinetic energy is dissipated in shorter time. However, the different thermal distribution in the very first cycle compared to the subsequent ones cannot be explained on the basis of the brake time. As the only explanation the previous bedding-in procedure remains.

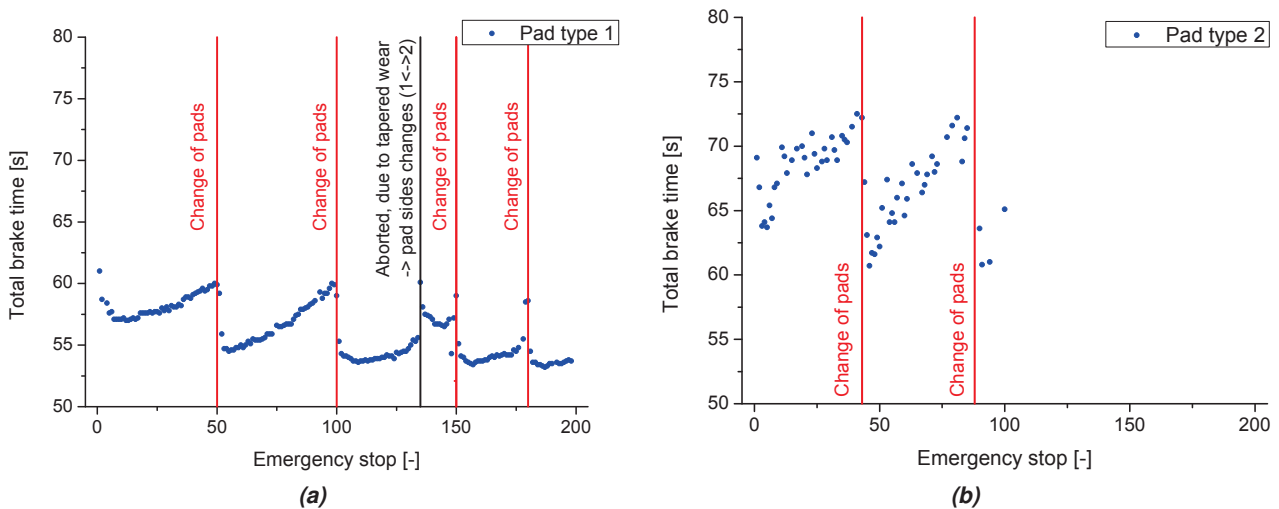


Figure 3.25: Evolution of total brake time for a) pad type 1 and b) pad type 2.

Fig. 3.27 shows a sequence of brakings after the only pad replacement that was recorded for pad type 2. The previous cycle was not recorded. The sequence reveals that the phenomenon of alternating inversions of the thermal distribution discussed in Section 3.4.2 still takes place during later brakings in the test run. The inversions consistently occur upon each braking, i.e. all the previously discussed observations still apply. It remains unclear, however, whether this process is reinitiated by the pad replacement or taking place over the whole sequence of brakings, independent from the use of new pads. Regarding this problem from the point of view of damage accumulation, which is a substantial issue treated in Chapter 5, a series of several brake cycles should be taken into account in order to obtain a representative result.

Fig. 3.25 shows that also in the case of the second pad type replacements greatly affect the total brake time. The brake time drops fast and increases slowly, but this time an obvious level of scatter occurs in the brake times, which is likely related to the inversion phenomenon.

Finally it should be considered that the emissivity might change during the bedding-in, but in this study it is not possible to quantify the impact on the recorded temperatures. The overall picture, however, is still consistent.

3. CHARACTERIZATION OF LOADING CONDITIONS

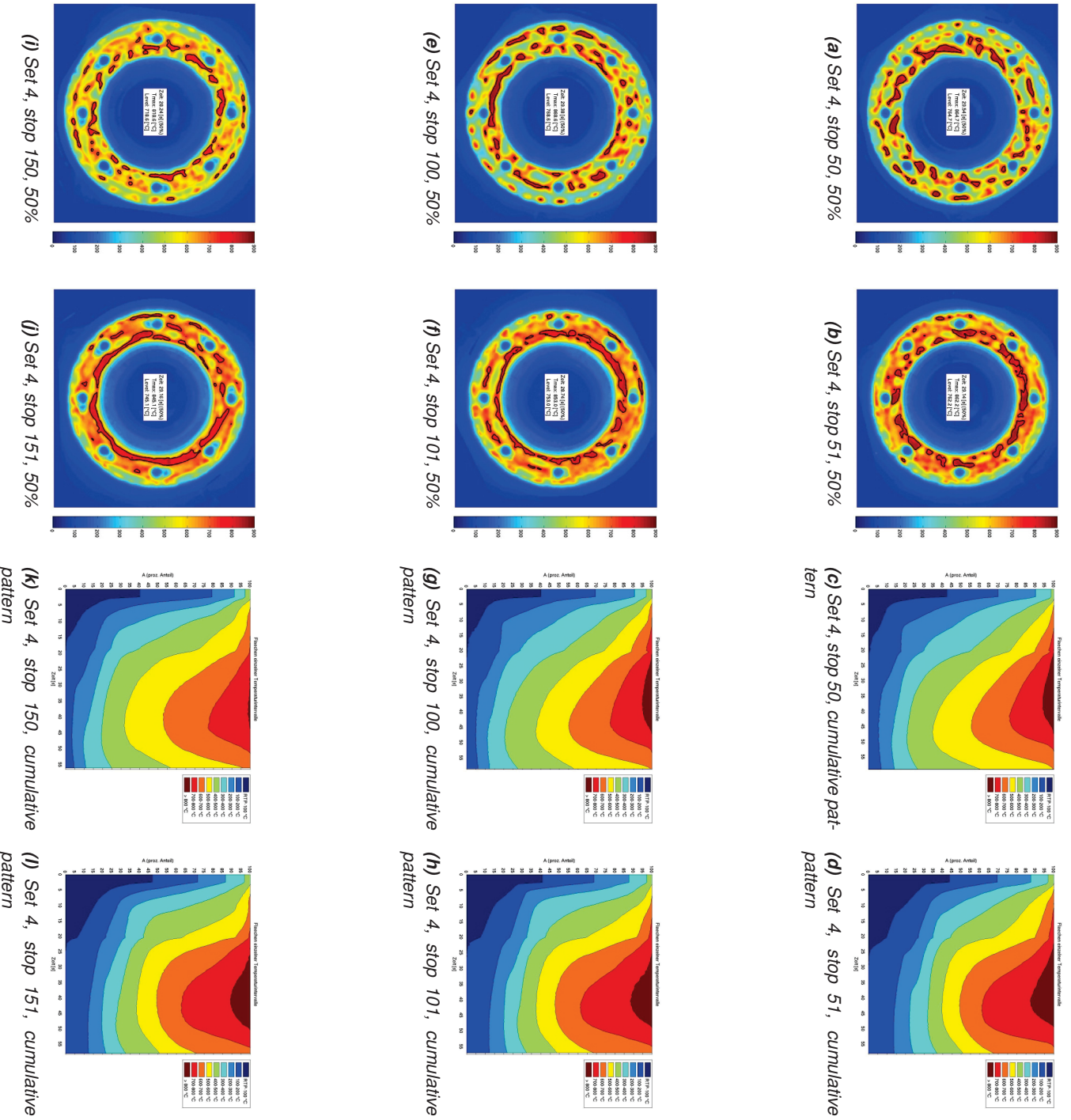


Figure 3.26: Comparison of thermal images and sum diagrams for the brake applications before and after pad replacement.

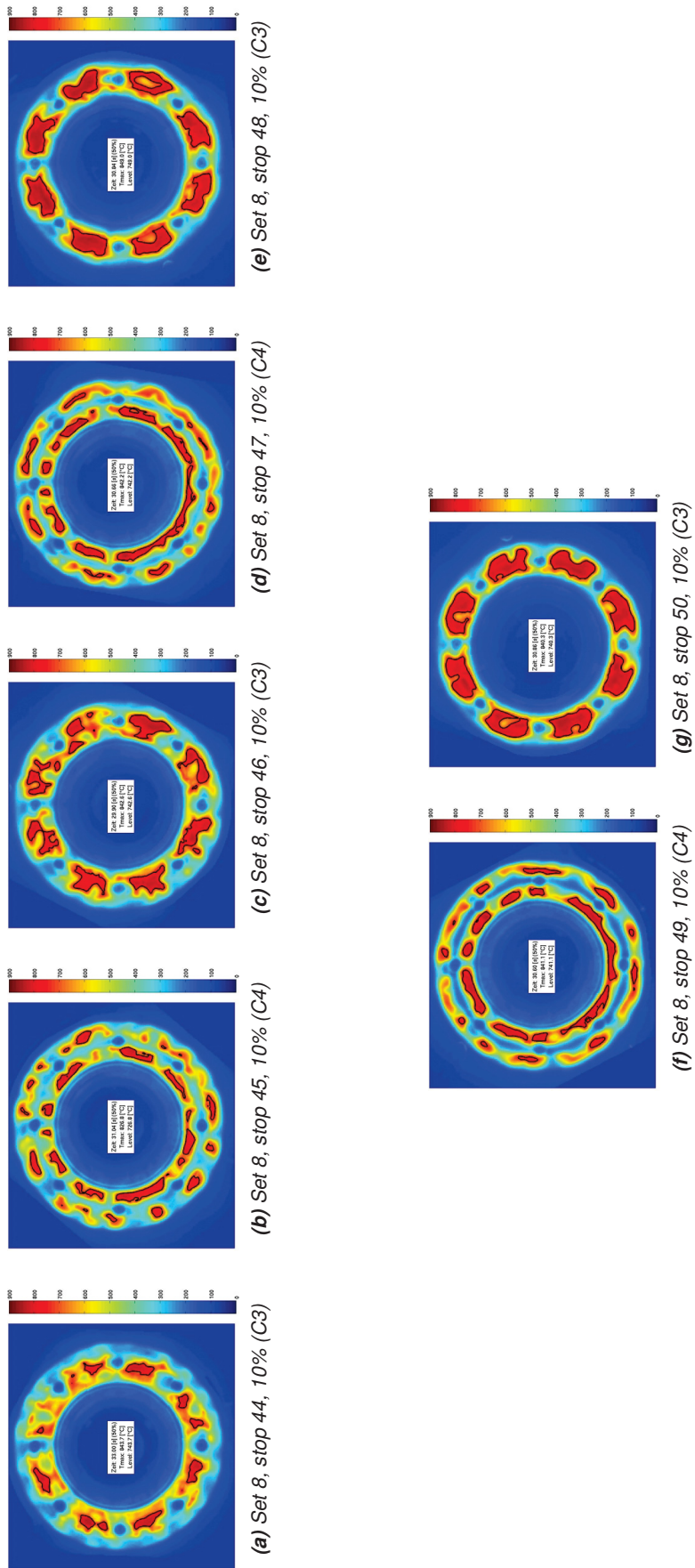


Figure 3.27: Comparison of thermal patterns of brakings 44 to 50 of test run 8. The designation in brackets refers to the type of thermal configuration.

3. CHARACTERIZATION OF LOADING CONDITIONS

3.4.5 Thermal distribution in tests carried out on scaled test rig

In addition to the experiments on the 1:1 test rig, two tests have been carried out on a scaled test rig (1:4). The rationale behind these tests is to investigate the comparability of results between the two systems in order to be able to carry out further testing on the smaller test rig. Given the fact that testing on a smaller scale is less costly and more efficient from the point of view of available test time, this method would provide a powerful means to speed up testing procedures. At least if the comparability is sufficient for the specific investigation.

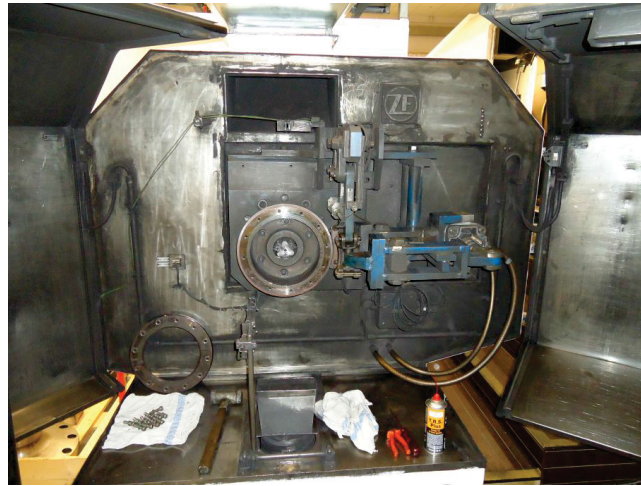


Figure 3.28: Scaled test rig.

Fig. 3.28 provides an overview of the scaled test rig including the test geometry, which is mounted at the center. The used disk geometry for this study is 460 mm in diameter, but in contrast to the mounted disk in Fig. 3.28, manufactured without holes. Furthermore, this test configuration is based on symmetric braking, viz. test conditions applying for axle mounted disks. As brake lining several pins from pad type 1 are used leading to a total pad area of 45.24 cm^2 . The flywheel mounted in the scaled test rig corresponds to an inertia of 80 kgm^2 . The braking force and the motor torque are set to 4kN and 700 Nm, respectively. The test parameters are summarized in Table 3.2. All data apart from those for the flywheel are average values since they are subjected to fluctuations.

Table 3.2: Test parameters for scaled test rig and material A

| Braking force | Flywheel | Brake torque | Specific power |
|---------------|------------------|--------------|--------------------------|
| [N] | $[\text{kgm}^2]$ | [Nm] | $[\text{W}/\text{mm}^2]$ |
| 4000 | 80 | 700 | 29 |

The exact conversion rules from full scale to reduced scale are not available to the author. The industrial partner carrying out the test has developed procedures for testing at reduced scale, which have been applied for this study. One major criterion in this procedure is to obtain comparable temperature levels on

both scales. The braking mass and the top speed on the scaled test rig are limited compared to the full scale test rig. For this reason it is not possible to obtain the same temperature levels after one severe brake application. Therefore another strategy has been chosen. Instead of one brake application corresponding to an emergency stop on the 1:1 test rig, a series of two consecutive brakings is carried out. The whole test sequence consists of 200 double stops.

In accordance with the previous sections, individual brake events have been recorded by a thermal imaging system in the form of consecutive frames. For the analysis of the results, the relevant time frame is divided in 10 intervals and images are extracted in steps corresponding to 10% of the overall brake time — in this case two brake applications. Since this study only aims at a coarse investigation without subsequent simulation activities, the data are only converted to temperatures but not processed any further. The angular position of the temperature field thus changes from image to image. The thermal evolution during a typical braking is not shown, instead its evolution over the whole test sequence is directly plotted in Figures 3.29 and 3.30 for two characteristic points in brake time. Fig. 3.29 illustrates the evolution at 20% of the overall brake time. Local temperature variations are indicated right from the beginning. It takes several load cycles, however, until the formation of 9 hot spots becomes really obvious. This point is reached around cycle number 7 (stops 13 and 14, Fig. 3.29e). From then on the situation stays rather stable until a quarter of the test is over (Fig. 3.29h). In the subsequent image (Fig. 3.29i) the hot spots appear to be more focused and this state increases till the end of the test.

The corresponding discussion can be carried out from a different point of view, i.e. a different point in time. Fig. 3.30 shows the thermal distribution at 80% of the overall brake time. During the first brake cycle (Fig. 3.29a) no thermal gradients are visible apart from elevated temperatures along the mean radius. This distribution is normal for uniform thermal loading because at the sides of the disk more thermal energy can be emitted by convection than at the center. In contrast to the preceding discussion formation of hot spots becomes clearly evident in the third brake cycle, i.e. at an earlier stage. In accordance to the situation at 20% of the brake time, this thermal distribution stays rather stable during the first quarter of the test sequence. From then on a further increase of thermal concentration in the area of 9 hot spots is evident. In Fig. 3.29j a very strong difference in the temperature level at the hot spots and the adjacent areas is visible. At this point a result from the damage analysis discussed in Chapter 4 will be anticipated: The hot spots are stationary since the occurrence of metallurgical transformations is limited to specific regions on the disk. This is further supported by the fact that the hot spots appear very early (10%) during braking, indicating that non-uniform contact conditions are established immediately. Combining this fact with the previous discussion leads to the conclusion that the mechanism based on progressive waviness distortion presented by Panier et al. in [59] fits well for the greatest parts to the present case. In contrast to the wheel mounted disk type discussed earlier, symmetric braking conditions apply, as for TGV brake disks discussed in [59]. The authors show that in the case of an asymmetric disk/hub system a temperature moment $M_T \neq 0$ is present causing a wavy axial displacement around the contact region with the pad yielding two maxima in the axial deformation. If plastic deformation occurs, the number of maxima increases and reaches a stabilized state since cyclic plastic deformation continues to occur, but always at the same positions. The number obtained in [59] is 6 in contrast to 9 in this study. As mentioned by Panier, the number of macroscopic hot spots depends on the ratio of mean disc circumference and pad length,

3. CHARACTERIZATION OF LOADING CONDITIONS

since the pad must have sufficient contact in order to maintain kinematic contact as outlined in [57]. The minimum requirement is that the pad length contains a full sinusoid, thus determining the number of hot spots. A number of 9 hot spots was also obtained in the study conducted by Kasem et al. [149] for high energy levels.

Whether the initial perturbation by the temperature moment is exactly as described by Panier cannot be verified in this study. It can be said, however, that a wavy axial deformation is introduced in the system and that the deformation reaches a stabilized state by plastic deformation. On the basis of the individual thermal images in Fig. 3.30 this stabilization is abrupt and takes only one brake cycle. The cyclic plastic deformation in the subsequent brake applications further contributes to the stabilization of the thermal distributions and the hot spots become more focused. This process is more evident from Fig. 3.29, illustrating the thermal distributions at an early point of the brakings. The temperature level is thus lower and thermal gradients appear with a different contrast. In this sequence the process of stabilization is on the one hand an abrupt process as well — although more than one cycle is required for the hot spots to build up — but on the other hand a further stabilization occurs in the form of a continuous process taking place from the beginning to the end.

3. CHARACTERIZATION OF LOADING CONDITIONS

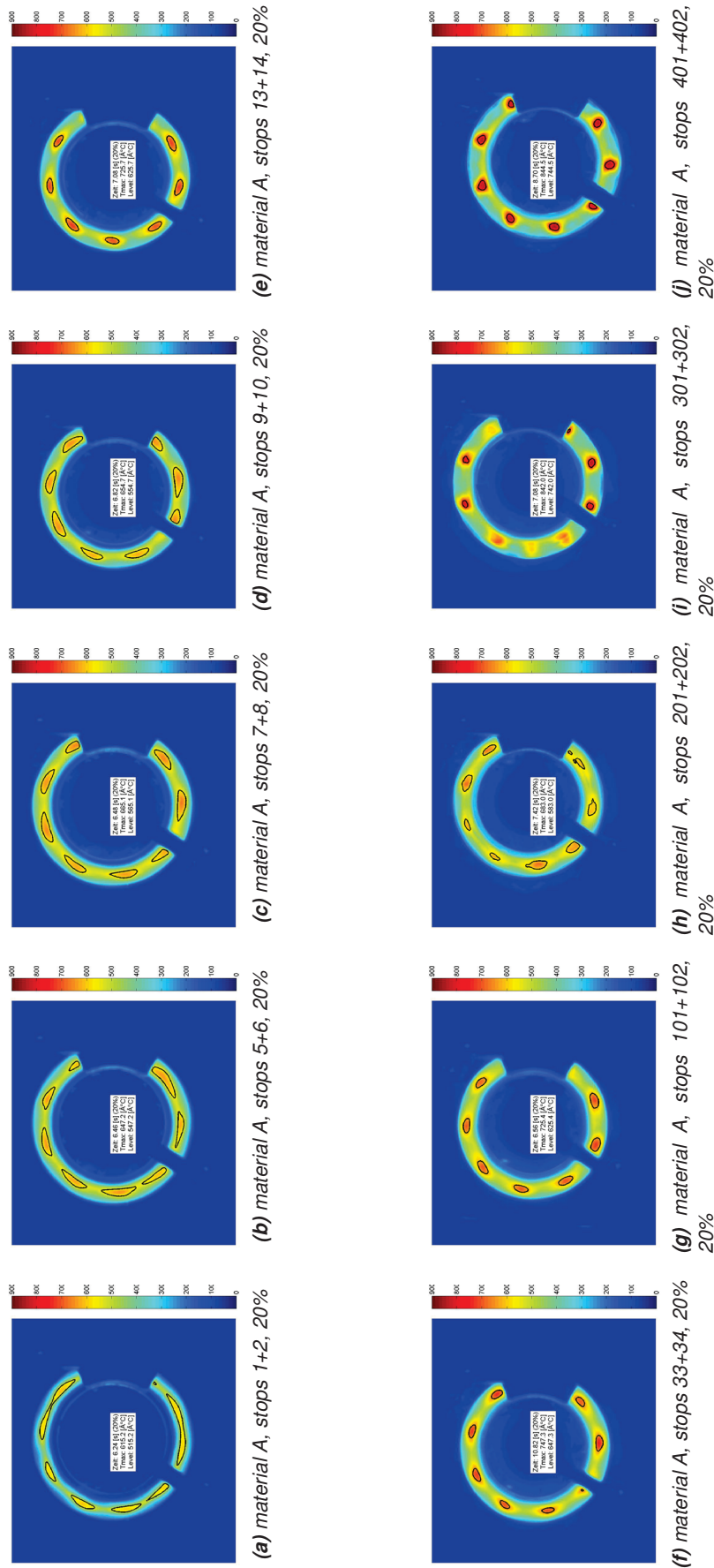


Figure 3.29: Evolution of the thermal distribution on scaled test rig over 201 double stops for material A. The images of the series correspond to the thermal distribution at 20% of the total brake time for each double stop. The series shows the formation of 9 hot spots situated along the disk circumference. At the beginning of the test sequence (3.29a) the formation of an inhomogeneous thermal distribution is indicated but the hot spot formation is clearly pronounced beginning with 3.29e. The maximal thermal concentration at the hot spots is reached during the final 100 double stops 3.29i-3.29j.

3. CHARACTERIZATION OF LOADING CONDITIONS

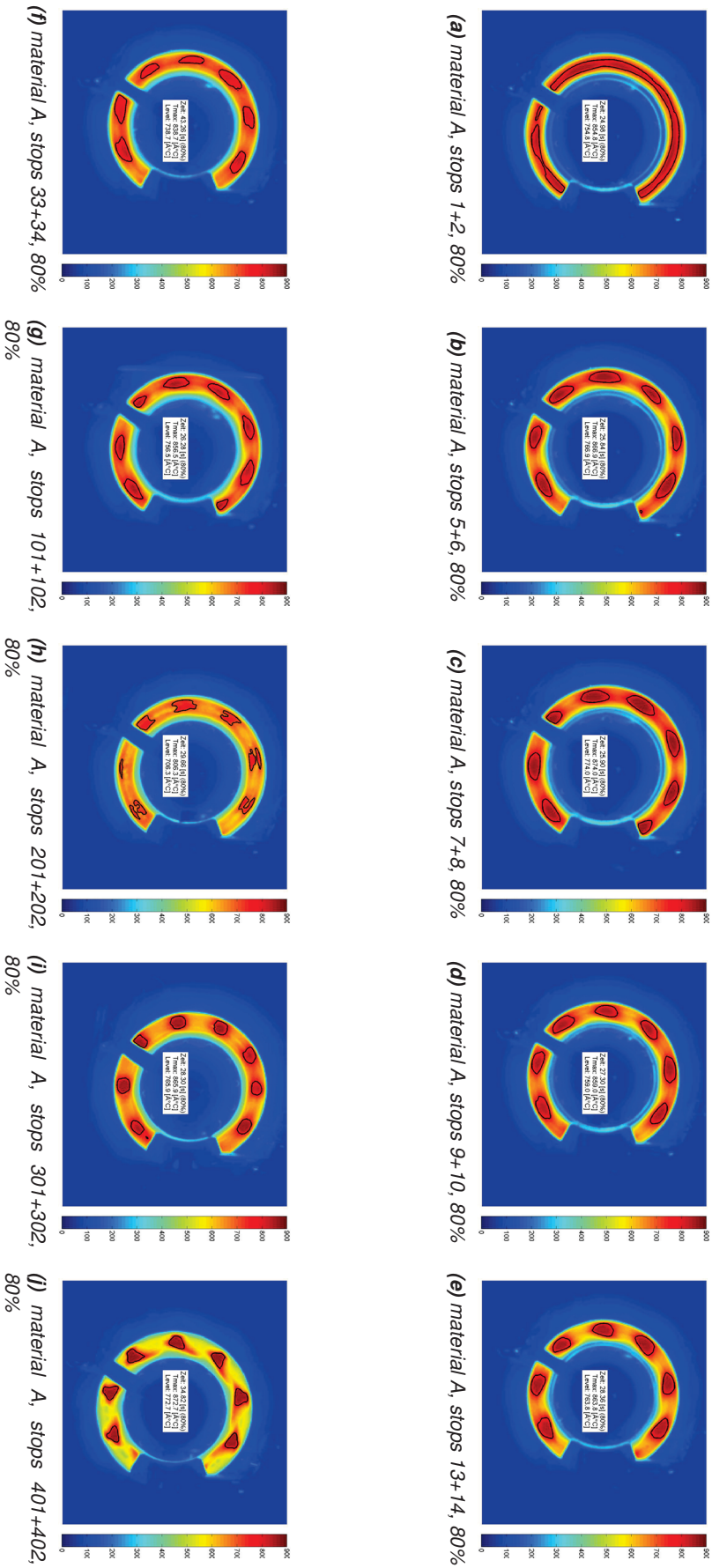


Figure 3.30: Evolution of thermal distribution on the scaled test rig over 201 double stops for material A. The images of the series correspond to the thermal distribution at 80% of the total brake time for each double stop. The series shows the formation of 9 hot spots situated along the disk circumference. At the beginning of the test sequence (3.30a) no severe thermal surface gradients can be seen apart from an usual elevated temperature level along the disk center. Beginning with the third double stop 3.29b the formation is clearly visible. The thermal concentration at the hot spots increases over the test sequence and reaches a clear maximum state at the end 4.38a.

3. CHARACTERIZATION OF LOADING CONDITIONS

A second material was investigated on the scaled test rig in this study. The second material — material B — is a ductile cast iron meant for less severe loading conditions. Besides a different pad type, a lower brake torque was thus applied for the testing procedure. The parameters are summarized in Table 3.3 again referring to average values. Fig. 3.31 illustrates the thermal distributions during selected brake cycles at 80% of the brake time. In contrast to the previous test sequence for material A, no thermal surface gradients appear, apart from the usual higher temperature level along the mean radius. Beside the different brake lining the lower brake torque and thus lower dissipated energy is the main difference to the previous case. Again this correlates with findings in the literature [80] where the occurrence of macroscopic hot spots is linked to a certain level of dissipated energy in sufficiently short time. Similarly to the present case it has been observed that for the same initial speed and mass hot spots only appear above a certain level of dissipated energy.

Table 3.3: Test parameters for scaled test rig and material A

| Braking force | Flywheel | Brake torque | Specific power |
|---------------|-------------|--------------|----------------|
| [N] | [kgm^2] | [Nm] | [W/mm^2] |
| 4000 | 80 | 575 | 10 |

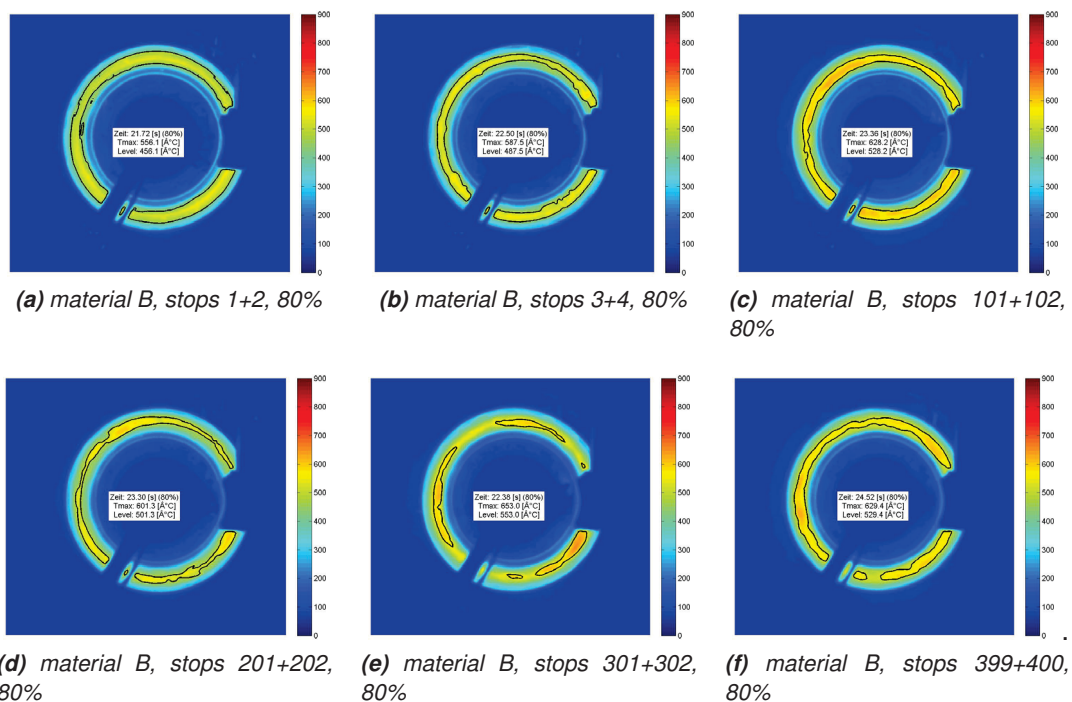


Figure 3.31: Evolution of thermal distribution on the scaled test rig over 200 double stops for material B. The images of the series correspond to the thermal distribution at 80% of the total brake time for each double stop. In the case of material B which was exposed to less severe loading conditions no thermal surface gradient are visible apart from the usual elevated temperature levels at the disk center.

3. CHARACTERIZATION OF LOADING CONDITIONS

As far as the thermal distributions on the friction surface are concerned, the results from the full scale test rig and the scaled rig significantly differ. While the results for the wheel mounted brake disks are rather unique, the patterns found on the test geometry conform to the literature. Usually, the first reaction to the differing results would be to check the assumptions made for the test on the reduced scale. As outlined in [79; 145] there are principal rules of similitude as described by Eq. (3.12) concerning parameters for the design of the scaled rig. The similitude factor k links the governing quantities between the two scales: The dissipated energy Q/q , the disk friction area S_d/s_d and the pad friction area S_p/s_p .

$$k = \frac{Q}{q} = \frac{S_p}{s_p} = \frac{S_d}{s_d} \quad (3.12)$$

In general it is not possible to establish similitude according to Eq. (3.12) alone because satisfying all ratios given by the similitude factor during the design of a scaled test rig is not feasible. Further considerations are necessary concerning the test parameters. In [79] Desplanques and coworkers provide a discussion of a test parametric triplet factor linking the initial speed, the braking force and the brake duration between the two scales leading to comparable results. The rules of similitude, however, also include the type of contact and consequently the principal reason for the differing results is the difference in the loading conditions, which are asymmetric in the case of the wheel mounted brake disks and symmetric for the test geometry. Given this fact, similitude between the loading conditions would have to be established first before going on to further considerations as previously noted, at least as far as wheel mounted brake disks are concerned. Nevertheless, for low and intermediate energy levels, when the thermal distribution is homogeneous, the scaled test rig can be used for wear tests. A comparison of various combinations of disk and pad material are possible, at least when test conditions at intermediate energy levels also correspond to service conditions. From the point of view of hot spot formation, however, the two scales are not comparable given the applied test configurations. The discussion will be continued in Chapter 4 from the point of view of damage.

3.4.6 Discussion of the thermal gradients in view of TMF

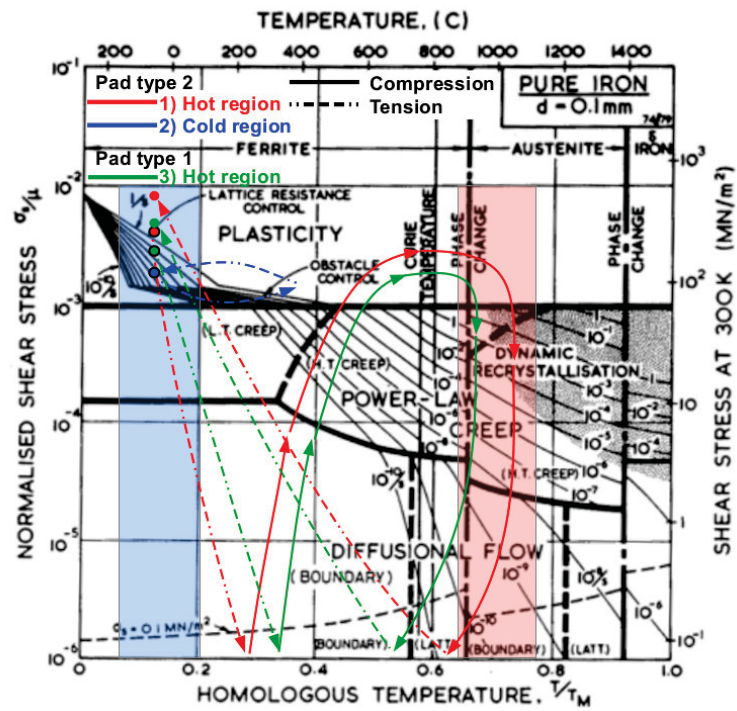
The discussion points to a major aspect for thermomechanical (TMF) life, which is now apparent from the cumulative patterns and the thermal images: The way how the thermal energy is introduced into the disk, i.e. which thermal patterns appear and how homogeneously the disk surface is heated up. Although thermal surface gradients are clearly present in Fig. 3.17 the temperature field caused by pad type 1 is by far more homogeneous as the one entailed by pad type 2. Fig. 3.18 reveals large hot areas in direct vicinity to large cold areas. The thermal heat input is not at all homogeneous causing severe thermal gradients in thickness direction as well as in the plane of the disk surface. Since thermal gradients are ensued by stresses, plastic yielding in various directions is more likely and more severe in the case of pad type 2. From this discussion three important assessment criteria can be identified that must be taken into account for the assessment of thermal images in view of the disk loading:

1. The maximal thermal level, because the mechanical strength properties decrease with increasing temperature.
2. The time elapsed to reach high thermal levels, since this determines the local stress level and thus the severity of the loading conditions.

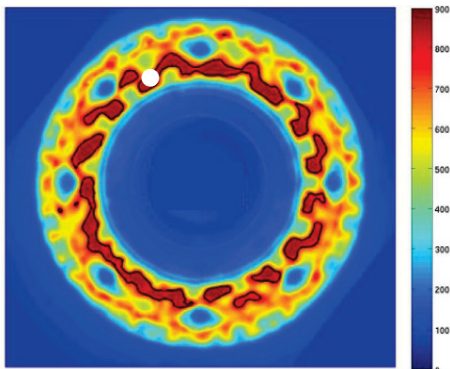
3. The homogeneity of the thermal distribution on the friction surface, since homogeneity ensures that no additional effects occur that are detrimental to the disk.

The main focus of this work is the development of methods for the service life evaluation of brake disks. The discussion in this section sheds some light on one paramount aspect in this context, i.e. the thermal loading conditions. A link to further aspects, such as stress levels and the deformation behavior, is still unclear. With the aid of the information given in Chapter 2 it is possible to establish some of those links, at this point in a qualitative way, without the information from the subsequent chapters on damage analyses and simulation techniques. Based on the preceding discussion, the different loading conditions in hot and cold regions on a disk surface during braking can be qualitatively represented in an Ashby map, as depicted in Fig. 3.32a. Fig. 3.32b and Fig. 3.32c show two thermal distributions, one for pad type 1 and pad type 2. Both of them will be discussed in more detail in Section 3.4.2 and serve only as illustrative examples in this discussion. For pad type 1 a reference position is indicated at the inner disk half, where the highest temperatures occur for this pad type. For pad type 2 two reference positions are indicated, one in a distinctly hot area and one at a distinctly cold area. The discussion of the σ - T evolution at the three positions is supposed to link the three assessment criteria noted above for a qualitative evaluation of thermal images to physical mechanisms relevant for fatigue. Fig. 3.32a depicts an Ashby map for pure iron, which suffices for the purpose of this discussion. Furthermore, it contains the qualitative σ - T paths for the three reference positions. It is assumed that each disk has already been exposed to several brake cycles. For this reason, the starting point in all three cases is a certain level of tensile residual stresses. The reason for these stresses is outlined in Section 1.3. For the cold patch it is assumed that the loading conditions in some of the previous brake cycles have been significantly higher, leading to higher residual stresses than at the other positions. Ashby maps do not take into account hardening and the normalized yield stress is plotted as horizontal line. However, hardening is an important aspect in TMF loading. This is why the beginning and the end of the σ - T paths are qualitatively located above σ_y . The yield stress after several brake cycles is higher than at the beginning. For pad type 2 a significant difference occurs between the hot and the cold patch. In the case of the hot patch, the σ - T path (1) exhibits a fast and significant input of thermal energy causing severe thermal expansion as well as large temperature gradients in thickness direction. Consequently, the stress level decreases rapidly and changes from tension to compression. The compressive stress level increases along with the temperature and the σ - T path reaches areas where viscoplastic deformation is clearly indicated. Furthermore, the temperature reaches the austenitic region and a metallurgical transformation occurs. How much austenite forms depends both on the temperature level and on the dwell time. Whether there is a partial or complete phase transformation is not known at this point but transformation during heating and consequently during cooling are indicated. After a section that corresponds to a dwell time with stress relaxation — and probably phase transformations — the temperature decreases and the compressive stress changes back to the tensile regime. Finally, a tensile stress level higher than at the beginning is obtained, which is due to the unequal inelastic deformation under compression and tension. During the high temperature-compressive phase a significant amount of plastic deformation occurs, which is not completely compensated by inelastic deformation during cooling. This gives rise to additional tensile residual stresses after cooling. In the σ - T path, however, austenitization takes place followed by the formation of a hardened microstructure during cooling. The plastic deformation and the corresponding residual stresses are thus partially annihilated yielding lower stress levels. At

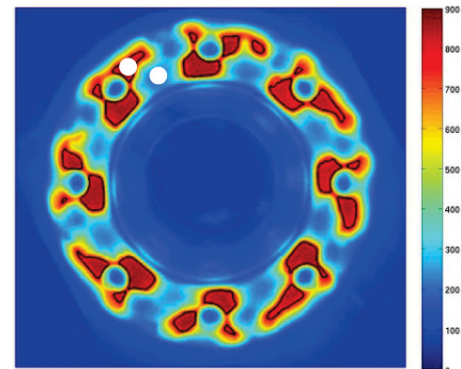
3. CHARACTERIZATION OF LOADING CONDITIONS



(a)



(b)



(c)

Figure 3.32: Qualitative illustration of temperature-stress paths at selected positions: a) Ashby map for pure iron (based on [15]), b) thermal image and reference position for pad type 1, c) thermal image and reference position for pad type 2.

this stage this influence is not considered in the σ - T evolutions in Fig. 3.32a and a proper discussion of the red and blue zone is left for Chapter 4. The critical evolution at the cold patch (2) stays in the tensile regime throughout the braking. The residual stress level originating from the precedent cycles is maintained and modulated by the increase in temperature, which is significantly lower than for (1). No phase transformations occur in the brake cycle but a microstructure altered in previous cycles is likely to prevail, which will be discussed in Chapter 4. The viscoplastic region is reached but due to the previous hardening and the low rates for dislocation creep, no significant inelastic deformation occurs. The start and the end point are thus coincident. If an influence from the surrounding regions occurs, however, the end point could be located at a higher or lower position. A detailed discussion is left for Chapter 5. The σ - T path for pad type 1 (3) resembles (1) but due to the more homogeneous thermal distribution, the σ - T

3. CHARACTERIZATION OF LOADING CONDITIONS

paths reveals less severe values for stress and temperature. In the case of pad type 1 the evolutions for the hot patch and a cold patch (not shown) yield situations between the two clearly differing σ - T path for pad type 2. This is due to the fact that the thermal distribution is more homogeneous than in the case of pad type 2.

3. CHARACTERIZATION OF LOADING CONDITIONS



Chapter 4

Characterization of damage

4.1 Introduction

The previous chapter dealt with the characterization of the thermal loading conditions of brake disks made of material A under emergency braking with two different pad types. This chapter will elaborate on the different forms of damage in the disks. In this context the term “damage” is not only used in the sense presented in Chapter 2, i.e. the density and the length of cracks. Damage is used in a wider sense including the mechanisms that eventually lead to crack initiation and propagation:

- The formation of residual stresses due to local inelastic deformation.
- Global disk deformation due to general plastic deformation at the friction surface.
- Phase transformations due to elevated temperature levels.
- The formation and growth of cracks as a result of the previous mechanisms.

The occurrence of inelastic deformation during TF/TMF loading has been discussed in detail in Section 2.3 and chapter 3, as well as its relation to residual stress formation. In [65] a preliminary investigation on damage in brake disks is presented. It is shown that damaging processes can be discussed on the basis of residual stress measurements (RSMs) and metallographic specimens. Furthermore, it was shown that in view of the residual stress level two competing mechanisms take place. On the one hand this is the formation of residual stresses due to plastification and the reduction of residual stresses due to annealing effects and phase transformations (subsequently abbreviated PT). The current work follows a corresponding strategy. The investigated disks, however, were subjected to higher levels of dissipated energy and the competition between plastification and PTs is expected to lead to a different picture.

4.2 Investigations and methods

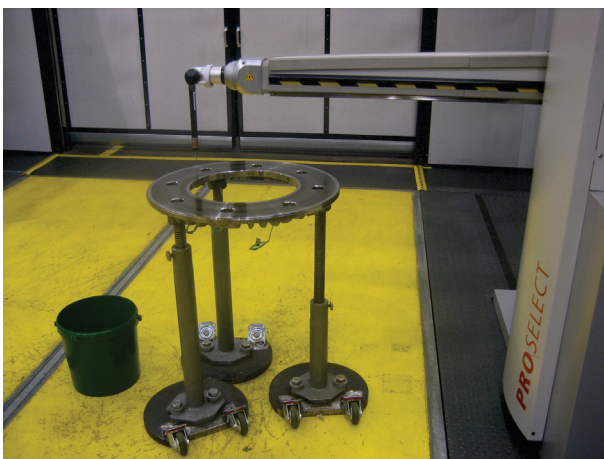
In accordance with [65], the friction surfaces of the investigated brake disks show discolored regions. They relate to areas of increased contact pressure in the previous cycle(s) and can be chosen as reference positions for the damage analysis. A summary of the applied methods is given below:

4. CHARACTERIZATION OF DAMAGE

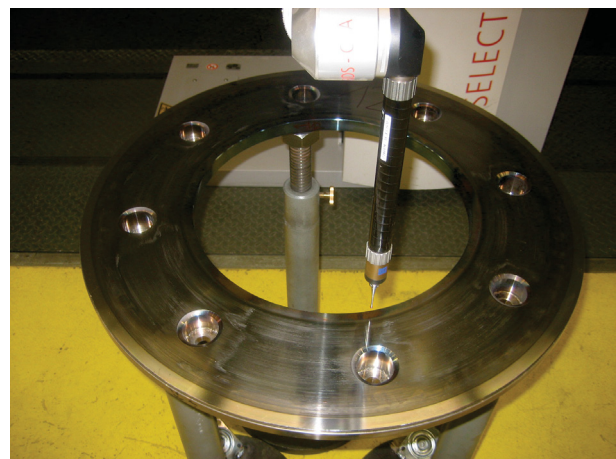
- A coordinate measurement machine (CMM) is used to characterize the axial deformation of the disks mentioned in Chapter 3. The CMM type is a Pro Select[®] horizontal-arm measuring machine manufactured by Zeiss.
- The stresses are measured by means of X-ray diffraction using $CrK\alpha$ radiation. At various positions the in-plane surface stresses are investigated and at characteristic positions in-depth residual stress profiles down to a depth of about 1.5 mm are measured. This is accomplished by a stepwise removal of material with the aid of electro-chemical polishing. The measurement system is a XStress 3000 G2 manufactured by Stresstech[®].
- Microstructural changes and fatigue cracking are investigated by means of different metallographic methods. For that reason several cross-sections are taken from the disk mentioned in Chapter 3. The samples are etched with an acid (Nital), in order to reveal the microstructure, and investigated with an optical microscope and a scanning electron microscope (SEM).

The measurement with a CMM was carried out at another location away from the test rig. Therefore both friction rings were unmounted and prepared for shipping after each test run. The obtained results thus correspond to residual deformation after removing the external force from the screws. After the CMM measurements the disks were brought to the laboratory at MCL¹ for further investigations. First, residual stresses were measured at characteristic positions on each friction ring. Second, the disks were coarsely separated by a water-jet cutting. Third, metallographic specimens were prepared for microscopic analysis by high-grade cutting, embedding in resin and etching with Nital. In a final step the samples were systematically investigated with an optical microscope.

4.2.1 Global disk deformation



(a)



(b)

Figure 4.1: a) Overview of configuration for coordinate measurements, b) close up of sensor.

¹Materials Center Leoben Forschung GmbH

4.2.1.1 Coordinate measurement machine

Fig. 4.1 depicts the measurement configuration. Because of the heavy loading during the test rig program a wavy deformation was anticipated. For the measurements it was thus essential to guarantee an even and stable position of the disks that prevents any sort of tilting during the measurement. This problem was resolved by positioning the disks one after another on a tripod, as shown in Fig. 4.1a. The measurement program was predefined according to the sketch in Fig. 4.2 based on the assumption that lower order oscillations as well as higher order oscillations occur along the circumference. The lower order ones correspond to the mounting points, while the ones of higher order may be caused by the cooling fins at the reverse side. However, it was not assumed that higher orders possibly caused by hot spotting can be measured by the applied method. In order to capture all possible stationary oscillations that are of interest a certain number of measurements are necessary, which is twice the highest order that should be detectable (Nyquist sampling criterion [150]). Thus, twice the number of the cooling fins was chosen for each investigation carried out along a specific radius. Consequently, 96 measurement positions were predefined along 4 selected radii close to the inner and the outer radius, each being either above a fins or between two fins. In an initial step a reference coordinate system was determined by the CMM for each friction ring. For this purpose the sensor, depicted in Fig. 4.1b, was manually guided to three mounting positions in order to determine the disk center and the orientation of the holes. Afterwards the CMM took over and determined the axial position of the points at the friction surface. This way, the reference plane was defined and the subsequently determined axial displacements were defined as normal to this plane.

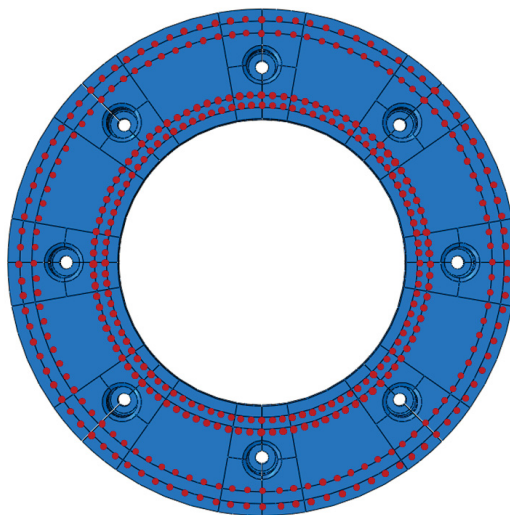


Figure 4.2: Illustration of the measurement positions at the inner and the outer perimeter.

4.2.1.2 Harmonic analysis

The collected data can be simply and efficiently analyzed by performing a harmonic analysis. The procedure is based on the assumption that an oscillating signal can be represented by a superposition of individual harmonic oscillations in the form of a *Fourier Series*. Hence, it represents an application of *Fourier Analysis* to oscillating signals, which in the current case is the discrete axial deformation measured along

4. CHARACTERIZATION OF DAMAGE

a specific radius. The term *Fourier Transform* (FT) refers to the generalization of the representation of periodic continuous functions by a Fourier series to non-periodic functions. In general, the technique is applied to transform signals from the time domain to the frequency domain and to display them in comprehensive plots. The *Discrete Fourier Transform* is the corresponding technique for discrete signals, i.e. data evenly sampled over a certain period. The results from the CCM can be seen as a discrete periodic signal and thus a simple Discrete Fourier Series (DFS) is sufficient for this study. As outlined in [151] a discrete and periodic signal can be represented by a periodic array $x[*]$, see Eq. (4.1).

$$x[n + N] = x[n] \quad (4.1)$$

The smallest N for Eq. (4.1) still to hold is called fundamental period N_0 . For common signals N_0 usually is the time period of the basic oscillation but in the present problem N_0 corresponds to 360° and a periodic continuation after 360° is assumed. For this reason, the basic oscillation corresponds to a sinusoidal wave along the circumference or, in other words, the axial deformation on the disk with the largest possible period. The base oscillation may be represented by Eq. (4.2), where Ω_0 refers to a periodic sequence with period N_0 . In contrast to a continuous signal where Eq. (4.2) is periodic for any ω_0 ¹, Ω_0 for a discrete signal must be rational. The investigated interval is commonly chosen as $0 \leq \Omega_0 \leq 2\pi$ or $-\pi \leq \Omega_0 \leq \pi$.

$$x[n] = e^{j\left(\frac{2\pi}{N_0}\right)n} = e^{j\Omega_0 n} \quad \Omega_0 = \frac{2\pi}{N_0} \quad (4.2)$$

A general signal with fundamental period N_0 can be represented as a *Discrete Fourier Series* (DFS) according to Eq. (4.3)².

$$x[n] = \sum_{k=0}^{N_0-1} c_k e^{jk\Omega_0 n} \quad (4.3)$$

The coefficients can be computed with Eq. (4.4):

$$c_k = \frac{1}{N_0} \sum_{n=0}^{N_0-1} x[n] e^{-jk\Omega_0 n} \quad (4.4)$$

4.2.2 Residual stresses

Localized plastic deformation, due to severe loading, leaves detectable traces behind, i.e. residual stresses. Their investigation yields important insights into the prevailing loading conditions and provide valuable information to interpret simulation results correctly. It must be taken into account, however, that the residual stress state is not only due to inelastic deformation. Metallurgical transformations, which are expected to occur at the friction surface, reduce or delete the previous history of the material and thus also the residual stresses.

¹Lower case and upper case letters are used to indicate the difference between the continuous and the discrete framework

²An alternative representation based on a sine and a cosine is possible. The link to the present formulation is given by Euler's formula: $x[n] = e^{j\Omega_0 n} = \cos(\Omega_0 n) + j \sin(\Omega_0 n)$

4.2.2.1 Measurement technique

As outlined in [28; 152] the basis for all techniques using X-ray diffraction on crystalline materials is Bragg's law:

$$n\lambda = 2d\sin(\theta) \tag{4.5}$$

Eq. (4.5) includes the lattice spacing d , the angle of the incident radiation θ and the wavelength λ of the radiation. The equation defines the angles where constructive interference occurs. If the angle of an incident X-ray beam, which consists for the most parts of a single wavelength, is varied the intensity of the reflected radiation varies distinctly. At the angles defined by Bragg's law peak values are observed and this behavior can be used for a variety of investigation techniques. Since X-ray diffraction yields information on the lattice spacing it can be used in the present study for the measurement of residual stresses. The stresses cause a distortion of the crystal lattice, which affects the parameter d and establishes a link between the lattice parameter and strain and stresses.

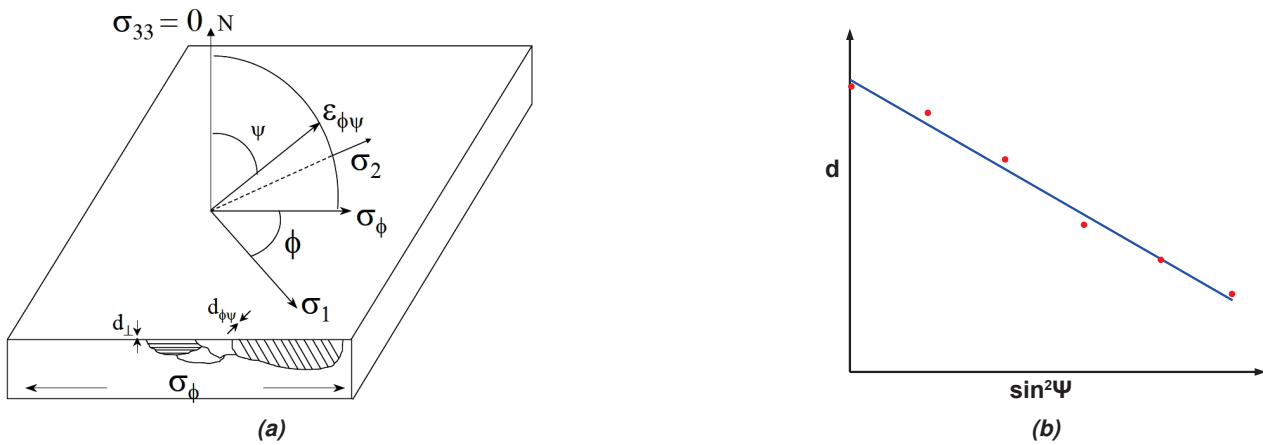


Figure 4.3: a) Illustration of strain and stress measurements by X-ray diffraction [28], b) illustration of the $\sin^2\Psi$ -method.

Fig. 4.3a shows a reference coordinate system and the definition of a plane parallel to the surface. The plane is determined by the angles Φ and Ψ . A measurement system consists of a radiation source and a detector. If the incident beam is normal to the sample surface, the strain in z-direction can be determined by moving the detector along an arc. It should be noticed that the surface is under plane stress conditions. This means that the stress but not necessarily the strain in normal direction is zero. The angular position yielding a peak in the detected signal is used in conjunction with Eq. (4.5) in order to get the lattice parameter in normal direction, d_n . Subsequently, ϵ can be determined from Eq. (4.6). By tilting the sample, the X-ray beam penetrates the surface under the angles Φ and Ψ . Determining the peak angle by moving the detector in the Φ and Ψ plane, the lattice parameter in this direction can be calculated. The corresponding strain is given by Eq. (4.7). This method requires the knowledge of the unstrained lattice parameter d_0 , which must be determined from an undeformed sample.

$$\epsilon_z = \frac{d_n - d_0}{d_0} \tag{4.6}$$

$$\epsilon_{\Phi\Psi} = \frac{d_{\Phi\Psi} - d_0}{d_0} \tag{4.7}$$

4. CHARACTERIZATION OF DAMAGE

The determination of stresses draws on Hooke's law. The normal strain can be expressed in the form of Eq. (4.8). Combining this equation with Eq. (4.6) yields an expression for the sum of the principal stresses (Eq. (4.9)).

$$\epsilon_z = -\nu(\epsilon_x + \epsilon_y) = -\frac{\nu}{E}(\sigma_x + \sigma_y) \quad (4.8)$$

$$\frac{d_n - d_0}{d_0} = -\frac{\nu}{E}(\sigma_x + \sigma_y) \quad (4.9)$$

For an expression yielding the stress in a specific direction Φ the equation needs to be generalized for arbitrary directions. Furthermore, the stresses need to be expressed by strains, which in turn can be expressed in terms of lattice parameters. This procedure finally yields Eq. (4.10). σ_Φ can be determined from two measurements, one normal to the surface and another one in the direction Φ - Ψ .

$$\sigma_\Phi = \frac{E}{(1 + \nu)\sin^2\Psi} \frac{d_\Psi - d_n}{d_n} \quad (4.10)$$

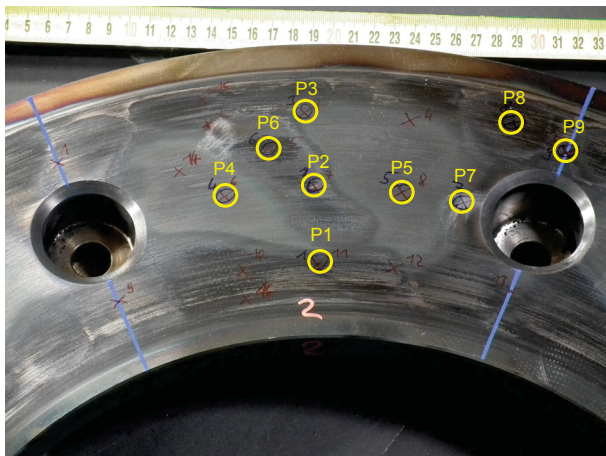
As outlined in [28], the most common method for residual stress measurement is the $\sin^2\Psi$ -method, which is based on the relation above. Besides the measurement in normal direction ($\Psi = 0^\circ$) a multitude of values for Ψ is investigated. In each case the θ -angle is measured and the lattice spacing is determined. In the next step d is plotted versus $\sin^2(\Psi)$, and the resulting data points can be approximated by a linear fit (Fig. 4.3b). The fit yields the slope m , which can be used to determine σ_Φ according to Eq. (4.11).

$$\sigma_\Phi = \frac{E}{1 + \nu} m \quad (4.11)$$

With this method, the in-plane stress in a specific direction can thus be determined without the unstrained lattice parameter d_0 .

4.2.2.2 Investigation methodology

From thermal images it is evident that there is a significant variation in the local loading conditions in each cycle. Additionally, the local loading varies from cycle to cycle, which causes a cyclic formation and deletion of residual stresses. For the purpose of a comprehensive investigation of the residual stresses a combined approach was chosen for the selection of the sampling positions. On the one hand, a predefined grid was used for all investigated friction rings in order to obtain results from corresponding positions. On the other hand, sampling positions were defined within distinct surface features, if present. Such features are e.g. worn or discolored areas. All measurements are restricted to a specific segment of the disk corresponding to 22.5° . The same segment is used later on for metallographic investigations. An example for a specimen location plan is presented in Fig. 4.4a. The residual stresses were determined by a mobile X-ray diffraction unit (Stresstech XStress 3000 G3). For the measurements, the disks were positioned on a flat surface and the machine was set on top (see Fig. 4.4b). The stresses were measured at the surface as well as in-depth at selected positions. For this purpose material was locally removed at the surface step by step by electrochemical polishing and each time the measurement was repeated. The procedure was continued with increasing step sizes until a maximum depth of 1.5 mm was reached. This depth poses the limit where the geometric influence of the established hole starts to have a significant impact on the stress state.



(a)



(b)

Figure 4.4: a) Example for selected positions for residual stress measurement, b) Configuration for residual stress measurement.

4.2.3 Microstructure

Due to the high temperature levels at the friction surface during high energy braking significant changes in the microstructure of the material can occur. The resulting microstructure is highly dependent on thermal levels and heating/cooling rates. For this reason, metallographic investigations yield a significant amount of information on the thermal loading conditions. A correlation with thermal images and simulation results is possible and valuable in view of the interpretation and verification of results.

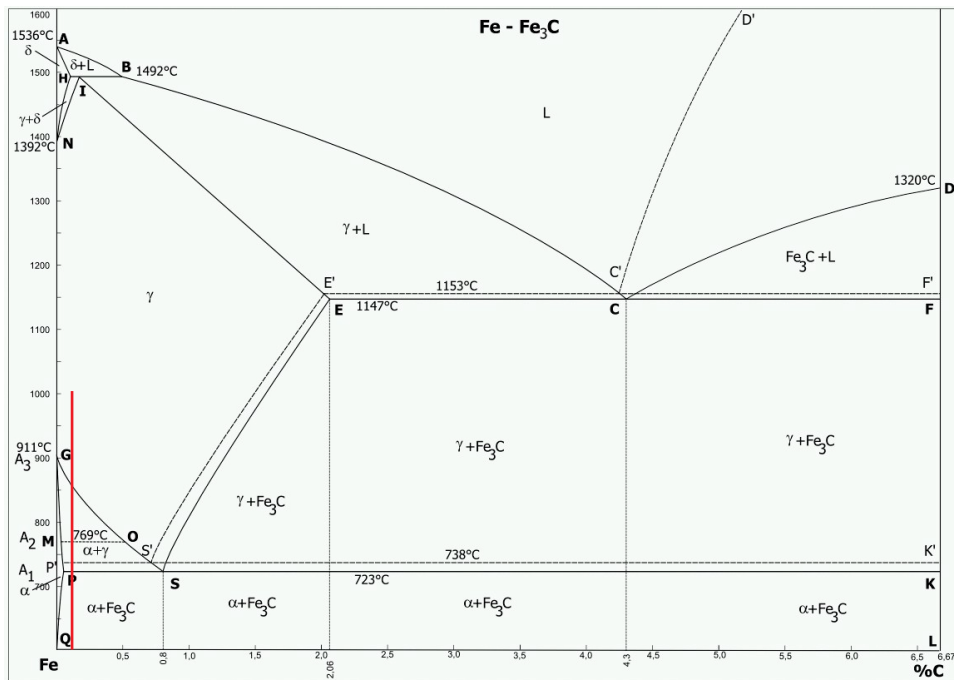
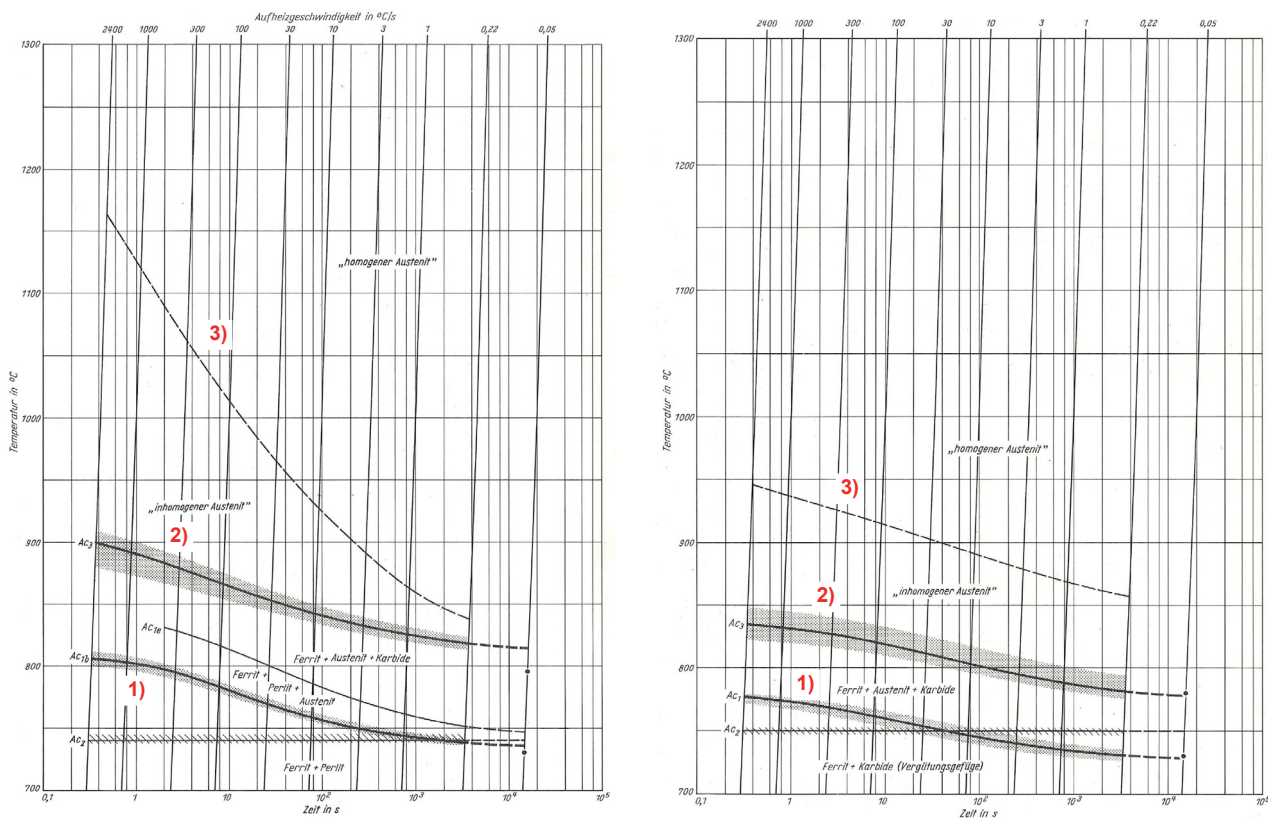


Figure 4.5: Iron carbon phase diagram [29].

4. CHARACTERIZATION OF DAMAGE

4.2.3.1 Background information on the characterization of metallurgical transformations

An overview of the relevant phase changes in iron based materials is commonly given in the form of the *Iron-Carbon Phase Diagram*, as depicted in Fig. 4.5. The solid lines correspond to the metastable system $Fe - Fe_3C$ (iron-cementite), which applies for slow but not infinitely slow cooling. The dashed lines refer to the thermodynamically stable $Fe - C$ system, which is less relevant for industrial processes. The carbon content for material A is low and it corresponds to a hypoeutectoid steel, as indicated in Fig. 4.5 for the relevant temperature range. At 723°C (A_1 temperature) the ferrite+austenite ($\alpha+\gamma$) 2-phase region is reached. At around 860°C (A_3) the indicated vertical line passes into the austenite region. The validity of the metastable $Fe - Fe_3C$ diagram is limited to rather slow processes with sufficient time for the indicated phases to build up. In many applications, like railway braking, the heating and the cooling are comparatively fast and the kinetics of the phase transformations must be considered. From Fig. 4.5, it is not clear how much austenite forms during heating, even if the A_3 temperature is surpassed, since the time of the loading is rather short and far away from an equilibrium state. Furthermore, rapid cooling causes metallurgical transformations not represented in Fig. 4.5. Limited diffusion gives rise to the formation of bainite or martensite. In order to describe the processes during heating *Time-Temperature-Austenitisation* (TTA)



(a) 34 CrMo 4 (0.34%C, 1.07%Cr, 0.17%Mo, 0.65%Mn) [153]

(b) 42 CrMo 4 (0.37%C, 1.06%Cr, 0.21%Mo, 0.64%Mn) [153]

Figure 4.6: Continuous TTA diagrams for two hypoeutectoid low alloyed steels with a) a ferritic-perlitic base microstructure and b) a hardened and tempered base microstructure.

diagrams can be applied. Fig. 4.6 shows two continuous TTAs for 34 CrMo 4 and 42 CrMo 4 taken from [153]. Formally, the latter material has a higher carbon content but the investigated lot has a very similar

chemical composition as the first material. The basic difference, however, is the microstructure before heating. For the first material it is a ferritic-pearlitic microstructure and for the second material a hardened and tempered microstructure, which commonly consists of tempered martensite or bainite. Due to this difference the formation of austenite in Fig. 4.6b begins and finishes at lower temperatures as compared to Fig. 4.6a. Since material A is also hardened, Fig. 4.6b is taken as a representative approximation for material A. The TTA shows three different regions, separated by the solid lines 1) and 2). At 1) austenite starts to form in the base microstructure and the transformation is completed above 2). Between the two lines both the base microstructure and austenite are present. An even distribution of carbon is obtained above the dashed line 3).

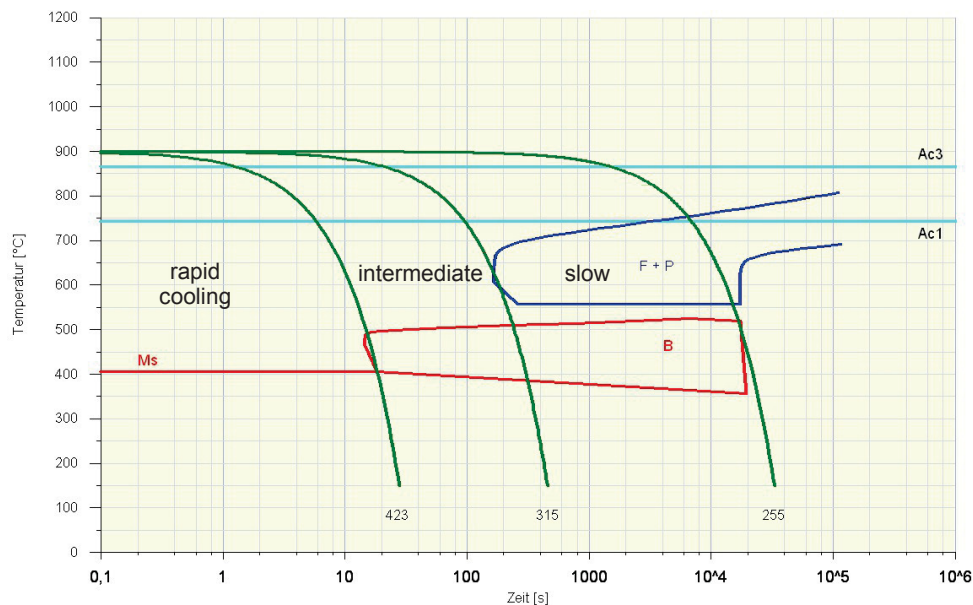


Figure 4.7: Characterization of phase transformations upon cooling: CCT diagram for material A (A courtesy of Schmiedag GmbH).

In the region, where austenitization has taken place, PTs occur during cooling. Which product phase is formed is largely determined by the cooling rate. An efficient means to illustrate this relation is a *Continuous Cooling Transformation* (CCT) diagram, as depicted in Fig. 4.7. The figure shows three different cooling rates, each causing a specific microstructure. The first green curve indicates the formation of a martensitic/bainitic microstructure, the second one a bainitic and the last one a ferritic/pearlitic microstructure. These are usually used in the context of industrial heat treatments but they can be applied as well for severely loaded brake disks. Fig. 4.8 lists the important transformation temperatures for the case of fast, intermediate and slow cooling. For the last case, the transformation is in accordance with Fig. 4.5. Figures 4.7 and 4.8 are valid for material A.

4. CHARACTERIZATION OF DAMAGE

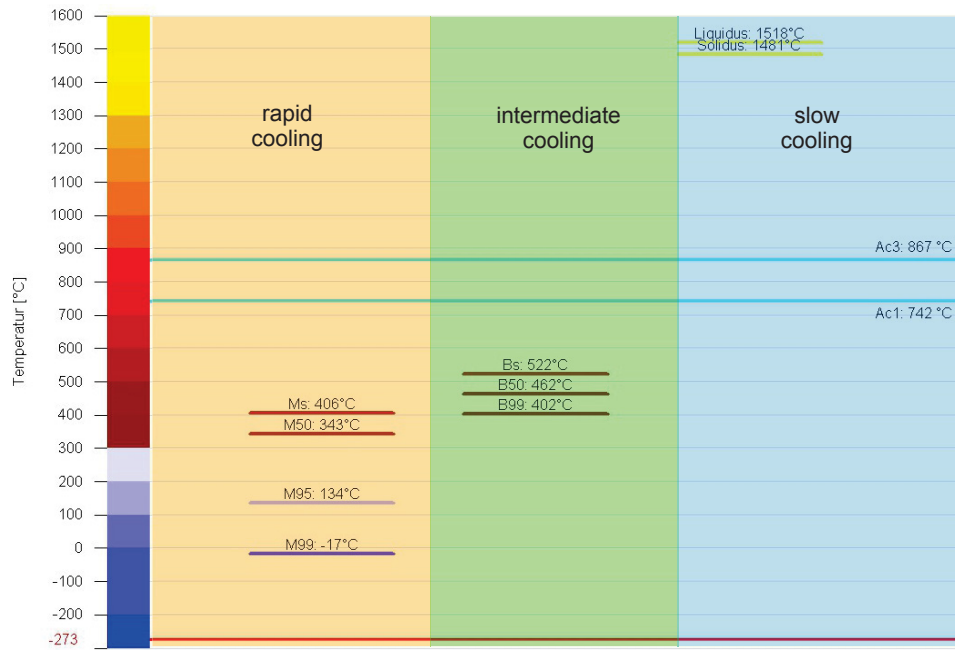


Figure 4.8: Characterization of phase transformations upon cooling: Individual transformation temperatures for material A (A courtesy of Schmiedag GmbH).

4.2.3.2 Investigation methodology

After the measurement of residual stresses were completed, each friction ring was separated into eight segments. The same segment that was used for the previous investigation was selected. The positions for metallographic specimens were predefined, as depicted in Fig. 4.9b. For each friction ring a row of samples was defined in radial and tangential direction. This way, the sampling points on the predefined grid are situated at least within one metallographic specimen. Since additional residual stress measurements (RSMs) were carried out at distinct surface features outside the standard grid, additional specimens were taken. The segment was separated by a precision cutting machine according to the sampling plan. Each specimen was embedded, ground and etched to be suitable for investigations with a light microscope. Fig. 4.9b provides an illustration of a prepared specimen and the expected regions of interest. In the depicted example a measurement site for residual stresses is situated at the center of the specimen. This allows a correlation between the two investigations.

4.3 Results

This section illustrates the results obtained by the techniques previously described. In order to be prepared for the performance of the analyses and the interpretation of the results, a preliminary study was carried out. A short summary is given at the outset of this section and further details can be found in [65]. Thereafter, the results of the present study are laid out in Section 4.3.2, Section 4.3.3, Section 4.3.4 and Section 4.3.5.

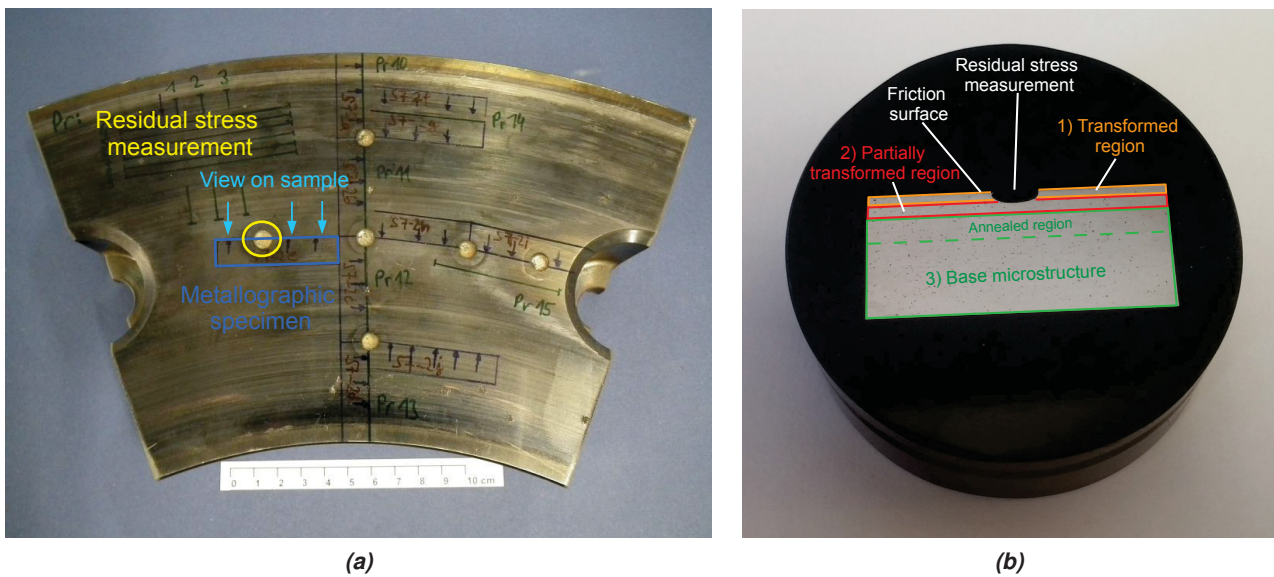


Figure 4.9: Illustration of a sample extracted for metallographic investigations, a) sample positions on disk segment, b) embedded sample with the expected regions of interest.

4.3.1 Preliminary studies

Fig. 4.10a shows the microstructure at a characteristic position in the surface region of a tested brake disk. The disk was exposed to 200 emergency stops similar to the long test runs in the current study. The initial speed, however, was 160 km/h as opposed to 250 km/h and the disk material is the cast version of material A. The disk diameter is 940 mm as opposed to 680 mm, for the present disks. The observable damage is thus less distinct but the basic mechanisms are the same. Fig. 4.10a reveals the three distinct zones

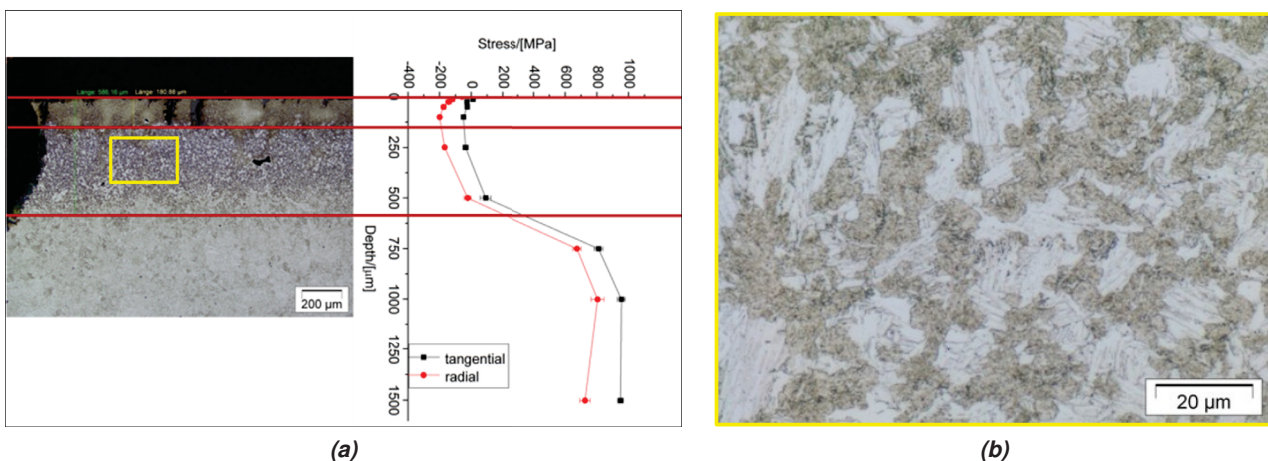


Figure 4.10: a) Correlation of microstructure and residual stress level, b) Partially transformed region in zone 2.

already mentioned in the context of Fig. 4.9b. It was found that these zones directly correlate with the in-depth evolution of the residual stresses. The expected evolution due to cyclic inelastic deformation without phase transformations would start with a significant level of tensile stresses at the surface which gradually diminishes with increasing depth. In Fig. 4.10a deviations clearly occur in the surface region. At depths, where the initial microstructure is still present and no annealing occurred, the evolution in Fig. 4.10a is

4. CHARACTERIZATION OF DAMAGE

as expected. The stress level is higher in tangential direction, which is also the main loading direction. Tensile residual stresses above 800 MPa occur due to compression dominated cyclic plasticity. Closer to the surface, where the microstructure has not transformed but annealing effects have occurred, the tensile stress level does not increase, on the contrary, it decreases. The surface zone with metallurgical transformations, either partially or complete, shows a sharp decrease and the stress level changes into the compressive regime. This makes sense since the previous plastic history is deleted by the austenitization during heating and the formation of bainite and martensite during cooling is linked to an increase in the volume of the metallic crystal structure.

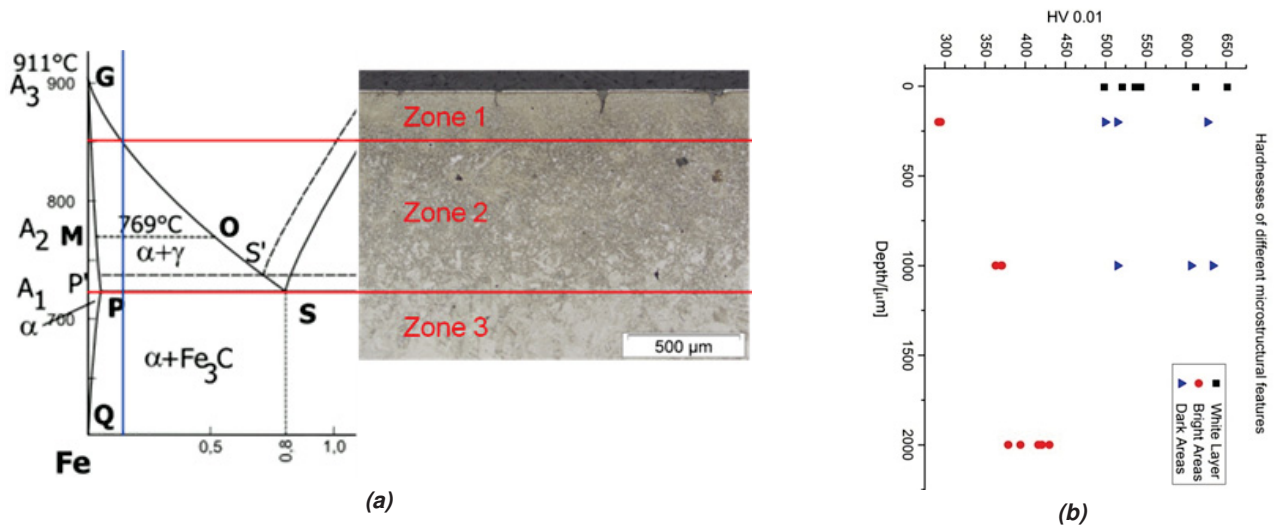


Figure 4.11: Correlation of a) microstructure and b) hardness.

Fig. 4.11a depicts a micrograph from a position below a hot spot, where PTs reach greater depths. The three zones are indicated and related to the relevant portion of the Fe-C diagram. This representation neglects the kinetics of PTs but it coarsely indicates the temperature levels above which partial and complete PTs can occur. The top 10 μm consist of friction martensite (white layer) containing retained austenite, which was detected by X-ray diffraction. The complete austenitization and hardening in the top 250 μm indicate temperatures beyond 860°C. Due to the kinetics of phase transformations the temperature level might have been higher regarding the relatively short periods of heating. The region between 250 and 1000 μm in depth was exposed to temperatures in the α + γ region in the range of 720-860°C followed by an area subjected to conditions similar to stress relaxation annealing. The results of microhardness testing in the individual microstructural features are depicted in Fig. 4.11b. The hardness of the so called white layer consisting of martensite and retained austenite scatters significantly. For the strongly etched and hence darker regions, comparable hardness values and scatter are obtained. The scatter stems from the different orientation of substructures in the martensite/bainite and the localized measurement. These features consist of extraordinarily fine structures formed by martensite and bainite. The less intensely etched areas appear white and show less hardness, also less scatter compared to the darker regions. With increasing depth the hardness in these areas increases towards the level of the unaffected microstructure. A possible explanation for the formation of the microstructure is given at this point. The white areas in zone 2 correspond to areas that have not been austenitized. The bainitic base microstructure consists of

fine carbides dispersed in a ferrite matrix. Carbides are not stable at temperatures that are higher than the A_1 temperature. Thus, in zone 2 carbides in bainitic regions dissolve and carbon diffuses into the austenite. Furthermore, recrystallization has occurred in the upper parts of zone 2. In lower parts of zone 2 the carbides have also dissolved but the stacked structure of the original bainite matrix is still present since no recrystallization has taken place. This microstructure can be observed in Fig. 4.10b.

Due to the fact that the disk was subjected to 200 emergency stop brakings, austenitization and subsequent cooling occurred many times. The achieved cooling rates are high enough to cause martensitic/bainitic hardening during cooling. The high cooling rates are due to the very high thermal gradients in the surface region. Thus, the heat flux away from the disk surface is large and the temperature level approaches the cooler bulk temperature fast. For these reasons, every position in zone two could have been austenitized with a subsequent formation of a new refined microstructure during the test rig program. This is not likely, however, since the higher carbon content of austenitized and subsequently martensitic/bainitic hardened regions, formed in the first phase transformation process, favors reaustenitization of these regions in subsequent heating cycles. Hence, the white areas in Fig. 4.10b could be part of the original grains.

The mentioned temperature ranges in the previous discussion are only rough estimates for two reasons. First, the alloying elements in material A change the transformation temperatures in the phase diagram. Second, the transformation kinetics is essential for the formation of austenite. It takes very long for the microstructure to transform completely to austenite if the temperature is only slightly above A_3 . Basically, the kinetics describe the formation of specific phases as a function of time and temperature. The heating times during braking are short, which points towards higher temperatures for complete transformations. The investigations presented in Section 4.3.4 can draw on TTA and CCT diagrams yielding more precise information on the occurring phase transformations.

4.3.2 Evolution of the global disk deformation

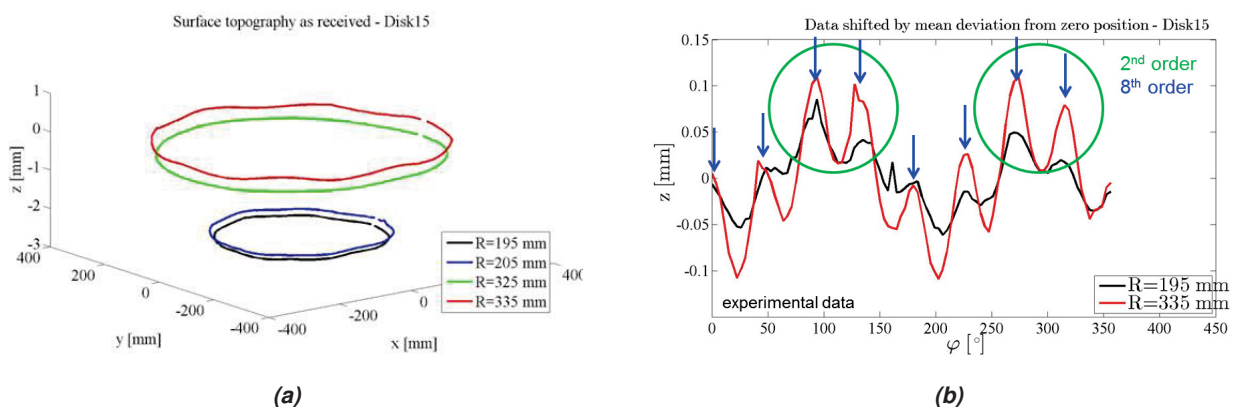


Figure 4.12: Measured waviness after test run 8 (friction ring 15; 100 emergency stops), a) 3D representation of measurement results b) Waviness along the inner and the outer circumference with local and global maxima.

Fig. 4.12a shows the results from the CMM for friction ring 15 from test run 8 (100 emergency stops; see table 3.16) obtained at four different radial positions. R=195 mm and R=335 mm correspond to areas on the friction system that have not been in contact with the pad and are unworn. R=205 mm and

4. CHARACTERIZATION OF DAMAGE

R=325 mm correspond to positions being situated slightly closer to r_{mean} and consequently to worn areas. Fig. 4.12a is an illustrative example for the results since test run 8 caused large deformations compared to other tests in the program. On the one hand, residual disk coning is visible as the results from the inner and the outer regions show a distinct difference in the axial displacement. On the other hand, a wave-like residual deformation along the circumference is visible, although the z-axis is scaled for the disk coning, which is naturally more pronounced than any waviness. Furthermore, the amplitude at R=195 mm is clearly lower than for R=335 mm. This indicates that wear has reduced the maxima of the waves. On the inside, where the amplitudes are in general smaller, this impact is not obvious. Fig. 4.12b shows the results for R=195 mm and R=335 mm in a more comprehensive way, as a 2D plot. The figure reveals two distinct maxima apparently superimposed by eight local maxima. As previously noted, the amplitudes are larger at the outside than on the inside. From the plot it is clear that the orders 2 and 8 in the spectrum play important roles. It is not clear, however, if there are other significant oscillations with smaller amplitudes. These would disappear in a representation of the form of Fig. 4.12b. Therefore it makes sense to transform the signal into a simple DSF.

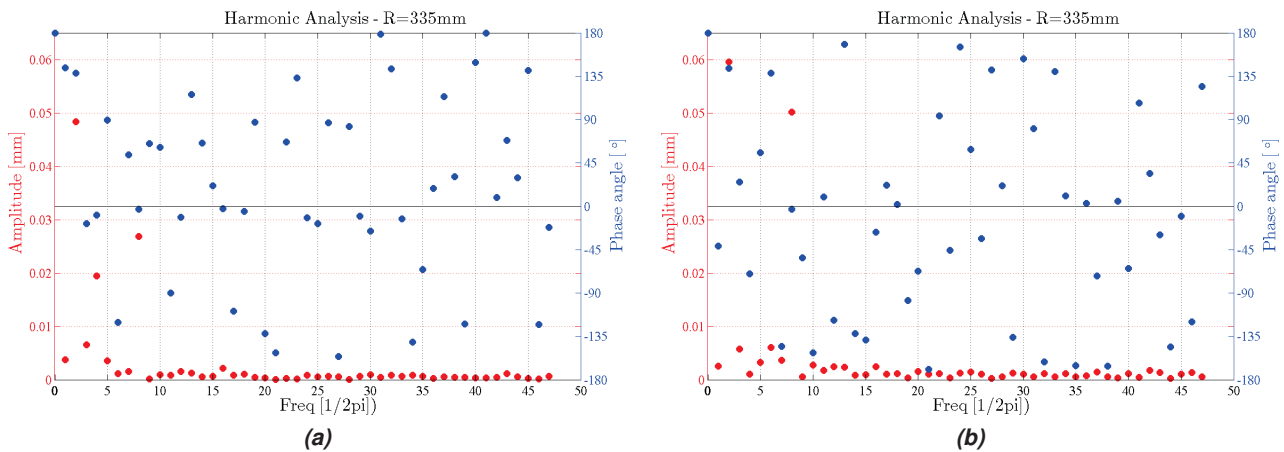


Figure 4.13: Harmonic analysis of a) friction ring 7 (200 ES) and b) 15 (100 ES).

Fig. 4.13 shows the results for the friction rings 7 and 15 (see Fig. 3.16), which were subjected to 200 and 100 emergency stops (ES), respectively. The blue dots refer to the amplitudes of the respective orders, while the green dots represent the phase shift of the oscillation with respect to the angular reference position. It is always situated at one of the mounting points with a stiffer design (see Section 1.5.1). The meaning of the lower orders can be explained as follows (see Table 4.1):

Table 4.1: Meaning of stationary oscillations along the circumference.

| Order | meaning |
|-------|---|
| 0 | Mean value of the oscillation corresponding to an axial shift with respect to the reference plane. |
| 1 | Either an inclination of the reference plane or a disk thickness variation (DTV). |
| 2 | This order indicates some sort of instability (e.g. potato chip effect) during braking, which becomes permanent due to plastic deformation. |

| | |
|---|--|
| 4 | Waviness linked to the fact that 4 of the 8 mounting points have a stiffer design. Even if the occurring plastic deformation is homogeneously distributed, the local stiffness variations lead to permanent waviness |
| 8 | A similar explanation as for the 4th order applies. The eight mounting positions are clearly stiffer than the regions in-between. |

Fieldhouse et al. [154] discuss possible origins of the static 2nd order deformation for automotive brake disks. On the one hand, the stresses in tangential direction can exceed the critical buckling load during braking. When plastification occurs, the resulting 2nd order becomes permanent. On the other hand, there might be a residual stress state from manufacturing. The results from dynamometer and CMM tests presented in [154] suggest that stress relaxation due to high temperatures, obtained during braking, gives rise to permanent 2nd order deformation as well.

The highest order that can be detected with 96 measurement points from the CCM is 48, which corresponds to the number of the cooling fins on the reverse side. Although there might be some influence, the amplitudes beyond order 8 are too small to yield comprehensive information. They disappear in the measurement inaccuracy. The orders 2 and 8 on the other hand are distinct for both measurement. For friction ring 7 also the order 4 is clearly present. The 0th order has been removed from the data before the analysis since it does not yield any important information in this context. Nevertheless, the 0th order can be used for the characterization of the disk coning because it corresponds to the average axial displacement along the investigated circle. This will be discussed further below.

Fig. 4.14 depicts the evolution of the amplitudes of the orders 2, 4 and 8 for an increasing number of load cycles and the two pad types. Each diagram contains three lines. One for each side, where a friction ring was mounted. The third line represents the average value from both sides. Here, it should be noticed that each line consists of the data points for individual friction rings rather than a continuously measured single ring.

The first test run corresponds to bedding-in only. At this point the order 2 is already present but the orders 4 and 8 are hardly visible for both pad types. With increasing load cycles there is a general increase of the amplitudes, but some scatter occurs between the two sides. The highest scatter occurs in Fig. 4.14d, where opposing trends are visible. The trends in run 3 in Fig. 4.14b and run 2 in Fig. 4.14e deviate. Apart from these data points the trends are identical. Especially in Fig. 4.14b (except the deviating point), Fig. 4.14c and Fig. 4.14f the amplitudes on both sides match well. During the first emergency stop the amplitudes increase more distinctly for pad type 2 than for pad type 1. Furthermore, the highest amplitudes occur for pad type 2 (orders 2 and 8). This observation can be correlated with the inhomogeneous thermal loading presented in Chapter 3. It was shown that for pad type 2 alternating thermal patterns appear consisting of coarse hot and cold patches. This sort of thermal loading indicates that also the plastic deformation at the disk surface is localized and coarsely distributed. Besides the local variation in stiffness due to the mounting points the inhomogeneous plastification contributes to the waviness. A further impact may be the phase transformations, which are linked to the thermal loading as well. In fact, they delete the plastic history in the hot regions and the severe plastification is removed. The plastic deformation and residual stresses in the other regions remain, however. The amplitudes, which do not match the trend

4. CHARACTERIZATION OF DAMAGE

suggest that either a homogenization has taken place or a change of the thermal configuration that causes impeding effects. The corresponding amplitudes are thus lower. A steady increase of the plastification in the disk occurs for both pad types and globally the amplitudes increase correspondingly.

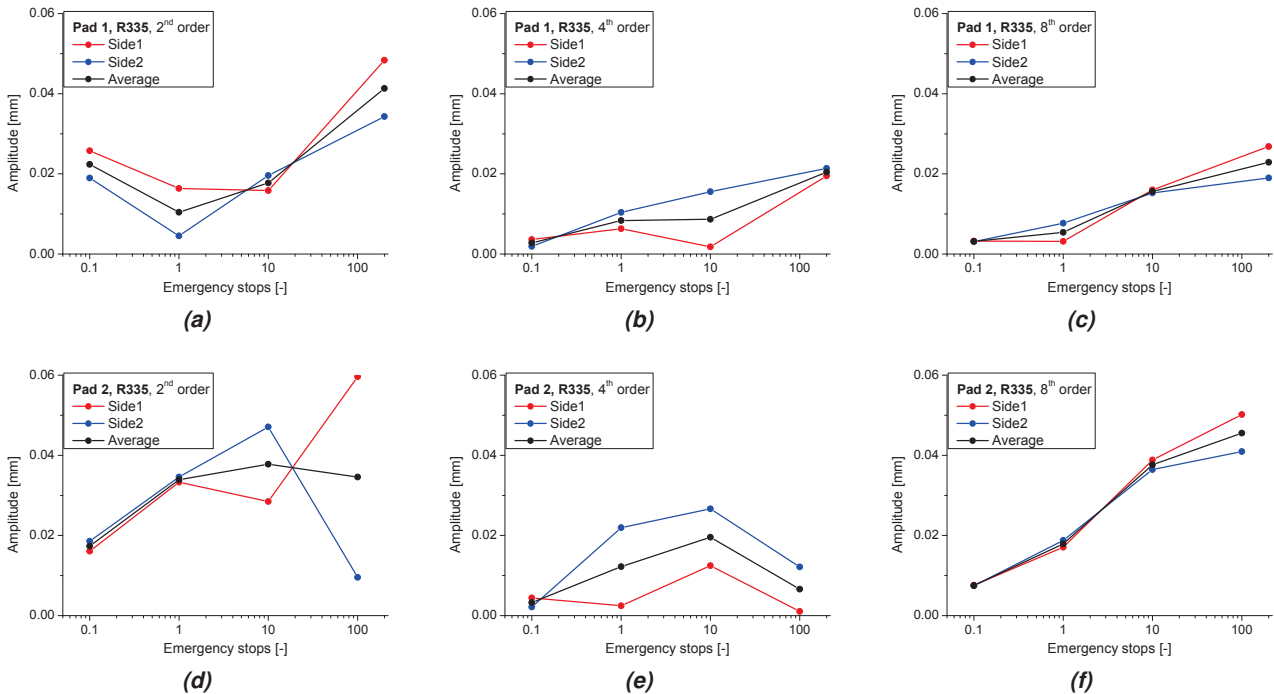


Figure 4.14: Evolution of amplitudes with increasing number of brake applications ($R=335$ mm). The state after bedding-in without emergency stops is indicated by the value 0.1.

In the diagrams a stabilization is not visible, which indicates that the maximal number of load cycles was not sufficient to reach a stabilized state. It must be considered, however, that the load cycles corresponding to the test runs are 0, 1, 10 and 200/100 emergency stops, respectively. Saturation is thus nearly achieved in the test program for the order 8, and for pad type 1, also for the order 4. As noted above, the 2nd order may be due to an instability or to a relief of manufacturing stresses. The evolution depicted in Fig. 4.14d supports the buckling theory combined with plastification. The thermal pattern occurring during the last braking of the test run has a great impact on the 2nd order. Fig. 4.14d suggests that different patterns occurred at each side at the end of the test runs 3 and 4. The resulting instability/plastification on each side yield different amplitudes. If the order 2 is triggered by an instability it is questionable if stabilization will ever occur.

In summary it can be said that there is a systematic evolution of the amplitudes on both sides. Occasional deviations may be related to random processes occurring in the tribological system during braking, which sometimes but not always occur. For pad type 2, it is likely that the random processes are linked to the inversion of thermal patterns discussed in Chapter 3.

The findings concerning the variations of the amplitudes with the radial position are summarized in Fig. 4.15:

10 emergency stops: An increase of the amplitudes with the radius is visible for both pad types. This is expected, since the disk is more flexible at the outside. The amplitudes are higher for pad type 2.

200/100 emergency stops: The impact of the disk wear starts to play a role after a high number of brake applications but it is difficult to pinpoint a clear trend. Especially the measurements in the worn regions yield ambiguous results. This is due to the fact that the wear is not homogeneous along the radius, as outlined in [65]. For this reason, measurements at two radii in the worn area cannot yield comprehensive results apart from some fundamental observations, such as the 8th order shown in Fig. 4.15e. Without wear the amplitude increases significantly from the inside to the outside. The CMM measurements at R=325 mm are situated exactly in a valley of the wear pattern, which can be seen and sensed by touching the friction surface. Hence, the peaks of the 8th order waviness are clearly worn along the circumference at this radius. This fact has already been mentioned in the discussion of Fig. 4.12a, where the waviness itself is depicted. At another radial position the impact of the wear would be different, however. This is clear at R=205 mm where wear is barely indicated on the friction surface. The other curves yield less distinct results but they indicate that wear may decrease but may also increase the amplitudes. The latter effect is not clearly understood but it may be related to the increased flexibility of the disk to deform in areas with slightly reduced thickness due to wear.

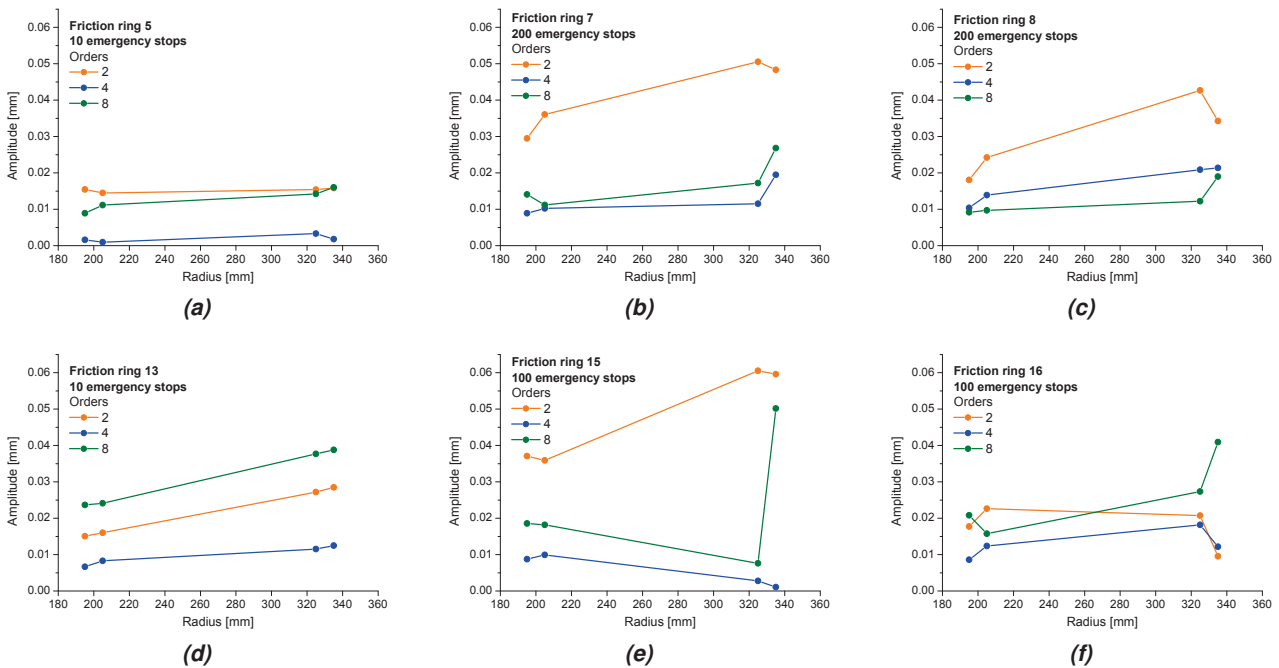


Figure 4.15: Evolution of the amplitudes of the orders 2, 4 and 8 as functions of the radial position.

As indicated in Fig. 4.12a, the disk coning can be derived from the CMM data. As noted above, the 0th order corresponds to the average axial shift along the circumference with respect to the reference plane. The difference between the results at R=335 mm and R=195 mm is thus the static disk coning, which is a measure for the plastic deformation in the brake disk. The results depicted in Fig. 4.16 reveal two things. First the increase in disk coning seems almost linear with respect to the test runs. Note the non-linear scale of the abscissa in , which indicates that the curves approach a saturation value. Second, the results are very consistent between both sides, suggesting that random processes have less impact on the coning than on the waviness. For pad type 1 the static coning increases from ~0.25 mm after bedding to ~3.9 mm after 200 emergency stops. For pad type 2 the increase is from ~0.42 mm after bedding to ~5

4. CHARACTERIZATION OF DAMAGE

mm after 100 emergency stops. These data are suitable for the verification procedure of simulation data. The data for the waviness can be used as well but significant scatter needs to be taken into account.

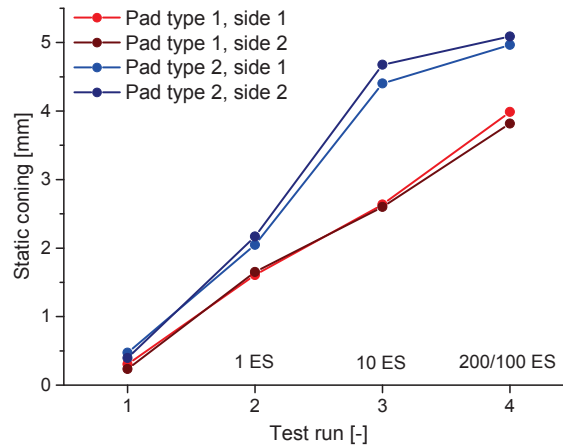


Figure 4.16: Computed disk coning from CMM measurements.

4.3.3 Distribution and evolution of the residual stresses on and under the friction surface



Figure 4.17: Standard positions for residual stress measurements for all friction rings.

This section deals with the characterization of residual stresses formed in the brake disks due to cyclic plasticity and metallurgical transformations. From each brake disk, the friction ring facing the thermal camera was chosen for the investigations. Fig. 4.17 shows the positions P1, P2 and P3, where RSMs were carried out for all friction rings. Fig. 4.18 provides an overview of the results for each position and applied pad type. The results are not conclusive at the first glance but some trends can be discerned:

Bedding-in: The stress evolution after the bedding-in process consists of compressive stresses at the surface and a tensile peak within the top 100 μm . At greater depths the stresses diminish. For the rings tested with pad type 1 the stress falls slightly below 0 within the measured range (1.5 mm). For pad type 2

the zero-crossing is not situated within the top 1.5 mm. For pad type 1 the tensile peak is in the range from 160 to 310 MPa. For pad type 2 the scatter and the maximum of the stress evolution is significantly higher. It varies in the range from 450 to 875 MPa. All of these evolutions are typical for cyclic plastic deformation in the region between the surface and a certain depth superimposed by phase transformations limited to the near surface region. A similar observation has been discussed in Section 4.3.1. The severity and penetration depth of the plastic deformation is clearly higher for pad type 2.

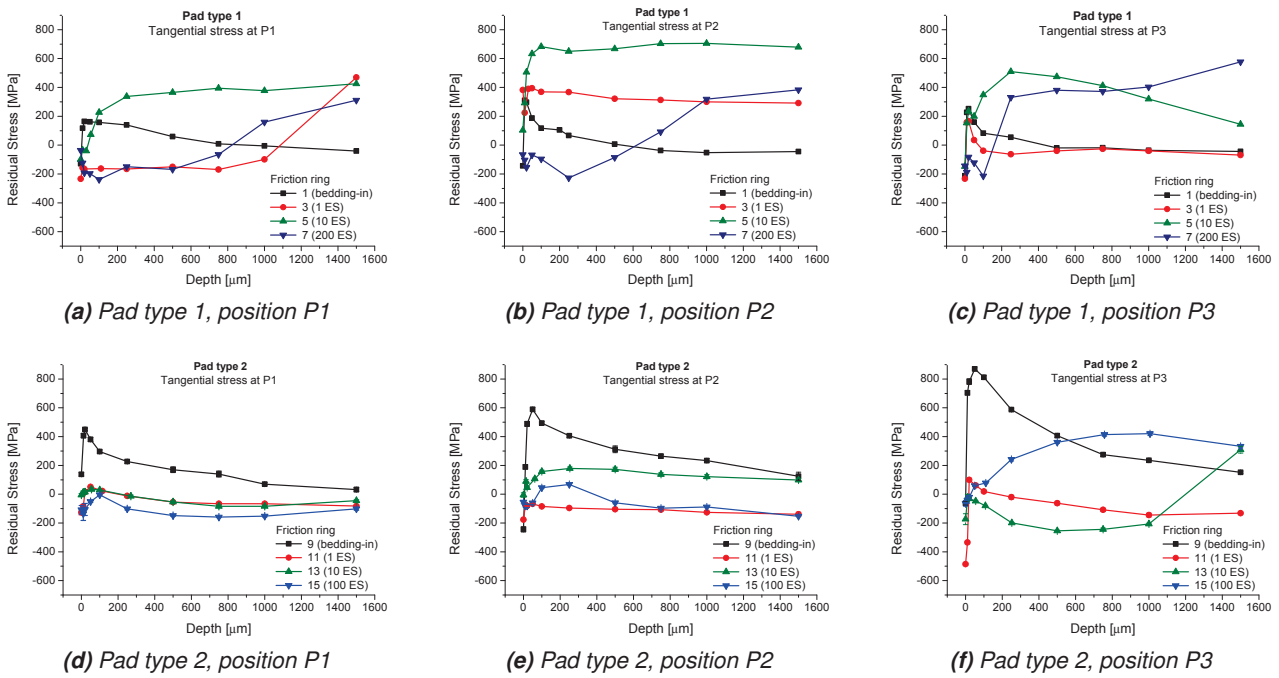


Figure 4.18: Comparison of residual stresses at the positions P1, P2 and P3 for all friction rings.

Emergency stops with pad type 1: The interpretation of the results obtained from friction rings exposed to high-energy braking is more difficult for an obvious reason. The penetration depth of phase transformations is much higher than during bedding-in and also higher as in the case of the brake disk used for preliminary studies. Additionally, the hot regions move from braking to braking, for pad type 1 on a local scale and for pad type 2 even at a global scale. The history of the formation and the deletion of residual stresses is thus very complex and requires a comparison with thermal images and the microstructure. This will be treated in Section 4.3.4. At this point some basic observations can be discussed.

- For pad type 1 the patches where the highest temperatures occur are situated along the inner disk half. The stress evolutions in Fig. 4.18a for friction rings 3 and 7 exhibit a distinct plateau in the compressive regime. This indicates phase transformations down to 800 to 1000 μm , which matches the observations from thermal images see the results presented in Section 4.3.4. At 1.5 mm depth the stresses are in the range of 310 to 470 MPa.
- As depicted in Fig. 3.20 the hot patches sometimes reach the mean radius, but on the outer half the thermal loading is distinctly lower. This matches the stress evolutions in Fig. 4.18b and Fig. 4.18c. For the rings 3 and 5 a high stress level is present right below a small transformed region. For ring

4. CHARACTERIZATION OF DAMAGE

7 apparently a hot patch and a more profound transformation region occurred at P2 during the last braking of the test run.

- At the position P3 the thermal loading was in general less than at P1 and P2. During the only emergency stop for friction ring 3, the thermal loading was very low at P3 and the stress evolution after bedding-in was largely retained. The results for the rings 5 and 7 indicated that harsher loading conditions occur as well after multiple brakings, but not in a comparable intensity as at smaller radii. Cyclic plastic deformation clearly occurred, but the temperature levels were not sufficient to cause far-reaching austenitization.
- The residual stresses measured in friction ring 5 do not show a plateau and are higher than the other results. This indicates sufficient loading for plastification, but temperatures below the A_1 temperature apart from the near surface region. Fig. 4.19 provides an explanation how this situation could have emerged. The thermal image belongs to the test sequence of friction ring 5. It shows a typical configuration of hot and cold areas where P1-3 do not coincide with hot patches. Therefore, phase transformations at P1-3 in the respective load cycle are restricted to regions in direct vicinity to the friction surface. The temperature at P3 seems rather cold to cause distinct residual stresses. The heat input at the surface is a local influence. The plastic deformation is in turn influenced by the local temperature field, but the formation of residual stresses is also influenced by the processes at a greater distance. For this reason, residual stresses build up, either due to local plastic deformation or plastic deformation/phase transformations in the surroundings. In configurations as depicted in Fig. 4.19, the formation of residual stresses is apparently favored, since the corresponding regions are spared from profound phase transformations. Fig. 3.20 shows the thermal images for the first 10 emergency stops for friction ring 7. In Chapter 3 it was shown that the results are reproducible in different test runs. Based on this observation it can be assumed that the series of thermal images would look similar for ring 5. Given the fact that the images are processed and rotated to an angular reference position one can find segments where conditions similar to Fig. 4.19 apply during successive brakings at the end of the test run. This indicates that the residual stresses may have built-up over multiple cycles.

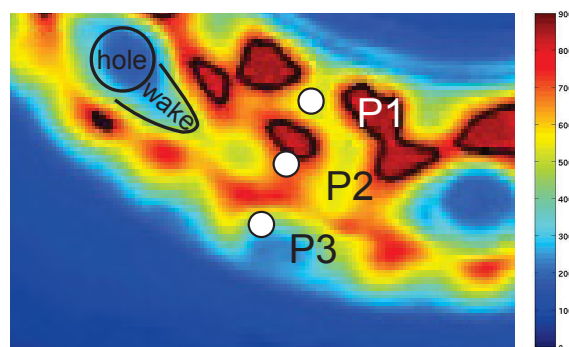


Figure 4.19: Residual stress measurements situated at positions with low thermal loading and less profound phase transformations.

Emergency stops with pad type 2:

- The final stress levels are generally lower than for pad type 1. Distinct plateaus in the compressive regime occur exceeding the investigated depth. Many measurements show values clearly below the stress levels after bedding. This situation indicates profound phase transformations reaching further into the material than the RSMs recorded (1.5 mm). Fig. 3.21 suggests that the hot patches move significantly from one braking to the next and even inversions of the patterns occur. It is thus possible that a random process occurs on a local scale, where phases of residual stress formation and deletion alternate.
- This effect can be discerned in Fig. 4.18f. After one emergency braking the whole measured depth has transformed and no effect of plastic deformation is visible. The tensile peak close to the surface will be discussed below. After 100 emergency brakings a similar tensile stress level is obtained at 1.5 mm depth. The distribution with increasing depth is almost inverse, however, and no compressive plateau occurs. This suggests that only metallurgical changes near the surface took place and residual stresses formed. These were partially deleted in the surface region due to annealing effects. This process may have occurred over multiple cycles towards the end of the test run. The stress evolution at P3 after 10 load cycles is similar to the one obtained after 1 cycle. The difference, however, is that tensile stresses are present at 1.5 mm. This shows that profound plastic deformation occurred during the test sequence that was not completely deleted. The phase transformations during the last cycle(s) were not sufficiently far-reaching.
- The stresses after one emergency braking (ring 11) at P3 are distinctly lower than after bedding. This can be explained by austenitization of the complete measurement range. The stress evolution right below the surface (20-40 μm) seems to stem from a different effect. The formation of friction martensite (white layer) is indicated from metallographic samples and it is also described in [65]. The precise mechanism is beyond the scope of this work. However, the stress evolution for friction ring 11 in Fig. 4.18f allows the conclusion that the formation of friction martensite follows a different mechanism, which is independent from the transformations at greater depths. Furthermore, it seems to induce higher compressive stresses at the surface and a tensile peak at the interface to the “normally” transformed zone. This peak may sometimes coincide with the peak caused by plasticity as in the case of the results for bedding in. Another possible source of localized tensile peaks may be the machining during manufacturing. Surface stresses in the range from 400 to 540 MPa were measured on the virgin brake disks. It can be excluded that these stresses are still present after bedding because the distributions do not match the very localized peaks close to the surface that would usually occur. It should be noted that the measurements directly at the surface (0 μm) are subject to a certain measurement error due to the surface conditions.

Fig. 4.21 provides an alternative overview of the RSMs obtained from the brake disks tested with pad type 1. This time the results are plotted individually for each friction ring and measurements outside the standard grid are included. The sampling positions for the friction rings 5 and 11 are depicted in Fig. 4.20. For a complete documentation of all friction rings see Appendix C.8.

Pad type 1:

- The results after bedding in are consistent for all positions. This indicates very homogeneous contact conditions due to the flexible design of this pad type. This is not visible anymore in the stress

4. CHARACTERIZATION OF DAMAGE

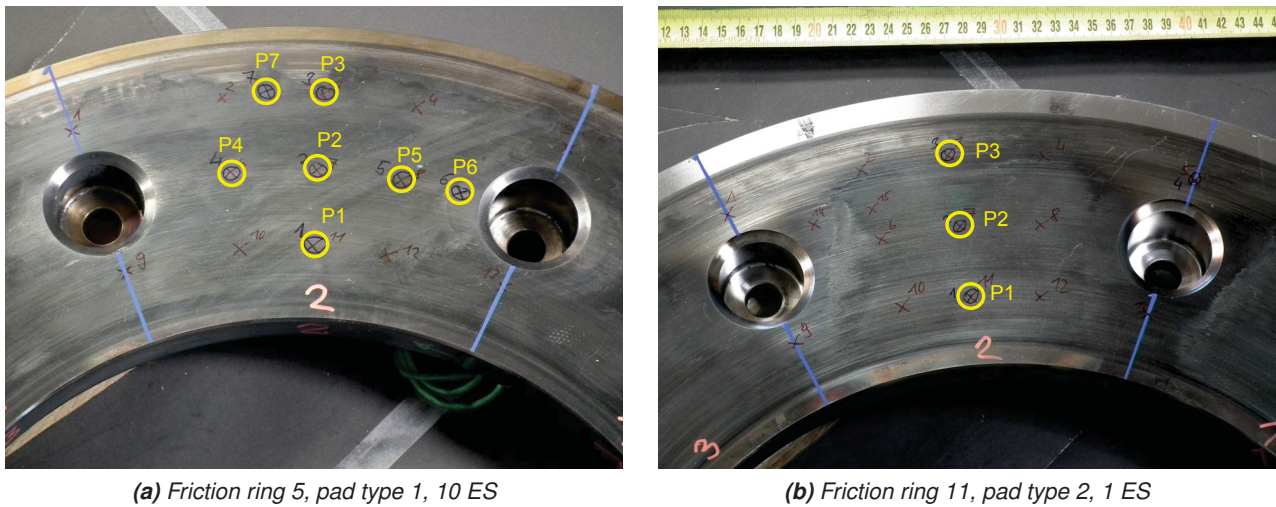


Figure 4.20: Positions for residual stress measurements on a) friction ring 5 and b) friction ring 11.

evolutions at higher brake energies.

- After 1 emergency stop (ES) pronounced plateaus in the compressive as well as in the tensile regime were detected.
- After 10 ESs the maximal stress level is higher (700 MPa) and plateaus, if present, are shifted towards the tensile region. Fig. 4.20a depicts all measured positions. The blue circles with blue labels refer to in-depth measurements, while red crosses with red labels correspond to surface measurement. The latter ones will be skipped because the results are not conclusive without in-depth information. At position P6 a classic evolution due to cyclic plasticity at a moderate level is visible, while an interaction between plasticity and phase transformations is present directly at the surface. This correlates well with the positions of the measurements documented in Fig. 4.20a. P6 is situated in the wake of a mounting point. The contact pressure between pad and disk is obviously decreased when the pad slides over a hole. For this reason, less wear is observed in the wakes of the mounting points. Correspondingly, it can be seen in Fig. 3.20 that the temperature levels are often distinctly lower after a mounting point. An example is also depicted in Fig. 4.19. The stress evolution at P6 is thus primarily dominated by cyclic plasticity. P7 on the other hand is situated on the outer half of the friction ring, where high temperature levels occur but they are moderate in comparison to the inner half. The stress evolution is thus dominated by phase transformations/annealing close to the surface and plasticity at greater depths.
- After 200 ESs the stress evolutions seem to be shaped by multiple phases of build-up and deletion. P5 and P6 are situated in the wake of a mounting point. A similar discussion as above applies with the difference that the stress level reaches deeper into the material.

Pad type 2:

- The stress evolutions after bedding (Fig. 4.22a) suggest that the contact conditions significantly vary from the inside to the outside. The peak stress increases from 450 MPa up to 875 MPa.

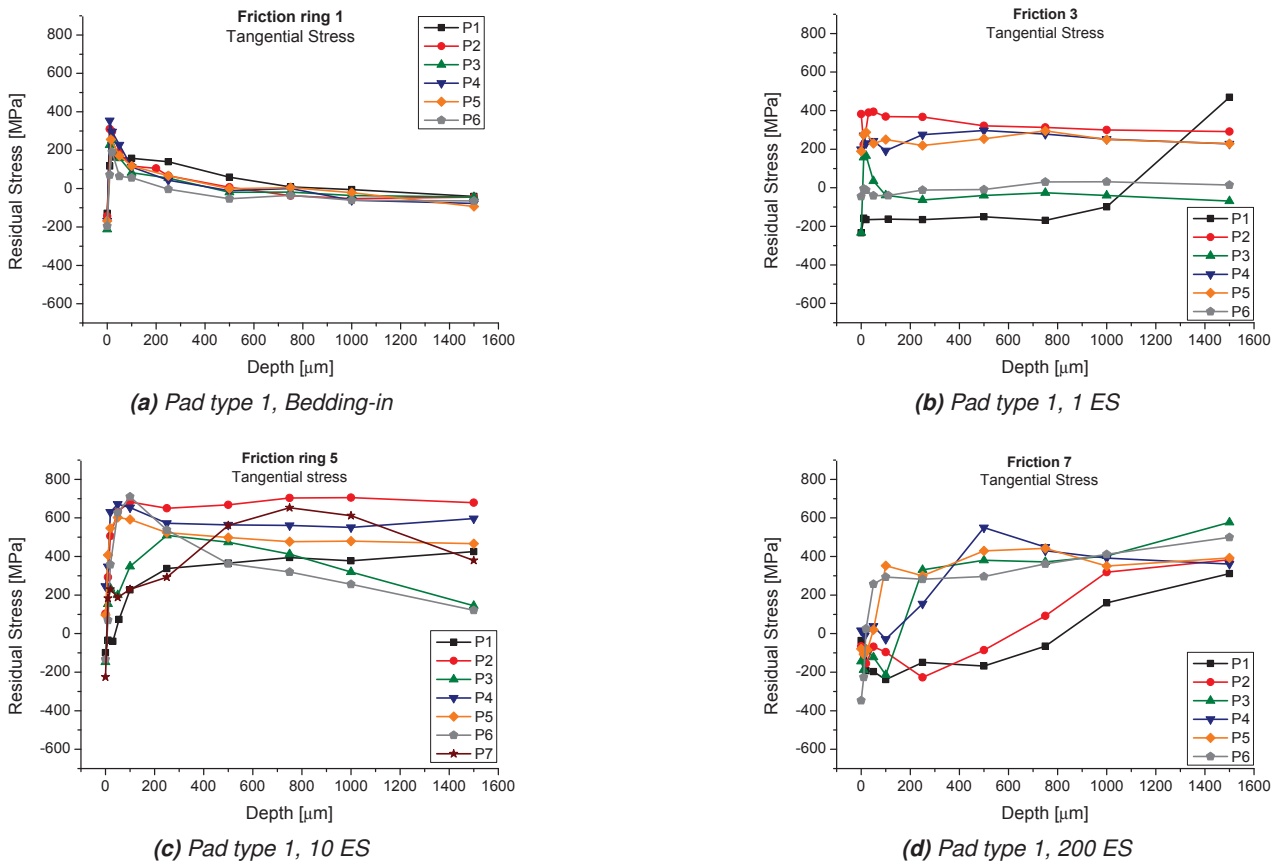


Figure 4.21: Overview of residual stress measurements carried out for pad type 1.

- The thermal distribution during the first ES was focused on the region between the mounting positions. This is evident from the wear pattern and from thermal images. Nevertheless, the thermal input was homogeneous in this area and the temperature levels were lower than in subsequent brakings (see Fig. 3.21). These loading conditions caused moderate plastic deformation and annealing effects, which have reduced the stress levels at P1-3 built-up during bedding and the emergency braking (Fig. 4.22b). At P2 (center position) phase transformations are indicated, since the stress evolution is entirely in the compressive regime. P4 is situated directly above a hole (see Fig. 4.20b), where temperatures stayed rather low. Apparently, the thermomechanical loading conditions were high enough to cause plastification and thus residual stresses, which are still present at P4 because no or little annealing has occurred.
- Friction ring 13 (10 ES) has the most conspicuous wear pattern from all brake disks resembling butterfly wings, as can be seen in Fig. 4.23. After 10 ESs a whole range of more or less distinct plateaus at different stress levels was measured (Fig. 4.22c). P2 is situated in the area separating the two “wings” that have been hot during the last load cycles. Maximum stresses around 200 MPa occur, which indicates plasticity and annealing effects. P1 and P3 are situated at the boundaries of the wings, where higher temperatures occurred than at P2. The compressive plateau indicates distinct phase transformations. The tensile level at 1.5 mm depth at P3 indicates profound plastic deformation in the preceding load cycles. P4 and P5 correspond to residual stress measurements at

4. CHARACTERIZATION OF DAMAGE

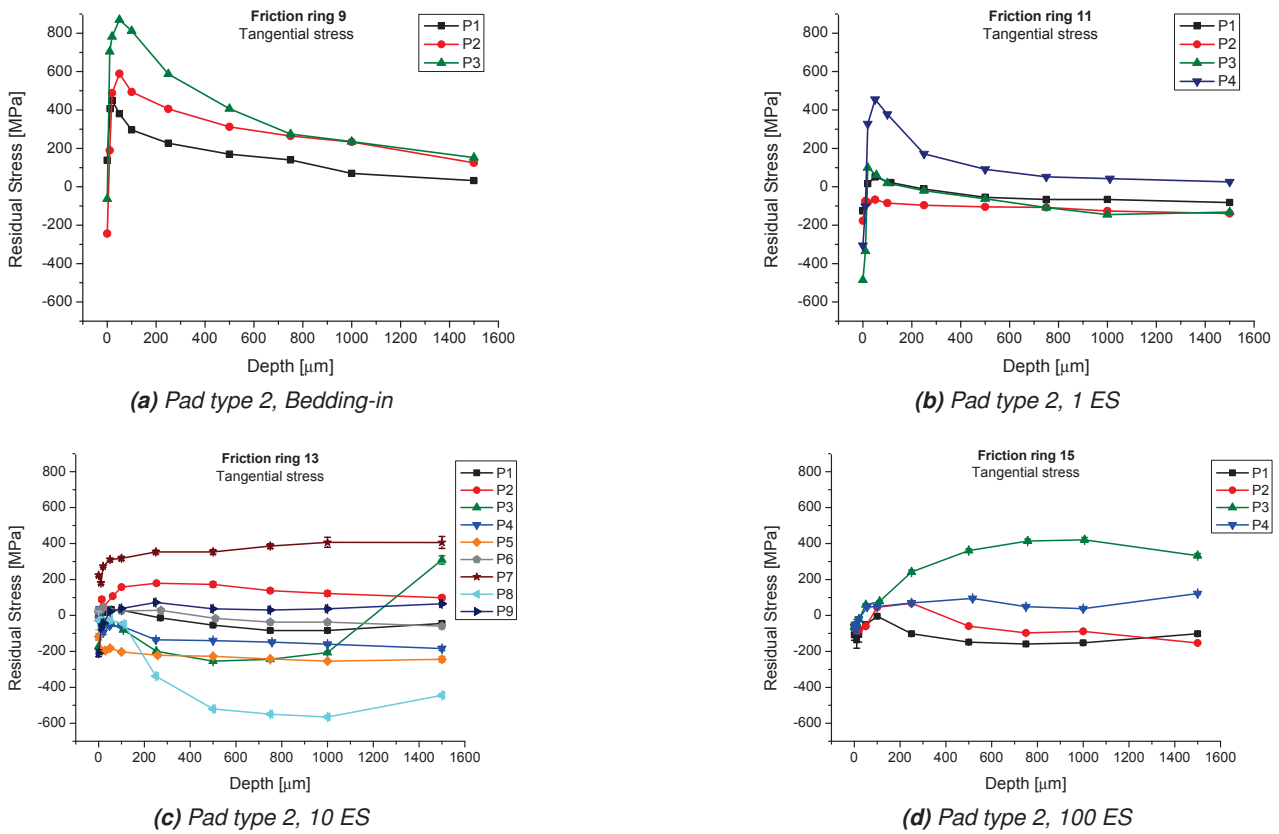


Figure 4.22: Overview of residual stress measurements carried out for pad type 2.

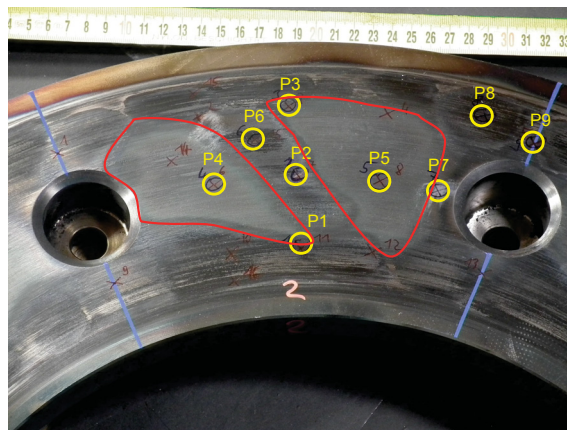


Figure 4.23: Positions for residual stress measurements on friction ring 13 (10 ES). Two hot patches that have occurred during the last of 10 ES are indicated.

the centers of the left and the right wing. Based on the distinct plateaus in the compressive regime it can be concluded that phase transformations reaching beyond the measured depth took place. P7 is situated in the wake of a mounting point and similar conclusions apply as before. P8 shows the stress evolution of region with a severe metallurgical transformations giving rise to compressive residual stresses of -550 MPa. Based on the surface pattern in Fig. 4.23 this occurred during brake cycles close to the end but not during the final one. The increased stress level at the surface indicates a moderate level of plastic deformation during the last braking.

- The results for friction ring 15 (100 ES) have, for the most part, been discussed above. However, Fig. 4.22d shows the stress evolution at an additional position P4 right beside P3. Fig. 4.24b shows a thermal image of a braking towards the end of the 100-stop-test. On the inner and the outer disk half hot spot patterns occur and corresponding positions can also be discerned from the wear pattern in Fig. 4.24a. P3 is situated in-between two spots, while 4 is situated directly on top of a spot. At P3 a significant tensile level occurs (420 MPa), while the stress evolution at P4 resembles a plateau at 100 MPa. This result is another illustration of the interrelation of thermal loading, residual stresses and the microstructure. The latter one will be further discussed in the subsequent section.

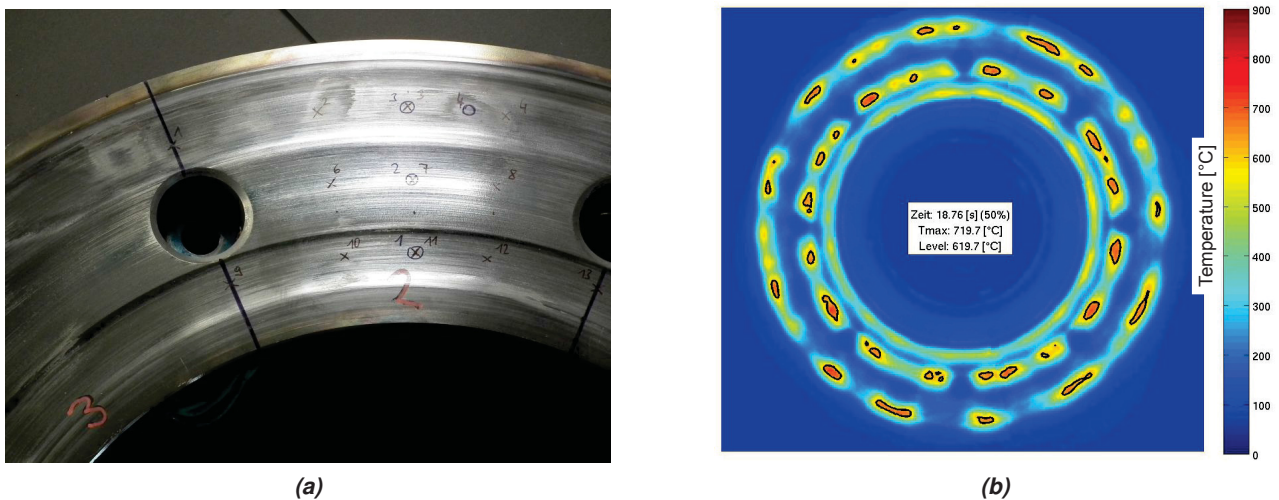


Figure 4.24: a) Positions for residual stress measurements on friction ring 13 (pad type 2, 10 ES), b) thermal pattern during brake application 89.

4.3.4 Distribution and evolution of the microstructure on and under the friction surface

The characterization of the principal mechanisms having influence on the development of the microstructure during braking are laid out in [65] and Section 4.3.1. The microstructural characterization of the brake disks tested in the scope of the present work draws on the findings of Chladil and Raninger summarized in [155]. At this point, the results will be embedded in the general framework of this work.

Fig. 4.25 and Fig. 4.26 provide an overview of the friction rings 5 (pad type 1, 10 ES) and 13 (pad type 2, 10 ES), which were exposed to 10 emergency stops. Furthermore, the two figures relate the investigated disk segments to the thermal loading conditions during the last cycle(s) and the resulting microstructure. As previously noted, the thermal loading for pad type 1 is higher on the inner disk half than on the outer one. The thermal images and the metallographic samples extracted in radial direction are conclusive. Phase transformations are pronounced at the inner half and moderate at the outer half. For the characterization of the microstructure a sample position deep into the transformation zone and with an orientation in tangential direction was selected. The position Pos1 is plotted in Fig. 4.27.

After 10 emergency brakings with pad type 2 the whole surface region has massively changed apart from areas in the wake of the mounting points. Due to the conspicuous wear pattern on friction ring 13, which directly correlates with thermal images, a series of metallographic samples was prepared along a line in

4. CHARACTERIZATION OF DAMAGE

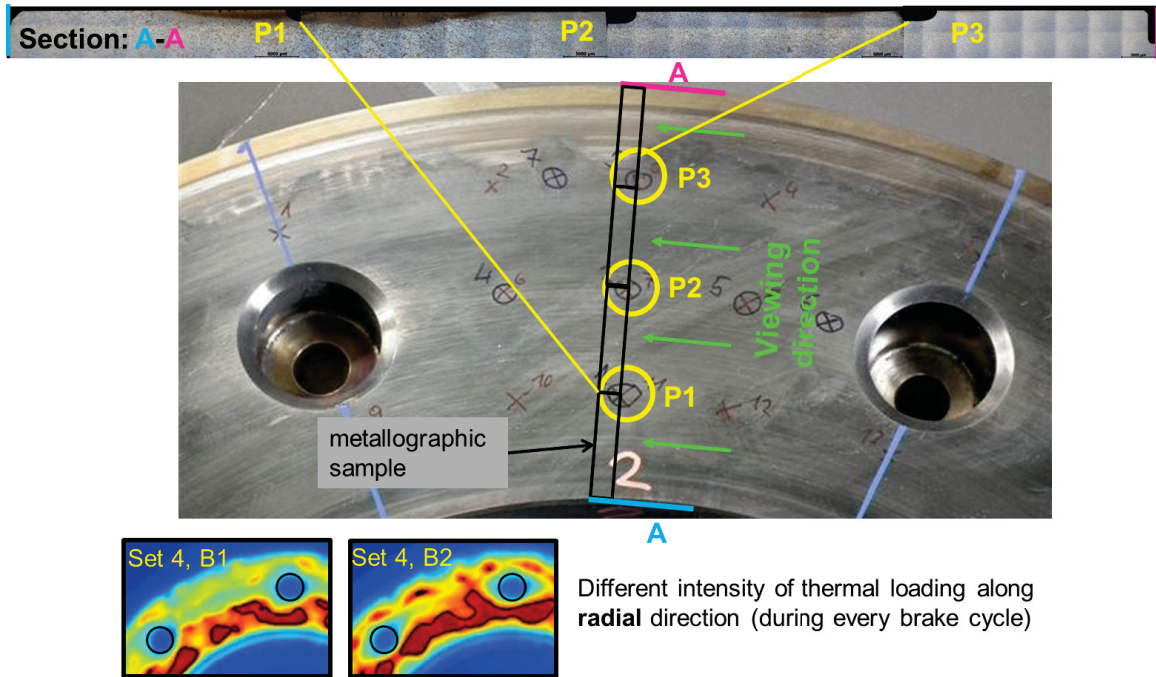


Figure 4.25: Overview of sample positions in a brake disk tested with pad type 1 (friction ring 5, 10 ES). Additionally, the figure shows the thermal loading and the microstructure in the section A-A.

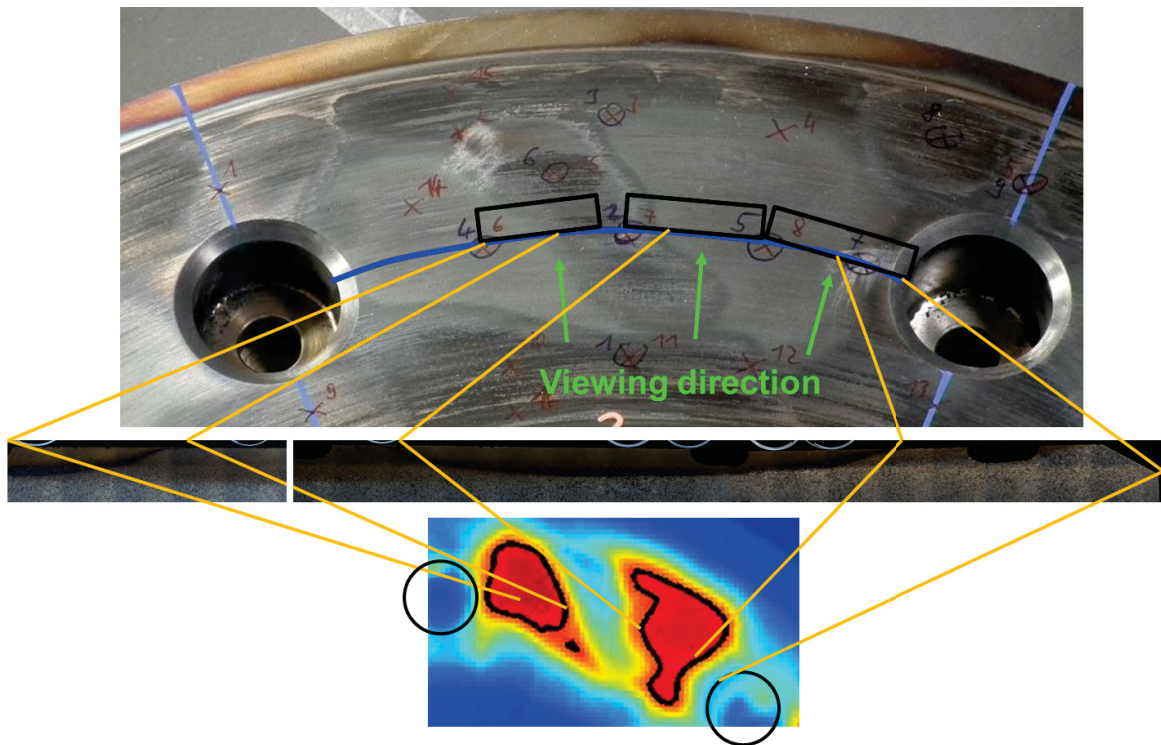


Figure 4.26: Overview of sample positions in a brake disk tested with pad type 2 (friction ring 13, 10 ES). Additionally, the figure shows the thermal loading and the microstructure. The yellow lines connect corresponding positions on the disk surface, the thermal image and the micrographs.

tangential direction. From the etching behavior and the shape of the transformed zones it can be derived which parts of the microstructure have transformed during the last ES and which ones have undergone transformations in precedent brake cycles. Again the thermal images are consistent with the transformed

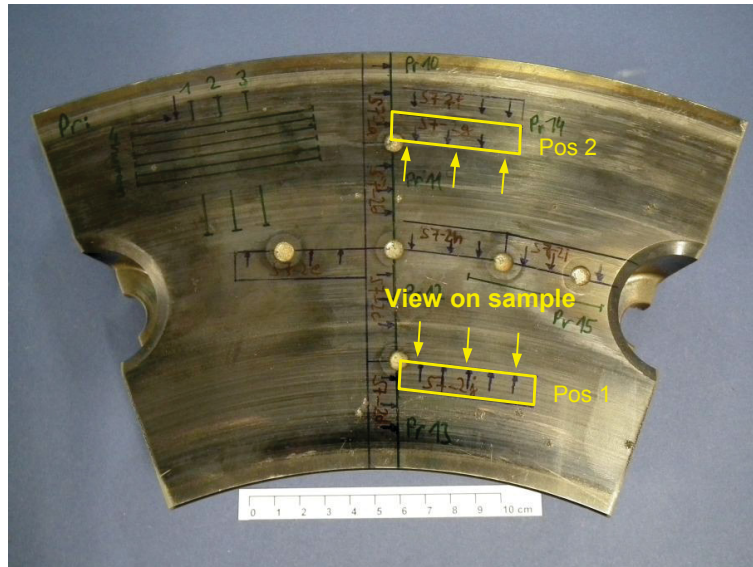


Figure 4.27: Sample positions selected for the base characterization of the microstructure.

regions and additionally with the wear pattern. Due to the fact that profound transformed regions are present at all radial positions the same reference position (Pos1) as in the case of pad type 1 was chosen. An additional position Pos2 further outside was selected for pad type 2. Other points of interest will be discussed after the base characterization.

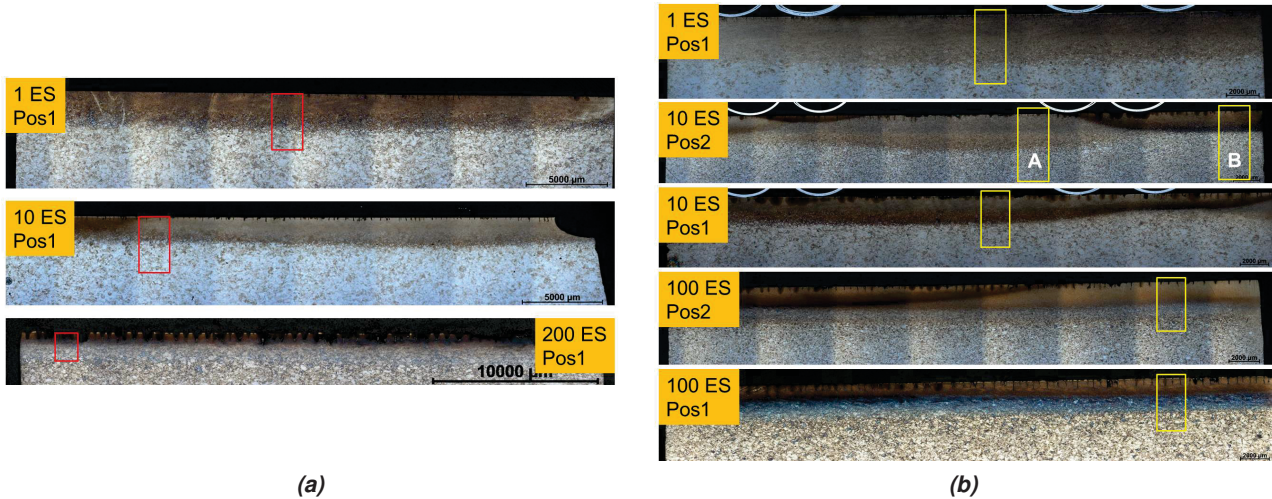


Figure 4.28: Representative metallographic samples taken from brake disks, which were tested with a) pad type 1 and b) pad type 2. The transformed regions in the upper part of each micrograph is clearly visible.

Fig. 4.28 shows a global view on the prepared metallographic specimens and the investigated positions. Based on these specimens the base microstructure, the individual transformed zones and their penetration depths are determined, as was already indicated in Fig. 4.9b (three zones). Since the discussion of the microstructure for one sample is representative for the others as well, only the specimen taken from friction 3 (1ES) at Pos1 will be discussed in detail.

Zone 3: The base microstructure of the tested disks (material A) is depicted in Fig. 4.31a-c). The fine, dispersed carbides (dark) in the ferrite matrix (white) in combination with the visible sheaves of parallel

4. CHARACTERIZATION OF DAMAGE

layers suggest a bainitic microstructure. The CCT in Fig. 4.29 indicates the quenching conditions after austenitization during manufacturing. Based on this information martensite can be expected as well, especially in the surface region of the virgin disk. Due to the subsequent annealing the martensite becomes tempered, though. The structure of tempered martensite is very close to bainite and the two can hardly be distinguished. During emergency braking the microstructure remains unaffected in this region.

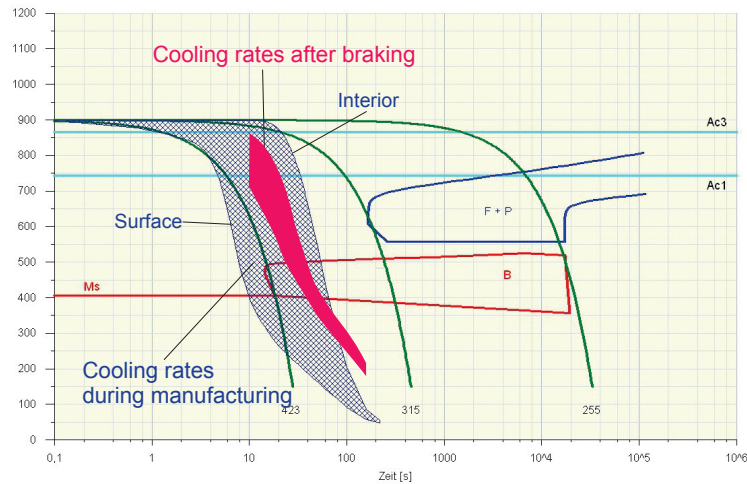


Figure 4.29: CCT for material A with cooling rates occurring during manufacturing and after emergency braking.

Zone 2: Fig. 4.31d-f) depicts regions closer to the friction surface, where temperatures in the two phase region have occurred. The temperature levels can be estimated from the TTA in Fig. 4.30. The relevant range of heating rates for emergency braking is indicated. The intersections with line 1) mark the temperature level where austenitization begins within the base microstructure ($\sim 760\text{ }^{\circ}\text{C}$). The intersections with line 2) indicate temperature levels where the base microstructure has completely transformed to austenite — although with an inhomogeneous carbon distribution. Obviously, this region has undergone temperatures between $\sim 755\text{ }^{\circ}\text{C}$ at the lower boundary and $\sim 815\text{ }^{\circ}\text{C}$ at the upper boundary of zone 2. Correspondingly, the size of the transformed patches increases from 0% up to 100%. The microstructure formed during cooling can be derived from Fig. 4.29. Besides the quenching conditions during manufacturing it also shows the range of cooling rates after braking (they already anticipate the simulation results). The cooling rates pass through the bainitic region of the CCT diagram and martensite formation is not indicated — friction martensite is a different issue. The maximum temperature at a hot patch decreases from the surface to greater depths. In-depth the temperatures become homogeneous very quickly and the cooling rates below the surface are also situated in the indicated region in Fig. 4.29. In the austenitized areas a similar microstructure as in the surface region can thus be expected. The microstructure depicted in Fig. 4.31d-f) occurs in the middle of zone 2 and consists of dark (strongly etched) and white (weakly etched) patches. It is likely that the white patches correspond to the bainitic base microstructure. In the dark areas austenite has formed, which has a higher solubility for carbon. Carbon diffused from the ferrite into the austenite and for this reason the sheaves — parallel layers of ferrite and carbides — disappear in the ferrite. The microstructure formed in the austenite during cooling is again bainitic but it is distinctly finer than the original one. Especially along the original grain boundaries of the austenite, formed during the industrial heat treatment after forging, very fine structures are visible. From the lower limit of zone 2 ($\sim 755\text{ }^{\circ}\text{C}$) to its upper limit ($\sim 815\text{ }^{\circ}\text{C}$) changes of the morphology of the microstructure take place. The portion of newly formed

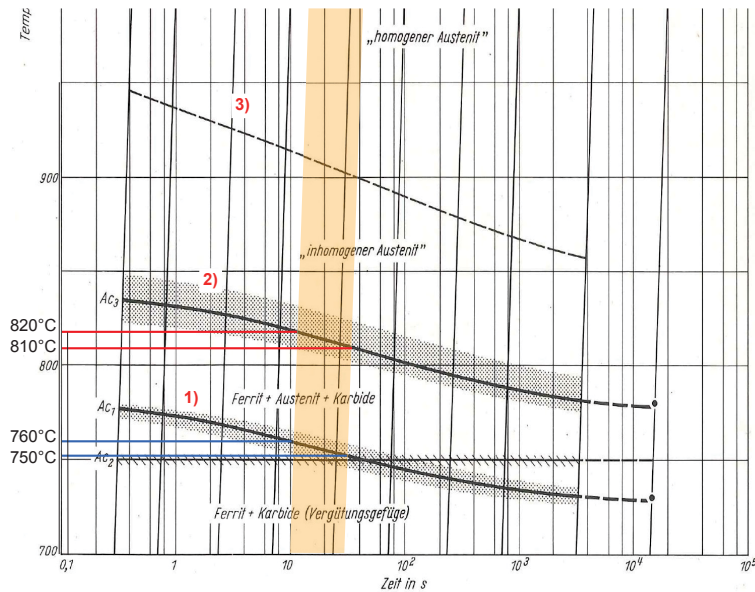


Figure 4.30: Relevant portion of continuous TTA diagram for 42CrMo4. The region of typical heating rates during emergency braking is indicated as well as the corresponding transformation temperatures.

bainite increases, while the one for the original bainite decreases. Close to the lower end of zone 2 only areas along the original grain boundaries have austenitized, since these are preferred nucleation sites. It is clearly visible that the newly formed structures are much finer than the original grains. Closer to the surface austenite has formed throughout the grains. In addition, the original bainite sheaves become more and more dissolved until they are not visible any more. At the upper limit of zone 2 the original microstructure has been completely consumed by newly formed fine bainite.

Zone 1: Fig. 4.31g-i) show the completely austenitized and quenched microstructure directly under the friction surface. The fineness of the structures makes it hard to distinguish between bainite and martensite in the optical microscope and in the scanning electron microscope (SEM). From the TTA and the CCT, however, two conclusions can be drawn. First, temperatures in excess of 815 °C must have prevailed for complete austenitization. Second, cooling conditions favoring the formation of bainite have occurred at the surface and also further below. Another conclusion becomes obvious when the sample from the 10-stop and the 200/100-stop tests are investigated. The phase transformations have occurred multiple times. For pad type 1 they occur predominantly on the inner disk half and for pad type 2 they wander on the friction surface, leaving transformed zones with different etching behavior.

Fig. 4.32 shows the measured penetration depth of zone 1 and zone 2 from the specimens in Fig. 4.28. Zone 2 reaches deepest after 1 emergency stop for both pad types. On the one hand this may be pure chance related to the sample position, on the other hand it may be caused by disk wear. If the contact conditions become more homogeneous after the first couple of brake cycles, wear can reduce the penetration depth of phase transformations, because the initial temperature levels are not obtained anymore. On average zone 1 reaches a depth of 860 μm for pad type 1 as opposed to 1160 μm for pad type 2. On average Zone 2 was found down to a depth of 2135 μm and 2575 μm , respectively. These observations confirm the conclusions drawn in Chapter 3, stating that pad type 2 causes higher temperatures on the friction surface. Furthermore, this information can be used to compare simulation results to

4. CHARACTERIZATION OF DAMAGE

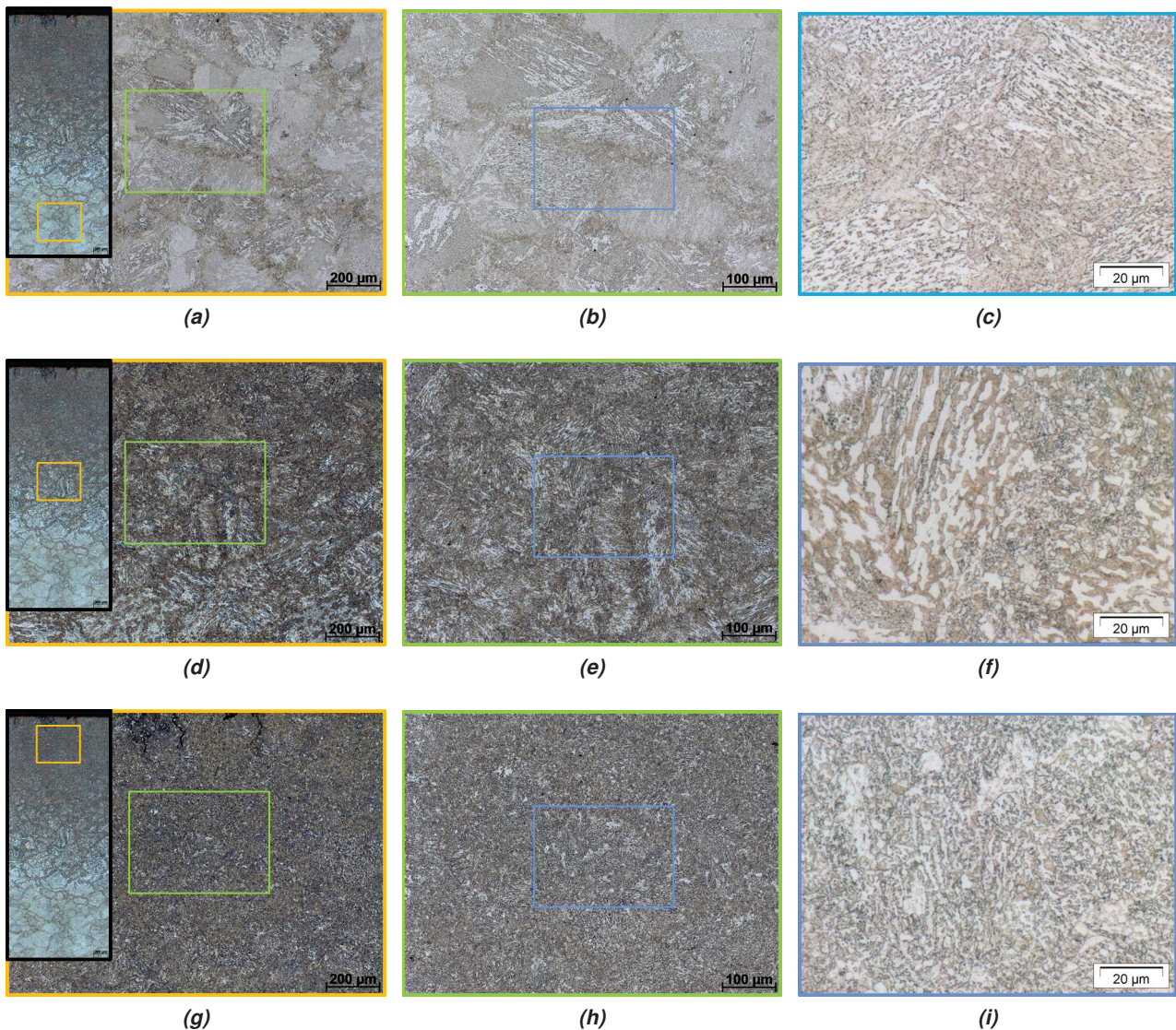


Figure 4.31: a-c) Zone 3: The base microstructure consists of bainite/tempered martensite, d-f) Zone 2: Quenched microstructure after austenitization in the two phase region, g-i) Zone 1: Quenched microstructure after full austenitization.

the real temperature levels that have occurred during braking.

Figures 4.33 and 4.34 relate the metallographic specimens depicted in Fig. 4.26 to a thermal image taken during the last of 10 brake cycles of the test run and to residual stress measurements at characteristic positions.

Pad type 2: The sample in Fig. 4.33 is situated in the left butterfly wing and stretches to the right into the vertical strip that has remained at low temperatures. As noted above, the whole surface region has undergone phase transformations but the thermal image, the wear pattern and the differently etched regions in the microstructure indicate that different regions have transformed in different load cycles. The residual stress measurement at position P4 is situated in the newly formed microstructure, while P2 corresponds to an area that has remained stable during the last braking. The effect on the residual stresses is in agreement with the conclusions from the previous discussion. At P4 the stresses are compressive reaching

4. CHARACTERIZATION OF DAMAGE

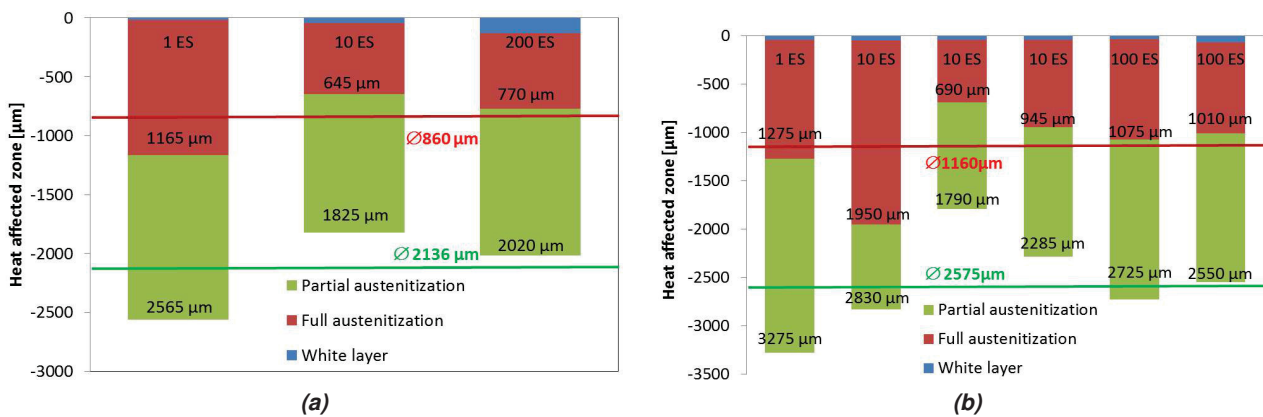


Figure 4.32: Depth of the transformed zones at characteristic positions (see Fig. 4.28) for a) pad type 1 and b) pad type 2. The average penetration depths of zone 1 and zone 2 are indicated by horizontal lines.

-180 MPa in tangential and -400 MPa in radial direction. The opposite situation applies at P2, where 65 MPa in radial and 180 MPa in tangential direction occur — the top 20-50 μm are a special case as already mentioned. The results indicate plastic deformation that has not been deleted by phase transformations. At greater depths, both stress evolutions decrease. This evolution is typical for cyclic plasticity but the slight compressive levels in radial direction point to influences from old phase transformations, which still show their effect.

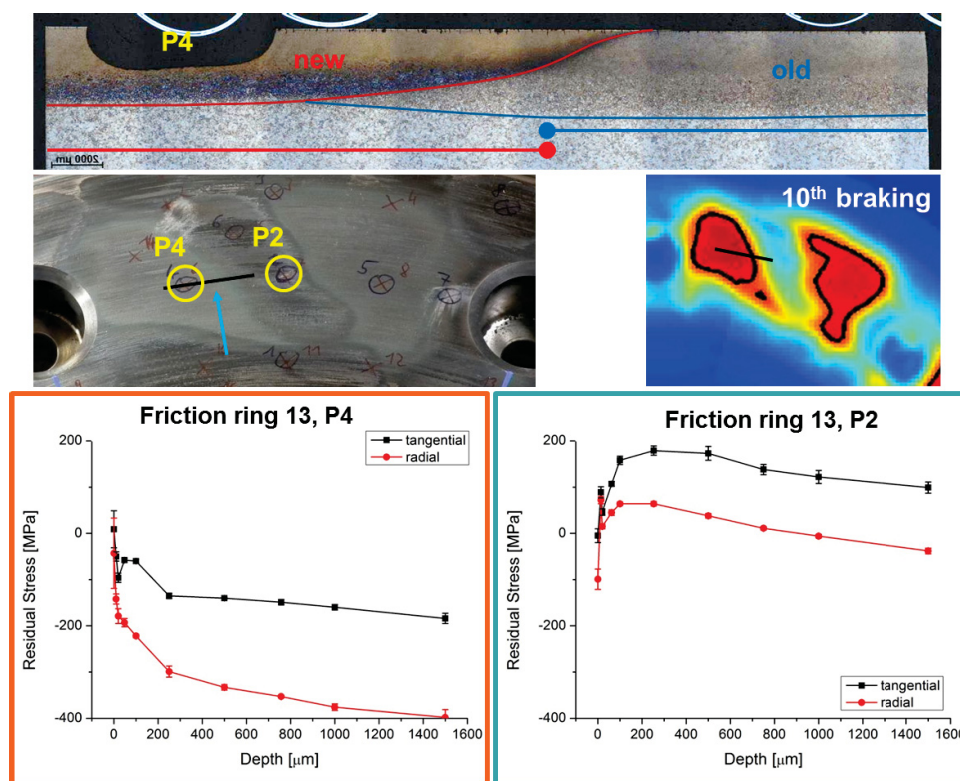


Figure 4.33: Comparison of thermal image, microstructure and residual stresses at position 1 after 10 ES with pad type 2.

Fig. 4.35 shows a specimen stretching from the cold strip into the right butterfly wing. Here, the stress evolution at P2 is compared to the measurement at P5 and a similar result as before is obtained. Fig. 4.33

4. CHARACTERIZATION OF DAMAGE

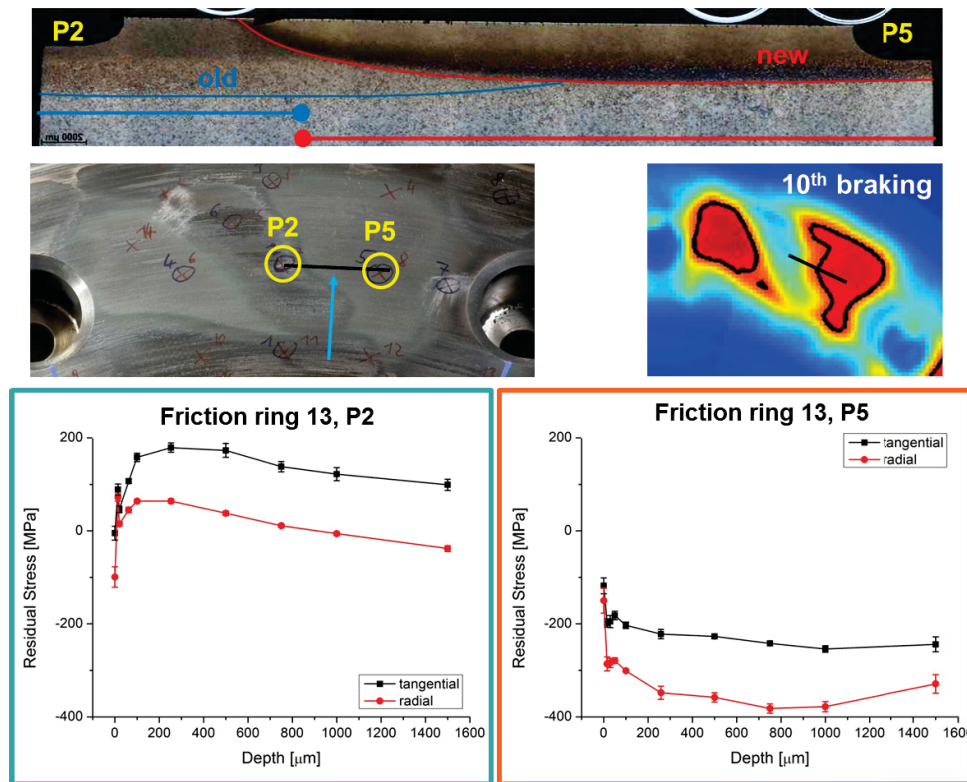


Figure 4.34: Comparison of thermal image, microstructure and residual stresses at **position 2** after 10 ES with **pad type 2**.

shows the results for a specimen extending from P5 to the mounting point on the right. As noted in Section 4.3.3 the wakes of the mounting points were mostly spared from extreme temperature levels (with both pad types). Measurement position P7 is situated close to a mounting point in a slightly transformed microstructure (2 phase region). The thermal images in Fig. 3.21 show that this region was higher loaded during the first brake cycles than later on and the phase transformations are thus deemed as “old”. The stress level at P7 after 10 ES is significantly higher than at the previous positions and the scale of the diagrams was thus changed. Tensile stresses up to 400 MPa in tangential and up to 650 MPa in radial direction are present at 1.5 mm depth. Annealing effects have lowered the stress levels closer to the surface.

Pad type 1: Fig. 4.36 illustrates the situation for a friction ring exposed to 10 ES with pad type 1. The position of the metallographic sample is plotted in Fig. 4.25 (second from the bottom) and captures the region from the hot ring to the mean radius. Apart from the near surface region both measurement positions P1 and P2 show tensile residual stresses. Since P1 is directly situated inside the deep transformation zone underneath the hot ring, tensile stresses can lead to two different conclusions. Either the profound transformations occurred only during the first braking, leading to more focused loading at the ring than later on (Fig. 3.20) or incidentally a patch has been picked for measuring that stayed rather cold during the last braking. The situation at position P2 is similar but distinctly higher tensile stresses have formed. The results show that processes corresponding to the case of pad type 2 have taken place but in a more systematic way. While for pad type 2 hot patches and phase transformations move on a global scale from cycle to cycle, the situation is globally very stable for pad type 1.

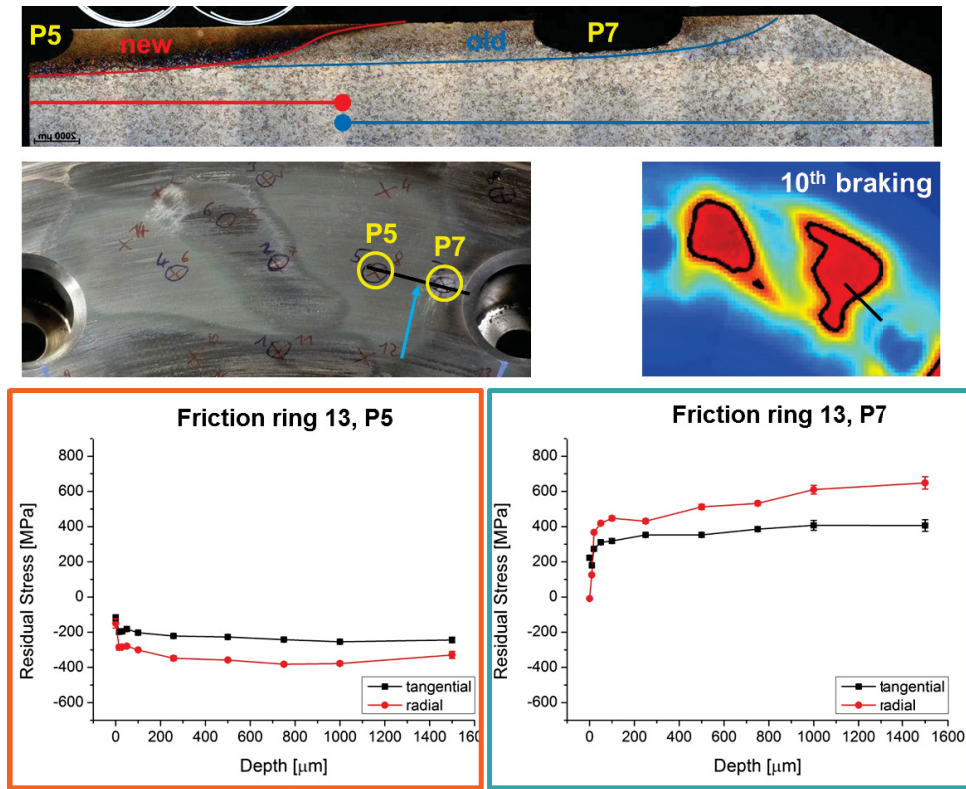


Figure 4.35: Comparison of thermal image, microstructure and residual stresses at **position 3** after 10 ES with **pad type 2**.

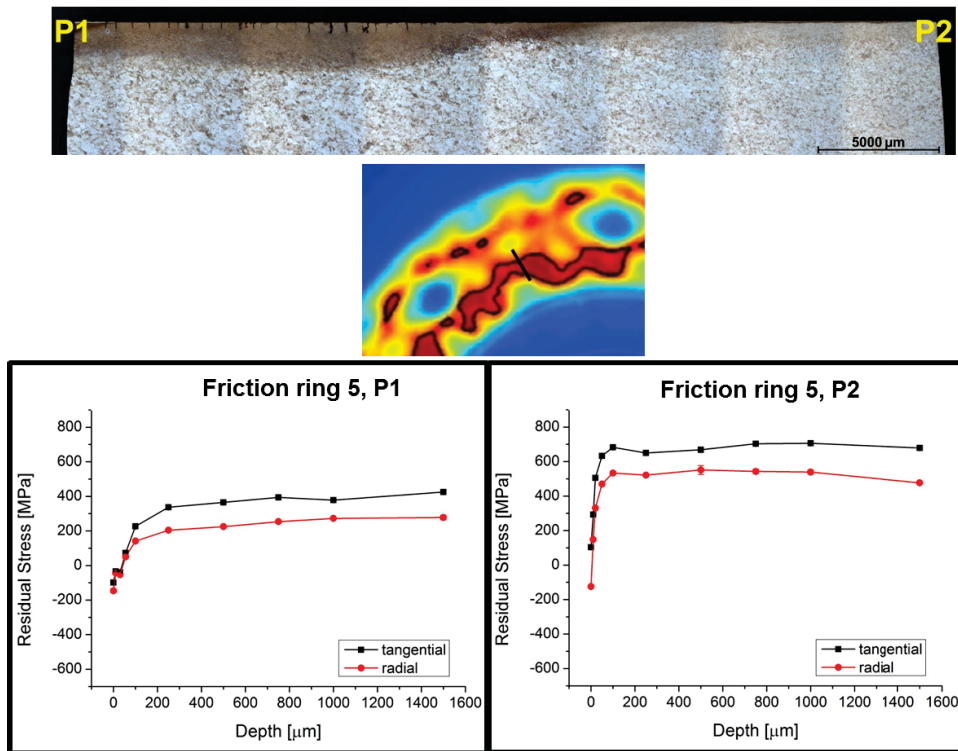


Figure 4.36: Comparison of thermal image, microstructure and residual stresses after 10 ES with **pad type 1**.

The formation of a network of surface cracks was observed for both pad types. Some cracks are

4. CHARACTERIZATION OF DAMAGE

initiated during the first ES and others emerge later forming a network of surface cracks that is engulfed by transformed microstructure. A typical state after 200/100 ES is depicted in Fig. 4.37a and Fig. 4.37b. The cracks do not exceed the depth of the transformed region but stay within the fully austenitized region. The observed crack lengths are mostly below the depth for zone 1 listed in Fig. 4.32. The average crack length in Fig. 4.37a is about 450-500 μm and in Fig. 4.37b about 450 μm .

It is very likely that the continuous changes of the volume of transformed regions have contributed largely to the initiation of cracks. This explains why they are predominantly situated in zone 1. Furthermore, phase transformations delete tensile residual stresses and evoke compressive stress levels, which explains why the cracks did not grow out of the transformed zones. They are initiated by the cyclic changes in volume but they are not viable in the residual stress field. Since the spacing in the network is similar or even smaller than the predominant crack lengths, strong crack shielding effects occur. The residual stresses are relieved because the cracks open and ΔK_{th} is not reached at the crack tips. The formation of crack networks is another explanation for the reduced tensile residual stresses in the surface region, at least after 10 and 200/100 ES.

Concluding, no macroscopic cracks growing into the bulk of the disk have been observed, neither for pad type 1 nor for pad type 2.

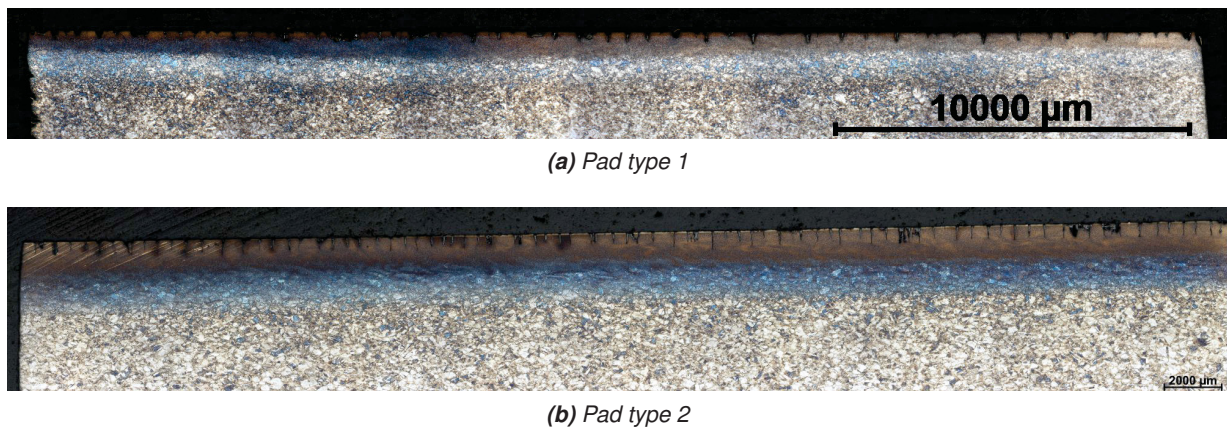


Figure 4.37: Characteristic crack arrays found in disks exposed to 200/100 ES with pad type 1 and pad type 2, respectively.

There is one danger, however, at positions where a hot spot occurs in an early brake cycle but not any more thereafter due to a homogenization of the contact conditions. A couple of cracks can be initiated with a rather large spacing. During later brake cycles, when the hot spot has moved to another position, residual stresses build up and the cracks may propagate without any shielding effects that could stop them. From the point of view of simulation techniques it is reasonable sense to investigate the propagation rates of single cracks in the residual stress field that forms in the absence of metallurgical transformations. The situation represents the most conservative case, which can be used as a guideline for design purposes. The laborious investigations of crack propagation in networks, as outlined in [33; 34] is thus redundant, since crack propagation in this case is always significantly slower than in the most conservative case, which usually determines the end of the life time. One step in the verification strategy of the simulation is to verify that all measured residual stress distributions are enveloped by the simulated stress field, i.e. the simulations assume a worst case scenario. This way, it can be made sure that the computed crack propagation rates are not underestimated.

4.3.5 Damage in brake disks tested on the scaled test rig

As noted in Section 3.4.5 high energy braking for material A on a scaled test rig caused classical hot spotting as opposed to average energy levels for material B, where homogeneous temperature distributions were found. Fig. 4.38 compares a characteristic thermal image to a sampling plan for material A for a stress measurement and metallographic specimens.

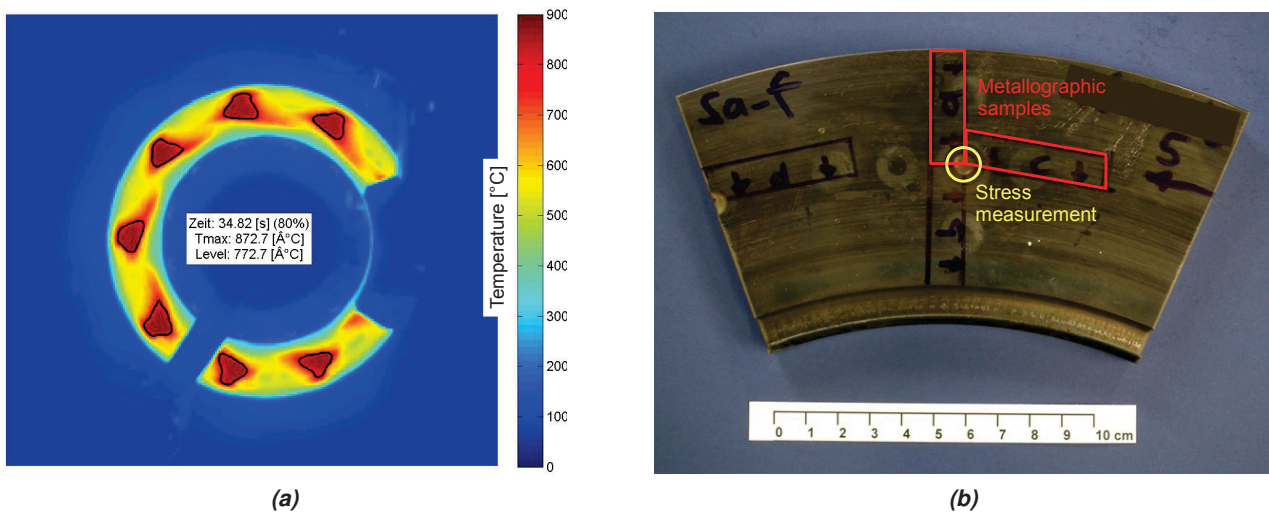


Figure 4.38: a) Thermal loading during test run on scaled test rig (material A) , b) overview of sample positions in the scaled brake disk.

Fig. 4.39a depicts the corresponding microstructure in radial and tangential direction. A transformed region with a distinct maximum depth and limited dimensions can be discerned in both directions. This result indicates that a site corresponding to one of the 9 hot spots in Fig. 4.38a was found. Due to the finite dimensions of the transformed zone it can be concluded that in contrast to the full scale tests, the hot patches formed during scaled braking were stationary. Corresponding to the full scale tests, cracks are

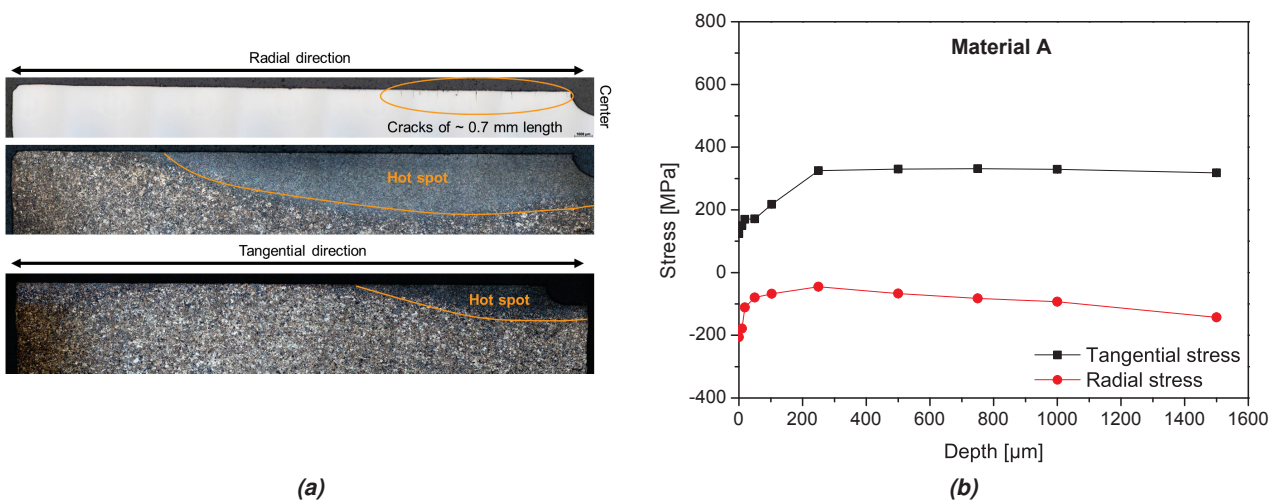


Figure 4.39: a) Microstructure around stationary hot spot in scaled brake disk made of material A, b) residual stresses.

visible in the transformed region but they are completely confined within it. The cracks are thus limited

4. CHARACTERIZATION OF DAMAGE

in-depth as well as in lateral direction by the dimensions of the hot spot. In contrast to [62; 73] no cracks parallel to the surfaces were found underneath the hot spot.

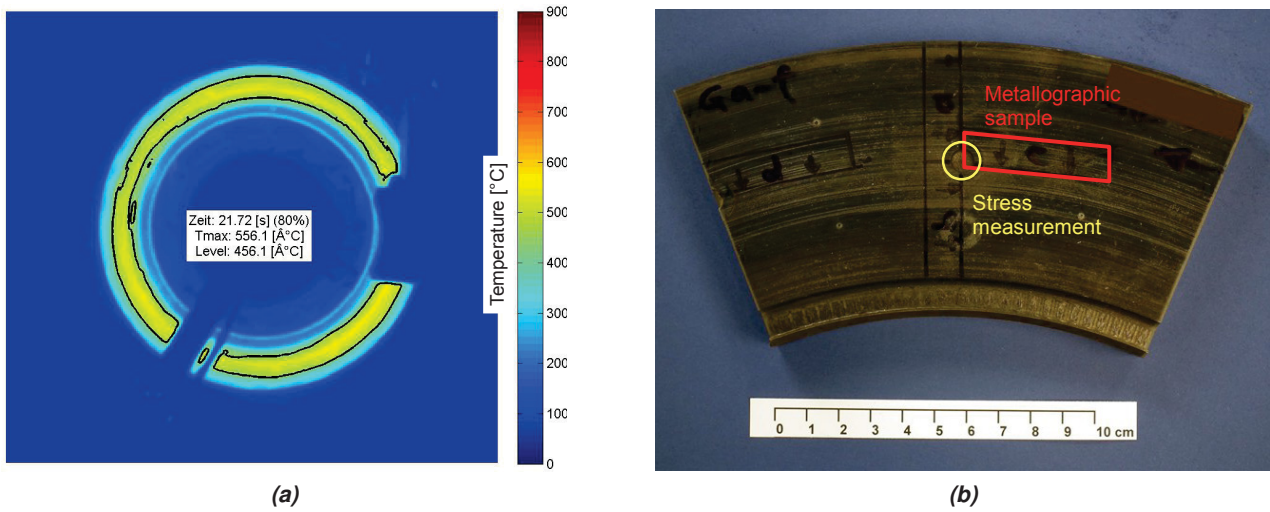


Figure 4.40: a) Thermal loading during test run on scaled test rig, b) overview of sample positions in the scaled brake disk made of material B.

The residual stress measurement has been performed inside the transformed zone. The distribution in radial direction is in the compressive regime, as expected due to the stationary position of phase transformations. In tangential direction, however, tensile stresses of about 320 MPa have formed. This indicates a global mechanism generating a tensile stress everywhere along the circumference.

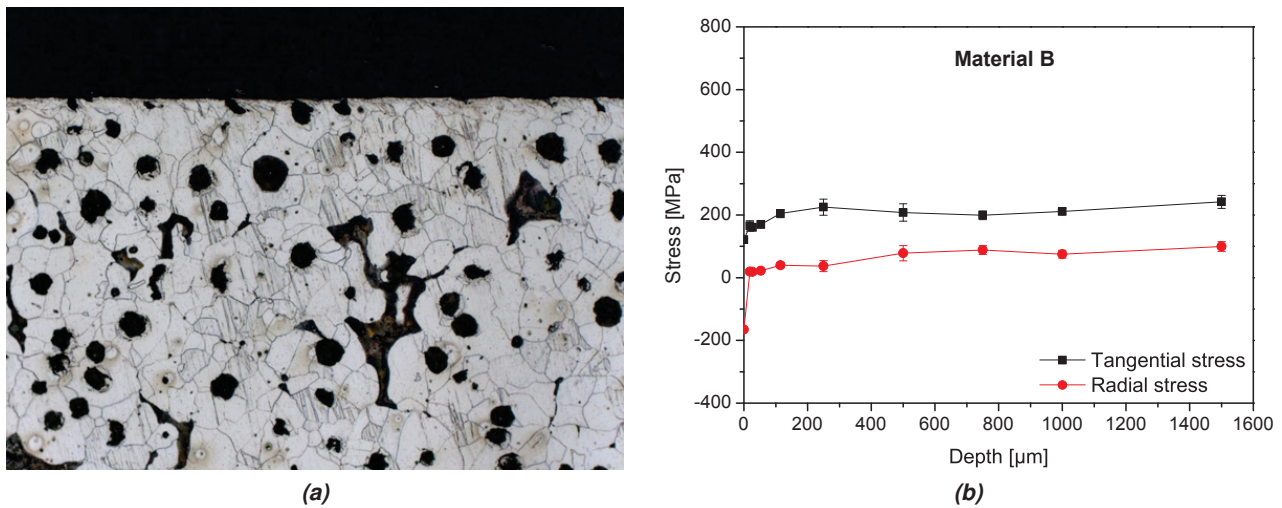


Figure 4.41: a) Microstructure around stationary hot spot in scaled brake disk made of material B. The ferritic-pearlitic base microstructure of the ductile cast iron is visible but no metallurgical transformations from braking, b) residual stresses.

Fig. 4.40 shows the loading situation and the sampling points for material B, which was less intensely loaded. Apart from the region directly under the friction surface ($\approx 10\mu\text{m}$), no changes of the microstructure and no cracks are visible (Fig. 4.41a). This observation also holds for other positions in the disk, which corresponds to the homogeneous thermal distribution in the thermal images. A moderate level of tensile residual stresses was measured, 100 MPa in radial and 240 MPa in tangential direction. Cyclic plastic

deformation has clearly occurred.

Given the vast variation of the damage observed in the full scale brake disks the results from scaled tests provide very limited information. A direct comparison is not possible but preliminary investigations of different combinations of pad material, disk material and load scenario are reasonable, as long as scaled disk geometries are available.

4.3.6 Discussion of residual stress formation in view of TMF

In analogy to the discussion at the end of Chapter 3, the findings of this chapter are represented in the global context in the form of an Ashby map. Fig. 4.42 shows an Ashby map for a CrMoV steel, taken as an approximation for material A. It contains a loading path starting from a residual stress state in the tensile regime, which is due to cyclic plasticity in the previous cycles without phase transformations. In accordance with the previous discussions, the σ - T path changes from tensile to compressive stresses as the temperature increases. In contrast to the representation in Fig. 3.32 the σ - T path splits into two alternative evolutions, which could both apply for brakings with pad type 1 or pad type 2. One branch

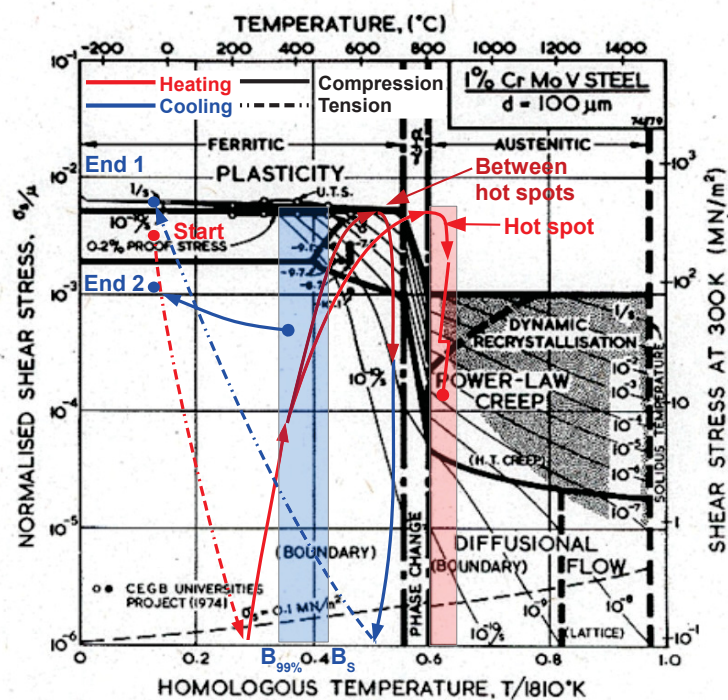


Figure 4.42: Schematic σ - T paths during TF/TMF loading at a hot spot and between hot spots.

loosely relates to the loading situation at a hot spot and the other one to a position where lower maximum temperatures prevail, e.g. between hot spots. Section 2.3 and Section 3.4.6 have already elaborated on the latter σ - T path and the corresponding residual stress formation. Important questions on the impact of phase transformations on residual stresses were discussed in this chapter and they can, to some extent, be summarized by the σ - T path in Fig. 4.42 that reaches the austenitic region. A phase transformation occurs according to Fig. 4.30 and during cooling again a phase transformation occurs between the temperatures B_S and $B_{99\%}$ according to Fig. 4.29. In contrast to the first σ - T path, a compressive residual stress occurs, which is related to volume changes during the phase transformations. Unfortunately, the σ - T

4. CHARACTERIZATION OF DAMAGE

evolution after the first transformation cannot be represented for the following reasons:

- The transformation behavior depends on the external loading.
- The local stress state becomes so complicated that it cannot be plotted in Fig. 4.42. The stress state is likely to exhibit a high hydrostatic component and circumferential stresses around the hot spot.
- The hydrostatic component changes the deformation behavior.
- The main loading direction is not necessarily in tangential direction anymore. Hence, it is not obvious if the stress state, represented by a single scalar σ_{eq} , is tensile or compressive.
- Simulations with complex material models describing both the plasticity and the development of the microstructure are necessary to understand the involved mechanisms.

This example is an illustration of the complex processes that take place at the friction surface during high energy braking. The situation is further complicated by the fact that in the subsequent brake cycle both σ - T paths might occur starting from either of the two end points indicated in Fig. 4.42. What happens depends on the evolution of the thermal distribution with each new brake cycle and the migration of hot regions.

Chapter 5

Modeling of the TMF behavior of brake disks

5.1 General considerations and motivation

The aim of the modeling part is a description of the thermomechanical fatigue loading of brake disks that is applicable in 1) the design process of brake disks and 2) friction brake systems. Furthermore, the established concepts should prepare the way for 3) an online health monitoring system that gives a signal during service when a critical state has been achieved. The models should yield qualitative results in a wide parameter range but also quantitative results in a narrower range of material and process parameters. The three application ranges mentioned before can be further detailed:

- Disk design: A whole range of modifications and alternatives are possible for the design of railway brake disks. At the beginning of the design process, however, it is often not clear, what a weight saving design, split-disk design or a design with alternative cooling ribs will mean in terms of fatigue life. A profound simulation tool establishes a link between the relevant design, material, loading parameters, etc. and fatigue life, both in view of crack initiation and crack propagation. This way, a simulation tool can greatly support the design process.
- Definition of the brake blending: Each train uses multiple brake systems and the friction brake is one of them. For various trains (especially multiple-unit trains) even the friction brake system is subdivided into axle mounted and wheel mounted brake disks and additionally, wheel mounted brake disks with variable diameters may be used on the same train type (e.g. at the wheels of trailer and motor bogies). When the brake system is planned certain standards must be met. Nevertheless, many variables remain, in the case of the friction brake system the total number of brake disks, the configuration of different disk types on the train, the material and the distribution of braking force/thermal input into the different disk sets. Moreover, the blending of the different brake systems outlined in Chapter 1 must be predefined in a sensible and safe way for the relevant brake scenarios for the specific train on a specific track. Again, a simulation tool that takes into account all the necessary influences is a valuable support.
- Online health monitoring: Currently brake disks are replaced based on wear or due to a predefined

schedule. Usually, the impact of fatigue damage is only roughly considered in the design process and mostly in terms of allowable maximum temperatures that have been empirically determined. The appearance of macroscopic cracks during service is an undesirable event and usually necessitates disk replacement. The standard DIN 27200, however, regulates the criteria for the replacement of wheel mounted railway brake disks. This standard allows the occurrence of surface cracks as well as cracks that reach the reverse side in a limited area of the cross section. In the case of specific crack lengths and through-thickness cracks spanning the whole cross-section, the disk must be changed. Critical situations can be avoided by proper disk design as previously mentioned. Since real in-service conditions can deviate from the assumptions during design, adding an online monitoring system is advisable. On the one hand it can indicate necessary disk replacement before the service interval is over and on the other hand it can be used for the assessment whether the disk can be used for another service interval or not.

Proper simulation tools are able to assist in the design process. They are based on suitable experiments and can capture the governing mechanisms without having to take into account all the complex processes identified in Chapter 3 and Chapter 4 (metallurgical transformations, which interact with the formation of residual stresses). The simulations have a certain range of validity and this range must be a predefined target at the outset and a verified fact at the end of the modeling chain. The modeling strategy is based on the following reasoning:

- The description of the local temperature evolution on the friction surface can be modeled with different techniques, which are suitable in different contexts.
 - Qualitative description of TMF behavior: For the design process it is often sufficient to have fast qualitative simulation results at hand. They are supposed to show whether the fatigue life will increase or decrease, severely or at a moderate level. The material behavior and the global loading conditions must be captured for this purpose but general simplifications can be made. The main simplification is the assumption of a uniform dissipation of the generated frictional heat on the surface.
 - Quantitative description of TMF behavior: The precision of the predicted service life can be greatly improved by taking into account the local thermal distribution, which has been characterized in detail in Chapter 3. For this purpose, a range of possible modeling strategies can be used:

One example is the computation of thermo-elastic instabilities according to e.g. [57; 156]. This method can be applied for the efficient prediction of the formation of hot spots and hot bands in dependence of multiple parameters, such as the thermal conductivity and thermal expansion of the brake disk and the pad stiffness. However, the concept yields results on the formation of thermal surface gradients but only qualitative results on the temperatures. Furthermore, it does not take into account plastic deformation. Another strategy is the thermomechanical modeling of the braking process with or without disk-pad interaction, as presented e.g. in [3; 59; 83; 85]. With these methods the thermal input is introduced in a non-uniform manner in order to obtain quantitative results on the damage behavior. The non-uniform nature is either established by a simplified and predefined input of thermal energy or by the modeling of the disk-pad interaction.

All of these works were carried out for axle mounted railway brake disks. The present work investigates wheel mounted brake disks used in combination with two specific brake pads. The resulting thermal distributions on the friction surface are not known in the literature. For this purpose a specific test rig program has been carried out and analyzed within the scope of this work as illustrated in Chapter 3. The types of thermal surface gradients are thus known and the thermal history over several brake cycles is available in the form of processed thermal image data. Besides uniform loading, this work uses thermal image mappings in order to obtain quantitative results for service life predictions.

- TMF modeling is highly dependent on suitable material data for 1) the thermophysical properties, 2) the inelastic deformation behavior and 3) the damage behavior. In general, it is very laborious and costly to obtain all the three necessary data sets. This work aims at a thermomechanical modeling scheme, which is accompanied by a very comprehensive experimental program.
- The influence of metallurgical transformations is neglected on the basis of three assumptions.
 - First, the modeling of phase transformations in conjunction with cyclic viscoplasticity is a field of research on its own and it cannot be treated in this work.
 - Second, the phase transformations do not increase but decrease residual stresses. This way, they oppose the effect of cyclic plasticity, which cause detrimental tensile residual stresses. When phase transformations are neglected, life time predictions based on crack growth are conservative. For this reason, a modeling strategy without considering metallurgical transformations is an admissible approach.
 - Phase transformations can cause crack initiation. This mechanism is different and also faster than the one of classical fatigue as outlined in Chapter 2. The criticality of the initiated cracks can be assessed by fracture mechanical analyses of the viability and the propagation rates of cracks. For a conservative but reasonable assessment the cracks are introduced in the high tensile stress field formed by cyclic plasticity. This corresponds to the critical case where hot spots initiate cracks in early cycles but cyclic plasticity prevails in later cycles causing tensile residual stresses.

5.2 Modeling strategies

This section elaborates on the modeling of the TMF loading of brake disks. The strategy follows the representation in Fig. 5.1, which has already been introduced in Chapter 1. The blue boxes represent the cornerstones of the modeling carried out with the commercial finite element package Abaqus [45]. The orange boxes refer to the results obtained from the specific modeling stages, which will be presented in Chapter 6. The red box refers to the analysis of the loading conditions in Chapter 3, which are used for the thermal image mapping. The green box refers to the damage analysis presented in Chapter 4. The diagram further indicates that the results obtained from Chapter 3 and Chapter 4 will be used for verification purposes.

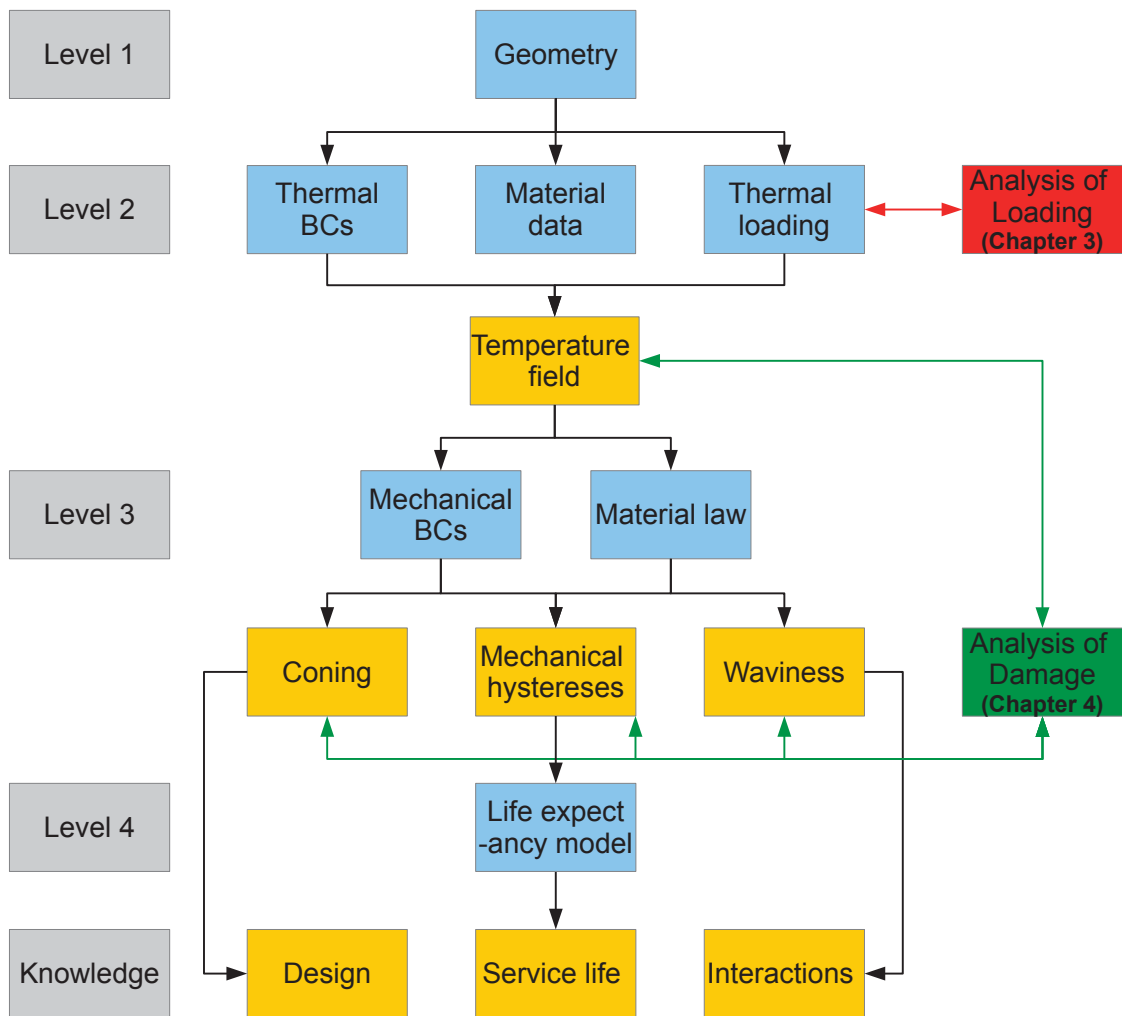


Figure 5.1: Modeling strategy for the service life prediction of a brake disk exposed to TF/TMF

5.2.1 Geometry

5.2.1.1 Selection of a representative geometrical model

Section 5.2.1.1 illustrates the wheel-disk assembly of the wheel mounted brake disk in focus. Additional detailed views are given in Chapter 1. Due to the eight mounting positions certain symmetries are present in the geometry which can be used to reduce the model size for the subsequent FE-calculations. Intuitively a 16-fold symmetry would be assumed to apply for the concerned brake disk as long as only the top view is considered. The whole disk could be generated by mirroring-, copying- and rotation-operations. By mirroring, one eighth of the disk is obtained and 7 copy-operations followed by proper rotation of the resulting parts yields the whole disk. Fig. 5.2 illustrates the rear side with the cooling fins and the regions that get into contact with the wheel. From this view it is apparent that every other mounting point is realized in a different manner than the others. Due to this feature the disk is of 8-fold symmetry. Since the second order waviness has low influence on the local loading, one eighth of the disk must be modeled to capture all geometric information. The meshed geometry is depicted in Fig. 5.2d) and e). It can be seen that the mesh is divided into two main regions, viz. the friction surface and the region of the cooling fins. The former

one is meshed with hexahedral (or brick) elements because on the one hand they offer a higher accuracy compared to comparable tetrahedral elements and on the other hand they can be used for structured meshes. This is important for the precise modeling of the heat flow whose principal orientation is in thickness direction. For this purpose the element size in thickness direction is varied from 0.27 mm at the surface to 1.64 mm at 12.5 mm depth where the zone of brick elements end. The curved structure at the rear side, especially at the cooling fins, necessitates the use of tetrahedral elements, unless the geometry of the fins is simplified. Since studies on the global deformation behavior are carried out, the original shape of the fins is maintained and tetrahedral elements are used. Additionally to the two previously mentioned main regions the sections at the mounting points are meshed with brick elements.

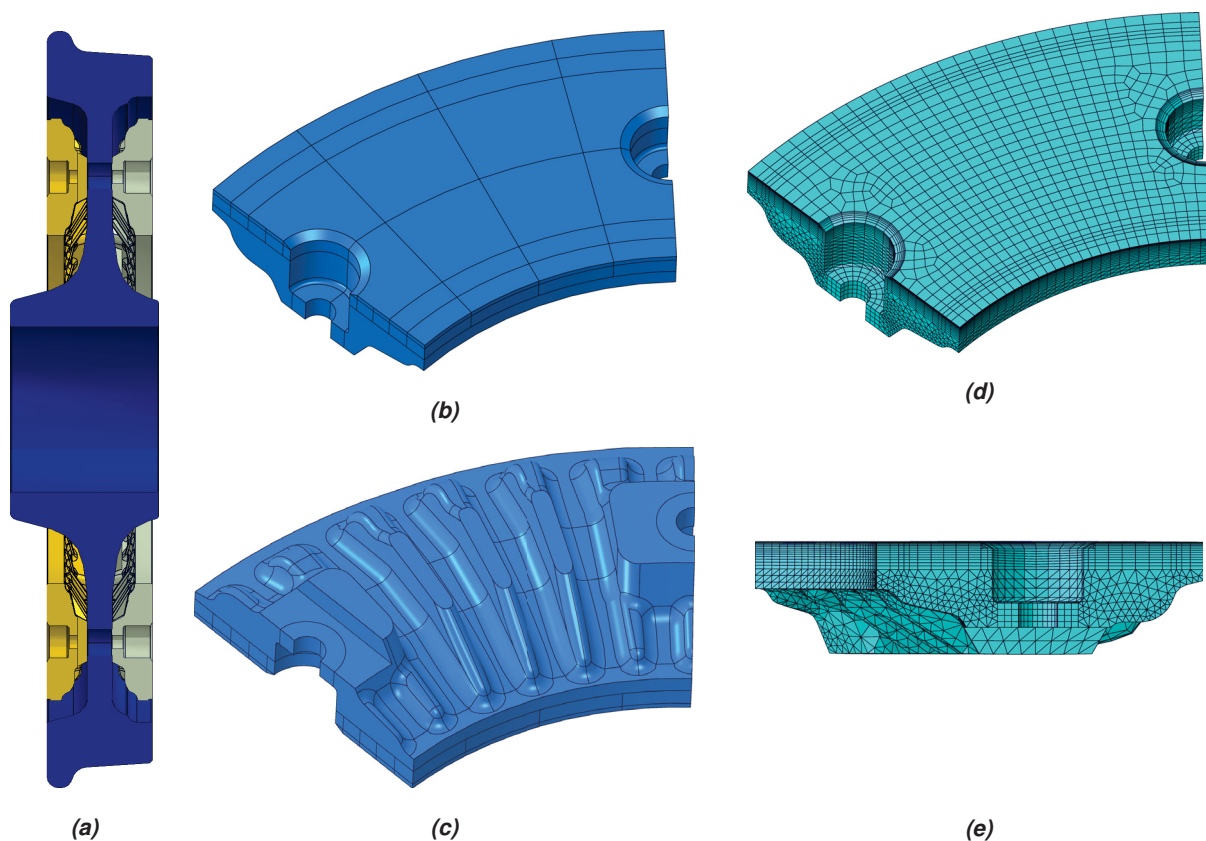


Figure 5.2: a) Overview wheel-disk, b) FE-geometry top view, c) FE-geometry bottom view, d) FE-mesh top view, e) FE-mesh front view

5.2.1.2 Choice of element type

Thermal model: For the thermal model a linear element formulation in both mesh regions is chosen. The corresponding element specifications are *C3D8R* and *C3D4* and a tie connection is established between them. They are explained in detail in [45]. These element types are preferred over quadratic elements, which tend yield non-physical, oscillating solutions. This is especially critical for the thermal image mapping.

Mechanical model: Table 5.1 lists the element formulations, which are considered for the mechanical part of the TMF modeling. They are used for a range of preliminary studies in order to decide on a

5. MODELING

sufficiently precise and time efficient element formulation for the simulations carried out in this work. All hexahedral elements apart from the incompatible modes elements (*C3D8I*) are use reduced integration to avoid an overly stiff bending behavior. *C3D8I* are special elements in Abaqus for the efficient but precise computation of bending problems. Fig. 5.3 summarizes the results for transient and static disk coning as well as for an evaluation of crack initiation life for different element types in the hexahedral and tetrahedral region. The solutions for quadratic elements are taken as reference values. Static coning that

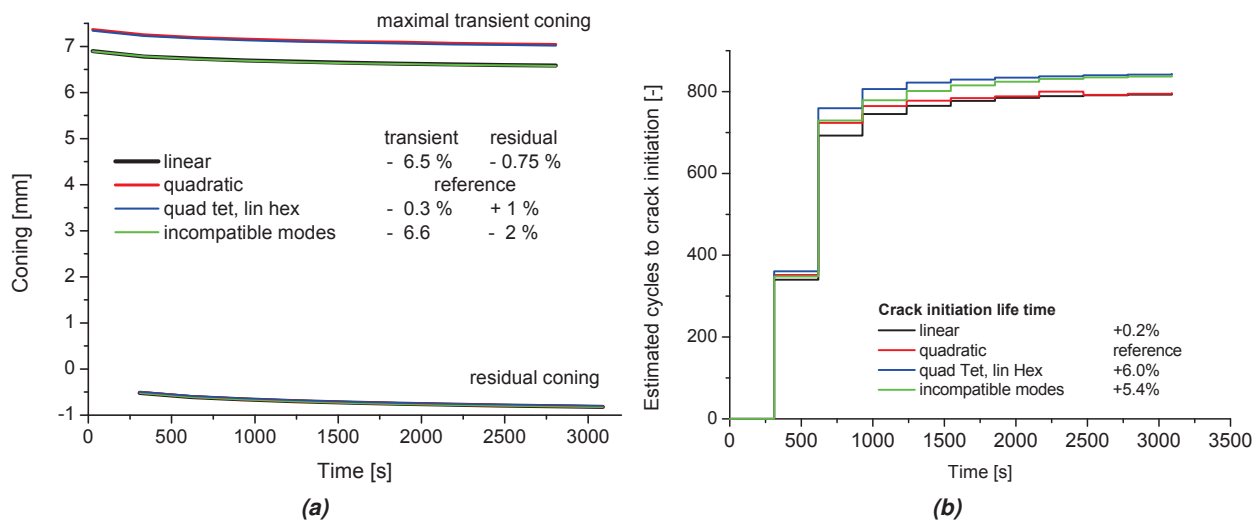


Figure 5.3: a) Evolution of disk coning and b) estimated crack initiation life.

remains after the brake sequence is a global measure for the accumulated plastic deformation in the disk. The linear element formulation yields the closest match to the quadratic one. For the maximal transient coning during braking the combination of *C3D8R* and *C3D10* is closest to the reference value. In view of life time estimation the combination of *C3D8R* and *C3D4*, both using linear shape functions, yields only 0.2% deviation after the 10 brake cycles, which are necessary for a stabilization of the σ - ϵ field. Before stabilization, the linear formulation is a conservative approximation.

Table 5.1: Computation times for 10 uniform emergency brakes with different element formulations [45].

| Description | Element type hexahedral region | Element type tetrahedral region | Computation time [h] | Factor |
|---------------------------------|--------------------------------|---------------------------------|----------------------|--------|
| quadratic | C3D20R | C3D10 | 178.5 | 1 |
| quad tet/lin hex | C3D8R | C3D10 | 34.3 | 0.2 |
| incompatible modes hex/ lin tet | C3D8I | C3D4 | 24 | 0.14 |
| linear | C3D8R | C3D4 | 12 | 0.07 |

Table 5.1 compares the corresponding computation times. Due to the good match between the linear and quadratic formulation and the fact that computation time is key for parameter studies linear elements are chosen for the mechanical model. Table 5.2 summarizes the selected element types.

Table 5.2: Element types used for FE-calculations in this work

| Hexahedral sections | Tetrahedral section |
|---------------------|---------------------|
| thermal | |
| DC3D8 | DC3D4 |
| mechanical | |
| C3D8R | C3D4 |

5.2.2 Thermophysical properties

In Fig. 5.4 the thermophysical properties for material A are plotted as a function of temperature. The measurements have been carried out at the ÖGI (Österreichisches Gießerei-Institut). The geometries of the specimens are documented in Appendix C. A short overview of the testing procedures is given in the subsequent table:

Table 5.3: Overview of the determination of physical properties [46; 47]

| Property | Measurement | Standard |
|---|---|--------------------------|
| Thermal expansion | Dilatometry | DIN 51 045 Teil 1 (2005) |
| Technical coefficient of thermal expansion | Calculated relative to 20°C | DIN 51 045 Teil 1 (2005) |
| Density | Archimedean balance | |
| Specific heat capacity | DSC | ÖNORM EN 821-3 (2005) |
| Thermal diffusivity | Laser-flash method | ÖNORM EN 821-2 (1997) |
| Thermal conductivity | Calculated according to $\lambda(T) = a(T) \cdot c_p(T) \cdot \rho(T)$ | |

The thermal expansion coefficient (α) can be defined as the derivation of the measured thermal expansion (ΔL vs. T) or as the slope of the lines connecting α_{Ref} with α_i , where Ref represents the thermal expansion at the reference temperature (20°C for the present data) and α_i at the sampling points (100°C, 200°C, 300°C,...). The first option results in the differential expansion coefficient while the latter leads to the technical coefficient of thermal expansion with respect to 20°C. In the case of phase transformations in the relevant measurement range the latter method avoids rapid changes in the data during transformation [30].

Beside the mechanical properties, which are decisive in view of the bearable cyclic strains/stresses the thermophysical properties play a pivotal role in TF/TMF. This discussion can be limited to the impact of thermal conductivity λ since it is determined by a range of other thermophysical properties as indicated by

5. MODELING

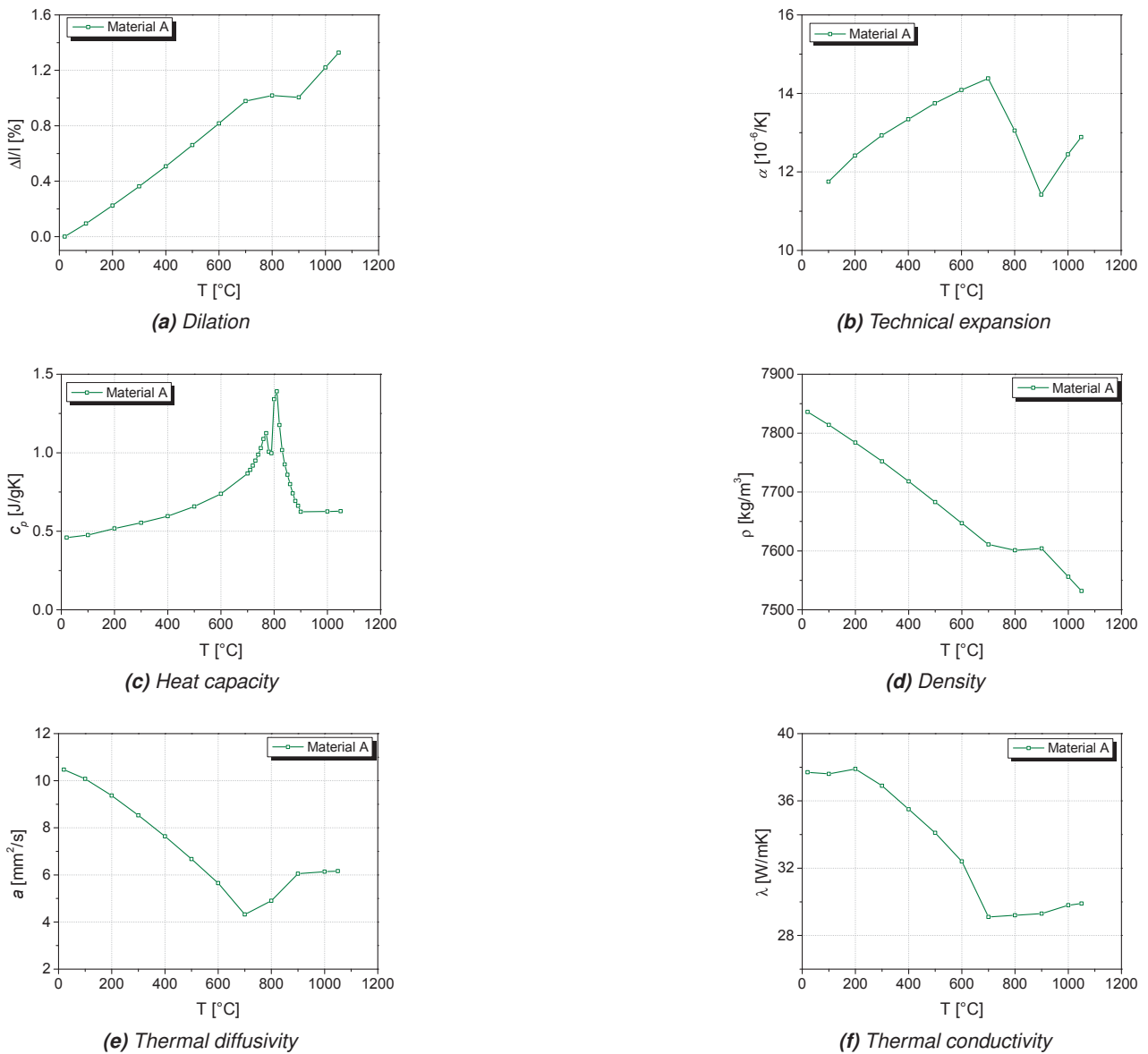


Figure 5.4: Thermophysical data for material A

Eq. (5.1).

$$\lambda(T) = a(T) \cdot c_p(T) \cdot \rho(T) \quad (5.1)$$

The importance of the thermal conductivity lies in the way the temperature field evolves in a component. For identical thermal input, a lower thermal conductivity means that the heat propagates more slowly through the component. In the case of brake disks, the temperature level at the friction surface will thus be higher while the bulk remains at low temperatures. Apart from the fact that the mechanical properties at the surface decrease due to the higher temperatures, the temperature gradient and the corresponding thermal stresses are higher. As previously noted, the full sequence of investigations from load analyses to damage analyses and TMF simulations is carried out for material A. For specific aspects, the comparison to other materials is pointed out. The discussion of the impact of thermophysical properties on the overall behavior of materials under TMF loading is continued in Section 6.4.1.

5.2.3 Thermal boundary conditions

For the **convective boundary conditions** the disk surface is partitioned in four zones, which are depicted in Fig. 5.5a to Fig. 5.5d. In general form the boundary condition can be stated in the following form [157]:

$$q_x n_x + q_y n_y + q_z n_z = h (T_s - T_{am}) \quad q_x, q_y, q_z \dots \text{components of the heat flux vector} \quad (5.2)$$

$n_x, n_y, n_z \dots$ components of the surface normal

$h \dots$ film coefficient

$T_s \dots$ surface temperature

$T_{am} \dots$ ambient temperature

The film coefficients indicated in Fig. 5.5 are provided for a speed of 160 km/h by one of the industrial partners. They are assumed as average values for brakings from 250 km/h to 0 km/h. For the cooling period after braking the corresponding values for 0 km/h are available.

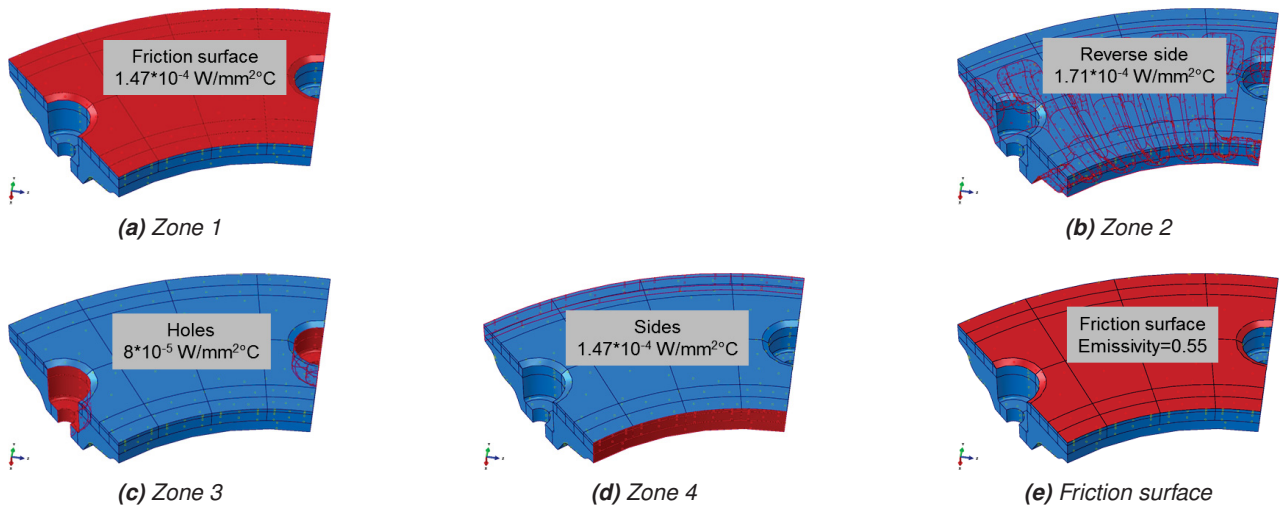


Figure 5.5: a)-d) Boundary conditions for convection: Film coefficient for four different zones, b) boundary condition for radiation.

Radiation is taken into account at the friction surface, as shown in Fig. 5.5e. The coefficient of emissivity is chosen as the stabilized value measured by Kasem et al. during a test rig program [140]. The boundary condition can be stated as follows:

$$q_x n_x + q_y n_y + q_z n_z = \sigma \epsilon T_s^4 - \alpha q_r \quad \sigma \dots \text{Stefan-Boltzmann constant} \quad (5.3)$$

$\epsilon \dots$ coefficient of emissivity

$\alpha \dots$ coefficient of absorption

$q_r \dots$ heat flux from incident radiation

5. MODELING

Due to the fact that the disk heats up to much higher temperatures than the surroundings, q_r is not considered for the modeling.

5.2.4 Thermal loading

5.2.4.1 Uniform loading

This work draws on two different approaches for modeling the thermal loading. The first one applies heat fluxes at the friction surface:

$$q_x n_x + q_y n_y + q_z n_z = -q_s(x, y, z, t) \quad q_s \dots \text{heat flux from external heat source} \quad (5.4)$$

In view of the braking problem the quantity q_s is a function of time, space and the brake scenario as discussed in [59; 73]. This offers a wide range of possibilities for parameter studies on the governing influences on fatigue life.

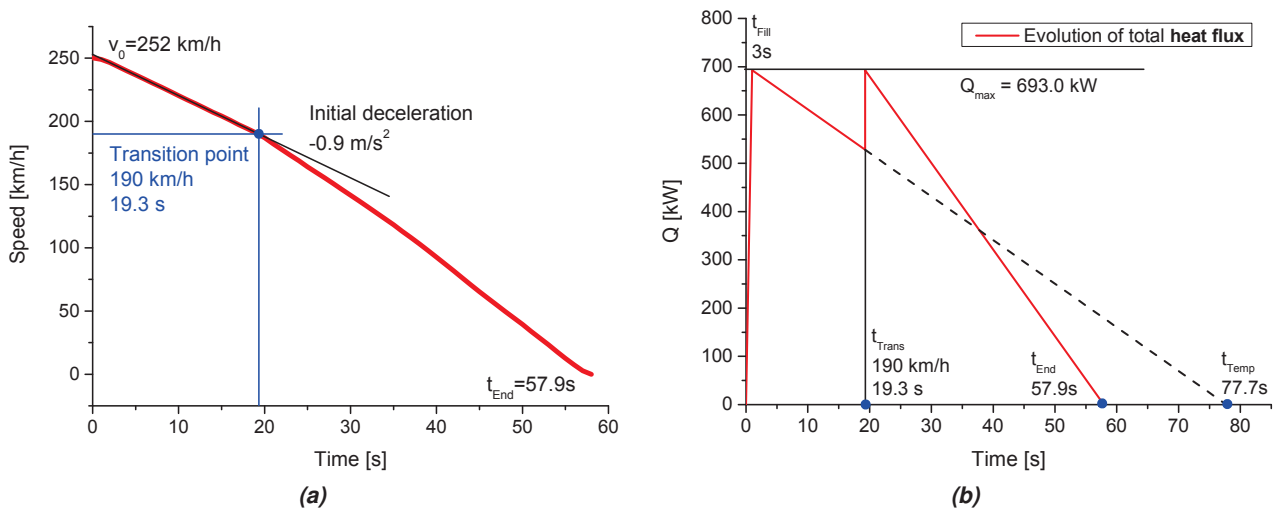


Figure 5.6: a) Evolution of velocity during the reference emergency braking and b) the corresponding total heat flux Q into the disk

Fig. 5.6a shows the velocity evolution of a high speed train during emergency braking from 250 km/h to full stop. This brake scenario is taken as the reference case for a test rig program and also for simulation purposes. The corresponding data are summarized in Table 5.4. At the beginning of the emergency stop a braking force F_B of 30.1 kN is applied. It takes about 3s for the brake cylinder to fill (fill time, t_{fill}) and transmit the full force. As indicated in Fig. 5.6b the total heat flux acting on the disk decreases along with the speed. When the train has slowed down to 190 km/h F_B is increased to 45.1 kN and the specific power reaches the initial level. The increase of F_B enables the train to stop faster. At the same time the brake blending redistributes the braking force so the mass to be decelerated by the disk set increases. Further information on the brake management of a test rig is given in Section 3.1.

Table 5.4: Test parameters for full scale test rig and material A

| Speed range | Braking force, F_B | Braking mass M_B | T_{ini} | Energy E_d |
|-------------|----------------------|--------------------|-----------|--------------|
|-------------|----------------------|--------------------|-----------|--------------|

| [km/h] | [kN] | [kg] | [°C] | [MJ] |
|---------|------|------|------|------|
| 250-190 | 30.1 | 9000 | 40 | 25 |
| 190-0 | 45.1 | 9500 | | |

Table 5.5 summarizes the necessary input data for a simple parametric description of the uniform total heat flux $Q(t)$ in Fig. 5.6b and the values chosen for the reference case. The linear decrease of Q is also known from e.g. [59; 73] but additionally the increase of F_B must be considered. The integral over the curve in Fig. 5.6b equals the dissipated energy. In order to specify the evolution of $Q(t)$ as a simple function of t in the FE software the peak value P_{max} must be known. The area under $Q(t)$ can be split into four parts as indicated in Fig. 5.7a and Eq. (5.5). The expression can be solved for P_{max} according to Eq. (5.6), which can be implemented in Abaqus in the form of the subroutine DFLUX.

$$E_d = \frac{t_{fill} Q_{max}}{2} + \frac{Q_{max} (t_{temp} - t_{fill})}{2} - \frac{Q_{max} - \frac{Q_{max}(t_{trans}-t_{fill})}{t_{temp}-t_{fill}} (t_{temp} - t_{trans})}{2} + \frac{Q_{max} (t_{End} - t_{trans})}{2} \quad (5.5)$$

with

$$t_{temp} = \frac{v_{End} - v_0}{a_0} \quad t_2 = \frac{v_1 - v_0}{a_0}$$

yielding

$$Q_{max} = \frac{2E_D (t_{fill} - t_{temp})}{t_{temp}t_{fill} - t_{temp}t_{trans} + t_{trans}^2 - t_{End}t_{temp} + t_{End}t_{fill} - t_{fill}t_{trans}} \quad (5.6)$$

Since DFLUX applies heat fluxes to the integration points, the heat flux must refer to the unit area:

$$q_{max} = \frac{Q_{max}}{A_C} \quad (5.7)$$

In the FE solver the heat flux density is automatically multiplied by the corresponding surface area. An example for a DFLUX subroutine is given in the appendix (Code B.2).

Table 5.5: Required input for uniform heat source

| Parameter | Meaning | Reference value |
|-------------|----------------------------|----------------------|
| v_0 | Initial speed | 250 km/h |
| v_{End} | Final speed | 0 km/h |
| v_{trans} | Transition speed | 190 km/h |
| a_0 | Initial deceleration | $-0.9 \frac{m}{s^2}$ |
| t_{fill} | Fill time | 3 s |
| E_d | Dissipated energy per disk | 25 MJ |

5. MODELING

| | | |
|-------|------------------------------|--------------------|
| A_C | Total contact area with pads | 0.38 m^2 |
| BS | Number of brake stages | 2 |

In contrast to [59; 73] no spatial variation of the heat flux due to hot bands and hot spots is applied. For this reason no parameters describing the influence of the disk-pad combination on the thermal distribution are taken into account and the parameter studies thus yield qualitative results. For quantitative predictions a different approach will be chosen.

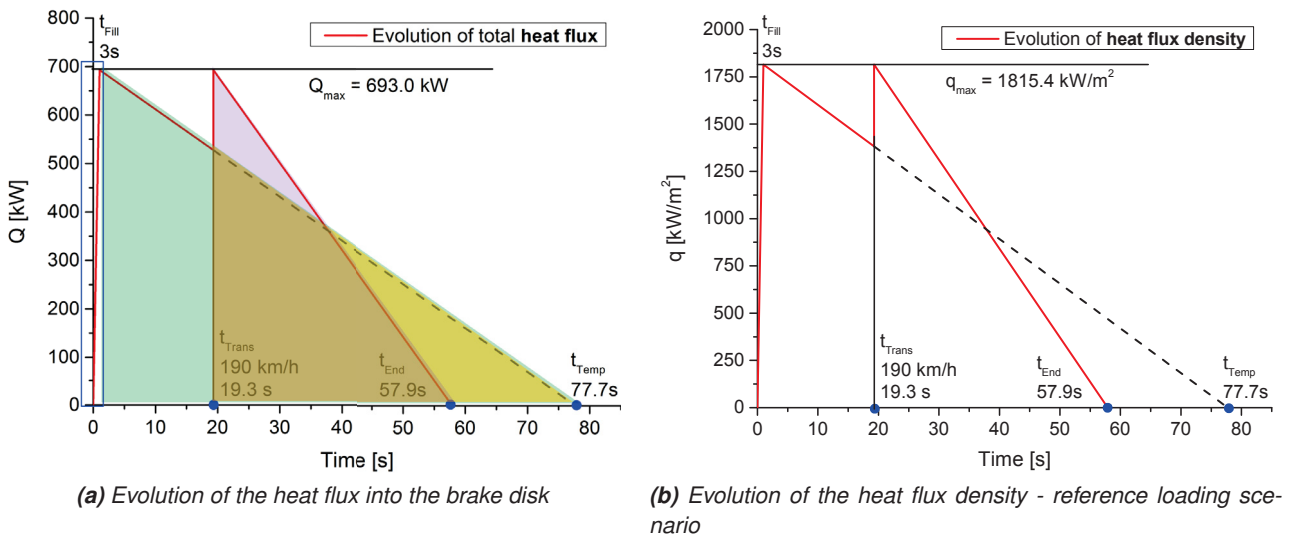


Figure 5.7: a) Derivation of the loading conditions from the evolution of the velocity in Fig. 5.6a and the total energy input. The colors refer to the four terms in Eq. (5.5). b) heat flux per unit area applied by DFLUX

5.2.4.2 Non-uniform loading

Chapter 3 elaborates in depth on the thermal image data obtained from the test rig program and the according data processing. In addition to the uniform heat source, which can be used efficiently for parameter studies on the general braking process the processed data are used for thermal image mappings. This way the non-uniformity and the transient history of the thermal input is taken into account. Since the discovered thermal patterns are complex and change during each braking and also over the course of several brakings, this strategy is favored over the application of non-uniform heat fluxes. For the investigated friction system this is left for future work.

Fig. 5.8 provides an illustration of the corresponding procedure. Instead of prescribing the heat flux as a function of time at the integration points at friction surface the temperatures from the processed thermal images are used as boundary conditions at the surface nodes:

$$T_s = T(x, y, z, t) \quad (5.8)$$

The strategy is realized with the user subroutine DISP, which allows the user defined specification of boundary conditions. DISP is usually applied to impose displacements on a mechanical FE model but in the case of a heat transfer problem the temperature degree of freedom (11) can be addressed as well.

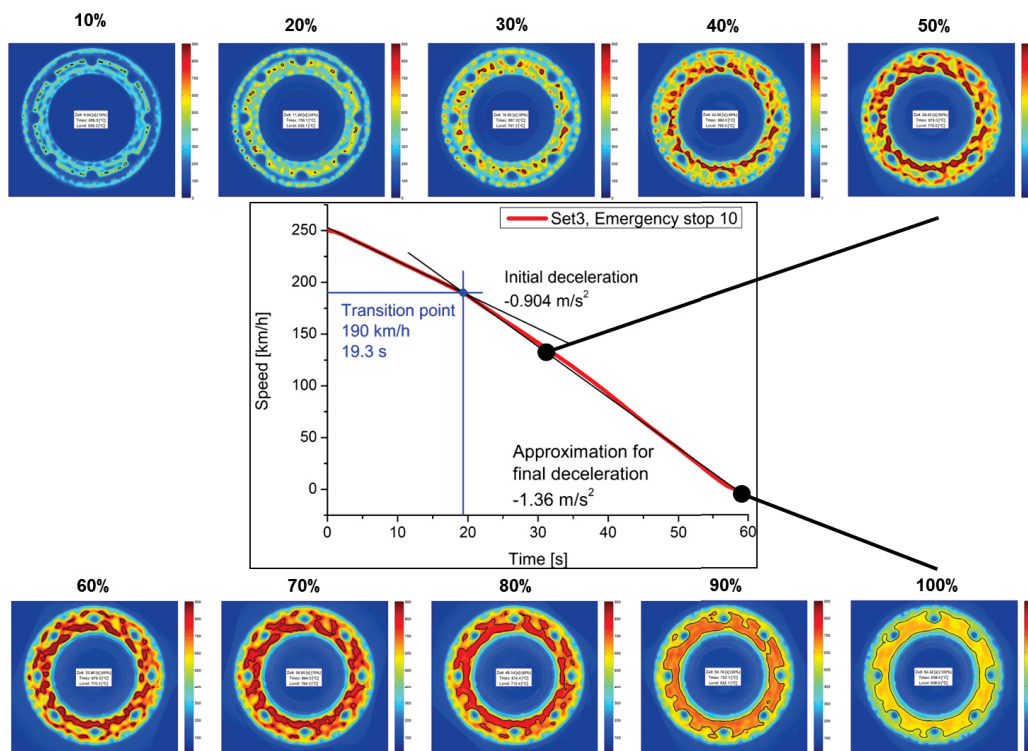


Figure 5.8: Illustration of thermal image mapping for one brake cycle.

If the temperature is known as a function of space and time $T(x, y, z, t)$, DISP can be used to apply the function at the nodes at the friction surface. The thermal image data for each recorded braking are available as individual frames, which are processed as discussed in detail in Section 3.3. Each data set represents a discrete function $T(x, y, t)$. Obviously the out-of-plane z -coordinate is not required for the present study. After the processing each data set is stored in a text file, as a 2D representation of a 3-dimensional array. For the thermal FE-calculation the desired data sets are selected in advance. DISP reads the corresponding text files and applies the thermal data at the friction surface. The incrementation of the FE-calculation is set to 0.01s at the beginning of the load step and coarsens to 1s. Since 50 frames per second are available from the thermal images, data interpolation is required. Similarly, the spatial resolution differs between the thermal image data and the FE-mesh. For this reason the data are linearly interpolated in time and bilinearly in space. The method is thus independent of the temporal and spatial resolution of the thermal camera. An example for a DISP subroutine used for a thermal image mapping of 10 consecutive brake cycles is given in the appendix (Code B.3).

5.2.5 Material law

5.2.5.1 Modeling of cyclic plasticity

The behavior of metallic materials at elevated temperatures as well as the available models have been discussed in detail in Chapter 2. As outlined in Section 2.5.3, material models for viscoplasticity can be divided into two principal classes:

- Unified models: Elastic-viscoplastic framework for the description of inelastic strains. Subsequently,

5. MODELING

the unified model used in the scope of this work will be designated **evp-model**.

- Non-unified models: Separate descriptions of the plastic strain and creep strain. Subsequently, the non-unified model used in the scope of this work will be designated **epc-model**.

These designations refer to the description of the inelastic strains (ϵ_{in}) originating from the effects illustrated in Section 2.5.3. Unified models compute the individual inelastic strain contributions as a combined quantity without distinguishing between them in the final result. The single variable is called viscous strain ϵ_v . The non-unified models on the contrary use two separate variables ϵ_{pl} and ϵ_{cr} . In the present work the main focus is laid on the unified modeling of viscoplasticity in line with the work of Chaboche [110; 113; 114]. Since the required constitutive equations are not implemented in most general purpose FE solvers such as Abaqus Standard, one of two alternatives must be chosen: Either the algorithms have to be programmed as a user defined material (UMAT subroutine) or the material model must be made available to Abaqus by an additional software. For this study the latter option is chosen and Abaqus is coupled with Zmat, the material model library of the commercial software package Zebulon [158]. The required constitutive equations can be summarized as follows¹:

$$\sigma_{eq} = (3J_2^{\mathbf{s}})^{\frac{1}{2}} = \left(\frac{3}{2} \mathbf{s} : \mathbf{s} \right)^{\frac{1}{2}} \quad \text{Equivalent stress} \quad (5.9)$$

$$\Omega = \frac{K}{n+1} \left\langle \frac{J_2(\mathbf{s} - \underline{\chi}) - \sigma_{y,0}}{K} \right\rangle^{n+1} \quad \text{Viscoplastic potential} \quad (5.10)$$

$$\dot{p} = \left\langle \frac{J_2(\mathbf{s} - \underline{\chi}) - \sigma_{y,0}}{K} \right\rangle^n \quad \text{Equivalent plastic strain rate} \quad (5.11)$$

$$\dot{\epsilon}_{pl} = \dot{p} \frac{\partial \Omega}{\partial \boldsymbol{\sigma}} = \frac{3}{2} \dot{p} \frac{\mathbf{s} - \underline{\chi}}{\sigma_{eq}} \quad \text{Normality rule} \quad (5.12)$$

$$\left. \begin{aligned} \underline{\mathbf{X}}_i &= \frac{2}{3} c_i \underline{\boldsymbol{\alpha}}_i, & \dot{\underline{\mathbf{X}}}_i &= \frac{2}{3} c_i \dot{\underline{\boldsymbol{\alpha}}}_i, & \dot{\underline{\boldsymbol{\alpha}}}_i &= -\frac{\partial \Omega}{\partial \underline{\mathbf{X}}_i} \\ \dot{\underline{\boldsymbol{\alpha}}}_i &= \dot{\epsilon}_{pl} - \frac{3}{2} \frac{\gamma_i}{c_i} \underline{\mathbf{X}}_i \dot{p} - \frac{3}{2} \left(\frac{J_2(\underline{\mathbf{X}}_i)}{M_i} \right)^{m_i} \frac{\underline{\mathbf{X}}_i}{J_2(\underline{\mathbf{X}}_i)} \\ \dot{\underline{\mathbf{X}}}_i &= \frac{2}{3} c_i \dot{\epsilon}_{pl} - \underbrace{\gamma_i \underline{\mathbf{X}}_i \dot{p}}_2 - c_i \underbrace{\left[\frac{J_2(\underline{\mathbf{X}}_i)}{M_i} \right]^m \frac{\underline{\mathbf{X}}_i}{J_2(\underline{\mathbf{X}}_i)}}_2, & \underline{\mathbf{X}} &= \sum_i^3 \underline{\mathbf{X}}_i \end{aligned} \right\} \text{Kinematic hardening with recovery} \quad (5.13)$$

The material parameters, which have to be determined from experiments are marked red. Furthermore, the parameters are listed in Table 5.6. The variables are discussed in detail in Section 2.5. The parameter identification will be discussed in Section 5.2.5.4.

¹Since Mises plasticity is used, the backstress and its deviatoric counterpart are equal $\underline{\mathbf{X}} = \underline{\chi}$

²In the literature (e.g. [110]) this term is often stated in the form: $\gamma_i^* [J_2(\underline{\mathbf{X}}_i)]^{m-1} \underline{\mathbf{X}}_i$. The two forms are equivalent but they use different material parameters M_i and γ_i^* , respectively.

Table 5.6: Parameters for the *unified* viscoplasticity model for material A

| Parameter | i | Interpolation points [°C] |
|--|-----|-----------------------------|
| E | - | 20, 400, 600, 660, 700, 800 |
| $\sigma_{y,0}$ | - | |
| c_i | 1-3 | |
| γ_i | 1-3 | |
| M_i | 1-3 | |
| m_i | 1-3 | |
| K | - | |
| n | - | |
| Parameters per temperature/Total: 16/96 | | |

The material model can be used in multiple ways. On the one hand it can be coupled with a continuum mechanical damage model, which necessitates the simulation of the whole crack initiation life time. On the other hand, it can be used to compute a stabilized state, which yields the input parameters for empirical life estimation models. Due to the fact that only the simulation of a limited number of load cycles is possible within reasonable computation times, the later option is chosen. The constitutive equations are used for the computation of a hardening state, which is representative for the life time of a brake disk and the consideration of isotropic hardening is thus not necessary. Instead, kinematic hardening is used to describe the hystereses at half life ($\frac{N_f}{2}$) as illustrated in Fig. 5.9 for the example of a strain controlled LCF test. In the case of the uniform heat source as many brake cycles need to be computed with the

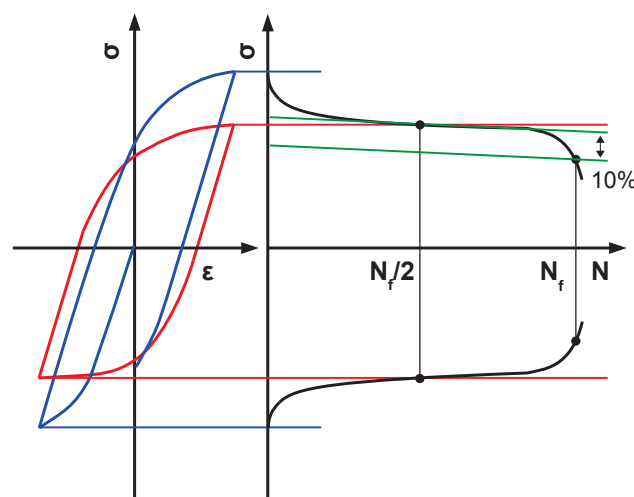


Figure 5.9: Material exhibiting cyclic softening in a strain controlled LCF test with $R_e = 0$ and the hysteresis loop at $N=1$ and $N=\frac{N_f}{2}$.

mechanical FE-model as necessary for the stress redistribution and the plastic shakedown to stabilize.

5. MODELING

For the simulation of a series of non-uniform load cycles no stabilization can be achieved. The hystereses in each braking are representative, however, and need to be treated with a damage accumulation rule.

As an alternative to the unified plasticity model, a non-unified combination of rate-independent plasticity (see Section 2.5.1) and creep (see Section 2.5.2) is used. Both are available in Abaqus. Again the constitutive equations can be summarized¹:

$$\sigma_{eq} = (3J_2^{\underline{\mathbf{s}}})^{\frac{1}{2}} = \left(\frac{3}{2} \underline{\mathbf{s}} : \underline{\mathbf{s}} \right)^{\frac{1}{2}} \quad \text{Equivalent stress} \quad (5.14)$$

$$f = \left(\frac{3}{2} (\underline{\mathbf{s}} - \underline{\boldsymbol{\chi}}) : (\underline{\mathbf{s}} - \underline{\boldsymbol{\chi}}) \right)^{\frac{1}{2}} - \sigma_{y,0} = 0 \quad \text{Yield criterion} \quad (5.15)$$

$$\dot{\underline{\mathbf{X}}}_i = \frac{2}{3} c_i \dot{\epsilon}_{pl} - \gamma_i \underline{\mathbf{X}}_i \dot{p}, \quad \underline{\mathbf{X}} = \sum_i^3 \underline{\mathbf{X}}_i \quad \text{Kinematic hardening} \quad (5.16)$$

$$\dot{\epsilon}_{pl} = \dot{p} \frac{\partial f(\underline{\boldsymbol{\sigma}})}{\partial \underline{\boldsymbol{\sigma}}} \quad \text{Normality rule} \quad (5.17)$$

$$\dot{f}(\underline{\boldsymbol{\sigma}}, \underline{\mathbf{X}}) = 0 \quad \text{Consistency condition} \quad (5.18)$$

$$\dot{\epsilon}_{cr} = \frac{3}{2} A \sigma_{eq}^{b-1} (\epsilon_{eq}^{cr})^c \underline{\mathbf{s}} \quad \text{Odquist's law for strain hardening} \quad (5.19)$$

The constitutive equations correspond to a rate-independent Chaboche model and the multiaxial form of the strain hardening creep law for primary creep. The material parameters are indicated in red and summarized in Table 5.7.

Table 5.7: Parameters for the *non-unified* viscoplasticity model for material A

| Parameter | i | Interpolation points [°C] |
|--|-----|-----------------------------|
| E | - | 20, 400, 600, 660, 700, 800 |
| $\sigma_{y,0}$ | - | |
| c_i | 1-3 | |
| γ_i | 1-3 | |
| A | - | |
| b | - | |
| c | - | |
| Parameters per temperature/Total: 11/66 | | |

The material law is used for the description of a stabilized material state, hence c is set to zero in order to obtain a power law for secondary creep. Consequently, the number of parameters reduces from

¹Since Mises plasticity is used, the backstress and its deviatoric counterpart are equal $\underline{\mathbf{X}} = \underline{\boldsymbol{\chi}}$.

66 to 60 for the present work.

5.2.5.2 Experiments for the characterization of the mechanical material behavior

Table 5.8 provides an overview of the mechanical tests available in the scope of this work. The suitability for special application ranges is indicated (orange means suitable, green very suitable). Tensile tests

Table 5.8: Illustration of the importance of individual mechanical experiments (orange: suitable, green: very suitable)

| Exp. Inform. | Tensile test | LCF test | Block test | TMF test | Static FM ¹ | Cyclic FM |
|-----------------------------------|--------------|----------|------------|----------|------------------------|-----------|
| Quick material comparison | Green | | Orange | | Green | |
| Large strain ranges | Green | | | | | |
| Empirical damage parameters | | Orange | | Green | | |
| Bauschinger effect | | Green | Orange | | | |
| Shakedown | | Green | Orange | | | |
| Strain rate dependence | | | Green | Orange | | |
| Relaxation | | | Green | Orange | | |
| Verification of plasticity models | | | | Green | | |
| Critical failure | Green | | | | Green | |
| Crack growth/arrest | | | | Orange | | Green |

in the temperature range from 20°C to 800°C at different strain rates are used to identify the temperature where viscoplasticity takes effect over plasticity. This information determines the experimental program for strain controlled LCF tests and block tests. Fig. 5.10a shows the tensile tests for material A for the relevant strain range from 0 to 1%. Between 20°C and 200°C the strength decreases. At 300°C and 400°C the typical embrittlement in this temperature range causes a deviation from the previous trend — the curves show higher values. From 500°C on embrittlement is not visible and the strength continually decreases. The greatest impact of the temperature occurs between 600°C and 700°C. Fig. 5.10b shows tensile tests for different strain rates at 600°C. The results indicate that rate dependence is minimal at this temperature level and the onset of viscoplastic behavior is assumed from here on.

From the previous considerations the temperatures for LCF tests are defined, as already indicated in Table 5.6. LCF tests are primarily used for the temperature dependent parameter identification of the kinematic hardening variables (c , γ) at a strain rate of $\dot{\epsilon} = 10^{-2} \frac{1}{s}$. Isotropic hardening is not considered in the material law as previously discussed and the hystereses at half life ($\frac{N_f}{2}$) from the LCF tests are used for the parameter identification. Fig. 5.11a shows three examples from the experimental program. The comparatively high $\dot{\epsilon}$ allows cost and time efficient testing. Fig. 5.11b compares the first five load cycles for LCF tests carried out at $R_\epsilon = -1$ and $R_\epsilon = -5$. In the first case no mean stress relaxation occurs because the external loading is symmetrical. In the latter case the imposed strain is five times higher under compression than under tension. Nevertheless, the resulting R_σ equals -1 as for the other hysteresis. The

¹Fracture mechanics.

5. MODELING

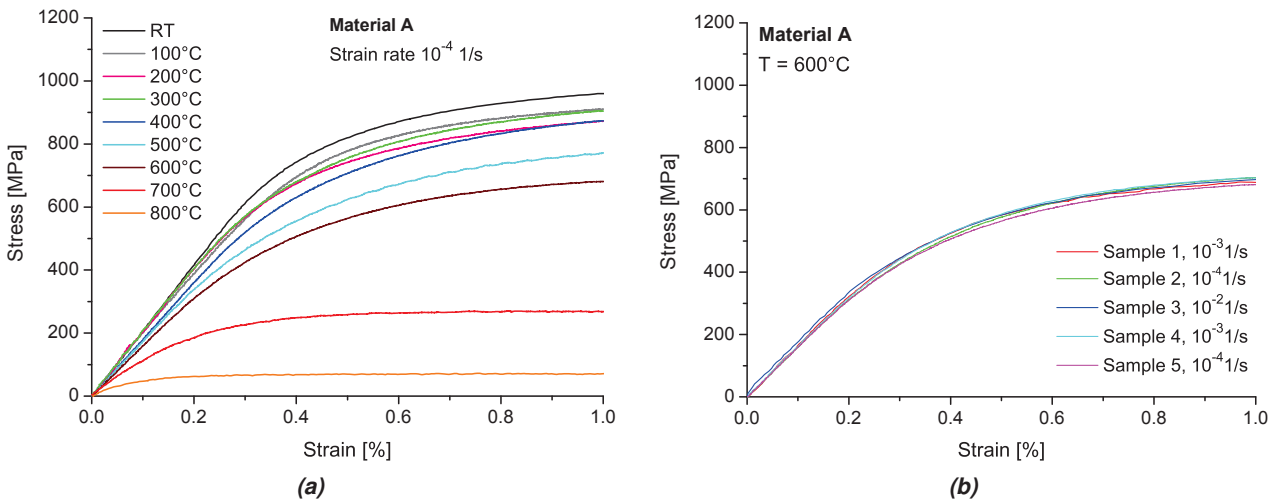


Figure 5.10: a) Tensile tests from 20°C to 800°C , b) investigation of strain rate dependence at 600°C .

greatest portion of the mean stress relaxation occurs during the first load cycle and is completed within three cycles. This behavior also occurs at the other temperature levels and thus most of the LCF tests are carried out with $R_\epsilon = -1$ supplemented with some tests with $R_\epsilon \neq -1$. The material parameters

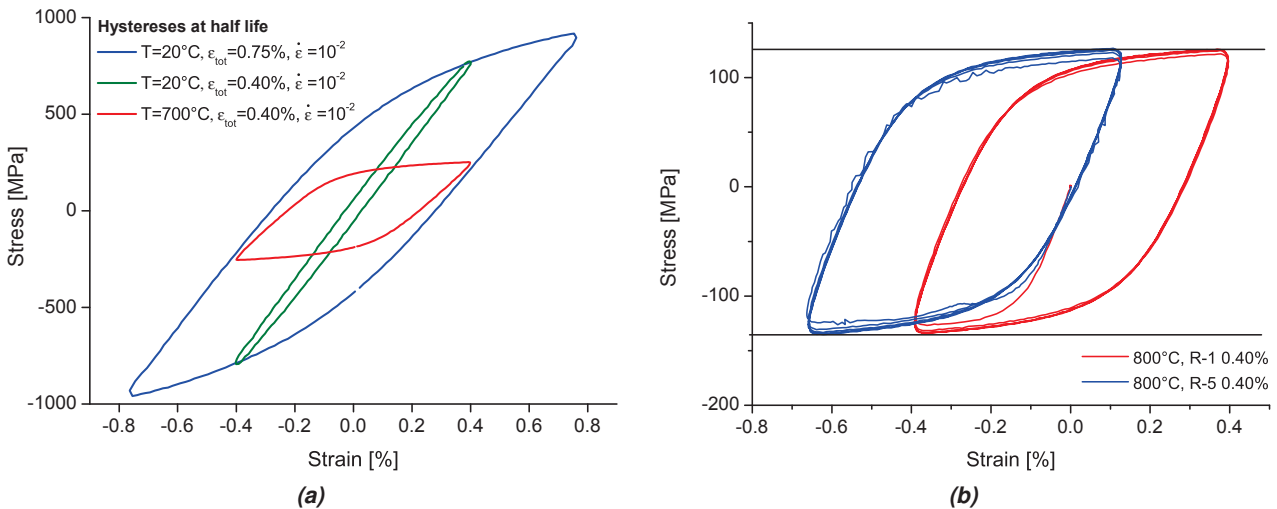


Figure 5.11: a) Examples for LCF hystereses at $\frac{N_f}{2}$, b) investigation of mean stress relaxation.

governing the rate dependence of the material behavior are identified from block tests: The experimental program pertaining to the block tests follows the strategy outlined in [20], which comprise different strain rates ($10^{-2} \frac{1}{\text{s}}$, $10^{-3} \frac{1}{\text{s}}$, $10^{-4} \frac{1}{\text{s}}$) and hold times under compression (30s, 90s, 600s). Both block types are plotted in Fig. 5.12. The block tests are carried out simultaneously with the LCF tests from 600°C to 800°C . As will be discussed in Section 5.2.7.1, the parameter identification for empirical damage models is carried out based on TMF tests, since they capture the brake disk loading more precisely than LCF tests. At the same time they are used for the verification of the material model. Section 5.2.7.2 will expand on the fracture mechanical tests.

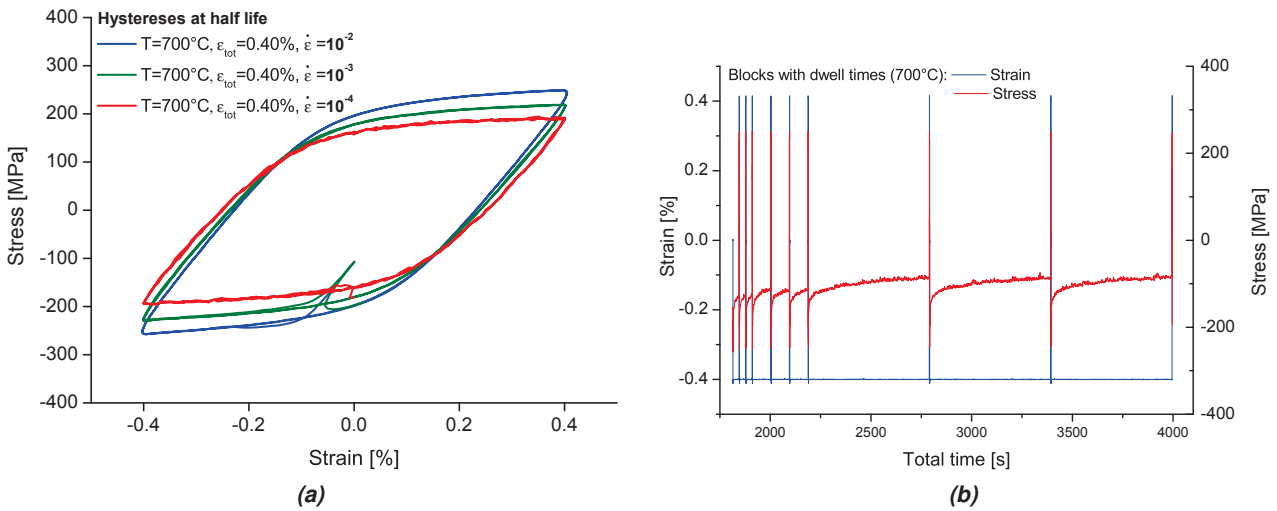


Figure 5.12: a) Investigation of strain rate dependence, b) investigation of stress relaxation at 700° C.

5.2.5.3 Sampling and sample manufacturing

Fig. 5.13 indicates the sampling positions of the mechanical and thermophysical specimens required for this project. The first cracks in brake disks commonly initiate in radial direction. The orientation of the samples for mechanical testing is thus chosen in tangential direction. This way the initiation of damage and crack propagation matches the radial direction in the disks. The position of thermophysical samples should follow the heat flow in the component, which is the axial direction for brake disks. It is assumed that the thermophysical properties are isotropic and due to the limited space available for sample extraction, the thermophysical specimens are oriented in tangential direction as well. Due to the geometry each friction

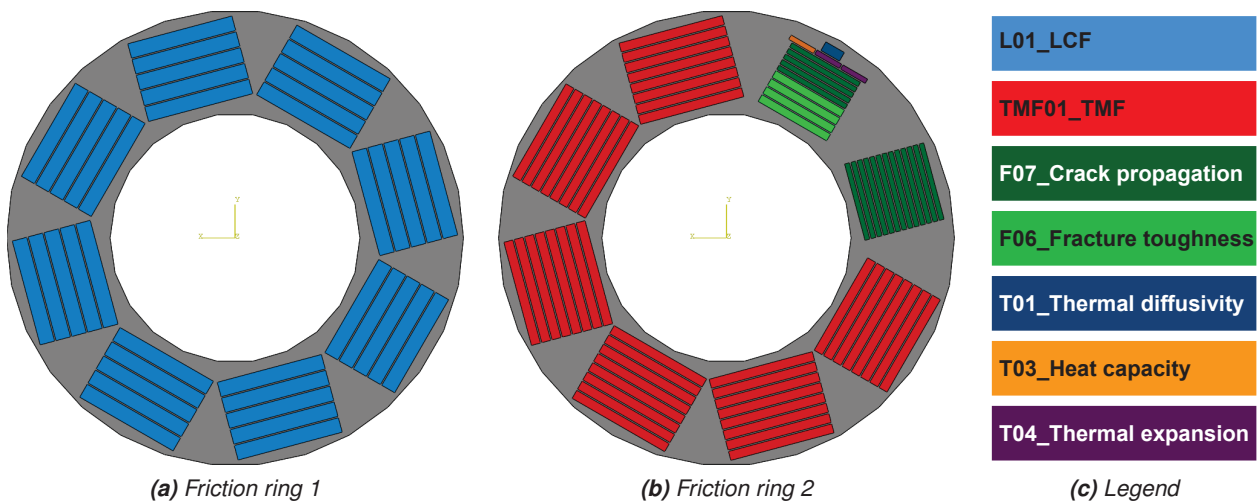


Figure 5.13: Exemplary sample orientation in a brake disk

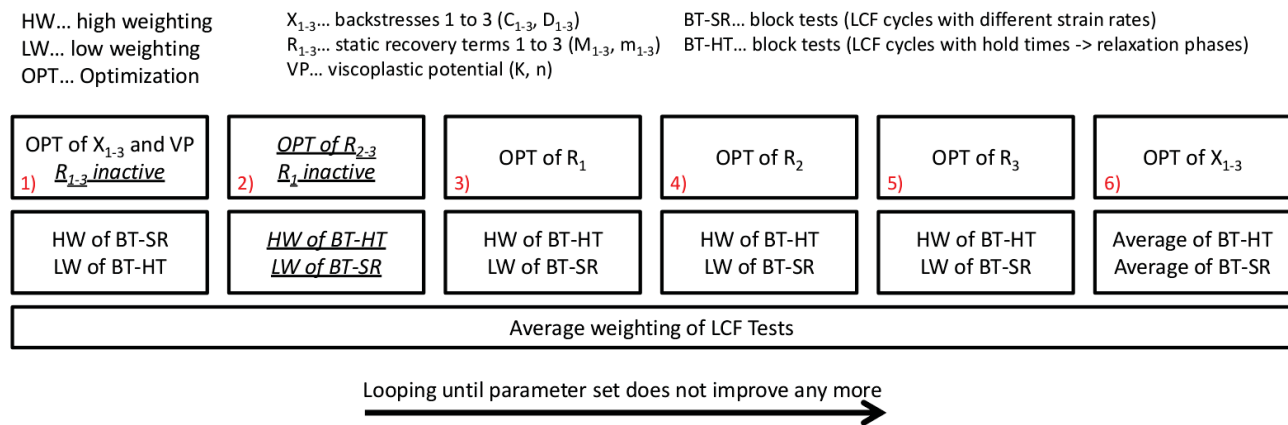
ring can be divided into eight sections for sample taking as indicated in Fig. 5.13. Each ring is separated into these segments and further on into cuboids. Water-jet cutting is preferred over mechanical machining at this point due to the fact that the temperature levels must stay low in order to avoid any metallurgical changes of the material. The final machining was carried out on a numerically controlled lathe according

5. MODELING

to the drawings in Appendix C.

5.2.5.4 Parameter identification

This section treats the identification of the material parameters listed in Table 5.6. The procedure is carried out separately for each temperature level. In order to determine the material parameters the hysteresis loops at $\frac{N_f}{2}$ are extracted from the LCF data as well as the individual blocks from the block tests. In a first step E and $\sigma_{y,0}$ are manually determined as average values from several LCF hysteresis loops. Afterwards, the hystereses are stored in text files and read by an optimization routine, which is programmed in Python [159] and draws on the commercial optimizer Z-opt [160]. The routine performs an iterative optimization process (Levenberg-Marquardt) as illustrated in Fig. 5.14 in order to approximate individual parameter sets step by step. For the non-unified model an adapted optimization strategy is used. In general the settings for the optimizations are chosen such that they yield a consistent trend with rising or falling temperature.



Underline -> Only applicable in first loop

Figure 5.14: The process of parameter identification for the unified viscoplasticity model. The procedure begins with a first approximation of the parameters for the backstresses X_{1-3} and the viscoplastic potential (1). Next, the parameters for the static recovery terms R_{1-3} are approximated in four steps (2-5). Finally, the parameters for the backstresses X_{1-3} are determined again (6). In each step the weighing of the individual experiments can be chosen accordingly. If necessary the whole optimization loop can be carried out several times.

Fig. 5.15a compares experimental hystereses for $\Delta\epsilon = 0.4\%$ and the tested temperature range to their counterparts, which are simulated based on the identified material parameters. Fig. 5.15b plots the corresponding data of the block tests. The simulation results represent the best found compromise to describe all of the 64 LCF hystereses and the 72 hystereses from 4 block tests. Deviations occur within acceptable limits, which will further be investigated and verified by TMF tests in Section 5.2.7.1.

5.2.6 Mechanical boundary conditions

The brake disk are connected to the wheel in a flexible way that minimizes the external constraint and thus the TMF loading during braking. One of the eight mountings is shown in Fig. 5.16a as a complete assembly. The two friction rings attached to wheel mounted brake disk are represented in green, while the cut through wheel is displayed in grey. The bolt and the spring washers keep the friction rings attached to the wheel,

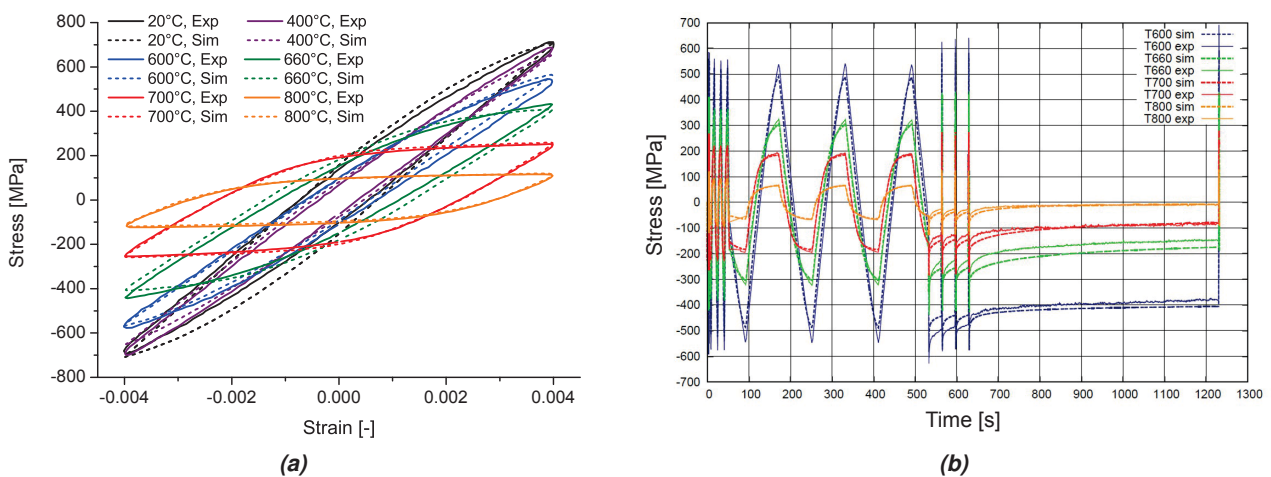
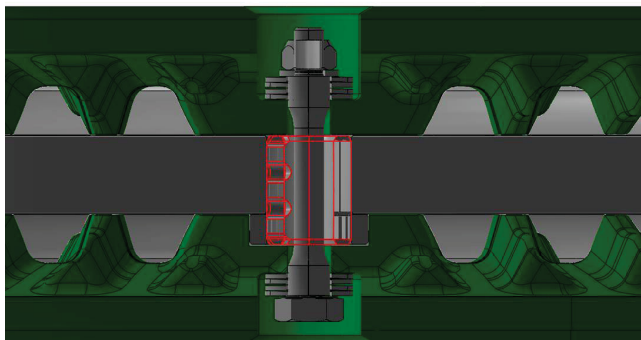
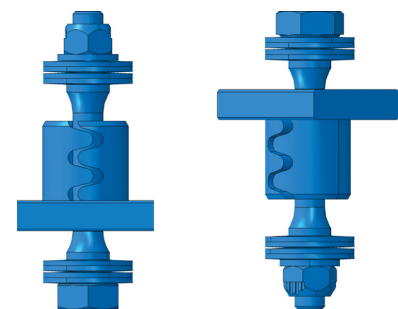


Figure 5.15: a) Exemplary illustration of experimental and simulated mechanical hysteresis for $\Delta\epsilon = 0.4\%$, b) results for block tests. See Section 5.2.5.2 for more information on the tests.



(a) Assembly including wheel and wheel mounted brake disk



(b) Assembly of bolt, adapter, sliding block and spring washers

Figure 5.16: a) Detailed view on the fastening, b) illustration of the antisymmetric arrangement of subsequent mounting points.

while the adapter (marked red) and the sliding block transfer the braking moment from the brake disk to the wheel. In Fig. 5.16a the moment is only transferred on one side (lower half in Fig. 5.16a). Fig. 5.16b shows that the arrangement at the next mounting position is mirrored and the moment is transferred onto the opposite side. By virtue of this assembly, the moment can efficiently be transferred and at the same time the disk can expand in radial direction. Additionally, the disk can move in tangential direction at each mounting position as well, which is important when thermal patterns are not symmetrically distributed along the circumference.

For the symmetrical FE-model the specifics of the disk mounting need to be taken care of by suitable boundary conditions, as far as necessary. The applied boundary conditions are illustrated in Fig. 5.17 and Fig. 5.18. As depicted in Fig. 5.17, the springs are modeled by multiple connector elements in order to avoid stress concentrations. These are unavoidable to a limited extent, since the connectors are attached to individual nodes. The elastic behavior of the spring washers is modeled with the aid of connector elements, which can be given an arbitrary behavior. In the present case it is simple elastic behavior based on the spring characteristic. The prestress of the bolts is considered by the application of a pressure load

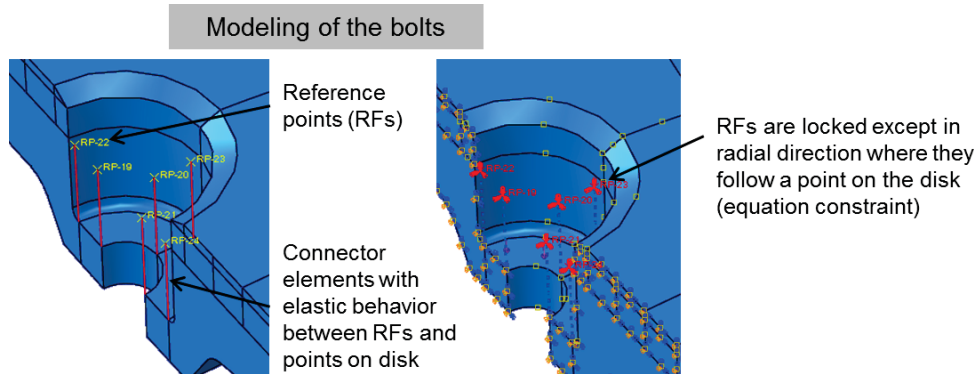


Figure 5.17: Modeling of the bolts.

on the contact areas with the disk (Fig. 5.18a). The prestress is sufficient to firmly attach the disk to the wheel but small compared to the forces caused by the disk coning during braking. The assembly allows the disk to expand in axial direction due to coning and this behavior is reflected by the boundary conditions. Due to the fact that the mechanical load due to the friction force is significantly lower than the TMF loading due to the transient temperature field in the disk, the braking force F_B is neglected. This allows to assume an eight-fold symmetry, which is realized by symmetry conditions on the two bounding faces indicated in Fig. 5.18b. Note that symmetry pretends the application of symmetric braking forces F_B . However, since F_B is much smaller than the TMF loading due to the temperature field, F_B can be neglected as a whole. The contact of the cooling fins with the wheel (Fig. 5.18c) is modeled using a penalty contact formulation for both the normal and the tangential direction. In the tangential direction a friction coefficient of 0.1 is applied for the mere purpose of numerical stabilization, when the disk expands in radial direction. As contact partner representing the wheel, an analytical rigid surface is used.

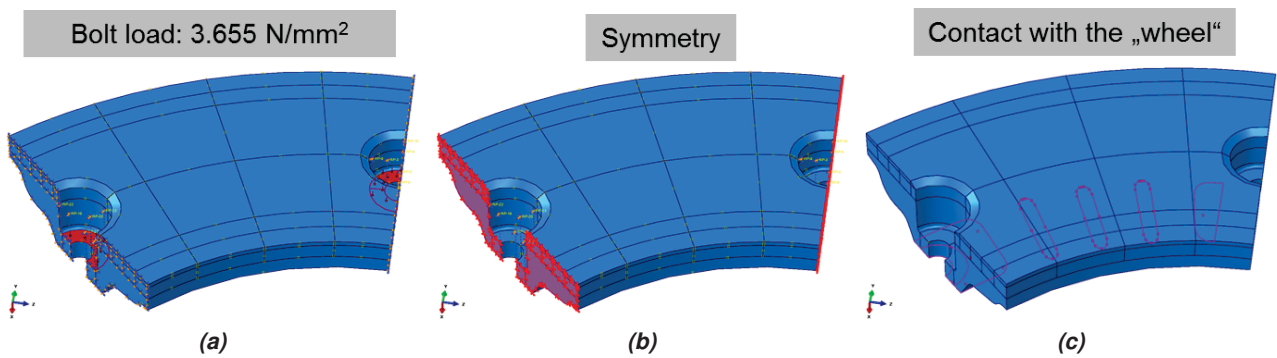


Figure 5.18: Mechanical boundary conditions.

5.2.7 Life time estimation models

For the modeling of crack initiation life time commonly one of two strategies is followed. The first approach is based on a full coupling between the behavior of the material for the material behavior and a continuum mechanical damage description, e.g. according to Lemaitre [124]. The second option is the post processing of the stabilized σ - ϵ field in combination with an empirical damage parameter. Due to the greater flexibility this option is chosen for the present work and discussed in Section 5.2.7.1.

Additionally a fracture mechanical evaluation is included in the service life assessment as outlined in Section 5.2.7.2.

5.2.7.1 Modeling of service life until crack initiation

Non-isothermal testing As isothermal high temperature testing in general yields non-conservative data for life time prediction [71], special measurement techniques have been developed to allow for non-isothermal testing as described e.g. in [30; 69; 70]. The most relevant parameters for LCF and TMF testing are indicated in Table 5.9. Since $\dot{\epsilon}$, ϵ_a , R_σ , R_ϵ result from the thermal control curve and K_{TM} , TMF

Table 5.9: Parameters for LCF and TMF testing

| LCF (isothermal) | | | TMF (non-isothermal) | | |
|------------------|------------------|--|----------------------|----------------|---|
| Parameter | Symbol | Comments | Parameter | Symbol | Comments |
| Temperature | T | Isothermal testing | Initial temperature | T_{ini} | Non-isothermal testing. T_{ini} is the starting point of the test where the sample is clamped and K_{TM} is established |
| Strain rate | $\dot{\epsilon}$ | At low temperatures not significant | Lower temperature | T_{min} | |
| Strain amplitude | ϵ_a | A set of important ϵ_a can be derived from first simulations | Upper temperature | T_{max} | |
| Stress ratio | R_σ | Ratcheting may occur in stress controlled LCF | Dwell time | t_{dwell} | Decisive for service life at high temperatures |
| Strain ratio | R_ϵ | Mean stress relaxation is fast so $R_\sigma \approx -1$ is obtained very quickly | Heating rate | \dot{T}_h | Set according to loading characteristics of the component |
| | | | Cooling rate | \dot{T}_c | |
| | | | Constraint factor | K_{TM} | Determines mechanical strains |
| | | | Initial stress | σ_{ini} | Consideration of residual stress |

testing involves more parameters than LCF testing that are more closely related to service conditions. For this reason, it is possible to describe the loading conditions in the component more precisely under laboratory conditions as it would be the case with LCF testing. Fig. 5.19 provides an illustration of the two main operating modes, in-phase (IP) and out-of-phase (OP). Fig. 5.19a shows the control curve consisting of the temperature evolution that is applied externally and the evolution of mechanical strain, which results indirectly from the temperature and the constraint.

- **IP:** The maximum mechanical strain coincides with the highest temperature in the cycle which promotes creep damage in the high temperature phase of the load cycle where tensile stresses prevail. Stress-strain hystereses typically show a decreasing level of stress in the tensile regime before load reversal (Fig. 5.19b). This feature is a characteristic difference compared to isothermal test and can be explained by the fact that the Young's modulus drops with increasing temperature.

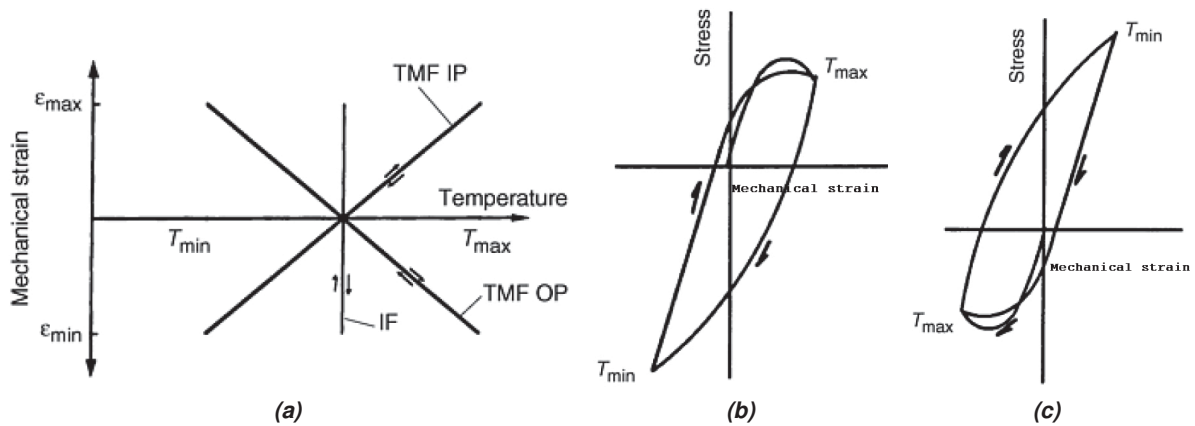


Figure 5.19: a) Comparison of isothermal testing, in-phase and out-of-phase TMF testing. Mechanical hystereses for b) in-phase and c) out-of-phase TMF testing [30].

- OP:** The minimum mechanical strain coincides with the highest temperature in the cycle, which is in the pressure regime in this case (see Fig. 5.19c). This affects the link between processes around T_{max} , where the surface oxidizes and T_{min} , where crack initiation and growth occur due to tensile stresses. Around T_{max} oxide layers might form that are increasingly brittle with falling temperature. At T_{min} , however, tensile stresses are highest which promotes cracking of the oxide layer and thus early crack initiation in the sample/component. Damage due to oxidation is thus critical in OP-TMF. This work is focused on TMF of brake disks. Therefore it should be pointed out that the formation of oxides at the friction surface of brake disks is a very special and complex case. In general, wear particles from the disk and the pad are mixed and compacted at the interface of this tribological system (contact surface). This way, a solid layer is formed that adheres to the disk surface. Due to its independent nature and its impact on the characteristics of the tribological system, it is called the third body [78]. Because of this layer and the low but constant wear at the friction surface of the disk that constantly removes crack initiation sites, oxidation damage plays a minor role for the damage of the component.

In both cases a shift of the mean stress (σ_{mean}) can be observed since plastic yielding differs between the high and low temperature phases of each load cycle. Equivalently to isothermal tests, a strongly elevated level of plasticity occurs during the first cycle accounting for most of the shift of σ_{mean} . Furthermore, thermal ratcheting may occur in TMF test where one region of the sample is hotter than the surrounding material [161]. This can be equivalent to the mechanical situation at hot spots, which will be discussed in Chapter 6. In the case of IP-TMF a shift towards the compressive regime is common, because the material is extended at T_{max} . For OP-TMF the opposite is true due to compression of the material at T_{max} . When T_{ini} is established the material is shorter or longer than in the original state, respectively, causing a $\sigma_{mean} \neq 0$ [16]. Due to the demanding testing techniques and long cycle times, however, TMF testing is more costly and sometimes it is necessary to depart from real service conditions in order to reduce machine time. This can be achieved by using K_{TM} factors that lead to higher mechanical strains during each load cycle and thus a corresponding reduction in N_f for these tests in comparison to TMF test using real K_{TM} factors. Although isothermal tests cannot capture the real in-service conditions isothermal tests are still essential for the determination of parameters for plasticity models (see Section 5.2.5.2).

The test parameters for material A are summarized in Table 5.10. In total an experimental program comprising 20 TMF tests is carried out. Details on the experimental procedure and an overview of the individual tests is given in [162].

Table 5.10: Parameters for TMF testing for material A

| Test parameter | Values |
|----------------|-----------------------|
| T_{ini} | 50°C |
| T_{min} | 50°C |
| T_{max} | 580°C-680°C |
| K_{TM} | -1, -0.75 |
| \dot{T}_h | 10°C $\frac{1}{s}$ |
| \dot{T}_c | 10°C $\frac{1}{s}$ |
| t_{dwell} | 5s, 60s , 180s |
| σ_{ini} | 50 MPa |

T_{ini} equals T_{min} and corresponds to the initial temperature of the brake disk at the beginning of each braking in the test rig program. The heating \dot{T}_h and the cooling rate \dot{T}_c are constant at 10°C $\frac{1}{s}$, which is in the relevant parameter range indicated in Fig. 4.30 and Fig. 4.29. The pivotal parameters T_{max} and K_{TM} are systematically varied in order to cover the TMF life from about 100 to 10000 load cycles. Since the current maximum design temperature for the bulk of the investigated disk type and material A is 660°C, T_{max} is varied around this value. Due to technological reasons it is not possible to reach maximum temperatures of 800°C as in the case of the LCF program. Since the service life is described in terms of stress and plastic strain as will be further discussed in Section 5.2.7.1, the parameters obtained from the experimental program also yield reasonable results to some extent outside the tested parameter range. The standard dwell time t_{dwell} at T_{max} is set to 60s, which corresponds well to the time frame of an emergency stop. The brake disk is exposed to temperature T_{max} only a fraction of the brake time. Therefore, the tested dwell time of 60s shifts the obtained results for N_f in the conservative direction. Additional TMF tests with $t_{dwell}=5s$ and $t_{dwell}=180s$ show that the major impact of the dwell time occurs between 0s and 60s. The result for $t_{dwell}=180s$ is inside the natural scatter band of the data points tested with $t_{dwell}=60$. This can be explained qualitatively with the aid of the isothermal block test in Fig. 5.12b carried out at 700°C. From the blocks with dwell time it is obvious that the greatest part of the stress relaxation occurs within the first 60s. The relaxation is effected by a viscoplastic strain, which accumulates but also saturates to a large extent during these 60s. Thereafter the stress level stays rather constant. The major impact on the TMF life thus occurs in this time frame. The tests are carried out with an initial stress level of $\sigma_{ini}=50$ MPa. The reason for this setting lies in the machine control of the test facility rather than the intention to investigate the impact of residual stresses in the service life prediction. This aspect is left for future work.

Fig. 5.20 depicts two TMF tests, which correspond to the same T_{max} . They were tested with the constraint factors -0.75 and -1, respectively, which causes a significant difference in the resulting mechanical strains. They increase with K_{TM} along with the corresponding hysteresis areas and thus the dissipated plastic energies. With K_{TM} and the other parameters listed in Table 5.9 in-service conditions of a component can thus be well approximated. Fig. 5.20 also shows two LCF tests carried out at T_{min} , respectively T_{max} of the TMF tests. It is evident that the LCF hystereses significantly differ. It is possible to vary $\dot{\epsilon}$, ϵ_a , R_ϵ and the temperature but the in-service loading cannot be approximated as well as with TMF tests. This comparison illustrates the reason why LCF tests are used for the identification of the parameters of constitutive laws (Section 5.2.5.4) but TMF tests for empirical life estimation models as well as for verification purposes.

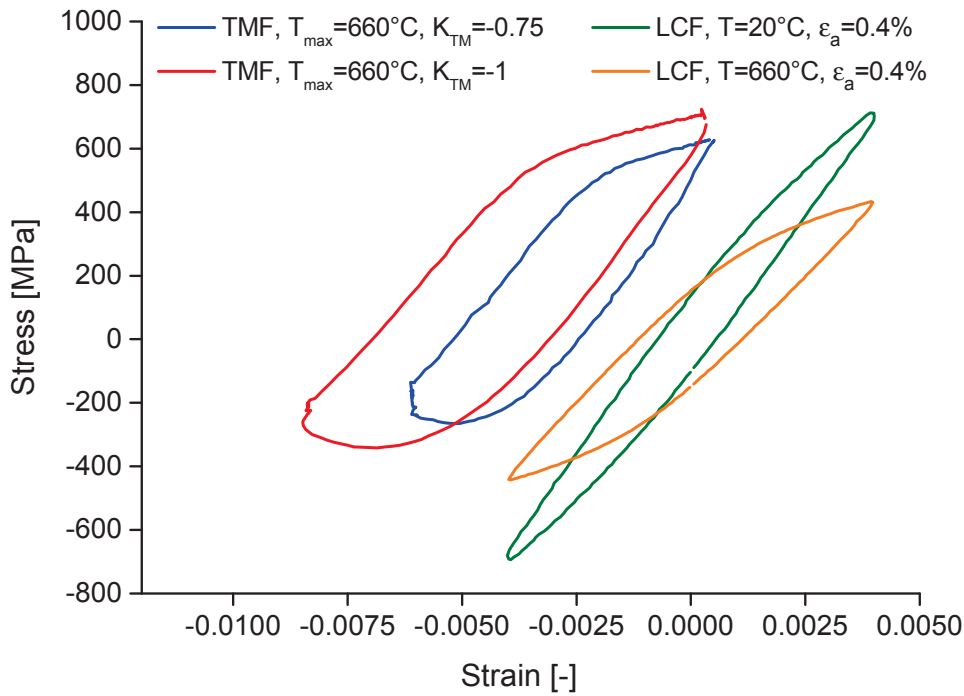


Figure 5.20: Exemplary illustration of TMF tests carried out in the experimental program and comparison to LCF tests at T_{min} and T_{max} .

Conventional empirical life estimation models In a preliminary study the life estimation models according to Manson-Coffin (MC), Smith-Watson-Topper (SWT) [128], Ostergren (Ost) [129], Riedler [69] and Winter [130] have been investigated and calibrated with the available TMF data. It was found that Manson-Coffin and Ostergren yield acceptable scatter bands, while the Riedler model and SWT are not suitable for material A. The Winter model yields the smallest scatter band but this is due to its formulation, which is less general than the other models. For this reason, it is suitable but its range of validity must be considered very carefully.

Manson-Coffin is based on the plastic strain amplitude $\epsilon_{pl,a}$ of stabilized hystereses or the hystereses at $\frac{N_f}{2}$, which can be interpreted as the damage parameter $P_{MC} = \epsilon_{pl,a}$. The relation between the damage parameter $\epsilon_{pl,a}$ and the load cycles until crack initiation is given by Eq. (5.20). Two empirical material constants, appear in the expression. In the case of Manson-Coffin a is called the fatigue ductility coefficient and often the label ϵ'_f is used. The label originates from the fact that in the case of an isothermal exper-

imental basis the constant relates with the fracture strain of a tensile test, i.e. one half cycle that leads to failure. This is also the reason why ϵ - N curves for LCF data are often plotted over $2N_f$. This way $N = 1$ refers to the first half cycle. For non-isothermal data this relation is not relevant. The life time is designated N_f and the constants a, b are determined from the complete experimental data. The procedure is illustrated in Fig. 5.21a. For each TMF test, $\epsilon_{pl,a}$ at half life is plotted versus N_f in a double logarithmic diagram. The constant b corresponds to the slope of a linear fit through the data points, while the constant a is the interception point of the fit at $N = 1$. As noted above this position can be determined from a tensile test in the case of an isothermal experimental basis and the alternative notation on the horizontal axis. In the present case $N = 1$ has no specific meaning and is merely the reference position for the fit.

$$\epsilon_{pl,a} = a_f N_f^b \tag{5.20}$$

$$N_f = \left(\frac{\epsilon}{a}\right)^{\frac{1}{b}} \tag{5.21}$$

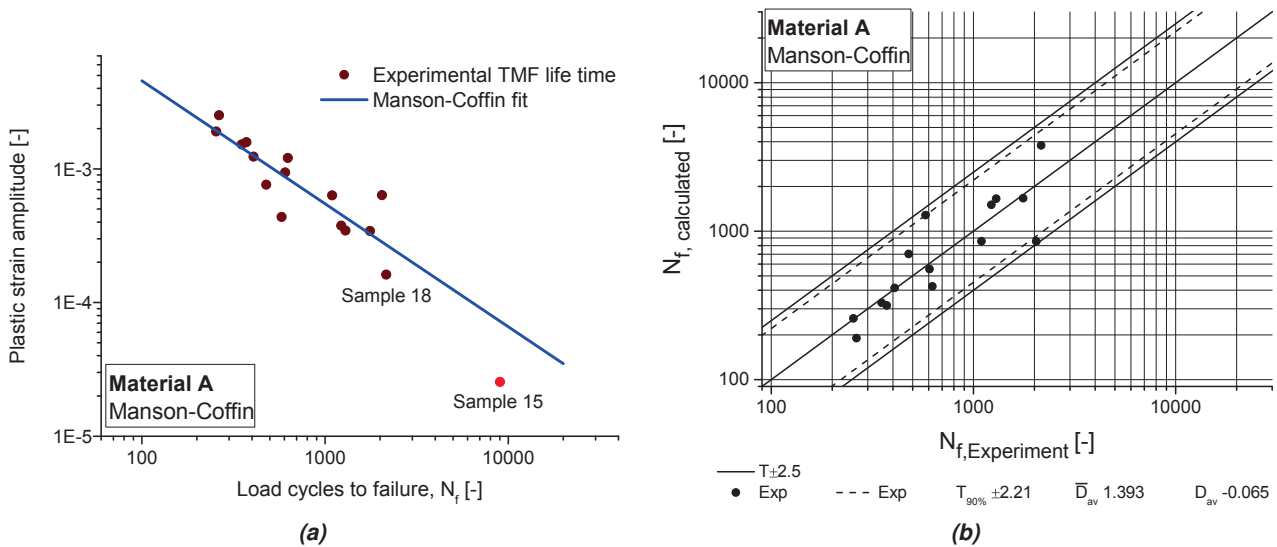


Figure 5.21: a) Determination of parameter set for Manson-Coffin and b) the corresponding scatter band. $T_{90\%}$ corresponds to the scatter band enclosing 90% of the results. D_{av} refers to the average deviation and \bar{D}_{av} to the average of the absolute deviation values.

One of the data points in Fig. 5.21a corresponding to sample 15 is marked red. The TMF test was carried out with $t_{dwell}=5s$. From the discussion in Section 5.2.7.1 is clear that dwell times, which are shorter than the time period for the stress level to approach saturation have a large impact on N_f . The values for N_f are higher compared to dwell times where the stress level is nearly saturated. For sample 15 the plastic strain is so small that it will be interpreted as elastic shakedown occurs. Its counterpart (sample 18) tested with $t_{dwell}=60s$ clearly shows a plastic response and $N_f=2160$ compared to $N_f=9000$ for sample 15. The impact of short dwell times cannot be captured by Manson-Coffin and an individual data set would be required for each value of t_{dwell} . Due to the fact that $\epsilon_{pl,a}$ for sample 15 is very small it cannot be considered for a damage model that is based on plastic strains. In the case of isothermal testing, experiments showing elastic shakedown can be taken into account by the model of Basquin, which is used in addition to Manson-Coffin. For TMF this is not possible, however. The result for sample 15 is thus

5. MODELING

not considered for the data fit and the range of validity is set to a threshold below which $\epsilon_{pl,a}$ becomes too small to be used as damage parameter. This will be discussed further below.

When the constants a and b are determined the quality of the damage model must be determined. This is done by plotting the N_f values computed with Eq. (5.21) and the experimental input values versus the experimental N_f as shown in Fig. 5.21b. In the optimal case all data points would lie exactly on the diagonal. Since scatter is an inherent part of fatigue experiments this ideal case is not achievable. Instead it is common practice to define a $T_{90\%}^{2.5}$ scatter band as the limit for an acceptable data set. This means that 90% of the data points must be within a scatter band defined by $N_f/2.5$ at the lower bound and by $2.5 N_f$ at the upper bound. This requirement is fulfilled and the precise scatter band $T_{90\%}$ equals 2.21. Additionally to $T_{90\%}$ the average deviation D_{av} and the average of the absolute deviation values \bar{D}_{av} are given in Fig. 5.21b. $D_{av}=-0.065$ means that on average the data set underestimates N_f by 6.5%. $\bar{D}_{av}=1.393$ specifies the average deviation (scatter) from the experimental N_f is a factor of ± 1.393 . The scatter band $T_{90\%} = 2.21$ signifies that for safety reasons a deviation of ± 2.21 must be assumed for all N_f values computed with the data set.

The damage parameter P_{Ost} according to Ostergren combines the plastic strain and the maximum stress σ_{max} as stated by Eq. (5.22). P_{Ost} thus corresponds to an approximation of the hysteresis energy in the tensile regime. For this reason it is a more general description of N_f than Manson-Coffin, because it considers the mean stress. The procedure for the identification of a and b is the same as in the previous case. Eq. (5.22) shows P_{Ost} versus N_f and the data fit. Again sample 15 is not included since the result is outside the range that can be captured by the model. The corresponding scatter band is plotted in Fig. 5.22b. $D_{av}=+0.18$ indicates an average overestimation of the computed results by 18%. $\bar{D}_{av}=1.495$ signifies an average scatter by a factor of ± 1.495 . The $T_{90\%}$ scatter band that needs to be considered for every estimation of crack initiation life is ± 2.2 .

$$P_{Ost} = \sigma_{max} \Delta \epsilon_{pl} = a N_f^b \quad (5.22)$$

$$N_f = \left(\frac{P_{Ost}}{a} \right)^{\frac{1}{b}} \quad (5.23)$$

The third empirical damage model considered in this work is the model according to Winter, which can be stated in the form of Eq. (5.24).

$$T_{max} = a (K_{TM}) N_f^{b(K_{TM})} \quad (5.24)$$

$$N_f = \left(\frac{T_{max}}{a (K_{TM})} \right)^{\frac{1}{b(K_{TM})}} \quad (5.25)$$

This approach differs from the previous two since it does not predict crack initiation in terms of stress and strain but in terms of the loading parameters T_{max} and K_{TM} . The advantages and disadvantages of this strategy will become obvious in Section 5.2.7.1. At this point the calibration of the model is discussed. In a first step the TMF data are plotted individually for each tested K_{TM} in the form of Fig. 5.23a as outlined by Winter in [130]. In the present case, the TMF tests are split into two sets, each corresponding to a specific K_{TM} (-1, -0.75). Each line can be fitted with a power law as indicated yielding two data sets for

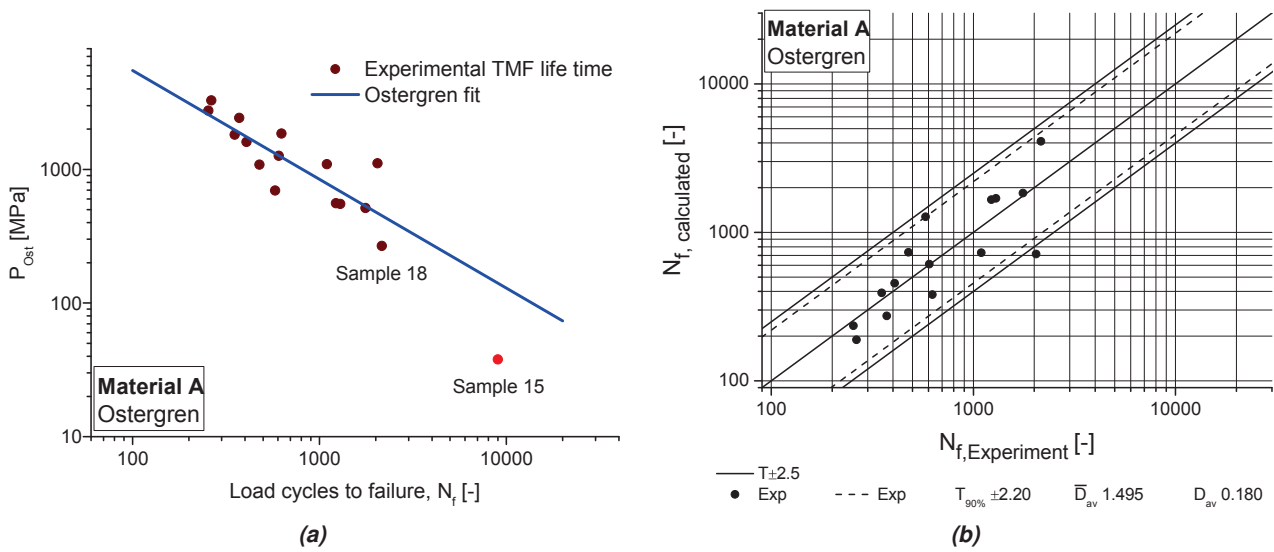


Figure 5.22: a) Determination of parameter set for Ostergren and b) the corresponding scatter band.

a and b . Both quantities can be defined as functions $f(K_{TM})$ instead of constants as in the Manson-Coffin and Ostergren models. In the case of a a simplification can be applied. The difference between the two curves decreases with increasing temperature and a corresponds to the theoretical temperature where the sample fails after one cycle. The data fits for $K_{TM}=-0.75$ and $K_{TM}=-1$ yield $T_{max}=972^{\circ}\text{C}$ and $T_{max}=977^{\circ}\text{C}$, respectively, which indicates that for both K_{TM} failure after one cycle would occur almost at the same T_{max} . Hence, a can be defined as a constant, while the slope b is defined as $b(K_{TM})$ as shown in Fig. 5.23b. Due to the definition of the Winter model and the corresponding procedure for the parameter

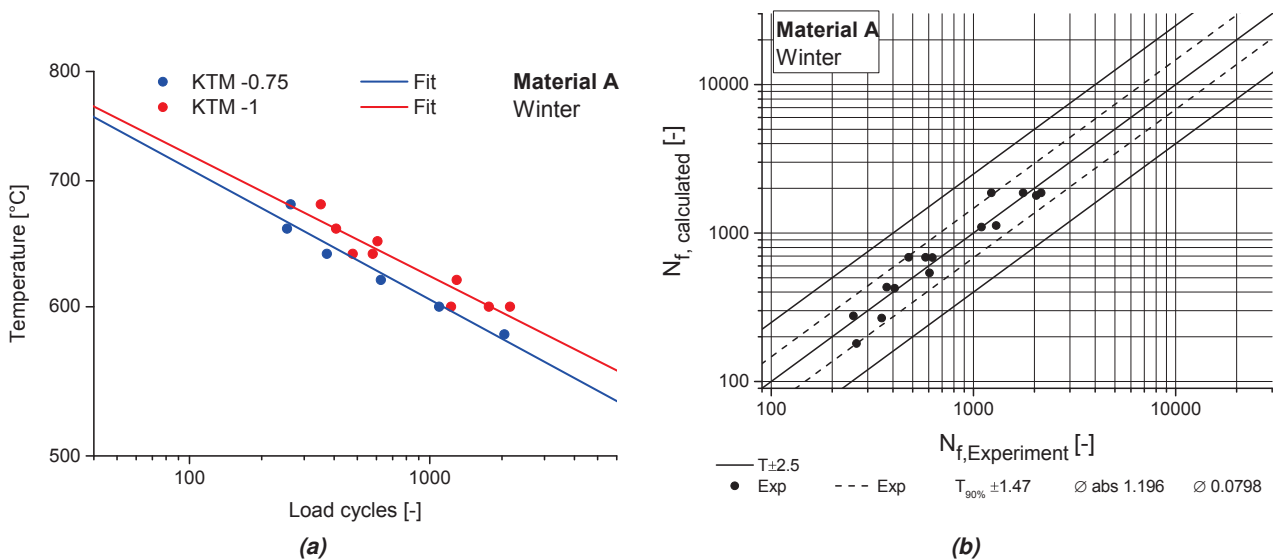


Figure 5.23: a) Determination of the parameters for the Winter model and b) the corresponding scatter band.

identification it shows the smallest scatter band $T_{90\%}=1.47$. The approach used in the Winter model is very different from the Manson-Coffin and Ostergren models and the resulting scatter bands must be assessed in the right context. While the approach of Manson-Coffin and Ostergren estimate crack initiation

5. MODELING

life based on the plastic strain and stress, the approach by Winter refers directly to the quantities describing the loading conditions during TMF-testing. Due to this fact, this model exhibits the smallest scatter band of all tested life estimation models. The approaches by Manson-Coffin and Ostergren on the other hand are more general and yield reasonable results outside the tested parameter range as long as T_{max} is not too far outside the tested region. The approach by Winter automatically extrapolates the experimental basis to other loading conditions, which may be far outside the tested parameter range. Although the scatter band is smallest for the experimental basis this may not be the case for extrapolated data points. Outside the experimental basis the model loses more precision compared to other models. Furthermore, the definition of the K_{TM} -factor in components is not always straightforward and a direct comparison with test conditions might not be possible. In these cases K_{TM} as an input quantity is questionable.

Verification procedure and range of validity In the last section the quality of the three damage models for the estimation of crack initiation life N_f was discussed in terms of scatter bands. The parameters of the models are determined from TMF tests and afterwards the scatter bands are determined by feeding each model with input data. In this case the input data correspond to $\epsilon_{pl,a}$, σ_{max} , T_{max} , K_{TM} from the TMF tests. From the point of view of simulation another, global verification of the models is required. For this purpose, each TMF test must be simulated and the experimental loading conditions, the viscoplasticity model and the damage models must be included. The input parameters for the damage models are now taken from the simulation and the resulting scatter bands indicate the overall quality. For the simulation

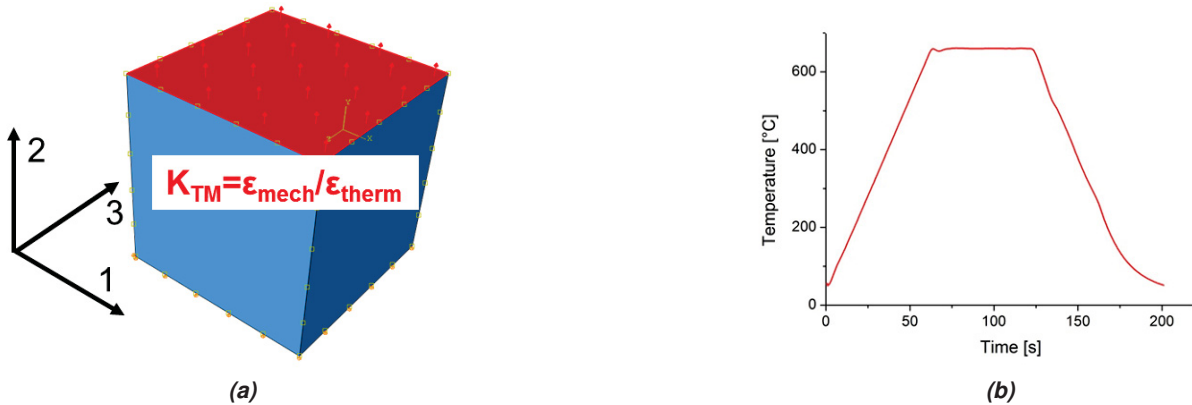


Figure 5.24: a) Single element for simulations at sample level, b) evolution of the element temperature.

a single element, a cube, is used as shown in Fig. 5.24a, which represents a material point in a TMF sample. The mechanical boundary conditions represent a statically determinate support, which provides for homogeneous σ - ϵ states inside the entire element. The prestress of 50 MPa that was used in the experiments is considered by a distributed force. The measured temperature evolution during the corresponding experiment is used to heat and cool the cube homogeneously (Fig. 5.24b). The temperature is the control signal of the experiment/simulation but the mechanical load is also dependent on the constraint. For this reason, a user defined boundary condition is defined for the degree of freedom 2 at the top plane with a DISP subroutine. In each increment DISP takes the thermal strain as input value and imposes the displacement on the model that corresponds to the desired K_{TM} . The result for one of the TMF tests for material A is depicted in Fig. 5.25. It compares the experimental hysteresis at half life with the simulation.

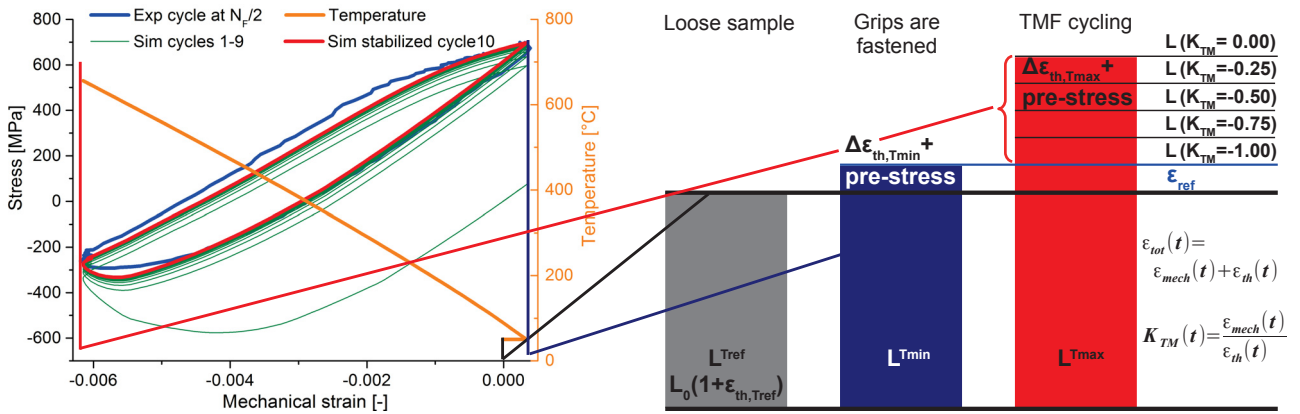


Figure 5.25: illustration of the simulation of a TMF test. The bars represent the length of the specimen at different stages of the test.

It is necessary to simulate about 10 TMF cycles in order to obtain a stabilized material response. An overestimation of the compressive stresses occurs but the overall accordance is acceptable. The overall quality will be assessed in terms of scatter bands further below. Fig. 5.25 further illustrates the previously discussed loading and boundary conditions. In the experiment the sample is mounted at $T_{ref}=20^{\circ}\text{C}$ but the grips are not yet fastened. The sample is heated to T_{min} and the prestress is applied. At this point the grips are fastened and the thermal cycling between T_{min} and T_{max} begins. Depending on the effected constraint factor the maximal total strain minus the reference strain $\epsilon_{tot}^{max}-\epsilon_{ref}$ at T_{max} may vary from 0 for $K_{TM}=-1$ to $\Delta\epsilon_{th}^{max}$ for $K_{TM}=0$, where the sample can expand freely. Positive K_{TM} are not relevant for this work and thus not discussed.

For the evaluation it is important to know the required output quantities that represent the input parameters for the damage models. Fig. 5.26 compares the material response for a simulated TMF test for the two viscoplastic models. For the unified viscoplasticity model (evp-model) the mechanical hysteresis is plotted over the total strain ϵ_{tot} and over the inelastic strain ϵ_{in} . For the discussion only two hystereses are shown but in practice as many cycles need to be computed as required for a stabilized material response. The half width of the latter hysteresis provides $\epsilon_{pl,a}$ as input for the Manson-Coffin model. It should be noted that the subscript pl that is commonly used in Eq. (5.20) and Eq. (5.21) refers to all inelastic strains. For the Ostergren model additionally σ_{max} is required, which can be obtained from both hystereses in Fig. 5.26a. The non-unified viscoplasticity model (epc-model) yields a different output due to its non-unified formulation as illustrated in Fig. 5.26b. The black curve corresponds to the plastic material response and the green curve to the creep response. Plastification occurs both under compression (T_{max}) and under tension (T_{min}) but a creep strain only occurs under compression, when the temperature levels are sufficiently high. The desired result is obtained by adding the two hystereses, which is indicated in blue, so $\epsilon_{pl,a}$ and σ_{max} can be determined. It should be noted that this procedure can cause an overestimation of σ_{max} , because an overestimation of the combined inelastic strains under compression can cause a drift of the hysteresis towards the tensile regime. This is due to convergence issues, i.e. the Abaqus option for computing creep and plasticity sequentially has been chosen as opposed to a simultaneous treatment. The plastic law can thus not prevent an overestimation of the creep strain. This problem is completely avoided by the evp-model where both behaviors are inherently interconnected.

Fig. 5.27 shows again the scatter bands for the Manson-Coffin and Ostergren models but this time includ-

5. MODELING

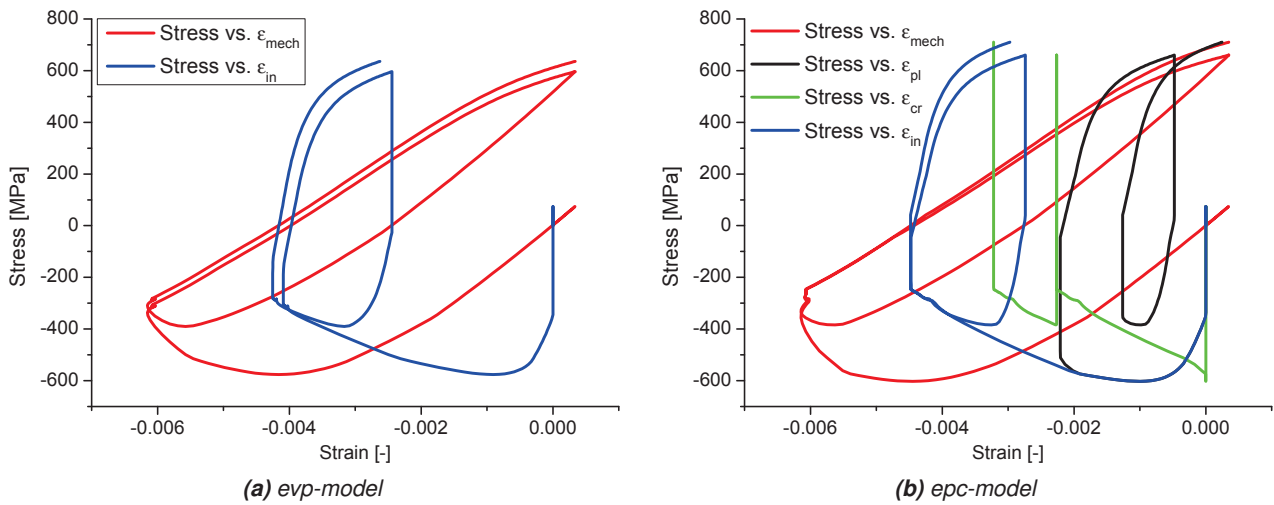


Figure 5.26: Comparison of the results data from a) the unified viscoplasticity model (**evp**) and b) the non-unified model (**epc**).

ing the simulated results for ϵ_{pl} and σ_{max} . The green dots refer to the results with the unified viscoplasticity model (evp-model), which is available in the software package Zmat and can be coupled with Abaqus. The red dots refer to the non-unified viscoplasticity model (epc-model) that is directly available in Abaqus. All four combinations of the viscoplasticity and the damage models fulfill the requirement of a scatter band below 2.5 as indicated in the lower part of Fig. 5.27a and Fig. 5.27b. The evp-model describes the inelastic material response more precisely than the epc-model and thus yields smaller scatter bands. Another advantage of the evp-model is that the average deviation D_{av} is negative and not positive as in the case of the epc-model. For Manson-Coffin $D_{av} = -0.422$ and for the Ostergren model $D_{av} = -0.349$, which means that the Manson-Coffin model on average underestimates the crack initiation life time N_f by 42% and Ostergren by 35%. On average the estimates are conservative, while the opposite applies for the epc-model where D_{av} is +70% and +41%, respectively. In general, the best result is obtained with the combination of the evp-model for the viscoplastic material behavior and the Ostergren model for the prediction of crack initiation life time. Based on this investigation this combination is chosen for the evaluations in Chapter 6. Nevertheless, all other combinations are also inside the required scatter band ± 2.5 and therefore suitable for the estimation of crack initiation. It is, however, important that the quality of the results is judged individually based on the scatter that has been determined for the experimental results and for the simulated data. At this point the other materials are introduced. An overview of the material types is given in the subsequent list:

material A Forged low alloyed steel, hardened and tempered

material B Forged unalloyed steel, hardened and tempered

material C Cast steel

material D Ductile cast iron

material E Grey iron

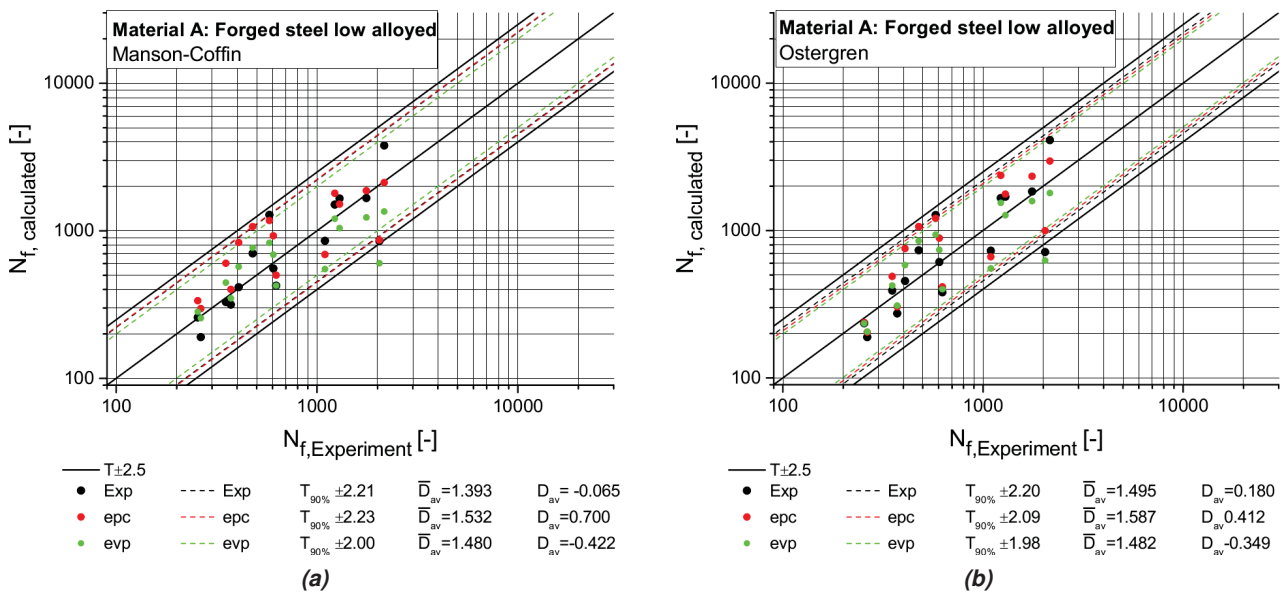


Figure 5.27: Experimental and simulated scatter bands for material B a) Manson-Coffin and b) Ostergren.

The scatter bands are plotted in Fig. 5.28, Fig. 5.29, Fig. 5.30 and Fig. 5.31a. For the two cast irons the criteria are not met since $T_{90\%}$ is greater than 2.5. For material D the limit is only slightly surpassed and the data set for the Ostergren model will be used in the context of a material comparison in Chapter 6. For material E the criteria are clearly violated. Additionally, the plastic behavior of grey iron exhibits a strong tension compression antisymmetry, which makes the viscoplasticity models used in this work non-applicable. A different strategy is chosen, which draws on the Winter model (Fig. 5.31a) and elastic FE-calculations. This strategy is reasonable as long as the loading of the brake disks is strain controlled and K_{TM} is independent of the inelastic strains, as will be verified in Chapter 6.

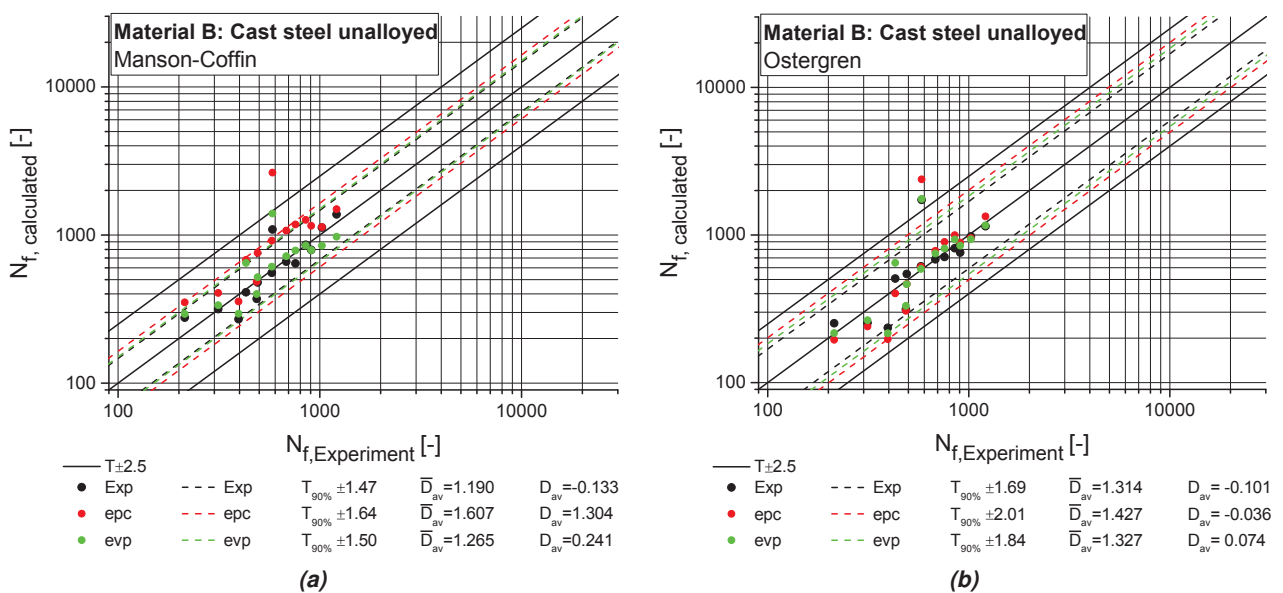


Figure 5.28: Experimental and simulated scatter bands for material B a) Manson-Coffin and b) Ostergren.

5. MODELING

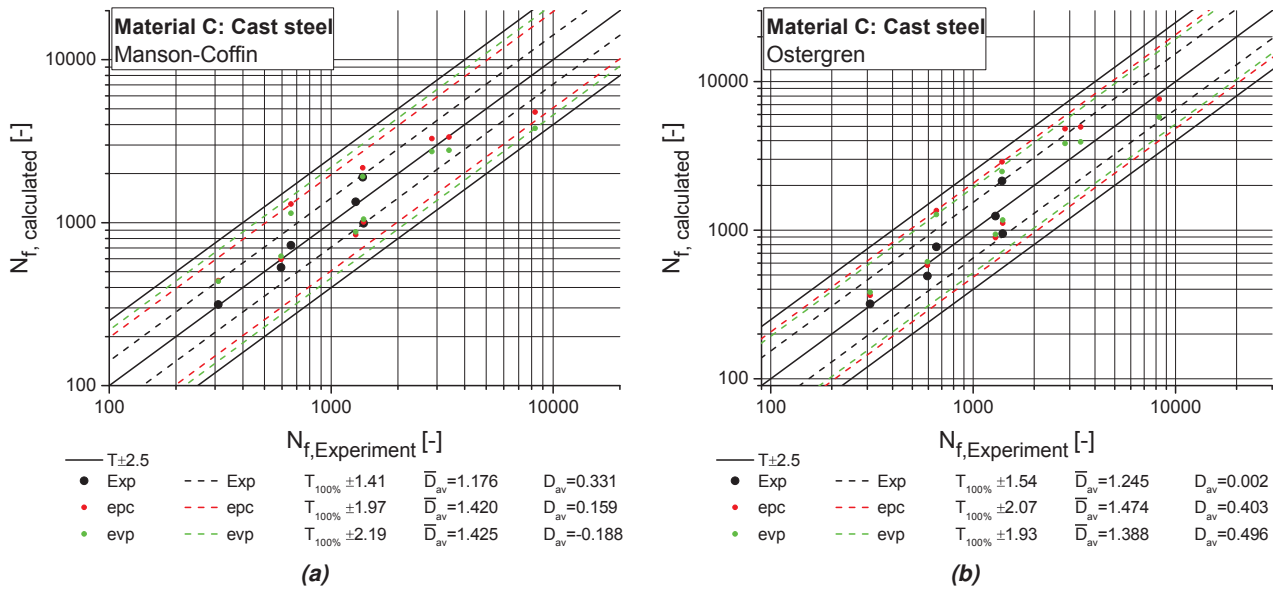


Figure 5.29: Experimental and simulated scatter bands for material C a) Manson-Coffin and b) Oostergren.

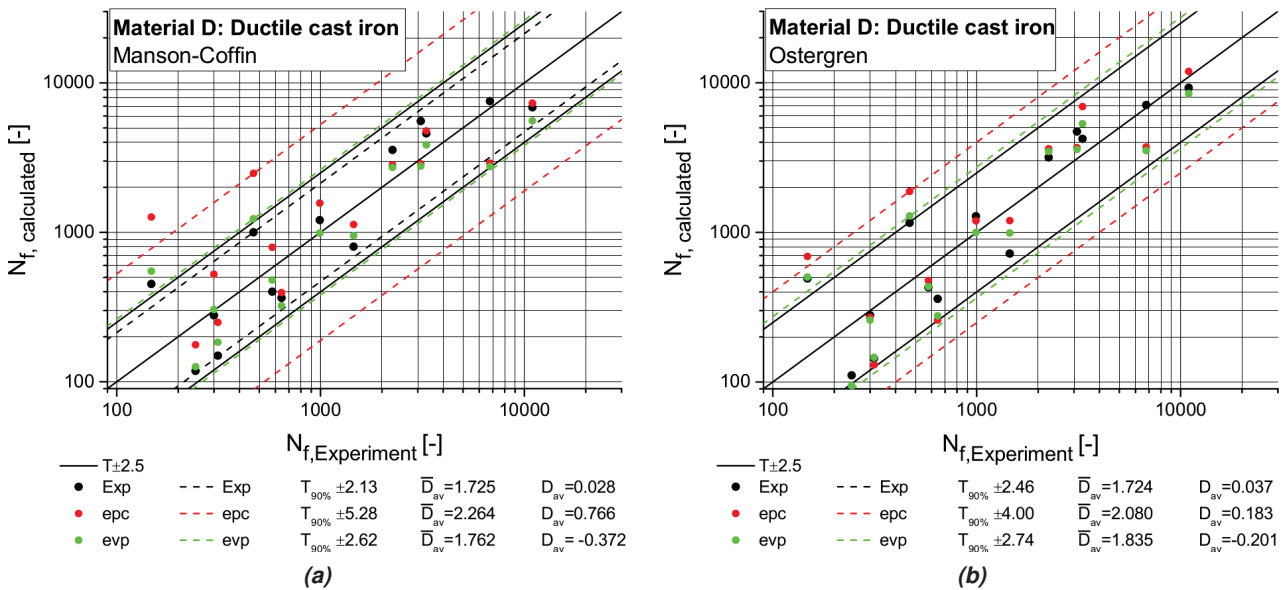


Figure 5.30: Experimental and simulated scatter bands for material D a) Manson-Coffin and b) Oostergren.

In contrast to the other life expectancy models the quality of the model in combination with the simulation framework cannot be tested on sample level with a single element test, since the input parameters for the Winter model are the loading parameters K_{TM} and T_{max} . This reflects both the advantage and the drawback of this method:

- + No stress or strain data are required. The input is directly T_{max} and K_{TM} rather than the resulting mechanical quantities.
- + Scatter is reduced because the quantities governing the loading (T_{max} and K_{TM}) are directly linked to the experimental basis.

- The link to the resulting mechanical quantities (σ and ϵ) and thus one strong link to the physics of the problem of life time prediction is lost.

The resulting damage parameter is suitable for:

- Quick estimations on load cycles to crack initiation.
- Online health monitoring: A characteristic K_{TM} factor can be determined in advance for each disk type on a specific train. Only the temperature has to be monitored in service. A rule for damage accumulation can be applied.

The life estimation model according to Winter is strictly valid for the tested experimental basis as indicated for all materials in Fig. 5.31b. Loading conditions outside that basis may occur and yield questionable results although the scatter band for the tested parameter range is low. This may happen unnoticed, if the data in Fig. 5.31b is neglected. Apart from material E the Manson-Coffin model and the Ostergren model are applicable and the latter one is preferred for the assessment of the component in Chapter 6. The range of validity needs to be assessed in a different manner, as indicated in Fig. 5.32a and Fig. 5.32b. On the one hand the range of validity of the material model must be considered, which is shown in Fig. 5.32a. In the present case, the validity is defined by the tested and modeled temperature range and strain rates. On the other hand the transition from the TMF/LCF region to the HCF region must be taken into account, because the Manson-Coffin model and the Ostergren model are based on the plastic strain. When the loading is too low the plastic strains may be too small to be within the validity range. From the experimental results the limit can be set to $\epsilon_{pl,a} = 3 \times 10^{-4}$ [-]. The corresponding number of load cycles within the validity limit can be determined as shown in Fig. 5.32b. Within the validity range the quality of the results can be assessed with the scatter bands. Outside, the life time estimations are conservative since the plastic strains diminish.

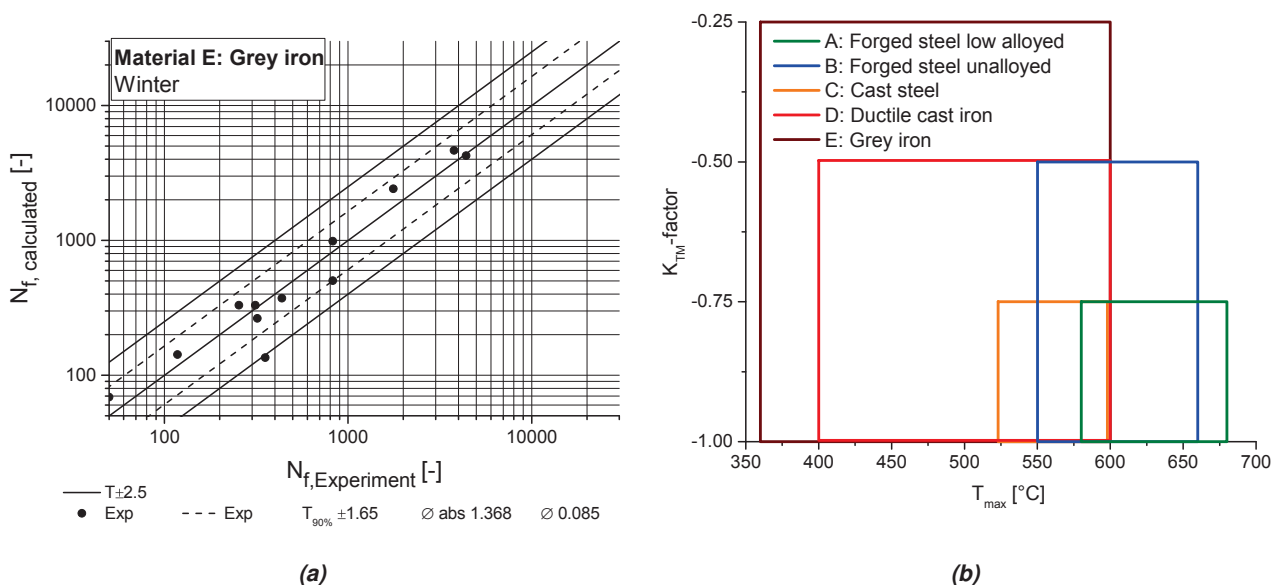


Figure 5.31: a) Experimental and simulated scatter bands for material E for the damage model according to Winter, b) Experimental basis for TMF tests. The boxes indicate the tested parameters and thus the area of validity for the Winter model.

5. MODELING

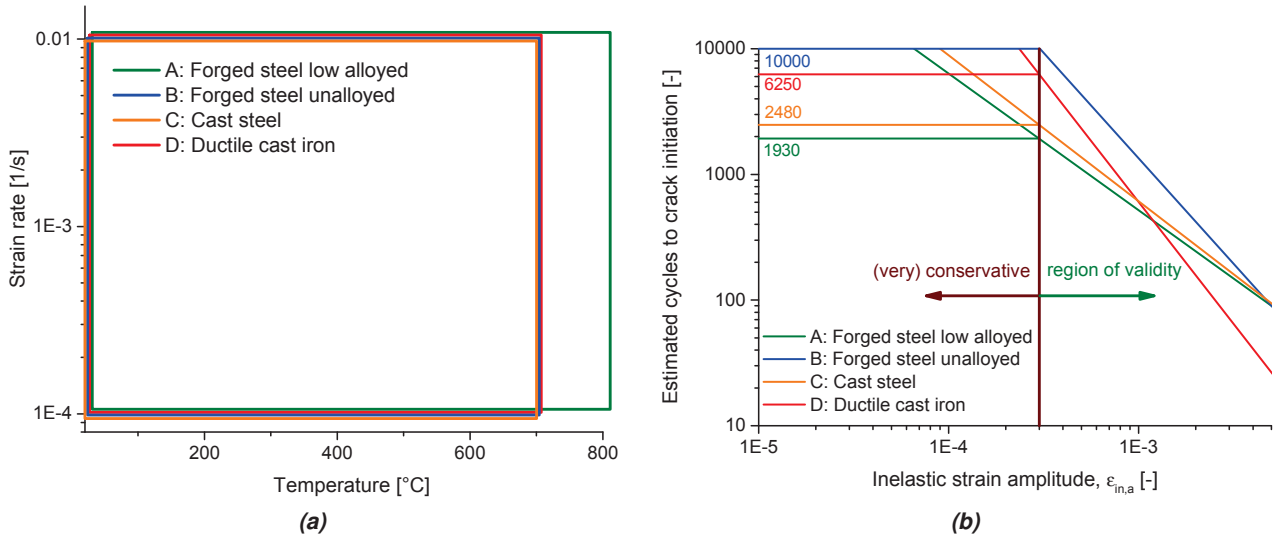


Figure 5.32: a) Range of validity for material models based on LCF tests, b) Range of validity for the Manson-Coffin model and the Oostergren model.

5.2.7.2 Modeling of the fracture mechanical service life

Numerical description of crack tip loading and crack propagation Chapter 2 expands on the meaning of the stress intensity factor K and the cyclic stress intensity factor ΔK as crack driving forces in the framework of linear elastic fracture mechanics (LEFM). K characterizes the stress field around the crack tip as long as plastic deformation due to loading of the flanks of the crack is limited to the near crack tip region. In LEFM the concept of K for the stress field is equivalent to the concept of the energy release rate G , which describes the release of potential energy — due to elastic deformation — during crack propagation:

$$G = \frac{K_I^2 + K_{II}^2}{E'} + \frac{K_{III}^2}{2G} \quad E': \quad E \text{ for plane strain} \quad (5.26)$$

$$\frac{E}{1 - \nu^2} \text{ for plane stress, axisymmetry and 3-D models} \quad (5.27)$$

The subscripts I , II and III refer to the mode of loading: crack opening, in-plane shear and out-of-plane shear. For the brake disks only K_I is of interest and the subscript will be dropped. In elastic-plastic fracture mechanics (EPFM) the J-integral takes the place of G . Both quantities are discussed in detail in Appendix A.2. Numerically, the J-integral can be expressed as a contour integral over a domain in a FE model and the corresponding procedures are implemented in Abaqus (see [45]). In the validity range of LEFM the J-integral coincides with G and for this reason, K can be determined in Abaqus by a contour integral. Beside other methods it is common practice to use collapsed quadratic elements around the crack front [36] as illustrated for the 2-D case in Fig. 5.33a. *Collapsed* means that at the crack tip the corner nodes are moved on top of the center node. This way, rectangular elements degenerate to triangular elements in 2-D and brick elements degenerate to wedge elements in 3-D. The desired $\frac{1}{\sqrt{r}}$ singularity in LEFM can be established with higher accuracy by tying the collapsed nodes at the crack tip and by moving the midside nodes at the lateral edges from the position $\frac{1}{2}$ to $\frac{1}{4}$. Moving the lateral midside nodes of non-collapsed quadratic elements establishes the singularity along the edges but not inside the element.

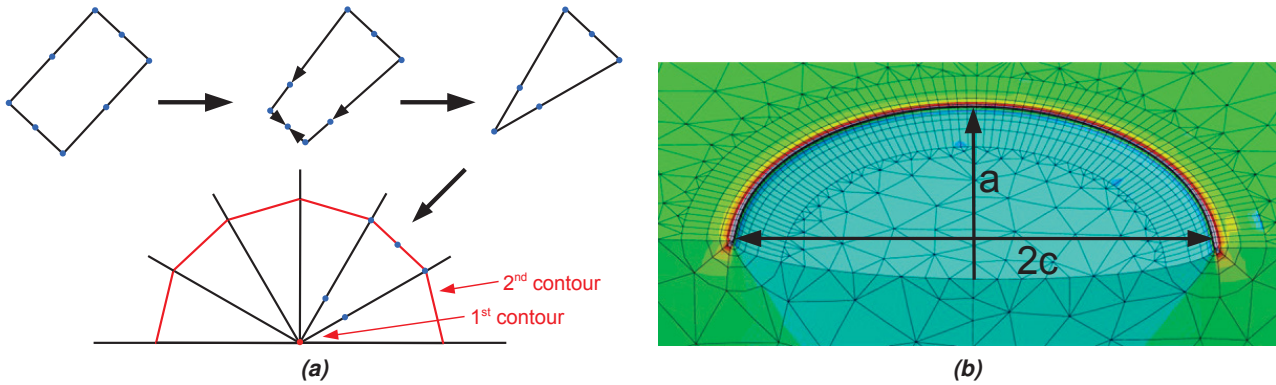


Figure 5.33: a) 2-D illustration of a crack tip modeled with collapsed elements, b) Semi-circular half-crack in a symmetrical 3-D FE-model.

This difference is illustrated in the appendix of [36]. With normal elements the desired singularity in the stress field can be achieved but a finer mesh is required. If the stress distribution close to the crack tip is not important and additionally a contour integral method is chosen, the mesh quality is less important. For numerical reasons, however, the results from first contours around the crack tip will deviate from the stable solution obtained further outside. The problem is tackled by modeling a spider web pattern and evaluating K at an outer contour, e.g. $n=5$. In a 3D model K is determined for each node along the crack front as can be derived from the FE-model depicted in Fig. 5.33b. The spider web is not obligatory, however.

The FE-method has some significant drawbacks in view of the desired parameter studies. The viability of cracks needs to be investigated under different loading conditions and for different crack geometries. The presented method necessitates individual TMF-modeling strategies for each brake scenario with all relevant crack geometries. The required time frame for the modeling and computation of the individual FE-models suggest the application of a more reasonable method within the scope of the current work.

Virtual crack method: The method presented subsequently is based on an alternative determination of K as presented by Brückner [31] and an extended numerical implementation by Gänser [32]. Fig. 5.34a and Eq. (5.28) illustrate an analytical solution for a 3-D crack with a straight crack front.

$$K_I = \frac{\sqrt{2}P}{(\pi b)^{\frac{3}{2}}} \frac{1}{1 + \left(\frac{z}{b}\right)^2} \quad (5.28)$$

This solution can be extended to Eq. (5.29), which can be used for the approximation of the stress intensity factors along a curved crack front as illustrated in Fig. 5.34b.

$$K_I(\underline{S}) = \frac{\sqrt{2}}{\pi^{\frac{3}{2}}} \iint_{\underline{R} \in A} \frac{\sigma_n(\underline{R})}{b_R^{\frac{3}{2}} \left[1 + \left(\frac{d_R}{b_R}\right)^2\right]} dA \quad (5.29)$$

The crack opening force P in Eq. (5.28) is now determined by an integral. The stresses normal to the virtual crack flank $\sigma_n(\underline{R})$ are integrated over the area of the flank A . The significant advantage of this method is that the crack does not need to be modeled in the FE mesh and virtual cracks can be inserted in the post processing in the stress field of an FE-calculation. In order to obtain ΔK the transient stress field during braking must be evaluated from increment to increment, which yields K_{min} and K_{max} . The procedure permits the fast investigation of crack propagation rates for various crack geometries, orienta-

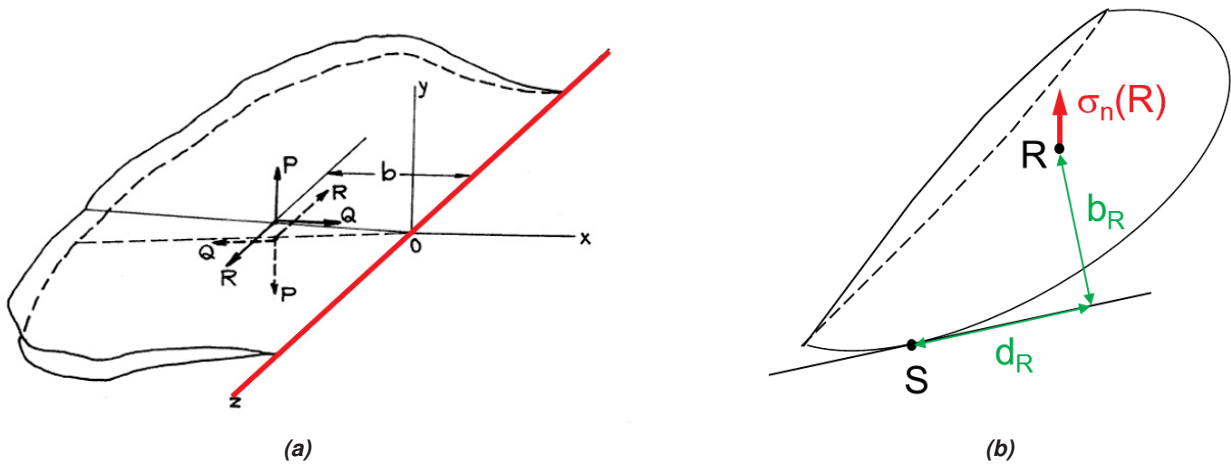


Figure 5.34: Analytical solutions for 3-D cracks with a) Eq. (5.28), straight crack front (P, Q, R ...forces, b ...distance of the application point of the force P from the crack front) and b) Eq. (5.29), curved crack front [31; 32] (S ...current point of interest, b_R ...distance of the normal stress σ_n at position R from the tangent in S).

tions and various disk positions.

The results along the crack front are approximations rather than exact solutions. A deviation from the more precise fracture mechanical FE-models occurs, because for the integration the crack front is assumed to be a tangent at the evaluated position S . It was shown by Gänser that the deviation is less than 10% in the angular range from 30° to 150° of the crack front. The deviation has a minimum at 90° and increases clearly towards the outermost points (0° and 180°). In order to determine the deviation for the current work and to investigate further improvements of the method, a cube model as depicted in Fig. 5.36a has been analyzed. As illustrated in Fig. 5.35 the cube model is used to determine stress intensity factors of a semi-elliptical crack with an analytical approximation, with finite elements and with the virtual crack method. In the first step a crack is modeled in the FE mesh and evaluated for a single a/c -ratio. In the second step an analytical method, which is available for the simple geometry is applied and verified by the FE solution. Finally, the analytical solution is determined for various a/c ratios and compared to the corresponding virtual crack solutions. The deviation is assessed and corrected if possible.

The analytical solution along the crack front of a semi-elliptical crack under tension can be found using e.g. Eq. (5.30) [106]:

$$K_I(\theta) = \sigma \sqrt{\pi a} F_I(\theta) \tag{5.30}$$

$$F_I = \frac{2}{\pi} (1.211 - 0.186 \sqrt{\sin(\theta)}) \quad 10^\circ < \theta < 170^\circ \tag{5.31}$$

The residual stresses in brake disks are high at the friction surface and diminish with increasing depth. For the brake disk problem a bending load is thus more relevant and a general analytical solution for tension and bending from the FKM guideline is used [40]. The procedure is more complex than Eq. (5.30) and it is outlined in the appendix (Fig. D.2). Fig. 5.36b compares the FE solution along the crack front (Fig. 5.33b) to the analytical solution, which is available for the positions 0° and 90° . The accordance is sufficient and the FKM solution can be used as reference for the next step. Fig. 5.37a additionally shows the virtual crack solution. For $a/c = 1$ the analytical K_a deviates by 2.3% from the FE solution and the virtual crack

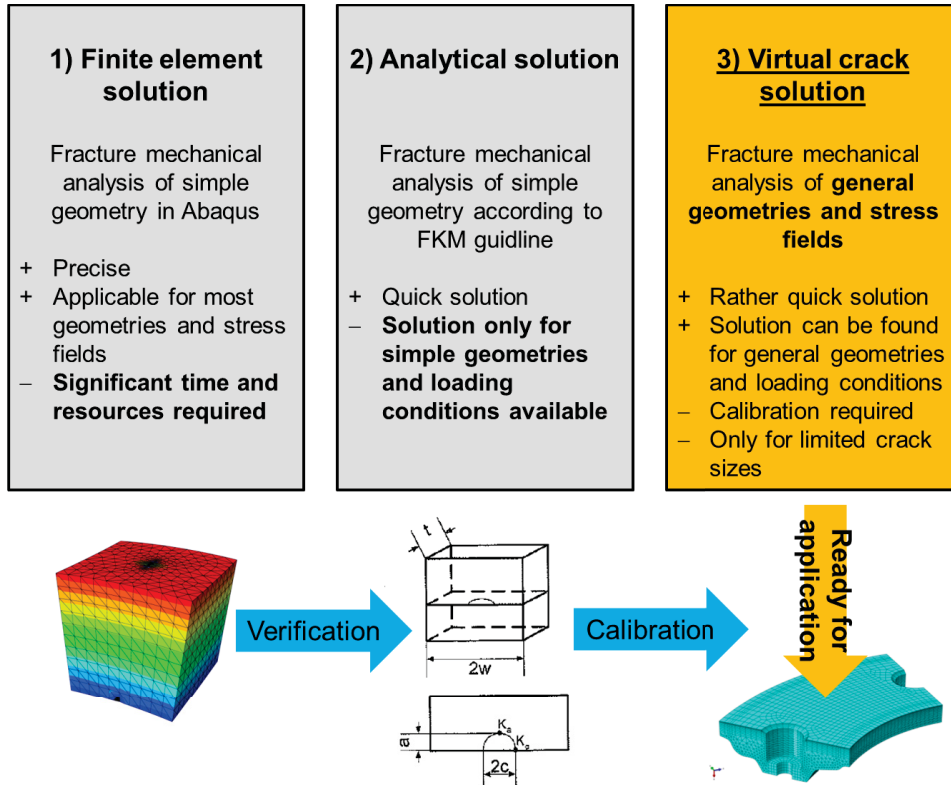


Figure 5.35: Illustration of the verification procedure for the virtual crack solution.

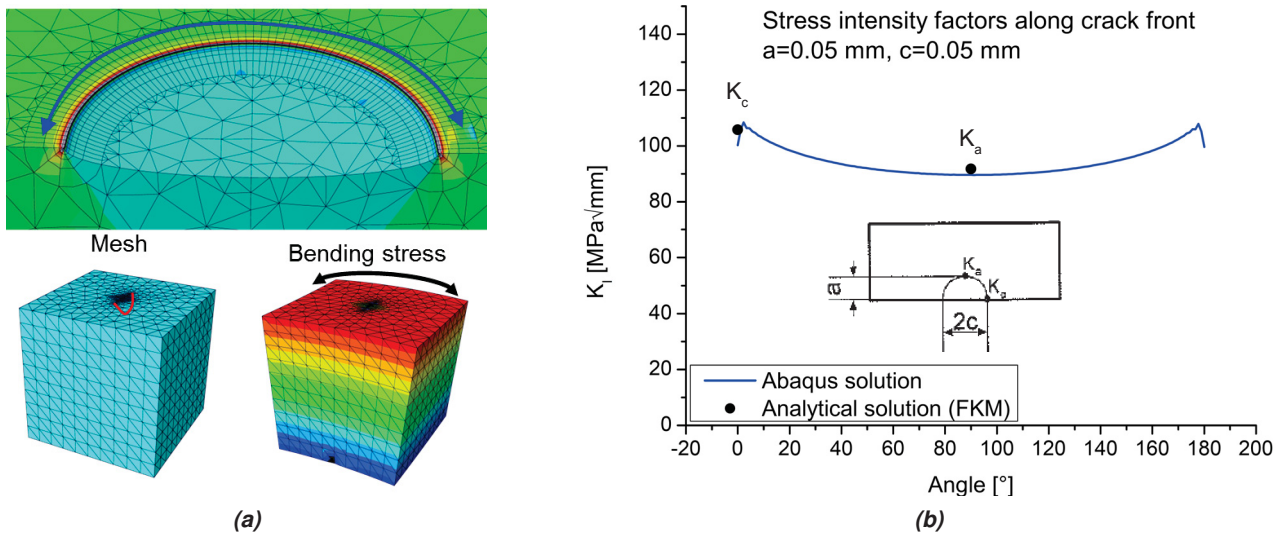


Figure 5.36: a) Example of a cube model used for verification purposes, b) Comparison between FE solution and analytical solution for K_I along the front of a semi-elliptical crack

solution (VCS) by 4.9%. For K_a the results are conservative and acceptable. The same conclusion holds in the case of K_c for the analytical approximation but the VCS deviates in the non-conservative direction. A parameter study investigating a range of a/c -ratios and crack dimensions shows that the deviations are systematic and depend on the a/c -ratio and the angular position. The corresponding data are plotted in Fig. 5.37b for tensile and for bending load. Due to the systematic deviation the correction functions f_a and f_c can be fitted through the data for K_a and K_c . Both functions are included in the numerical evaluation

5. MODELING

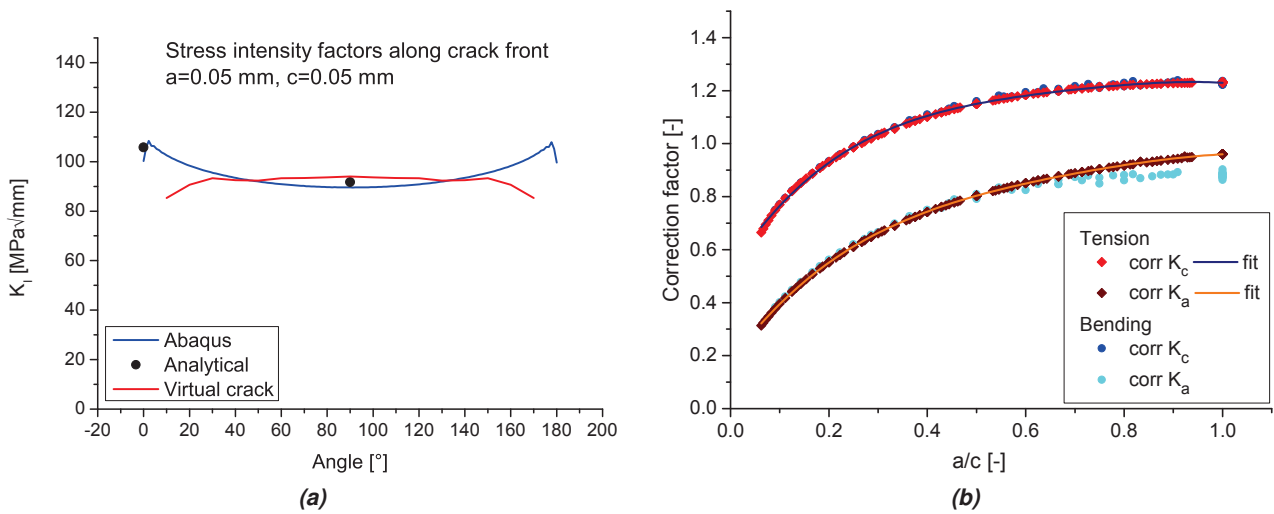


Figure 5.37: a) Comparison between FE solution, analytical solution and virtual crack solution for K_I along the front of a semi-elliptical crack, b) correction functions for K_a and K_c

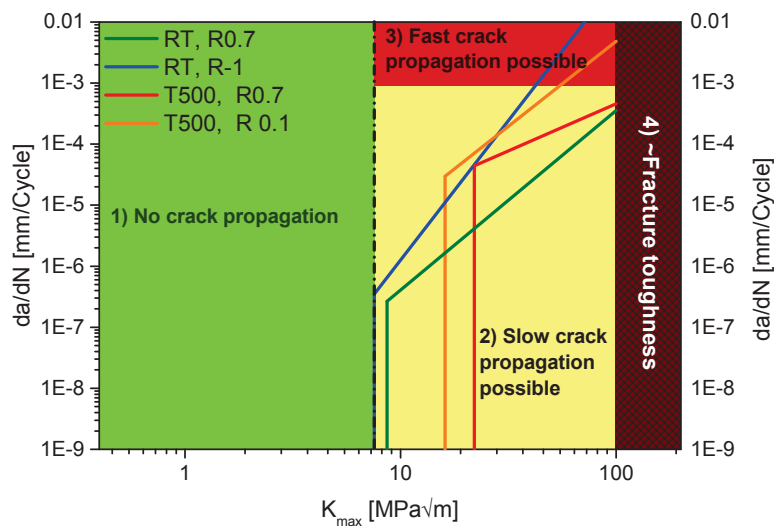


Figure 5.38: Overview of crack propagation data collected for material A for two temperature levels and two stress ratios.

tool developed by Gänser and this way the virtual crack method is ready to use for the brake disk problem.

Experimental characterization of crack propagation Chapter 2 expands on the theory of static and cyclic crack growth and additional information is given in Appendix A.2. At this point an overview of the experimental program is given. Table 5.11 lists influencing parameters on crack propagation during testing. The influences have been characterized in the scope of this work and parallel projects. The focus for this study is laid on the characterization of crack propagation and for this purpose cyclic tests are carried out at 20°C and 500°C. At 500°C the test frequency f_{test} becomes important due to the onset of oxidation. In order to achieve crack propagation f_{test} is much higher than TMF load cycles. This is conservative, however, because oxidation gives rise to crack closure and lower propagation rates. With increasing cycle times as in the case of railway braking this effect becomes more pronounced.

Table 5.11: Parameters for static and cyclic fracture mechanical testing

| static | | | cyclic | | |
|-----------------------------|------------|---|---------------------------------------|------------|---|
| Parameter | Symbol | Comments | Parameter | Symbol | Comments |
| Temperature | T | 20°C | Temperature | T | 20°C, 500°C |
| Sample geometry | S_G | 3SENB | Sample geometry | S_G | 8SENB |
| Sample thickness | B | Set for plane strain | Sample thickness | B | Set for plain strain |
| Sample width | W | Set according to standards | Sample width | W | Set according to standards |
| Test frequency | f_{test} | The results are highly speed dependent at all temperatures. | Test frequency | f_{test} | Speed dependence at high T |
| Precracking | R_{pre} | The applied method determines the stress/strain state in the sample | Precracking | R_{pre} | The applied method determines the stress/strain state in the sample |
| Calculation of crack growth | - | Method that transforms potential to crack length | Stress ratio Calculation crack growth | R_σ | 0.7, -1 Method that transforms potential to crack length |

Fig. 5.38 shows the obtained data for material A in terms of K_{max} ¹. The reason for this representation will be discussed in Chapter 6. The diagram can be subdivided into 4 regions:

1. Green area: The region below the lowest determined threshold value $K_{max,th}=7.56 \text{ MP}\sqrt{\text{m}}$. If the simulated K_{max} is below this value no crack propagation is expected.
2. Yellow area: In this region crack propagation is possible but no more than a crack length of $c=40 \text{ mm}$ is expected within 10000 high energy stops. 40 mm long cracks close to the mounting holes are the criterion for disk replacement for steel disks. 10000 high energy brakings is a conservative assumption for in-service conditions until the disk must be replaced due to wear or predefined maintenance schedules.
3. Red area: In this region crack lengths exceeding $c=40 \text{ mm}$ are possible even for less than 10000 high energy brakings.
4. Brown area: K_{max} approaches the fracture toughness K_{IC} . The corresponding loading conditions may induce immediate disk failure. This region must be avoided at all costs and a safety margin must be observed.

¹ $K_{max} = \frac{\Delta K_{th}}{1-R}$



Chapter 6

Simulation results

The first part of this section treats the results for material A obtained with uniform and non-uniform thermal loading, respectively. The second part focuses on the comparison of material A with the other four materials mentioned in Section 5.2.7.1. These comparisons are based on uniform thermal loading.

6.1 Results for material A — Uniform loading

In this section the non-uniform nature of the temperature is not taken into account. The thermal loading is applied as outlined in Section 5.2.4.1, which provides the necessary flexibility for parameter studies and comparisons of different brake scenarios. The resulting temperatures can be interpreted as average values at the disk surface, which coincide with the non-uniform solution further below.

6.1.1 Temperature evolution

Fig. 6.1 shows the temperature evolution at a central position on the friction surface (red). The other lines represent the temperature evolutions below the friction surface down to a depth of 12.5 mm (black). The thermal loading corresponds to the reference case, which was tested on a test rig. The reader is referred to Fig. 5.7 for the applied thermal input. A depth of 12.5 mm marks the boundary between the structured mesh consisting of brick elements and the non-structured tetrahedral region comprising the cooling fins (see Fig. 5.2). As outlined in Chapter 4, the surface region, especially the top 2 mm, are of special interest in the current work since inelastic deformation and cracks occur there. The discussion of the simulation results will thus focus primarily on the surface region.

Starting from $T_{ini}=40^{\circ}\text{C}$ the friction surface reaches a temperature of 610°C after 19.3s. This is the point in time where the braking force is increased from 30 kN to 45 kN. $T_{max}=740^{\circ}\text{C}$ is reached after 32s, which corresponds roughly to half of the brake time t_{end} . Towards the end of the braking the temperature drops down 515°C , followed by a cooling period of 250s. At the end of the simulation the temperature field in the whole disk is reset to $T_{ini}=40^{\circ}\text{C}$. With increasing depth the maximum temperature occurs after 32s and at lower temperature levels. In 12.5 mm depth, $T_{max}=460^{\circ}\text{C}$ occurs after 54s when the braking has almost finished. The thermal gradient in thickness direction corresponds to the distances between the curves plotted in Fig. 6.1. The curve at the friction surface is the steepest and for the other curves the slopes decrease with depth. The largest gradients occur between the beginning of the brake application and

6. SIMULATION RESULTS

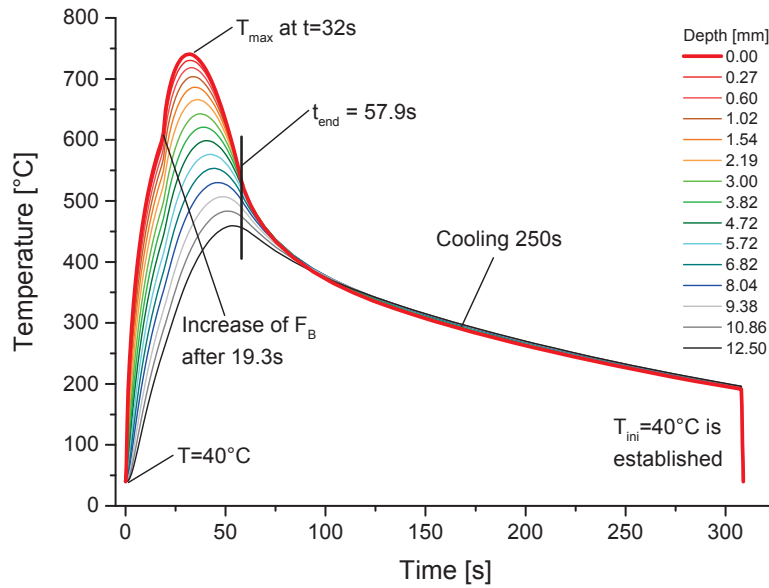


Figure 6.1: Temperature evolution at a central position on the friction surface indicated by the red dot and positions underneath down to 12.5 mm depth. The mesh is finer in the surface region than at greater depths. Hence, it should be noted that the corresponding distances between the plotted lines steadily increase. Characteristic points in time are commented.

T_{max} at the surface (32s). At 19.3s where F_B is increased the present gradients are augmented due to the additional thermal input. The temperature levels at different depths as well as the forming temperature gradients are paramount factors for the resulting viscoplastic response of the material as will be discussed in Section 6.1.3.

Fig. 6.2a compares the red curve in Fig. 6.1 to corresponding results for lower dissipated energies in order to assess the entailed changes in the temperature field. In later sections this comparison will be further discussed in view of other quantities such as the inelastic strain ϵ_{in} . 100% refers to the reference braking discussed above. Lower dissipated energies can be obtained by a different brake blending of the individual

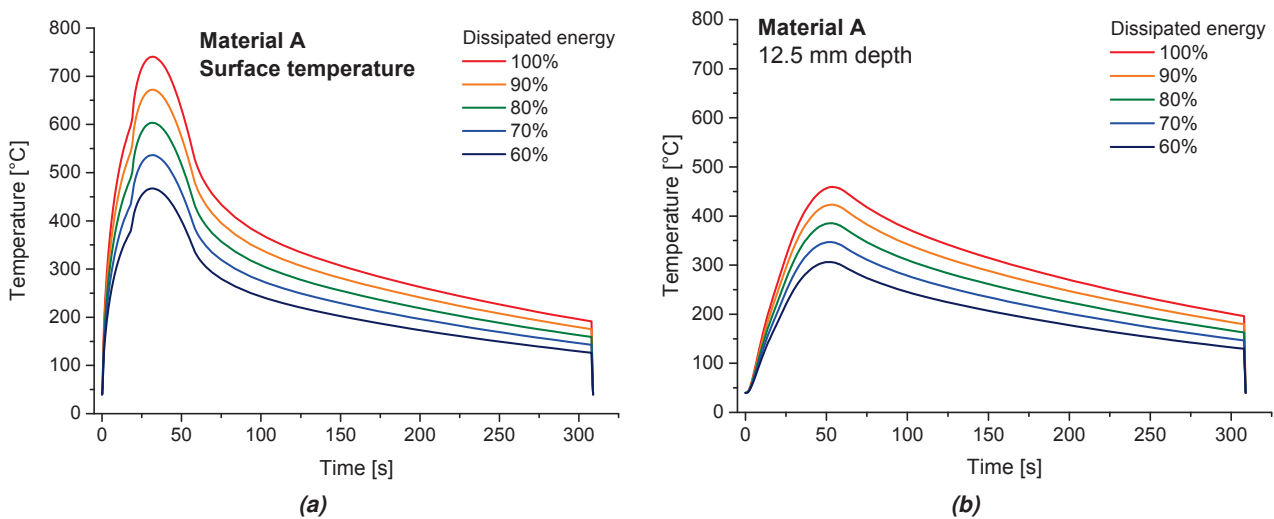


Figure 6.2: Comparison of the evolution of the temperature due to different thermal input a) at the friction surface and b) in 12.5 mm depth.

brake systems, by a greater number of brake disks or by more massive disks. The opposite case is also

applicable and can be assessed with the simulation tool. The thermophysical properties and thus the thermal calculations are valid up to 1000°C (see Section 5.2.2). For the mechanical simulations, however, the according ranges of validity must be considered, which are outlined in Section 5.2.7.1. The impact of thermophysical properties will be discussed within the scope of the material comparison in Section 6.4.

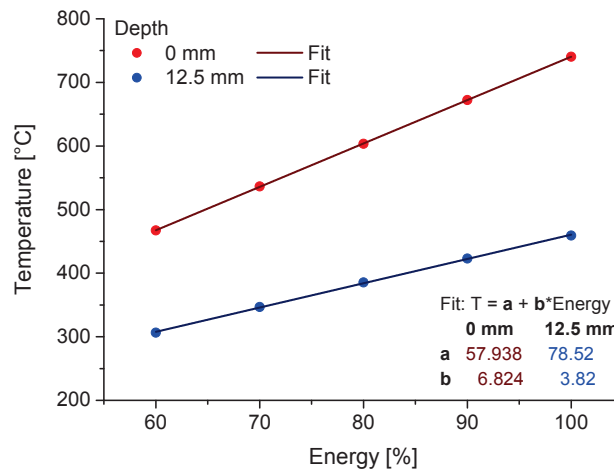


Figure 6.3: Values for T_{max} at the friction surface (0 mm) and 12.5 mm depth.

Fig. 6.3 summarizes the data in Fig. 6.2a and Fig. 6.2b in terms of the maximum temperatures. The expected linear increase of T_{max} with dissipated energy is evident and both data sets can be described by a linear fit as indicated. The interception points do not meet exactly at $T_{ini}=40^{\circ}\text{C}$ for zero heat input, since this area is not of interest and no data points were generated. The fits can be used for rough estimations of maximum temperatures in different depths for the investigated disk type and variable energy input. It should be noted that brake scenarios with shorter or longer brake time and different settings for the increase of F_B yield different slopes for the curves in Fig. 6.3. The representation in Fig. 6.3 can easily be extended in order to capture these influences. This is left for the industrial application and will not be discussed in this work.

6.1.2 Disk coning and waviness

Due to the temperature field during braking the surface region of the brake disk expands. As a consequence of the temperature variation in thickness direction from the surface to the cooling fins, the disk cannot expand homogeneously and disk coning occurs. This situation is depicted in Fig. 6.4 for the reference thermal input (100%) for the point in time with maximal coning. In the case of inelastic deformation in the surface region during braking the coning is not fully reversible and static coning remains. Since the material deforms under compression, a shortening of each volume element close to the surface takes place. This is the reason why inverse coning is present after cooling.

Fig. 6.5a shows the evolution of the maximal dynamic coning C_{DM} and static coning C_{St} in mm with increasing number of simulated brake cycles. Since isotropic hardening is not considered only a low number of cycles are required to stabilize stress redistribution due to inelastic deformation, mean stress relaxation and recovery in the disk. As discussed in Chapter 5 the stabilized stress/strain state must be determined in order to have a representative state for the largest part of the service life at hand. The curves in Fig. 6.5a have not yet stabilized but judging from the scales used in the diagram and the shape of the two evolutions

6. SIMULATION RESULTS

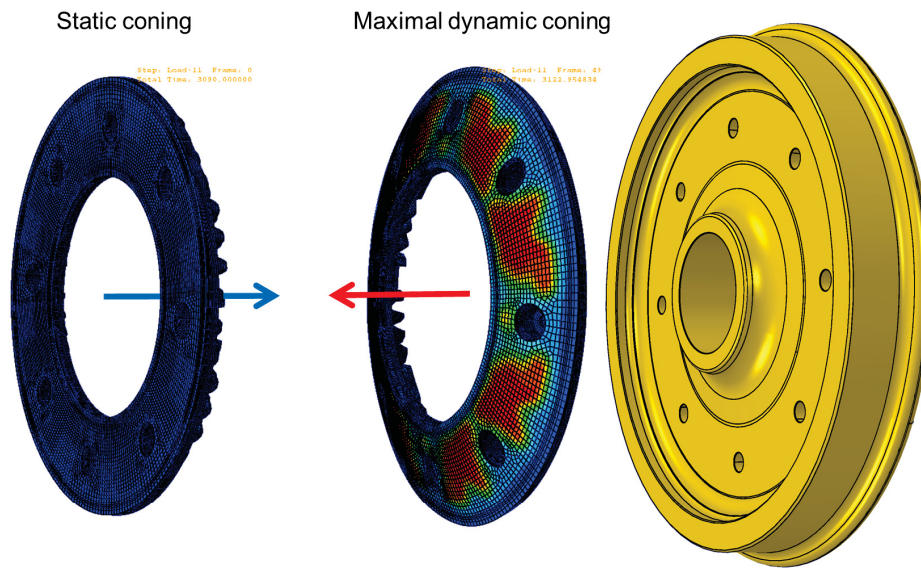


Figure 6.4: Illustration of dynamic and static disk coning (exaggerated). The arrows show in the direction where the inner disk radius moves.

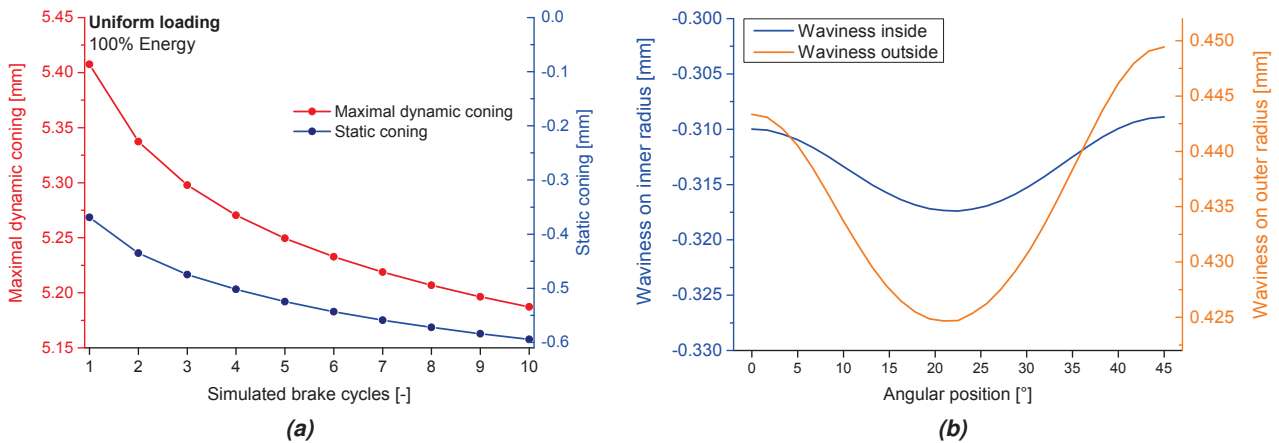


Figure 6.5: a) Stabilization of maximal dynamic coning and static coning with increasing number of simulated brake cycles, b) Stabilized waviness after 10 cycles.

sufficient stabilization can safely be assumed after 10 load cycles. C_{DM} begins with 5.40 mm and stabilizes around 5.20 mm. C_{St} is -0.37 mm after the first braking and increases to -0.6 mm. The change in C_{DM} is obviously due to the evolution of the static coning with each brake cycle. These data will be used for verification purposes in Section 6.3.

Inelastic deformation during braking gives not only rise to static disk coning but induces waviness in tangential direction as depicted in Fig. 6.5b. Along the inner disk circle the axial coordinate is negative due to the static coning. Nevertheless, a clear wave is visible when the scale is reduced. The wave along the outer disk circle is situated in the positive coordinate range. On the outside the wave is naturally more pronounced than on the inside but the amplitude is still small compared to the deformation due to disk coning. Fig. 6.6 shows the amplitudes of the individual oscillation orders detected by a simple Fourier analysis. The only orders being physically reasonable in the symmetrical FE-model are the orders 2 and

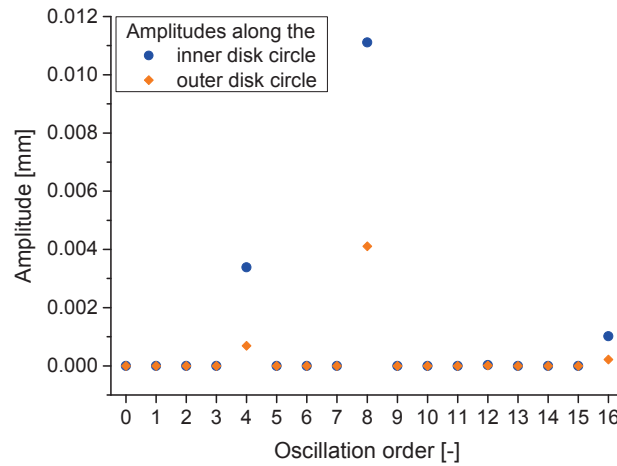


Figure 6.6: Simulated waviness split up into individual oscillation orders.

8 as already mentioned in Section 4.2.1. The amplitude for the order 16 is a numerical artifact and may have been detected at the costs of the orders 2 and 8. On the inner disk circle the amplitudes for the orders 4 and 8 are 6.89×10^{-4} mm and 4.11×10^{-3} mm, respectively. On the outer circle the corresponding values are 3.4×10^{-3} mm and 1.12×10^{-2} mm, respectively. As outlined in Section 4.2.1, the amplitudes in the tested disk are subject to significant scatter. Nevertheless, they will be compared to the simulated data in Section 6.3.

6.1.3 Damage mechanical evaluation of service life

Fig. 6.7 depicts σ - ϵ hystereses in the main loading direction (tangential) for the first simulated brake cycle (green) and cycle 10 (blue). In the case of TMF loading it is necessary to distinguish between the total strain ϵ_{tot} and the mechanical strain ϵ_{mech} because a thermal strain ϵ_{th} occurs, which does not contribute to the stress formation:

$$\epsilon_{mech} = \epsilon_{tot} - \epsilon_{th} \quad (6.1)$$

Additionally the temperature is plotted versus ϵ_{mech} in order to correlate the mechanical hystereses with the corresponding temperatures during the TMF cycle. In the TMF tests presented in Section 5.2.7.1 the T - ϵ hystereses are due to the used control signal straight lines (zero area), while the hystereses in Fig. 6.7 are clearly open. On the one hand this difference arises from the direct use of a linear temperature evolution as the control signal during testing and on the other hand from the indirect control signal, i.e. the resulting heat flux from friction into the brake disk. Furthermore, the temperature field in the TMF samples is uniform while a temperature gradient occurs in the brake disk. Nevertheless, TMF tests capture the relevant physical processes for TMF loading, as long as the constraint factor K_{TM} , T_{max} and the heating/-cooling rates are properly chosen.

From the four depicted hystereses it is evident that the onset of reverse deformation sets in before T_{max} is reached. Although the temperature lowers the yield strength of the material, T_{max} is not the only factor for inelastic deformation. Another factor is the temperature gradient in thickness direction, which is represented in Fig. 6.1. The gradients are highest between the onset of the braking and the incidence of T_{max} . At the surface significant plastic deformation under compression occurs, which is less severe at greater

6. SIMULATION RESULTS

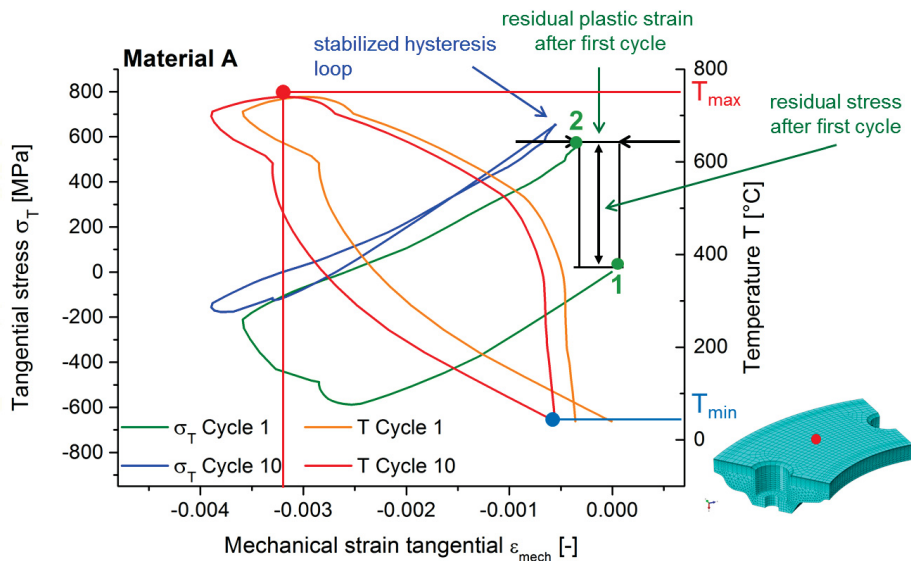


Figure 6.7: Stress-strain response during load cycle 1 and cycle 10 at the friction surface and correlation with the temperature evolution depicted in Fig. 6.1 in the form of T - ϵ hysteresses.

depths, as can be seen in Fig. 6.8a for the first simulated brake cycle. Fig. 6.8a compares the inelastic strain ϵ_{in} in tangential direction for different depths. At the surface a significant compressive ϵ_{in} occurs,

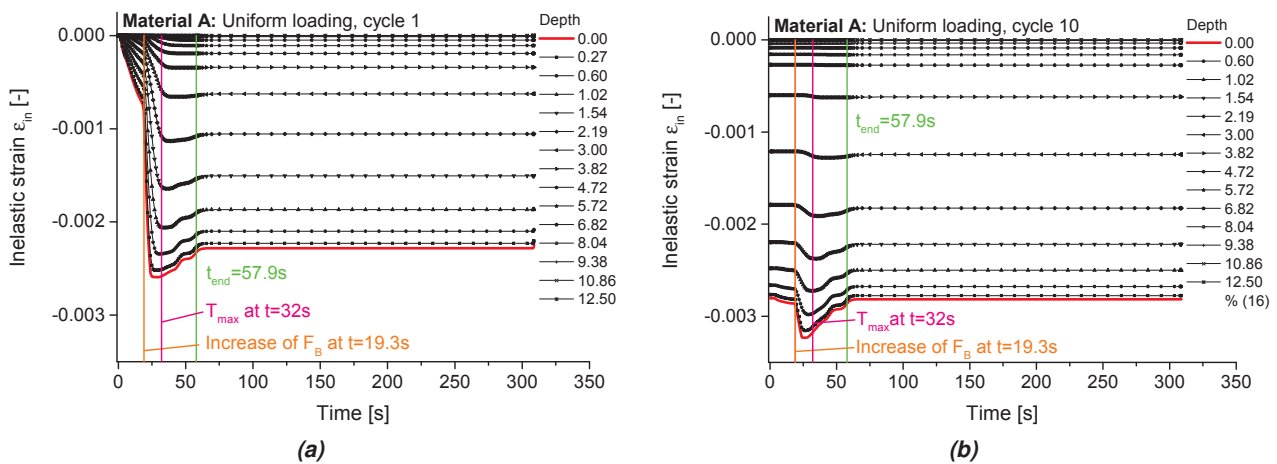


Figure 6.8: Inelastic strain in tangential direction for various depths during a) simulated brake cycle 1 and b) 10.

which increases clearly when F_B is increased from 30 to 45 kN after 19.3s. Between this point in time and T_{max} reverse plastification begins. This can be explained by the distinct inelastic shortening of each volume element in the surface region, which is more pronounced than at greater depths. Since the whole disk has heated up it expands as a whole and stretches the shortened volume elements. The more plastification under compression the more reverse plastification is thus expected, which is largest at the surface. During cycle 1 inelastic deformation occurs down to a depth of 6.8 mm. Reverse plastification, however, only occurs down to a depth of 3.0 mm, which means that the expansion of the disk only causes elastic reverse deformation below 3 mm. The reverse plastification is finished shortly after t_{end} . Down to a depth of 0.6 mm a small increment of ϵ_{in} is visible, which is caused by the decrease of the dynamic coning. After 10 load cycles (Fig. 6.8b) the plastification under compression and the reverse plastification under

tension at the surface are equal and also the strain increment after cooling has disappeared. Plastification occurs down to a depth of 4.7 mm and reverse plastification down to 3 mm as in the previous case. In the transition area where the reverse plastification starts to decrease but plastification under pressure is still present, a negative increment in ϵ_{in} remains and this explains the fact that disk coning is nearly but not completely saturated after 10 cycles.

The evolution of ϵ_{in} in tangential direction at the friction surface in cycle 1 and 10 is directly compared in Fig. 6.9a. The figure shows the significantly higher plastification under compression during the first cycle compared to cycle 10.

For this reason, the starting point and the end point of the green hysteresis in Fig. 6.7 cannot coincide, which can be explained by the significant residual stress formation and mean stress relaxation as noted above. The horizontal distance between point 1 and point 2 in Fig. 6.7 corresponds to the residual inelastic strain that was not reversed during the load cycle (see Fig. 6.9a). It has a negative sign and indicates that inelastic deformation under compression prevailed over deformation in the tensile phase of the local load cycle, which is obvious from Fig. 6.8a. The vertical distance between point 1 and 2 in Fig. 6.7 equals the residual stress σ_{res} remaining after the first cycle. Since inelastic deformation under compression prevails σ_{res} is tensile. In this case σ_{res} reaches 550 MPa after the first cycle. This mechanism has been discussed in detail in Section 1.3 and Section 2.3. The largest part of σ_{res} forms during the first cycle and it further increases in the course of the subsequent cycles until a stabilized state is obtained. In accordance with the discussion in Section 6.1.2 multiple load cycles are computed to obtain a stabilized material response that can be used for life time assessment. For the hysteresis from cycle 10 (blue) in Fig. 6.7 the start point meets the end point, i.e. in terms of the σ - ϵ response of the material at the investigated position stabilization is accomplished. The hysteresis area is significantly smaller than during the first cycle since

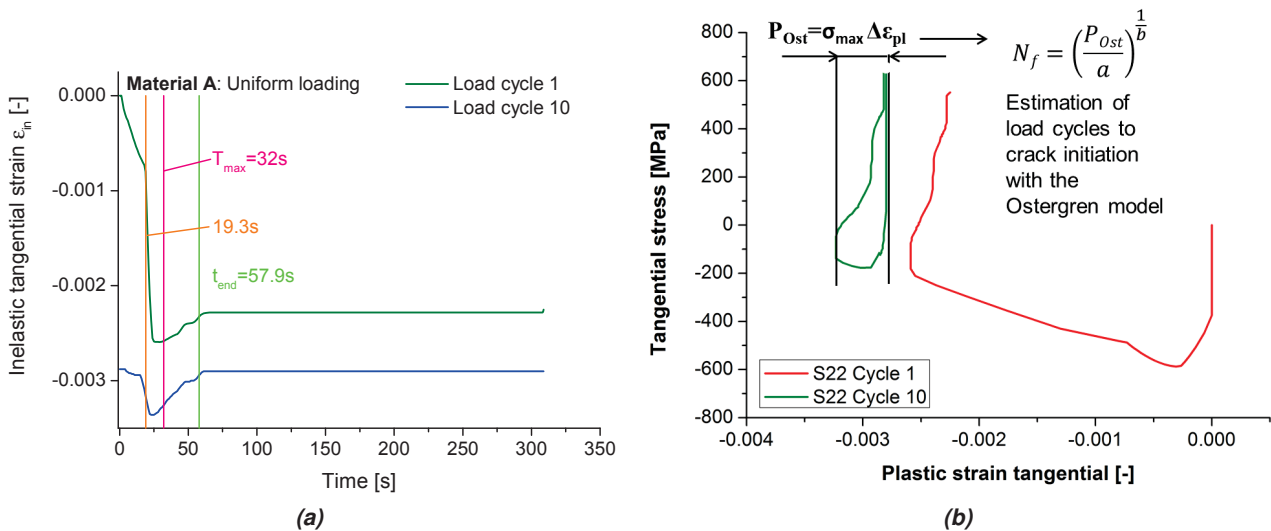


Figure 6.9: a) Inelastic strain in tangential direction at the friction surface after load cycle 1 and 10 in tangential direction as a function of time, b) Stress versus inelastic strain.

mean stress relaxation and stress redistribution have stabilized. This means that plastification and reverse plastification are equal during each cycle that follows as previously mentioned. In contrast to isothermal LCF testing the stress ratio R_σ does not reach -1 since plastic deformation under compression and tension

6. SIMULATION RESULTS

are obviously unbalanced during the first cycles and the temperature varies. This affects the σ - ϵ response significantly because stresses can be reduced at elevated temperatures ($> 600^\circ\text{C}$) by recovery, while this is not possible when tensile residual stresses form towards the end of the brake cycle. The hysteresis branches intersect, which is due to elastic deformation caused by the different temperature levels during the heating and the cooling branch and consequently by the corresponding temperature dependent Young's moduli. All of these effects are captured accordingly by the chosen material law (see Section 2.2, Section 2.5.3 and Section 5.2.5). The material law thus establishes the link between the stress levels and the inelastic strains that is not captured in the Ashby maps in Fig. 2.11, Fig. 3.32 and Fig. 4.42. The hystereses from cycle 1 to 10 move in σ - ϵ space due to the static disk coning and the corresponding inelastic strain increments. The two phenomena interact and the position of the hysteresis stabilizes along with the static coning after roughly 10 cycles.

Fig. 6.9b shows the two mechanical hystereses in Fig. 6.7 in terms of ϵ_{in} rather than ϵ_{mech} . This representation is relevant for the application of the Ostergren model for the estimation of the load cycles until crack initiation. For this model the hysteresis width $\Delta\epsilon_{in}$ is required as indicated and the maximum stress σ_{max} . The hysteresis from cycle 1 gaps open and yields a value for $\Delta\epsilon_{in}$, which is too high and is not representative for the whole service life of a brake disk. Furthermore, σ_{res} has not yet obtained its stabilized level and the value is too low to be representative. After 10 cycles the hysteresis has nearly closed and σ_{res} is stable. As shown in Fig. 6.9b the required values for the Ostergren model can be determined and used for the prediction of N_f^1 according to Eq. (5.23). For the extension to multiaxial loading as in the present case, the von Mises equivalent stress σ_{eq} and the change of the equivalent plastic strain Δp (see Eq. (2.64)) will be used, while the representation in principal loading direction, here the tangential direction will be maintained for the discussion of the diagrams. Fig. 6.10a compares the in-depth distribution of the

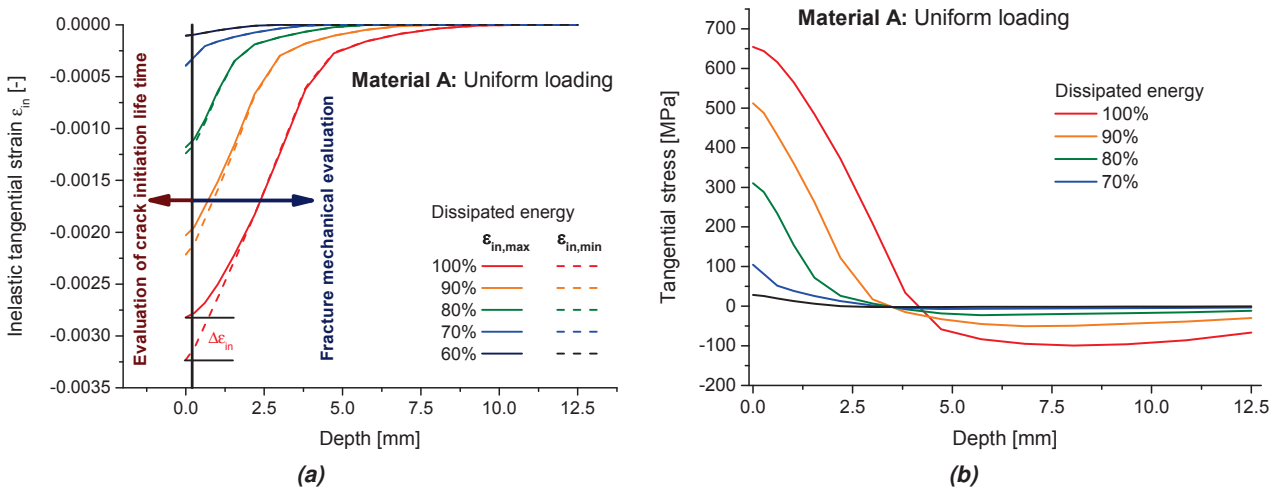


Figure 6.10: a) Comparison of the stabilized minimal and maximal in-depth distribution of ϵ_{in} for varying energy input. The regions of validity for damage mechanical (crack initiation) and fracture mechanical (crack growth) evaluations are indicated. b) The corresponding stabilized residual stress field at the end of load cycle 10.

minimal and the maximal inelastic strain in tangential direction for variable energy input. For each level of dissipated energy $\Delta\epsilon_{in}$ corresponds to the vertical distance between the two corresponding curves. The simulations allow to assess how much this quantity decreases with decreasing dissipated energy. Already

¹within the scope of this work N_f refers to the number of load cycles until crack initiation rather than to failure.

a decrease of E_d by 10% entails a decrease of $\Delta\epsilon_{in}$ by 55%. This result shows that the optimal application range of brake disks is rather small for brake configurations preventing early failure but also avoiding oversizing. For this reason a simulation tool is key in the design process.

The value for σ_{max} equals the residual stress σ_{res} after the disk has cooled down to T_{ini} as depicted in Fig. 6.10b. A decrease of E_d by 10% causes a decrease of σ_{res} by 22%. The necessary data for the Ostergren model are now available for the investigated position but also for the complete FE-model and the evaluation of N_f can be carried out for different brake energies and positions within the brake disk. It must be kept in mind, however, that a damage mechanical evaluation aims at the prediction of the number of load cycles to crack initiation. This makes only sense in the surface region since predictions further below yield higher values for N_f , where a crack is already present and changes the local σ - ϵ field. The service life evaluation in the regions below the surface can only be based on fracture mechanical methods (or damage mechanical methods including crack propagation). The crack driving forces stem from the transient stress field where σ_{res} depicted in Fig. 6.10b gives rise to the maximal stress intensity factor during the load cycle. The fracture mechanical evaluation where cracks are positioned in the stress field will further be discussed in Section 6.1.5, while in the remainder of this section the focus is laid on crack initiation.

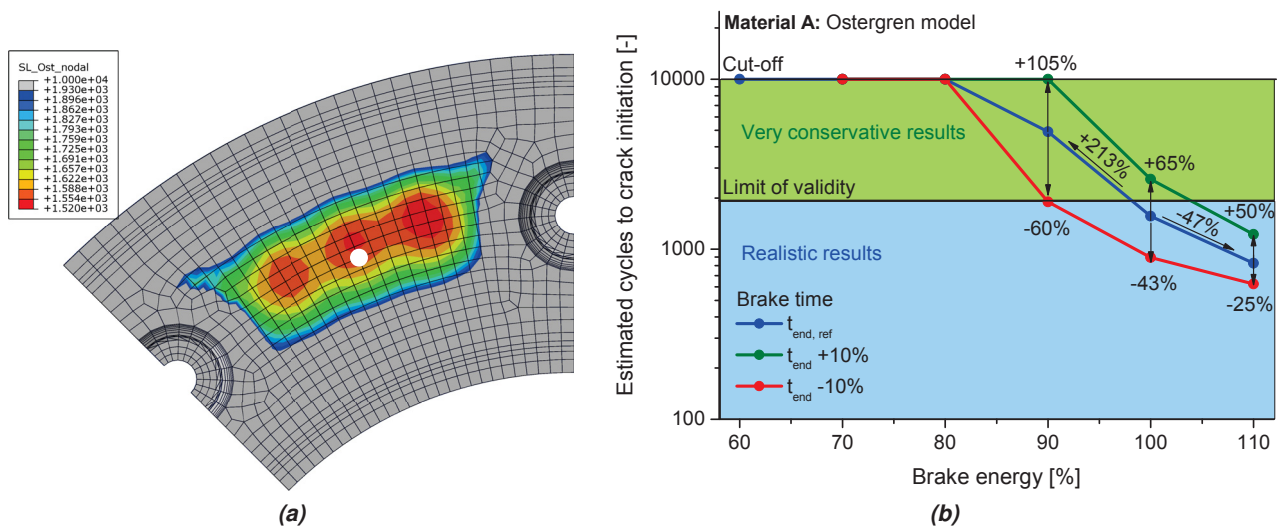


Figure 6.11: a) Predicted crack initiation life time N_f based on the Ostergren model for different values of dissipated energy E_d and brake time t_{end} , b) Local distribution of N_f on the friction surface within the validity range.

Fig. 6.11a shows the computed N_f for the reference brake scenario as a distribution on the friction surface. At the lower end the distribution is limited by the minimum value of 1520 brake cycles and on the upper end by the validity limit of 1930 cycles. With this scale the influence of the three cooling fins at the reverse side is visible (3 circular spots) as well as the fact that one of the mounting holes is stiffer than the other one (the spot on the right is more pronounced than the left one). The difference between the regions plotted red and orange is only 30 cycles and between red and yellow 100 cycles, i.e the influence of the cooling fins is low compared to $N_{f,min}=1520$ cycles. A specific position, the central position on the friction surface, is indicated by a white dot in Fig. 6.11a. This position is evaluated in order to compare the results of simulations with variable values for E_d and t_{end} as depicted in Fig. 6.11b. The comparison is carried out for $E_d=60$ -110% of E_d^{ref} of the reference value and for t_{end} in the range of $\pm 10\%$ of the reference case.

6. SIMULATION RESULTS

The results in the blue field are within the validity range of the Ostergren model as defined in Fig. 5.32b. Results in the green field are very conservative since the onset of elastic shakedown takes place. The results clearly show the impact of E_d . From 100% to 110% N_f decreases by 47% and from 100% to 90% of $E_{d,ref}$ N_f increases by 213%. The result for 90% of $E_{d,ref}$ is outside the validity range and N_f is thus underestimated, i.e. the real difference is greater than 213%. The brake time has a significant impact as well since the material behavior is time and rate-dependent. At 110% of E_d^{ref} and a decrease of t_{end} by 10% decreases N_f by 25%. Conversely, an increase by 50% occurs when t_{end} is extended by 10%. With decreasing E_d the impact of t_{end} becomes stronger and at 90% E_d^{ref} N_f changes by +105%/ -60%. The accumulated plastic strain at the reverse side of the brake disk is zero after 10 simulated brake cycles, which is as required according to design standards. The same applies for the other investigated loading conditions and the reverse side can thus be neglected for the LCF evaluation.

6.1.4 Influence of disk wear

A further influence not taken into account so far is disk wear. It reduces the thickness and the mass of the brake disk, which changes the resulting temperature levels and temperature gradients. This influence can be quickly assessed by the application of the previous procedure to the worn geometry. Fig. 6.12 displays the mesh of the original geometry alongside with the mesh of the worn disk, assuming 5 mm wear, which is the current wear limit. The region with brick elements is reduced in thickness and the mesh is changed in order to obtain a similar mesh size. Fig. 6.13a shows the temperature evolution in three different depths.

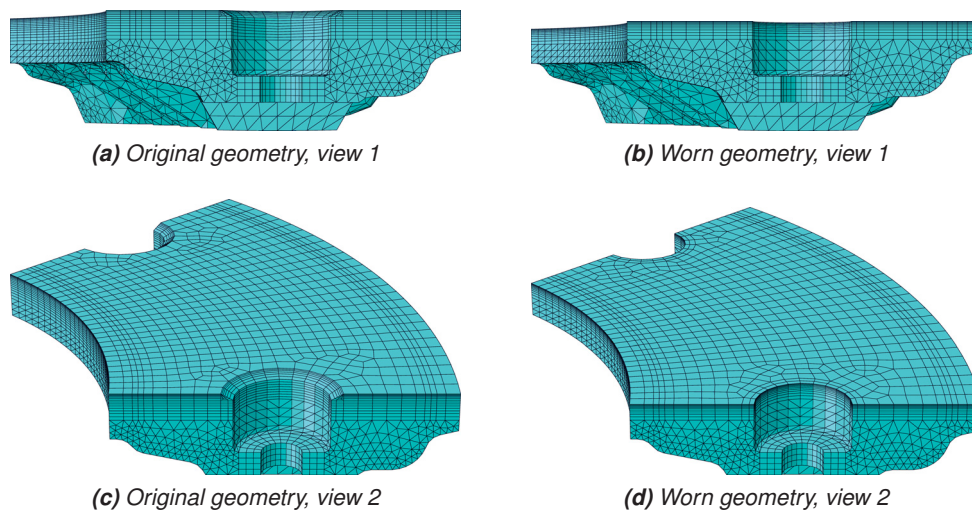


Figure 6.12: Comparison between original geometry and geometry based on a wear limit of 5 mm

In the surface region the temperature during braking for both geometries correspond well to each other with minor deviations. At the reverse side between the cooling fins, however, a clear difference is visible. T_{max} is higher for the worn geometry. During cooling the temperature evolutions at all positions deviate since the temperature field in both geometries becomes homogeneous and cools at a different speed. The homogenization in the worn geometry is faster and the disk cools sooner. This can be explained by the reduced disk mass and the smaller thickness. The total heat capacity of the worn disk is lower and the temperature in the disk bulk reaches higher values. Additionally, the temperature field reaches the cooling

fins faster. This accounts for the higher T_{max} at the reverse side and also for the faster cooling. The same E_d is introduced into both geometries but the reverse side of the worn disk reaches a higher temperature maximum in a shorter time. This enables the disk to emit more heat by convection, while the unworn disk stores the introduced heat longer.

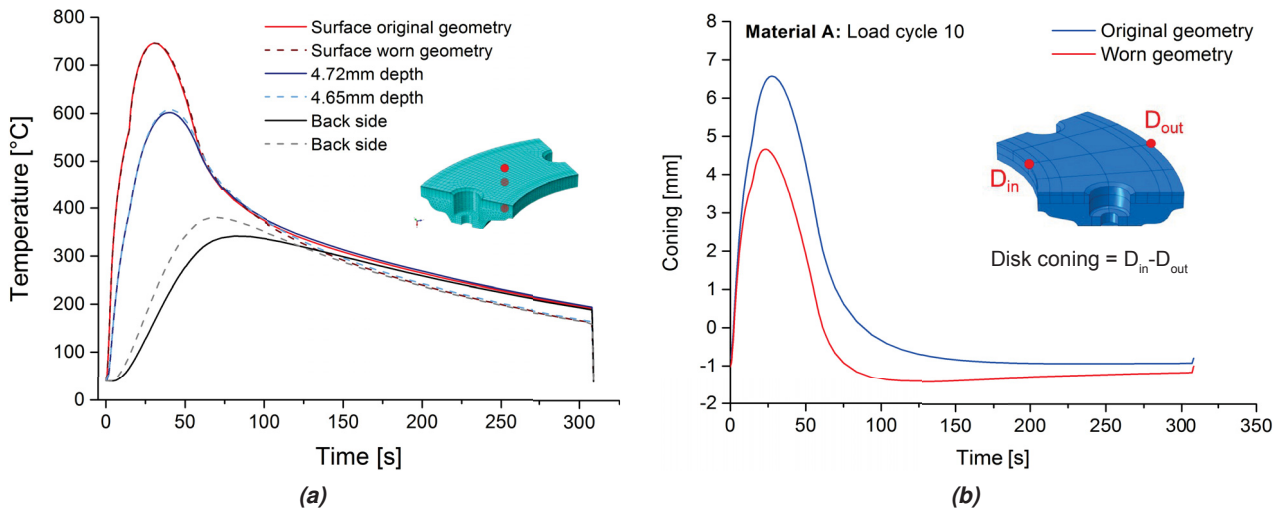


Figure 6.13: a) Comparison of the temperature evolution in the original and the worn geometry and b) the corresponding disk coning during load cycle 10.

One consequence of the change of the temperature field and the disk stiffness with increasing wear is a change of the disk coning as shown in Fig. 6.13b. Due to the fact that the temperature field in the worn disk is more homogeneous and the decreased thickness allows more thermal expansion, the maximal dynamic coning C_{DM} reduces from 6.6 mm to 4.7 mm. The static coning C_{St} , however, increases from -0.81 mm to .1.02 mm because the undeformed bulk that tries to force the whole disk back into its initial shape is smaller due to the wear.

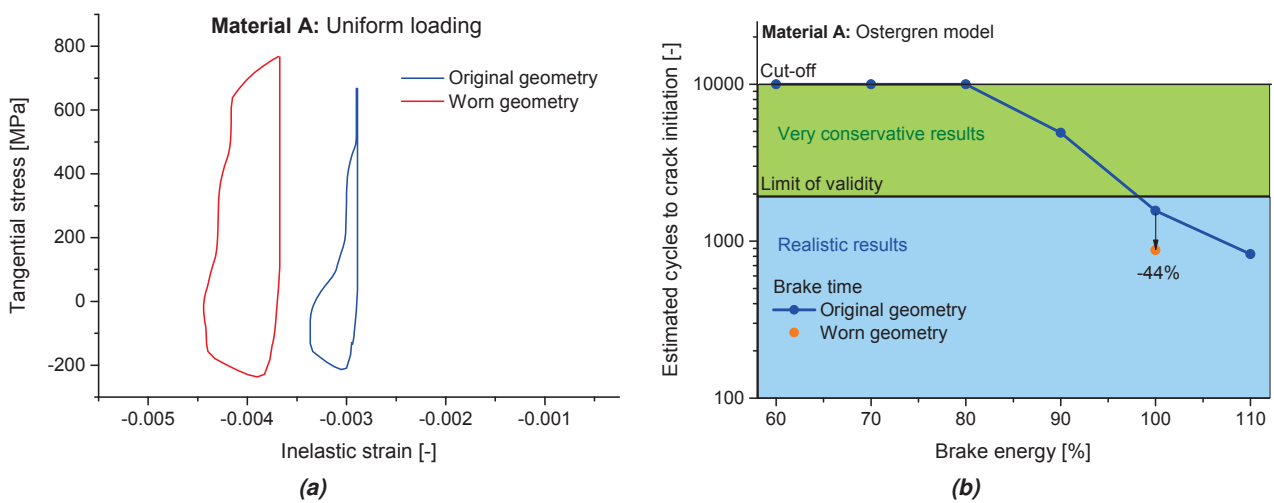


Figure 6.14: Comparison of the original and the worn disk geometry in view of a) the stabilized hystereses at the center of the friction surface and b) estimated crack initiation life time.

Fig. 6.14a reveals that the hysteresis shape significantly changes due to wear despite the similar tem-

6. SIMULATION RESULTS

perature evolution at the friction surface. This can be explained by the local constraint at the evaluated positions which increases, e.g. at the surface from $K_{TM}=-0.33$ to $K_{TM}=-0.47$ due to the overall loading conditions. The hysteresis width increases along with the residual stress level, which causes lower values for N_f . Fig. 6.14b compares the results obtained with the Ostergren model for both disk geometries. The comparison shows a 44% drop in N_f for the wear limit of 5 mm. The expected N_f is situated between the two results since wear is a gradual process over the whole service life.

6.1.5 Fracture mechanical evaluation of service life

So far the number of brake cycles until the initiation of a crack has been estimated. As noted above the propagation behavior of the crack must be assessed with fracture mechanical methods, discussed in this section. Fig. 6.15 illustrates schematically the crack growth in brake disks. This example refers to growth of a single fatigue crack rather than the formation of crack networks consisting of heat checks, which is a different and a less dangerous issue (see [33; 34]). Crack initiation is governed by the accumulated plastic strain in slip systems of the metallic crystal structure as outlined in Section 2.1. It is thus a micromechani-

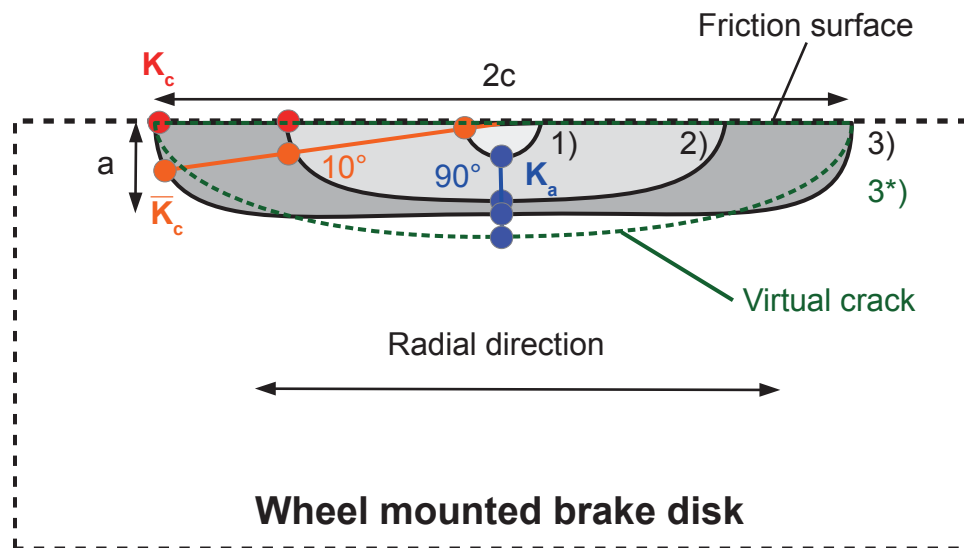


Figure 6.15: Schematic illustration of crack growth on a brake disk. The schematic crack is oriented in radial direction which is normal the main loading direction (tangential).

cal process not only linked to the macroscopic stress field but also to the orientation of the crystals. After a crack has initiated and is viable in the stress field, it will orient itself normal to the main loading direction, i.e. according to the greatest crack opening forces in mode 1. This way, the crack becomes describable by continuum mechanical means. Away from the mounting holes the main loading direction is in tangential direction apart from the direct surface region where thermal surface gradients may change the principal direction of the stress field. Further below, however, where the temperature and the stress field are homogeneous the main loading direction is tangential. The crack in Fig. 6.15 is oriented in radial direction and is opened and closed by the transient tangential stresses during each brake cycle. The highest stress intensity K occurs at the end of the braking due to the residual stress field depicted in Fig. 6.10b. In the schematic in Fig. 6.15 it is assumed that the crack has a semi-circular shape shortly after initiation. As can be seen in Fig. 6.10b the stress decreases in-depth significantly along with the inelastic stain. In

this stress field K_c at the outer rim is always higher than K_a at the deepest part of the crack front. On the condition that the crack is viable it will grow faster in lateral direction than in depth as indicated by the second contour. At some point of crack propagation K_a will drop below the threshold value K_{max}^{th} and from then on propagation is only possible in lateral direction indicated by the third crack contour in Fig. 6.15. In this study the virtual crack method discussed in Section 5.2.7.2 is applied. This means that semi-elliptical cracks are positioned in the computed stabilized stress field exemplarily indicated by the green dashed curve. The dimensions a and c are varied systematically in order to identify crack shapes where K factors above the K_{max}^{th} appear. Before the results are discussed the chosen strategy must be elaborated in more detail. Fig. 6.16a depicts the stress distribution for all increments of the TMF simulation. The upper en-

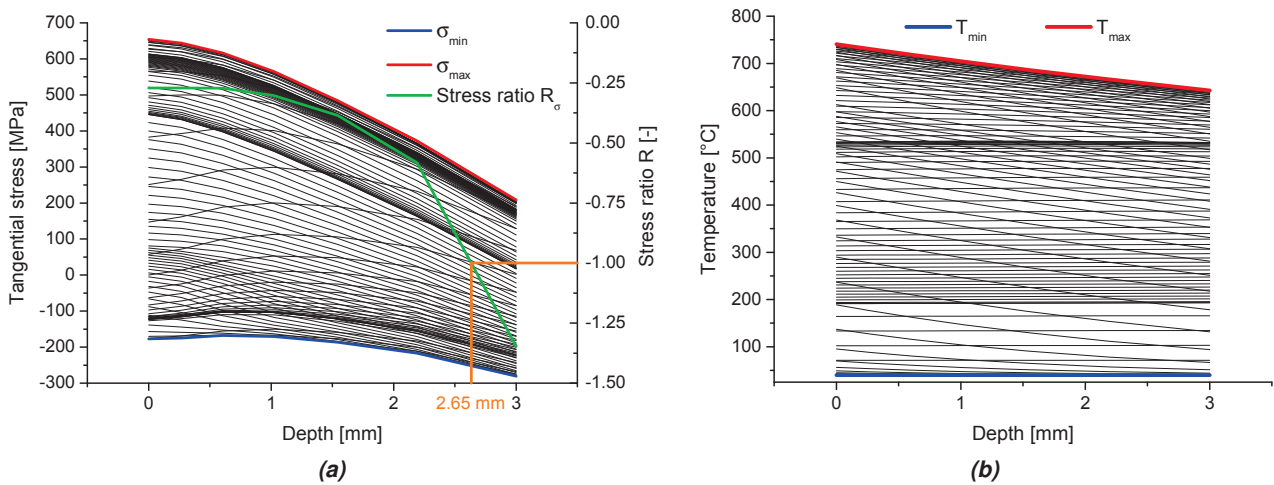


Figure 6.16: a) Envelopes of the stress field and the resulting stress ratio in main loading direction as a function of depth and b) the envelopes of the transient temperature field.

velope corresponds to the residual stress after cooling and the lower one results from multiple increments during the brake application. One essential quantity for the fracture mechanical assessment is the stress ratio R_σ :

$$R_\sigma = \frac{\sigma_{min}}{\sigma_{max}} \tag{6.2}$$

The importance of this quantity stems from the fact that the impact of the determined stress intensity range ΔK or maximum stress intensity K_{max} on the rate of crack propagation changes with R_σ . Above $R_\sigma > \sim 0.7$ the crack is fully open during the whole load cycle and ΔK equals the effective stress intensity range ΔK_{eff} , which is the real crack driving force. For $R_\sigma < \sim 0.7$ plasticity induced crack closure takes effect. Material is transported to the crack tip by plastic deformation, which fills the region behind the crack tip to a certain degree. As a consequence the stress intensity factor where the crack closes K_{cl} is not equal to K_{min} predicted by FE-methods. This influence is neither taken into account by the virtual crack method since the contact of the crack flanks is not considered nor by the FE procedure discussed in Section 5.2.7.2. For the virtual crack method negative K_{min} are by far too low since no contact of the crack flanks is taken into account and the physically meaningful range can be exceeded. The solution for the problems occurring below $R_\sigma < \sim 0.7$ is the use of K_{max} in combination with R_σ . This is the reason why the data in Fig. 6.17a, which was already introduced in Section 5.2.7.2 is expressed in terms of K_{max}

6. SIMULATION RESULTS

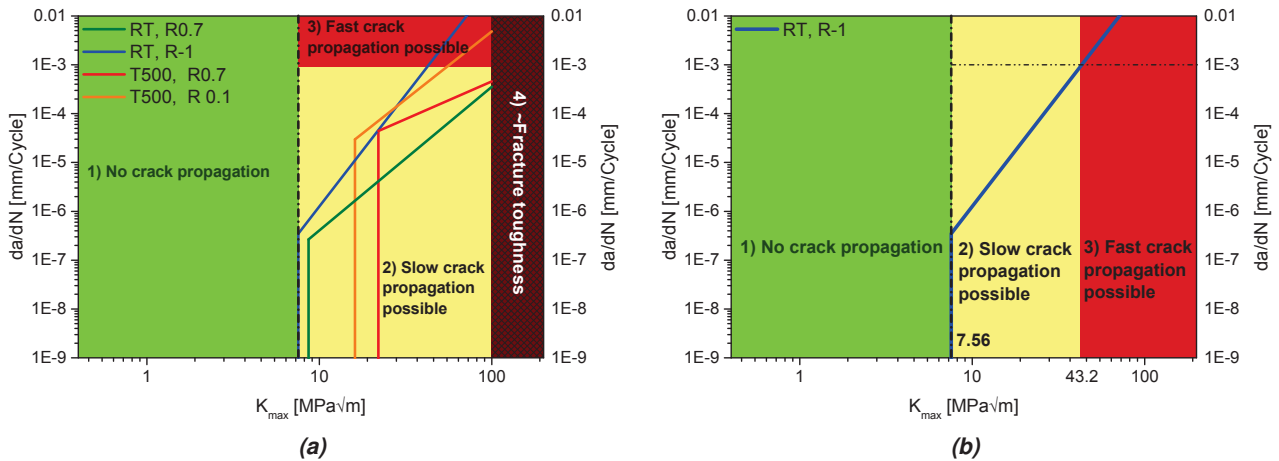


Figure 6.17: a) Illustration of the data basis for the evaluation of crack propagation based on K_{max} , R_σ and the temperature and b) simplified approach based on K_{max} and the most conservative experiment

rather than ΔK . The diagram contains the data of crack propagation experiments (the data for 300°C are not shown). The precise procedure would be to determine K_{max} , R_σ and the maximum temperature in the crack region. Subsequently the proper curve is selected and the propagation rate da/dN is determined. Based on the measured data an important simplification can be applied. The most conservative curve in terms of K_{max} is the one measured at room temperature for $R_\sigma = -1$. The fact that the threshold value K_{max}^{th} at elevated temperatures is situated higher than at room temperature can be attributed to a significant influence of oxidative crack closure effects. At elevated temperatures the region behind the crack tip becomes filled with oxides, which reduces ΔK_{eff} . This effect is amplified at the friction surface of the

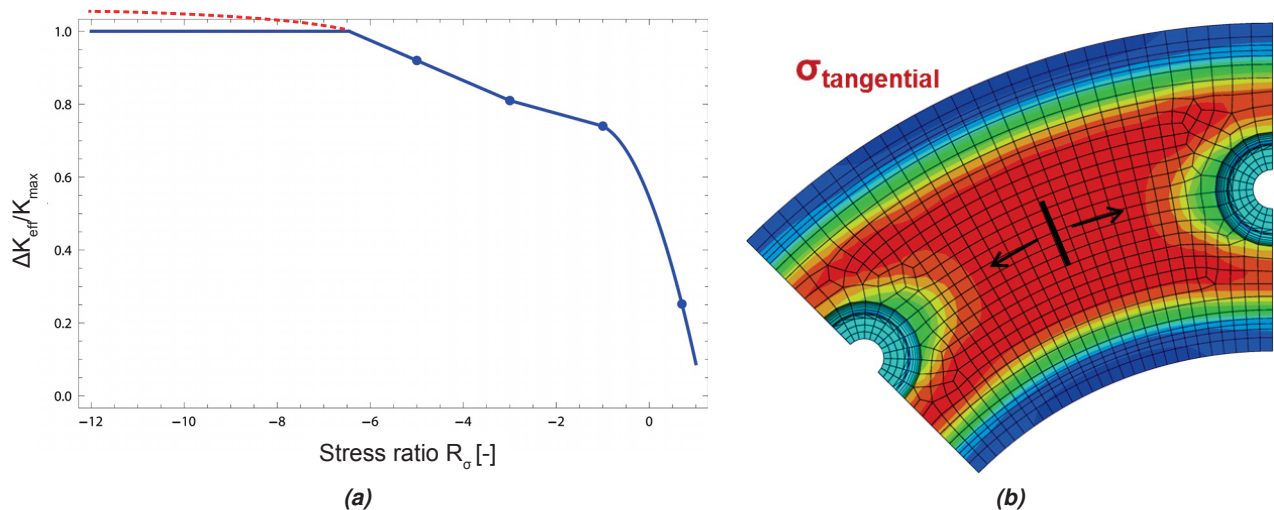


Figure 6.18: a) Correlation of K_{max} and ΔK_{eff} at room temperature as a function of R_σ for a tool steel and small scale yielding conditions (blue line). In the case of large scale yielding the red line applies [33; 34], b) Position of the virtual cracks in the brake disk.

brake disk because wear particles and oxides are forced into the cracks until they are partially or completely filled. This observation was made during investigations with the optical microscope. The reason why $R_\sigma = -1$ yields the most conservative result is the representation in terms of K_{max} instead of ΔK . For $R_\sigma = 0.7$

K_{min} is larger than zero and K_{max} is thus larger than ΔK , respectively ΔK_{eff} . For $R_\sigma=-1$ ΔK_{eff} can be smaller than K_{max} due crack closure effects or higher under high compressive loads. Fig. 6.18a illustrates this for small scale yielding conditions for a tool steel. At $R_\sigma=0.7$ ΔK_{eff} is significantly lower than K_{max} . With decreasing stress ratios the situation changes. At $R_\sigma=-1$ $\Delta K_{eff}/K_{max}=0.74$. Below $R_\sigma=-1$ this ratio further increases until $\Delta K_{eff}/K_{max}=1$ is reached around $R_\sigma=-6.5$. In [33] the curve was cut off at this point since no further experimental data are available. It cannot be excluded, however, that $\Delta K_{eff}/K_{max}$ can exceed 1. This is due to the tensile residual stress field around the crack tip forming under inelastic deformation under compression. At $R_\sigma=-6.5$ the compressive load is 6.5 times higher than the tensile load. If the amplitude of the loading is large, inelastic deformation is indicated and large scale yielding occurs. Under these loading conditions the resulting tensile stresses force the crack open in the unloaded condition which increases the effective stress intensity range. For the current study either the corresponding function depicted in Fig. 6.18a must be known for material A, or as a simplification an experimental curve that is conservative for the prevailing stress ratios must be used as a reference. Fig. 6.16a shows the in-depth distribution of R_σ for a standard braking. At the surface R_σ is around -0.25 and decreases with depth. $R_\sigma=-1$ is reached at a depth of 2.65 mm. Hence, evaluations based on the data in Fig. 6.17b are conservative up to this depth but non-conservative beyond, which must be kept in mind for the interpretation of the results.

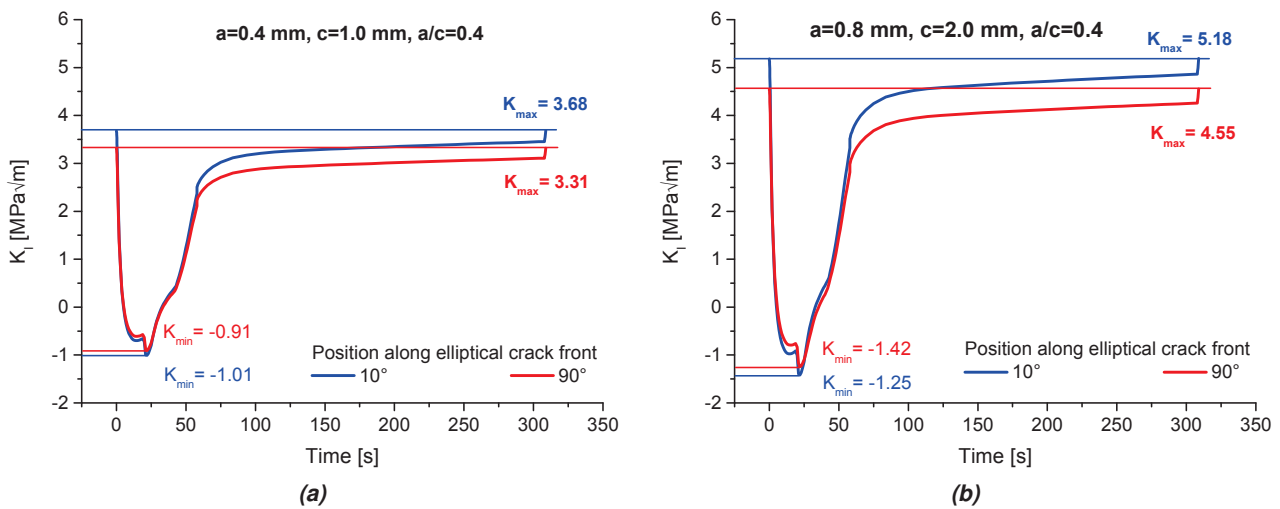


Figure 6.19: Evaluation of the stress intensity K_I during a reference brake cycle for a) a crack with $a=0.4$ mm and $c=1.0$ mm and b) a crack with $a=0.8$ mm and $c=2.0$ mm

Fig. 6.19a shows the evolution of the stress intensity for a crack within the validity range over the course of a braking for the positions 10° and 90° along the crack front. The position of the crack and the angular positions along the crack front are illustrated in Fig. 6.18b. The a/c ratio of 0.4 loosely correlates with the findings in [3]¹. The position at 10° is favored over 0° as indicated in Fig. 6.15 since this evaluation avoids the zone with pronounced phase transformations in the near surface region. This region is beyond the validity range of the experimental data. This is especially important for the evaluation of the non-uniform load case in Section 6.2. The results for K_{min} are negative as expected and the results for K_{max} occur at the end of the load cycle with $K_a=3.31$ and $K_c=3.68$. K_a is below K_c as noted above. Fig. 6.19b shows

¹It should be noted that the crack investigated in [3] is situated in an axle mounted brake disk, which affects its shape.

6. SIMULATION RESULTS

the results for a larger crack that is still within the validity range. The magnitudes of the relevant K -factors increase and the difference between the K_{max} values K_a and K_c slightly increases. This supports the conclusion that the crack grows faster in lateral direction, i.e. along the surface, than in thickness direction. Of course this applies only on the condition that the crack is viable at all. This can be assessed with the data in Fig. 6.17b, which shows that the conservative threshold value for crack propagation K_{max}^{th} is $7.56 \text{ MPa}\sqrt{\text{m}}$. Since all determined values for K_{max} are below, the investigated cracks are not viable in the computed stress field.

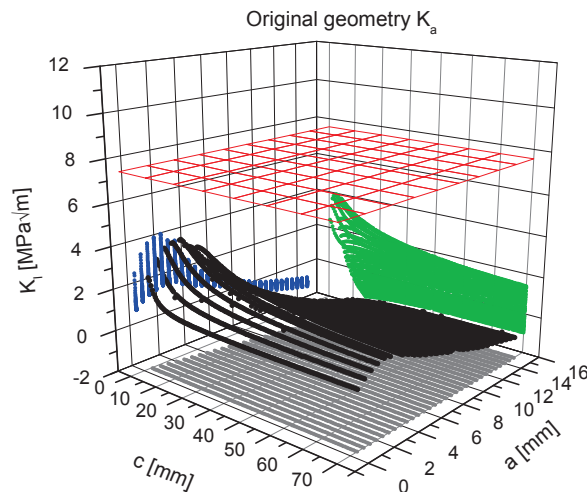


Figure 6.20: K_a for semi-elliptical cracks with different sizes in the stabilized residual stress field of the **original geometry**. All results are below the threshold for crack propagation, which indicates that crack growth in thickness direction is not possible.

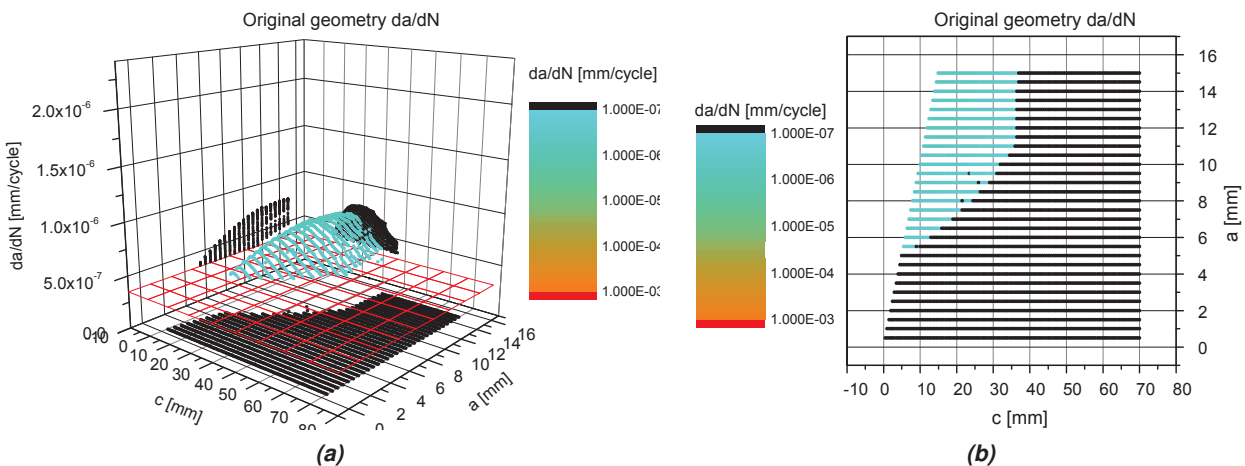


Figure 6.21: Crack propagation rates in lateral direction computed with K_c for semi-elliptical cracks with different sizes in the stabilized residual stress field of the **original geometry** a) 3D view and b) 2D representation.

In order take into account the possible case of an unexpected overload, such as a jammed friction brake, the parameters a and c are varied in a wider range. Fig. 6.20 reveals that K_a always stays below K_{max}^{th} indicated by the red grid. With a maximal value of $5.34 \text{ MPa}\sqrt{\text{m}}$ the viability of an initiated crack in thickness direction is thus not given and subsequently focus is laid on K_c . Fig. 6.21 shows the resulting propagation rates determined by K_c and Fig. 6.17b in 3D and 2D. The areas plotted in black correspond to

crack dimensions where K_c is below the threshold value. The lab measurement of the lowest propagation rate da/dN after K_{max}^{th} is 3.49×10^{-7} indicated by the red grid in Fig. 6.21a. There exist configurations

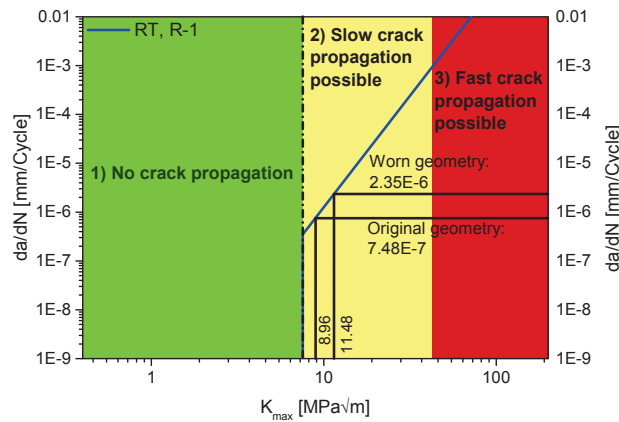


Figure 6.22: Theoretical maximum propagation rates for the original and the worn disk geometry (5 mm) exposed to the standard braking.

where crack propagation is possible but the corresponding propagation rates are at the lower end of the logarithmic scale beside the diagrams. da/dN around the threshold value and the relevant propagation rates for resulting crack lengths requiring disk replacement indicated in red are separated by several orders of magnitude. On the one hand it must additionally be considered that the viable crack dimensions are outside the range of validity of the crack propagation experiments. On the other hand these configurations cannot be reached because K_a is below the threshold. Fig. 6.21b further shows that beside a minimum

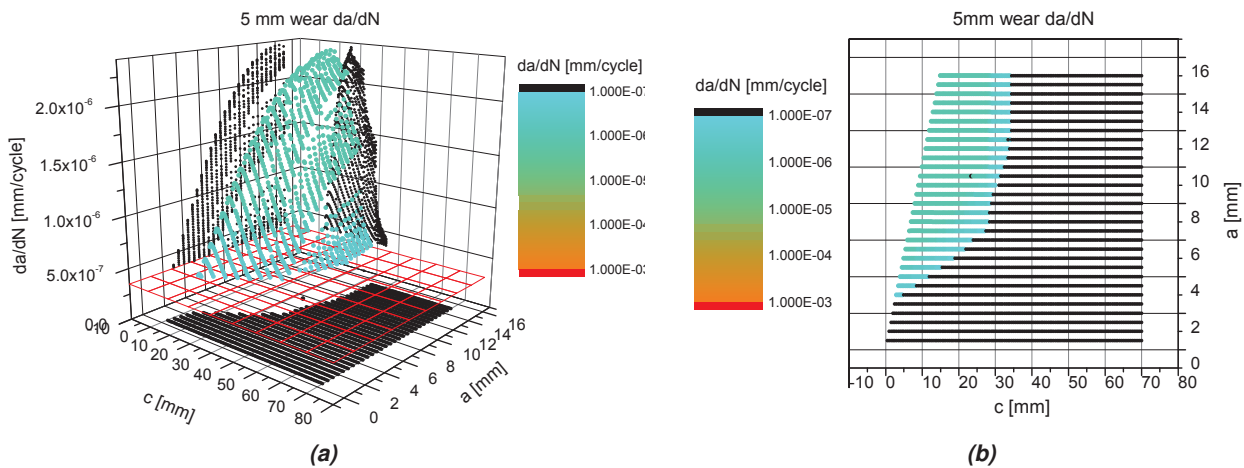


Figure 6.23: Crack propagation rates for semi-elliptical cracks with different sizes in the stabilized residual stress field of the worn geometry (5 mm) a) 3D view and b) 2D representation.

crack depth of 5.5 mm a minimum crack length of 11 mm ($c=5.5$ mm) would be required. On the assumption that an unforeseen event induces a crack of this size, crack propagation can still be assessed as negligible due to the low propagation rates in the investigated stress field. It is not likely that a criterion for disk replacement according to DIN 27205-5:2005-10 (see Appendix D.1 for a short overview) is met within the service life time with 2000 to 10000 high energy brakings. This is further illustrated in Fig. 6.22. The required propagation rates for a crack with $c=20$ mm (replacement criterion) are marked red. The

6. SIMULATION RESULTS

difference to the highest theoretical estimation of the propagation rate is a factor of 1340. This explains why no macroscopic cracks could be identified in the course of the metallographic investigations presented in Section 4.3.4.

Fig. 6.23 presents the corresponding data obtained for the worn disk geometry. The maximal value for K_a (not plotted) is $7.05 \text{ MPa}\sqrt{m}$. This is still below the threshold value of $7.56 \text{ MPa}\sqrt{m}$. If this value were reached the propagation rate would be far too low to obtain the required crack depth to enable crack growth in lateral direction. The smallest size for a viable crack in lateral direction decreases to $s=3 \text{ mm}$ and $c=3 \text{ mm}$ and the crack propagation rates are slightly higher. Due to the overall situation and the logarithmic scale of the range of da/dN crack propagation can still be neglected. The highest calculated da/dN is still separated from the relevant rate by a factor of 425. Nevertheless, this investigation should be carried out as well for the stress field caused by non-uniform loading.

6.2 Results for material A — Non-uniform thermal loading

This section presents an extension of the methods applied above to simulations with non-uniform loading conditions. The procedure was explained in Section 5.2.4.2 and the required input data was characterized and discussed in detail in Chapter 3. Based on these investigations the evolution of thermal surface gradients are known and available in the form of processed data matrices. After extensive discussion the sequence of brake cycles in Fig. 3.20 — for the sake of simplicity represented by one thermal image for each braking — was found to be representative for the service life of a brake disk made of material A and used with pad type 1. As illustrated in Fig. 6.24, which was already introduced in the previous chapter, the

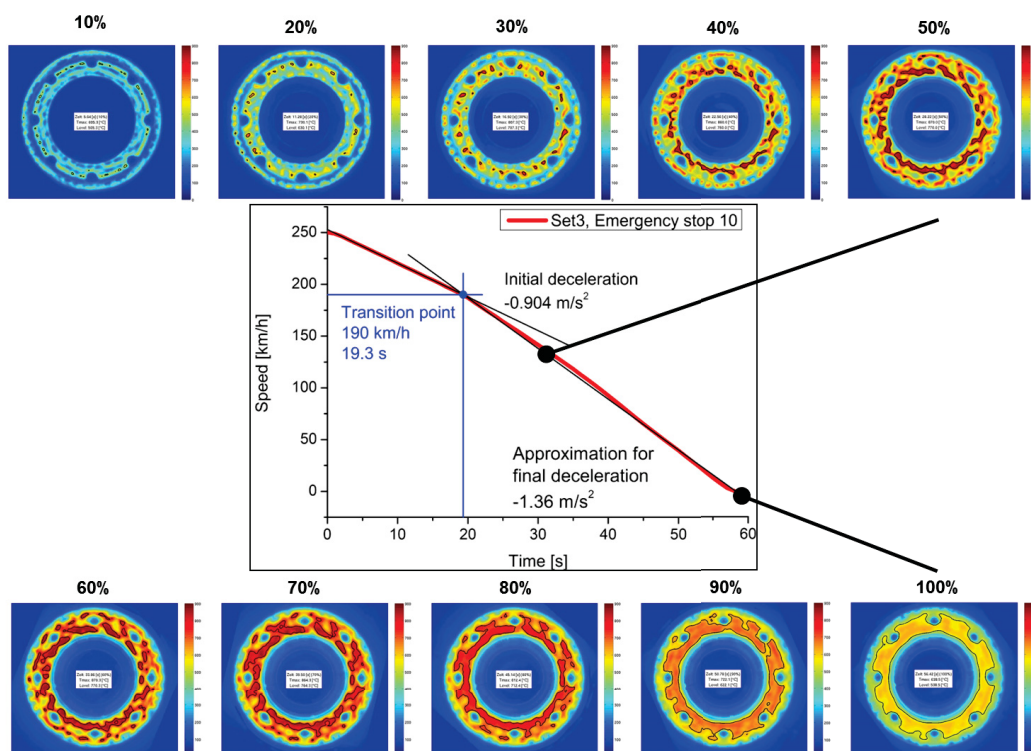


Figure 6.24: Illustration of thermal image mapping for one brake cycle. In this study the method is applied to perform the thermal image mapping for the brake sequence of 10 consecutive high energy stops represented in Fig. 3.16.

data of each individual frame (see Fig. 3.3) measured with a thermal camera during the test rig program (Fig. 3.16) is available for the simulation. For the non-uniform loading the complete data for each brake cycle of the sequence represented in Fig. 3.20 is read by the DISP subroutine shown in the appendix (Code B.3). This way the thermal history of the ten consecutive load cycles is mapped on the FE-model that has already been used for the investigations with the uniform heat source. Since the number of available frames per second is constant at 50 Hz whereas the incrementation in the FE computation is flexible, the required thermal image data are interpolated from the neighboring frames in time. Due to the fact that the increment size is augmented from its start value of 0.01s to 1s during each braking it is also sufficient to use a data set that only contains every 10th frame in order to reduce the file size that needs to be read into Abaqus. Since the data grid defined by the pixels of the camera does evidently not match the FE mesh bilinear interpolation is applied to correlate the data from the pixels with the surface nodes of the mesh. The method is thus independent of the image frequency and the resolution of the thermal camera. The results of the damage analysis presented in Chapter 4 show that for high energy brakings with pad type 2 the whole friction surface undergoes metallurgical transformations multiple times. Additionally, the transformed zones reach deeper into the material. This limits the range of validity of the modeling strategy elaborated in Chapter 5. Pad type 2 is usually not used in the tested application range and it was selected for the project to promote crack formation hence yielding data for verification purposes. Since neither of the two pads produced macroscopic cracks after 200, respectively 100 high energy stops, this section focuses on non-uniform loading generated by pad type 1.

6.2.1 Temperature evolution

The complete load sequence is rather complex as outlined in Section 3.4.1 and Section 3.4.2. At the outset of this section the non-uniform temperature field is thus characterized on the basis of brake cycle 7 represented by the data frame in Fig. 6.25a corresponding to 50% brake time. It was selected because

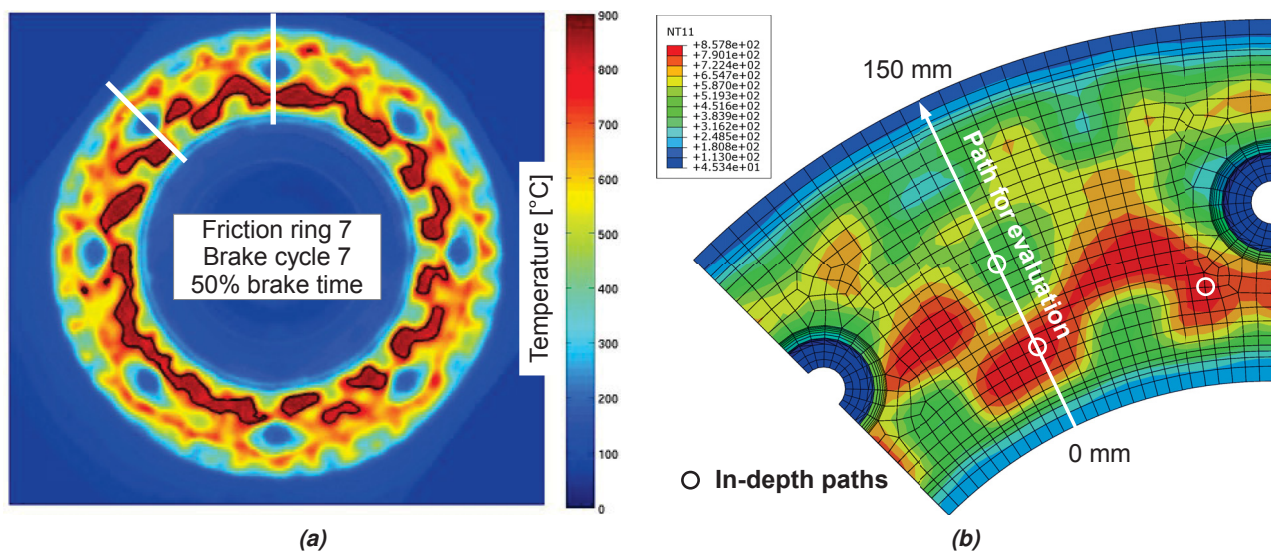


Figure 6.25: a) Selected thermal image from brake cycle 7 of the 200 stop test and the section considered in the thermal image mapping, b) Corresponding temperature field in the simulation with points of interest for further investigation.

of the characteristic and illustrative thermal distribution in the simulated sector marked by white lines. The

6. SIMULATION RESULTS

computed temperature field at a similar point in time is depicted on the right side (using a different scale). For the characterization of the transient temperature field a radial path is plotted in Fig. 6.25b. It intersects a region that reaches high temperature levels during the braking and an area that stays comparatively cold. Later on the discussion will proceed with in-depth investigations at the additional indicated positions. Fig. 6.25a shows the temperature levels along the radial path for different phases of the brake cycle. In this representation the focus is laid on the temperature ranges that occur during the braking rather than the transient evolution. The figure contains the temperature limits for the austenite start temperature, for the sake of simplicity in the following designated as T_1 and T_2 for the austenite finish temperature. Both values can be determined from Fig. 4.30 for the relevant heating rates. The value on the abscissa describes the distance from the inner disk circle to the outer one. Corresponding to the findings of the damage analysis the temperature on the inner disk half exceeds T_1 as well as T_2 , while the temperatures on the outer half stay within the limits of zone 3 where annealing effects may occur but phase transformations will not take place. The extent of zone 1 (full austenitization) in lateral direction is about 21 mm and for the partially

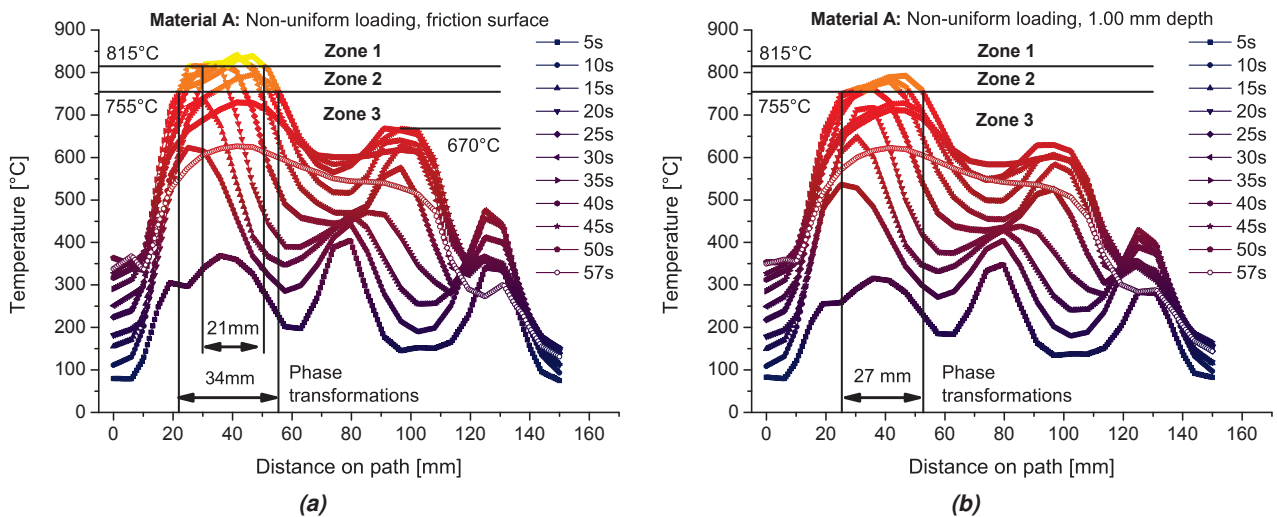


Figure 6.26: a) Transient temperature evolution at the surface along the path plotted in Fig. 6.25b. The focus is laid on the incident temperature levels in the zones 1-3 rather than the evolution itself. The three zones are important in view of phase transformations as outline in Section 4.3.4, b) The corresponding data 1 mm below the surface.

transformed zone 2, 34 mm. These values are estimates since the emissivity was assumed constant for the infrared investigations. Furthermore, the temperature distributions may be cut off since the measurement range of the camera is limited to 850-870°C. Nevertheless these distributions are significantly closer to the reality than the results from uniform loading. At elevated temperatures the temperature distributions show a minimum around the mean radius, which was already mentioned in the discussion of the thermal image data in Chapter 3. The results so far can directly be obtained from the thermal image data. However, the paramount difference between the thermal image data and the FE results is the corresponding temperature field *inside* the brake disk that now becomes accessible. The temperature distributions at various points in time below the friction surface can now be compared to the surface temperatures. Fig. 6.26b shows the achieved temperature levels in a depth of 1 mm. The shape of the distributions corresponds to the results from the surface but the maximum temperature has already dropped below T_2 . This favors a penetration depth of zone 1 in the order of 1 mm. The penetration depth of zone 2 cannot be assessed at this point

but the width of zone 2 is still 27 mm. Fig. 6.27a shows the corresponding results at a depth of 2.2 mm.

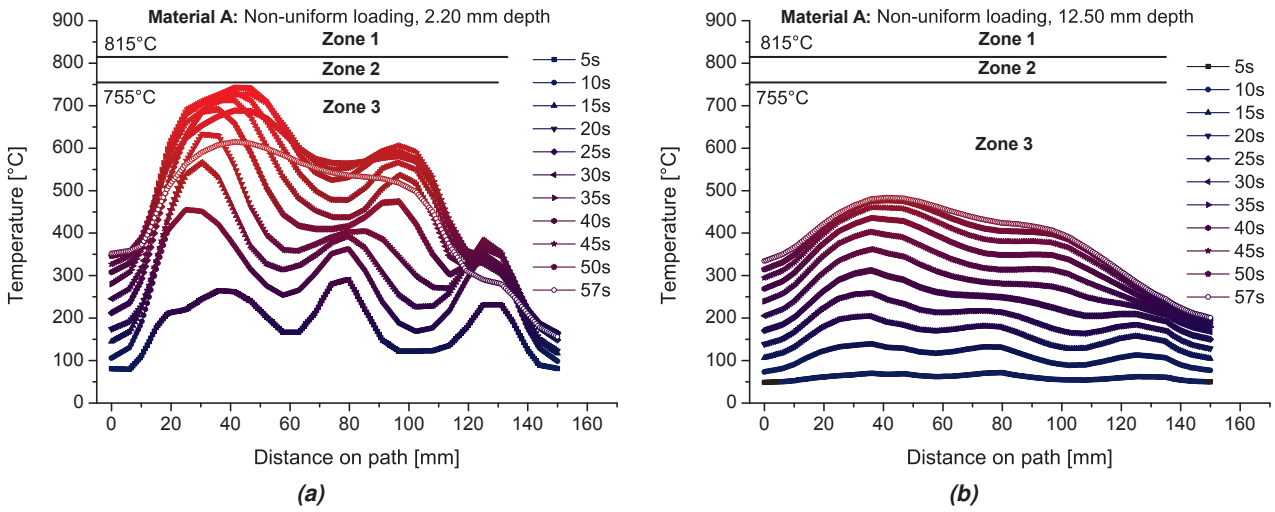


Figure 6.27: a) Temperature levels 2.2 mm below the radial path plotted in Fig. 6.25b and b) the data for 12.5 mm depth.

The characteristic shape of the distributions is still visible but homogenization of the temperature field in lateral direction already begins to take place. Since T_2 is almost reached, the penetration depth of zone 2 in this brake cycle and at this positions can be assumed as 2.2 mm. Fig. 6.27b shows the temperature distributions at the interface between the brick elements and the tetrahedral elements in 12.5 mm depth. The distributions have further homogenized. Furthermore, the influence of convection at the sides and the increased thermal input on the inner disk half are visible. The positions of two in-depth paths for further

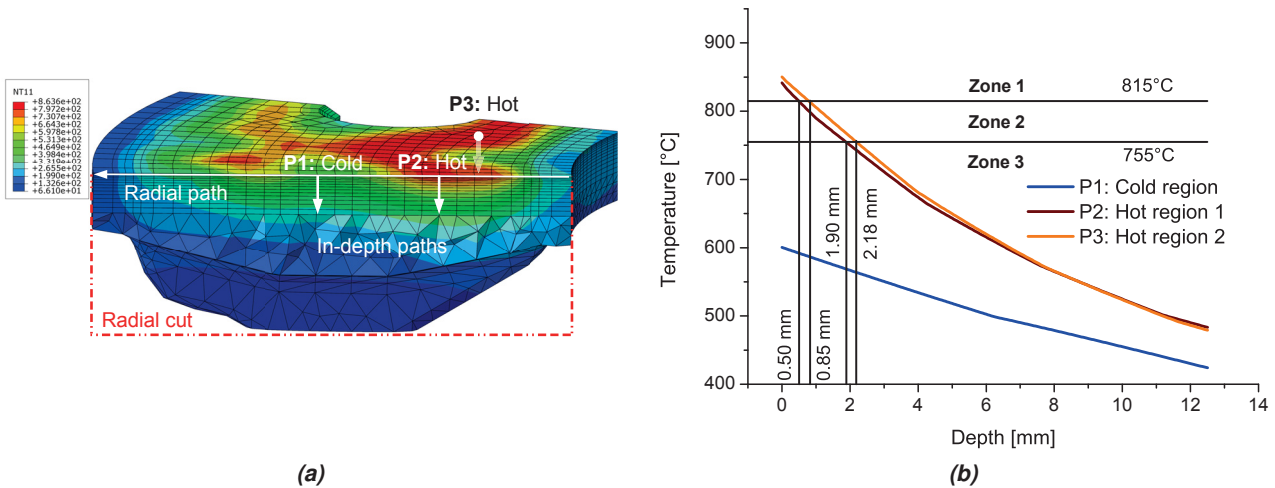


Figure 6.28: a) Radial cut through the FE-model revealing the temperature field in depth direction. The three in-depth paths for further investigations indicated in Fig. 6.25b are now clearly visible, b) Upper envelopes of the in-depth temperature distributions at the three positions P1, P2 and P3. The penetration depths of the transformation zones 1 and 2 are indicated.

evaluations indicated in Fig. 6.25b are plotted in the cutting plane through the FE-Model in Fig. 6.28b. The position P1 is in a region that stays at rather low temperatures during the emergency stop (ES) 7. P1 corresponds to the valley in the previous figures and position P2 to the temperature peak on the inner disk half. Additionally, position P3 closer to the mounting hole is evaluated. Fig. 6.28b compares the

6. SIMULATION RESULTS

upper envelopes of the temperature distribution, i.e. the maximum temperatures during the braking in each depth, at the three positions. As noted above the temperatures at P1 are too low to cause phase transformations. The envelopes at P2 and P3 are comparable and result in zone 1 reaching to a maximum penetration depth of 0.5-0.85 mm. At P2 and P3 zone 2 is limited to a depth of 1.9 to 2.18 mm. These data can be used in the verification procedure where the simulations are compared to the results from the test rig program in Section 6.3.

6.2.2 Disk coning and waviness

Fig. 6.29 compares the results from the mechanical FE calculation on disk coning and the waviness for the uniform and the non-uniform loading. For this purpose a sequence of 20 brakings has been simulated. The first 10 ES correspond to the reference case and uniform loading. Thereafter the viscoplastic behavior has stabilized and the sequence of 10 non-uniform brakings discussed above is simulated. In the case of static and dynamic coning a clear reduction of coning can be observed when the non-uniform sequence begins. For the dynamic coning this can be explained by the fact that an inhomogeneous temperature field hinders deformation of the disk. This case was discussed in the introduction in Section 1.3 where the meaning of internal and external constraints was clarified. An inhomogeneous temperature field generates an internal constraint since the flexibility of the disk is lowered and disk deformation cannot reduce the stress field as in the homogeneous case. In Section 1.3 this problem is illustrated with a simple beam. A beam subjected to a linear temperature distribution, i.e. a constant gradient, can release the thermal stresses by simple bending and is thus stress free. In the case of a non-linear temperature distribution the stress field cannot be released completely due to the internal constraints. A wheel mounted brake disk is always subjected to thermal stresses. It can reduce the stresses by coning and waviness but a certain amount of stress remains. Due to an inhomogeneous temperature field coning is suppressed to a certain extent and the internal constraint is increased. This is also the reason why the magnitude of the static coning becomes higher when the non-uniform loading begins. The higher constraint entails higher inelastic strains, which are the reason for static coning. Fig. 6.29b compares the amplitudes of the 4th and 8th order waviness

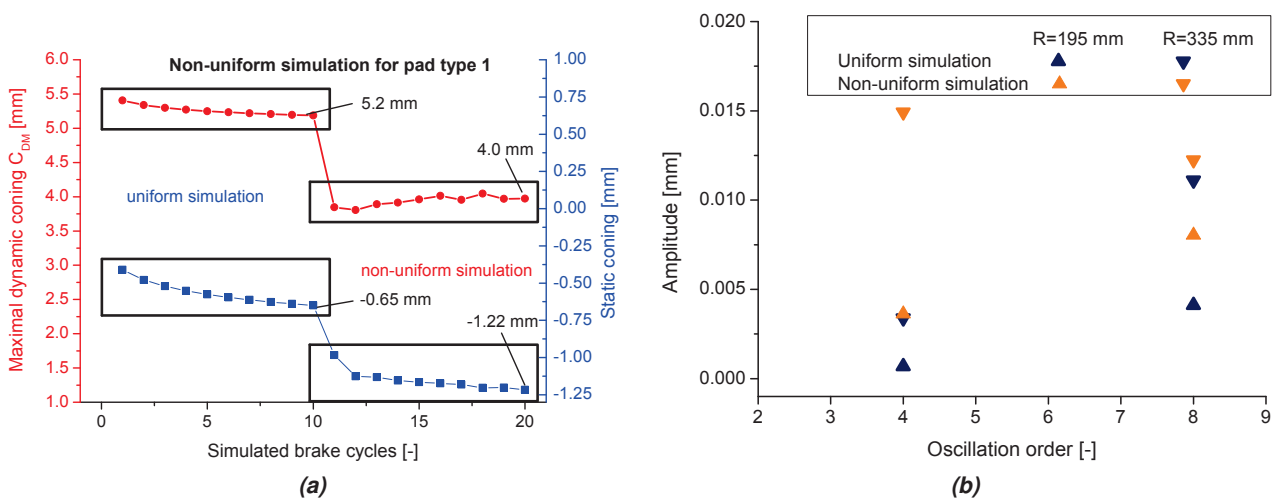


Figure 6.29: a) Maximal dynamic disk coning per load cycle. The first ten simulations are based on uniform loading in order to stabilize the σ - ϵ field followed by the thermal image mapping, b) simulated amplitudes of the 4th and 8th order static waves.

in circumferential direction. The diagram contains data from the uniform and the non-uniform computation at the inner disk circle as well as the outer one. The general trend is an increase of the amplitude for non-uniform loading. This can be attributed to the increased and more localized plastification. Another point is the magnitude of the 4th order waviness that exceeds the one for order 8. The data can be used for a comparison with the measured waviness. Due to significant scatter of the experimental results presented in Section 4.3.2 and the limited suitability of the FE-model using linear element formulations for the prediction of small amplitudes other means should be used for verification purposes.

6.2.3 Damage mechanical evaluation of service life

For the discussion of TMF damage the same positions as above are investigated (see Fig. 6.28a). Fig. 6.30a compares the inelastic strain and the residual stress at P2 at the end of brake cycle 7 for the radial and the tangential direction. Also under non-uniform loading the main loading direction coincides with the tangential direction, which is also apparent from the representation of the tangential stress field and the principal stress field in Fig. 6.31. The subsequent discussion will focus on the loading in tangential direction. Fig. 6.30b shows σ_{res} and ϵ_{in} at the positions P1, P2 and P3. The highest loading is indicated for P2, where residual stresses around 730 MPa occur together with a higher level of plastification compared to P1 and P3. The results for the cooler position P1 indicate that harsher loading conditions prevailed during previous brakings giving rise to a residual stress level of 650 MPa. The mechanical hystereses of

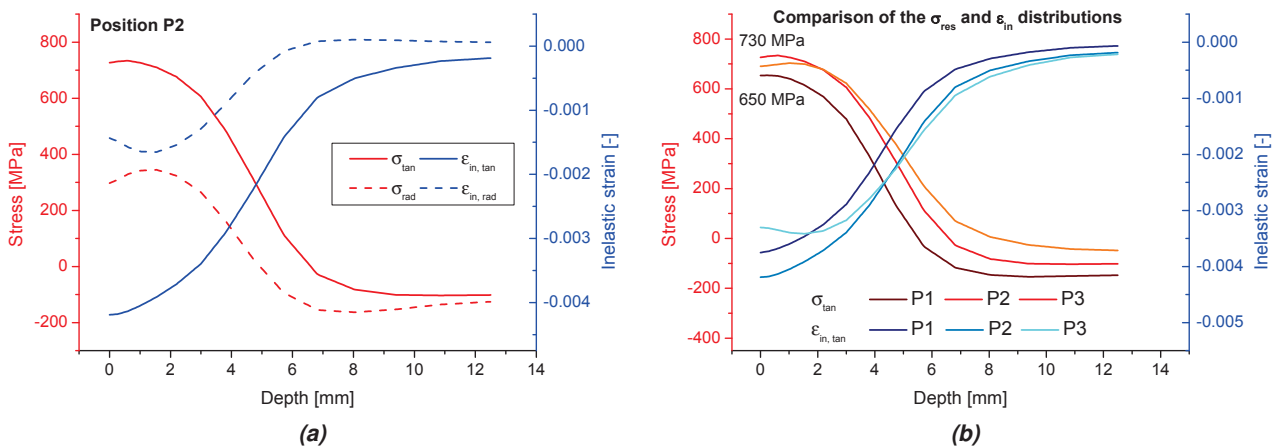


Figure 6.30: a) In depth distribution of residual stress and ϵ_{in} at position P2 in tangential and radial direction at the end of brake cycle 7. The main loading direction in the bulk is oriented in tangential direction, b) Residual stress and ϵ_{in} in tangential direction at P1, P2 and P3.

σ_{tan} vs. $\epsilon_{in,tan}$ are depicted in Fig. 6.32a for the whole simulated sequence of 20 high energy brakings. The simulation of the first 10 ES is carried out with a uniform heat source in order to obtain a reasonably stabilized σ - ϵ field before the thermal image mapping is started. After the very first ES the hysteresis stabilizes rather quickly for the given uniform loading conditions. The situation changes, however, when non-uniform loading is applied. On the one hand the hystereses are wider due to the elevated loading resulting from the higher temperatures but also from the faster heating. On the other hand the hystereses do not stabilize at a specific position in σ - ϵ space and shift to a certain degree with changing loading conditions. Instead of the computation of a stabilized hysteresis a modified strategy must be applied. Fig. 6.32b

6. SIMULATION RESULTS

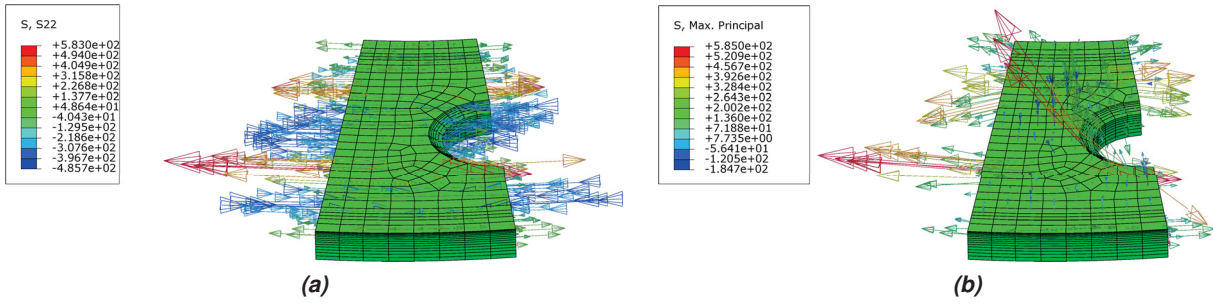


Figure 6.31: Illustration of the a) tangential stresses and b) principal stresses during braking.

shows the evolution of the equivalent plastic strain p and the equivalent stress σ_{eq} over the ten brake cycles simulated on the basis of thermal image mapping. The value $p=0.02$ stems from the plastic history of the corresponding material point during the first 10 cycles. Without the application of methods for cycle counting and the assembly of closed hysteresses described in Section 2.6.3 a simplified procedure can be used. Each double step in Fig. 6.32b corresponds to the plastification and the reverse plastification during the corresponding brake cycle. The double step appears to be a single steps in the present case because of the smooth transition from compressive to tensile plastification. On the condition that the σ - ϵ hysteresis has stabilized to a sufficient degree the increment Δp over a brake cycle can be used as an approximation for $\epsilon_{pl,a}$ according to the following relation:

$$\epsilon_{pl,a} = \frac{\Delta p}{4} \quad (6.3)$$

This procedure is conservative since open hysteresses are treated as closed thus yielding a larger strain

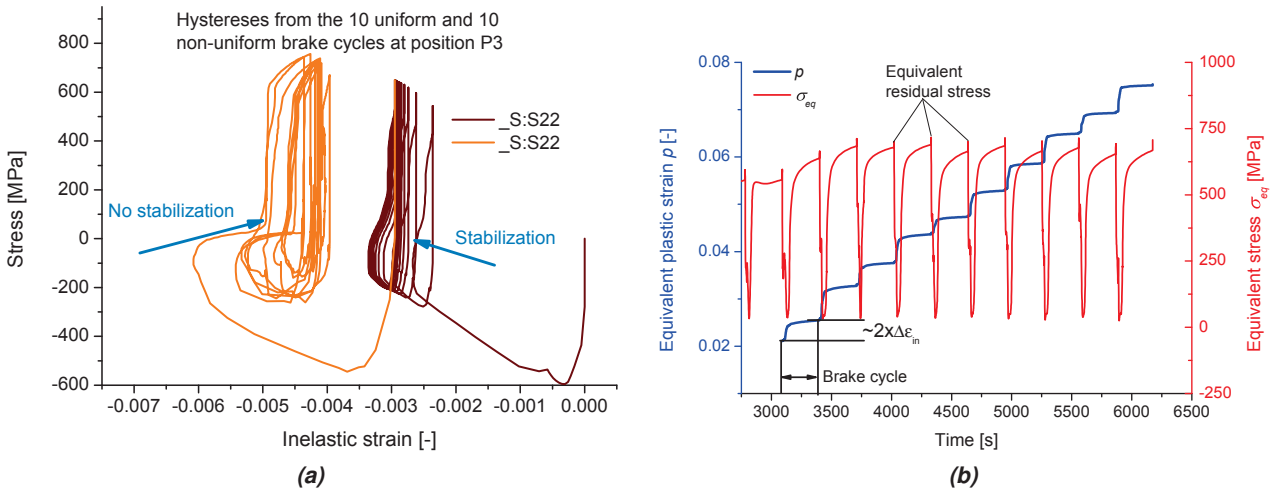


Figure 6.32: a) Mechanical hysteresses for the 20 simulated high energy brakings. The applied uniform heat source during the first 10 brakings promotes the formation of a stabilized hysteresis. During the subsequent thermal image mapping completely stabilized hysteresses cannot be obtained due to the varying loading conditions, b) Evolutions of the accumulated (equivalent) inelastic strain p and the von Mises equivalent stress over the course of the ten non-uniform brake cycles.

amplitude than cycle counting methods. Since the TMF loading is primarily strain controlled — apart from the influence of the disk coning — the hysteresses are rather stable on the horizontal axis. Possible overestimations of $\epsilon_{pl,a}$ are small compared to the hysteresis widths as long as the first non-uniform cycle is ignored, which provides a significant level of stabilization for the subsequent cycles. An approach

based on the Manson-Coffin model and the Palmgren-Miner rule for linear damage accumulation is thus applicable and does not require much additional effort. In order to consider the multiaxial loading case¹ Δp is determined over the course of each brake cycle and along with it $\epsilon_{pl,a}$ according to Eq. (6.3). The contribution of each cycle to the overall damage is taken into account by the Palmgren-Miner rule and after the evaluation of the ten brake cycles a prediction can be made on how often the disk can bear the corresponding load sequences until a macroscopic crack appears:

$$N_f^{sequence} = \frac{1}{\sum_i ES \frac{n_i}{N_f^i}} \quad (6.4)$$

It is important to investigate a load sequence, which is characteristic for the predominant loading conditions during the service life of the component. For the wheel mounted brake disk investigated in this work this topic has been discussed in detail in Chapter 3. The procedure can be performed with the Ostergren model as well, which is preferred in this work. Additionally the stress maximum per cycle must be taken into account. For the brake disk problem this is always at the end of a braking after cooling. For the more general multiaxial description the maximal signed equivalent stress is used. In cases where it is not clear when σ_{eq} describes a compressive or a tensile stress state the sign can be determined from the first invariant, $Tr(\boldsymbol{\sigma})$. Fig. 6.33 depicts the distribution of N_f on the friction surface. The life times in the legend

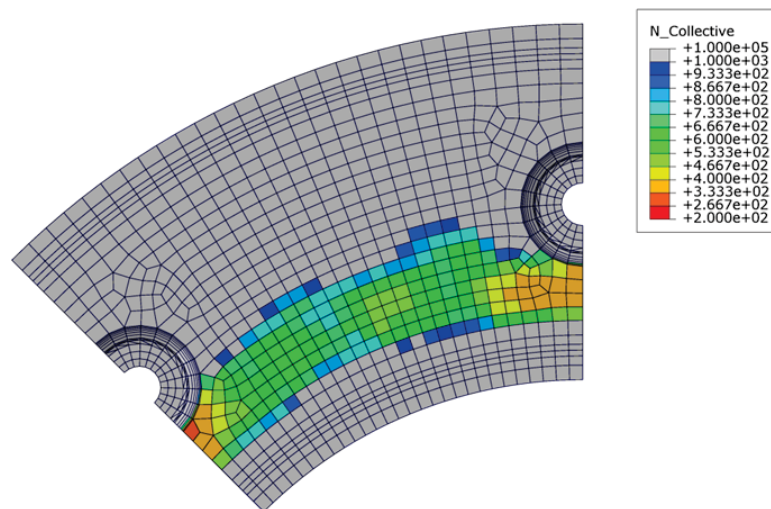


Figure 6.33: Resulting distribution of the estimated N_f on the friction surface.

correspond to individual average brake cycles rather than the whole sequence. The evaluation is based on the evaluation of the last 9 of the 10 non-uniform load cycles with the Manson-Coffin model and the Palmgren-Miner rule. The resulting minimum N_f is compared to the corresponding result obtained with the Manson-Coffin model from a uniform simulation. The result around P3, which has only been discussed for brake cycle 7 so far, corresponds to a 70% reduction in crack initiation lifetime due to non-uniform loading as compared to the uniform case. This figure should be kept in mind for the interpretation of results obtained with uniform heating. It is a relative quantity and it also holds when the Ostergren model is used. Nevertheless, this estimation is only valid for the investigated disk type used in combination with pad type 1.

Position P2, which is the highest loaded position during brake cycle 7 shows higher values for N_f after

¹Multiaxial in the sense of 3-dimensional but without significant influence of non-proportional loading.)

6. SIMULATION RESULTS

the evaluation of the whole brake sequence. This underlines the importance of evaluating a characteristic load sequence and rather than individual brake events only.

6.2.4 Fracture mechanical evaluation of service life

In analogy to Section 6.1 the damage mechanical analysis is followed by a fracture mechanical evaluation of crack growth. As in the case of the uniform loading the tensile residual stresses at the surface are fully developed at the end of each load cycle after cooling. This is the point where the maximal stress intensity K_{max} reaches its extreme value over the cycle. The residual stresses σ_{rad} in radial and in tangential direction σ_{tan} are plotted side by side in Fig. 6.34. The maximal values for σ_{rad} are in the range of 650 MPa. The maximum level of σ_{tan} is around 770 MPa and coincides with the probable sites of crack initiation determined in the last section. For this reason, the growth of cracks oriented in radial direction, i.e. normal to the greatest crack opening forces, will be investigated. For this purpose two positions are selected as

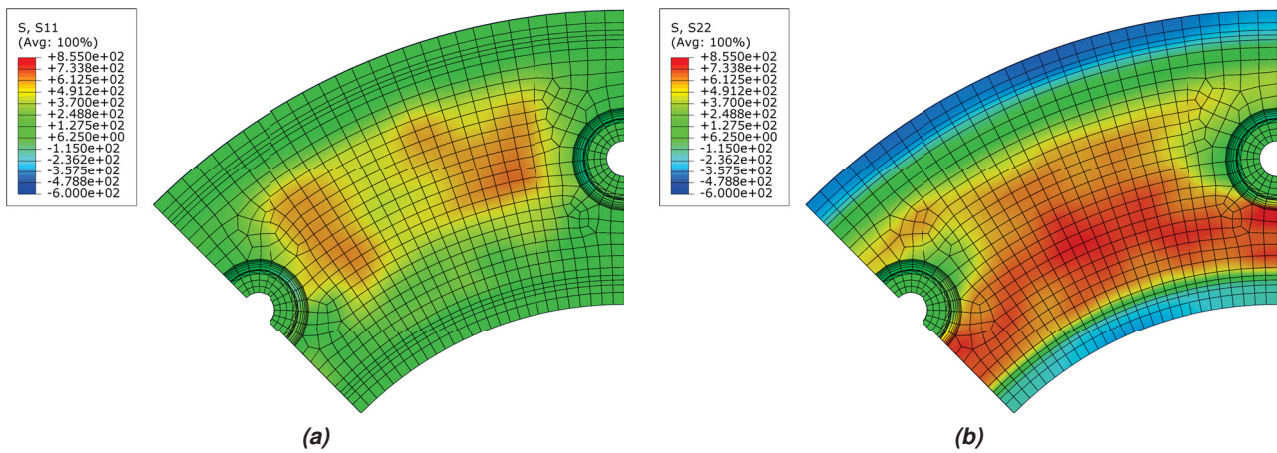


Figure 6.34: Residual stresses a) in radial direction and b) in tangential direction after simulated brake cycle no. 17.

indicated in Fig. 6.35. Position A corresponds to the radial path, which was discussed in the context of the non-uniform temperature field in Section 6.2.1. Position B is situated in the area where the minimal crack initiation life time is estimated (see Fig. 6.33). In both cases a parameter study is performed on the geometric quantities a and c as was done for the uniform loading. The start values are 0.25 mm and 0.5 mm, respectively. At position A the crack has grown to $a=15$ mm and $c=30$ mm. The value for c corresponds to the maximal allowable crack length in the friction surface according to DIN 27205-5:2005-10 summarized in Appendix D.1. For position B the corresponding values are $a=10$ mm and $c=20$ mm. In this case the value for c equals the maximal allowable crack length at a mounting hole. Before the evaluation it must be determined whether the prevailing stress ratios in loading direction are situated within the range of validity or not. The in-depth distribution of R_σ in the stress field shown in Fig. 6.34b is plotted in Fig. 6.36a. The in-depth path corresponds to the one of the hot region designated with P2 in Section 6.2.1. The results show that down to a depth of 4.75 mm R_σ is greater than -1. This value corresponds to the experiment with the lowest fatigue threshold within the experimental program. As noted in Section 6.1.5 the threshold K_{max}^{th} for the onset of crack growth and the predicted propagation rates are based on this experiment. For $R_\sigma > -1$ the results are thus conservative but the opposite case applies for stress ratios below. Fig. 6.36b shows

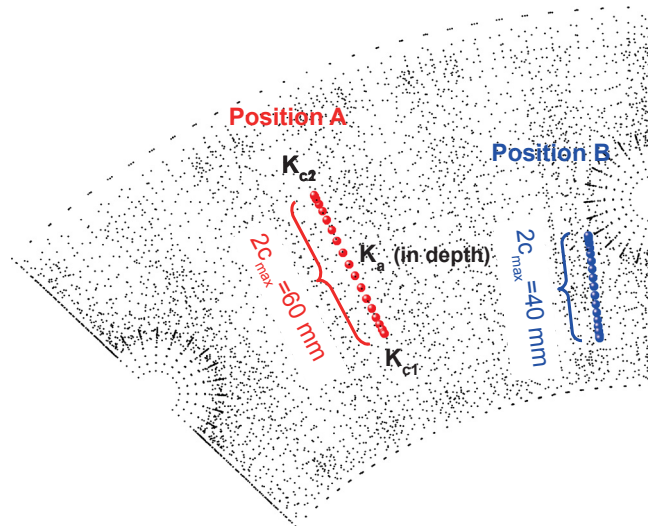


Figure 6.35: Virtual cracks positioned in the stress field plotted in Fig. 6.34b. The crack sizes are varied and only the largest crack dimension is shown.

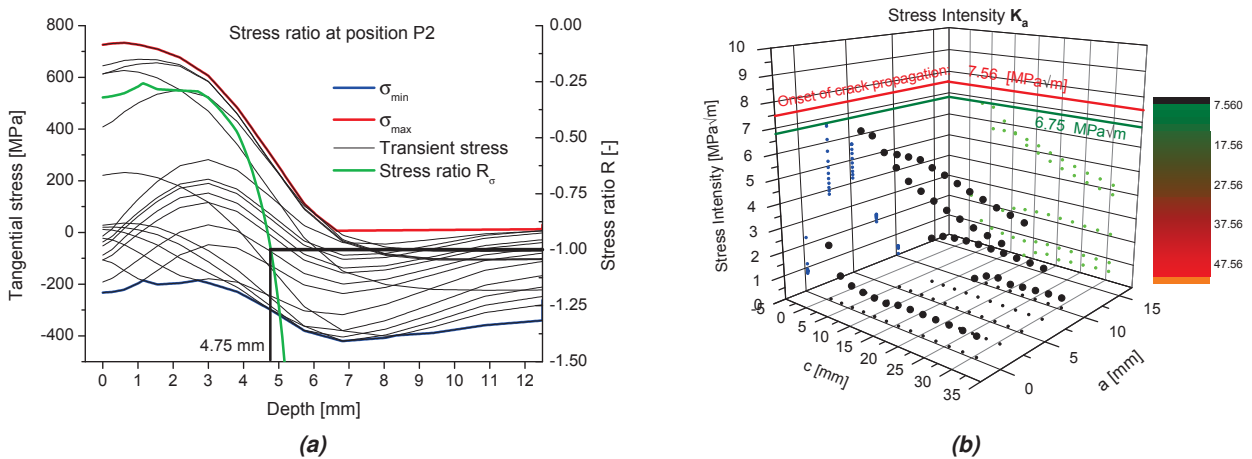


Figure 6.36: a) Stress ratio R_σ as a function of depth at position P2 in Fig. 6.28a, b) Overview of the stress intensity factors K_a obtained at position B.

the stress intensity at the deepest point along the crack front (K_a) as a function of a and c . The threshold value $K_{max}^{th} = 7.56 \text{ MPa}\sqrt{\text{m}}$ is never exceeded and a crack initiating at the surface is not viable in thickness direction. Outside the validity range $a > 4.75 \text{ mm}$ the computed K_a drops significantly. Even if the threshold decreases for lower stress ratios, K_a is too low. For the case that an unforeseen event induces a crack the possible range of propagation rates at the outer positions K_{c1} and K_{c2} are investigated. Fig. 6.37a and Fig. 6.37b provide an overview of crack geometries where crack propagation in lateral direction is possible. The maximal value K_{c2} corresponds to a propagation rate of $3.80 \times 10^{-6} \text{ mm/cycle}$. For K_{c1} , which corresponds to positions on the inner half of the disk with higher temperatures and stresses, da/dN is 1.88×10^{-5} . The difference in the propagation rate of one order of magnitude seems to be significant at the first glance. However, the necessary da/dN in order to obtain a crack with $2c = 60 \text{ mm}$ within 10000 high energy brakings is $1.00 \times 10^{-3} \text{ mm/cycle}$, i.e. another 2 orders of magnitude higher. On the basis of these results it can be concluded that crack propagation is not an issue at position A. This is true if the

6. SIMULATION RESULTS

stress field after load cycle 17 is characteristic for the whole life time. A damage accumulation rule as in the previous section is not applied in this work. The stress field is unlikely to increase any further since the maximum residual stress is limited by the yield stress. Evaluating the critical positions in the stress field resulting after multiple non-uniform simulations suffices to assess the fatigue risk.

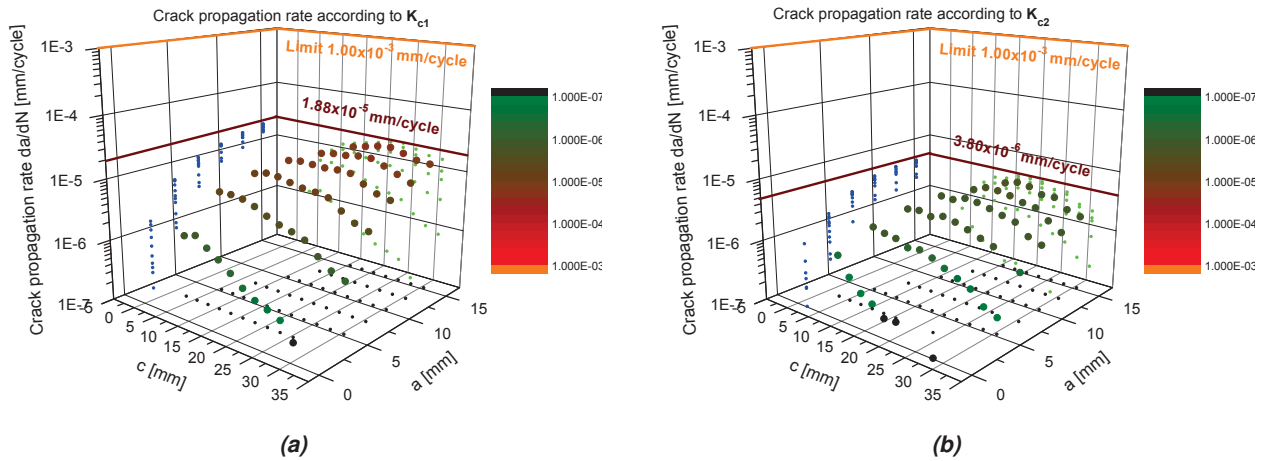


Figure 6.37: Overview of propagation rates entailed by the stress intensities a) K_{c1} and b) K_{c2} at outer bounds of cracks at position A

The corresponding procedure was carried out at position B. Fig. 6.38 reveals that none of the determined stress intensities K_a , K_{c1} and K_{c2} reaches $K_{max}^{th} = 7.56 \text{ MPa}\sqrt{\text{m}}$. Taking into account the analysis of the previous section it can be concluded that the loading conditions at position B lead to faster crack initiation compared to other positions on the disk surface but after initiation a large crack cannot propagate under mode 1 loading. Thus the risk of failure due to crack propagation can be precluded.

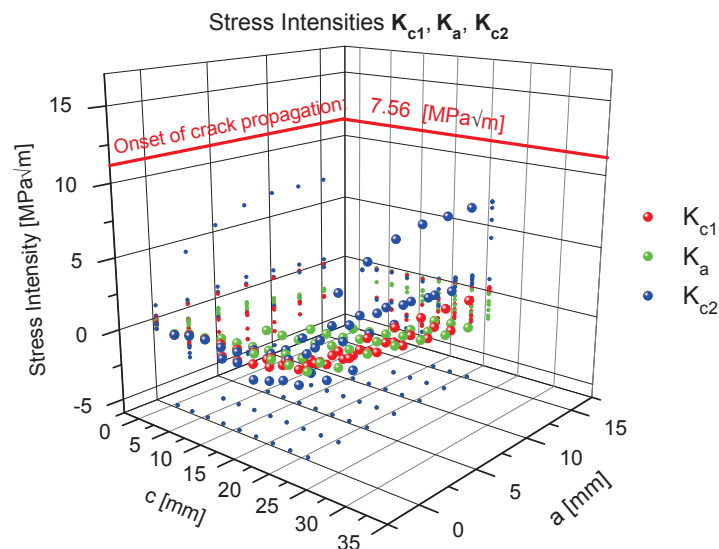


Figure 6.38: Overview of the stress intensity factors K_{c1} , K_a and K_{c2} obtained at position B.

6.3 Comparison of the simulations to the results from the test rig program.

The investigations carried out in Chapter 4 provide data that can be used to verify the simulated results. One of the primary targets in this work is a thermomechanical simulation that considers the non-uniformity of the temperature distribution on the friction surface. As outlined in Section 4.3.4 a profound investigation of phase transformations in the brake disks used in the test rig program. Using the methods presented in Section 4.3.4 it is possible to determine the temperature levels that have occurred at a certain depth below the friction surface. These temperatures can be compared to the start and finish temperatures of phase transformations. Fig. 6.39 shows the discovered penetration depths of zone 1 (full austenitization+quenching) and zone 2 (partial austenitization+quenching). Considering the alloy composition of material A and the kinetics of the transformations the temperatures corresponding to the boundaries of zone 1 and 2 are 815°C and 755°C, respectively. The average penetration depth determined from the samples represented in Fig. 6.39 as well as other investigated samples is 0.86 mm for zone 1 and 2.135 mm for zone 2. This result can directly be correlated with the simulation data on temperature distributions in hot regions depicted in Fig. 6.28b. The data plotted in Fig. 6.39 show that the experimental findings and the simulations are in good agreement.

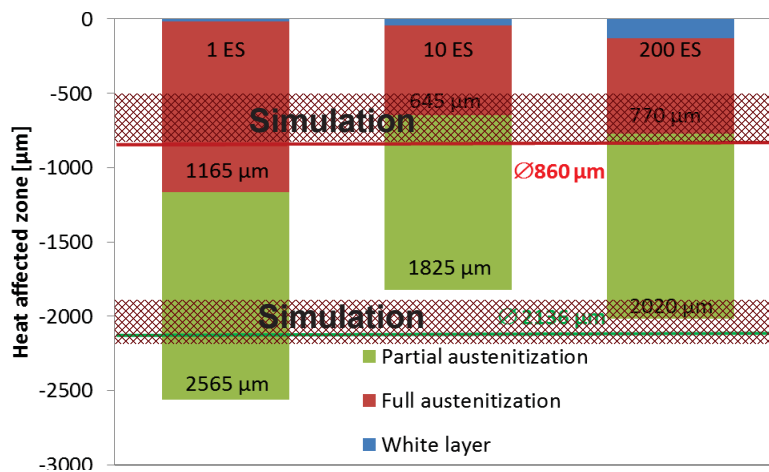


Figure 6.39: Comparison of the temperature field simulated with non-uniform loading conditions and real temperatures in terms of phase transformation temperatures.

In the next step the results of the disk deformation are compared. Fig. 6.40 shows the maximal dynamic as well as the static disk coning measured during the test rig program (200 emergency stops). The blue and the green lines correlate the measured and the simulated static coning. The simulations aim at the description of the stabilized disk coning. After 10 uniform simulations the average of the measured values after the initial phase of the test run (-1.15 mm) is underestimated by 43%. After subsequent 10 non-uniform cycles the magnitude of the average static coning is overestimated by only 6%. The maximal dynamic disk coning is generally overestimated. After 10 uniform cycles the measured average value of 2.6 mm is overestimated by 100%. After additional 10 non-uniform simulations the overestimation is reduced to 50%. One reason for this deviation might be the good but not exact approximation of the temperature field. As previously mentioned inhomogeneities in the temperature field tend to suppress the disk deformation to a certain degree. Some of the information in the thermal images has been lost due to the use of a constant coefficient of emissivity, the interpolation of the data during the processing (see Chapter 3) and the

6. SIMULATION RESULTS

thermal image mapping. Nevertheless, the good accordance between the measured and simulated static coning indicates that the overestimation of the dynamic coning does not lead to an incorrect prediction of the plastic deformation in the disk.

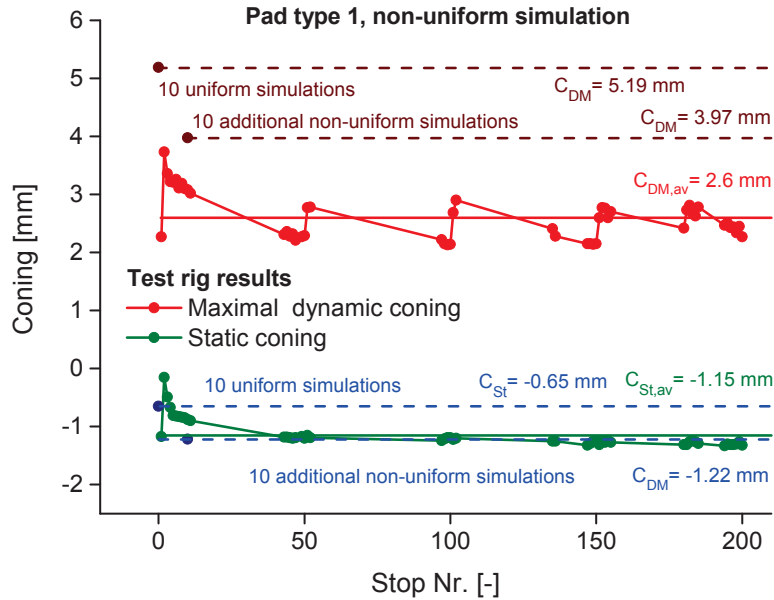


Figure 6.40: Comparison of simulated and measured disk coning.

Fig. 6.41 correlates the results from the Fourier analysis of the coordinate measurements presented in Section 4.3.2 to simulation data. As previously noted the symmetrical model can capture the 4th and 8th order waviness, which is represented by the red and green data points. For both orders the the amplitudes are underestimated by the uniform simulations, while the non-uniform loading conditions induce waviness that is in better accordance with the measured data. It should be kept in mind, however, that the experimental results show a high degree of scatter. An exact match is thus neither necessary for the functionality of the simulation tool nor an explicit aim for the modeling activities. Nevertheless, the conclusion holds that the non-uniform loading increases the waviness to an extent that is in the observed data range. One of

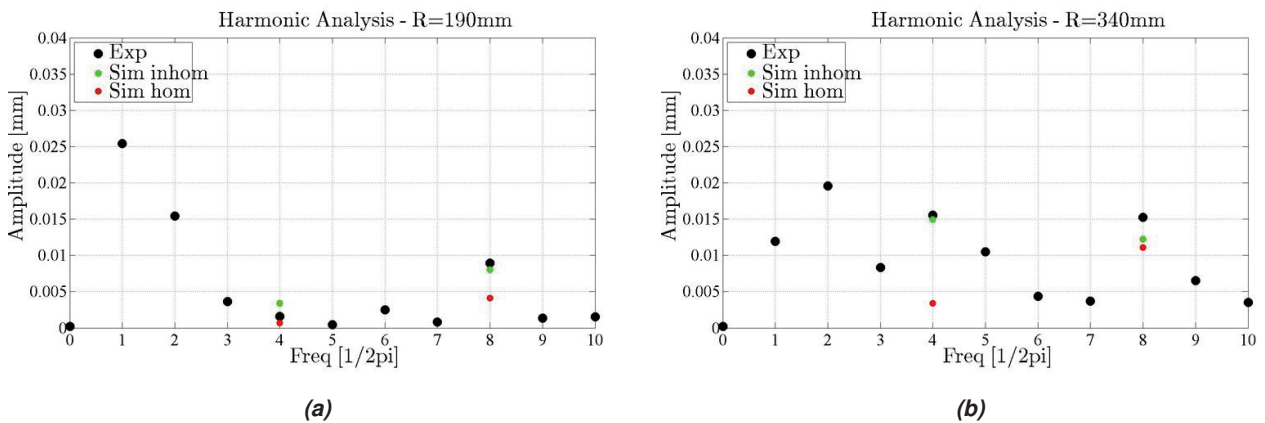


Figure 6.41: Comparison of the amplitudes of the 4th order and 8th order waviness at a) the inner and b) the outer disk circle. The experimental data after 10 emergency stops are compared to the simulated amplitudes after 10 uniform and 10 non-uniform simulations.

the most important quantities in the verification process is the residual stress distribution from the friction surface in thickness direction. The damage analysis presented in Chapter 4 treats this topic in detail and on the basis of a multitude of in-depth residual stress measurement. The residual stress level formed by cyclic inelastic deformation can reach a significant tensile level but becomes clearly reduced, deleted or even partially shifted into the compressive regime when phase transformations occur. Evidently, phase transformations in the near surface region are not detrimental but on the contrary a means to lower the stress level. From the point of view of FE modeling, however, taking into account phase transformations is a huge challenge. The combined description of cyclic viscoplasticity and phase transformations under variable thermal and mechanical loading conditions is clearly beyond the scope of this work. Since phase transformations generally reduce the residual stresses in the brake disk, simulations taking into account the deformation behavior represent a conservative approach. Nevertheless, the procedure is not overly conservative because it captures the realistic scenario where hot spots in early brake cycles initiate cracks and migrate to other positions during later cycles. From then on positions where cracks may have been initiated are subjected to cyclic viscoplastic deformation, which causes high tensile residual stresses but will not undergo phase transformations and annealing effects that would reduce them. The residual stress field computed on the basis of the developed modeling approach thus fulfills the requirement of describing the realistic worst case scenario, which is always the basis of component design. As a consequence the simulated residual stress field must be higher than or equal to all measured results. This condition is graphically displayed in Fig. 6.42a, Fig. 6.42b and Section 6.3. After one high energy braking the measurements

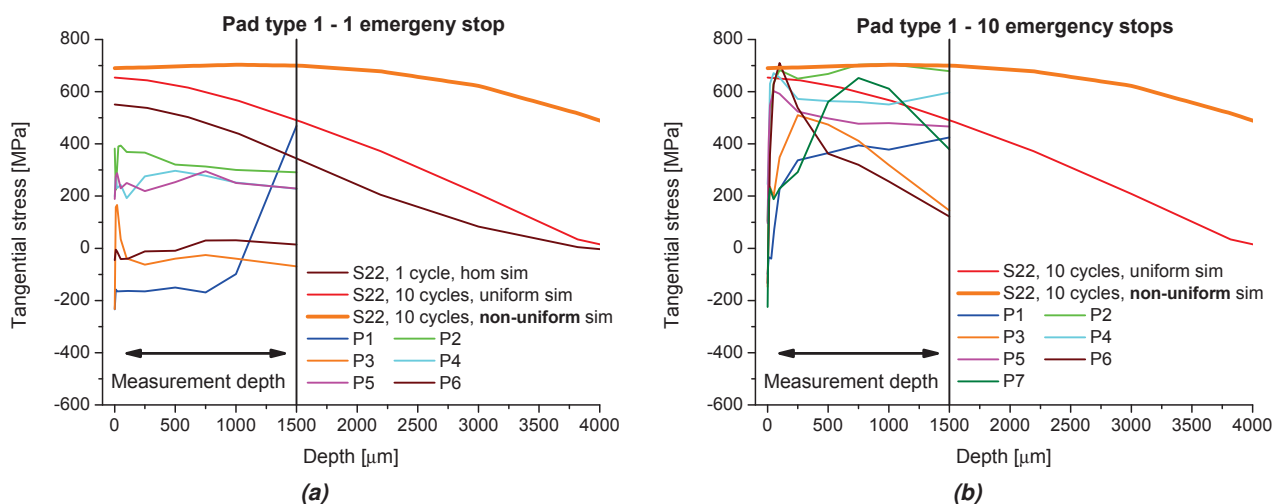


Figure 6.42: Comparison of measured and simulated residual stress distributions a) 1 and b) 10 emergency stops. The measurements correspond to multiple positions on the friction surface. The measured results are influenced by the viscoplastic material response and the occurrence of phase transformations. The simulations only take the viscoplastic material behavior into account an aim at the description of the highest possible stress level.

are completely enveloped by the stabilized stress field obtained with the uniform heat source. The result from the non-uniform simulation corresponds to the distribution depicted in Fig. 6.30b for position P2. This result seems to be very conservative but the situation changes when the measurements are taken after 10 high energy brakings. At this stage the highest stress levels were measured since the residual stresses have completely formed and have not yet been reduced or deleted as later on during the test run. The results from the uniform simulation underestimate some of the measurements and are hence not conser-

6. SIMULATION RESULTS

vative. The result from the non-uniform simulation on the other hand envelope and match the stress level with a very good accordance. After 200 emergency stops most of the measurements show an influence from annealing or transformation. For this reason the uniform solution is again conservative but only in the surface region where these effect have an influence. At greater depths some of the measured values are underestimated. The results from the non-uniform simulation give the only solution that envelopes all measured results without being too conservative (see Fig. 6.42b). The only solution that that can be used for quick qualitative results and for more laborious but at the same time more profound and quantitative results has been reached.

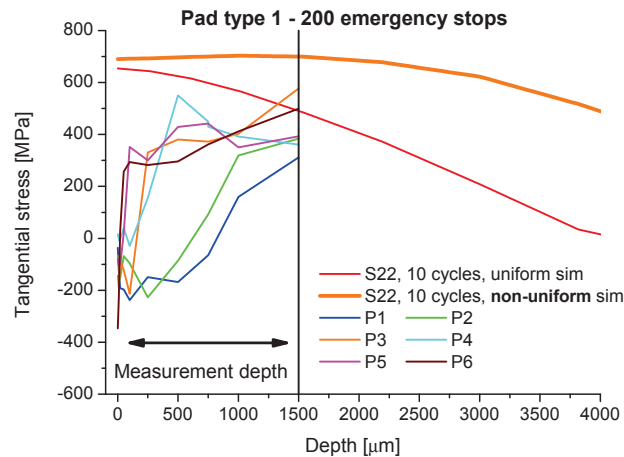


Figure 6.43: Comparison of measured and simulated residual stress distributions after 200 emergency stops. The measurements correspond to multiple positions on the friction surface. The measured results are influenced by the viscoplastic material response and the occurrence of phase transformations. The simulations only take the viscoplastic material behavior into account an aim at the depiction of the highest possible stress level.

The subsequent section shows how the uniform description can be applied for efficient material comparisons.

6.4 Material comparison

6.4.1 Impact of thermophysical properties

Fig. 6.44a shows the evolution of the thermal conductivity λ with temperature for a set of engineering materials used for brake applications. The background for the discussion in Section 5.2.2 becomes evident when material D is compared to material B. Both materials are cast irons. While material B exhibits a higher strength — due to its globular graphite shape and the higher alloying content — the thermal conductivity of material D is significantly higher — due to the lamellar graphite shape. This is the classical advantage of this inexpensive material that has been introduced a long time ago. At room temperature λ of material D is by a factor of 2 higher compared to material B. With increasing temperatures the differences decrease but at 400°C the difference is still a factor of 1.3. The three steels in Fig. 6.44a are situated in between the two cast iron variants from the point of view of λ . Their mechanical properties, however, are far beyond the levels of cast irons and thus their suitability to bear higher loads is given in any case — at higher costs, however. Fig. 6.44b depicts the corresponding measurements for the technical coefficient of expansion α . This is another critical quantity for the resulting TMF loading. The thermal conductivity has a great impact

on the evolution of the temperature field in the brake disk — beside the specific heat c_p — and the resulting T_{max} . The thermal expansion on the other hand affects the thermal strain ϵ_{th} and thus the constraint. The data in Fig. 6.44b suggests that up to 700°C both cast irons have lower expansion coefficients than the three steels. The material with the lowest mechanical properties, i.e. material E, shows very favorable thermophysical properties, at least below the A_1 temperature (see Section 4.2.3.1 for general information on metallurgical transformations). The influence of the unfavorable mechanical properties of material E prevails in view of N_f but to which extend this drawback is relativized by λ and α can only be assessed by the aid of simulations.

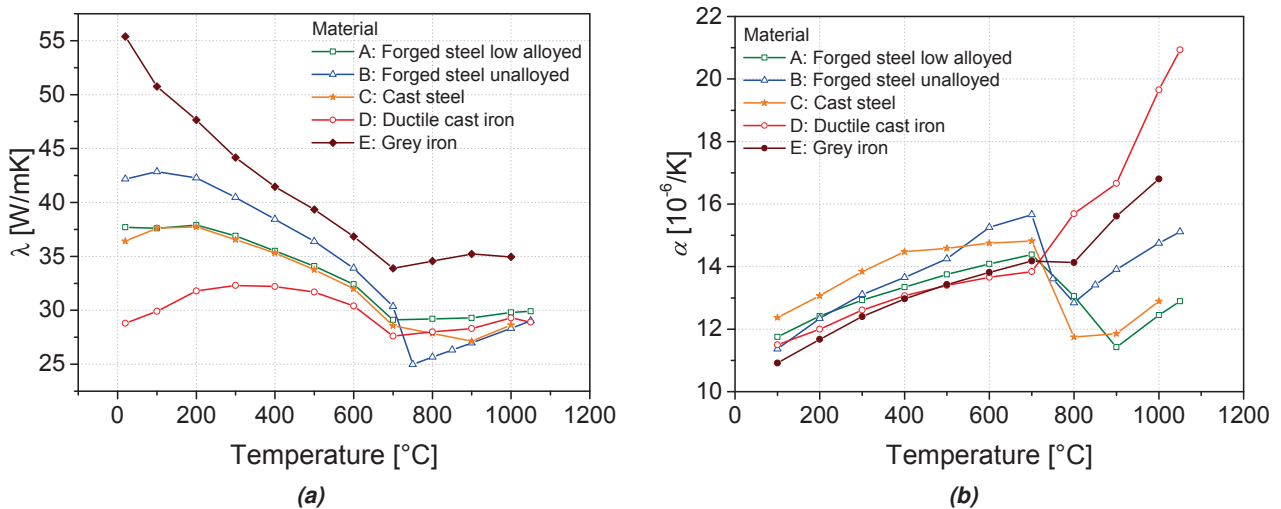


Figure 6.44: Material comparison for a) the thermal conductivity λ and b) the engineering thermal expansion coefficient α ($T_{ref} = 20^\circ\text{C}$).

From the point of view of the resulting temperatures the influence of λ and c_p can quickly be assessed by thermal computations as presented in Fig. 6.45a for the reference braking. Fig. 6.45b compares the materials with the highest and the lowest temperature levels (material D and material E) and it can be seen that a difference of 80°C occurs in T_{max} . This difference is already present at an earlier stage around the time when the brake force is increased at 19.3s. This means that the impact of the thermophysical properties coincides with the time period where most of the inelastic deformation takes place. The temperature difference is thus significant in terms of TMF damage. The diagram also reveals the clear influence of λ on the entire temperature field in the brake disk, which directly affects the disk coning as previously noted. This comparison is only qualitative for loading conditions typical for the main material in this work, material A. The cast irons are exposed to less severe loading conditions and the temperature difference is lower. In the case of the steels the difference is less and the curves for material A and material C nearly coincide. T_{max} for material B is lower since it contains a lower content of alloying elements, which act as lattice defects in the metallic grid thus lowering λ . The influence of alloying elements is apparent from Fig. 6.44a, where the ductile cast iron exhibits the lowest values due to its high content of alloying elements in order to produce graphite in spherical shape. The unalloyed steel has the second highest values for λ . Grey iron shows the highest values for λ , which stems from another physical mechanism, the elevated heat flow through the graphite lamellae. The impact of the thermophysical properties on the overall performance should become evident — at least for materials with comparable mechanical properties — from component testing carried

6. SIMULATION RESULTS

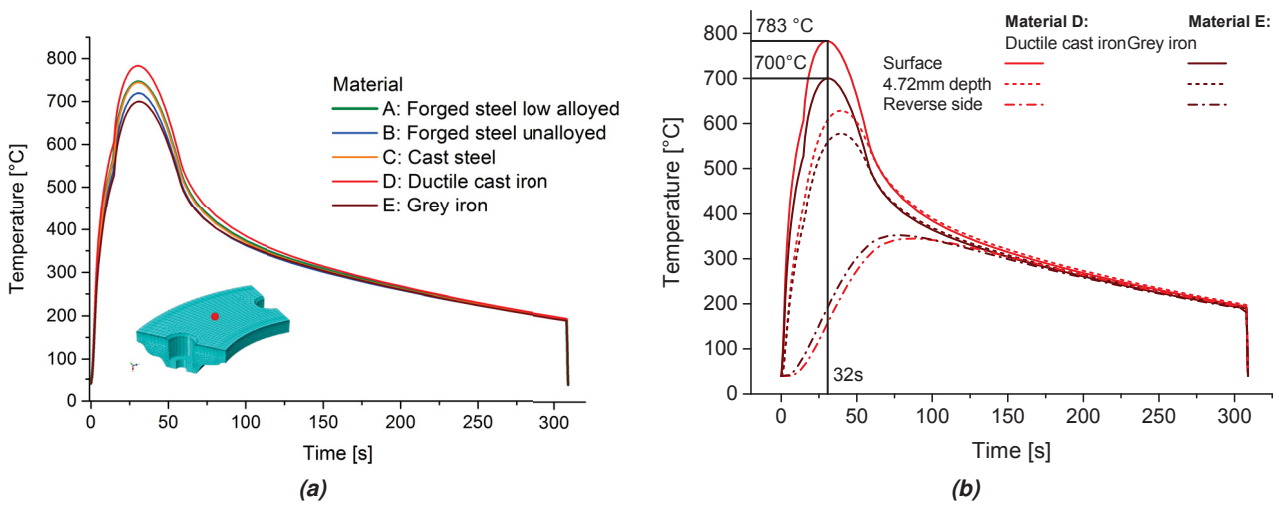


Figure 6.45: a) Evolution of the surface temperature for the reference braking for representatives of five different classes of metallic brake disk materials, b) Comparison of the temperature fields of materials D and E, which exhibit the greatest difference in thermophysical properties.

out until crack initiation at similar testing conditions. Because this is not always possible, due to the long time frames for crack initiation to take place under realistic brake applications, it is an advantage to have TMF simulations at hand. Using precisely measured thermophysical properties in thermal FE computations combined with a material model for cyclic (visco)plasticity in a subsequent mechanical calculation yields the required information for material selection purposes. The resulting plastic strains for loading conditions in the LCF range or the stress levels in the HCF range can be compared to life time curves and an objective comparison can be done as previously discussed for the LCF region of material A.

6.4.2 Application maps for material selection

In this section the impact of the thermophysical properties is complemented with the influence of the mechanical properties and the damage behavior on crack initiation life N_f . Fig. 6.46a compares the stabilized minimal and the maximal in-depth strain distribution¹ for materials A-D during a reference braking. The $\Delta\epsilon_{in}$ at the friction surface is one of the two input parameters for the Ostergren model. In view of $\Delta\epsilon_{in}$ the materials can be ordered in the sequence material A, material C, material B and material D. The second input parameter is σ_{max} , which can be derived from Fig. 6.46b. The diagram compares the minimal² and the maximal stress distribution for each material. Due to the higher strength of the steel materials, which is qualitatively illustrated in Fig. 6.47a and Fig. 6.47b the maximal stress (=residual stress) is significantly higher than for the ductile cast iron — and of course grey iron. The combined effect can be assessed on the basis of a verified damage parameter as noted in Section 5.2.7.1.

The results for N_f for variable energy input are depicted in Fig. 6.48b along with the individual ranges of

¹The maximal distribution, in terms of magnitude, is in fact the lower envelope of the results from the individual points in time during braking. For the sake of simplicity the result with the most relevant maximal magnitude at the surface is represented, which is relevant for crack initiation.

²Again the minimum distribution is the lower envelope of the results for all computed increments. For the sake of simplicity the distribution with the minimal stress at the surface is represented. For the Ostergren-model this distribution has no influence on the estimated N_f but in view of crack propagation it determines $\Delta\sigma$ at the crack tip.

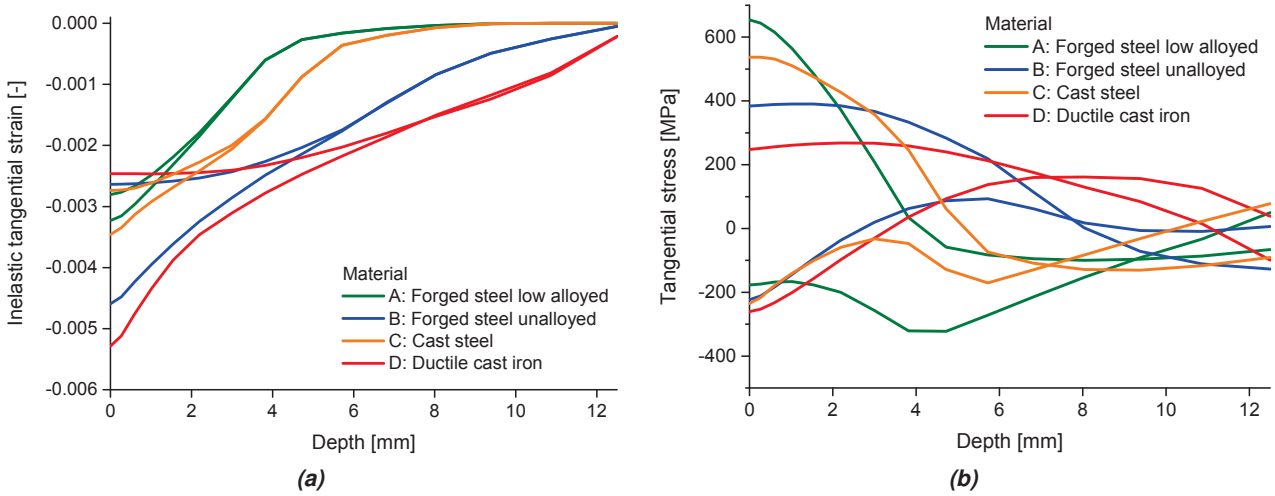


Figure 6.46: a) Comparison of the stabilized inelastic response for the reference braking for material A-D from the surface down to 12.5 mm depth and b) the corresponding residual stress field.

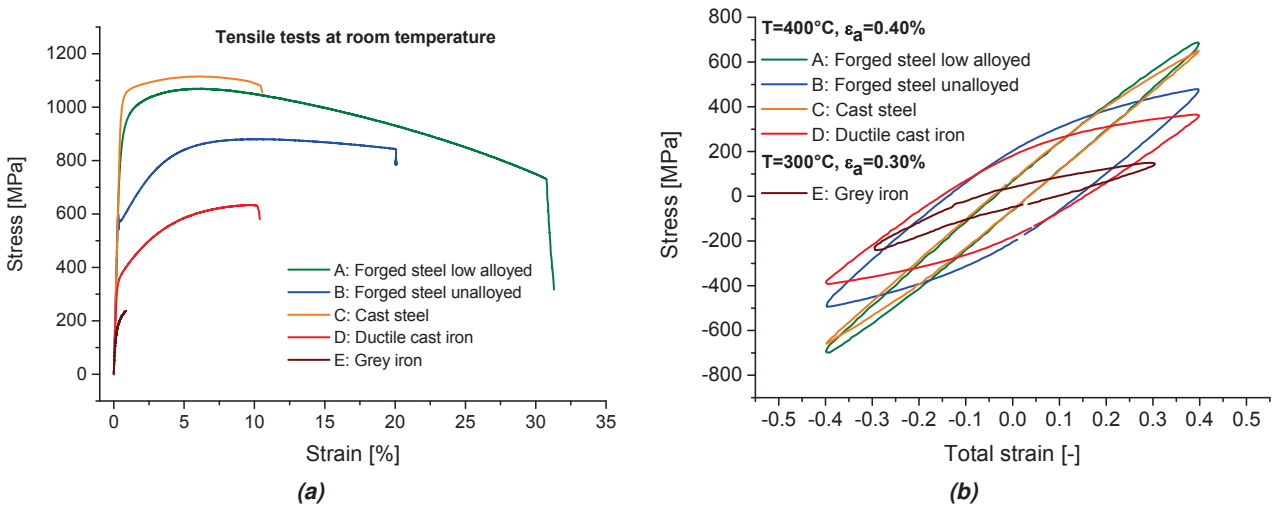


Figure 6.47: Qualitative material comparison with a) tensile tests at room temperature and b) LCF tests at elevated temperature.

validity for each material (Fig. 6.48a). The validity range is limited by an inelastic strain amplitude $\epsilon_{in,a}$ of 3×10^{-4} as discussed in Section 5.2.7.1. It should be noted that the validity range of the viscoplasticity models must also be kept in mind. For this reason, Fig. 6.48b should be used in combination with Fig. 5.32a and Fig. 6.45a.

From Fig. 6.48b it can be concluded that the improved mechanical properties of material A and material C due to alloying prevail over the decreased thermal conductivity. This is also due to the impact of the alloying elements on the thermal expansion α (Fig. 6.45b). Below the phase transformation temperature this quantity is clearly lower for material A than for the other two steels. At elevated temperatures material C shows a more favorable thermal expansion than material B¹. The low thermal expansion of material D cannot make up for the lower strength and the low thermal conductivity. Nevertheless, it is sufficient at

¹By alloying α can be significantly influenced at the cost of λ . Which influence prevails can be assessed by thermomechanical simulations.

6. SIMULATION RESULTS

lower values of E_d .

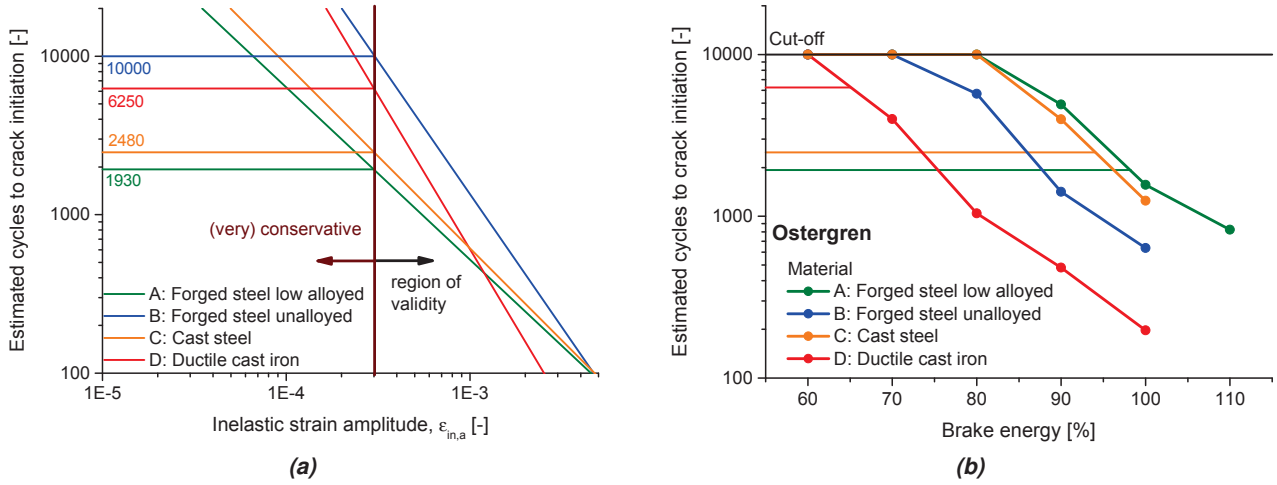


Figure 6.48: Material comparison in terms of crack initiation life time. a) Validity range for each material and b) N_f versus E_d for the reference brake scenario and variable energy input.

In the present work the comparison is carried out for the reference braking with varying energy input. The reference brake scenario is relevant for high speed braking, which is the application range for material A but not for the other materials. They are exposed to load scenarios, which cause different energy dissipation but also different brake times. With the presented simulation tool and the material models the comparison can be performed for any brake application, especially if only the parameters in Table 5.5 need to be changed. This topic is left for the industrial application of the simulation tool.

6.4.3 Alternative assessment for online health monitoring

In Section 5.2.7.1 an alternative prediction of the crack initiation life time N_f based on the work of Winter [130] has been proposed (Eq. (5.25)). On the one hand, this model is useful for the assessment of material E since the prediction of N_f based on stress and strain is not possible for this material within the scope of this work. On the other hand, it is applicable for online health monitoring as long as the input parameters are within the validity range. The input for the Winter model are the local maximum temperature T_{max} and the local constraint factor K_{TM} . The definition of K_{TM} follows Eq. (6.5).

$$K_{TM} = \frac{\epsilon_{mech}}{\epsilon_{th}} \quad \epsilon_{mech} = \epsilon_{tot} - \epsilon_{th} \quad (6.5)$$

Its determination from the FE-model at a specific point in time is straightforward if the main loading direction is clear as in the present case. A problem arises from the fact that K_{TM} is a function of time and it is not straightforward to obtain a value that is characteristic for the damage behavior. Fig. 6.49b shows the evolution of the temperature, K_{TM} in tangential direction and the equivalent plastic strain p . Fig. 6.49b compares the results of simple and more complex estimations of characteristic K_{TM} factors at a position in the component. The first estimation is the $K_{TM}^{T_{max}}$, which corresponds to the constraint at the maximum temperature of the load cycle. Since inelastic deformation occurs during the high temperature phase this is deemed a reasonable approximation. However, inelastic deformation does not only occur at T_{max} but around T_{max} with variable inelastic strain increments. This requires the investigation of additional methods,

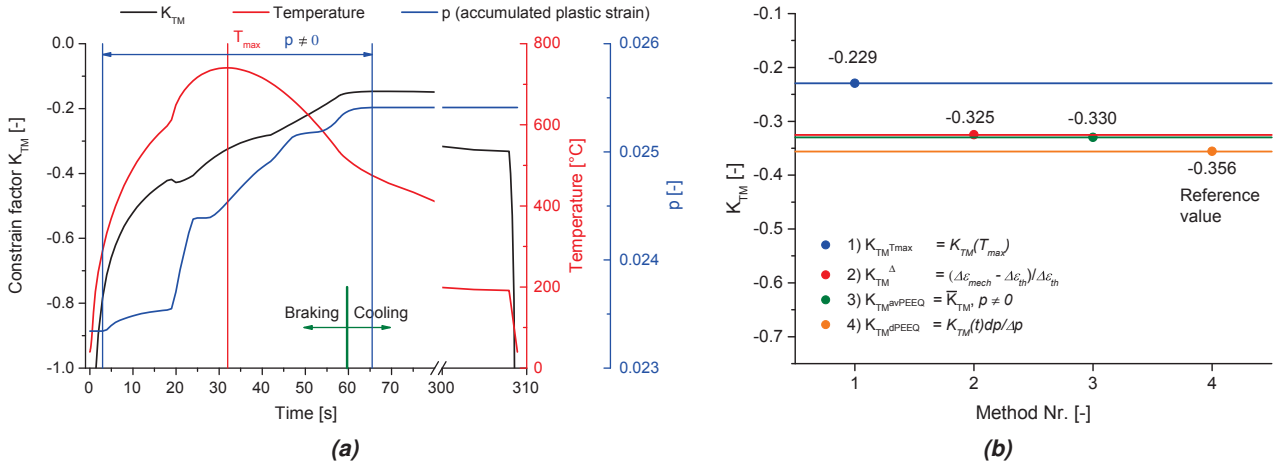


Figure 6.49: Possible definitions of K_{TM} in a component: a) Evolution of $K_{TM}(t)$ in main loading direction and the governing quantities of damage and b) comparison of the results for different definitions of a characteristic K_{TM} . The results are extracted from the simulation of a reference brake cycle and material A.

which take into account the relevant period in the cycle where $\dot{\epsilon}_{in} \neq 0$. The first estimation is K_{TM}^{Δ} , which uses the mechanical strain range $\Delta\epsilon_{mech}$ and the thermal strain range $\Delta\epsilon_{th}$ over the whole cycle. This method has the disadvantage that stages during the load cycle, where deformation is purely elastic are also taken into account. For the brake disk the length of the cooling period influences fallaciously the result. K_{TM}^{avPEEQ} resolves the problem by averaging $K_{TM}(t)$ over the time period, where dp is non-zero. $K_{TM}(t)$ has the greatest impact during the periods where inelastic deformation occurs. K_{TM}^{avPEEQ} can be further improved by the application of weighted averaging according to Eq. (6.9). In this work it is thus assumed that the weighted average of $K_{TM}(t)$ with dp as weighting factor K_{TM}^{dPEEQ} is the quantity with the most general and most physical meaning. Additionally the effect of variations of the brake time are automatically taken into account by this quantity. Fig. 6.49b shows that for the reference brake scenario the result for K_{TM}^{Δ} is 35.5% less than the reference result obtained with K_{TM}^{dPEEQ} . K_{TM}^{Tmax} and K_{TM}^{avPEEQ} underestimate the reference result by 8.5% and 7.3%, respectively. Due to the acceptable approximation K_{TM}^{Tmax} can be applied as the most simple and sufficiently accurate quantity for the assessment of brake disks. The variation of the brake time and brake energy is taken into account by the position of T_{max} only making this quantity less general than K_{TM}^{dPEEQ} .

$$K_{TM}^{Tmax} = K_{TM}(T_{max}) \quad (6.6)$$

$$K_{TM}^{\Delta} = \frac{\Delta\epsilon_{mech} - \Delta\epsilon_{th}}{\Delta\epsilon_{th}} \quad (6.7)$$

$$K_{TM}^{avPEEQ} = \bar{K}_{TM} \quad dp \neq 0 \quad (6.8)$$

$$K_{TM}^{dPEEQ} = K_{TM}(t) \frac{dp}{\Delta p} \quad dp \dots \text{current increment, } \Delta p \dots p \text{ during load cycle} \quad (6.9)$$

A further question that needs to be answered is whether K_{TM}^{Tmax} is admissible for purely elastic FE computations without taking into account the inelastic deformation. For material E this is a necessary requirement since no viscoplasticity model is available and for the other materials it would simplify the application for

6. SIMULATION RESULTS

online health monitoring significantly. For stress controlled loading conditions the elastic calculations are not sufficient because inelastic deformation adds to ϵ_{mech} . The loading of brake disks is primarily strain controlled, which means that ϵ_{mech} is rather unaffected by inelastic deformation. Due to other influences on the constraint, such as the static disk coning, the deviations between the results from elastic and viscoplastic FE calculations must be compared. Fig. 6.50a shows the stabilization of $K_{TM}^{T_{max}}$ over 10 reference

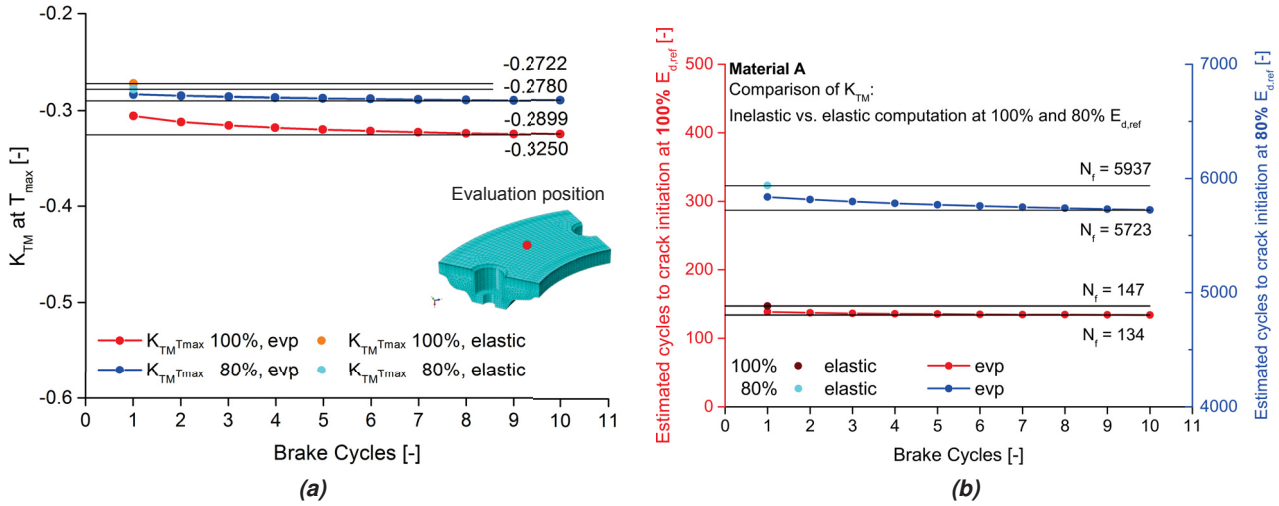


Figure 6.50: Comparison of the K_{TM} factor obtained from the stabilized σ - ϵ field of a viscoplastic FE-calculation and K_{TM} from an elastic calculation. The results are extracted from the simulation of a reference brake cycle and material A.

brakings and the evp-model for material A. At 100% E_d^{ref} (25 MJ/disk) $K_{TM}^{T_{max}}$ stabilizes at -0.325 and at 80% E_d^{ref} at -0.270 indicating that K_{TM} is not only a function of time but evidently of the energy input as well. The corresponding results for the elastic calculations are -0.278 and -0.271, respectively. For 100% E_d^{ref} this corresponds to an underestimation by 16% and for 100% E_d^{ref} by 4%, which implies that the impact of the disk coning on $K_{TM}^{T_{max}}$ is relevant but only to a minor extent. The impact of these deviations in the prediction of N_f is illustrated in Fig. 6.51b. In terms of N_f the difference between the elastic and the viscoplastic calculation is +10% for 100% E_d^{ref} and +4% for 80% E_d^{ref} . For the investigated reference braking a prediction of N_f based on an elastic FE-calculation is admissible. The deviation decreases with falling values for E_d and thus the inelastic deformation. This is of special interest for material E, which is used for less severe loading conditions. Fig. 6.51a shows values for T_{max} and K_{TM} determined for materials A-D based on the viscoplastic calculations used for the data in Fig. 6.48b and for material E, which is based on elastic calculations. The data are marked with a frame showing the validity limits of the Winter model, which reveals that the results for materials A-D are clearly outside the range of validity, especially material A and material C. The tested K_{TM} factors are very conservative compared to the simulation results but due to the fact that the Winter model extrapolates from the tested parameter range to other values outside this range the quality of the extrapolated results is not known. T_{max} is critical for the validity, while K_{TM} has less impact. For material A, however the simulated constraint is 60% below the lowest tested K_{TM} (low in terms of the magnitude). Furthermore, the lower and upper bound of the tested range for K_{TM} is rather narrow. For material D the validity range is wider and closer to the simulated K_{TM} factors (\sim 35%). For material E the tested parameter range, i.e. the region of validity, encloses the simulated results up to $T_{max}=600^\circ\text{C}$, which is clearly above the usual design temperature.

Fig. 6.51b depicts the data from Fig. 6.48b with the additional data for material E obtained from elastic

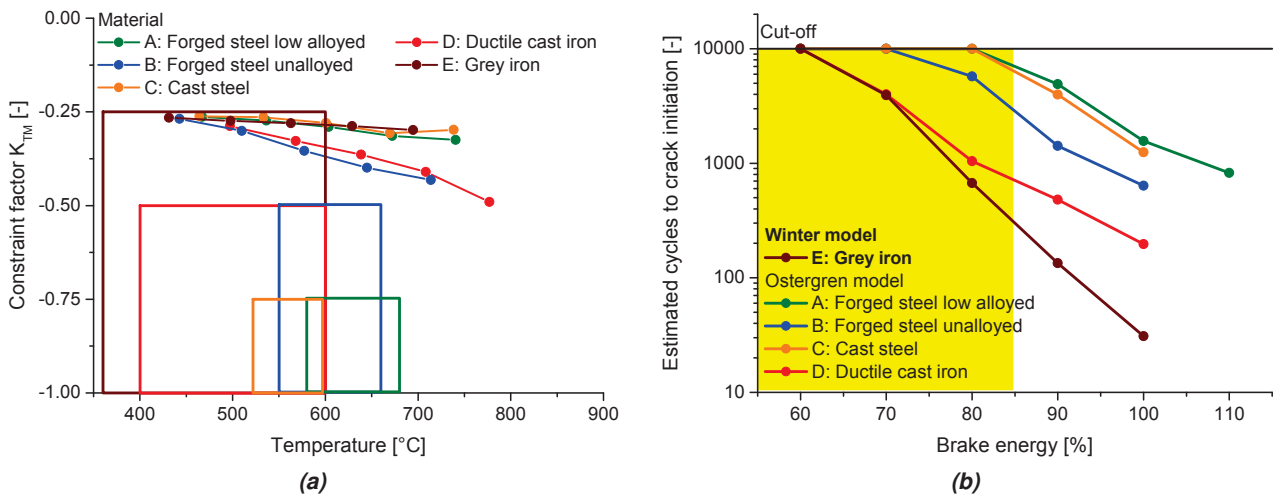
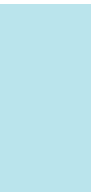


Figure 6.51: Material comparison in terms of crack initiation life time. a) Validity range of the Winter model for each material and b) N_f versus E_d . For material E the range of valid predictions of N_f based on the Winter model is indicated in yellow.

FE calculations and the Winter model. For the materials A-D the evaluation procedure based on inelastic strain and stress from viscoplastic computations is preferable. For material E the alternative strategy is applicable for general estimations in the design process and online health monitoring in the validity range indicated in yellow. It must be considered, however, that a fracture mechanical evaluation needs to be taken into account as well. This is especially the case for grey iron due to the inherent defects in the form of graphite lamellae. The role of fracture mechanics in the context of online health monitoring is left for future work.



Chapter 7

Conclusion

In the introduction the main objectives of this work have been stated in the following form:

1. Characterization of the non-uniform loading conditions of a wheel mounted brake disk used for high speed trains in combination with a relevant pad type used in service. For this purpose thermal image data from a test rig program are analyzed and processed for the subsequent use in thermomechanical simulations.
2. Characterization of the processes contributing to damage at the friction surface of the tested brake disks. The obtained knowledge is the basis for the development of a simulation tool that captures the necessary mechanisms. Furthermore, the analyses provide data for the verification of the simulation results.
3. The development of a simulation tool, which is capable 1) of supporting the design process of brake disks, 2) of facilitating the design and the optimization of the brake management (blending) and 3) of providing knowledge and methods for online health monitoring systems.

Analysis of loading conditions: A program on a full scale test rig consisting of individual test runs with an increasing number of brake cycles was carried out for the combination of a steel disk and a flexible pad type for regular use in the high speed segment. In order to investigate the damage behavior of the brake disk under increased loading the test rig program was carried out with a second pad type. A non-flexible type (pad type 2) usually applied at lower speeds was chosen in order to cause more severe TMF loading conditions with consequent crack initiation and propagation. A specific brake scenario for emergency braking was chosen as the reference braking for the test rig program. It corresponds to the relevant worst case scenario on track. The program was planned as a step test with a number of load cycles from 0 to 200 brakings in order to investigate the evolution of the thermal loading, its reproducibility and the evolution of the corresponding damage. Cycle 0 corresponds to bedding-in only at low brake energies without emergency testing. In the other test runs the bedding-in process was followed by 1, 10 and 200 emergency stops, respectively, each beginning with a new disk set. Individual brake cycles were recorded with a thermal camera and systematically analyzed. The results show the transient nature of the disk surface temperature caused by each pad type. The evolution of the temperature distribution during individual brake cycles as well as changes in this evolution over the course of several brake cycles was

7. CONCLUSION

characterized and documented in Chapter 3. Pad type 1 shows increased thermal loading on the inner disk half. On a global scale the thermal patterns are stable but on the local scale significant changes occur during each cycle and from one cycle to the next. Pad type 2 causes very pronounced thermal surface gradients that change on a global scale. It was possible to identify a systematic alternation between two opposing hot spot configurations, where the term *hot spot* is not applicable in the classical sense. The thermal patterns are reproducible in different test runs for both pad types. The thermal image data was processed and prepared for simulation purposes. Characteristic load sequences were identified, which can be used in the simulations in order to capture transient thermal loading that essentially determines the service life of a brake disk.

Analysis of the damage: After component testing on the test rig the global residual deformation, the residual stresses and the microstructure were characterized individually for each disk. Data on the static disk coning and waviness have been obtained. These were compared for the individual test runs and pad types. The data are subject to significant scatter but they clearly indicate increased inelastic deformation caused by pad type 2. The residual stresses can reach a level of 700 MPa for pad type 1 and even higher values for pad type 2. However, the stress level does not systematically increase and stabilize as typically observed in other components under TMF loading. This is due to the interaction of cyclic viscoplastic deformation and phase transformations in the regions where increased temperature levels occur. Residual tensile stresses are continually formed by inelastic deformation and reduced or deleted by phase transformations. This effect is more pronounced in brake disks tested with pad type 2. The strongly varying thermal distributions cause systematic transformation of the whole surface region. For pad type 1 this effect is mostly concentrated on a ring on the inner disk half, while the other regions are only subject to stress relaxation effects. After the maximum number of brake cycles neither of the two pad types has induced macroscopic cracks on the friction surface. The detailed results are collected and discussed in Chapter 4. The obtained data are available for the verification of the simulations.

Modeling and simulation of the braking process: Based on the knowledge obtained from the analyses of the thermal loading conditions and the damage mechanisms a modeling strategy was developed. It considers the thermal loading, either in a uniform manner for quick qualitative results or in a non-uniform manner based on the thermal image data for quantitative results. Furthermore, it takes into account the inelastic time and rate-dependent material behavior by means of a viscoplastic material law. The required material parameters were identified from extensive lab experiments. The additional modeling of the phase transformations is beyond the scope of this work. However, it can be shown that omitting phase transformations yields results overestimating the stresses thus making the simulations a conservative approach. The crack initiation behavior is captured by an empirical damage parameter and the results from extensive TMF tests. The fracture mechanical behavior was evaluated with a method that introduces virtual cracks into the computed stress fields and provides the corresponding stress intensities. Crack propagation experiments are available for the interpretation of the results. On the basis of the discussions in the corresponding chapters (Chapter 5 and Chapter 6) the following fundamental conclusions can be drawn: The evaluation of crack initiation life based on the presented strategy clearly shows the impact of geometrical, material and process parameters on the overall behavior of brake disks. It thus significantly supports

the design process. The evaluation of a damage parameter provides insights into the combined effect of thermophysical properties, mechanical properties, disk geometry and the brake scenario on the suitability for service. The importance of a damage parameter for quantitative estimates on crack initiation life is limited by the rather large scatter and its dependence on other factors, such as the material model and the assumptions about the loading conditions. It clearly shows, however, that small changes in the overall system settings may easily cause an increase or a reduction of the estimated crack initiation lifetime by one order of magnitude. This quantitative information is expected to hold in real applications.

The investigations on crack initiation life and fracture mechanical life show that a quantitative description of service life necessitates a fracture mechanical analysis. For the reference case crack initiation happens at an early stage of service life, i.e. after several 100 high energy brakings. Emergency stops are only one type of high energy brakings beside other more frequent brake events. For this reason the predicted crack initiation after only several hundred brakings is low compared to the estimated 2000-10000 high energy brakings during the service life of a brake disk. In the present case the predicted number of brake cycles to crack initiation does not mark the end of the service life. The fracture mechanical analyses show that only a limited amount of crack propagation will occur in the computed stress fields. This explains the observation that cracks do not appear at early stages of service on the investigated disk type. Since maintenance procedures mostly rely on visual inspection, initiated cracks of 0.5-2 mm length may not be seen or might not be distinguishable from heat checks. Longer cracks only form under more severe conditions than the reference case or after an unrealistically high number of load cycles.

The comparison of the simulated results to the experimental data confirm the higher quality of the results from the non-uniform heat source over the ones obtained with uniform loading. Qualitative investigations on the overall behavior can be carried out based on uniform thermal loading conditions. For the flexible pad type, which is relevant for real applications, it was shown that taking into account non-uniform loading conditions predicts a crack initiation life time of 30% of the uniform assumption. This result can be used for correlating the uniform simulations and the non-uniform reality. The methods and the knowledge from this work can be taken as the basis for the development of online health monitoring systems. Such systems will be part of the onboard system of modern trains. It assesses the condition of brake disks based on continuous measurements, e.g. of the temperature, and based on an implemented combination of verified damage and fracture mechanical models.

7. CONCLUSION

Appendix A

Supplementary background information

A.1 Dislocation structures

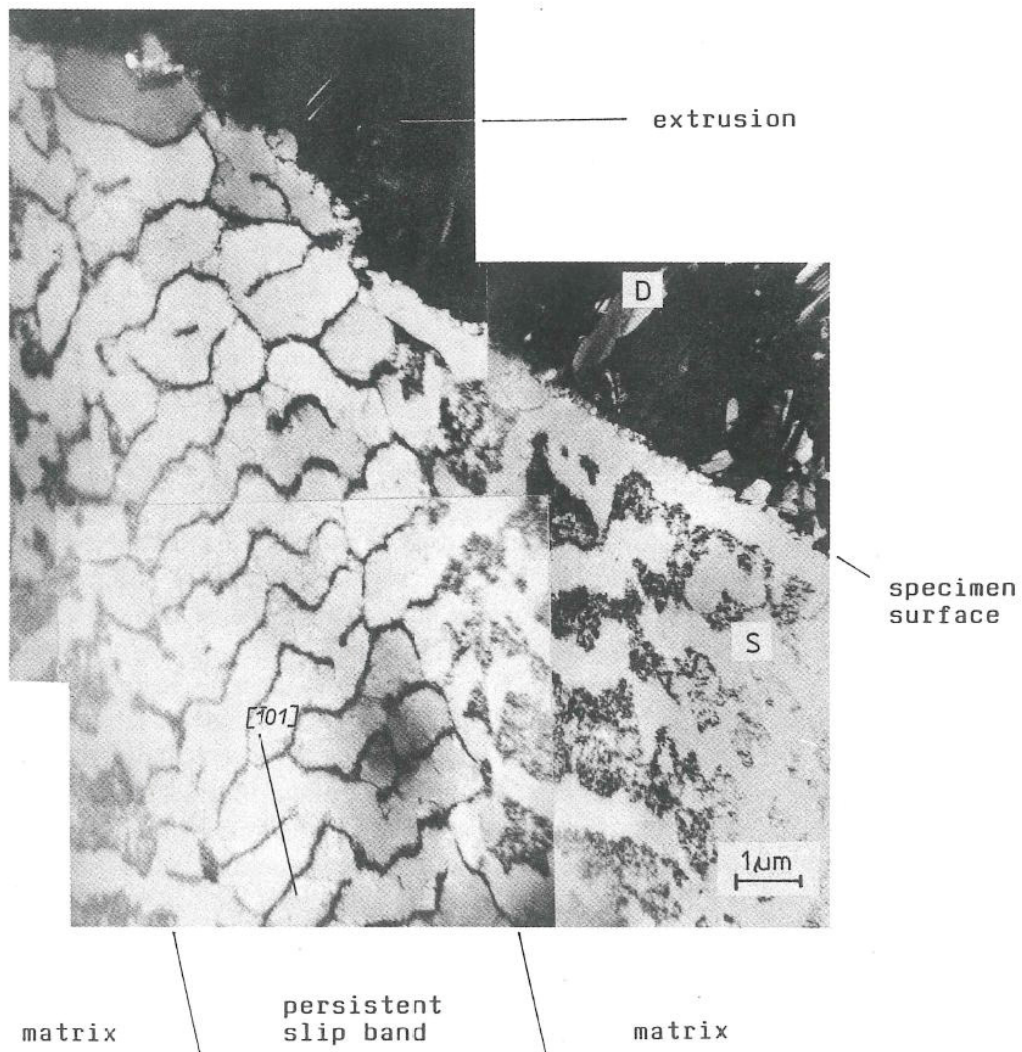


Figure A.1: Illustrative image showing the formation of an extrusion by a persistent slip band in *s* copper single crystals [13].

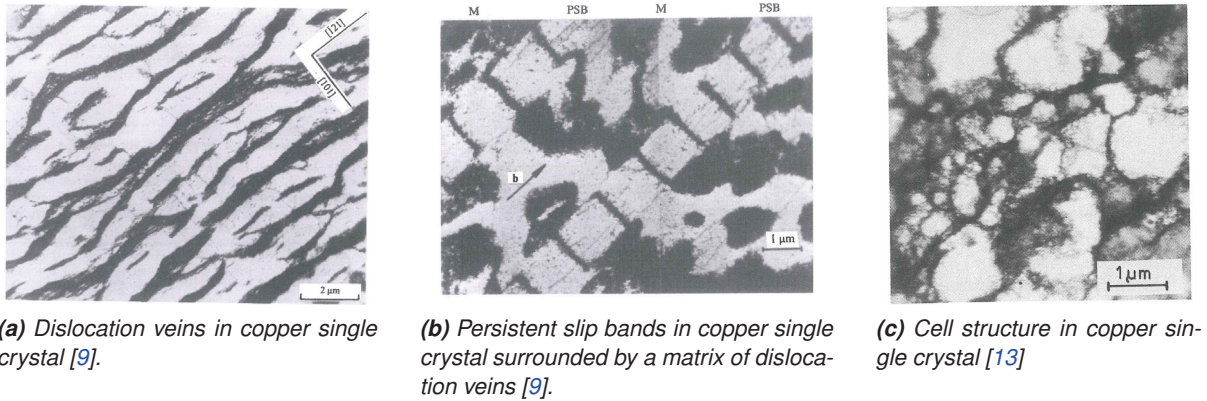


Figure A.2: Various types of dislocation structures

A.2 Determination of fracture mechanical quantities

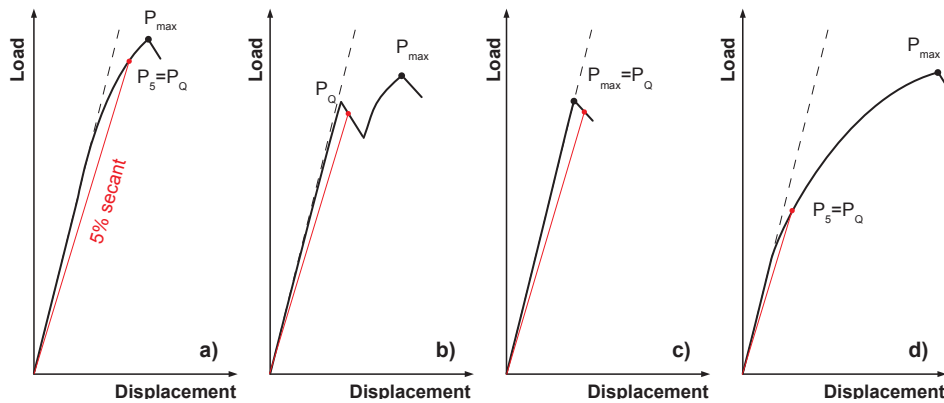


Figure A.3: Determination of the critical load P_Q [35; 36]

Fig. A.3 plots four possible examples of the load displacement curve of fracture toughness tests. Equations (A.2) and (A.3) below are recommended to be used for preliminary estimations of the necessary sample dimensions to produce valid results for K_{IC} . The variables a , B and W refer to the characteristic dimensions of the specimen. The sample geometries most commonly used are Single Edge Notch Bend specimens (SENB, see Fig. A.4) and Compact specimens (CT). Since tensile tests are often run in parallel for the material characterization the tensile strength can be obtained readily. An estimate for the expected K_{IC} value may be obtained from the literature on similar materials. By using sample dimensions according to Equations (A.2) and (A.3) the plastic zone size is likely to be about 50 times smaller than these dimensions which in turn would guarantee the validity of assuming small scale yielding [36]. The restriction on the sample size stated by Eq. (A.2) is linked to the ductile fracture mode. In thin samples a plane stress state prevails, which implies that plastic deformation normal to the surface is possible (3D strain state). The overall appearance of this sort of fracture includes shear lips indicating very ductile deformation that consumes high amounts of energy in the process of crack extension. In thick samples this fracture appearance can be found at the sides where plane stress conditions are present. At the center the situation is different, however, as plastic deformation in thickness direction is constrained by the surrounding material which gives rise to plane strain conditions. The lack of deformation in the third direction

induces stress in this orientation, which increases the hydrostatic part of the stress state to a considerable extent. The impact of the hydrostatic stress can be seen in two ways: First, the plastic zone is smaller at the inside than at the outside of the sample. This can be explained by the aid of Mohr's circle. The largest circle in this diagram shrinks compared to the plane stress state due to the third stress component. Since the maximum radius determines the maximum shear stress, the region in the sample affected by plastic yielding is smaller at the interior than at the outside. Second, the ductile fracture mode is different under plane strain conditions because the high hydrostatic stress enables the growth and coalescence of pores, which is the preferred fracture mode for K_{IC} -testing, since it consumes less energy and entails more conservative values for K_{IC} . In terms of ductile fracture mode, the contribution of the shear lips A further increase of the sample thickness would not lead to any changes in the fracture toughness, i.e. the determined K_{IC} is characteristic for the tested material. As mentioned above, this plane strain value fulfilling the size requirement given by Eq. (A.2) is designated K_{IC} while for the plane stress value K_C is used. K_C is still applicable for fracture mechanical evaluations but the thickness of the component, e.g. a metal sheet, must be similar to the sample thickness. Otherwise the tested fracture toughness could be significantly higher or lower than the one of the component.

As previously mentioned small scale yielding is the uppermost limit for plastic deformation for LEFM to be applicable. Moreover, plane strain conditions must prevail for the measurement of K_{IC} which is a material property and not depending on the sample thickness. Whether these conditions really hold may be influenced a priori by choosing proper sample dimensions but under all circumstances they need to be checked by further measures after testing. A 5% drop from the elastic regime as indicated in Fig. A.3 in samples with $a/W=0.5$ either indicates:

1. stable crack growth before failure of 2% the length of the ligament or
2. the formation of a plastic zone around the crack tip causing 2% apparent crack growth

Whether 1) or 2) is the case is not evident but a plastic zone that has possibly formed up to the intersection with a 5% secant line is guaranteed to be 50 times smaller than the uncracked ligament. If stable crack growth occurs before failure an uncertainty is introduced in the calculation of K_Q since it is unclear what the final crack length a was before failure. Again, this uncertainty is limited by the 5% secant line. The quantity P_Q used to calculate the provisional fracture toughness K_Q according to Eq. (A.1) is determined from this intersection (Fig. A.3 a)) unless there has already been a higher point on the experimental curve before the intersection (Fig. A.3 b) and c)).

$$K_Q = \frac{P_Q}{B\sqrt{W}} f\left(\frac{a}{W}\right) \quad (\text{A.1})$$

Since the crack usually propagates differently along the sample thickness the average of several measurements along the thickness is used for the crack length before failure. The variation along the thickness is attributed to plane stress conditions at the sides and plane strain at the center. At the sides more energy is thus absorbed by plastic deformation and crack propagation lags behind compared to the center region. The function $f(a/W)$ is given by the standard [35]. Whether the provisional value is a valid fracture toughness or not is checked in a first step by evaluation Equations (A.2) and (A.3), which have already been applied for the estimation of the sample dimensions. At this point, they can be reevaluated with the determined K_Q but yet, the conditions noted so far still do not suffice. Fig. A.3 d) shows an experiment similar to Fig. A.3 a) that would also yield a valid result in terms of Equations (A.2) and (A.3). Nevertheless, the

obtained value P_Q would entail a fracture toughness not characteristic for this material since failure occurs significantly above P_Q due to extensive plastic deformation. Eq. (A.4) excludes this kind of results as it demands P_Q to be in the range of P_{max} .



Figure A.4: Illustration of relevant sample dimensions at the example of an SENB specimen

$$a, B \geq 2.5 \left(\frac{K_Q}{\sigma_{ys}} \right)^2 \tag{A.2}$$

$$0.45 \leq \frac{a}{W} \leq 0.55 \tag{A.3}$$

$$P_{max} \leq 1.10P_Q \tag{A.4}$$

If one of the conditions discussed above is not fulfilled there are still three possibilities to characterize the conditions for critical failure of a material.

First, the sample dimensions can be increased to promote plane strain conditions which allow less plastic deformation [37]. This way it is more likely that all conditions are met since the plastic zone is smaller under plane strain conditions which prevail within the sample than under plane stress conditions which prevail at the sides of the sample. For many engineering alloys, however, it can be seen from Eq. (A.1) that the required dimensions are not feasible. The values for an ASTM 533B steel of $K_{IC} = 208MPa\sqrt{m}$ and $\sigma_{ys} = 470MPa$ [11] lead to the dimensions $B=0.5$ m and $W=2a=1.0$ m. Since this is only an estimate, the thickness may still not be sufficient or the material behavior makes it impossible to meet all the requirements mentioned so far as in the case shown in Fig. A.3 d).

Second there is the possibility to determine K_{IC} as a quantity that is both dependent on metallurgical features and sample dimensions [37]. This method is called *K-R curve testing* or *plane stress fracture toughness testing* in some cases and it is suitable for materials behaving predominantly linearly elastic but exhibiting a rising R-curve. Since this will entail stable crack growth before failure, this will cause problems with the measurement of a valid plain strain fracture toughness as described above. The curvature in Fig. A.3 d) may result from such behavior, although this case is rather rare [39] and usually observed in very wide and thin samples like sheets. The second more common reason for the curvature will be discussed later in this section. Before the measurement of an R-cure (resistance curve) is discussed, the meaning of the R-curve as a failure criterion will be further developed by the aid of Fig. A.5 a). Two equivalent quantities characterizing the crack driving force exist in LEFM which are the stress intensity factor K and the energy release rate G. While K describes the local stress and strain field G is a global measure of the potential energy of the system. In LEFM both quantities are connected by Eq. (A.5), where E' is either E for plane strain conditions or $E/(1 - \nu)$ for plain stress conditions. The situation is similar in terms of the quantities describing the resistance of the material against crack growth which are the fracture toughness

ΔK_{IC} and the crack resistance R. Graph A.5 a) illustrates how G and R may be used to identify a critical loading situation. In the case of a perfect brittle material or often a material subjected to SSY and strict plane strain conditions, the horizontal line at $G_{c,brittle}$ corresponds to a critical quantity characteristic for the material resistance against crack propagation. The R-curve consists of only one point which can be computed to a ΔK_{IC} value as will be discussed below. For the first case, an ideal brittle material, this crack resistance is due to the specific surface energy [163]. For the latter case the crack resistance value would be higher due to plastic deformation along the crack flanks, i.e. there would be a second horizontal line in Fig. A.5 a) situated above the first one valid for the most frequent case of a material under SSY conditions and a flat R-curve. The shape of the R-curve depends on the stress state the fracture mechanism and the size of the structure. Microvoid coalescence in combination with a increasing plastic zone with crack extension, for example, may lead to rising R-curves [36] as depicted in Fig. A.5 a) which will be discussed in the following. It should be noted that K stays a valid measure for the crack driving force if stable crack propagation occurs. As will be shown below, this property is challenged when J is used as characteristic value in EPFM [12].

The three red curves correspond to force controlled loading where the curve corresponding to the load P1 is in the vertical part of the R-curve. This means the energy released by crack propagation would be less than the energy necessary to brake bonds in the material (and plastification of the crack flanks in the case of SSY). The P2 curve on the other hand intersects the R-curve above the vertical part. The intersection means that between a_0 and $a_0 + \Delta a_{P2}$ the released energy is larger or equal than the energy required for crack growth. The initial crack will thus propagate up to the length $a_0 + \Delta a_{P2}$ and stop there. This kind of propagation is called stable crack growth. The load P3 entails G-curve which is tangent to the R-curve at one position. The released energy is thus larger or equal than the energy required inducing unstable crack propagation at all times, i.e. instantaneous failure that cannot be stopped anymore once P3 is applied. All loads above P3 will have the same effect. The tangent point defines the critical loading situation whose identification is the main objective in static fracture mechanics. In this case it corresponds to a critical energy release rate G_C that coincides with a critical point on the R-curve. In terms of stress intensity this would correspond to condition 2.12 which can be obtained by the application of Eq. (A.5). It must be noted that the shape of the G-curves is highly dependent on the shape of the specimen or the component since these determine the potential energy state during loading and unloading due to crack growth. This means that any ΔK_{IC} determined by this method can only be a technological quantity valid for the very test conditions. The shape of the R-curve on the other hand is rather stable except shifting on the x-axis with different initial crack lengths, causing some shift in the position of the tangent point. Thus, the R-curve can be used in many different situations while the G-curve must always be determined for the loading situation in question.

For the experimental measurement of the R-curve it is more convenient to use displacement control as indicated by the blue lines in A.5 a). In displacement control the potential energy decreases with increasing crack length. This prevents the occurrence of critical failure as discussed above until very large displacements. This way, the R-curve can be identified up to crack lengths much larger than in load control.

$$G = \frac{K^2}{E'} \quad (\text{A.5})$$

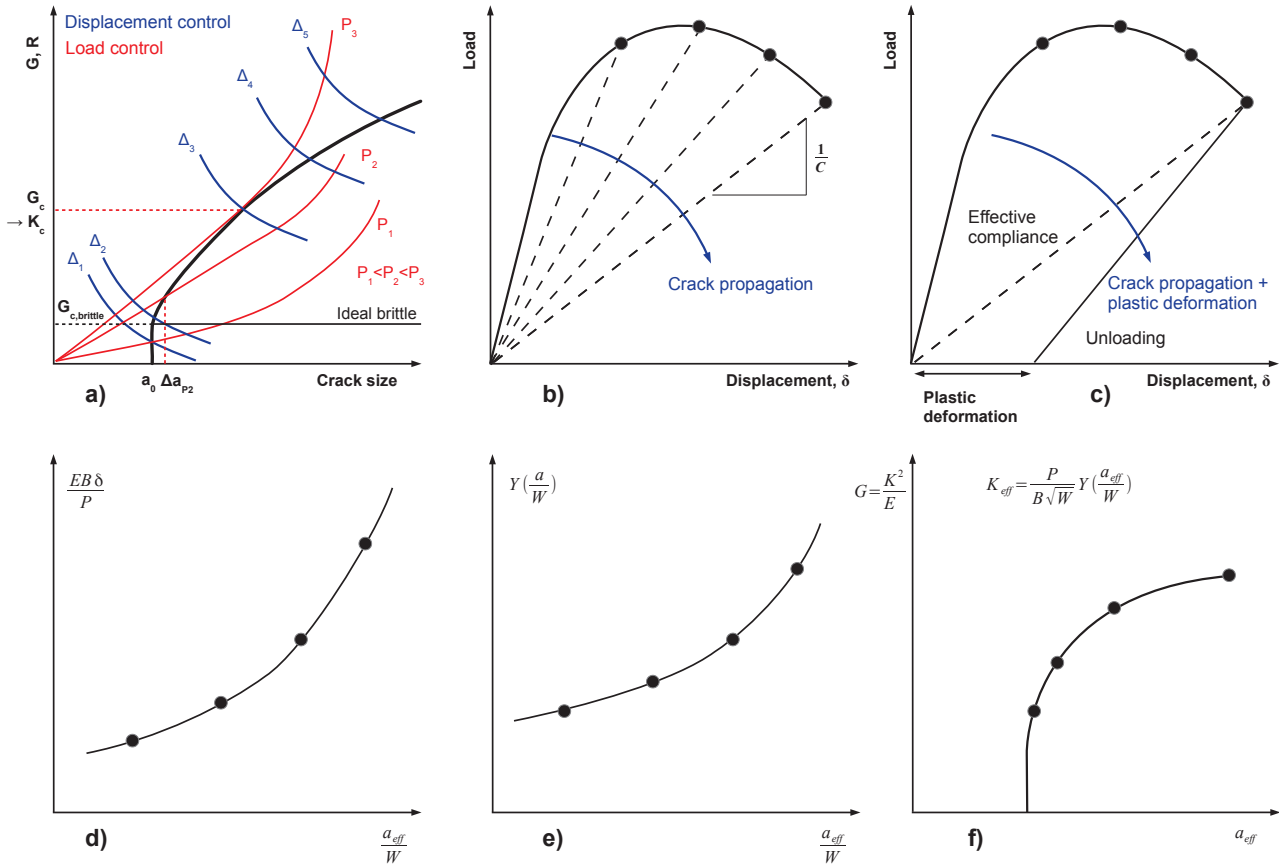


Figure A.5: Procedure for the measurement of a crack resistance curve (synthesized from [22; 30; 36; 37])

The procedure illustrated in A.5 b)-f) draws on several sources [22; 30; 36; 37] with the intention to give a complete picture of the course of action. The key issue in the experiment is the determination of the crack length at each point of the load-displacement curve in Fig. A.5 b). This can be done optically or by the systematic evaluation of the compliance of the sample (P/δ). The ASTM standard [164] or the literature, e.g. [36], provide polynomials for the evaluation of the crack elongation in terms of a/W . Equations (A.6) and (A.7) give the polynomials for CT-specimens and SENB-specimens, respectively. In the case of SENB-specimens, S refers to the load span and V to the crack mouth opening displacement (CMOD). Fig. A.5 d) plots the crack elongation for the case of a CT-specimen which relates the quantity $EB\delta/P$ in Eq. (A.6) with a/W .

$$\frac{a}{W} = 1.00196 - 4.06319U_{LL} + 11.242U_{LL}^2 - 106.043U_{LL}^3 + 464.335U_{LL}^4 - 650.677U_{LL}^5$$

$$U_{LL} = \frac{1}{Z_{LL} + 1}, \quad Z_{LL} = \frac{BE\delta}{P}, \quad \text{CT-specimen} \tag{A.6}$$

$$\frac{a}{W} = 0.999748 - 3.9504U_V + 2.9821U_V^2 - 3.21408U_V^3 + 51.51564U_V^4 - 113.031U_V^5$$

$$U_V = \frac{1}{\sqrt{\frac{4Z_V W}{S} + 1}}, \quad Z_V = \frac{BEV}{P}, \quad \text{SENB-specimen} \quad (\text{A.7})$$

Nowadays, the potential drop method provides another alternative that yields precise and precise values for the crack length and is easy to use [39]. From this point on a stress intensity factor K can be calculated according to Eq. (A.8) (analogously to Eq. (A.1)) provided that the function $f(a/W)$ has been determined. This correction function considers the crack geometry (a/W) and is given in ASTM E399 [35] for various specimen types. Fig. A.5 e) shows a schematic calibration curve obtained from [35] with the crack elongation data shown in Fig. A.5 d). In a final step the K values are transformed to energies according to Eq. (A.5). Since the finally determined energy release rates correspond to points on the sought-after R-curve, a fit through the data points yields the very R-curve as illustrated in Fig. A.5 f).

$$K_{eff} = \frac{P}{B\sqrt{W}} f\left(\frac{a_{eff}}{W}\right) \quad (\text{A.8})$$

The reason why the expressions a_{eff} and K_{eff} have been used in Fig. A.5 d)-f) can be seen in Fig. A.5 c). In case the curvature of the load displacement curve is not only due to stable crack propagation but also a limited amount of plastic deformation (still in line with the requirements of LEFM), the unloading path would not end at the origin. If an effective compliance is used, as indicated in Fig. A.5 c), the procedure for creating the data in Fig. A.5 d) automatically yields the effective crack length according to Eq. (A.9). An alternative approach would be partial unloading during the experiment, which yields the crack length a . This value still has to be corrected by the Irwin approach for crack tip plasticity [36] according to Eq. (A.9), which necessitates an iterative solution due to the interdependence of Eq. (A.8) and Eq. (A.10). In practice, however, the iteration is often neglected [39].

$$a_{eff} = a_0 + \Delta a + r_y \quad (\text{A.9})$$

$$a_{eff} = a + \frac{1}{2\pi} \left(\frac{K}{\sigma_y} \right) \quad (\text{A.10})$$

The use of the energy release rate provides a further advantage for multiaxial loading since it is a scalar quantity (see Eq. (A.11)) and this may be used for the definition of a mode invariant failure criterion. The additivity according to Eq. (A.11) is only valid for self similar crack growth, i.e. planar cracks remain planar, and different methods apply otherwise [36].

$$G = G_I + G_{II} + G_{III} = \frac{K_I^2 + K_{II}^2}{E'} + \frac{K_{III}^2}{2G} \quad (\text{A.11})$$

If the conditions for SSY are not fulfilled, the energy release rate as well as the stress intensity lose their meaning and LEFM is at its end.

Additionally to the first two possibilities for producing a meaningful quantity for the characterization of static crack behavior there is now the **third** possibility to draw on methods of EPFM, like J-integral

measurement, which will be discussed subsequently. The J-integral was introduced by Rice [165] as a mathematical construct of the form of a closed line integral around a crack tip (Eq. (A.12)).

$$J = \int_{\Gamma} \left(w dy - T_i \frac{\partial u_i}{\partial x} \right) ds \quad (\text{A.12})$$

1. w ...strain energy density ($w = \int_0^{\epsilon_{ij}} \sigma_{ij} d\epsilon_{ij}$)
2. T_i ...traction vector ($T_i = \sigma_{ij} n_j$)
3. u_i ...displacement vector
4. ds ...length increment on the contour Γ

He then showed that the value obtained from solving this integral corresponds to the energy release rate in a nonlinear elastic material. It is important to give attention to the term *nonlinear elastic* at this point because this limits the applicability of the model to pure loading without unloading phases. This is due to the fact that a plastic material response is equal to a nonlinear elastic one until unloading occurs. With a mathematically feasible construct considering nonlinear material behavior, the stress and strain fields of elastic-plastic materials can thus be described as long as the loading conditions are monotonic and there is a zone ahead of the crack tip that can be described by J-Integral. Fig. A.6 illustrates the various zones where K and J can be used for different loading conditions. Fig. A.6 a) refers to the case where two stress-strain fields exists ahead of the crack which can be characterized by a single value, i.e. the J-Integral and K, respectively. The corresponding σ - ϵ field between the large deformation zone and the elastic zone in the sample can be approximated by the HRR field (named after Hutchinson, Rice and Rosengren) which holds for small strain conditions ($< \sim 10\%$) and contains J as parameter. The hardening behavior in the HRR is modeled by the Ramberg-Osgood equation, which is also used in other mechanical context as will be discussed in Section 2.6 and the constitutive behavior is based on deformation theory. The In Fig. A.6 a) the plastic zone is still small enough to leave a region where the σ - ϵ field follows the description by LEFM and K as fitting parameter. This zone is situated between the plastic zone and the elastic region where Eq. (2.7) is no longer valid without the higher order terms, i.e there is still a stress field following the description by the singular term with K as parameter. Fig. A.6 b) shows the case where EPFM is required since the plastic zone has consumed the K-dominated region of the stress field, leaving only the J-dominated region. In the case of Fig. A.6 c) even the single parameter description by J is not valid anymore since the zone obeying large strain theory becomes too big. In this extreme case, two parameter approaches like the J-Q theory are necessary, as discussed e.g. in [9].

For the experimental measurement of J it is useful to split J into an elastic and a plastic [12] part according to Eq. (A.13).

$$J = J_{el} + J_{pl} = \frac{K^2(1 - \nu)}{E} + \frac{\eta A_{pl}}{Bb}, \quad \eta = 2.0 \quad \text{for SENB}, \eta = 2 + \frac{0.522b_0}{W} \quad \text{for CT} \quad (\text{A.13})$$

The elastic part is determined from the stress intensity factor obtained from Eq. (A.1) and corresponds to the elastic part A_{el} of the area under the load displacement curve. The term for the plastic part involves the area below the load-displacement curve ($A_{pl} = A_{tot} - A_{el}$), the sample thickness (B) and the initial ligament length (b). In order to determine a critical value for J a whole series of J-values must be obtained and represented as a curve. These values can either be determined by a multiple specimen or a single specimen technique, as illustrated in Eq. (A.13). For the first option several precracked samples are subjected to different displacements and unloaded. In a second step the amount of stable crack propagation

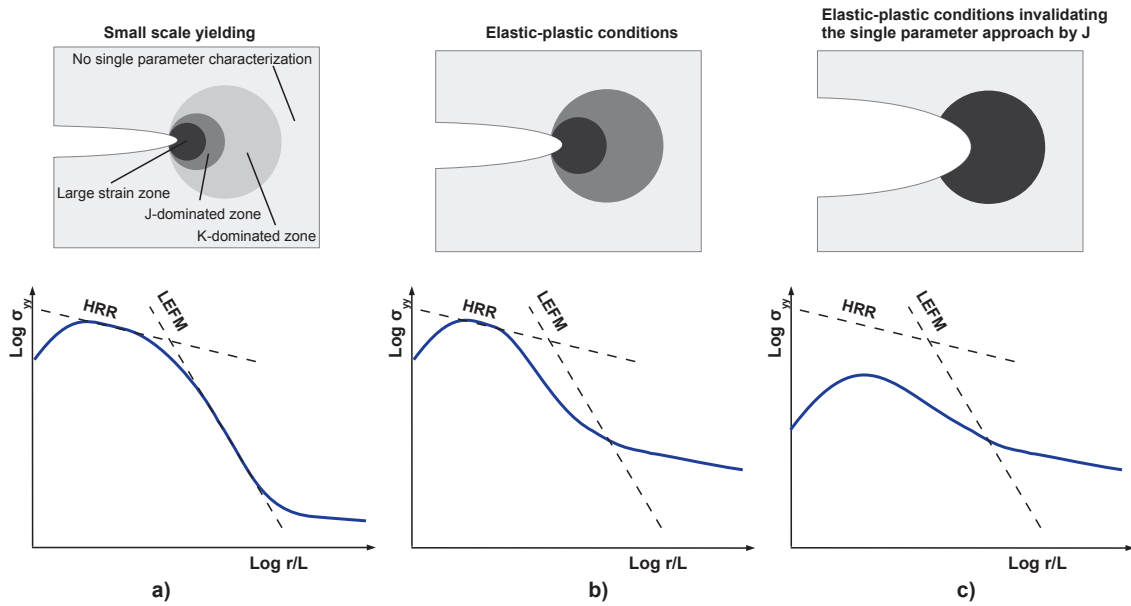


Figure A.6: Stress fields ahead of the crack for various loading conditions [36]

has to be identified. Therefore the crack propagation zones has to be marked before the sample is broken to measure Δa . This can be done by heat tinting or by the application of a fatigue load. In the former case the crack propagation zone is clearly distinguishable as in Fig. A.7 b), in the latter case the crack propagation zone is situated between two fatigue crack propagation zones which can be distinguished from one another in the microscope. From the area indicated in Fig. A.7 a) the J-integral can be computed and correlated with the corresponding crack length. Fig. A.7 c) shows the single specimen procedure, where the sample is systematically partially unloaded by 10% of the current load [37]. The corresponding crack lengths can be obtained from Equations (A.6) and (A.7), which have already been mentioned in the context of LEFM crack resistance curves. Alternatively the potential drop method could be used. Fig. A.7 d) plots the evaluation of these procedures. The first step for the determination the provisional value J_Q is to draw an exclusion line at 0.15 and 1.5 mm, respectively. Both lines have a slope of $\sigma_{flow} = (\sigma_y + \sigma_{TS})/2$, which is an approximation for crack blunting, when drawn through the origin. Next, all J values situated within the exclusion lines are fitted with expression A.14 and last, J_Q is determined from the intersection of Eq. (A.14) and an 0.2 mm offset line.

$$J = C_1(\Delta a)^{C_2} \tag{A.14}$$

If the criterion defined by Eq. (A.15) is satisfied J_Q is a valid value for J_{IC} . Furthermore, the hardening of the material needs to be sufficient for J to be controlling the state at the crack tip [106]. With decreasing hardening the J controlled region gets smaller and disappears for an ideal-plastic material.

$$B, b \geq \frac{25J_Q}{\sigma_y} \tag{A.15}$$

Even if these criteria are fulfilled some difficulties still remain, as outlined in [166]:

1. The J-integral is based on deformation theory, i.e. the plastic strain ϵ_{pl} is modeled as a function of the equivalent stress σ_{eq} like it is the case for nonlinear elastic materials. In other words, elastic-plastic materials are treated as non-linear elastic. Hence, the meaning of the J-integral approach suffers

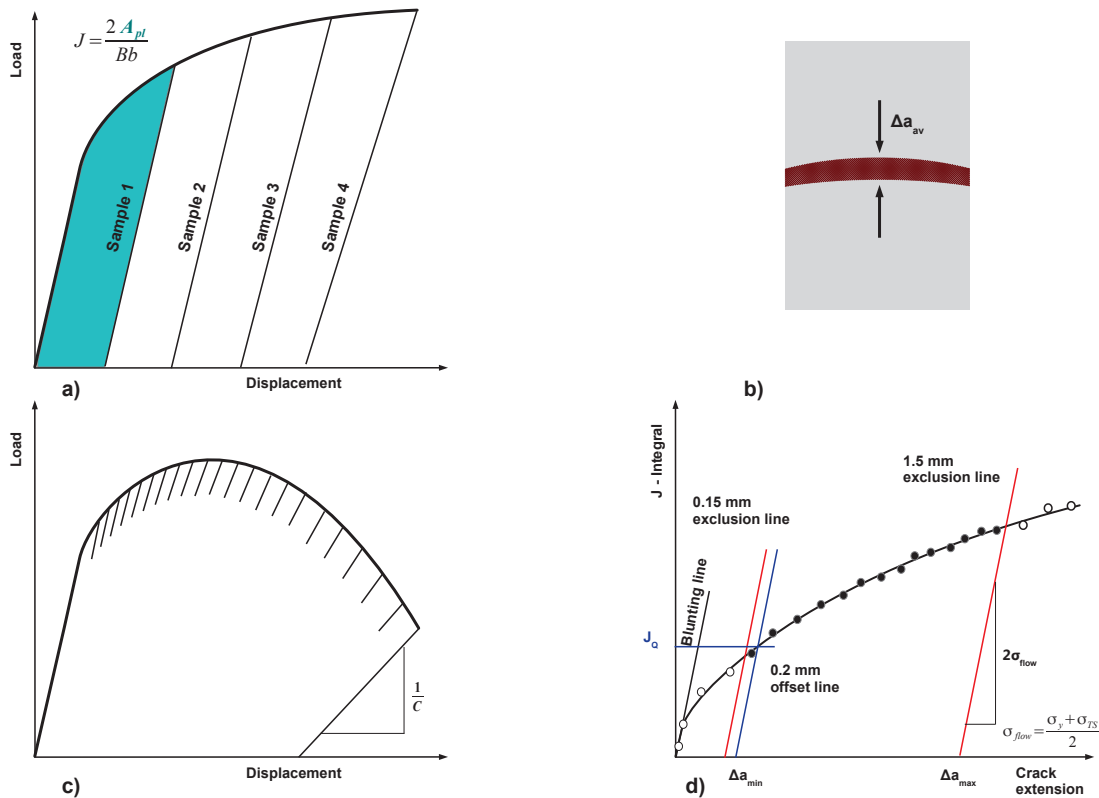


Figure A.7: Testing procedure the determination of J_{IC} . a) and b) multiple specimen technique, c) single specimen technique, d) Evaluation of results [37; 38]

when unloading occurs, e.g. due to crack extension, void formation or unloading of the component.

2. The classic J-integral characterizes the crack driving force for non-linear elastic and not elastic-plastic materials. J can still be used as distinctive parameter for the σ - ϵ field at the tip of a stationary crack in an elastic-plastic material. With increasing crack propagation and and in the case of cyclic loading the physical meaning of J diminishes.

Kolednik et al. further discuss the concept of configurational forces that allows the definition on an elastic-plastic J-integral J^{ep} based on incremental plasticity where the plastic strain increment $d\epsilon_{pl}$ is a function of the equivalent stress σ_{eq} . This description is appropriate for elastic-plastic materials. The physical restrictions of the classical J due to its constitutive behavior based on deformation plasticity are thus overcome and J^{ep} can be applied in the case of 1) and 2). Since J^{ep} is path dependent they further expand on the meaning of the elastic-plastic J evaluated at the crack tip J_{tip}^{ep} , a contour around the active plastic zone J_{PZ}^{ep} and the far field value J_{far}^{ep} .

- J_{far}^{ep} ...driving force inserted into the sample by external loading
- J_{tip}^{ep} ...driving force for translational movement of the crack tip. Since its value is zero an apparent oxymoron occurs in view of crack propagation. This is accounted for by the fact that an individual crack driving force is not meaningful at the crack tip, which can only propagate in conjunction with the surrounding process zone and plastic zone.
- J_{PZ}^{ep} ...the elastic-plastic J-integral evaluated around the active plastic zone is recommended as a critical driving force parameter for the evaluation of crack extension and fracture.

The comparison of Eq. (A.15) and Eq. (A.2) points out that the necessary sample size for a valid J_{IC} is about 20 times less than for fracture toughness measurement [37]. It is also important to notice that that K_{IC} corresponds to 2% real or apparent crack extension (blunting) while J_{IC} corresponds to 0.2 mm crack propagation. Both quantities are thus technical measures but they do not pinpoint exactly the onset of crack propagation. If the multiple specimen technique is used for J_{IC} determination the initiation values J_i can be determined as well very precisely [39]. The single specimen technique which is often used in combination with the potential drop method, however, makes it difficult to yield precise data on the crack propagation when the crack is still very small. This is also the reason why the blunting line is used in the region where it is not clear whether blunting or crack extension is present. An equivalent procedure for defining an R-curve with J instead of the energy release rate G exists and is summarized in the form of Eq. (A.16):

$$R = \frac{(W - a)}{\eta} \frac{dJ_{pl}^{exp}}{d(\Delta a)} + \frac{\gamma}{\eta} J_{pl}^{exp} \tag{A.16}$$

The crack growth resistance is thus proportional to the slope of the $J - \Delta a$ curve and not to the curve

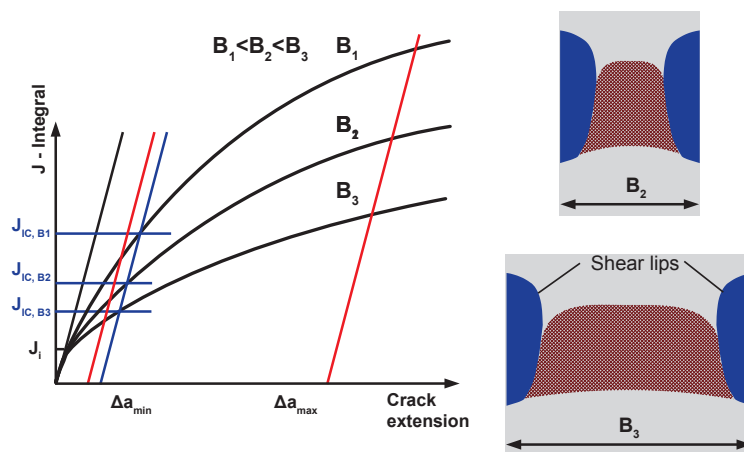


Figure A.8: Illustration of the possible influence of the sample thickness on J_{IC} [39]

itself. The procedure is further described in the literature (i.e. [36; 166]) and in standards [38]. It should be noticed, however, that in contrast to the R-curve in LEFM the R-curve in EPFM is strongly dependent on the geometry. Combined with the problem of the classic J losing its validity under unloading conditions and thus with crack extension, the use of R-curves in EPFM for the characterization of crack growth is tedious. In addition, the definition of the point of final unstable failure is also more demanding than in the case of LEFM as discussed in [166]. The determined value J_{IC} is a technical criterion for the onset of stable crack propagation and this criterion may be used as safety limit in the design process of components. A characterization of the stable propagation by a J-R curve according to [38] would thus be superfluous. The J-integral provides a further application in LEFM. Whenever the requirements on the sample thickness Eq. (A.2) cannot be met, J_{IC} or better J_i can be determined from a much smaller sample and transformed to a K_{JC} value according to Eq. (A.17). If J_i cannot be properly determined and J_{IC} is used instead, the sample thickness should not be chosen very small, however, because this may yield non-conservative

values for the fracture toughness as indicated in Fig. A.8.

$$J_{LEFM} = G = \frac{K^2}{E'} \quad (\text{A.17})$$

The greater contribution of the shear lips in thinner samples leads to a higher crack growth resistance corresponding to steeper curves. Since J_{IC} is determined from the 0.2 offset line, the corresponding values increase for thinner samples. J_{IC} characterizes the onset of stable crack propagation and for this reason a small difference in J_{IC} is not dangerous. If the value is used, however, for the computation of the fracture toughness K_{JC} , which characterizes unstable failure, non-conservative values may be dangerous since the computed K_{JC} might be too high.

A.3 Tensor notation

Table A.1: Types of tensors [18]

| Tensors | | |
|--------------------------------|--|---------------|
| | symbolic | index |
| 0 th -rank (scalar) | X | X |
| 1 st -rank (vector) | $\underline{\mathbf{X}}$ | X_i |
| 2 nd -rank | $\underline{\underline{\mathbf{X}}}$ | X_{ij} |
| 3 rd -rank | $\underline{\underline{\underline{\mathbf{X}}}}$ | X_{ijk} |
| 4 th -rank | $\underline{\underline{\underline{\underline{\mathbf{X}}}}}$ | X_{ijkl} |
| Unit tensor | $\underline{\underline{\underline{\underline{\mathbf{I}}}}}$ | δ_{ij} |

Table A.2: Some tensor operations [18]

| Contracted product | | Dyadic product | |
|--|----------------------------|--|----------------------------|
| symbolic | index | symbolic | index |
| $X = \underline{\mathbf{a}} \cdot \underline{\mathbf{b}}$ | $X = a_i b_i$ | $\underline{\underline{\mathbf{X}}} = \underline{\mathbf{a}} \otimes \underline{\mathbf{b}}$ | $x_{ij} = a_i b_j$ |
| $\underline{\mathbf{X}} = \underline{\mathbf{a}} \cdot \underline{\underline{\mathbf{b}}}$ | $X_i = a_{ij} b_j$ | $\underline{\underline{\underline{\mathbf{X}}}} = \underline{\mathbf{a}} \otimes \underline{\underline{\mathbf{b}}}$ | $x_{ijkl} = a_{ij} b_{kl}$ |
| $\underline{\underline{\mathbf{X}}} = \underline{\underline{\mathbf{a}}} \cdot \underline{\underline{\underline{\mathbf{b}}}}$ | $X_{ij} = a_{ik} b_{kj}$ | $\underline{\underline{\underline{\underline{\mathbf{X}}}}} = \underline{\underline{\mathbf{a}}} \otimes \underline{\underline{\underline{\mathbf{b}}}}$ | $x_{ijkl} = a_{ik} b_{jl}$ |
| $X = \underline{\underline{\mathbf{a}}} : \underline{\underline{\underline{\mathbf{b}}}}$ | $X_{ij} = a_{ij} b_{ij}$ | $\underline{\underline{\underline{\underline{\mathbf{X}}}}} = \underline{\underline{\underline{\mathbf{a}}}} \otimes \underline{\underline{\underline{\mathbf{b}}}}$ | $x_{ijkl} = a_{il} b_{kj}$ |
| $\underline{\underline{\mathbf{X}}} = \underline{\underline{\underline{\mathbf{a}}}} : \underline{\underline{\underline{\underline{\mathbf{b}}}}}$ | $X_{ij} = a_{ijkl} b_{kl}$ | | |
| $X = \underline{\underline{\underline{\underline{\mathbf{a}}}}} :: \underline{\underline{\underline{\underline{\mathbf{b}}}}}$ | $X = a_{ijkl} b_{ijkl}$ | | |

Table A.3: Some general tensor calculus [48]

| Selected tensor calculus | | |
|--------------------------|--|--------------------|
| | symbolic | index |
| Symmetric tensor | $\underline{\underline{\mathbf{X}}} = \underline{\underline{\mathbf{X}}}^T$ | $X_{ij} = X_{ji}$ |
| Antisymmetric tensor | $\underline{\underline{\mathbf{X}}} = -\underline{\underline{\mathbf{X}}}^T$ | $X_{ij} = -X_{ji}$ |

| | | |
|---|--|--|
| Separation of a tensor in its symmetric and skew-symmetric part | $\underline{\mathbf{X}}^{sym} = \frac{1}{2} (\underline{\mathbf{X}} + \underline{\mathbf{X}}^T)$ $\underline{\mathbf{X}}^{asym} = \frac{1}{2} (\underline{\mathbf{X}} - \underline{\mathbf{X}}^T)$ | $X_{ij}^{sym} = \frac{1}{2} (X_{ij} + X_{ji})$ $X_{ij}^{asym} = \frac{1}{2} (X_{ij} - X_{ji})$ |
|---|--|--|

A.4 Thermodynamic potential

The constitutive equations for plasticity and viscoplasticity can be discussed within a thermodynamical framework. As outlined in [17; 114], the thermomechanical formalism in the formulation of constitutive equations is based on the assumption of two potentials. The first one, the thermomechanical potential is used to describe reversible processes:

$$\Psi = \Psi(\underline{\epsilon}_{el}, T, \alpha_i) \quad \text{Thermodynamic potential, as function of the observable} \quad (\text{A.18})$$

$$\text{variables } (\underline{\epsilon}_{el}, T) \text{ and internal variables } (\alpha_i) \quad (\text{A.19})$$

The partial derivation yields $\dot{\Psi}$, which can be inserted into the Clausius-Duhem inequality:

$$\dot{\Psi} = \frac{\partial \Psi}{\partial \underline{\epsilon}_{el}} : \dot{\underline{\epsilon}}_{el} + \frac{\partial \Psi}{\partial T} : \dot{T} + \frac{\partial \Psi}{\partial \alpha_i} : \dot{\alpha}_i \quad (\text{A.20})$$

$$\left(\underline{\boldsymbol{\sigma}} - \rho \frac{\partial \Psi}{\partial \underline{\epsilon}_{el}} \right) \dot{\underline{\epsilon}}_{el} + \underline{\boldsymbol{\sigma}} : \dot{\underline{\epsilon}}_{pl} - \rho \left(s + \frac{\partial \Psi}{\partial T} \right) \dot{T} - \rho \frac{\partial \Psi}{\partial \alpha_i} : \dot{\alpha}_i - \frac{\mathbf{q}}{T} \underline{\mathbf{grad}}(T) \geq 0 \quad (\text{A.21})$$

From the expression above the state laws, or laws of thermoelasticity can be derived. These laws connect the state variables α_s (α_i and α_j) with the associated variables ($\underline{\boldsymbol{\sigma}}$, s , and α_a). α_a refers to the associated variables for the internal variables α_i . The associated variables represent thermomechanical forces.

$$\text{State laws} \left\{ \begin{array}{l} \underline{\boldsymbol{\sigma}} = \rho \frac{\partial \Psi}{\partial \underline{\epsilon}_{el}} = \rho \frac{\partial \Psi}{\partial \underline{\epsilon}} = -\rho \frac{\partial \Psi}{\partial \underline{\epsilon}_{pl}} \\ s = -\frac{\partial \Psi}{\partial T} \\ \alpha_a = \rho \left(\frac{\partial \Psi}{\partial \alpha_i} \right) \end{array} \right.$$

The first equation is the generalized form of Hooke's law. $\underline{\boldsymbol{\sigma}}$ and s are thermodynamic forces associated with $\underline{\epsilon}_{el}$ and T , respectively [114]. Similarly, α_a are the thermodynamic forces associated with α_i .

A.5 Dissipation potential

The correlation between the observable state variables and their associated variables has been established based on the thermodynamic potential. For the internal state variables, associated variables have been defined as well. Nevertheless, irreversible processes linked to dissipation phenomena have not yet been taken into account. In order to describe dissipation, which correlates mostly with the evolution of the

internal variables, the concept of the dissipation potential is introduced. In a first step, it is shown that the dissipation must be positive. This is established by introducing the state laws into the Clausius-Duhem inequality:

$$\Psi_2 = \underbrace{\underline{\sigma} : \dot{\underline{\epsilon}}_{pl} - \alpha_a \dot{\alpha}_i}_{\text{intrinsic dissipation}} - \underbrace{\frac{\mathbf{q}}{T} \underline{\mathbf{grad}}(T)}_{\text{thermal dissipation}} \geq 0 \quad (\text{A.22})$$

The intrinsic dissipation is also called mechanical dissipation and it is due to plastic dissipation and the dissipation caused by the change of other internal variables. The thermal dissipation is caused by heat conduction. Each of the three terms in Eq. (A.22) consist of a flux variable and a dual variable.

In a next step, the existence of a dissipation potential Φ is assumed. This potential can either be defined as a function of the dual variables $\Phi_1(\underline{\sigma}, \alpha_a, \underline{\mathbf{grad}}(T))$ or the flux variables $(\Phi_2(\dot{\underline{\epsilon}}_{pl}, \alpha_i, -\frac{\mathbf{q}}{T}))$. The transformation from the space of flux variables to the space of dual variables is effected by the Legendre-Fenchel transformation, as shown in [17], and the resulting functions for Φ_1 and Φ_2 are called dual functions. For the potential to fulfill the second principle of thermodynamics, Φ must be a nonnegative function that is convex and zero at the origin. The complementary laws for the evolution of the internal variables obtained from the thermodynamic potential can then be defined by the application of the normality rule. This way the second principle is satisfied. The dual variables are thus the components of the gradient of the dissipation potential, $\underline{\mathbf{grad}}(\Phi_2)$, in the space of the flux variables. For the corresponding potential defined in the space of the dual variables, the flux variables are the components of $\underline{\mathbf{grad}}(\Phi_1)$. The latter option is more convenient and generally used for the definition of the complementary laws.

$$\text{Complementary laws} \left\{ \begin{array}{l} \overbrace{\dot{\underline{\epsilon}}_{pl} = \frac{\partial \Phi_1}{\partial \underline{\sigma}}}^{\Phi_2} \\ \overbrace{-\dot{\alpha}_i = \frac{\partial \Phi_1}{\partial \alpha_a}}^{\Phi_2} \\ \overbrace{-\frac{\mathbf{q}}{T} = \frac{\partial \Phi_1}{\partial \underline{\mathbf{grad}}(T)}}^{\Phi_2} \end{array} \quad \begin{array}{l} \overbrace{\underline{\sigma} = \frac{\partial \Phi_2}{\partial \dot{\underline{\epsilon}}_{pl}}}^{\Phi_1} \\ \overbrace{\alpha_a = -\frac{\partial \Phi_2}{\partial \dot{\alpha}_i}}^{\Phi_1} \\ \overbrace{\underline{\mathbf{grad}}(T) = -\frac{\partial \Phi_2}{\partial \frac{\mathbf{q}}{T}}}^{\Phi_1} \end{array} \right.$$

The key issue in the modeling of material behavior based on thermodynamics is to formulate Ψ and Φ and to identify the parameters in these expressions. Φ cannot be measured directly but the flux variables and dual variables can be determined by proper experiments, i.e. the complementary laws can be directly determined. Φ is still used, however, for formalism and the definition of analytical expressions. The dissipation potential is often written in a generalized form, including the state variables: $\Phi(\underline{\sigma}, \alpha_a, \underline{\mathbf{grad}}(T); \underline{\epsilon}_{el}, T, \alpha_i)$. It should be noticed that the state variables $\underline{\epsilon}$ and $\underline{\epsilon}_{pl}$ do not appear in any expression. This is due to the fact that the strains are generally decomposed into $\underline{\epsilon}_{el} = \underline{\epsilon} - \underline{\epsilon}_{pl}$ and thus only one of these variable is required. $\underline{\epsilon}_{el}$ also includes the thermal strain $\underline{\epsilon}_{th}$. Beside other simplifications of the dissipation potential, a decoupling of intrinsic and thermal dissipation can be done:

$$\Phi_1 = \Phi_{1a}(\underline{\sigma}, \alpha_a) + \Phi_{1b}\left(-\frac{\mathbf{q}}{T}\right) \quad (\text{A.23})$$

Both parts must satisfy the second principle, which can be shown using the Clausius-Duhem inequality Eq. (2.44). The function $\Phi_{1b}\left(-\frac{\mathbf{q}}{T}\right)$ leads to the definition of Fourier's law of heat conduction. $\Phi_{1a}(\underline{\sigma}, \alpha_a)$

on the other hand is important in view of plasticity. In the case of rate-independent plasticity, the function $\Phi_{2a}(\dot{\epsilon}_{pl}, \alpha_i)$ is positive, homogeneous and of first order. The dual function $\Phi_{1a}(\sigma, \alpha_a)$, however is non-differentiable. Based on the formulation of a subdifferential and the assumption that $\dot{\epsilon}_{pl}$ is part of that subdifferential, the normal dissipative laws can be redefined as follows:

$$\text{Complementary laws for rate-independent plasticity} \left\{ \begin{array}{ll} \overbrace{\dot{\epsilon}_{pl} = \dot{\lambda} \frac{\partial F}{\partial \sigma}}^{\text{non-associated}} & \overbrace{\dot{\epsilon}_{pl} = \dot{\lambda} \frac{\partial f}{\partial \sigma}}^{\text{associated}} \\ \overbrace{-\dot{\alpha}_i = \dot{\lambda} \frac{\partial F}{\partial \alpha_a}} & \overbrace{-\dot{\alpha}_i = \dot{\lambda} \frac{\partial f}{\partial \alpha_a}} \end{array} \right.$$

$f(\sigma, \alpha_a)$ is a potential and can be used as a criterion whether $\dot{\epsilon}_{pl}$ belongs to the subdifferential or not. The multiplier $\dot{\lambda}$ can be determined from the consistency condition $\dot{f} = 0$. F is the corresponding function for the case of non-associated flow rules. In this case three potentials are necessary for the representation of plasticity. The thermodynamic potential Ψ , the yield surface (or plastic potential) f and the potential surface F . For associated plasticity F coincides with f .

Table A.4 summarizes the variables mentioned in the last sections.

Table A.4: Overview of variables in the thermodynamic framework of constitutive equations [17]

| Thermodynamic variables | | | Dissipation variables | |
|-------------------------|--------------------|-----------------------|-------------------------|----------------------|
| State variables | | | Flux variables | Dual variables |
| Observable variables | Internal variables | Associated variables | | |
| $\underline{\epsilon}$ | | $\underline{\sigma}$ | $\dot{\epsilon}_{pl}$ | $\underline{\sigma}$ |
| T | | s | $-\dot{\alpha}_i$ | α_a |
| | ϵ_{el} | $\underline{\sigma}$ | $-\frac{\mathbf{q}}{T}$ | $\text{grad}(T)$ |
| | ϵ_{pl} | $-\underline{\sigma}$ | | |
| | α_i | α_a | | |

A.6 Tertiary creep

The tertiary region of a creep experiment exhibits softening effects due to the evolution of damage that has been initiated in the primary or secondary stage. Creep damage manifests itself as the formation of pores. During the first two stages they are too small to have an impact on the global behavior but this changes in the third stage. The pores grow and coalesce thus affecting the effective cross section that bears the external load. The third stage can be taken into account in creep simulations by empirical laws that allow to fit the whole creep curve by an appropriate choice of parameters. One of these laws would

draw on the model introduced by Graham and Walles, i.e. the sum of individual time hardening terms:

$$\epsilon_{cr} = \sum_{i=1}^n C_i \sigma^{n_i} t^{m_i} \quad (\text{A.24})$$

According to [43] four terms are sufficient to describe all three stages in a creep curve:

$$\epsilon_{cr} = C_1 \sigma^{n_1} t^{\frac{1}{3}} + C_2 \sigma^{n_2} t + (C_3 \sigma^{n_3} + C_4 \sigma^{n_4}) t^3 \quad (\text{A.25})$$

In a similar fashion it should be possible to use strain hardening terms. In both cases, however, the creep strain is a function of the time or the accumulated creep strain. The problem with these approaches is the negligence of the stress state, which could change the evolution of the creep strain or creep strain rate for different load situations and load histories. A more general description of tertiary creep can be obtained by the implementation of damage mechanical laws and damage parameters to take into account increased creep rates as a function of the current damage. One example would be the isotropic damage parameter according to Robotnov. As outlined in [5; 104], the equivalent stress is updated based on the current value of the damage ($0 \leq \omega \leq 1$):

$$\sigma_{eq}^* = \frac{\sigma_{eq}}{1 - \omega} \quad (\text{A.26})$$

The challenge is to find a proper evolution equation for the damage ($\dot{\omega}$). The evolution equation is a function of a multitude of parameters $\dot{\omega}(\sigma_{eq}, T, \omega, \dots)$ but often a simplified law is used:

$$\dot{\omega} = A \left(\frac{\sigma_{eq}}{1 - \omega} \right)^B \quad (\text{A.27})$$

A and B are material parameters.



Appendix B

Source codes

Source Code B.1: Creep subroutine for Abaqus - Strain hardening law with two terms implemented in Fortran.

```
0  C23456789012345678901234567890123456789012345678901234567890123456789012
  SUBROUTINE CREEP (DECRA, DESWA, STATEV, SERD, EC, ESW, P, QTILD,
  1  TEMP, DTEMP, PREDEF, DPRED, TIME, DTIME, CMNAME, LEXIMP, LEND,
  2  COORDS, NSTATV, NOEL, NPT, LAYER, KSPT, KSTEP, KINC)
5
  C
  INCLUDE 'ABA_PARAM.INC'
  C
  CHARACTER*80 CMNAME
  C
  DIMENSION DECRA (5), DESWA (5), STATEV (*), PREDEF (*), DPRED (*),
10  1  TIME (3), COORDS (*), EC (2), ESW (2)
  C
  C DEFINE CONSTANTS
  C
  REAL A1, n1, m1
15  REAL A2, n2, m2
  REAL e_cr
  C First term - Primary creep and transition to secondary creep
  A1=1.021E-22
  m1=-0.6
20  n1=9.597
  C Second term - If m is set to 0, the term describes secondary creep according to Norton's law
  A2=2.5E-22
  m2=0.0
25  n2=8.8
  C
  LEND=0...beginning of increment, 1... end of increment
  IF (LEND.EQ.0) THEN
  e_cr=EC(1)
  ELSE
30  e_cr=EC(2)
  END IF
  C
  IF (KSTEP .EQ. 1 .AND. KINC .EQ. 1) THEN
  DECRA(1) = 0.00001
  ELSE
35  C In the case of metal creep QTILD corresponds to the equivalent stress
  DECRA(1) = (A1*QTILD**n1*((m1+1)*e_cr)**m1)**(1/(m1+1))*DTIME+
  &(A2*QTILD**n2*((m2+1)*e_cr)**m2)**(1/(m2+1))*DTIME
  C For implicit integration the derivative of the creep law is required (de/ds)
40  IF (LEXIMP.EQ.1) THEN
  DECRA(5) = ((A1*QTILD**n1*((m1+1)*e_cr)**m1)**(1/(m1+1))*
  &n1*DTIME)/((m1+1)*QTILD)+((A2*QTILD**n2*((m2+1)*e_cr)**m2)**
  &(1/(m2+1))*n2*DTIME)/((m2+1)*QTILD)
  END IF
45  END IF
  C
  RETURN
  END
50
  C For the case debugging is necessary: Write data to file
  C OPEN (UNIT=100, FILE=
  C  &'Path/Filename', STATUS='UNKNOWN', ACCESS='APPEND')
  C WRITE (100,1000) KSTEP, KINC, DECRA(1)
  C CLOSE (100)
55  C 1000 FORMAT (I5, I5, F15.100)
```

Source Code B.2: DFLUX subroutine for Abaqus - Parameterized uniform heat flux.

```
0  CCCCCCCCCCCCCCCCCCCCCCCCCCCCCCCCCCCCCCCCCCCCCCCCCCCCCCCCCCCCCCCCCCCCCCCCC
  C 1) Flux(1) -> Time dependent heat flux imposed at the friction surface
```

APPENDIX B

```

C   of the brake disk.
C   The heat flux can be imposed as triangular or double triangular
C   distribution.
5  C   All variables marked with XXX are inserted by the main python
C   script
CCCCCCCCCCCCCCCCCCCCCCCCCCCCCCCCCCCCCCCCCCCCCCCCCCCCCCCCCCCCCCCC
C2345678901234567890123456789012345678901234567890123456789012
10 SUBROUTINE DFLUX (FLUX,SOL,KSTEP,KINC,TIME,NOEL,NPT,COORDS,
1  JLTYP,TEMP,PRESS,SNAME)
C
C   INCLUDE 'ABA_PARAM.INC'
C
15 DIMENSION FLUX(2), TIME(2), COORDS(3)
CHARACTER*80 SNAME
INTEGER*4 BCycle,nStep,modulus,firstCall,FirstRun,stages,numRep
INTEGER*4 CycleSteps
REAL tFill, tTrans,tTemp, tend, Pmax
20 REAL cStepTime,cTottime,TimeVarDflux
REAL arrScenarios(1,2)
REAL charScenarios(1,6)
COMMON BCycle,nStep,modulus,firstCall,FirstRun,stages,tFill,
&tTrans,tTemp,tend,Pmax,TimeVarDflux,arrScenarios,
25 &charScenarios,numRep
cStepTime=TIME(1)
cTottime=TIME(2)
C   Some parts of the program are executed only once. This is done
C   during the first call of the subroutine.
30 IF (firstCall .NE. 1) THEN
BCycle=1
numRep=0
firstCall=1
END IF
35
C   Number of brake scenarios
arrScenarios(1,1)=1
C   Number of brake cycles
arrScenarios(1,2)=10
40
CycleSteps=3
C   modulus is determined once per step
IF (nStep .NE. KSTEP) THEN
45 nStep=KSTEP
modulus=mod(KSTEP,CycleSteps)
IF (modulus .EQ. 1) THEN
numRep=numRep+1
END IF
50
IF (numRep .EQ. arrScenarios(BCycle,2) +1) THEN
BCycle=BCycle+1
numRep=0
END IF
55
charScenarios(1,1)=1.0
charScenarios(1,2)=21.2232670086
charScenarios(1,3)=85.4440144467
charScenarios(1,4)=63.69
charScenarios(1,5)=1814.0480435
60 charScenarios(1,6)=2
tFill=charScenarios(BCycle,1)
tTrans=charScenarios(BCycle,2)
65 tTemp=charScenarios(BCycle,3)
tend=charScenarios(BCycle,4)
Pmax=charScenarios(BCycle,5)
stages=charScenarios(BCycle,6)
END IF
70
IF (TimeVarDflux .NE. cStepTime) THEN
FirstRun=0
TimeVarDflux=cStepTime
ELSE
75 FirstRun=1
END IF
C   Time(1)...Current value of step time => continuous
C   Time(2)...Current value of total time => discrete
80 IF (stages .EQ. 2.0) THEN
IF (TIME(1) .LE. tFill) THEN
FLUX(1)=Pmax/tFill*TIME(1)
Else IF (TIME(1) .GT. tFill .AND. TIME(1) .LE. tTrans) THEN
85 FLUX(1)=Pmax-Pmax/(tTemp-tFill)*(TIME(1)-tFill)
ELSE IF (TIME(1) .GT. tTrans .AND. TIME(1) .LE. tend) THEN
FLUX(1)=Pmax-Pmax/(tend-tTrans)*(TIME(1)-tTrans)
EndIF
ENDIF
90
IF (stages .EQ. 1.0) THEN
IF (TIME(1) .LE. tFill) THEN
FLUX(1)=Pmax/tFill*TIME(1)
ELSE
95 FLUX(1)=Pmax-Pmax/(tend-tFill)*(TIME(1)-tFill)
EndIF
ENDIF

```

```

RETURN
END

```

Source Code B.3: DISP subroutine for Abaqus - Thermal image mapping for non-uniform loading.

```

0  C-----
C   Thermal image mapping
C   U -> Temperature at each node of the model.
C-----
5  C23456789012345678901234567890123456789012345678901234567890123456789012
   SUBROUTINE DISP (U, KSTEP, KING, TIME, NODE, NOEL, JDOF, COORDS)
C
C   INCLUDE 'ABA_PARAM.INC'
C
10  DIMENSION TIME(2), COORDS(3)
C
C   Insert dimensions of matrix!!!! -> lengthX, lengthY
C   INTEGER*4 i1,i2,nFrame,firstCall1,firstCall2,nStep,nMap
C   INTEGER*4 lengthX, lengthY, pixelY
C   INTEGER*4 IndX1Coord,IndX2Coord
15  INTEGER*4 IndY11Coord,IndY12Coord,IndY21Coord,IndY22Coord
   REAL x1Coord,x2Coord
   REAL y11Coord,y12Coord,y21Coord,y22Coord
   REAL xCoord,yCoord,zCoord,Temp1,Temp2, TSurrounding
20  REAL T11t1,T12t1,T21t1,T22t1
   REAL T11t2,T12t2,T21t2,T22t2
   PARAMETER(lengthX=322)
   PARAMETER(lengthY=69601)
   PARAMETER(lengthZ=10)
   PARAMETER(pixelY=240)
25  PARAMETER(TSurrounding=62.0)
   REAL dataArray,mapDims
   DIMENSION dataArray(1:lengthY,1:lengthX,1:lengthZ)
   DIMENSION mapDims(1:lengthZ,1:2)
C For debugging - Start
30  INTEGER*4 nStep2,nStep3
   COMMON nStep2,nStep3
C For debugging - End

C The length of the array has to match or to exceed the number of
C lines in the data file
C The length of the TMF test has to be set in the corresponding
C Abaqus step
40  REAL InterpFuncLinear, InterpFuncBilinear
   REAL cStepTime,cTotTime, cTEMP, FirstRun, TimeVarDisp
   REAL subTHE, u_Test, ktm
   COMMON /cDISP/ dataArray,mapDims, FirstRun,
   & TimeVarDisp, cStepTime,cTotTime, nFrame,firstCall1,firstCall2
   COMMON /cDFLUX/ cTEMP,nStep,nMap,modulus

45  cStepTime=TIME(1)
   cTottime=TIME(2)

C Some parts of the program are executed only once. This is done
C during the first call of the subroutine.
50  IF (firstCall1 .NE. 1 ) THEN
   nFrame=1
   firstCall1=1
C nMap is initialized with 0. It is updated at the beginning of each new step
55  nMap=0
   END IF

C Some parts of the program are executed only once per increment.
C This is done during the first call of the subroutine
C in the current increment.
60  IF (TimeVarDisp .NE. cStepTime) THEN
   FirstRun=0
   TimeVarDisp=cStepTime
   ELSE
65  FirstRun=1
   END IF

C modulus is determined once per step
70  IF (nStep .NE. KSTEP ) THEN
   nStep=KSTEP
   modulus=mod(KSTEP,3)
   IF (modulus .EQ. 1 ) THEN
   nMap=nMap+1
   IF (nMap .GT. lengthZ ) THEN
75  nMap=1
   END IF
   nFrame=1
   END IF
   END IF

80  C-----
C   The subroutine assumes that the surface is in the xy-plane
   xCoord=COORDS(3)
   yCoord=COORDS(2)
   zCoord=COORDS(1)
85  C Some parts of the program are executed only once. This is done
C during the first call of the subroutine.

```


APPENDIX B

```

    IF (firstCall2 .NE. 1 ) THEN
90    2000 FORMAT (F15.10, I5, I5, I5, I5, F15.10)

        nFrame=1
        firstCall2=1

95    C Data is read from text file and stored to array
        OPEN(UNIT=9,FILE='
            &/home-extra/p.raninger/Simulationsordner/Bremssche
            &iben/1_Simulations/Set4/S4_4_B_001_10.txt'
            &, STATUS='OLD')
100        READ(9,1002), ((dataArray(i1,i2,1),i2=1,322),
            &i1=1,69601)
            CLOSE(9)
            OPEN(UNIT=9,FILE='
            &/home-extra/p.raninger/Simulationsordner/Bremssche
            &iben/1_Simulations/Set4/S4_4_B_002_10.txt'
            &, STATUS='OLD')
105        READ(9,1002), ((dataArray(i1,i2,2),i2=1,322),
            &i1=1,66961)
            CLOSE(9)
            OPEN(UNIT=9,FILE='
            &/home-extra/p.raninger/Simulationsordner/Bremssche
            &iben/1_Simulations/Set4/S4_4_B_003_10.txt'
            &, STATUS='OLD')
110        READ(9,1002), ((dataArray(i1,i2,3),i2=1,322),
            &i1=1,68161)
            CLOSE(9)
            OPEN(UNIT=9,FILE='
            &/home-extra/p.raninger/Simulationsordner/Bremssche
            &iben/1_Simulations/Set4/S4_4_B_004_10.txt'
            &, STATUS='OLD')
120        READ(9,1002), ((dataArray(i1,i2,4),i2=1,322),
            &i1=1,66001)
            CLOSE(9)
            OPEN(UNIT=9,FILE='
            &/home-extra/p.raninger/Simulationsordner/Bremssche
            &iben/1_Simulations/Set4/S4_4_B_005_10.txt'
            &, STATUS='OLD')
125        READ(9,1002), ((dataArray(i1,i2,5),i2=1,322),
            &i1=1,64561)
            CLOSE(9)
            OPEN(UNIT=9,FILE='
            &/home-extra/p.raninger/Simulationsordner/Bremssche
            &iben/1_Simulations/Set4/S4_4_B_006_10.txt'
            &, STATUS='OLD')
135        READ(9,1002), ((dataArray(i1,i2,6),i2=1,322),
            &i1=1,65521)
            CLOSE(9)
            OPEN(UNIT=9,FILE='
            &/home-extra/p.raninger/Simulationsordner/Bremssche
            &iben/1_Simulations/Set4/S4_4_B_007_10.txt'
            &, STATUS='OLD')
140        READ(9,1002), ((dataArray(i1,i2,7),i2=1,322),
            &i1=1,65041)
            CLOSE(9)
            OPEN(UNIT=9,FILE='
            &/home-extra/p.raninger/Simulationsordner/Bremssche
            &iben/1_Simulations/Set4/S4_4_B_008_10.txt'
            &, STATUS='OLD')
145        READ(9,1002), ((dataArray(i1,i2,8),i2=1,322),
            &i1=1,63361)
            CLOSE(9)
            OPEN(UNIT=9,FILE='
            &/home-extra/p.raninger/Simulationsordner/Bremssche
            &iben/1_Simulations/Set4/S4_4_B_009_10.txt'
            &, STATUS='OLD')
155        READ(9,1002), ((dataArray(i1,i2,9),i2=1,322),
            &i1=1,65281)
            CLOSE(9)
            OPEN(UNIT=9,FILE='
            &/home-extra/p.raninger/Simulationsordner/Bremssche
            &iben/1_Simulations/Set4/S4_4_B_010_10.txt'
            &, STATUS='OLD')
160        READ(9,1002), ((dataArray(i1,i2,10),i2=1,322),
            &i1=1,64801)
            CLOSE(9)

        mapDims(1,1)=69601
        mapDims(1,2)=322
        mapDims(2,1)=66961
        mapDims(2,2)=322
170        mapDims(3,1)=68161
        mapDims(3,2)=322
        mapDims(4,1)=66001
        mapDims(4,2)=322
        mapDims(5,1)=64561
        mapDims(5,2)=322
175        mapDims(6,1)=65521
        mapDims(6,2)=322
        mapDims(7,1)=65041
        mapDims(7,2)=322
180        mapDims(8,1)=63361
        mapDims(8,2)=322
        mapDims(9,1)=65281

```

```

185     mapDims(9,2)=322
        mapDims(10,1)=64801
        mapDims(10,2)=322

        END IF

190     C23456789012345678901234567890123456789012345678901234567890123456789012
        C If the current time is larger than the time of the current frame (of the thermal image data) and the subsequent one in the
        C   ↳ file, nFrame is increased by 1
        C -> time window for time interpolation is changed. If time interpolation is not executed the second frame is mapped on the
        C   ↳ FE model
        IF (FirstRun .EQ. 0) Then

195     C pixelY*(nFrame)+1: last row in current frame; +1 -> first line in file is heading
    55     IF (INT(cStepTime*100000) .GT.
        &INT(dataArray(pixelY*(nFrame)+1,1,nMap)
        &*100000) .AND. INT(cStepTime*100000) .GE. INT(dataArray(pixelY*
200     &(nFrame+1)+1,1,nMap)*100000) .AND. cStepTime .LT.
        &dataArray(mapDims(nMap,1),1,nMap)) THEN
            nFrame=nFrame+1
            GOTO 55
        END IF
    END IF

205     C x-coord in grid that exceeds the current x-coord is searched
        i1=3
    56     IF (dataArray(1,i1,nMap) .LT. xCoord .AND. i1 .LE. lengthX) THEN
            i1=i1+1
210     GOTO 56
        END IF
        C y-coord in grid that is just below the current y-coord is searched
        i2=2
    57     IF (dataArray(i2,2,nMap) .GT. yCoord .AND. i2 .LE. pixelY) THEN
215     i2=i2+1
            GOTO 57
        END IF

220     C Data too close to the edges of the grid cannot be interpolated
        C This should never be the case but nevertheless errors are avoided by using the values on the grid
        IF ((i1 .GE. lengthX-2) .OR. (i1 .EQ. 3) .OR. (i2 .GE. pixelY)
        & .OR. (i2 .EQ. 2)) THEN
            U=cTEMP

225     ELSE
        C Indices of data in the grid that are used for interpolation
            IndX1Coord=i1-1
            IndX2Coord=i1
230     IndY11Coord=i2+pixelY*(nFrame-1)-1
            IndY12Coord=i2+pixelY*(nFrame-1)
            IndY21Coord=i2+pixelY*(nFrame)-1
            IndY22Coord=i2+pixelY*(nFrame)

        C Coordinates of data in grid for interpolation are stored
235     x1Coord=dataArray(1,IndX1Coord,nMap)
            x2Coord=dataArray(1,IndX2Coord,nMap)
            y11Coord=dataArray(IndY11Coord,2,nMap)
            y12Coord=dataArray(IndY12Coord,2,nMap)
            y21Coord=dataArray(IndY21Coord,2,nMap)
            y22Coord=dataArray(IndY22Coord,2,nMap)

240     C Data for interpolation are stored
        C First frame of interpolation window
            T11t1=dataArray(IndY11Coord,IndX1Coord,nMap)
            T12t1=dataArray(IndY11Coord,IndX2Coord,nMap)
            T21t1=dataArray(IndY12Coord,IndX1Coord,nMap)
245     T22t1=dataArray(IndY12Coord,IndX2Coord,nMap)
        C Second frame of interpolation window
            T11t2=dataArray(IndY21Coord,IndX1Coord,nMap)
            T12t2=dataArray(IndY21Coord,IndX2Coord,nMap)
            T21t2=dataArray(IndY22Coord,IndX1Coord,nMap)
250     T22t2=dataArray(IndY22Coord,IndX2Coord,nMap)

            IF ((T11t1 .NE. TSurrounding) .OR. (T12t1 .NE. TSurrounding)
        & .OR. (T21t1 .NE. TSurrounding) .OR. (T22t1 .NE. TSurrounding) .OR.
255     &(T11t2 .NE. TSurrounding) .OR. (T12t2 .NE. TSurrounding) .OR.
        &(T21t2 .NE. TSurrounding) .OR. (T22t2 .NE. TSurrounding)) Then

        C spatial interpolation for each frame
            Temp1=InterpFuncBiLinear(
260     &xCoord,x1Coord,x2Coord,yCoord,y11Coord,y12Coord,
        &T11t1,T12t1,T21t1,T22t1,cStepTime)

            Temp2=InterpFuncBiLinear(
265     &xCoord,x1Coord,x2Coord,yCoord,y21Coord,y22Coord,
        &T11t2,T12t2,T21t2,T22t2,cStepTime)

        C time interpolation between frames
        C Interpolation between two sampling times -> good if thermal images are rotated on top of each other
270     U=InterpFuncLinear(dataArray(IndY12Coord,1,nMap),
        &dataArray(IndY22Coord,1,nMap),Temp1,Temp2,cStepTime)

        C No time interpolation -> better if images are as received
        C U=Temp2
        C U=T22t2
275     ELSE
            U=cTEMP

```

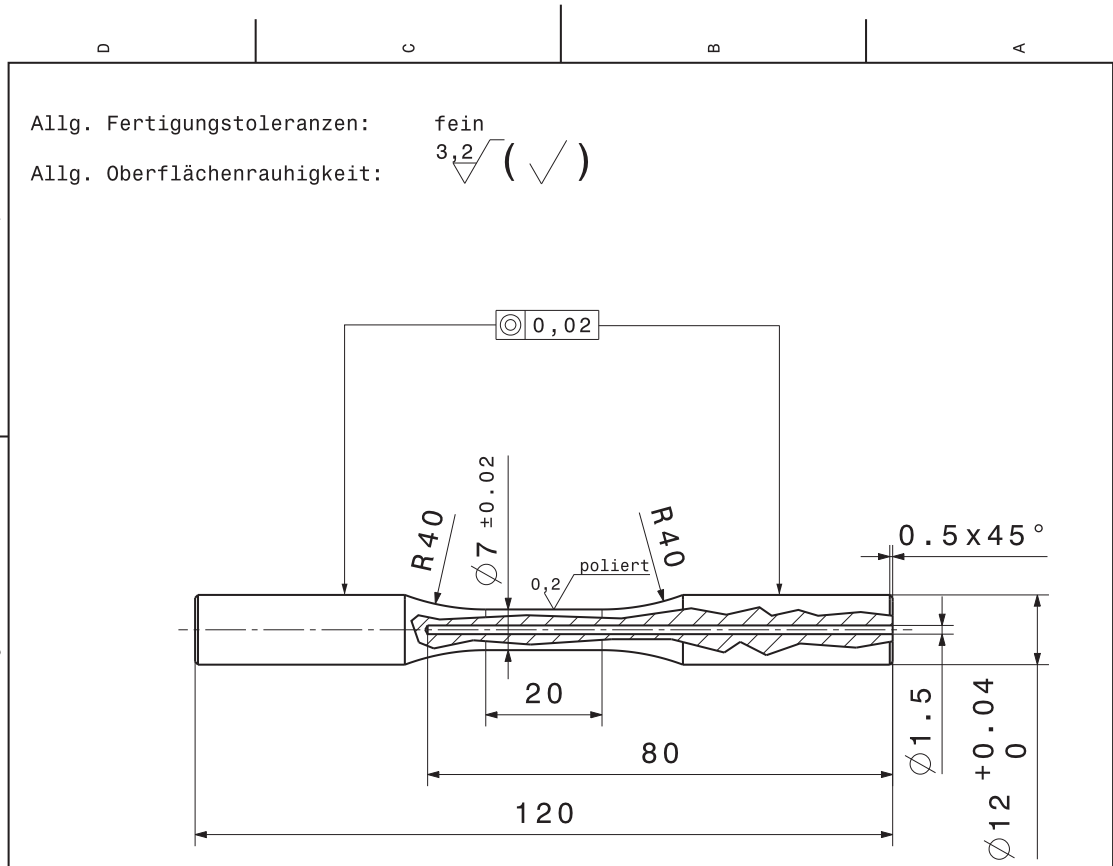
APPENDIX B

```
280     END IF
280     END IF
1002 FORMAT (<lengthX>F12.5)
RETURN
END
285
C23456789012345678901234567890123456789012345678901234567890123456789012
C   Interpolation Function
REAL FUNCTION InterpFuncLinear(x1,x2,f0,f1,ctime)
290
REAL x1, x2, f0, f1, ctime
InterpFuncLinear=f0+(f1-f0)/(x2-x1)*(ctime-x1)
RETURN
END
295
C23456789012345678901234567890123456789012345678901234567890123456789012
C   Interpolation Function
REAL FUNCTION InterpFuncBiLinear(
300 &x,x1,x2,y,y1,y2,f11,f12,f21,f22,ctime)
REAL x,x1,x2,y,y1,y2,f11,f12,f21,f22,ctime
InterpFuncBiLinear=
&f11/((x2-x1)*(y2-y1))*(x2-x)*(y2-y)+
&f12/((x2-x1)*(y2-y1))*(x-x1)*(y2-y)+
305 &f21/((x2-x1)*(y2-y1))*(x2-x)*(y-y1)+
&f22/((x2-x1)*(y2-y1))*(x-x1)*(y-y1)
RETURN
END
```

Appendix C

Sample geometries and sampling positions

C.2 TMF



| | | | | |
|---|----------------------------------|--|------------|------------|
| Datum: | Ansprechperson: | Projektname: | Werkstoff: | Stückzahl: |
| Gezeichnet: Stanojevic Datum: 29.04.2008 | | TMF - 120 - 12 - 7 - 20 - Ru | | |
| Format A4 | | Lehrstuhl für Allgemeinen Maschinenbau | | |
| Maßstab 1:1 | Zeichnungsnummer TMF01 | Blatt 1/1 | | |

C.3 Fracture toughness

Vormmaß

$6,3 / \left(Ra_{1,6} / Ra_{0,8} \right)$

Endmaß

Beschriftung Unterseite Rand BEIDSEITIG!

auf Rechtwinkeligkeit achten

Detail und Clip On Verwendung

Clip On Aufnahme

Radius an die Erodiermaschine anpassen

Fertigungsvorschrift

- Vormaterialblock vorschneiden
- Block planparallel auf Endlänge schleifen
- Proben auf Vormmaß erodieren
- stempeln (laut Angabe)

Wärmebehandlung

- Proben auf Endmaß fertigen (Längsschleifen)
- (Breite: beidseitig 0,5 mm abarbeiten)
- (Höhe: kerbseitig 0,2 mm abarbeiten)
- Kerbe und Clip On Aufnahme erodieren

| | | | | | |
|-------|----------|-----------------|-----------|-------------------------------|---------------|
| | | (Allg. Tol.) | (Oberfl.) | Maßstab 1:1 | (Gewicht) |
| | | ISO2768-M | | SENB-Probe nach ISO12135:2002 | |
| | | Datum | Name | F06_KIC-20X10X100MM | |
| | | Bearb. 05-03-12 | SBR | | |
| | | Gepr. 05-03-12 | SMA | | |
| | | Freig. | | | |
| | | | | F06-__ | Blatt |
| | | | | | Blätter |
| Zust. | Änderung | Datum | Name | Ursprung | Ersatz für: |
| | | | | | Ersatz durch: |

C.4 Crack propagation

Vormaß

Endmaß

Beschriftung Unterseite Rand

Fertigungsvorschrift


- Vormaterialblock vorschneiden
- Block planparallel auf Endlänge schleifen
- Proben auf Vormass erodieren
- stempeln (laut Angabe)

Wärmebehandlung

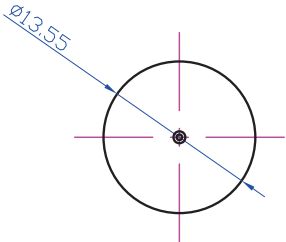
- Proben auf Endmaß fertigen (Längsschleifen)
(Breite: beidseitig 0,5 mm abarbeiten)
(Höhe: kerbseitig 0,2 mm abarbeiten)
- Kerbe einbringen

| | | | | | |
|------------|----------|-------------------------------|-----------|---------------------|--|
| Version: 2 | | (Allg. Tol.) MITTEL | (Oberfl.) | Maßstab MAßSTAB | (Gewicht) |
| | | | | F07-DADN-20X6X110MM | |
| | | | | F07-__ | |
| | | | | Blatt | |
| | | | | Blätter | |
| Zust | Änderung | Datum | Name | Ursprung | Ersatz für: _____ Ersatz durch: _____ |

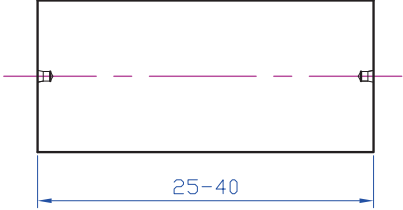
C.5 Thermal diffusivity



Vormaß



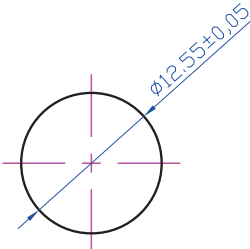
Ø13,55



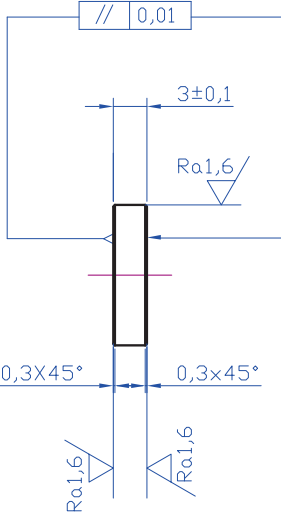
25-40

- die 1. Probe bei min. 20mm abstechen
- die 2. Probe bei min. 25mm abstechen
- die 3. Probe bei min. 30mm abstechen

Endmaß




Ø12,55±0,05




3±0,1
Ra1,6
0,3x45°
Ra1,6

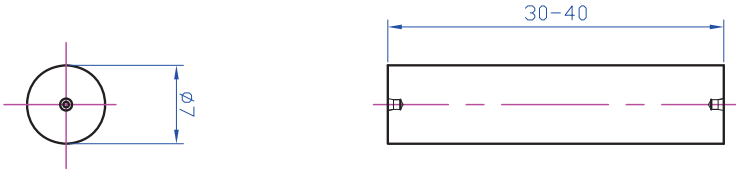
Kanten brechen

| | | | | | | |
|---|----------|-------|-------------------------------|-----------|----------------------------------|---------------|
| Version: 2 | | | (Allg. Tol.) MITTEL | (Oberfl.) | Maßstab MAßSTAB 2:1 | (Gewicht) |
| | | | | | T01-LASERFLASH-PR.__(TLF) | |
| | | | Datum | Name | | |
| | | | Bearb. | 18-10-11 | SBR | |
| | | | Gepr. | 18-10-11 | SMA | |
| | | | Freig. | | | |
|  | | | | | T01-__ | Blatt |
| | | | | | Blätter | |
| Zust | Änderung | Datum | Name | Ursprung | Ersatz für: | Ersatz durch: |

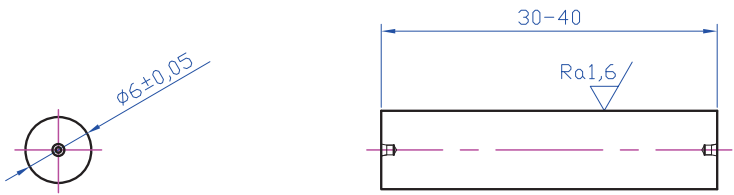
C.6 Heat capacity




Vormmaß



Endmaß

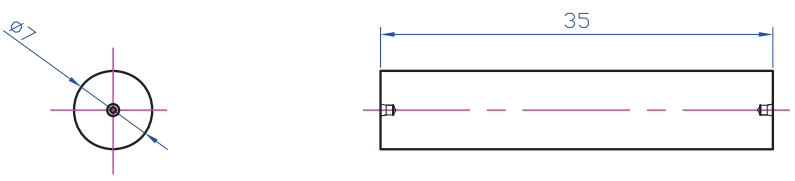


| | | | | | | |
|---|----------|-------|-------------------------------|-----------|------------------------------|------------------|
| Version: 2 | | | (Allg. Tol.) MITTEL | (Oberfl.) | Maßstab MAßSTAB 2:1 | (Gewicht) |
| | | | Datum | Name | T03-CP-PROBENZYLINDER | |
| | | | Bearb. 18-10-11 | SBR | | |
| | | | Gepr. 18-10-11 | SMA | | |
| | | | Freig. | | | |
|  | | | | | T03-__ | |
| Zust. | Änderung | Datum | Name | Ursprung | Ersatz für: | Ersatz durch: |
| | | | | | | Blatt Blätter |

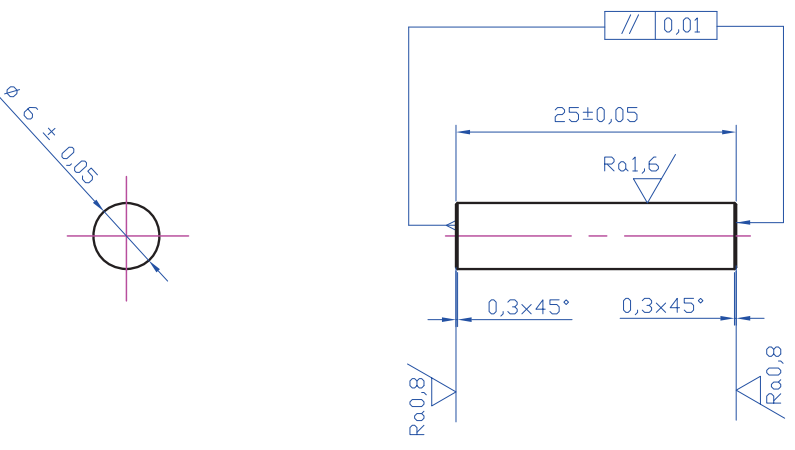
C.7 Thermal expansion

$\checkmark \left(\begin{matrix} Ra1,6 \\ \nabla \\ , \\ \nabla \\ Ra0,8 \end{matrix} \right)$


Vormaß



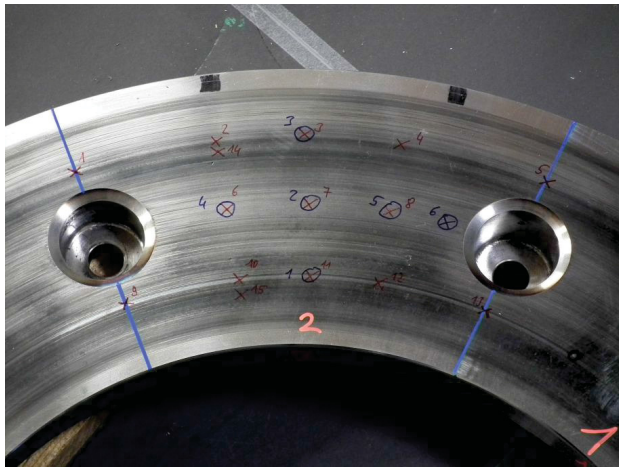
Endmaß



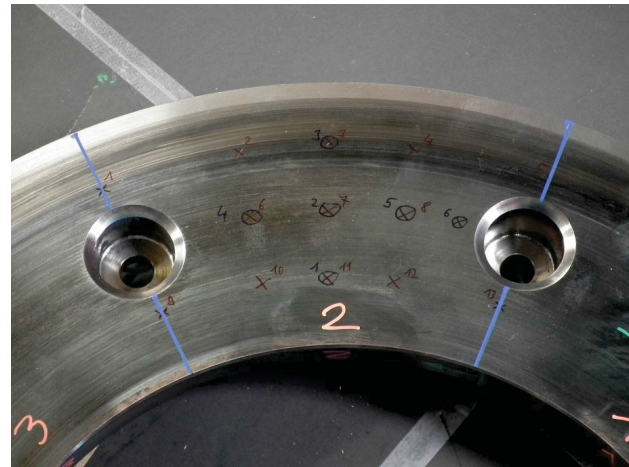
Kanten brechen

| | | | | | | |
|---|----------|-------|-----------------|-----------|------------------------------|---------------|
| Version: 2 | | | (Allg. Tol.) | (Oberfl.) | Maßstab MAßSTAB 2:1 | (Gewicht) |
| | | | MITTEL | | | |
| | | | Datum | Name | T04-WÄRMEAUDEHNUNGSP. | |
| | | | Bearb. 18-10-11 | SBR | | |
| | | | Gepr. 18-10-11 | SMA | | |
| | | | Freig. | | | |
|  | | | | | T04-__ | Blatt |
| | | | | | Blätter | |
| Zust. | Änderung | Datum | Name | Ursprung | Ersatz für: | Ersatz durch: |

C.8 Positions for residual stress measurements and metallographic specimens



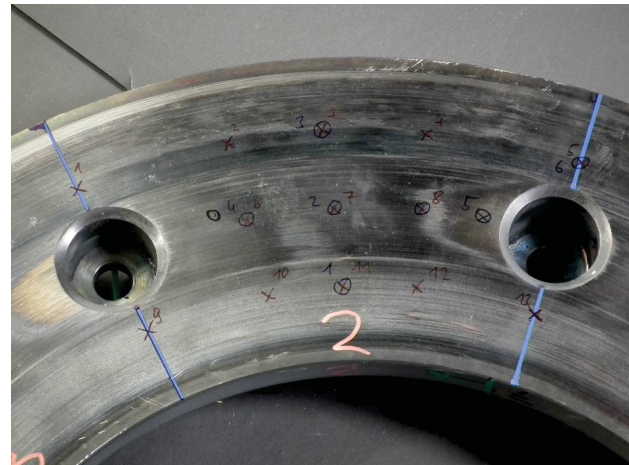
(a) Friction ring 1, Bedding



(b) Friction ring 3, 1ES



(c) Friction ring 5, 10ES



(d) Friction ring 7, 200ES

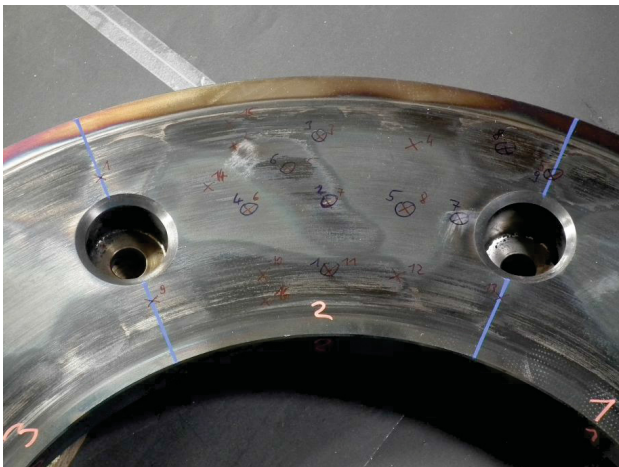
Figure C.1: Positions for residual stress measurements. The images show segments tested with pad type 1



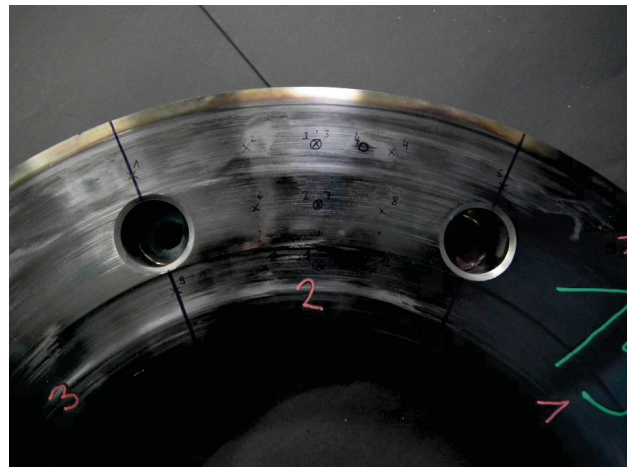
(a) Friction ring 9, Bedding



(b) Friction ring 11, 1ES



(c) Friction ring 13, 10ES



(d) Friction ring 15, 100ES

Figure C.2: Positions for residual stress measurements. The images show segments tested with pad type 2 (ES...emergency stops).



(a) Friction ring 1, Bedding



(b) Friction ring 3, 1ES



(c) Friction ring 5, 10ES



(d) Friction ring 7, 200ES

Figure C.3: Positions for residual stress measurements and metallographic specimens. The images show segments tested with pad type 1



(a) Friction ring 9, Bedding



(b) Friction ring 11, 1ES



(c) Friction ring 13, 10ES



(d) Friction ring 15, 100ES

Figure C.4: Positions for residual stress measurements and metallographic specimens. The images show segments tested with pad type 2 (ES...emergency stops).

Appendix D

General data and standards

D.1 Extract from DIN 27205-5:2005-10: Zustand der Eisenbahnfahrzeuge - Bremsen - Teil 5: Radbremsscheiben

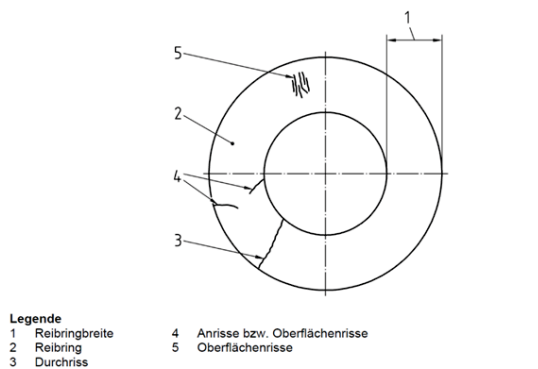


Bild 5 — Belüftete Radbremsscheibe mit Darstellung möglicher Rissformen

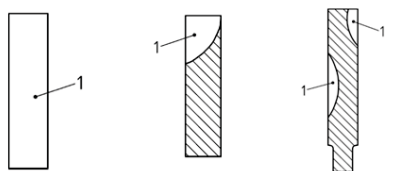


Bild 2 — Durchriss

Bild 3 — Anriss

Bild 4 — Oberflächenriss

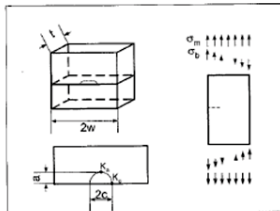
| | | |
|--|---|--|
| <u>Durchriss unzulässig</u> | | Feststellung der Risse durch Sichtprüfung nach DIN 27200 |
| RBS aus Kugelgraphit (GJS), Stahlguss (GS), bzw. geschmiedetem Stahl RBS aus Grauguss (GJL) | <u>Anrisse:</u> Es sind mehrere Anrisse in willkürlicher Anordnung zulässig, wenn eine Länge von: | Feststellung der Risse durch Sichtprüfung nach DIN 27200 |
| | — <u>60 mm</u> — <u>30 mm</u> | |
| nicht überschritten wird und der Abstand zum nächsten Anriss bzw. Oberflächenriss (mit $l \leq 60$ mm bei GS und GJS und geschmiedetem Stahl bzw. $l \leq 30$ mm bei GJL) mindestens 50 mm beträgt. Zu messen ist die kürzeste Entfernung. | | |
| <u>Oberflächenrisse:</u> | | Feststellung der Risse durch Sichtprüfung nach DIN 27200 |
| RBS aus Kugelgraphit (GJS), Stahlguss (GS) und geschmiedetem Stahl RBS aus Grauguss (GJL) | — <u>60 mm zulässig</u> — <u>30 mm zulässig</u> | |
| RBS mit Mittenanbindung Senkbohrungen | Oberflächenrisse, die durch die Senkbohrung verlaufen bzw. den Rand der Bohrung erreichen, sind bis zu einer Länge von <u>40 mm</u> zulässig. | |

Figure D.1: Admissible and non-admissible crack configurations and crack lengths in wheel mounted brake disks [?].

D.2 Analytical solution for semi-elliptical cracks under tensile and bend loading according to FKM guideline

7.4.2.1 Scheibe unter Zug und Biegung

7.4.2.1.4 Halbelliptischer Oberflächenriss



Quellen Spannungsintensitätsfaktor

Newman, J.C., Jr., Raju, I.S., Stress-intensity factor equations for cracks in three-dimensional finite bodies subjected to tension and bending loads, NASA Technical Memorandum 85793, Langley Research Center, Hampton, VA, 1984

Quelle plastische Grenzlast

Sattari-Far, I., Dillerföm, P., Local limit load solution for surface cracks in plates and cylinders using finite element analysis, International Journal of Pressure Vessels and Piping 81, 57-66, 2004

Spannungsintensitätsfaktoren K_a (Scheitel), K_s (Oberflächenpunkt)

$K_a = K(\phi = \frac{\pi}{2}), K_s = K(\phi = 0)$ Solution at 0° and 90°

$$K = (\sigma_n F_m + \sigma_b F_b) \sqrt{\frac{\pi a}{Q}}$$

$$F_m = \left[M_1 + M_2 \left(\frac{a}{t}\right)^2 + M_3 \left(\frac{a}{t}\right)^4 \right] g_\phi f_w$$

$$F_b = F_m [H_1 + (H_2 - H_1) \sin^2 \phi]$$

$$f_w = \left[\sec \left(\frac{\pi}{2w} \sqrt{\frac{a}{t}} \right) \right]^2$$

Für $\frac{a}{c} \leq 1$:

$$M_1 = 1,13 - 0,09 \frac{a}{c}, M_2 = -0,54 + \frac{0,89}{0,2 + \frac{a}{c}}, M_3 = 0,5 - \frac{1}{0,65 + \frac{a}{c}} + 14 \left(1 - \frac{a}{c}\right)^{24}$$

$$g = 1 + \left[0,1 + 0,35 \left(\frac{a}{t}\right)^2 \right] (1 - \sin \phi)^2$$

$$Q = 1 + 1,464 \left(\frac{a}{c}\right)^{1,65}, f_\phi = \left(\sin^2 \phi + \frac{a^2}{c^2} \cos^2 \phi \right)^{\frac{1}{4}}$$

$$p = 0,2 + \frac{a}{c} + 0,6 \frac{a}{t}$$

$$H_1 = 1 - 0,34 \frac{a}{t} - 0,11 \frac{a}{c} \frac{a}{t}$$

$$H_2 = 1 + \left(-1,22 - 0,12 \frac{a}{c} \right) \frac{a}{t} + \left[0,55 - 1,05 \left(\frac{a}{c}\right)^{0,75} + 0,47 \left(\frac{a}{c}\right)^{1,5} \right] \left(\frac{a}{t}\right)^2$$

Für $\frac{a}{c} > 1$:

$$M_1 = \sqrt{\frac{c}{a}} \left(1 + 0,04 \frac{c}{a} \right), M_2 = 0,2 \left(\frac{c}{a}\right)^4, M_3 = -0,1 \left(\frac{c}{a}\right)^4$$

$$g = 1 + \left[0,1 + 0,35 \frac{c}{a} \left(\frac{a}{t}\right)^2 \right] (1 - \sin \phi)^2$$

$$Q = 1 + 1,464 \left(\frac{c}{a}\right)^{1,65}, f_\phi = \left(\cos^2 \phi + \frac{c^2}{a^2} \sin^2 \phi \right)^{\frac{1}{4}}$$

$$p = 0,2 + \frac{c}{a} + 0,6 \frac{a}{t}$$

$$H_1 = 1 + \left(-0,04 - 0,41 \frac{c}{a} \right) \frac{a}{t} + \left[0,55 - 1,93 \left(\frac{c}{a}\right)^{0,75} + 1,38 \left(\frac{c}{a}\right)^{1,5} \right] \left(\frac{a}{t}\right)^2$$

$$H_2 = 1 + \left(-2,11 + 0,77 \frac{c}{a} \right) \frac{a}{t} + \left[0,55 - 0,72 \left(\frac{c}{a}\right)^{0,75} + 0,14 \left(\frac{c}{a}\right)^{1,5} \right] \left(\frac{a}{t}\right)^2$$

Gültigkeitsbereich: $0 \leq \frac{a}{t} < 1, 0 \leq \frac{a}{c} \leq 2, \frac{c}{w} < 0,5$.

Plastifizierungsgrad L_r

$$L_r = \frac{(1 - \xi)^{1,38} \frac{\sigma_b}{3} + \sqrt{(1 - \xi)^{3,16} \frac{\sigma_b^2}{9} + (1 - \xi)^{3,14} \sigma_m^2}}{(1 - \xi)^2 R_e}$$

$$\xi = \frac{ac}{t(t+c)}$$

Gültigkeitsbereich: $0 \leq \frac{a}{t} \leq 0,8, 0 \leq \frac{a}{c} \leq 1, w > c + t$.

Figure D.2: Analytical solution for stress intensity factors according to FKM guideline [40].

D.3 Data sheet for thermal imaging system

THERMACAM SC 3000 TECHNICAL SPECIFICATIONS

| IMAGING PERFORMANCE | |
|----------------------------------|-------------------------|
| Field of view/min focus distance | 20' x15' /0.3m |
| Spatial resolution (IFOV) | 1.1 mrad |
| Thermal sensitivity | 20 mK at 30°C |
| Image frequency | 50/60 Hz non-interlaced |
| Electronic zoom function | 4X continuous |

| DETECTOR | |
|------------------|--|
| Type | GaAs, Quantum Well Infrared Photodetector (QWIP), 320x240 pixels |
| Spectral range | 8 to 9 μ m |
| Detector Cooling | Stirling cooled to 70K, cool down time <6 minutes |

| IMAGE PRESENTATION | |
|--------------------|--|
| Video output | RS170 EIA/NTSC or CCR/PAL composite, S-video, and 14-bit digital serial link |

| MEASUREMENT | |
|-------------------------------------|--|
| Temperature range | -20°C to +1500°C (-4°F to 2732°F), 4 ranges Up to +2000°C (+3632°F), optional |
| Accuracy | $\pm 1\%$ or $\pm 1^\circ\text{C}$ (for measurement ranges up to +150°C) $\pm 2\%$ or $\pm 2^\circ\text{C}$ (for measurement ranges above +150°C) |
| Atmospheric transmission correction | Automatic, based on inputs for distance, atmospheric temperature and relative humidity |
| Optics transmission correction | Automatic, based on signals from 5 internal sensors |
| Automatic emissivity correction | Variable from 0.1 to 1.0 or select from listings in pre-defined materials list |

| IMAGE STORAGE | |
|---------------|--|
| Type | High capacity PC-Card, ATA compatible (160MB min) |
| File formats | 14-bit radiometric IR digital image (IMG), includes header file with all radiometric data 8-bit standard bitmap (BMP), image only or image with screen graphics Every image stored in both formats |

| LENSES (OPTIONAL) | |
|---------------------|--|
| Field of view | 2.5' x 1.88' • 5.0' x 3.75' • 10' x 7.5' 34mm x 26mm /90mm (close-up) 10mm x 7.5mm/25mm (close-up) |
| Lens identification | Automatic |

| POWER INPUT | |
|-------------------|-----------------|
| Voltage | 12V DC, nominal |
| Power Consumption | 22 watts |
| AC Adapter | Included |

| ENVIRONMENTAL SPECIFICATION | |
|-----------------------------|---|
| Operating temperature range | -15°C to +50°C (5°F to 122°F) |
| Storage temperature range | -40°C to +70°C (-40°F to 158°F) |
| Humidity | Operating and storage: 10% to 95%, non-condensing |
| Encapsulation | IP 54 IEC 529 (metal casing) |
| Shock | Operational: 25G, IEC 68-2-29 |
| Vibration | Operational: 2G, IEC 68-2-6 |

| PHYSICAL CHARACTERISTICS | |
|--------------------------|--|
| Weight | 3.2 kg (7.0 lbs.) |
| Size | 220mm x 135mm x 130mm (8.7" x 5.3" x 5.1") |

| INTERFACE | |
|------------------------|---|
| Remote-control options | Remote focus (standard), RS-232 (standard) Remote control panel (optional) |
| Sync | Gen Lock input |

SPECIFICATIONS ARE SUBJECT TO CHANGE WITHOUT NOTICE
 ©Copyright 2000, FLIR Systems, Inc.
 All other brand and product names are trademarks of their respective owners.

QWIP SPECTRAL RESPONSE (NOMINAL)

RESPONSIVITY

WAVELENGTH (μ m)

FLIR SYSTEMS, BOSTON
 USA Thermography Center
 16 Esquire Road
 North Billerica, MA 01862 USA
 Telephone: +1 (978) 901-8000
 Toll Free: +1 (800) GO-INFRA

FLIR SYSTEMS, AB
 Worldwide Thermography Center
 Rinkebyvägen 19
 SE-182 11
 Danderyd, SWEDEN
 Telephone: +46 (0) 8 753 25 00

FLIR SYSTEMS, LTD
 UNITED KINGDOM
 Telephone: +44 (0) 1732 220 011

FLIR SYSTEMS
 BELGIUM
 Telephone: +32 (0) 3 287 87 10

FLIR SYSTEMS, GMBH
 GERMANY
 Telephone: +49 (0) 69 95 00 900

FLIR SYSTEMS, SARL
 FRANCE
 Telephone: +33 (0) 1 41 33 97 97

FLIR SYSTEMS, SRL
 ITALY
 Telephone: +39 (0) 2 39 09 121

FLIR SYSTEMS LTD
 CANADA
 Telephone: +1 800 613 0507

FLIR SYSTEMS COMPANY, LTD
 HONG KONG
 Telephone: +852 2792 8955

1 (800) GO INFRA
www.flir.com/sc3000

I022100PL

References

- [1] G. Gfatter, P. Berger, G. Krause, and G. Vohla. *Grundlagen der Bremstechnik - Basics of Brake Technology*. Knorr-Bremse. xv, 2, 3
- [2] Seigo Uchida Izumi Hasegawa. Braking systems. *Railway Technology Today*, 7, 1999. xv, 2, 5
- [3] P. Dufrenoy and D. Weichert. A thermomechanical model for the analysis of disc brake fracture mechanisms. *Journal of Thermal Stresses*, 26(8):815–828, 2003. xv, 6, 13, 126, 192, 247
- [4] Zhiyong Yang, Jianmin Han, Weijing Li, Zhiqiang Li, Like Pan, and Xiaoling Shi. Analyzing the mechanisms of fatigue crack initiation and propagation in {CRH} {EMU} brake discs. *Engineering Failure Analysis*, 34(0):121 – 128, 2013. xv, 10
- [5] Konstantin Naumenko and Holm Altenbach. *Modeling of Creep for Structural Analysis (Foundations of Engineering Mechanics)*. Springer, 2007 edition, 3 2007. xv, xvi, xxvii, 11, 12, 48, 57, 67, 70, 72, 74, 78, 79, 80, 81, 293
- [6] Dieter Radaj, Cetin Morris Sonsino, and Wolfgang Fricke. *Fatigue assessment of welded joints by local approaches, Second Edition (Woodhead Publishing in Materials)*. CRC Press, 2 edition, 11 2006. xv, xvi, 24, 88
- [7] Jaap Schijve. The significance of fatigue crack initiation for predictions of the fatigue limit of specimens and structures. *International Journal of Fatigue*, 61(0):39 – 45, 2014. xv, 24, 27
- [8] Dieter Radaj and Michael Vormwald. *Ermüdungsfestigkeit: Grundlagen für Ingenieure*. Springer, 3., neubearb. u. erw. aufl. 2nd printing. 2007 edition, 8 2007. xv, xvi, 28, 30, 53, 97, 99
- [9] S. Suresh. *Fatigue of Materials (Cambridge Solid State Science Series) Second Edition*. Cambridge University Press, 2 edition, 11 1998. xv, 24, 25, 26, 28, 33, 93, 96, 278, 284
- [10] Mirco D. Chapetti. Fatigue propagation threshold of short cracks under constant amplitude loading. *International Journal of Fatigue*, 25(12):1319 – 1326, 2003. xv, 28, 29
- [11] O. Kolednik. Lecture notes on "werkstoff und bruchzähigkeit", 2010. xv, 30, 280
- [12] Luigi Nicolais, Assunta Borzacchiello, and Stuart M. Lee, editors. *Wiley Encyclopedia of Composites, 5 Volume Set (Lee: Enc. of Composites)*. Wiley, 2 edition, 5 2012. xv, 30, 281, 284
- [13] M. Klesnil and P. Lukác. *Fatigue of Metallic Materials, Volume 71, Second Edition (Materials Science Monographs)*. Elsevier Science, 2 edition, 4 1992. xv, xxvi, 24, 27, 31, 32, 277, 278

REFERENCES

- [14] Ralf Bürgel, Hans Jürgen Maier, and Thomas Niendorf. *Handbuch Hochtemperatur-Werkstofftechnik: Grundlagen, Werkstoffbeanspruchungen, Hochtemperaturlegierungen und -beschichtungen*. Vieweg+Teubner Verlag, 4., überarb. aufl. 2011 edition, 4 2011. [xvi](#), [10](#), [11](#), [36](#), [38](#), [40](#), [98](#), [99](#), [101](#)
- [15] H.J. Frost and M.F. Ashby. "deformation-mechanism maps, the plasticity and creep of metals and ceramics", <http://engineering.dartmouth.edu/defmech/>. [xvi](#), [xix](#), [xxvii](#), [12](#), [39](#), [40](#), [41](#), [42](#), [44](#), [45](#), [73](#), [150](#)
- [16] W Eichlseder. Betriebsfestigkeit ii, 2010. [xvi](#), [xvii](#), [53](#), [88](#), [96](#), [214](#)
- [17] Jean Lemaitre. *Mechanics of Solid Materials*. Cambridge University Press, 10 1994. [xvi](#), [xxvii](#), [xxviii](#), [48](#), [51](#), [53](#), [55](#), [57](#), [59](#), [60](#), [63](#), [84](#), [87](#), [101](#), [290](#), [291](#), [292](#)
- [18] Jacques Besson, Georges Cailletaud, Jean-Louis Chaboche, Samuel Forest, and Marc Blétry. *Non-Linear Mechanics of Materials (Solid Mechanics and Its Applications)*. Springer, 2010 edition, 12 2009. [xvi](#), [xxvii](#), [xxviii](#), [48](#), [53](#), [56](#), [59](#), [289](#)
- [19] Fionn Dunne and Nik Petrinic. *Introduction to Computational Plasticity*. Oxford Univ Pr, 6 2005. [xvi](#), [51](#), [57](#), [68](#), [69](#), [78](#), [84](#), [85](#)
- [20] W. Ecker. *Modeling of the thermo-mechanical behavior of pressure casting dies*. PhD thesis, Montanuniversität Leoben, 2008. [xvi](#), [85](#), [86](#), [208](#)
- [21] Lothar Issler, Hans Ruoss, and Peter Haefele. *Festigkeitslehre - Grundlagen (Springer-Lehrbuch) (German Edition)*. Springer, 2., corrected aufl. 2003. 3., korr. nachdruck 2005 edition, 11 2005. [xvi](#), [xvii](#), [88](#), [91](#), [92](#)
- [22] H.-J. Christ. *Ermüdungsverhalten metallischer Werkstoffe*. Wiley-VCH Verlag GmbH & Co. KGaA, 2. auflage edition, 5 2009. [xvii](#), [xxvi](#), [24](#), [25](#), [26](#), [93](#), [94](#), [95](#), [96](#), [282](#)
- [23] E. Haibach. *Betriebsfestigkeit: Verfahren und Daten zur Bauteilberechnung (VDI-Buch)*. Springer, 3., korr. u. erg. aufl. 2006 edition, 1 2006. [xvii](#), [96](#)
- [24] <http://en.wikipedia.org/wiki/pagoda>. [xvii](#), [97](#)
- [25] S. S. Manson and G. R. Halford. *Fatigue And Durability of Structural Materials*. ASM International, 12 2005. [xvii](#), [90](#), [92](#), [96](#), [97](#)
- [26] B. Oswald-Tranta. Infrarot thermographie - einföhrung, 2013. [xvii](#), [105](#), [107](#)
- [27] http://de.wikipedia.org/wiki/bilineare_filterung. [xvii](#), [122](#)
- [28] M.E. Fitzpatrick, A.T. Fry, P. Holdway, F.A. Kandil, J. Shackleton, and L. Suominen. A national measurement good practice guide no. 52: Determination of residual stresses by x-ray diffraction - issue 2, 2005. [xix](#), [157](#), [158](#)
- [29] <http://de.wikipedia.org/wiki/eisen-kohlenstoff-diagramm>. [xix](#), [159](#)

- [30] *ASM Handbook Volume 19 : Fatigue and Fracture*. ASM International, 1996. xxii, xxvi, 8, 9, 24, 26, 27, 197, 213, 214, 282
- [31] H. Bueckner. A novel principle for the computation of stress intensity factors. *ZAMM*, 50(9):529–545, 1970. xxiii, 227, 228
- [32] H.P. Gänser. Beurteilung der Betriebsfestigkeit eines Konverter-Links. 2010. xxiii, 227, 228
- [33] P. Raninger. Numerical studies on crack arrays in aluminum pressure die casting molds. Master's thesis, Montanuniversitaet Leoben, 2009. xxiv, 32, 34, 186, 244, 246, 247
- [34] P. Raninger, W. Ecker, T. Antretter, M. Leindl, and R. Ebner. Interaction of heat checks in aluminum pressure casting dies and their effect on fatigue life. *Key Engineering Materials*, 488-489:626–629, 2012. xxiv, 8, 186, 244, 246
- [35] ASTM. Standard test method for linear-elastic plane-strain fracture toughness K_{Ic} of metallic materials. *ASTM International, West Conshohocken, PA*, ASTM Standard E 399 – 09. xxvi, 35, 278, 279, 283
- [36] T. L. Anderson. *Fracture Mechanics: Fundamentals and Applications*. CRC Press, 3 edition edition, 2005. xxvi, 126, 226, 227, 278, 281, 282, 283, 285, 287
- [37] Richard W. Hertzberg, Richard P. Vinci, and Jason L. Hertzberg. *Deformation and Fracture Mechanics of Engineering Materials*. Wiley, 5 edition, 4 2012. xxvi, 23, 36, 37, 40, 280, 282, 285, 286, 287
- [38] ASTM. Standard test method for measurement of fracture toughness. *ASTM International, West Conshohocken, PA*, ASTM Standard E 1820 – 08. xxvi, 286, 287
- [39] O. Kolednik. pers. comm. Erich Schmid Institute of Materials Science, Leoben, Austria. xxvi, 280, 283, 287
- [40] *Bruchmechanischer Festigkeitsnachweis*. Forschungskuratorium Maschinenbau (FKM), 2009. xxvi, 228, 314
- [41] Jean Lemaitre, editor. *Handbook of Materials Behavior Models, Three-Volume Set: Nonlinear Models and Properties[C]*. Academic Pr Inc, 11 2001. xxvii, 59
- [42] Holm Altenbach and Jacek J. Skrzypek, editors. *Creep and Damage in Materials and Structures (CISM International Centre for Mechanical Sciences)*. Springer, 1 edition, 12 1999. xxvii, 72, 73
- [43] R.K. Penny and D.L. Marriott. *Design for Creep*. Springer, 2nd ed. 1995. softcover reprint of the original 2nd ed. 1995 edition, 10 2012. xxvii, 72, 73, 75, 293
- [44] J. Schemmel. *Beschreibung des Verformungs-, Festigkeits- und Versagensverhaltens von Komponenten im Kriechbereich unter instationärer Beanspruchung mit einem elastisch-viskoplastischen Werkstoffmodell*. PhD thesis, Materialprüfungsanstalt Universität Stuttgart, 2003. xxvii, 72
- [45] *Abaqus V6.13 Theory Manual*. xxvii, 31, 74, 193, 195, 196, 226

REFERENCES

- [46] E. Kaschnitz, P. Hofer, and W. Funk. Thermophysical properties of a hot-work tool-steel with high thermal conductivity. *International Journal of Thermophysics*, 34(5):843–850, 2013. xxvii, 197
- [47] <http://www.ogi.at/de/index.php>. xxvii, 197
- [48] Eberhard Klingbeil. *Tensorrechnung für Ingenieure (VDI-Buch)*. Springer, 1., aufl. edition, 1966. xxviii, 289
- [49] Bert Breuer and Karlheinz H. Bill, editors. *Bremsenhandbuch: Grundlagen, Komponenten, Systeme, Fahrdynamik (ATZ/MTZ-Fachbuch)*. Vieweg+Teubner Verlag, 3., vollst. überarb. u. erw. aufl. 2006 edition, 9 2006. 1, 2, 4, 21
- [50] W. Schlosser and S. Aurich. Modern brake systems for rail vehicles [moderne bremsysteme für schienenfahrzeuge]. *ZEV-Zeitschrift für Eisenbahnwesen und Verkehrstechnik - Journal for Railway and Transport*, 125(8):273–277, 2001. 2, 3
- [51] S. Sarip, A.J. Day, P. Olley, and H.S. Qi. Evaluation of a lightweight friction brake disc design for a regenerative braking system. In *6th European Conference on Braking, JEF 2010, Lille, France*, 2010. 2, 4
- [52] M. Tirovic. Development of a wheel mounted disc brake for a high-speed train. *Proceedings of the Institution of Mechanical Engineers, Part F: Journal of Rail and Rapid Transit*, 212(2):113–121, 1998. 3, 4
- [53] S. Teimourimanesh, R. Lundén, and T. Vernersson. Tread braking of railway wheels - state-of-the-art survey. In *6th European Conference on Braking, JEF 2010, Lille, France*, 2010. 4
- [54] M. Tirovic and A.J. Day. Disc brake interface pressure distributions. *Proceedings of the Institution of Mechanical Engineers, Part D: Journal of Automobile Engineering*, 205(2):137–146, 1991. 5
- [55] A.J. Day, M. Tirovic, and T.P. Newcomb. Thermal effects and pressure distributions in brakes. *Proceedings of the Institution of Mechanical Engineers, Part D: Journal of Automobile Engineering*, 205(3):199–206, 1991. 5
- [56] J.R. Barber. Thermoelastic instabilities in the sliding of conforming solids. *Wear*, 15(4):296 – 296, 1970. 5
- [57] Kwangjin Lee and J.R. Barber. Frictionally excited thermoelastic instability in automotive disk brakes. *Journal of Tribology*, 115(4):607–614, 1993. 5, 144, 192
- [58] Kwangjin Lee and J.R. Barber. An experimental investigation of frictionally-excited thermoelastic instability in automotive disk brakes under a drag brake application. *Journal of Tribology*, 116(3):409–414, 1994. 5
- [59] S. Panier, P. Dufrenoy, J.F. Brunel, and D. Weichert. Progressive waviness distortion: A new approach of hot spotting in disc brakes. *Journal of Thermal Stresses*, 28(1):47–62, 2005. 5, 13, 143, 192, 200, 201, 202

- [60] A.L. Christol, Y. Desplanques, W. Österle, and Degallaix G. Coupling between thermal localisation and friction mechanism: heat accumulation effect. In *6th european conference on braking JEF 2010*, 2010. 6
- [61] A. E. Anderson and R. A. Knapp. Hot spotting in automotive friction systems. *Wear*, 135(2):319 – 337, 1990. 6
- [62] H. Kasem, J.F. Brunel, P. Dufrénoy, M. Siroux, and B. Desmet. Thermal levels and subsurface damage induced by the occurrence of hot spots during high-energy braking. *Wear*, 270(5-6):355 – 364, 2011. 6, 13, 188
- [63] Claude Bathias. *Fatigue of Materials and Structures: Application to Design (Iste)*. John Wiley & Sons, 1. auflage edition, 1 2011. 6
- [64] W. Ecker, M. Leindl, T. Antretter, E. Ebner, I. Siller, and S. Nissle. Effect of material properties on the thermo-mechanical loading and damage of pressure casting dies—a numerical study. In *Tool Steels—Deciding Factor in Worldwide Production. Proceedings of the 8th International Tooling Conference. Aachen*, 2009. 8
- [65] P. Raninger, S. Marsoner, W. Ecker, R. Ebner, and T. Antretter. Characterization of damage at the friction surface of wheel mounted brake disks for railway applications. In *EuroBrake 2012*, 2012. 8, 153, 162, 169, 173, 177
- [66] Robert Minichmayr, Martin Riedler, Gerhard Winter, Heinz Leitner, and Wilfried Eichlseder. Thermo-mechanical fatigue life assessment of aluminium components using the damage rate model of Sehitoglu. *International Journal of Fatigue*, 30(2):298 – 304, 2008. 8
- [67] M Riedler, H Leitner, B Prillhofer, G Winter, and W Eichlseder. Lifetime simulation of thermo-mechanically loaded components. *Meccanica*, 42(1):47–59, 2007. 8
- [68] R.J. Lancaster, M.T. Whittaker, and S.J. Williams. A review of thermo-mechanical fatigue behaviour in polycrystalline nickel superalloys for turbine disc applications. *Materials at High Temperatures*, 30(1):2–12, 2013. 8
- [69] M. Riedler. *Simulation der Lebensdauer von Bauteilen unter thermomechanischer Ermüdungsbeanspruchung*. PhD thesis, Montanuniversitaet Leoben, Department of Product Engineering, Chair of Mechanical Engineering, Leoben, Austria, 2005. 9, 91, 213, 216
- [70] R. Minichmayr. *Modellierung und Simulation des thermomechanischen Ermüdungsverhaltens von Aluminiumbauteilen*. PhD thesis, Montanuniversitaet Leoben, Department of Product Engineering, Chair of Mechanical Engineering, Leoben, Austria, 2005. 9, 89, 97, 213
- [71] R.W. Neu and H. Sehitoglu. Thermomechanical fatigue, oxidation, and creep: Part i. damage mechanisms. *Metallurgical Transactions A*, 20(9):1755–1767, 1989. 9, 102, 213
- [72] R.W. Neu and H. Sehitoglu. Thermomechanical fatigue, oxidation, and creep: Part ii. life prediction. *Metallurgical Transactions A*, 20(9):1769–1783, 1989. 9, 102

REFERENCES

- [73] P. Dufrenoy, H. Kasem, P. Wicker, P. Degallaix, and W. d'Hardivilliers. Quantitative identification of brake disc cracking parameters: hot spots, pad type, disc material. In *6th european conference on braking JEF 2010*, 2010. 9, 13, 188, 200, 201, 202
- [74] M. Fortin. Vorgehensweise zur implementierung von werkstoffmodellen in die lebensdauerbewertung von thermo-mechanisch beanspruchten komponenten. Master's thesis, Montanuniversitaet Leoben, Department of Product Engineering, Chair of Mechanical Engineering, Leoben, Austria, 2009. 10
- [75] Guenter Gottstein. *Physikalische Grundlagen der Materialkunde*. Springer, 3. aufl. 2007 edition, 6 2007. 10
- [76] Dominique Francois. *Mechanical Behaviour of Materials: Volume II: Viscoplasticity, Damage, Fracture and Contact Mechanics (Solid Mechanics and Its Applications)*. Springer Netherlands, 1998 edition, 12 2009. 12
- [77] M. Siroux, A.-L. Cristol-Bulthé, Y. Desplanques, B. Desmet, and G. Degallaix. Thermal analysis of periodic sliding contact on a braking tribometer. *Applied Thermal Engineering*, 28(17-18):2194–2202, 2008. 13
- [78] A.-L. Cristol-Bulthé, Y. Desplanques, and G. Degallaix. Coupling between friction physical mechanisms and transient thermal phenomena involved in pad-disc contact during railway braking. *Wear*, 263(7-12):1230 – 1242, 2007. 13, 214
- [79] Yannick Desplanques, Olivier Roussette, Gerard Degallaix, Reynald Copin, and Yves Berthier. Analysis of tribological behaviour of pad-disc contact in railway braking. part 1. laboratory test development, compromises between actual and simulated tribological triplets. *Wear*, 262(5-6):582 – 591, 2007. 13, 111, 148
- [80] S. Panier, P. Dufrenoy, and D. Weichert. An experimental investigation of hot spots in railway disc brakes. *Wear*, 256(7-8):764 – 773, 2004. 13, 147
- [81] Y. Desplanques, A.-L.-Bulthé, G. Degallaix, L. Sabatier, and J. Bertheau. Transient aspects of local physical mechanisms induced by friction in braking. In *Proceedings of the 5th European Conference on Braking (JEF 2006)*, page 89–97, Lille, France, GRRT (ed.) 20, rue Elisee Reclus-B.P.317 59666 Villeneuve d' AscQ CEDEX-France, 2006. 13
- [82] P. Dufrénoy, G. Bodovillé, and G. Degallaix. Damage mechanisms and thermomechanical loading of brake discs. In L. Rémy and J. Petit, editors, *Temperature-fatigue Interaction, International Conference on Temperature-Fatigue Interaction, Ninth International Spring Meeting*, volume 29 of *European Structural Integrity Society*, pages 167 – 176. Elsevier, 2002. 13
- [83] P. Dufrénoy, P. Wicker, G. Degallaix, and W. D'Hardivilliers. Thermal fatigue criticality of railway brake discs. pages 139–146, 2009. 13, 192

- [84] Haruo SAKAMOTO and Kenji HIRAKAWA. Fracture analysis and material improvement of brake discs. *JSME International Journal Series A Solid Mechanics and Material Engineering*, 48(4):458–464, 2005. 13
- [85] P. Dufrenoy. Two-/three-dimensional hybrid model of the thermomechanical behaviour of disc brakes. *Proceedings of the Institution of Mechanical Engineers, Part F: Journal of Rail and Rapid Transit*, 218(1):17–30, 2004. 13, 192
- [86] C.H. Gao, J.M. Huang, X.Z. Lin, and X.S. Tang. Stress analysis of thermal fatigue fracture of brake disks based on thermomechanical coupling. *Journal of Tribology*, 129(3):536–543, 2007. 13
- [87] A. Langmann. Dynamometer test report, high speed days 2010. Technical report, FaiveleyTransport Witten GmbH, 2010. 21
- [88] Z.S. Basinski and S.J. Basinski. Fundamental aspects of low amplitude cyclic deformation in face-centred cubic crystals. *Progress in Materials Science*, 36(1):89–148, 1992. 24
- [89] Michael D. Sangid. The physics of fatigue crack initiation. *International Journal of Fatigue*, 57(0):58–72, 2013. 26
- [90] Michael D. Sangid, Hans J. Maier, and Huseyin Sehitoglu. A physically based fatigue model for prediction of crack initiation from persistent slip bands in polycrystals. *Acta Materialia*, 59(1):328–341, 2011. 27
- [91] A. Weidner, R. Beyer, C. Blochwitz, C. Holste, A. Schwab, and W. Tirschler. Slip activity of persistent slip bands in polycrystalline nickel. *Materials Science and Engineering: A*, 435–436(0):540–546, 2006. 27
- [92] F.O. Riemelmoser and R. Pippan. Consideration of the mechanical behaviour of small fatigue cracks. *International Journal of Fracture*, 118(3):251–270, 2002. 28
- [93] M.H. El Haddad, T.H. Topper, and K.N. Smith. Prediction of non propagating cracks. *Engineering Fracture Mechanics*, 11(3):573–584, 1979. 29
- [94] Mirco D. Chapetti. Application of a threshold curve model to high-cycle fatigue behavior of small cracks induced by foreign-object damage in ti-6al-4v. *International Journal of Fatigue*, 27(5):493–501, 2005. 29
- [95] B. Tabernig and R. Pippan. Determination of the length dependence of the threshold for fatigue crack propagation. *Engineering Fracture Mechanics*, 69(8):899–907, 2002. 31, 32, 33
- [96] O. E. Wheeler. Spectrum loading and crack growth. *J Basic Eng Trans ASME*, 94 Ser D(1):181–186, 1972. 32
- [97] J. Schijve. Fatigue of structures and materials in the 20th century and the state of the art. *International Journal of Fatigue*, 25(8):679–702, 2003. 34

REFERENCES

- [98] M. Leindl. *Untersuchung des Risswachstums in einem Druckgießwerkzeug mit Hilfe der Finite-Elemente-Methode*. PhD thesis, Montanuniversitaet Leoben, 2008. 34
- [99] Josef Cadek. *Creep in Metallic Materials*. Academia Prague/Elsevier Science Publishers, 1988. 38, 81
- [100] Harold J. Frost and Michael F. Ashby. *Deformation-Mechanism Maps: The Plasticity and Creep of Metals and Ceramics*. Pergamon Press, 10 1982. 39, 42
- [101] Michael E. Kassner. *Fundamentals of Creep in Metals and Alloys*. Elsevier Science, 2 edition, 2 2009. 40, 41
- [102] F.R.N. Nabarro. Do we have an acceptable model of power-law creep? *Materials Science and Engineering: A*, 387–389(0):659 – 664, 2004. 40
- [103] Werner Schatt and Hartmut Worch, editors. *Werkstoffwissenschaft*. Wiley-VCH, 9th edition, 7 2003. 41
- [104] Holm Altenbach. *Kontinuumsmechanik: Einführung in die materialunabhängigen und materialabhängigen Gleichungen*. Springer, 2. aufl. 2012 edition, 8 2012. 48, 52, 71, 293
- [105] Dietmar Gross, Werner Hauger, and Peter Wriggers. *Technische Mechanik 4: Hydromechanik, Elemente der Höheren Mechanik, Numerische Methoden: Band 4: Hydromechanik, Elemente der Höheren Mechanik, Numerische Methoden (Springer-Lehrbuch)*. Springer, 6 edition, 1 2007. 48
- [106] Dietmar Gross. *Bruchmechanik: Mit einer Einführung in die Mikromechanik (German Edition)*. Springer, 4., bearb. aufl. edition, 11 2006. 48, 65, 228, 285
- [107] Miguel J. Bagajewicz and Han-Chin Wu. *Continuum Mechanics and Plasticity (CRC Series–Modern Mechanics and Mathematics)*. Chapman & Hall, 12 2004. 48
- [108] A. Acharya and T.G. Shawki. The clausius-duhem inequality and the structure of rate-independent plasticity. *International Journal of Plasticity*, 12(2):229 – 238, 1996. 51
- [109] T. H. Hyde, editor. *Creep of Materials and Structures*. Wiley, 1 edition, 3 1994. 51, 84
- [110] J. L. Chaboche. Constitutive equations for cyclic plasticity and cyclic viscoplasticity. *International Journal of Plasticity*, 5(3):247 – 302, 1989. 51, 58, 63, 64, 85, 86, 87, 204
- [111] Wilhelm Rust. *Nichtlineare Finite-Elemente-Berechnungen: Kontakt, Geometrie, Material*. Vieweg+Teubner Verlag, 2., überarb. + erw. aufl. 2011 edition, 4 2011. 53, 81
- [112] <http://www.continuummechanics.org/cm/hookeslaw.html>. 58
- [113] J.L. Chaboche. A review of some plasticity and viscoplasticity constitutive theories. *International Journal of Plasticity*, 24(10):1642 – 1693, 2008. 58, 63, 64, 85, 87, 204
- [114] J.-L. Chaboche. Thermodynamic formulation of constitutive equations and application to the viscoplasticity and viscoelasticity of metals and polymers. *International Journal of Solids and Structures*, 34(18):2239–2252, 1997. 58, 87, 204, 290

- [115] Fabien Szmytka, Luc Rémy, Habibou Maitournam, Alain Köster, and Myriam Bourgeois. New flow rules in elasto-viscoplastic constitutive models for spheroidal graphite cast-iron. *International Journal of Plasticity*, 26(6):905 – 924, 2010. 65, 87
- [116] Jacob Lubliner. *Plasticity Theory*. Dover Publications, 2006. 65, 66, 67
- [117] Joachim Rösler, Harald Harders, and Martin Bäker. *Mechanisches Verhalten der Werkstoffe*. Springer Vieweg, 4. aufl. 2012 edition, 9 2012. 66
- [118] *Abaqus V6.13 Subroutines Manual*. 69
- [119] F. Szmytka, M.H. Maitournam, and L. Rémy. An implicit integration procedure for an elasto-viscoplastic model and its application to thermomechanical fatigue design of automotive parts. *Computers and Structures*, 2013. 70
- [120] E.G. Miravete. *Classical and computational solid mechanics for materials engineers*, 2005. 71
- [121] Josef Betten. *Creep Mechanics*. Springer, 2nd ed. edition, 3 2005. 73, 78
- [122] Ansys® academic research, release 15.0, help system, 3.5.5. creep, ansys, inc. 74
- [123] Gijsbertus de With. *Structure, Deformation, and Integrity of Materials (2 Volumes)*. Wiley-VCH, 1 edition, 3 2006. 78
- [124] Jean Lemaitre. *A Course on Damage Mechanics*. Springer, 2nd rev. and enlarged ed. edition, 6 1996. 85, 97, 212
- [125] Martin Becker and Hans-Peter Hackenberg. A constitutive model for rate dependent and rate independent inelasticity. application to {IN718}. *International Journal of Plasticity*, 27(4):596 – 619, 2011. 87
- [126] S. Issler. *Entwicklung eines Verfahrens zur Lebensdauervorhersage für Schaufel-Scheibe-Verbindungen bei Gasturbinen*. PhD thesis, Materialprüfungsanstalt (MPA) Universität Stuttgart, 2002. 89, 100
- [127] S. Tabibian, E. Charkaluk, A. Constantinescu, F. Szmytka, and A. Oudin. Tmf criteria for lost foam casting aluminum alloys. *Fatigue and Fracture of Engineering Materials and Structures*, 36(4):349–360, 2013. 89, 91
- [128] KN SMITH, P WATSON, and TH TOPPER. Stress-strain function for the fatigue of metals. *J Mater*, 5(4):767–778, 1970. 91, 216
- [129] W.J. Ostergren. Damage function and associated failure equations for predicting hold time and frequency effects in elevated temperature, low cycle fatigue. *Journal of Testing and Evaluation*, 4(5):327–339, 1976. 91, 216
- [130] G. Winter. *Thermomechanische Ermüdung des Gusseisenwerkstoffes GJV450*. PhD thesis, Montanuniversitaet Leoben, Department of Product Engineering, Chair of Mechanical Engineering, Leoben, Austria, 2008. 97, 216, 218, 268

REFERENCES

- [131] Wolfgang Bleck, editor. *Werkstoffprüfung in Studium und Praxis*. Mainz, G, 15., überarb. aufl. edition, 2011. [98](#)
- [132] J. Colin. *Deformation history and load sequence effects on cumulative fatigue damage*. PhD thesis, The University of Toledo, College of Engineering, 2009. [99](#)
- [133] J. Colin and A. Fatemi. Variable amplitude cyclic deformation and fatigue behaviour of stainless steel 304l including step, periodic, and random loadings. *Fatigue and Fracture of Engineering Materials and Structures*, 33(4):205–220, 2010. [99](#)
- [134] S.S. Manson, G.R. Halford, and M.H. Hirschberg. Creep-fatigue analysis by strain-range partitioning. pages 12–24, 1971. [101](#), [102](#)
- [135] S. S. Manson and G. R. Halford. *Fatigue & Durability of Metals at High Temperatures*. ASM International, 9 2009. [101](#)
- [136] P. Raninger and W. Ecker. Internal mcl report on material modeling and parameter identification. [103](#)
- [137] G. Gaussorgues and S. Chomet. *Infrared Thermography (Microwave and RF Techniques and Applications)*. Springer, 1994 edition, 12 1993. [105](#)
- [138] J. Schlichting. *Integrale Verfahren der aktiven Infrarotthermografie*. PhD thesis, Fakultät V - Verkehrs- und Maschinensysteme der Technischen Universität Berlin, 2012. [105](#)
- [139] T Astarita, G Cardone, G.M Carlomagno, and C Meola. A survey on infrared thermography for convective heat transfer measurements. *Optics & Laser Technology*, 32(7–8):593 – 610, 2000. [105](#)
- [140] H. Kasem, J. Thevenet, X. Boidin, M. Siroux, P. Dufrenoy, B. Desmet, and Y. Desplanques. An emissivity-corrected method for the accurate radiometric measurement of transient surface temperatures during braking. *Tribology International*, In Press, Corrected Proof:–, 2010. [105](#), [199](#)
- [141] Jean Thevenet, Monica Siroux, and Bernard Desmet. Measurements of brake disc surface temperature and emissivity by two-color pyrometry. *Applied Thermal Engineering*, 30(6-7):753 – 759, 2010. [105](#)
- [142] M. Siroux J. Thevenet and B. Desmet. Brake disc surface temperature measurement using a fiber optic two-color pyrometer. 2008. [105](#)
- [143] J. Wong. *Analyse de l'endommagement par fatigue thermique et modelisation du comportement thermomecanique de couples disques-garnitures de type TGV*. PhD thesis, Ecole Centrale de Lille, Laboratoire de Mécanique de Lille, 2007. [105](#)
- [144] Stephane Panier, Philippe Dufrenoy, and Pierre Bremond. Infrared characterization of thermal gradients on disc brakes. volume 5073, pages 295 – 302, Orlando, FL, United states, 2003. [105](#)
- [145] Y. Desplanques, G. Degallaix, R. Copin, and Y. Berthier. A tribometer for the study of materials under railway braking conditions. *Tribology Series*, 39:381–391, 2001. [111](#), [148](#)

- [146] T. Kaltenbrunner, P. Raninger, and P. O'Leary. Development of a Matlab routine for the processing and the analysis of thermal image data from test rig programs. 2014. 116
- [147] <http://www.mathworks.de>. 116, 117
- [148] John Canny. A computational approach to edge detection. *Pattern Analysis and Machine Intelligence, IEEE Transactions on*, PAMI-8(6):679–698, Nov 1986. 117
- [149] H. Kasem, P. Dufrénoy, and Y. Desplanques. Relationships between surface thermal gradients and disc distortion during stop-braking with high energy dissipation. *Tribology Letters*, 48(2):169–181, 2012. 144
- [150] Monson Hayes. *Schaums Outline of Digital Signal Processing, 2nd Edition (Schaum's Outline Series)*. McGraw-Hill, 2011. 155
- [151] Hwei Hsu. *Schaum's Outline of Signals and Systems, Second Edition (Schaum's Outline Series)*. McGraw-Hill, 2 edition, 8 2010. 156
- [152] M.E. Fitzpatrick and Alain Lodini, editors. *Analysis of Residual Stress by Diffraction using Neutron and Synchrotron Radiation*. CRC Press, 1 edition, 2 2003. 157
- [153] J. Orlich, A. Rose, and P. Wieast. *Atlas zur Wärmebehandlung der Stähle. Band 3: Zeit – Temperatur – Austenitisierung – Schaubilder*. Verlag Stahleisen mbH, Düsseldorf, 1973. 160
- [154] J.D. Fieldhouse and C.J. Bryant, D.and Talbot. Hot judder - an investigation of the thermo-elastic and thermo-plastic effects during braking. *SAE International Journal of Passenger Cars - Mechanical Systems*, 4(2):1086–1101, 2011. 167
- [155] K. Chladil and P. and Raninger. Gefügeanalyse von Bremsscheibenmaterial. 2013. 177
- [156] M. Graf and G.P. Ostermayer. Efficient computation of hot bands and hot spots. In *EuroBrake 2013*, 2013. 192
- [157] Gennadiy P. Nikishkov. *Programming Finite Elements in Java(TM)*. Springer, 2010. 199
- [158] *Z-mat Version 8.4.2*. 204
- [159] <https://www.python.org>. 210
- [160] <http://www.zset-software.com/products/z-opt>. 210
- [161] W Eichlseder and M Riedler. Course in thermo-mechanical fatigue, 2006. 214
- [162] G. Winter and B. Strohhäussl. Tmf untersuchungen an stahl- und gusseisenwerkstoffen. 2014. 215
- [163] R. Pippan. Lecture notes on "ausgewählte kapitel der festkörpermechanik", 2011. 281
- [164] ASTM. Standard test method for k-r curve determination. *ASTM International, West Conshohocken, PA*, ASTM Standard E 561 - 10e2. 282

REFERENCES

- [165] J. R. Rice. A path independent integral and the approximate analysis of strain concentration by notches and cracks. *Journal of Applied Mechanics*, 35:379–386, 1968. [284](#)
- [166] O.a Kolednik, R.b c Schöngrundner, and F.D.c Fischer. A new view on j-integrals in elastic-plastic materials. *International Journal of Fracture*, pages 1–31, 2014. [285](#), [287](#)

<